LA DIVERSITÉ D'ENSO ET LE CHANGEMENT CLIMATIQUE

Aude Carreric

Université Fédérale
Toulouse Midi-Pyrénées

THÈSE

En vue de l'obtention du

DOCTORAT DE L'UNIVERSITÉ DE TOULOUSE

Délivré par l'Université Toulouse 3 - Paul Sabatier

Présentée et soutenue par

Aude CARRERIC

Le 5 juin 2019

La diversité d'ENSO et le changement climatique

Ecole doctorale : **SDU2E - Sciences de l'Univers, de l'Environnement et de l'Espace**

Spécialité : **Océan, Atmosphère, Climat**

Unité de recherche :
LEGOS - Laboratoire d'Etudes en Géophysique et Océanographie Spatiale

Thèse dirigée par
BORIS DEWITTE et Virginie Guemas

Jury

Mme Dacha GUSHCHINA, Rapporteure
Mme Maria BELéN RODRIGUEZ FONSECA, Rapporteure
M. Jérôme VIALARD, Rapporteur
Mme Myriam KHODRI, Examinatrice
M. Julien BOUCHAREL, Examinateur
M. Nick HALL, Examinateur
M. Boris DEWITTE, Directeur de thèse
Mme Virginie GUéMAS, Co-directrice de thèse

Résumé

ENSO, pour El Niño-Southern Oscillation, est le mode de variabilité dominant du système climatique à l'échelle inter-annuelle. C'est un phénomène couplé océan-atmosphère qui se produit dans le Pacifique tropical tous les 2 à 7 ans. Composé d'alternance d'événements chauds, El Niño, et d'événements froids, La Niña, cette oscillation naturelle entraîne de fortes déstabilisations du système météorologique qui s'étendent bien au-delà du bassin Pacifique par le biais de téléconnexions atmosphériques. En modifiant la circulation globale atmosphérique, ces événements impactent fortement les systèmes socio-économiques de nombreuses régions du monde.

ENSO se définit par rapport à l'état moyen du Pacifique tropical, qui est soumis au réchauffement climatique. Ainsi, en plus d'un réchauffement des eaux de surface plus rapide dans le Pacifique oriental que dans les régions alentours, une augmentation de la stratification moyenne est projetée dans le Pacifique tropical, tendance déjà observée dans le Pacifique central sur les 50 dernières années. Ces changements de stratification dans l'océan peuvent, d'un point de vue théorique, conduire à des modifications significatives des caractéristiques d'ENSO.

ENSO est donc susceptible d'être modifié avec le réchauffement climatique. Compte tenu de ses conséquences socio-économiques, et pour pouvoir atténuer ses dommages potentiels, il est important de mieux le comprendre afin de prévoir son évolution avec le réchauffement climatique. Or à l'heure actuelle, il reste encore beaucoup d'incertitudes sur la réponse d'ENSO au réchauffement climatique. Ceci tient en partie aux biais des modèles couplés de climat dans les régions clefs du Pacifique tropical pour ENSO, c'est-à-dire la région occidentale de la piscine d'eau chaude ("Warm Pool") et la région orientale ("Cold Tongue").

De plus, ENSO exhibe une grande diversité, en termes d'amplitude, de fréquence et de structures spatiales, en particulier entre les événements chauds El Niño. Cette diversité des événements El Niño peut se caractériser en particulier par deux régimes de variabilité statistiquement indépendants mais liés entre eux par la non-linéarité du système couplé du Pacifique tropical. L'existence de ces deux régimes invite à prendre avec précaution les résultats des études qui ne les discriminent pas.

Dans ce travail de thèse, nous nous sommes intéressés à la relation entre la diversité d'ENSO, en particulier des événements chauds El Niño, et l'état moyen du Pacifique tropical, qui va donc être modifié par le réchauffement climatique.

En premier lieu, nous avons cherché à réévaluer les caractérisations de la diversité des événements El Niño. Mieux comprendre cette diversité est primordiale car les impacts météorologiques diffèrent en fonction des types d'événements. Nous avons pour cela utilisé le modèle de climat couplé CESM-LE, qui fournit une simulation de longue durée (1801 ans) sans forçage anthropique ainsi qu'un grand ensemble de réalisations (40 à 42 simulations) du climat historique (1920-2005) et futur (2006-2100) sous l'hypothèse du scénario RCP8.5 d'émission soutenue de gaz à effet de serre. Nous avons ensuite analysé le changement des statistiques de la diversité d'ENSO avec le réchauffement climatique. En particulier, nous montrons que les événements El Niño forts, qui présentent un réchauffement important dans le Pacifique oriental, voient leur pic d'anomalies en températures de surface être décalé de l'hiver au début du printemps (Février-Mars-Avril, FMA). Cette analyse a été mise en perspective avec les résultats récents qui montrent que les événements El Niño extrêmes en précipitation

dans le Pacifique oriental doubleront d'ici 2100 d'après la génération actuelle des modèles de climat. En effet, cette période FMA est naturellement propice à provoquer des précipitations du fait de la position climatologique de la zone de convergence inter-tropicale (ITCZ), qui se trouve la plus au sud à cette saison. Le fort couplage saisonnier entre les anomalies chaudes de températures de surface des événements El Niño qui culminent en FMA et l'ITCZ explique ainsi un quart de l'augmentation des événements El Niño extrêmes en précipitation.

Enfin, les processus océaniques pouvant être associés à cette plus forte persistance des évènements EP El Niño et au décalage temporel de leur pic de réchauffement ont été diagnostiqués. Nous proposons l'hypothèse selon laquelle ces changements proviennent d'un processus de recharge plus important et d'une rétroaction de la thermocline plus efficace dans le Pacifique oriental, du fait d'une augmentation de la stratification verticale du Pacifique équatorial dans un climat plus chaud, tel que simulé par CESM-LE.

Mots clés : Oscillation australe El Niño, Changement climatique, Large Ensemble CESM, Variabilité décennale, El Niño extrêmes.

Abstract

El Niño-Southern Oscillation (ENSO) is the dominant mode of variability in the tropical Pacific on inter-annual scale. This phenomenon, alternating warm events, called El Niño, and cold events, called La Niña, affects weather events, ecosystems, agriculture and fisheries worldwide via atmospheric and oceanic teleconnections. Given the socio-economic and meteorological impacts that ENSO can cause, projecting its evolution with climate change presents strong challenges.

There are still many uncertainties about the evolution of ENSO in the context of global warming. This is partly due to biases of Coupled General Circulation Models (CGCMs) in ENSO key areas of the tropical Pacific, i.e. the western tropical Pacific ("Warm Pool" region) and the eastern tropical Pacific ("Cold Tongue" region). In addition to a faster warming of surface waters in the eastern Pacific than in the surrounding regions, global warming will lead to an increase in the equatorial Pacific mean stratification, a trend observed in the central Pacific over the past 50 years. From a theoretical point of view, these changes in ocean stratification can lead to significant modifications in the characteristics of ENSO.

ENSO exhibits an important diversity of amplitude and spatial patterns, especially between the warm El Niño events. This diversity of El Niño events is characterised in particular by two statistically independent variability regimes but linked together by the non-linearity of the coupled tropical Pacific system. The existence of these two regimes calls for caution in taking the results of studies that do not discriminate against them.

In this thesis, we focused on the changes in the statistics of El Niño's diversity and related changes in oceanic dynamics as a result of global warming.

We first assessed the characterisations of the diversity of El Niño in the CESM-Large Ensemble model. CESM-LE provides a long-term simulation (1801 years) without anthropogenic forcing, and multiple realisations of the climate (40 members) over the 1920-2100 period, with a combination of both natural and anthropogenic climate forcings. We analysed changes in ENSO diversity statistics (amplitude, seasonality) with global warming. This analysis has been put into perspective with recent results showing that ENSO-induced extreme precipitation events in the eastern Pacific will double by 2100. In particular, we show that the strong El Niño events, which show significant warming in the eastern Pacific, have their peak of sea surface temperature (SST) anomalies shifted fro winter to early spring (February-March-April, FMA). This FMA period is naturally conducive to precipitation due to the southernmost climatological position of the inter-tropical convergence zone (ITCZ). The strong seasonal coupling between the positive SST anomalies of the El Niño events that peak in FMA and the ITCZ thus explains one quarter of the increase in the frequency of extreme precipitation El Niño events in the future.

Finally, the oceanic processes that may be associated with a greater persistence of EP El Niño events and the time lag of their warming peaks have been diagnosed. We propose that these changes are due to a larger recharge process and a more effective thermocline feedback in the eastern Pacific, two characteristics related to the increase in vertical stratification of the equatorial Pacific.

Keywords: El Niño Southern Oscillation, Climate Change, CESM Large ensemble, Decadal Variability, extreme El Niño.

List of acronyms

AGCM	Atmospheric General Circulation Model
APE	Available Potential Energy
CAM	Community Atmosphere Model-
CCSM	Community Climate System Model
CESM-LE	Community Earth System Model-Large Ensemble
CGCM	Coupled General Circulation Model
CHI	Center of Heat Index
CMIP	Coupled Model Intercomparison Project
CNRS	Centre National de la Recherche Scientifique
COP	Conference of the Parties
CP	Central Pacific
CRW	Convectively-coupled Rossby Wave
CT	Cold Tongue
DJF	December-January-February
ELI	ENSO Longitude Index
EMI	El Niño Modoki Index
ENSO	El Niño Southern Oscillation
EOF	Empirical Orthogonal Function
ERSST	Extended Reconstructed Sea Surface Temperature
EP	Eastern Pacific
FMA	February-March-April
FFT	Fast Fourier Transform
GFDL	Geophysical Fluid Dynamics Laboratory
GHG	Greenhouse Gas
GIEC	Groupe d'experts intergouvernemental sur l'évolution du climat
GPCP	Global Precipitation Climatology Project

HadISST	Hadley Center for Climate Prediction and Research Sea Surface Temperature
IOD	Indian Ocean Dipole
IPCC	Intergovernmental Panel on Climate Change
ITCZ	Inter-Tropical Convergence Zone
JAS	July-August-September
LANL	Los Alamos National Laboratory
LWR	Long Wave Radiation
MJO	Madden-Julian Oscillation
NASA	National Aeronautics and Space Administration
NCAR	National Center for Atmospheric Research
NDH	Non-linear Dynamical Heating
NOAA	National Oceanic and Atmospheric Administration
NPMM	North Pacific Meridional Mode
NPO	North Pacific Oscillation
OLR	Outgoing Longwave Radiation
ONDJ	October-November-December-January
ONI	Oceanic Niño index
PC	Principal Component
PDO	Pacific Decadal Oscillation
PI	Pre-Industrial
PMM	Pacific Meridional Mode
POP	Parallel Ocean Program
QB	Quasi-Biennal
QQ	Quasi-Quadriennal
RCP	Representative Concentration Pathway
RD	Recharge-Discharge
RMSE	Root Mean Square Error
SFM	Seasonal Footprinting Mechanism
SLP	Sea Level Pressure
SODA	Simple Ocean Data Assimilation
SPCZ	South Pacific Convergence Zone
SPMM	South Pacific Meridional Mode

SSS	Sea Surface Salinity
SST	Sea Surface Temperature
SSTA	Sea Surface Temperature Anomalies
STC	Sub-Tropical Cells
SWR	Short Wave Radiation
TCF	Thermocline Feedback
TIW	Tropical Instability Wave
TNI	Trans-El Niño index
TOA	Top of the Atmosphere
TOGA	Tropical Ocean Global Atmosphere
TPDV	Tropical Pacific Decadal Variability
TPDO	Tropical Pacific Decadal Oscillation
WACCM	Whole Atmosphere Community Climate Model
WCRP	World Climate Research Programme
WES	Wind-Evaporation-Sea Surface Temperature
WMO	World Meteorological Organization
WP	Warm Pool
WWB	Westerly Wind Burst
WWV	Warm Water Volume
ZAF	Zonal Advective Feedback

Contents

Introduction générale

L'Oscillation Australe - El Niño, ou ENSO (l'acronyme anglais d'El Niño-Southern Oscillation), est le mode de variabilité dominant du Pacifique tropical à l'échelle inter-annuelle. Ce phénomène couplé océan-atmosphère, alternance d'événements chauds, El Niño, et d'événements froids, La Niña, entraîne de fortes déstabilisations du système météorologique, qui s'étendent bien au-delà du bassin Pacifique par le biais de téléconnexions atmosphériques. Ce déséquilibre de la circulation atmosphérique à l'échelle globale impacte fortement les systèmes socio-économiques de nombreuses régions. Parmi ses impacts, on peut citer une perturbation de la mousson, des sécheresses et des feux de forêts en Indonésie, en Inde et dans le nord-est de l'Australie pendant l'été précédant le pic de l'événement El Niño, une intensification de la formation de cyclones tropicaux dans le Pacifique nord-ouest, des inondations et des glissements de terrain pendant l'hiver en Équateur, au Pérou et dans le sud-ouest des États-Unis, une interruption des conditions favorables à la pêche industrielle aux anchois au large des côtes péruviennes et un blanchissement qui peut être dévastateur du corail du Pacifique tropical (Goddard and Dilley, 2005; McPhaden et al., 2006). A titre d'exemple, l'événement El Niño de 1997-98 a entraîné des coûts estimés à 33 milliards de dollars dans le monde. Compte tenu des répercussions sur les systèmes économiques d'agriculture et de pêche, sur les écosystèmes marins et terrestres, il est indispensable de mieux comprendre ce phénomène afin de mieux le prévoir et de pouvoir mettre en place des systèmes d'alerte et de réduction des vulnérabilités des sociétés touchées.

ENSO est une perturbation du cycle saisonnier du Pacifique tropical. En conditions normales, les températures de surface de la mer (SST pour Sea Surface Temperatures) dans l'ouest du Pacifique tropical sont les plus chaudes au monde (supérieure à 28 °C) alors que les SST dans le Pacifique oriental sont plus froides de 4–10 °C. Cette "piscine d'eaux chaudes" (ou "Warm Pool" en anglais) à l'ouest est maintenue par les alizés qui soufflent d'est en ouest le long de l'équateur. Au-dessus de ces SST chaudes, la convection atmosphérique profonde peut se développer, générant de fortes précipitations sur le continent maritime, l'ouest du Pacifique tropical et l'est de l'océan Indien. Dans le Pacifique est, les alizés entraînent une remontée d'eau froide plus profonde le long de la côte et de l'équateur, ce qui refroidit la surface et forme la "langue d'eau froide" (ou "Cold tongue" en anglais). Ce contraste de SST entre l'est et l'ouest, dû aux vents accélérés vers la convection profonde atmosphérique à l'ouest, entraîne une pression plus élevée à l'est qu'à l'ouest, ce qui renforce les alizés. L'état moyen du Pacifique tropical est ainsi maintenu par une boucle positive couplée océan-atmosphère, appelée rétroaction de Bjerknes (Bjerknes, 1969).

De faibles changements de l'état moyen du Pacifique tropical peuvent entraîner la croissance d'ENSO grâce à la rétroaction de Bjerknes. Pendant les événements El Niño, des anomalies positives de vents d'ouest dans le Pacifique équatorial occidental et central vont déclencher une onde de Kelvin chaude qui, en approfondissant la thermocline lors de son déplacement vers l'est, va entraîner le réchauffement des eaux de surface dans le Pacifique équatorial central et oriental. Ces anomalies positives de SST à l'est vont renforcer le relâchement des alizés, ce qui va continuer d'affaiblir l'upwelling des eaux froides à l'est, renforçant les anomalies chaudes de SST. La rétroaction de Bjerknes va alors être contrée par plusieurs rétroactions négatives, venant de l'ajustement dynamique lent de l'océan. Parmi les théories des rétroactions négatives retardées, l'oscillateur recharge-décharge (Jin, 1997a,b) est le paradigme le

plus largement accepté. L'ajustement lent de l'océan aux coups de vents d'ouest (aux alizés) a pour effet de décharger (recharger) le contenu en chaleur du Pacifique équatorial, ce qui met fin à l'événement El Niño (La Niña) et fait basculer dans la phase négative (positive) d'ENSO. L'océan joue ainsi le rôle de force compensatrice du système couplé instable océan-atmosphère. Cela procure le caractère déterministe de la dynamique d'ENSO, rendant possible sa prévision à 6-9 mois. Pendant les événements La Niña, la boucle inverse conduit à des SST en dessous de la normale dans le Pacifique équatorial central et oriental, renforcées par des alizés plus forts que la moyenne.

Cependant, ces théories oscillatoires sur lesquelles repose la vision cyclique auto-entretenue d'ENSO n'expliquent pas l'irrégularité de sa fréquence d'occurrence, l'asymétrie entre les événements chauds (El Niño) et froids (La Niña), ni la diversité des événements. En plus d'être plus forts en intensité, les événements El Niño exhibent en effet une diversité spatiale plus prononcée par rapport aux événements La Niña. L'intérêt grandissant pour la diversité des événements El Niño ces vingt dernières années a soulevé la question de leur définition, compte tenu de la multiplicité de leurs structures spatiales, de leurs amplitudes, de leurs évolutions temporelles ou encore de leurs impacts météorologiques. De nombreuses métriques (et dénominations) ont ainsi été proposées et il est maintenant reconnu qu'au moins deux degrés de libertés sont nécessaires pour décrire El Niño dans sa diversité. Suivant les méthodes utilisées, la diversité d'El Niño est mise en avant à travers ses structures spatiales (Trenberth and Stepaniak, 2001; Ashok et al., 2007; Kug et al., 2009; Kao and Yu, 2009; Yeh et al., 2009a; Ren and Jin, 2011), ou l'intensité de certaines de ses caractéristiques dont le réchauffement de l'océan de surface (Takahashi et al., 2011; Dommenget et al., 2013; Takahashi and Dewitte, 2016), ou les précipitations induites en particulier dans le Pacifique oriental (Cai et al., 2014, 2015a, 2017; Williams and Patricola, 2018).

Cette thèse s'inscrit dans ce contexte riche en études sur la diversité et la complexité d'ENSO (Timmermann et al., 2018). Un état de l'art des avancées sur cette problématique est décrit au chapitre 1 *"Background"*. La compréhension des processus physiques sous-jacents à la diversité spatiale, temporelle et d'amplitude est primordiale pour une meilleure prédictibilité d'ENSO, en particulier dans un contexte où ENSO est susceptible d'être modifié dans un climat plus chaud.

Le développement exponentiel des ressources numériques ces dernières décennies a permis d'améliorer la capacité des modèles couplés de climat global (CGCMs pour Coupled General Circulation Models) à simuler de manière réaliste la variabilité du climat et ENSO. Même si des biais persistent, en particulier dans la simulation de la diversité et de l'asymétrie d'ENSO, les modèles de climat sont des outils indispensables à l'amélioration de la compréhension de ce phénomène complexe couplé océan-atmosphère et à la projection des changements induits par le réchauffement climatique. Mes travaux de thèse se basent principalement sur les simulations du modèle couplé de climat issu du projet Community Earth System Models Large Ensemble (CESM-LE) développé par le National Center for Atmospheric Research (NCAR) (Kay et al., 2015). L'un des grands intérêts du projet CESM-LE est qu'il fournit différents types de simulations : une simulation longue durée (1801 ans) sans forçage anthropique, qui permet d'analyser la variabilité interne du système climatique simulé sans changement de forçage externe, et un grand ensemble de réalisations (40 à 42 simulations) du climat historique (1920-2005) et du climat futur (2006-2100) sous l'hypothèse du scénario RCP8.5 d'émission de gaz à effet de serre tel que définit par le Groupe d'experts intergouvernemental sur l'évolution du climat (GIEC). Ce modèle, ainsi que les jeux de données d'observation sont décrits au chapitre 2 *"Data and methods"*. Il y est également décrits les outils statistiques utilisés tout au long de cette thèse, ainsi que les hypothèses de calcul du bilan de chaleur effectué sur la grille native du modèle CESM-LE. L'évaluation de la simulation de la variabilité du Pacifique tropical et d'ENSO par CESM-LE est aussi présentée dans ce chapitre.

Le premier objectif de cette thèse sera de réévaluer les caractérisations de la diversité d'ENSO et plus particulièrement de sa phase positive El Niño dans le modèle couplé de climat CESM-LE. Quels sont les indices qui caractérisent le mieux la diversité d'ENSO ? Sont-ils statistiquement robustes pour différents jeux de données d'observations ou de simulations de modèles couplés de climat ? Pour répondre à ces questions, nous nous sommes plus particulièrement intéressés à deux approches distinctes et couramment utilisées. La première méthode consiste à distinguer les événements El Niño par leurs structures spatiales dans les régions historiques Niño-3 (5°S-5°N, 210°E-270°E) et Niño-4 (5°S-5°N, 160°E-210°E) qui mesurent la variabilité associée au Pacifique central et oriental respectivement. Deux types d'événements El Niño sont ainsi classifiés, les événements "Central Pacific" (CP) et les événements "Eastern Pacific" (EP) (Kug et al., 2009). La seconde méthode distingue les événements El Niño par l'intensité de leur réchauffement dans le Pacifique oriental en utilisant les modes de variabilité principaux du Pacifique tropical dans toute sa largeur. Elle définit les événements "forts" et les événements "modérés", qui ont par définition une signature de réchauffement des eaux de surface moins marquée dans le Pacifique oriental. Un des intérêts de cette méthode est qu'elle permet de ne pas être contraint d'analyser les événements chauds à partir de leur structure spatiale pendant leur pic hivernal. Elle permet à l'inverse de couvrir l'ensemble de leur évolution spatio-temporelle dans une large région de forte variabilité du Pacifique est. Cette analyse comparative fait l'objet du chapitre 3 *"Characterising ENSO diversity"*.

Les asymétries d'ENSO, qu'elles soient mesurées entre les événements chauds El Niño et froids La Niña ou entre les événements chauds entre eux, sous-tendent la notion de processus non-linéaires intervenant dans les mécanismes d'ENSO. Parmi les sources de ces non-linéarités, on peut citer la convection profonde atmosphérique et les processus océaniques d'advection de chaleur. Plusieurs études ont suggéré que les processus océaniques non-linéaires étaient liés à la variabilité décennale du Pacifique tropical et à la modulation basse-fréquence d'ENSO lui-même (Rodgers et al., 2004). Ainsi, la modulation basse-fréquence d'ENSO pourrait produire des rectifications non-linéaires de la variabilité basse-fréquence du Pacifique tropical via ses asymétries. A l'inverse, certaines périodes caractérisées par des états moyens spécifiques du Pacifique tropical semblent favoriser un certain régime d'El Niño comme on a pu le constater ces dernières décennies avec un regain de la fréquence d'occurrence des événements CP El Niño. L'état moyen du Pacifique tropical influence-t-il les différents régimes des événements El Niño ? Est-ce que cette diversité rectifie en retour l'état moyen ? **Le second objectif de cette thèse sera de diagnostiquer la variabilité interne de la diversité d'ENSO et ses rétroactions sur l'état moyen dans le modèle CESM-LE.** Ces questions seront appliquées au modèle de climat CESM-LE et les résultats seront comparés à des résultats existants établis avec d'autres modèles de climat. Ces résultats sont présentés au chapitre 4 *"Low-frequency modulation of ENSO diversity"*.

Enfin, le chapitre 5 *"ENSO diversity and global warming"* est consacré à l'impact du réchauffement climatique sur ENSO, et en particulier sur les événements El Niño forts. Les modèles couplés de climat projettent des changements significatifs de l'état moyen du Pacifique tropical, dont certains avec un forts consensus entre les modèles. Ainsi, la Circulation de Walker, circulation zonale à l'échelle de l'océan Pacifique, est susceptible de s'affaiblir (Vecchi and Soden, 2007), ce qui va diminuer la puissance des alizés et altérer la structure thermique et les courants moyens du Pacifique tropical (DiNezio et al., 2009; Santoso et al., 2013). L'augmentation projetée de la stratification verticale de l'océan tropical peut conduire à d'importants changements dans les caractéristiques d'ENSO par l'impact qu'elle peut avoir sur la rétroaction de la thermocline, en particulier dans le Pacifique est (An and Jin, 2001; Dewitte, 2000). Cependant, les modèles couplés de climat présentent une forte dispersion de la projection de l'amplitude d'ENSO dans un climat plus chaud (Bellenger et al., 2014; Chen et al., 2017a). D'un autre côté, il a été montré que le nombre d'événements El Niño

extremes, c'est à dire qui sont accompagnés d'une forte signature en précipitation anormale dans l'est du Pacifique, est susceptible d'augmenter en situation future (Cai et al., 2014). Cette augmentation de fréquence est liée à l'augmentation des températures de surface de l'océan, plus rapide dans le Pacifique est, réduisant le gradient méridional de la SST et facilitant ainsi le déplacement vers le sud de l'ITCZ. Cependant, les mécanismes associés à ENSO lors de ce déplacement facilité de l'ITCZ restent peu clairs. Quels sont les changements de statistiques de la diversité d'ENSO avec le réchauffement climatique ? Comment concilier les deux résultats émanant des modèles couplés de climat qui paraissent contradictoires avec, d'un côté, une absence de consensus sur les changements de variabilité du Pacifique tropical oriental et, de l'autre côté, une augmentation significative du nombre d'événement extrême en précipitation induite par El Niño dans le Pacifique oriental ? Quels sont les (changements de) processus fondamentaux qui gouvernent les changements de diversité d'ENSO dans un climat plus chaud ? **Le troisième objectif de cette thèse sera de diagnostiquer les changements projetés de statistiques associés à la diversité d'ENSO lorsqu'elle est définie par son intensité dans la région de variabilité orientale du Pacifique tropical.** Cela requiert de distinguer dans le modèle CESM-LE le signal dû à la variabilité interne de celui dû à la réponse du système climatique à l'augmentation des gaz à effet de serre. Les processus thermodynamiques associés à ENSO et leur réponse au climat plus chaud seront également étudiés, par l'analyse du bilan de chaleur lors des événements El Niño. Quels sont les (changements de) processus fondamentaux qui contrôlent les variations d'amplitudes d'ENSO dans un climat plus chaud ? Comment les changements des processus thermodynamiques vont impacter la diversité d'ENSO ? **Le dernier objectif de cette thèse sera d'aborder certains aspects fondamentaux de la dynamique tropicale et portera plus spécifiquement sur la sensibilité de la réponse dynamique de la diversité d'ENSO au réchauffement climatique.**

General Introduction

El Niño-Southern Oscillation (ENSO) is a coupled ocean-atmosphere phenomenon that represents the dominant mode of year-to-year variability in the tropical Pacific. This phenomenon, alternating warm events, called El Niño, and cold events, called La Niña, affects weather events, ecosystems, agriculture and fisheries worldwide via atmospheric and oceanic teleconnections. These impacts include a monsoon disturbance, droughts and forest fires in Indonesia, India and north-eastern Australia in the boreal summer, winter floods and landslides in Ecuador, Peru and the south-western United States, an interruption of favourable conditions for industrial anchovy fishing off the Peruvian coast and a potentially devastating bleaching of the tropical Pacific coral (Goddard and Dilley, 2005; McPhaden et al., 2006). As an example, the 1997-98 strong El Niño event inflicted costs of approximately $33 billions in the world. Given the impact on economic systems such as agriculture and fisheries and on marine and terrestrial ecosystems, a better understanding of this phenomenon is essential in order to better predict it and to be able to set up warning systems and reduce the vulnerabilities of affected societies.

ENSO is a disruption of the tropical Pacific mean seasonal cycle. In normal conditions, the sea surface temperatures (SST) in the western tropical Pacific are among the warmest large-scale ocean temperatures in the world (greater than 28 °C), while the SST in the eastern Pacific are 4 to 10 °C colder. The "Warm Pool" in the west is maintained by the trade winds that blow from east to west along the equator. Above these warm SST, atmospheric deep convection can develop, generating heavy rainfall over "the Maritime continent", the western tropical Pacific and the eastern Indian ocean. In the eastern Pacific, the trade winds drive coastal and equatorial upwelling of deep cold water that cools the surface and forms the "Cold Tongue". The wind-driven zonal SST contrast, associated with deep atmospheric convection in the west, results in higher pressure in the east than in the west, which reinforces the trade winds. The tropical Pacific mean state is thus maintained by a positive loop coupled ocean-atmosphere, called the Bjerknes feedback (Bjerknes, 1969).

Small changes in the state of the tropical Pacific can lead to ENSO growth thanks to the Bjerknes feedback. During El Niño events, positive westerly wind anomalies in the western-to-central equatorial Pacific trigger a warm Kelvin wave that, by deepening the thermocline as it moves eastward, causes surface waters in the central and eastern equatorial Pacific to warm. These positive SST anomalies in the east reinforce the weakening of the trade winds, which further weakens the upwelling of cold waters in the east, reinforcing the warm SST anomalies. The Bjerknes feedback is then offset by several negative feedbacks, which have been suggested coming from the slow dynamic adjustment of the ocean as the restoring force of the unstable ocean-atmosphere interactions of ENSO. These delayed feedbacks include the widely accepted paradigm of the recharge-discharge oscillator (Jin, 1997a,b). The delayed oceanic adjustment to the westerly (easterly) winds acts to discharge (recharge) the equatorial upper-ocean heat content, which eventually terminates the El Niño (La Niña) event and transitions to the negative (positive) phase of ENSO. ENSO is then described as a self-sustained cycle. During La Niña events, the reverse loop leads to below-average SST in the central-to-eastern equatorial Pacific, reinforced by stronger trade winds.

However, the main limitation of these oscillatory theories is that they do not explain the irregularity of the frequency of occurrence of the phenomena, nor the strong asymmetry

between warm (El Niño) and cold (La Niña) events. El Niño and La Niña are not mirror images to each other. The complexity of ENSO is accentuated by the diversity of El Niño events. In addition to being stronger in magnitude, El Niño events exhibit a more pronounced spatial diversity compared to La Niña events. The growing interest in the diversity of El Niño events over the last twenty years has raised the question of their definition, given the multiplicity of their spatial structures, their amplitudes, their temporal evolution or their meteorological impacts. Numerous metrics (and denominations) have been proposed, highlighting the diversity of the spatial structures of the tropical Pacific (Trenberth and Stepaniak, 2001; Ashok et al., 2007; Kug et al., 2009; Kao and Yu, 2009; Yeh et al., 2009a; Ren and Jin, 2011), or the intensity of some of its characteristics, such as the warming of the ocean surface (Takahashi et al., 2011; Dommenget et al., 2013; Takahashi and Dewitte, 2016), or induced rainfall (Cai et al., 2014, 2015a, 2017; Williams and Patricola, 2018) in the eastern Pacific. A still on-going debate emerged to know whether the different regimes of El Niño represent a continuum (Capotondi et al., 2015) or distinct phenomena (Ashok et al., 2007; Karamperidou et al., 2015). The issue is directly linked to the definition of the diversity of El Niño, whose characterisation requires two degrees of freedom (Trenberth and Stepaniak, 2001; Yeh et al., 2009a; Takahashi et al., 2011; Ren and Jin, 2011).

This thesis is part of this rich context of studies on the diversity and complexity of ENSO (Timmermann et al., 2018). A state of the art of progress on this problem is described in Chapter 1 *"Background"*. Understanding, anticipating, and predicting ENSO behaviour on seasonal to decadal and longer time scales remains a great challenge, especially in the context of potential changes to ENSO in a warming climate.

The exponential development of computational resources in recent decades has improved the ability of Coupled General Circulation Models (CGCMs) to realistically simulate climate variability and ENSO. Although biases persist, in particular in the simulation of ENSO diversity and asymmetry, climate models are essential tools to improve the understanding of this complex ocean-atmosphere coupled phenomenon and the projection of its changes induced by global warming. My PhD work is mainly based on simulations of the coupled climate model from the Community Earth System Models Large Ensemble (CESM-LE) Project developed by the National Center for Atmospheric Research (NCAR) (Kay et al., 2015). The CESM-LE project provides a long-term simulation (1801 years) without anthropogenic forcing, which makes possible to analyse the internal variability of the simulated climate system. It provides also multiple realisations of the climate (40 to 42 members) over the 1920-2100 period, with a combination of both natural and anthropogenic climate forcings. Thanks to this large ensemble of simulations of the historical and projected climate, we have access to a large number of El Niño events that occur in climatic systems close to the observed climate, and thus to the variability of ENSO statistics. The observation datasets, the climate model and the statistical tools used in the thesis are described in Chapter 2 *"Data and methods"*. This chapter describes also the numerical calculation of the heat equation used in the analysis of ENSO physical processes as well as the assessment of the simulation of the Pacific variability and ENSO by CESM-LE.

The first objective of this thesis will be to reassess the characterisations of the diversity of ENSO and more particularly of its positive phase El Niño in the coupled model of climate CESM-LE. Which indices best characterise the diversity of ENSO? Are they statistically robust across observation datasets and simulations of climate models? To address these questions, we focused on two distinct and widely used approaches. The first method consists of distinguishing El Niño events by their spatial structures in historical regions Niño-3 (5°S-5°N, 210°E-270°E) and Niño-4 (5°S-5°N, 160°E-210°E), which measure the variability associated with the central and eastern Pacific respectively. Two types of El Niño events are thus classified, "Central Pacific" (CP) and "Eastern Pacific" (EP) events (Kug et al., 2009). The second method distinguishes El Niño events by the intensity of their warming in the eastern Pacific using the main modes of variability of the tropical

Pacific along the equator. It defines "strong" and "moderate" events, which by definition have a less pronounced surface water warming signature in the eastern Pacific. One of the advantages of this method is not to be constrained to analyse warm events from their spatial structure during their winter peak. An important aspect seems indeed to analyse ENSO not as a static spatial pattern at its winter peak but to cover its spatio-temporal evolution and in particular its evolution phase. This comparative analysis of the two methods is presented in Chapter 3 *"Characterising ENSO diversity"*.

The ENSO asymmetries, between El Niño and La Niña events on one hand, between warm El Niño events on the other hand, underpin the notion of non-linear processes, in particular in deep atmospheric convection and oceanic heat advection. Non-linearities in oceanic processes seem to be the link between the decadal variability of the tropical Pacific and the ENSO modulation. Indeed, numerical studies suggested that time-mean effect of ENSO may product a non-linear rectification onto the low-frequency variability of the tropical Pacific via ENSO asymmetries (Rodgers et al., 2004). Conversely certain periods, characterised by specific tropical Pacific mean states, seem to favour El Niño's flavours, as for example the prevalence of the occurrence of CP El Niño events in recent decades. Does the mean state of the tropical Pacific influence the type of El Niño events? Does ENSO diversity rectify the mean state? **The second objective of this thesis will be to diagnose the internal variability of the ENSO diversity and its rectification onto the mean state in the CESM-LE coupled model** (Chapter 4 *"Low-frequency modulation of ENSO diversity"*).

Finally, the Chapter 5 *"ENSO diversity and global warming"* is devoted to the impact of global warming on ENSO, and in particular on the strong El Niño events. Coupled climate models project significant changes in the mean state of the tropical Pacific, some with strong consensus between models. Especially, the Walker circulation is projected to weaken (Vecchi and Soden, 2007), which will decrease the strength of the trade winds and thus alter the thermal structure and the mean ocean circulation of the tropical Pacific (DiNezio et al., 2009; Santoso et al., 2013). From a theoretical point of view, the projected increase in the mean vertical stratification of the tropical Pacific can lead to significant modifications in the characteristics of ENSO, through the impact it can have on the thermocline feedback, especially in the eastern Pacific (An and Jin, 2001; Dewitte, 2000). However, there is still a weak consensus among CGCMs on the projected ENSO variability in a warmer climate. On the other hand, extreme El Niño events, which are associated with strong signature in anomalous precipitation in the eastern Pacific, are predicted to increase in frequency in the future (Cai et al., 2014). This increase in occurrence frequency has been argued to be due to the faster temperature warming in the eastern equatorial Pacific facilitating the southward migration of the Inter-Tropical Convergence Zone (ITCZ). While this offers a paradigm for the climate change impact on ENSO, the underlying mechanisms remain unclear. What are the changes in ENSO's diversity statistics with global warming? How to reconcile the two results emanating from coupled climate models that seem contradictory with, on the one hand, a lack of consensus on changes in ENSO variability in the eastern tropical Pacific and, on the other hand, a significant increase in the number of ENSO-induced extreme precipitation events in the eastern Pacific? **The third objective of this thesis will be to diagnose, in CESM-LE, projected changes in statistics associated with ENSO diversity, when defined by its intensity in the region of eastern tropical Pacific variability** This requires distinguishing the signal due to internal variability from that due to the response of the climate system to the increase of greenhouse gases. A directly related issue concerns the changes in ENSO mechanisms and feedback processes in a warmer climate. What are the (changes in) fundamental processes controlling ENSO amplitude variations in a warmer climate? How changes in thermodynamical processes would impact ENSO diversity? **The last objective of this thesis will be to address some fundamental aspects of tropical dynamics and specifically focus on the sensitivity of the dynamical response of the ENSO diversity to global warming.**

Chapter 1

Background

Contents

The El Niño-Southern Oscillation (ENSO), the alternation of warm El Niño and cold La Niña events, is a coupled ocean-atmosphere phenomenon and the most energetic mode of inter-annual variability in the climate system. This fluctuation occurs in the tropical Pacific and has meteorological, societal and economic impacts affecting the entire planet, via atmospheric and oceanic teleconnections.

Improving our understanding of ENSO is fundamental to better predict its impacts and ultimately reduce societal vulnerabilities by implementing an early warning system. Its predictability over several months is made possible thanks to the slow dynamic adjustment of the ocean, which slows down the evolution of the coupled ocean-atmosphere system, contrary to weather forecasts, limited to a few days.

Various theories explain different characteristics of this complex coupled phenomenon that interweaves many spatial and temporal scales. These theories emphasize different interactions and are sometimes distinct ways of seeing the same physical processes. But they are oftentimes complementary and indispensable to forecast the phenomenon. The exponential development of numerical resources over the last decades has improved the ability of Coupled General Circulation Models (CGCMs) to simulate El Niño. Nonetheless the diversity of ENSO representation by different CGCMs illustrates the models limitations to simulate this complex interplay of ocean and atmospheric processes. Understanding, anticipating, and predicting its behaviour on seasonal to multi-decadal time scales remain a great challenge, especially in the context of potential changes of ENSO in a warming climate.

This introductory chapter presents state-of-the-art knowledge on ENSO characteristics and, in particular, those discussed in this study. In section 1.1, ENSO general features are described (e.g. dynamics, mean state, impacts). We focus specifically on ENSO diversity, as the main background material for this thesis. We then review the main theories describing the oscillation's mechanisms, in particular those involving equatorial wave dynamics and explaining the transition from El Niño to La Niña events (section 1.2). However, the observed ENSO irregularity and asymmetry are not accounted for by these linear theories and understanding the complexity and diversity of the phenomenon have become a priority for ENSO researchers. Several lines of investigation are presented in this chapter, from the atmospheric stochastic forcing to the intrinsic non-linearities of the coupled ocean-atmosphere system. ENSO is also affected and modulated by mechanisms operating at a wide range of timescales. For instance, ENSO is strongly phase-locked to the tropical Pacific seasonal cycle. ENSO properties have also been shown to change according to the tropical pacific decadal mean state. This complicates the analysis of ENSO dynamics especially considering the short available instrumental records. This "ENSO timescale interaction issue" is discussed in section 1.3. Finally, we present in section 1.4 some of the most recent progresses on the understanding of ENSO response to global warming.

1.1 El Niño-Southern Oscillation

We first describe the main atmospheric and oceanic circulations in the tropical Pacific and their variations during the two phases of ENSO, El Niño and La Niña. In this first section, we immediately bring up the still open question of the El Niño events definition. It is still a matter of debate considering its diversity of spatial patterns, amplitudes, temporal evolution or impacts. We finally present a quick overview of the meteorological, environmental, but also economic and societal consequences of ENSO.

1.1.1 Main features

ENSO occurs in the equatorial Pacific Ocean, which is the seat of intense atmospheric and oceanic circulations related to general climate circulation. The solar energy, maximum at the equator, is the most important driver of the large-scale atmospheric circulation, which

is organised in cells: the meridional Hadley circulation and the zonal Walker circulation (Fig. 1.1).

(a) Hadley circulation

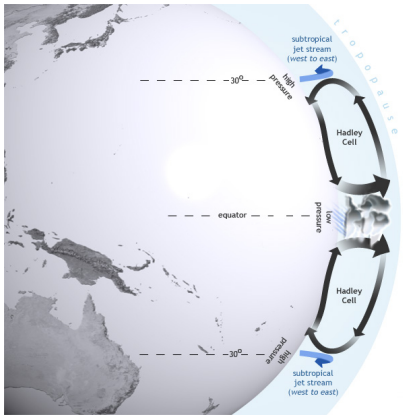

(b) Hadley and Walker circulations

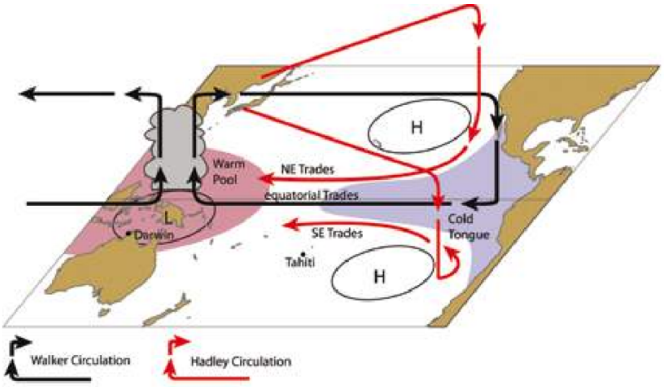

Figure 1.1 – Schematic representation of (1.1a) the Hadley Circulation (reprinted from NOAA Climate.gov[1]) and (1.1b) Walker (black lines) and Hadley (red lines) circulations in the tropical Pacific (reprinted from Lough et al. (2016)).

The Hadley circulation is organised in meridional cells that redistribute the accumulated energy in the equator towards higher latitudes in each hemisphere (Fig. 1.1a). Warm waters at the equator are primarily in the western tropical Pacific and along bands on both sides of the equator, forming the Inter Tropical Convergence Zone (ITCZ) and the South Pacific Convergence Zone (SPCZ). The ITCZ is more intense due to the larger continental landmass in the Northern Hemisphere and spans the entire Pacific. These convective zones in the equatorial band (10°S-10°N) lead to convergence of cold and dry coastal surface winds from the mid-latitudes to the tropics where they moisten and warm, constituting the north and south cells of the Hadley circulation. Through the conservation of the angular momentum, these winds are deflected to the right (left) in the northern (southern) hemisphere, resulting in the north-east (south-east) trade winds that blow on average from east to west in the equatorial Pacific (Fig. 1.1b). Crossing the Pacific Ocean along the equator, the trade winds gradually charge in moisture and heat through evaporation, reinforcing the warming of the western Pacific. Moist warm air rises spontaneously into cumulus towers above this "Warm Pool", which exceeds the convective instability threshold of $\sim 27.5\,°C$ (Graham and Barnett, 1987) causing significant rainfall. These convective towers constitute the ascending branch of the east-west oriented Walker circulation (Bjerknes, 1969). Aloft the air that has lost its moisture diverges in the upper troposphere to subside, dry, over colder (due to the upwelling) regions at the eastern edge of the ocean, that gets little precipitation. The trade winds close the large-scale Walker atmospheric circulation, blowing from east to west on the surface of the equatorial Pacific.

In the tropics, atmospheric circulation is the main driver of the upper ocean circulation, due to the strong oceanic vertical stratification characterised by a shallow layer of warm water over a deep layer of colder water, separated by the thermocline (i.e. the sharp boundary separating warm upper waters from cold deeper waters, typically marked by the 20 °C isotherm). The trade winds cause a divergence of the Ekman transport northward (southward) to the north (south) of the equator, which generates an equatorial upwelling of colder subsurface water forming a "Cold Tongue" that stretches from the south American coast to near the dateline (Fig. 1.2a). The trade winds pressure along the equator exerts a force onto the upper ocean directed westward that pushes the equatorial warm waters to the west, causing an accumulation of water in the "Warm Pool". The induced slope of the ocean surface, higher in the west than in the east, causes a mirror structure of the oceanic thermocline that shoals

[1] www.climate.gov

eastward. On average, the sea level is 60 cm higher and the thermocline 150 m deeper in the west (up to 200 m deep) than in the east Pacific (30 m in the far eastern Pacific). Because of the climatological mean depth of the thermocline, the east-west contrast of the Sea Surface Temperature (SST) increases. The deep thermocline in the west allows surface temperatures above 28 °C to hold up while in the east the shallow thermocline results in more efficient cooling of the surface layer by vertical mixing and upwelling of deep cold water. Finally, the trade winds maintain the zonal SST gradient, which confines the atmospheric convection in the western Pacific, reinforce the associated zonal atmospheric pressure gradient and thus the Walker circulation, which in turn reinforces trade winds and zonal SST gradient (forming a positive feedback loop).

The trade winds maintain also a westward zonal current, the South Equatorial Current, and induce a divergence of equatorial meridional currents. The amplitude of the trade winds, driving the divergence of the surface currents, accounts for the intensity of the vertical velocities in the superficial ocean and thus for the upwelling of cold water observed along the equator. The related changes in SST will in turn affect the equatorial atmospheric circulation, illustrating the strong coupling between the atmosphere and ocean in the tropics. The tropical Pacific mean state results then from the coupling between the large-scale Walker circulation in the atmosphere and the spatial structure of the underlying SST (Dijkstra and Neelin, 1995). These air-sea coupled mechanisms involve processes that are both thermal (via heat fluxes between the equatorial Pacific Ocean and the atmosphere) and dynamical (via the action of the wind on the ocean surface).

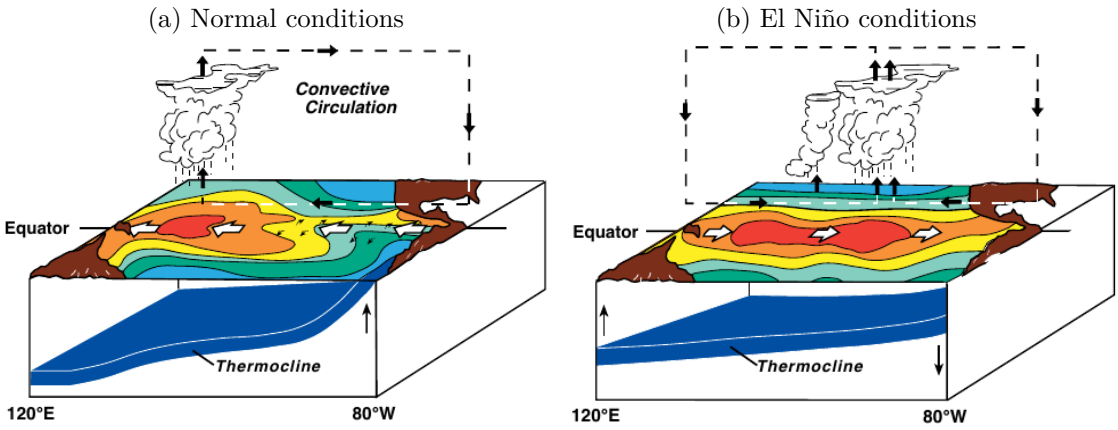

Figure 1.2 – Schematic showing (1.2a) the normal and (1.2b) El Niño conditions in the tropical Pacific (reprinted from McPhaden et al. (2010)).

However, the tropical Pacific is not in a steady state. Its variability arises from the strong air-sea coupling that can initiate an unstable disturbance.

El Niño conditions (Fig. 1.2b) are characterised by a relaxation of the trade winds that allows the eastward extension of the western Pacific Warm Pool as well as the weakening of the equatorial upwelling. This leads to the deepening of the thermocline in the eastern Pacific and thus to an anomalous warming of the oceanic surface layer off the coasts of Ecuador and Peru, which may warm by up to 2 to 4 °C. This warming in the east decreases the SST contrast along the equator, which further reduces the trade winds. This mutual reinforcement between the SST gradient and the winds strength, in a positive feedback loop called the "Bjerknes feedback" (see paragraph 1.2.1.1), causes the rapid development of El Niño. The Walker circulation is destabilised via the decrease of the zonal temperature gradient. The convective atmospheric cells follow the warm surface waters from the west to the central Pacific and therefore shift the location of intense tropical rainfalls. The ITCZ and SPCZ shift southward and north-eastward respectively. Essentially, the major source of heat for the atmospheric circulation moves towards the central Pacific, and the whole atmosphere responds to this

change, with important weather impacts. Actually, changes in sea surface temperature are both the cause and consequence of wind fluctuations, interacting as a positive air-sea feedback and causing a continuous horizontal redistribution of warm surface waters.

The reverse disturbance leading to the displacement of the ascending branch of the Walker circulation further west is called La Niña (Philander, 1990). During La Niña events, the Walker circulation is reinforced with strong trade winds confining the convective Warm Pool to the west and reinforcing the Cold Tongue cooling in the east.

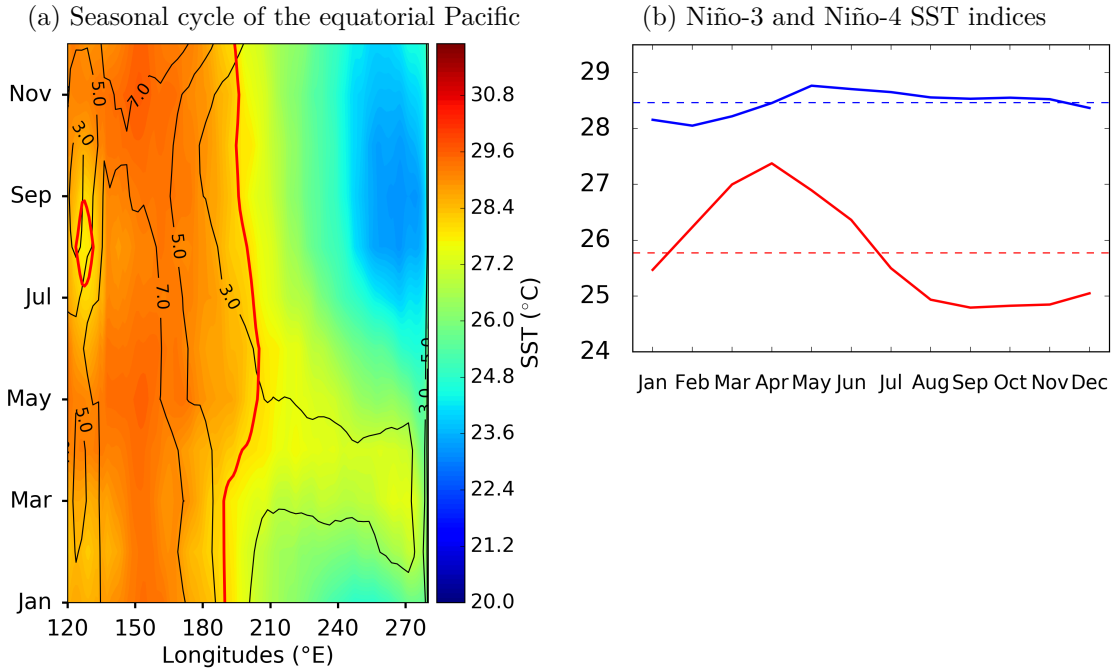

Figure 1.3 – (1.3a) Seasonal cycle of the equatorial Pacific (5°S-5°N) of SST (colour scale) and precipitation (contour, at intervals of 2 mm per day) in HadISST v1.1 (1950-2017) and GPCP v2.3 (1979-2017) datasets respectively. Red line materialises the 28 °C isotherm. (1.3b) Seasonal cycle of the eastern (red line) and the central (blue line) Pacific. The eastern and central Pacific regions are materialised by the SST averaged over the Niño-3 (5°S-5°N, 210°E-270°E) and Niño-4 (5°S-5°N, 160°E-210°E) regions respectively, over the same HadISST period.

ENSO is thus a year-to-year disruption of the seasonally evolving climatological state of the tropical Pacific, although the latter tends to favour its development in certain seasons. The climatological state of the tropical Pacific varies seasonally in response to the seasonal variations of solar irradiance with a slight lag due to the heat capacity of the ocean. Seasonal variations in the tropical Pacific reach their maximal values in boreal spring and fall (Fig. 1.3). In spring, the ITCZ moves equatorward and the southeasterly winds weaken. The equatorial and coastal upwelling weakens, which allows the warming of the Cold Tongue, and the eastern Pacific SST usually reaches its seasonal maximum. First, the vertical entrainment velocity of cold subsurface water toward the mixed layer remains constant but the thickness of the surface layer being increased (variations of the thermocline depth), the surface layer is less cooled on average and a warm SST anomaly appears in the eastern Pacific. The warming is then amplified through a weakening of cold water upwelling (variations in the mean upwelling velocity). However, as the surface gets warmer, evaporation increases, limiting the development of temperature above 30 °C and therefore the warm inter-annual anomalies (related to the seasonal cycle). The spring warm phase of the Cold Tongue propagates westward and reaches the central Pacific in boreal summer. The seasonal cycle of the central Pacific SST has smaller amplitudes than in the eastern Pacific and is staggered over time (Fig. 1.3b). The eastern SST seasonal cycle is driven by a strong ocean-atmosphere coupling while the seasonal cycle in the western Pacific results mainly from changes in solar radiative forcing.

In fall, the ITCZ moves towards 12°N when south-east trade winds are the most intense.

These seasonal changes, tied to the annual cycle of the insolation, in upwelling, ITCZ location and winds stress play a key role in the onset and termination of ENSO. El Niño and La Niña tend to develop during spring (April-June) and reach a maximum strength during the next boreal winter (December-February) (see paragraph 1.3.1).

It has been observed that this phenomenon is irregular and has a return period between 2 and 8 years. The duration of an El Niño event is also variable and lasts less than La Niña. This highlights one of the asymmetric features between the two ENSO phases. Ray and Giese (2012) showed in reanalysis data (1871-2008) that the time between events may range from several months to ten years and the duration of ENSO may vary from 5 to 27 months. Another asymmetric feature is that La Niña events have weaker amplitudes and tend to last longer (generally 2 years). Finally, ENSO is governed by multi-scale processes, from high frequency stochastic processes to mechanisms operating at decadal scales. All of these features will be addressed and reviewed throughout this introductory chapter.

1.1.2 ENSO diversity

1.1.2.1 History of the diversity

Generally, El Niño events characterise the anomalous warming occurring in the eastern equatorial Pacific, associated with the weakening and even potentially the reversal of the trade winds. However, "no two El Niño events are quite alike" (Wyrtki, 1975). He showed that the 1965 El Niño event was different in terms of wind stress and SST from the other two main events he studied (the 1957-1958 and 1972-1973 El Niño events). The 1965 event did not exhibit a second temperature peak during the winter following the first growth of SST anomalies.

A few years later, Rasmusson and Carpenter (1982) described the typical evolution of an El Niño, by building a composite from 6 recorded events from 1951 to 1972, in terms of SST anomalies, wind anomalies and velocity divergence. This composite is often referred to as the **canonical El Niño**. It is characterised by a development of SST anomalies along the coast of Peru and a subsequent spreading westward towards the central Pacific in boreal winter. Rasmusson and Carpenter (1982) pointed out that large SST anomalies in the central Pacific were unlikely during boreal winter unless significant SST anomalies were already in place along the coast of Peru a few months before. Yet, they mentioned that the 1963 El Niño was not preceded by positive SST anomalies in the far eastern tropical Pacific.

Conversely, Deser and Wallace (1990) showed that anomalous warming in this region may take place without a developing El Niño and that it may develop separately from an initial warming in the central Pacific. A change in the direction of propagation of El Niño events was also observed at this time. The El Niño events of 1957, 1965 and 1972-73 were propagating westward, from the far eastern Pacific to the central Pacific, consistently with the canonical El Niño event described by Rasmusson and Carpenter (1982), while the events of 1982-1983, 1986-87 and 1991 propagated eastward. Wang (1995) suggested that such changes in El Niño onset were linked to changes in the background state of the Pacific, determining whether a warming along the South American coast leads or follows the warming in the central Pacific. Boucharel et al. (2013) proposed that these changes in ENSO-related SST anomalies propagation were in fact an artefact from the modulation of the seasonal cycle amplitude in the eastern Pacific.

Another puzzling behaviour of ENSO was noticed by Latif et al. (1997). The warm period of 1990-1994 can be either defined as a succession of small El Niño events or as a long event of nearly 3 years depending on the studies. This raises the question of ENSO being actually an oscillation or a series of stochastic events. Finally, the 20th century ended with the strongest event ever recorded. The 1997-98 El Niño event could have caused $33 billion in damage and cost 23 000 lives worldwide (Kerr, 1999). This event has been extensively studied

(e.g. McPhaden (1999); Wang and Weisberg (2000); Vialard et al. (2001); Lengaigne et al. (2003); Vecchi and Harrison (2006)) and has distinct and pronounced characteristics including a propagation of SST anomalies eastward and an extraordinary amplitude of anomalous warming in the eastern Pacific (4–5 °C). More recently, the 2015-16 El Niño was likely the most widely anticipated event ever. It was preceded by nearly four decades of progress in observing and prediction systems. It rivalled the 1997-98 event, showcasing advancements in operational observing and prediction systems, while offering challenges for the future (early peak not well predicted, L'Heureux et al. (2017)).

The last twenty years showed a resurgence of events peaking in the central Pacific (CP) near the dateline. Such dissimilarities with the canonical view of El Niño revived the question of ENSO diversity. These CP events characterised by anomalous warming near the dateline induce different precipitation and temperature impacts around the world (Larkin and Harrison, 2005a,b). After the warm event of 2004, Ashok et al. (2007) defined a new flavour of ENSO, that they called "El Niño Modoki". Since the 2000s, the increase in such events brought a profusion of indices to characterise the different types of observed El Niño (see following paragraph 1.1.2.2 for a description of the SST indices and associated denominations). Despite the diversity and complexity of ENSO behaviours, it has been widely proposed to classify ENSO events simply into two categories. El Niño events with a stronger warming in the eastern Pacific are referred to as **Cold Tongue** El Niño (Kug et al., 2009) or **Eastern Pacific** El Niño (Kao and Yu, 2009; Yeh et al., 2009a). El Niño events with a stronger warming in the central Pacific are called **Dateline** El Niño (Larkin and Harrison, 2005a,b), El Niño **Modoki** (Ashok et al., 2007), **Warm Pool** El Niño (Kug et al., 2009), or **Central Pacific** El Niño (Kao and Yu, 2009; Yeh et al., 2009a).

Even if the vast majority of classifying methods uses the SST anomalies longitudinal location, some have suggested to look at other features, such as the intensity of the SST warming (**moderate** and **strong** El Niño of Takahashi et al. (2011)), the subsurface temperature (Yu et al., 2010b), the induced precipitations (**extreme** El Niño of Cai et al. (2014), variable also used by Williams and Patricola (2018)), the outgoing long-wave radiation (OLR) associated signal (Chiodi and Harrison, 2013), the event onset time (Wang, 1995; Xu and Chan, 2001), the propagation direction (Wang, 1995; McPhaden and Zhang, 2009), or the termination (Lee et al., 2014). Kao and Yu (2009) suggested that many of these different classifications share common features, mostly characterising different warming centres between two types of El Niño events, one in the eastern and the other in the central Pacific. This diversity is often referred to as the "flavours of El Niño". The following provides a brief review of current metrics to characterise ENSO diversity.

1.1.2.2 Metrics

In 2003, the National Oceanic and Atmospheric Administration (NOAA) defined El Niño "as a phenomenon in the equatorial Pacific Ocean characterised by a positive sea surface temperature departure from normal (for the 1971-2000 base period) in the Niño-3.4 region (5°S-5°N, 120°-170°W, see Figure 1.4a) greater than or equal in magnitude to 0.5 °C, averaged over three consecutive months" (which has become at least five consecutive overlapping seasons by the NOAA Climate Prediction Center). This index, called the Oceanic Niño Index (ONI), has been one of the most popular indices to characterise ENSO variability. However, this definition added El Niño events that were not considered as El Niño until then (Larkin and Harrison, 2005a). This is mainly because the criterion region, Niño-3.4 area, takes into account conditions in the central equatorial Pacific (see Figure 1.4a).

It is now recognised that at least two degrees of freedom are needed to describe El Niño events and their spatial diversity (Trenberth and Stepaniak, 2001; Yeh et al., 2009a; Takahashi et al., 2011; Ren and Jin, 2011). El Niño events characterisation is often based on metrics calculated from SST anomalies, a direct observation that may reflect the presence of an El Niño event. The metrics must allow taking into account the diversity of the phenomenon while

being relatively simple to compute. In the following, we present some of the most commonly used indices of SST anomalies in the El Niño classification. It should be noted that because there is less difference between the patterns of La Niña events, we focus exclusively in the thesis on the diversity of warm events, even if the problematic of defining diversity also applies to cold events and, in particular, to extreme La Niña events (Santoso et al., 2017). For a review of the different indices used in the literature, we invite the reader to refer to Capotondi et al. (2015).

Trans-El Niño : Trenberth and Stepaniak (2001) first proposed to use two indices to describe the distinct evolution of each El Niño or La Niña event. They proposed to use the Niño-3.4 index and the Trans-Niño Index (TNI). The TNI represents the difference between the normalised SST anomalies averaged in the Niño-1+2 (0°S-10°S, 90°W-80°W) and Niño-4 (5°S-5°N, 160°E-210°E) regions (see Fig. 1.4a).

El Niño "Modoki" : defined by Ashok et al. (2007) using the El Niño Modoki Index (EMI). The EMI is defined by a linear combination of mean SST anomalies over specific regions of the tropical Pacific:

$$EMI = [SSTA]_A - 0.5 \cdot [SSTA]_B - 0.5 \cdot [SSTA]_C \tag{1.1}$$

The brackets indicate the area-averaged SST Anomalies (SSTA) over the region A (165°E-140°W, 10°S-10°N), B (110°W-70°W, 15°S-5°N), and C (125°E-145°E, 10°S-20°N) (see Fig. 1.4b for the corresponding regions). An event is defined as a Modoki event when the EMI is greater than 0.7 times the standard deviation of the mean EMI. It should be noted for correspondence with other metrics, that the EMI is highly correlated with the second Principal Component (PC2) of the Empirical Orthogonal Function analysis (EOF, see paragraph 2.2.2.2) of the monthly SST anomalies over the tropical Pacific (Ashok et al., 2007). The EOF analysis is a statistical method which deconvolutes the spatio-temporal variability into orthogonal modes, composed of spatial pattern modes (called EOF maps) and associated time series (called principal component or PC). Often the first modes alone can capture most of the coherent variability of the data. The first two modes are thus very often used to study the variability of the tropical Pacific and ENSO in particular. According to Marathe et al. (2015), the EMI is also correlated to the C-index defined by Takahashi et al. (2011) (see "Strong and moderate El Niño" bullet point) and N_{WP} index defined by Ren and Jin (2011) (see "Warm Pool and Cold Tongue El Niño" bullet point). This method was questioned by Lian and Chen (2012) who suggested that the spatial pattern of the Modoki event could be an artefact due to the orthogonality constraint associated with the EOF technique. Dommenget and Latif (2002) and Dommenget et al. (2013) also raised the limitations of the interpretation of EOF modes as two physically independent modes, due to the tendency of many physical modes to superpose into a single EOF mode. Marathe et al. (2015) used various linear and non-linear approaches including an EOF and a cluster analysis to confirm that the El Niño Modoki and the canonical El Niño display different seasonal evolution and teleconnections, involving a different strength of the air-sea coupled feedback. Following the denomination of Jeong and Ahn (2017), this method is referred to as "AS" method.

"Warm Pool" and "Cold Tongue" El Niño : the terms were first defined by Kug et al. (2009) based on historical El Niño indices. They compared the value of the mean SST anomalies in the winter over the Niño-3 (5°S-5°N, 210°E-270°E) and Niño-4 (5°S-5°N, 160°E-210°E) regions (see Fig. 1.4a) to separate Warm Pool (WP) from Cold Tongue (CT) El Niño events. The Warm Pool events are so called because the centres of action of several atmospheric variables as well as the SST anomalies are related to the eastward extension of the Warm Pool. This method has been widely used owing to its relative

simplicity (Yeh et al., 2009a; Kug et al., 2009; Choi et al., 2011; Capotondi, 2013; Stevenson et al., 2017) and we will also investigate further this definition in Chapter 3 (see paragraph 3.2.3). This method is referred to as "KU" method.

Arguing that the previous indices from Kug et al. (2009) are highly correlated, Ren and Jin (2011) proposed other indices to characterise ENSO diversity:

$$\begin{cases} N_{CT} = & N_3 - \alpha\ N_4 \\ N_{WP} = & N_4 - \alpha\ N_3 \end{cases} \quad \text{with } \alpha = \begin{cases} 2/5, & \text{if } N_3N_4 > 0. \\ 0, & \text{otherwise.} \end{cases}$$

N_3 (N_4) corresponds to the SST anomalies averaged in the Niño-3 (Niño-4) areas. These two indices are a linear combination of the Niño-3 and Niño-4 indices conditioned by the ENSO phase. The parameter α is data-dependent and it is used to transform the base (Niño-3, Niño-4) into a base where the two clusters of CT and WP El Niño events are centred on the new axes. They defined these indices also because they are easier to calculate than the following indices of Kao and Yu (2009). This method is referred to as "RJ" method.

"Central Pacific" and "Eastern Pacific" El Niño : first named by Kao and Yu (2009) who used an EOF analysis combined with a linear regression. Before calculating the first EOF mode associated with the CP (EP) El Niño, they subtract the SST anomalies regressed onto the Niño-1+2 (Niño-4) index from the original SST anomalies field. This method is referred to as "KY" method.

Several studies then took over the same terms of "Central Pacific" and "Eastern Pacific" events using different methods of events classification. For instance Yeh et al. (2009a) used this terminology but with a method approaching that of Kug et al. (2009).

"Strong" and "moderate" El Niño : first defined by Takahashi et al. (2011) using the rotating leading EOF modes of the tropical Pacific SST anomalies. They suggested to rotate by 45° the PC1-PC2 phase space because of the privileged directions of the system: in the new base of the rotated indices, named E and C in Takahashi et al. (2011), the strong El Niño regime is distributed along the E axis and the moderate and cold regimes along the C axis. The axes appear to have dynamical meaning, when the PC1 and PC2 axes result from maximising the variance of the SST of the first two EOF modes. These indices (E and C) also allow the peak season as well as the location of the warming being independent. The same rotation is also used by Dommenget et al. (2013), based on similar arguments, calling the new axis $PC_{\text{El Niño}}$ and $PC_{\text{La Niña}}$ respectively. The work of this thesis is based on this method (see chapter 3 and paragraph 3.2.2 for more details). This method is referred to as "TD" method.

Finally, without explicitly seeking to separate two ENSO regimes, Giese and Ray (2011) defined the Center of Heat Index (CHI) that breaks down the great diversity of El Niño and La Niña behaviours into three components (longitude, amplitude and area). The CHI is based on the longitudinal location of SST anomalies greater than 0.5 °C in the tropical Pacific (5°S-5°N, 120°E-70°W) if the warm area is greater than the area of the Niño-3.4 region.

Other classifications of ENSO diversity based on spatial patterns has been proposed, using different statistical methods such as agglomerative hierarchical clustering (AHC) (Singh et al., 2011), self-organizing map (SOM) analysis (Johnson, 2013; Li et al., 2015), fuzzy clustering analysis (Chen et al., 2015a) or pattern correlation coefficients (Jeong and Ahn, 2017) among others.

1.1.2.3 Characterisation of ENSO diversity

Although the names and definitions of these El Niño types are slightly different, the Warm Pool, Central Pacific, Dateline and Modoki El Niño events are often considered to describe

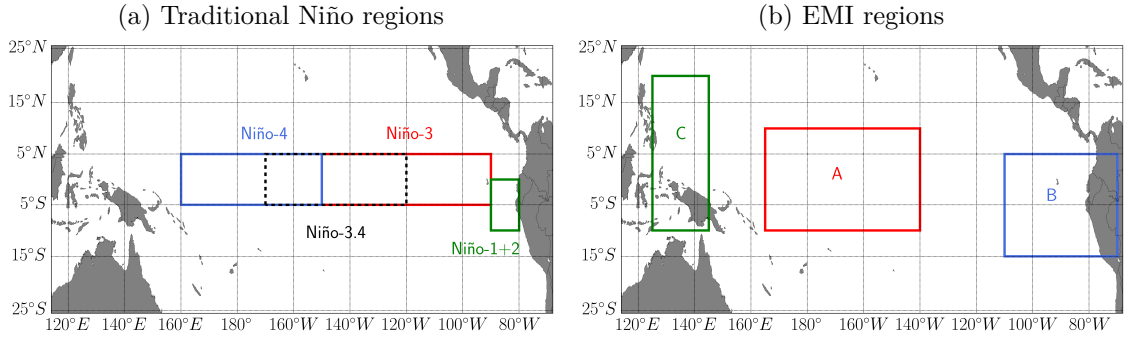

Figure 1.4 – Outline of regions over which SST anomalies (SSTA) are averaged to defined ENSO SSTA indices. (1.4a) Historical Niño regions, corresponding to assorted Niño SSTA indices, with Niño-4 (5°S-5°N, 160°E-210°E), Niño-3.4 (5°S-5°N, 120°-170°W), Niño-3 (5°S-5°N, 210°E-270°E) and Niño-1+2 (0°S-10°S, 90°W-80°W). (1.4b) Regions used to compute the EMI index of Ashok et al. (2007), with A (10°S-10°N, 165°E-140°W), B (15°S-5°N, 110°W-70°W), and C (10°S-20°N, 125°E-145°E).

the same type of events, in which the warmest SST anomalies occur in the western-to-central Pacific. By analysing the evolution of several El Niño events in the E-C phase space between May(0) (of their developing year) and January(1) (of their mature phase), Takahashi et al. (2011) confirmed that Modoki, CP and moderate El Niños can be grouped in the same category, distinct from extreme warm events (see their Figure 1). It should be noted that the *canonical El Niño*, referring to as the El Niño composite of Rasmusson and Carpenter (1982), is often compared to EP El Niño events in literature (Kug et al., 2009; Kim et al., 2009). However, it shares more features with moderate El Niños than with strong EP El Niños, despite an initial warming in the eastern Pacific that the CP events do not have (Takahashi et al., 2011; Dewitte and Takahashi, 2017). For instance, in the E-C phase space, the canonical El Niño event of 1957-58 (Rasmusson and Carpenter, 1982) is close to Modoki or CP El Niño events (Takahashi et al., 2011).

Commonly, the typical **Eastern Pacific (EP) El Niño** develops strongly in the (far) eastern Pacific (Niño-1+2 region, see Figure 1.4a) during boreal spring. Although sometimes the developing SST anomalies do not have propagating characteristics and are thus considered as quasi-stationary (Kug et al., 2009), it generally extends westward during summer (Kao and Yu, 2009), meeting a second warming zone that develops in the central Pacific following local westerly wind events (Wang and Weisberg, 2000). The peak of positive SST anomalies is reached in boreal winter, before retreating in an almost identically opposite way that restores the normal cold waters of the eastern Pacific Cold Tongue during the following spring. Typically, the Niño regions experience this decay in April of the second year except in the Niño-1+2 region, where the decay may occur later, in July (Kao and Yu, 2009). It should be noted however that some differences appear in the development of strong El Niño events: during the 1982-83 events for instance, no initial warming in the extreme east has been observed but the SST anomalies herein were amplified in the spring after the mature phase of the event.

The **Central Pacific (CP) El Niño** has a different structure with positive SST anomalies confined in the western-to-central Pacific (Kao and Yu, 2009). Positive SST anomalies often begin during the summer months near the international dateline (180° longitude). The event spreads meridionally with extension to the eastern subtropics, but fails to propagate zonally to the extent that the EP El Niño does. The mature phase of the event, with maximum SST anomalies amplitudes, is also often reached in winter and the event retreats during spring of the second year. Furthermore, CP (EP) El Niño events are characterised by weaker (stronger) SST anomalies and have a shorter (longer) duration, around 9 (15) months.

Lai et al. (2015) analysed the spatial evolution over the equatorial Pacific of all observed El Niño events over 1980-2013. They concluded that almost all events start with a warming

(+0.5 °C) in the central Pacific. They also showed that all CP El Niños and their hybrid El Niños decay with a warming in the central Pacific. Only EP El Niño, which correspond in their study to the two strong El Niño events of 1982-83 and 1997-98, end with a warming in the eastern Pacific. Thus, the initiation phase would be similar between El Niño events, which would then differ in their direction of propagation (see paragraph 1.2.2.4).

Some studies suggested that other classifications, such as moderate versus extreme El Niño events could be more relevant. Among the different SST anomalies metrics presented above, the "TD" classification also integrates information on the strength of the event. It leads to a categorisation between strong and moderate El Niño events, based on the underlying Bjerknes feedback (Takahashi and Dewitte, 2016) as well as between moderate CP and moderate EP El Niño events, based on the variability in the far eastern Pacific related to an air-sea interaction mode (Dewitte and Takahashi, 2017).

In addition to a possible more physical approach to the phenomenon, the differentiation of strong or extreme El Niño events is of prime importance because of the greater and dramatic socio-economics global impacts (Philander, 1990; McPhaden et al., 2006). Another approach for identifying extreme El Niño has been proposed by Cai et al. (2014) and focuses on precipitation anomalies rather than SST anomalies. Characterised by an important warming in the eastern Pacific with SST exceeding 28 °C, the two observed strong El Niño events of 1982-83 and 1997-98 induced precipitation anomalies in the eastern equatorial Pacific, normally dry and cold (Philander, 1983; McPhaden, 1999). Indeed, during strong El Niño events, the ITCZ moves from its climatological location (8°N) to the eastern equatorial Pacific (Rasmusson and Carpenter, 1982; Lengaigne and Vecchi, 2010) due to the weakening of the zonal and meridional SST gradients. It leads to atmospheric convection and exceptional rainfall (> 5 mm/day) in the eastern Pacific. Cai et al. (2014) showed that the precipitation in the eastern Pacific increases non-linearly with the increase of SST anomalies in Niño-3 and the decrease in the eastern Pacific meridional SST gradient. Cai et al. (2014, 2015a, 2017) defined thus an extreme El Niño event when the boreal winter (DJF) rainfall in the Niño-3 region is beyond an arbitrary threshold of 5 mm/day.

More recently, an index based on the longitude of the deep convection in the equatorial Pacific basin has been proposed by Williams and Patricola (2018). Based on the same idea as the precipitation index of Cai et al. (2014), it allows in addition to discriminate the effect of the increase in column water vapour due to warming in order to focus on the rain-related ENSO effect. The proposed ENSO Longitude Index (ELI) contains longitude information of where deep convection occurs along the equatorial Pacific. Surprisingly they proposed only one index to characterise ENSO diversity, arguing that it accounts for the non-linear, threshold-like response of deep convection to SST. The index is not weighted by how much SST exceeds the threshold, it is not an indication of total magnitude of the event. However, depending on the resulting longitude value, the index makes it possible to determine the displacement of the deep convection associated with El Niño events and so, indirectly, the qualitative importance of the warming in the eastern Pacific where the relationship rainfall-SST is non-linear (see paragraph 1.2.2.3). One of the main advantage of the index is that it is robust to changes in the SST background state since the convection threshold used for the calculation of the index is defined by comparison with the tropics-wide average SST.

Finally, Dewitte and Takahashi (2017) showed that CP and Modoki El Niño events may be apprehended as moderate CP events while canonical El Niño events as moderate EP events. This classification is close to that proposed by Chen et al. (2015a) who defined three distinct SST warm patterns: the extremely strong El Niño event, with large warming near the South American coast, the CP El Niño, a weak warm event centred near the dateline and the canonical El Niño event with moderate warming in the central-eastern Pacific. We will come back in more details on this classification in terms of amplitude (extreme versus moderate) closely related to the classification in terms of SST anomalies patterns (EP versus CP) in the chapter 3.

The different classifications agree that the observed El Niño events of 1983-83, 1997-98 and to a lesser extent 2015-16 are strong or extreme events (Takahashi et al., 2011; Santoso et al., 2017; Cai et al., 2017). However, even between extremes events with the same magnitude of SST anomalies across the central and eastern equatorial Pacific (L'Heureux et al., 2017) (see Niño-3.4 index in Fig. 1.5), the temporal and spatial evolutions of the tropical Pacific show important discrepancy (Abellán et al., 2017b). The anomalous warming of the 1997-98 El Niño develops in the eastern tropical Pacific in late boreal spring - early summer and then extends to the central Pacific the next winter. The anomalous warming of the recent El Niño event is less intense in the eastern Pacific and extends further west of the dateline. The associated precipitation field is even more contrasted with a spatial extension far eastward and a maximum of precipitation in the Niño-3.4 region in winter for the 1997-98 event while the displacement of the precipitation centre remains confined to the central Pacific with a maximum of precipitation located in the Niño-4 region in winter for the 2015-16 event (see spatial patterns in Fig. 1.5).

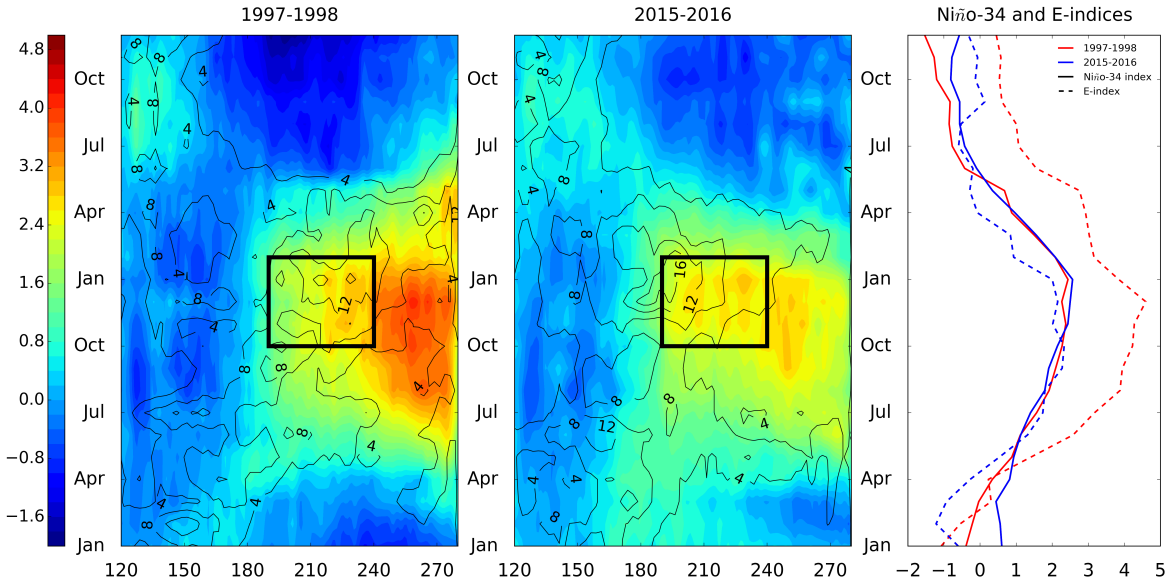

Figure 1.5 – Time-longitude sections of the equatorial band (2°S-2°N) SST anomalies (°C) for (left) the 1997-98 El Niño event and (middle) the 2015-16 El Niño event (HadISST v1 dataset). The contours represent the evolution of the precipitation (mm/day) with intervals every 4 mm/d (GPCP v2.3 dataset). On the right figure is shown the time-evolution of (solid lines) the Niño-3.4 index (SSTA averaged over 5°S-5°N, 190-240°E, black box of the left figures) and (dashed lines) the E-index during both events (1997-98 in red, 2015-16 in blue).

When using the E-index defined by Takahashi et al. (2011), differences between both events are significant (see E-index in Fig. 1.5): the maximal amplitude is of 2 °C greater for the 1997-98 event than for the 2015-16. The warm period of the 1997-98 El Niño, when the E-index is greater than 1.5 °C, lasts twice as long, from June 1997 to June 1998 when the 2015-16 event warm period lasts from July 2015 to January 2016. Finally, while the 1997-98 event presents a marked peak in December 1997, the 2015-16 event reaches a SST anomalies peak not as large but that persists more than the 1997-98 event. These differences of evolution of the E-index are reflected in the spatial pattern of the two events, with a significant warming in the extreme east of the Pacific Ocean (Niño-1+2 region) for the 1997-98 event (L'Heureux et al., 2017), the E-index explaining most of the variability of the eastern Pacific (see paragraph 3.2.2) when the 2015-2016 event had an important warming in the Niño-4 region in addition to the exceptional warming in Niño-3.4 region (Xue and Kumar, 2017; L'Heureux et al., 2017; Abellán et al., 2017b). Even if these two events are characterised as strong events, their temporal and spatial evolution is drastically different.

Williams and Patricola (2018) pointed out that the ONI index cannot effectively capture

the differences between the 1997-98 and 2015-16 El Niño events because the variation between them in the phase space PC1-PC2 is orthogonal to the variability explained by ONI (their figure 3a). Santoso et al. (2017) raised also the difficulty of defining strong El Niño since extreme El Niño, defined by Cai et al. (2014) from a threshold of precipitation in the eastern part of the tropical Pacific, does not necessarily propagate eastward as extreme El Niño events defined by Santoso et al. (2013) or McPhaden and Zhang (2009) do.

Thus, the El Niño classification into strong events may also depend on the metrics used. Similarly, the classification between CP and EP El Niños is dependent on the metrics used, as shown by Singh et al. (2011) and Jeong and Ahn (2017) in observations, or by Stevenson et al. (2017) using a large ensemble Coupled General Circulation Model (CGCM). These studies inter-compared different methods using several datasets. Singh et al. (2011) compared the "AS", "KY", "KU" methods among others to their Sea Surface Salinity (SSS) clustering. Jeong and Ahn (2017) compared "AS", "KY", "KU", "RJ" and "TD" methods. Stevenson et al. (2017) used the "KU", "KY" and Yeh et al. (2009a)'s methods.

The use of these different indices leads to different classifications of El Niño events type, which may question the validity of the results that estimate the projected evolution of El Niño statistics in a warmer climate. The use of simplified indices, useful for studying complex climate phenomena, is above all a tool for accessing the diversity of ENSO in a qualitative way. It must be kept in mind that compositing El Niño events via these metrics can mask significant differences between events of the same class.

Knowing that ENSO diversity causes different global impacts (see paragraph 1.1.3 and Larkin and Harrison (2005a); Ashok et al. (2007) among others) and may contribute differently to climate variability (see paragraph 1.3.2 and Lee and McPhaden (2010); Choi et al. (2012); Johnson (2013) among others), the characterisation of El Niño flavours by adapted metrics is crucial to understand their associated dynamics, from the atmospheric stochastic forcing to ENSO feedbacks (see section 1.2 of the chapter). The characterisation of the ENSO diversity is also of prime importance to estimate changes in frequency of occurrence of El Niño due to internal variability (see section 1.3) and due to global warming (see section 1.4).

1.1.2.4 A "wicked" problem

As mentioned by Christina Karamperidou at the recent ENSO conference in Guayaquil, Ecuador in 2018[2], ENSO is a "wicked" problem. A wicked problem is defined by its difficulty or impossibility to solve because of incomplete or contradictory knowledge and changing requirements that are often difficult to recognise[3]. The main feature of a wicked problem is that it has no definitive formulation, neither stopping rule, nor ultimate test of a solution. There is always more than one solution for a wicked problem, with the appropriateness of the solution depending greatly on the individual perspective of the designer of the solution. Taking into account the elements presented previously, it appears that ENSO diversity is difficult to define and can be assessed in many different ways, whether one want to diagnose the event's intensity or its spatial pattern for instance. This issue raises several questions.

How to define ENSO diversity? Which variable(s) should we use? Temperature or precipitation or more at once? Should the flavours be defined by their intensity or their spatial pattern? Should we analysed the climate variables at a fixed time, commonly during the mature phase of the events, or characterise their temporal evolution? If, conversely, the descriptive approach through climate variables is not the one chosen, should we rely on physical processes? If so, which ones? As long as one does not better understand the mechanisms that govern the different flavours of ENSO, it is difficult to consider putting forward a particular physical process. There is (for now) no definitive formulation for ENSO diversity and the many metrics proposed over the last twenty years reflect this ambiguity.

[2] http://www.ensoconference2018.org/
[3] Source: Wikipedia

An important underlying issue of the diversity definition is **how we should approach ENSO diversity?** As a **continuum representation** of an asymmetric phenomenon or as **two independent modes**? The underlying issue is to determine whether the two El Niño flavours involve different physics or can emerge fro the same dynamics.

The continuum view comes from the apparent continuous distribution of the longitudes of the ENSO SST anomalies peaks: El Niño and La Niña events have a large longitudinal distribution, and their anomaly centres intertwine. In this framework, weak or moderate El Niño and extreme La Niña have similar patterns with a broad range of longitudes while extreme El Niño are outliers with intense warming in the eastern Pacific. Johnson (2013), using observations over 1950-2011, suggested a framework representing ENSO as a continuum that can be explained by 9 statistically distinguishable patterns. In a CGCM capturing realistically ENSO diversity, the GFDL CM2.1 (see paragraph 2.1.2.1 for a description of the model), the peaks of the El Niño events shift eastward as they strengthen (Fig. 1.6a(b), reprinted from Capotondi et al. (2015)), a result also observed in the reanalysis dataset SODA v2.2.4 (see Figure 9a of Giese and Ray (2011) and paragraph 2.1.1 for a presentation of the reanalysis dataset). However, in the reanalysis dataset over the period 1871-2008, the central longitude of the ENSO warming is indistinguishable from a Gaussian distribution centred near 140°W (Giese and Ray, 2011) when a weak bi-modality appears in the pre-industrial (PI) control simulation of the CGCM (Fig. 1.6aa). Note that the centre of warming used by Giese and Ray (2011) is determined via the CHI index (see paragraph 1.1.2.2), which considers the warming over an area at least equal to the area of the Niño-3.4 region. The centre is calculated for each month of the event. In contrast, Capotondi et al. (2015) used maximum SST anomalies (5°S-5°N) in DJF to determine the associated longitude in the model. Although these two methods are not comparable, El Niño warming centres appear to occupy a wide range of longitudes. Fedorov et al. (2015) confirmed that CP and EP El Niños could be viewed as a continuum especially when focusing on the average warming magnitude and the anomaly heat centre rather than on the maximum SST anomalies and the exact longitude of this maximum. Characterising El Niños as strictly central or eastern events appears contradictory with this continuity in the distribution of longitudes (Giese and Ray, 2011; Johnson, 2013; Capotondi et al., 2015). Moreover, the spatial patterns of CP and EP events are often compared to the first two modes of the tropical Pacific variability obtained from an EOF analysis (Ashok et al., 2007). The second EOF mode, whose pattern may resemble CP El Niño spatial pattern (see paragraph 2.1.4.2 and Fig. 2.8), may rather be considered as a "modulator" for describing inter-event differences and requires a substantial projection onto the first EOF mode to appear. Indeed, an El Niño event may be considered as an appropriately weighted superposition of the two modes. Cai et al. (2015a) argued that this feature of ENSO involving both EOF modes represents a continuum. Another argument is that the existence of two modes of ENSO variability would imply the existence of different deterministic processes that favour one mode over the other. Lai et al. (2015) argued that observed El Niño events (1980-2013) form a continuum with CP and EP El Niño events at each end. The "location" of an El Niño event on this continuum depends on the respective value of two parameters, the zonal wind anomalies and the recharged state of the western Pacific (see paragraph 1.2.3.2). However, Newman et al. (2011) showed that the central and eastern Pacific variability associated with the two regimes may arise from natural random variation, as may the multidecadal variations in ENSO flavours characteristics (see paragraph 1.3.2). Note that they described ENSO flavours as different combinations of two orthogonal spatial patterns, precursors to CP and EP El Niño events and excited by stochastic atmospheric forcing, which can be assimilated to a continuum of mixed CP and EP patterns.

Conversely, numerous studies argued that EP and CP El Niños are distinct regimes because of the distinct seasonal evolution of their SST anomalies patterns, their distinct meteorological impacts, their distinct oceanic and atmospheric processes or their frequency change after the climate regime shift of 1977 (Ashok et al. (2007); Kao and Yu (2009); Kug et al.

(2010); Ren and Jin (2011) among many others). Ashok et al. (2007) raised first the question of whether the Modoki El Niño, with a pattern of warming in the central Pacific flanked by colder SST anomalies on both sides along the equator, is a part or not of El Niño evolution. They suggested that the two regimes are actually two major orthogonal modes of the ocean-atmosphere coupled system in the tropical Pacific. A comparative analysis of various linear and non-linear approaches and composite analysis techniques has been conducted on observed and reanalysed climate datasets to further investigate whether these regimes are two distinct phenomena (Marathe et al., 2015). In particular, they analysed the seasonal evolution of Modoki and canonical El Niño events and suggested that due to their distinct evolution in summer season, their persistent warming in central Pacific and their distinct teleconnections, Modoki El Niño events should be classified as distinct events. They called for considering the Modoki El Niño as a separate phenomenon, at least for the purpose of applications and impact studies. With a different approach, Ren and Jin (2011) showed that the two types of El Niño, named WP and CT El Niño in their study, may be considered as two independent modes of ENSO although the data is too short to be statistically significant. Indeed, the two modes correspond to different zonal propagation of ENSO SST anomalies and the climate shift in 1976-77 led to ENSO regime changes with the increase in CP ENSO regime.

The possible coexistence of two ENSO-like modes in the ocean-atmosphere coupled system under the present climate conditions was noted by Bejarano and Jin (2008). These modes resemble to the two observed regimes of ENSO. These two ENSO-like modes, called Quasi-Biennial (QB) and Quasi-Quadrennial (QQ), are further investigated in various studies in terms of dynamic processes or sensitivity to the mean state (Wang and Ren, 2017; Xie and Jin, 2018; Timmermann et al., 2018). These studies highlighted the role of the background state to be conducive in the preferential occurrence of one of the two modes. Especially, combining these previous results, Timmermann et al. (2018) suggested to apprehend ENSO complexity through the co-existence of two linear Eigen-modes, which can be derived from a deterministic, intermediate-complexity coupled model and a number of excitation mechanisms. This approach as well as its integration into the ENSO complexity, which has many others asymmetries, is discussed in paragraph 1.2.3.

However, one may argue that the dichotomy between EP and CP events is not well defined when using the different SST anomalies metrics presented above. The classification of some observed events depends on the methods used (see also chapter 3), suggesting that the longitudinal location of SST anomalies El Niño peaks is not an optimal variable to analyse ENSO diversity. Some suggested that other classifications than two spatial modes, such as moderate and extreme El Niño regimes, could be more relevant (Lengaigne and Vecchi, 2010; Takahashi et al., 2011; Takahashi and Dewitte, 2016; Takahashi et al., 2018). The diversity of El Niño and more generally of ENSO may thus be the response of the system to non-linearities as suggested by Takahashi et al. (2011) and Dommenget et al. (2013) (see also paragraph 1.2.2). When increasing the number of ENSO statistics through the use of long CGCM simulations, Takahashi et al. (2011) noticed a marked anisotropy of the main modes of variability of the tropical Pacific, and therefore ENSO. The phase space of the principal component (PC) timeseries associated with the two main EOF modes presents indeed a boomerang shape, revealing the non-linearity of the coupled system (see also Dommenget et al. (2013); Karamperidou et al. (2017) and the paragraph 2.1.4.5). They suggested that La Niña, weak and strong El Niño, EP and CP El Niño are part of the same non-linear phenomenon rather than independent modes of variability. No privileged cluster of Modoki or CP El Niño events appears in the ENSO phase space. However, when focusing on El Niño events solely, a bi-modality in the E-C phase space is revealed in the model, corresponding to the moderate and strong El Niño regimes (Fig. 1.6b). This bi-modality in the SST peaks distribution during El Niño events is suggested in observations (solid circles in Fig. 1.6b) even if the record of El Niño events is too short to statistically reject the null hypothesis of a uni-

(a) Longitudes bivariate distribution

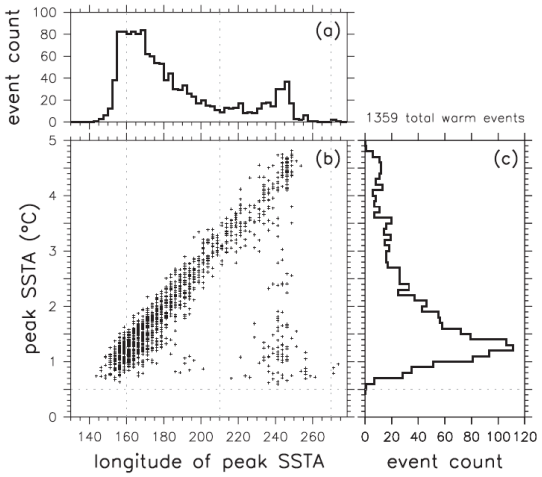

(b) El Niño asymmetry

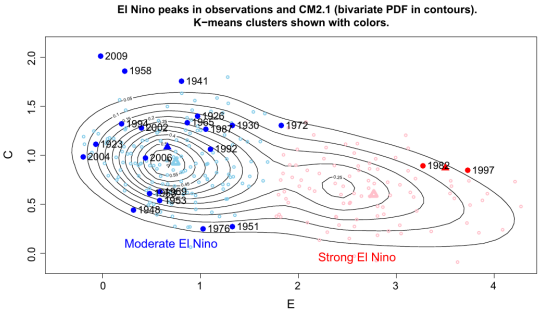

Figure 1.6 – (Fig. 1.6a) Distribution of the equatorial (5°S-5°N) DJF SST anomalies during El Niño events in GFDL CM2.1 PI-control simulation (4000 years). An El Niño event is defined when DJF Niño-3 SSTA exceeds 0.5 °C. (a) Distribution of peak SSTA longitudes (°E). (b) Scatterplot of the peak SSTA value (°C) vs the longitude (°E) at which it occurs. (c) Distribution of peak SSTA values (°C). The figure is reprinted from Capotondi et al. (2015). (Fig. 1.6b) Bivariate E-C probability density function of the El Niño peaks for GFDL CM2.1 PI-control and 20th century simulations (open circles). Observed El Niño peaks (HadISST, 1920-2013) are indicated in solid circles with the year corresponding. Reprinted from Takahashi and Dewitte (2016).

modal distribution based on observations alone. Recently, Takahashi et al. (2018) confirmed that the two El Niño regimes, moderate and strong, exist in a simplified model (recharge-discharge model, see paragraph 1.2.1.2) in which a single non-linearity is introduced.

As a response to the rising debate, the strong El Niño of 2015-16 occurred. Its positive SST anomalies have potentially exceeded the previous records observed in the Niño-3.4 region (L'Heureux et al., 2017; Xue and Kumar, 2017; Dewitte and Takahashi, 2017), classifying it as a strong El Niño event by the amplitude. However, the warming in the far eastern Pacific were not so pronounced (Fig. 1.5), which did not cause the convection to move as much in the eastern Pacific as during the other two observed strong EP El Niño events. As a result, the 2015-16 El Niño event did not have the expected rainfall impacts in Ecuador and Peru (Sanabria et al., 2018). The event was followed by a weak La Niña event whereas usually strong El Niños are followed by strong La Niñas. The 2015-16 El Niño may appear rather like an EP-CP hybrid El Niño (Paek et al., 2017) with wet conditions in the central Pacific or like a moderate-strong hybrid El Niño with an eastern Pacific signature not so pronounced.

Finally, **should we consider ENSO as two independent spatial modes modulated by the background state or as two modes arising from the non-linearities in the coupled system?** Chen et al. (2015a) proposed to reconcile the debates between the two different views, spatial versus amplitude. In their framework, ENSO appears to be a symmetric, canonical cycle in the central to eastern equatorial Pacific, representing a large portion of El Niño and La Niña events. Superimposed on this basic cycle are rare extreme El Niño events in the eastern Pacific, triggered by non-linearities or stochasticity, and weak but more frequent warm events near the dateline, forming the different flavours of El Niño. This approach adds a flavour to El Niño compared to the view of Takahashi et al. (2011); Takahashi and Dewitte (2016) and Dewitte and Takahashi (2017). The latter argued that CP El Niño and the canonical El Niño are the components of the same broad central-to-eastern Pacific phenomenon and that the El Niño phenomenon as a whole also includes some extremely strong EP El Niño.

Chen et al. (2015a) remind however that any classification is to some extent subjective, and is often chosen based on practical convenience rather than rigorous mathematics. A

minimal criterion for a valid classification is consistent with the physical picture from our current understanding of El Niño dynamics but therefore is evolving. Better understanding of the underlying processes will only improve it.

1.1.3 Impacts and teleconnections

ENSO exerts profound impacts that extend well beyond the Pacific basin. It affects global weather patterns through thermal exchanges during the displacement of the warm waters of the Pacific. The relocation of the convective areas of the Pacific disrupts the teleconnections of the tropical atmospheric circulation patterns with the mid-latitudes, which in turn modifies the mid-latitude jet streams and influences more distant areas.

El Niño events have large impact, whether in precipitations (Ropelewski and Halpert, 1987) than in surface temperature (Halpert and Ropelewski, 1992). Their impacts have been widely studied and resumed in Figure 1.7. The reorganisation of the tropical thermal machine disrupts weather particularly around the Pacific basin. In boreal summer (Fig. 1.7, bottom panel), it is known to cause serious droughts in north-eastern Australia, Indonesia and India, perturbing the monsoon in these places, causing eventually huge forest fires. In boreal winter (Fig. 1.7, top panel), it causes important precipitation in Ecuador and coastal Peru, as well as in the south-west of the USA, which can lead to floods and landslides. Conversely, it induces precipitation deficits over the northern part of South America, Indonesia and Australia. It alters biogeochemical activity through the decrease in the upwelling off the South American coast, which has repercussions on fishing activities, especially on anchovy fishing, one of the main driver of the Peruvian economy. The 1982-83 (Philander, 1983) and 1997-98 (McPhaden, 1999) extreme El Niño events were the most impacting and destructive. They were accompanied with devastating floods in Peru, severe droughts and forest fires in southeast Asia, disappearance of marine life and native bird populations of the Galapagos as well as severe coral bleaching in the Pacific, impacting marine and terrestrial ecosystems, agriculture, freshwater supplies, hurricane activity and other severe weather events worldwide (Goddard and Dilley, 2005; McPhaden et al., 2006).

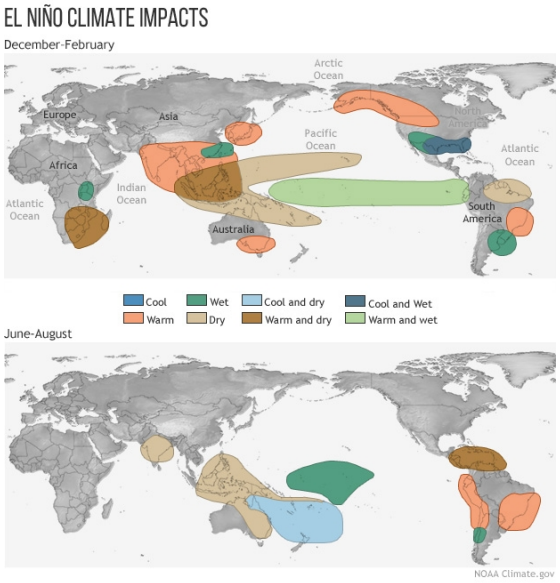

Figure 1.7 – El Niño common impacts around the world in (top) boreal winter and (bottom) boreal summer (Reprinted from NOAA Climate.gov[4]).

However, CP El Niño has a different footprint on regional climates worldwide (Larkin and Harrison, 2005b; Ashok et al., 2007; Yeh et al., 2009a). Central Pacific El Niño is associated

[4] www.climate.gov

with globally cool temperatures, except for parts of South America. During CP El Niño, northern India receives wet conditions in boreal summer and Australia experiences severe droughts. CP El Niño conditions intensify also the genesis of tropical cyclones over the western North Pacific during boreal summer since the early 1990s (Chen and Tam, 2010; Kim et al., 2011; Liu and Chen, 2018) as well as over the South China sea (Chen, 2011). These different impacts are explained by the sensitivity of the atmosphere to the oceanic warming. SST patterns are essential for determining the atmospheric response, particularly in the Warm Pool region, where subtle SST variations may have large impacts on the location and intensity of latent heat release in the atmosphere and thus on the global atmospheric circulation. Therefore, due to the potential combination of atmospheric sensitivity and anomalous warming in an already warm climatological region, the central Pacific plays a central role in remote off-equatorial impacts. Thus, even if CP El Niño events have smaller zonal scales and weaker SST anomalies than EP El Niño events, the atmospheric response to the SST anomalies is stronger indicating stronger teleconnections between Tropics and mid-latitudes (Weng et al., 2009).

But even strong El Niño events do not always have the expected impacts, such as the normal Indian summer monsoon rainfall in 1997 (McPhaden et al., 2010). External influences such as in that case the co-occurrence of an Indian Ocean Dipole or changes in decadal variability between ENSO and the monsoons (Kumar, 1999) may interfere. Predicting climate impacts associated with ENSO outside the tropics is likewise problematic because weather noise can obscure teleconnections from the tropics.

Finally, ENSO teleconnection can be systematically strengthened over many land regions with global warming, leading to increased inter-annual variability in regional temperature extremes and wildfire frequency (Fasullo et al., 2018). For instance, the strong 2015-16 El Niño event prolonged the longest global coral die-off started in 2014 due to record ocean temperatures and highly enhanced tropical cyclone activity (Brainard et al., 2018). All of these impacts usually accompany El Niño events but are reinforced by the SST background warming, likely due concomitantly to global warming and the positive phase of the Pacific Decadal Oscillation.

1.2 ENSO's theories

In the first part of this section, we present the canonical view of the ENSO quasi-oscillation, which develops under the influence of the Bjerknes air-sea coupled feedback. The positive anomalies will be offset by several negative feedbacks. Amongst them, the recharge-discharge oscillator is now a widely accepted paradigm to explain the delayed negative feedback due to oceanic processes, which eventually terminates the ENSO event. However, strong asymmetric features due to numerous multi-scales interactions and non-linearities make ENSO more complex than this simplified quasi-oscillatory theory. The second part of this section will attempt to present the main causes suspected of introducing asymmetries into the ENSO system.

1.2.1 The canonical view of ENSO

1.2.1.1 Growth of anomalous warming

Anomalous warming in the central-to-eastern equatorial Pacific is chosen as a starting point. By reducing the zonal SST gradient along the equator, the warming weakens the trade winds further reducing the zonal SST gradient. The direct response of the trade winds to zonal contrast of SST is the atmospheric component of the positive (amplifying) **Bjerknes feedback**.

The weakening of the trade winds also flattens the mean thermocline, deepening it in the eastern Pacific, and reduces the wind-driven equatorial upwelling, causing warming in the

eastern Pacific, decreasing the zonal SST gradient, which further weakens the trade winds.

Other positive feedbacks amplifying the warming in the eastern Pacific complement the Bjerknes feedback. The weakening of the trade winds increases the advection of warm waters of the Warm Pool towards the east and amplifies the initial warming: this is the **zonal advection feedback** or the zonal advection of mean SST by the anomalous current. The weakening of the upwelling reduces the vertical advection of deep cold water to the surface in the eastern Pacific and amplifies the initial warming: this is the **upwelling feedback** or the vertical advection of mean temperature by the anomalous vertical current. The deepening of the thermocline in the eastern Pacific results in warm surface water being spread over a greater depth in subsurface. Subsurface water upwelled are warmer than usual, which amplifies the initial warming: this is the **thermocline feedback** or the vertical advection of anomalous subsurface temperature by the mean upwelling.

It should be noted that coupling air-sea interactions are strong in the western Pacific (Picaut et al., 1997) while interactions between SST and thermocline depth are strong in the eastern Pacific (Vialard et al., 2001), which influences the balance between the different processes involved.

These positive ocean-atmosphere instabilities lead to a never ending warm state. The reverse situation with negative anomalies leads in the same way to a cooler permanent state (La Niña-like). A negative feedback is needed to turn the system around.

1.2.1.2 ENSO wave theories

In the 1980s and 1990s, the understanding of El Niño has progressed a lot thanks especially to the development and spread of observation network over the tropical Pacific (TOGA, McPhaden et al. (2010)) then satellite observations. New theories have emerged based on a mechanistic approach through highly parameterised simplified coupled models to explain the quasi-oscillatory nature of ENSO. In particular, linear theories based on equatorial wave theory introduced negative oceanic feedbacks.

Four conceptual ENSO oscillator models have been proposed: the delayed oscillator (Suarez and Schopf, 1988; Battisti and Hirst, 1989), the recharge oscillator (Jin, 1997a,b), the western Pacific oscillator (Weisberg and Wang, 1997), and the advective-reflective oscillator (Picaut et al., 1997). These oscillator models emphasise negative feedbacks on SST anomalies of respectively the delayed effect of reflected Kelvin waves at the ocean western boundary, a discharge process due to Sverdrup transport, western Pacific wind-forced Kelvin waves, and anomalous zonal advection. These negative feedbacks may work together for terminating El Niño warming, as suggested by the unified oscillator (Wang, 2001). In these models, the system oscillates owing to the presence of a fast positive feedback (e.g. the Bjerknes feedback), which causes the growth of El Niño and of a slow negative feedback (the slow adjustment of the ocean) that reverses the initial growth into its opposite phase. The oscillatory nature of ENSO can therefore be linked to the coupled nature of the equatorial ocean-atmosphere system, in which the ocean provides the memory of the system. We detail here the delayed oscillator as well as the widely used recharge-discharge paradigm. We invite the reader to refer to Wang and Picaut (2004) for a review of the main theories on these coupled oscillations and a discussion on their interaction with the shorter time-scale variability. The French-speaking reader can also refer to the thesis of Boucharel (2010).

Wyrtki (1975), observing a strengthening of the trade winds in the central Pacific the years preceding a warm event, first hypothesised that this resulting accumulation of warm water in the western Pacific (build-up) were part of the onset of El Niño. When the system reaches a critical state, a relaxing of the trade winds is enough for the accumulated warm waters to move towards the east in the form of Kelvin waves. He suggested that at the end of the warm event, these waters are redistributed to higher latitudes, especially along the coasts of South America. Cane and Zebiak (1985) suggested that this recharge of warm water in the western Pacific is a pre-conditioning ocean state necessary for the onset of a warm event.

The **delayed oscillator** (Suarez and Schopf, 1988; Battisti and Hirst, 1989) resuming the idea of a displacement of warm waters through Kelvin waves, also proposed a negative feedback by free propagation of equatorial oceanic waves (Fig. 1.8). A relaxing of the trade winds, which can even go as far as positive westerly wind anomalies, near the dateline in the central Pacific, generates equatorial downwelling Kelvin waves towards the east and upwelling Rossby waves toward the west. A downwelling Kelvin wave is an eastward propagating oceanic internal wave (∼3 m/s) that deepens the thermocline. An upwelling Rossby wave is a westward propagating oceanic internal wave (∼1 m/s) that shoals the thermocline and is characterised by two symmetric anomalies on both sides of the equator. The downwelling Kelvin waves deepen the thermocline in the eastern Pacific and reduce the efficiency of climatological upwelling, which warms the surface layer. The weakened zonal SST gradient then reinforces the original wind anomalies. Instability of the coupled ocean-atmosphere system is initiated, favouring the Bjerknes feedback. The upwelling Rossby waves generated by the initial warming in the central Pacific reflect at the western boundary of the equatorial Pacific as upwelling Kelvin waves, which counter the effect of the downwelling Kelvin waves by progressively shoaling the thermocline and cooling the SST. They can reverse positive SST anomalies and help start a cold event. The propagation of Kelvin and Rossby waves at different speeds explains the delay between fast positive feedback, by forced downwelling Kelvin waves, and slow negative feedback, by reflected upwelling Kelvin waves, giving the name to the delayed oscillator. The delayed oscillator states that ocean subsurface adjustment due to individual free Kelvin and Rossby waves provide memory of the oscillation between warm and cold phases. It should be noted that in reality the winds excite a continuum of waves rather than a few isolated ones.

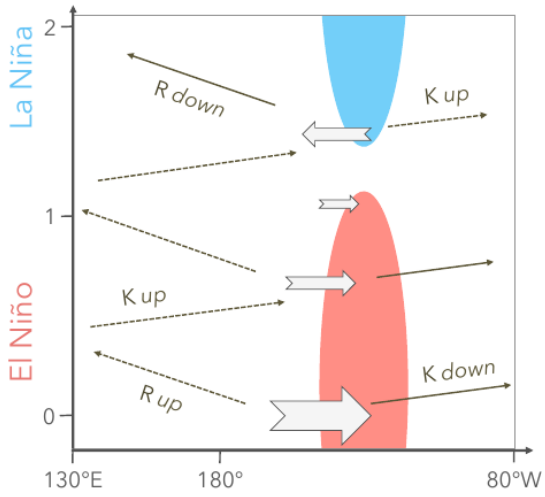

Figure 1.8 – Schematic diagram of the delayed oscillator. Positive SST anomalies (red) in the equatorial eastern Pacific cause westerly wind anomalies (large arrows) that drive downwelling Kelvin waves (thin solid arrow) eastward and act to increase the positive SST anomalies. The westerly wind anomalies also generate oceanic equatorial upwelling Rossby waves (thin dashed arrow), which propagate westward and eventually reflect from the western boundary as equatorial Kelvin waves. Since the thermocline anomalies for the reflected upwelling Kelvin waves have an opposite sign to those of the directly forced downwelling Kelvin waves, they provide a negative feedback for the coupled system to oscillate. (Reprinted from Saint-Lu and Leloup (2016), adapted from Wang and Picaut (2004)).

This mechanism is responsible for the low-frequency behaviour observed in the simplified coupled model of Zebiak and Cane (1987), which has successfully predicted El Niño event onsets and is still widely used in more complex forms in the study and prediction of ENSO (Neelin and Jin (1993); Fedorov and Philander (2000); Bejarano and Jin (2008) among many others). Many observational studies have attempted to confirm the theory and point out that while the termination of El Niño events has consistently occurred with the cyclic nature of the delayed oscillator (Boulanger and Menkes, 1999), their initiation is less obvious (Kessler and

McPhaden, 1995), which led Mantua and Battisti (1994) to limit the role of wave reflections on the western edge of the Pacific to the termination of the El Niño events. However, Boulanger (2003) demonstrated that 80 % of the Kelvin wave signal at 175°E over the observation period of 1993-2001 is wind-induced rather than being the adjusted contribution of the Rossby wave reflection suggested by the delayed oscillator.

The **recharge-discharge (RD) oscillator** (Jin, 1997a,b), a widely accepted paradigm of ENSO dynamics, is based on the oceanic heat transfer from the equatorial region toward the off-equatorial regions and vice-versa (Fig. 1.9). Echoing the ideas of Wyrtki (1975) and Cane and Zebiak (1985), Jin (1997a,b) proposed that the fundamental mechanism of ENSO oscillation is the delay between the adjustment of SST anomalies and that of the heat content over the entire basin. During an El Niño event (I), westerly wind anomalies decrease meridionally with latitude and the resultant wind stress curls drive meridional subsurface ocean transport, the zonally integrated Sverdrup transport (solid thick arrows). The meridional transport slowly discharges the equatorial heat content (characterised by the depth of the thermocline, to access the Warm Water Volume, WWV) poleward, which results in a homogeneous abnormally shallow thermocline at the end of the discharge (II). It allows cold water being pumped to the surface through the mean climatological upwelling in the eastern Pacific, which initiates the cold phase of La Niña (III). The greater zonal SST gradient and thus easterly anomalies cause equatorward heat content recharge through Sverdrup transport (IV) and possibly the repositioning in El Niño phase (I). The slow adjustment of the ocean is characterised through two zonal modes of the thermocline depth: the tilt mode (I and III) and the WWV mode (II and IV). Recharge-discharge processes play key role in initiation and termination of El Niño events.

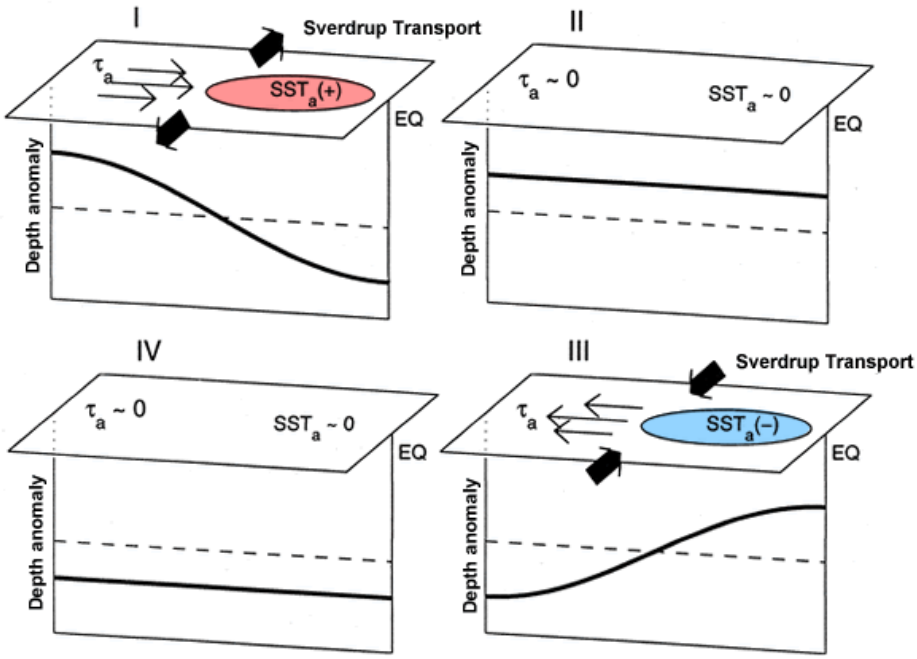

Figure 1.9 – Schematic diagram of the recharge oscillator. The four phases of the recharge-discharge oscillation: (I) the warm phase, (II) the warm to cold transition phase, (III) the cold phase, and (IV) the cold to warm transition phase (Reprinted from Meinen and McPhaden (2000) and adapted from Jin (1997a)).

Clarke et al. (2007) proposed a RD oscillator differing in that it emphasises the recharge-discharge of ocean heat content in the west-central Pacific region, rather than in the eastern Pacific. Jin and An (1999) proposed an extension of the RD oscillator by explicitly including the zonal advective feedback (ZAF) when previous oscillators focused on one oceanic feedback alone, the thermocline feedback (TCF) (Suarez and Schopf, 1988; Battisti and Hirst, 1989; Jin, 1997a,b) or the zonal advective feedback (Picaut et al., 1997) (see paragraph 2.3.1.4 for

the expression of these heat advection terms). They showed that both feedbacks are dynamically connected through the geostrophic balance between the upper-ocean zonal currents and the meridional gradient of the thermocline depth. They suggested that the two feedbacks contribute equally to the growth and transition of ENSO (An and Jin, 2001).

The RD paradigm is more general than the delayed oscillator by not relying explicitly on equatorial wave propagation. But the mechanism remains fundamentally the same, in both cases representing the slow adjustment of the equatorial ocean to wind anomalies (slow relative to the 2-3 months basin-crossing time of the Kelvin waves). In the case of the delayed oscillator, Rossby waves and their reflection are the means by which mass is added or removed from the equatorial surface layer. In the case of the RD oscillator, a disequilibrium between zonal winds stress and zonal-mean equatorial thermocline depth drive meridional convergence or divergence of Sverdrup transport. One interest of the RD oscillator formulation is that variables may be assessed easily in observations. Moreover, the zonal mean warm water volume (essentially Wyrtki's build-up) being in quadrature with east Pacific SST leading by about a quarter of the period of the oscillation, is a good predictor of ENSO (Meinen and McPhaden, 2000). Positive (negative) peaks of warm water volume anomalies produce then the transition from El Niño to La Niña (and vice-versa), with the memory of the system in the zonal mean thermocline depth. Meinen and McPhaden (2000) showed that the RD processes are observable, even if not symmetric. However, Kessler (2002) showed in observations that the coupled system is able to remain in a weak discharged La Niña state for up to two years, so that memory of previous influences would be lost. Moreover, the role of the western Pacific equatorial heat content, rather than the mean equatorial heat content along the entire Pacific, is recently again put forward (Boschat et al., 2013; Izumo et al., 2018). We return to some limitations of this schematic in paragraph 1.2.2.1.

Despite their relative simplicity, simplified oscillators models have forecast skills comparable to those of more complex models (Latif, 1998). They describe reasonably well ENSO dynamics, especially the termination of El Niño events, despite some intrinsic limitations indicated previously. However, being essentially linear, they are not sufficient to explain the complexity of the phenomenon, especially the cause of the observed irregularities in ENSO. Each El Niño event is different in terms of growth, development and decay, both temporally and spatially. The oscillatory theories do not explain the irregular frequency of occurrence of ENSO, asymmetries between warm and cold events, in magnitude and duration, or the asymmetrical phase transition. Indeed, El Niño events can reach larger amplitudes than La Niña events (Hoerling et al., 1997) but La Niña generally lasts longer (Okumura and Deser, 2010). El Niño events are often followed by La Niñas, while La Niña events are less frequently followed by El Niños (Kessler, 2002; Yu et al., 2010b). It seems however that CP El Niños are less followed by La Niñas than EP El Niños (Kao and Yu, 2009; Kug et al., 2009).

For instance, an indicator of the amplitude asymmetry between El Niño and La Niña is the skewness of SST anomalies-based ENSO indices. The skewness is the third moment of the probability distribution function of a variable and quantifies whether the distribution tails are long or short, thick or thin (see paragraph 2.2.1.1). Despite the apparent normality of the distribution of the Niño-3.4 index (top inset in Fig. 1.10), the skewness along the equator turns from slightly negative in the western-to-central Pacific (in Niño-4 region, it is equal to -0.5) to highly positive in the eastern Pacific, quantifying the fact that El Niño events reach larger amplitudes than La Niña events (Fig. 1.10). When removing the contribution of the extreme El Niño (4 events) and La Niña (7 events), the skewness decreases severely, demonstrating the non-linear nature of strong ENSO events.

Dommenget et al. (2013) showed that ENSO skewness is not only a characteristic of the amplitude asymmetry of events (El Niño events being stronger than La Niña events) but also of the spatial pattern and time evolution of ENSO. Their spatial patterns are asymmetric with strong (moderate) La Niña events in the central (eastern) Pacific and strong (moderate) El Niño events in the eastern (central) Pacific (Schopf and Burgman, 2006; Kao and Yu, 2009;

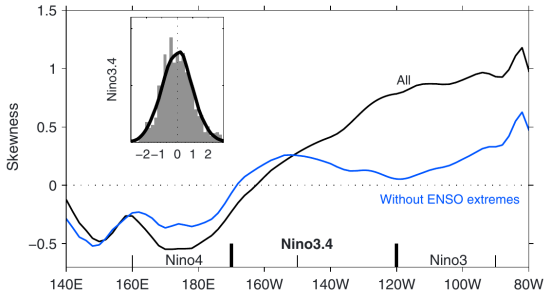

Figure 1.10 – Skewness of SST anomalies along the equatorial Pacific from 1950 to 2016 (black line) and comparison when strong ENSO (El Niño and La Niña) events are removed (blue line). The developing and decaying years (that is 12 months before and after the winter peak) of the strongest ENSO events are removed from the calculation of the skewness. The strong events are the 1972-73, 1982-83, 1997-98, 2015-16 El Niño, and the 1973-74, 1975-76, 1988-89, 1998-99, 1999-00, 2007-08, 2010-11 La Niña events. Inset shows histogram of standardized Niño-3.4 anomalies (grey shading), with the overlaid black curve indicating histogram of 10,000 random numbers generated from a normal distribution. (Reprinted from Santoso et al. (2017)).

Frauen and Dommenget, 2010; Yu et al., 2010b). Non-linear effects are neglected completely in oscillatory theories, although non-linearities cause the asymmetry between El Niño and La Niña events (An and Jin, 2004; Frauen and Dommenget, 2010).

Finally, ENSO spectrum does not show marked peaks at very specific frequencies but seems continuous and must certainly correspond to a very large number of excited modes. For instance, oscillatory theories do not take into account interactions with the seasonal forcing, that will disrupt inter-annual variability by favouring the phase locking of the events on the seasonal cycle, especially contributing to the termination of the events (Lengaigne et al., 2006; Lengaigne and Vecchi, 2010; McGregor et al., 2012; Stein et al., 2014).

All of these sources of non-linearities are discussed in the following paragraphs 1.2.2, 1.2.3 and section 1.3.

1.2.1.3 Coupled instabilities theory

Other theories seek in the ocean-atmosphere coupled modes themselves the origin of frequency oscillations compatible with those of ENSO. The ENSO cycle is partly due to a destabilisation of mean circulation, and the coupled instabilities approach allows us to consider this relationship. In these linearised ENSO models, the prescribed mean state acts as a source of energy for anomaly growth, controlling the spatial and temporal scales of the simulated ENSO cycle (growth rate, oscillation period, spatial structure, propagation). These theories identify negative and positive feedbacks in the equatorial Pacific that may trigger El Niño and La Niña events and the transition between them. Dominant instabilities from the ocean-atmosphere coupled system are identified for which a slight disturbance is potentially the most likely to develop.

The description of instabilities is generally understood through linear stability analysis, which is the Eigen modes analysis of a simplified coupled model, linearised with respect to a climatological basic state. The spatial and temporal scales of variability are then determined through the dominant instabilities of the linearised system, that is the leading coupled modes issued from linear stability. The objective is to study the tendency of the model to favour one coupled mode of oscillation over the other in response to changes in basic parameters of the mean state, such as intensity of the trade winds, thermocline depth, or temperature difference across the thermocline. Thus, they permit the exploration of the phase space of the ENSO mode (Neelin et al., 1998).

The temporal stability analysis of models has allowed the identification of various types of coupled modes of the equatorial Pacific. They are usually classified depending on the physical processes involved. Neelin and Jin (1993) classified coupled instabilities according

to the adjustment time of each of the coupled system components, which explain the low-frequency behaviour of numerous coupled models. They identified the spatial and temporal characteristic scales of three important dynamical and thermodynamical mechanisms for the ocean-atmosphere coupled system: the air-sea coupling ("coupling parameter"), the SST adjustment time to feedback and damping processes, and the "surface layer parameter" which governs the adjustment time to vertical advection. They distinguished two coupled modes:

- the fast-SST regime where the adjustment time of SST to coupled system is fast compared to the adjustment time of the ocean dynamics, and
- inversely, the fast-wave regime, or slow SST mode, where the velocity of the waves is infinite and the dynamic adjustment time of the ocean to wind variations through equatorial waves is fast compared to the thermodynamic adjustment time of the coupled system. The ocean is then in equilibrium with the wind.

The second mode gives a different view of the coupled system in which the slow adjustment of the ocean is secondary. The temporal scales of ENSO depend on the dynamic adjustment of the ocean but also on the thermodynamic adjustment of the mixed layer. Neelin et al. (1998) indicated later that the slow SST mode is closely related to the delayed oscillator, which does not involve coupling in the western Pacific and for which equatorial waves are responsible for time scales of dynamic and thermodynamic conditions. In nature, the observed (canonical) ENSO is in fact mixed fast-SST/wave modes of delayed oscillator type, for which ocean dynamics play an important role in the evolution of SST and ocean-atmosphere coupling.

Fedorov and Philander (2000, 2001) and An and Jin (2001) classified coupled instabilities through two oceanic processes important for the air-sea coupling in the tropical Pacific:

- the thermocline processes: the variability of the thermocline depth as well as the entrainment of water across the thermocline modify the sea surface temperature, in particular a deepening of the thermocline warms sea surface waters by decorrelating the upwelling of deep cold water from the mixed layer;
- the zonal advection processes: zonal currents bring heat through mean zonal temperature gradient.

Fedorov and Philander (2001) and An and Jin (2001) further suggested that the relative strength of these two processes could lead to different regimes of ENSO in terms of amplitude, frequency and propagation.

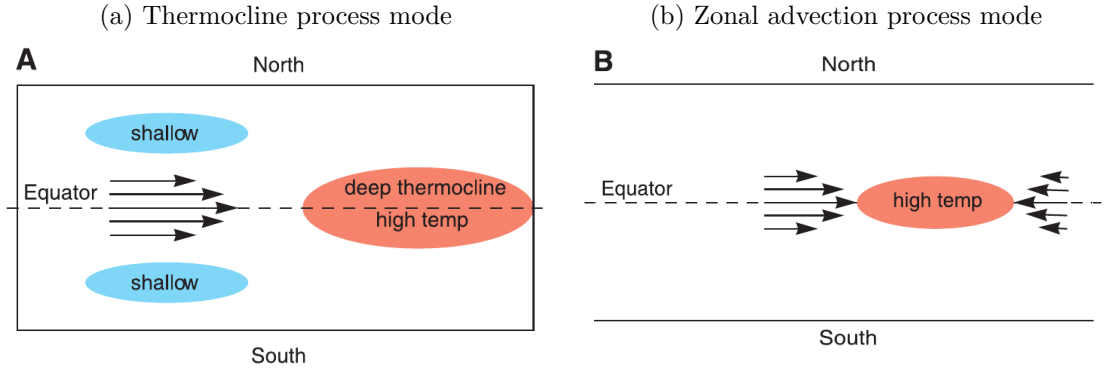

Figure 1.11 – Schematic diagrams of the spatial structure of the two idealized modes resulting from the stability analysis of Fedorov and Philander (2000, 2001). Arrows indicate winds, shaded areas show changes in thermocline depth ("temp" refers to surface temperature). These conditions, during El Niño, correspond to departures from a background state. 1.11a shows the mode associated with the thermocline process, known as the delayed oscillator. 1.11b shows the mode associated with the zonal advection process. Reprinted from Fedorov and Philander (2000).

Fedorov and Philander (2001) identified two unstable modes of coupled instabilities associated with these processes (Fig. 1.11). Thermocline processes induce remote feedback with SST variations occurring mainly in the eastern Pacific, in response to vertical movements of

the thermocline induced by wind fluctuations in the western Pacific. This mode is part of the adjustment of the ocean basin to wind variations, similar to that described in oscillatory models and often referred as the delayed oscillator mode. It has long periods of several years ($\sim$ 5 years) and a slight eastward propagation. Zonal advection processes induce a local coupled instability, propagating slowly westward. It does not involve any vertical movement of the thermocline but depends on the entrainment of cold water across a shallow thermocline. Winds that converge towards a warm disturbance can cause cooling on its eastern side (by westward advection and upwelling of cold water) and warming on the western side. The resultant local mode is associated with relatively short periods of one or two years. It is referred to as the SST mode. The low-frequency (high-frequency) mode is prominent when the background state has a deep (shallow) thermocline. Both require zonal winds of a certain intensity, to elevate the thermocline in the east in the case of the delayed oscillator, to create zonal temperature gradients in the case of the local mode. Fedorov and Philander (2001) suggested that ENSO is a hybrid type of these two modes whose properties change gradually with time as the background state changes.

An and Jin (2001) showed in their conceptual model that the two feedbacks tend to contribute to the growth and phase transition of ENSO for different strengths of the air-sea coupling, which characterises the intensity of the wind stress response to SST anomalies. However, these two feedbacks control the leading coupled mode in different ways. The main consequence of these sensitivities is that the growth rate and frequency of the ENSO mode may be sensitive to slight changes in basic-state parameters, which control the strength of these feedbacks.

The results from Fedorov and Philander (2000) and An and Jin (2001), even if they slightly differ in formalism (focus on the importance of the mean thermocline rather than the mean upwelling in Fedorov and Philander (2000)) resemble and confirm the importance of the mean state and the associated balance between the thermocline feedback (TCF) and the zonal advective feedback (ZAF) upon ENSO frequency.

Various studies have subsequently investigated these coupled modes, using a more complex Zebiak-Cane model (Zebiak and Cane, 1987) on which the stability analysis is based (Bejarano and Jin, 2008; Xie and Jin, 2018). They are discussed in the paragraph 1.2.3.1.

It is interesting to note that this approach reconciles all the theories reviewed previously, and, in particular, the possibility of the system to evolve from one mode of variability to another.

1.2.1.4 Is El Niño episodic or cyclic?

In the framework of the theories presented previously, processes involved in the ENSO cycle are shown schematically in Figure 1.12.

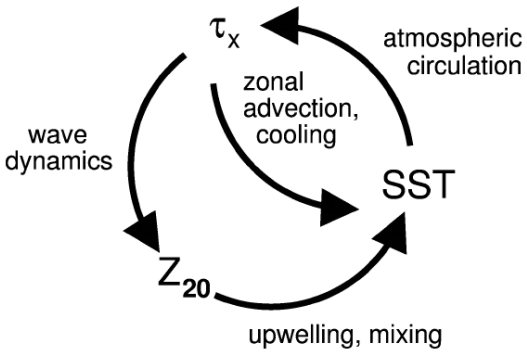

Figure 1.12 – Main positive feedbacks in ENSO as a cycle. Z_{20} denotes the thermocline depth through the depth of the isotherm 20 °C and τ_x denotes the zonal wind stress (Reprinted from Zelle et al. (2004)).

SST variations are still chosen as a starting point. Positive SST anomalies in the eastern equatorial Pacific change the strength of the trade winds, mainly in the central Pacific. This change directly influences local SST through anomalous zonal advection, Ekman pumping (upwelling of cold water), evaporative cooling and mixing (see also paragraphs 1.2.2.4 and 1.2.3.1). The reduction, or even reversal, of the trade winds also produces eastward Kelvin waves, which deepen the thermocline and warm the SST in the eastern Pacific, completing the cycle.

This loop of positive feedbacks requires to be reversed, through the discharge paradigm for instance. The oscillatory feature of ENSO is then explained by a growth through positive Bjerknes feedback and a phase transition through a delayed negative feedback. What does not appear explicitly in this diagram is that the loop is never the same for each event, in intensity, in spatial location or in temporal evolution. Moreover, an El Niño event rarely follows a La Niña event, not supporting a cyclic view of ENSO. The irregularities of ENSO, visible also in its broad inter-annual power spectrum, spanning 2-7 years per cycle, arise from non-linearities in the coupled system or from external influences, within a certain background state (see paragraphs 1.2.2 and 1.2.3). Their integration in the system depends on how to apprehend ENSO:

- as a *self-sustained, unstable oscillatory mode* of the coupled ocean-atmosphere system (Zebiak and Cane, 1987; Jin, 1997a; Meinen and McPhaden, 2000; Chen et al., 2004). In that case, the system uses an external source of power, without any corresponding periodicity, to maintain. The system itself modulates the phase at which the external source of power acts on it. A negative damping term is included in the system and causes an exponential growth over time of the amplitude of small perturbations, until the non-linearities of the system become important and limit their amplitude. The system, unstable enough, may be therefore self-regulated by internal non-linear processes whose characteristics (period, magnitude, spatial pattern) are determined by the background state. In that case, the system is sensitive to initial conditions due to its non-linearities, its predictability is thus limited;
- as a *stable weakly damped oscillatory system* maintained by random disturbances such as the atmospheric noise (Philander and Fedorov, 2003); The movement of the system is due to external forcing, necessary to maintain its variability.
- as a succession of independent and episodic events triggered randomly in a *strongly damped system* (Wyrtki, 1975; Kessler, 2002; Neske and McGregor, 2018). In that case, the stochastic atmospheric forcing is the essential El Niño trigger and random triggers at different times result in the impression of a continuous oscillation. ENSO is then only a direct response to random disturbances and becomes difficult to predict because it is controlled by atmospheric noise.

These two first views integrate that ENSO is a deterministic phenomenon. For each initial condition at time t_0, there is a single possible state at each next time-step. Even if the dynamic system is non-linear and its behaviours seem to be unpredictable through their random appearance, it is deterministic. This is called chaos.

A recent approach suggests that EP El Niño events can be considered as a self-sustained oscillation with a phase-reversal signal when CP El Niño events are local episodic events, triggered by external forcing rather than part of the cycle (Kao and Yu, 2009). Chen et al. (2015a) argued that by decomposing El Niño diversity into three different flavours, canonical, extreme and weak dateline El Niño events, ENSO can be viewed as an interplay between a self-sustained symmetric oscillation (central-to-eastern canonical El Niño and La Niña events acting as the Recharge-Discharge paradigm) and the atmospheric forcing (via the Westerly Wind Bursts, see paragraph 1.2.2.2) partially modulated by El Niño itself and giving rise to the different flavours of El Niño.

Whether ENSO is considered as a self-sustained or damped oscillator, or an interplay between them, it appears not truly cyclic. ENSO system is destabilised by noise-induced

instabilities or non-linearities whose different sources are invoked in the literature, without knowing the actual contribution of each of them. The irregularities of the ENSO cycle may arise from tropical or extra-tropical atmospheric forcing (paragraphs 1.2.2 and 1.2.3), multi-scale interactions, from the seasonal cycle to the mean state (section 1.3), but also from non-linearities in the different coupled atmosphere-ocean feedback processes, which are generally more intense during El Niño events (paragraphs 1.2.2 and 1.2.3).

The current and mostly still open questions can be summarised as: Where does the El Niño / La Niña asymmetry come from? And the diversity of El Niño events? Are the same processes involved? Is there a specific type of El Niño, strong versus moderate event, eastward versus westward propagating event, central versus eastern Pacific pattern, favoured by atmospheric precursors? Or by ocean pre-conditioning?

As described previously, different ENSO asymmetries can be identified. Despite the complexity of ENSO and the fact that its spatial and temporal multi-scales can not be easily decorrelated, I sought to address the complex issue of ENSO asymmetries via two angles: its asymmetries in amplitude (paragraph 1.2.2) and in spatial patterns (paragraph 1.2.3). In terms of amplitudes, the asymmetries between El Niño and La Niña are taken into account, as well as the asymmetries between strong and moderate El Niño. In terms of spatial patterns, the asymmetries between CP and EP El Niño are investigated. The fact that extreme El Niño events are all EP El Niños but not all EP El Niños are strong events remind us that it can not be so simple.

1.2.2 Amplitude asymmetry (and associated ENSO non-linearities)

Dommenget et al. (2013) recalled that both El Niño and La Niña extreme events are more likely than expected of a normal distribution. The propensity to extreme events as well as asymmetry of duration and phase transition may arise from:

- multiplicative noise (paragraph 1.2.2.2) acting under oceanic favourable conditions (paragraph 1.2.2.1);
- non-linear convective response to SST (paragraph 1.2.2.3);
- non-linear oceanic advection (paragraph 1.2.2.4).

1.2.2.1 Warm water volume asymmetry

The upper ocean heat content variations along the equator is suggested to play a key role as a precondition for El Niño and La Niña development by both theory (Recharge-Discharge oscillator, Jin (1997a,b)) and observations (Meinen and McPhaden, 2000). An unusual high (low) heat content tends to favour the development of an El Niño (La Niña). El Niño termination purges then excess heat to higher latitudes.

Meinen and McPhaden (2000) showed that two main modes of the EOF analysis (see paragraph 2.2.2.2) of the 20 °C isotherm depth describe respectively the tilt mode and the Warm Water Volume (WWV) mode (see Figure 1.9). The tilt mode has opposite signs in the eastern and western Pacific and is in phase with ENSO and the zonal wind forcing (Bunge and Clarke, 2014). The WWV mode is associated with the recharge and discharge of warm water in the off-equatorial Pacific. Meinen and McPhaden (2000) defined the WWV index as a volume of warm water with temperature greater than 20 °C in the equatorial Pacific region (5°S-5°N). This index, proxy of the equatorial heat content, is used as an ENSO predictor: westerly winds anomalies occurring in spring (6-9 months before the peak of an El Niño event) impact directly the WWV mode to give the tilt mode associated with El Niño. A build-up (deficit) of heat content leads El Niño (La Niña) SST variations by 2-3 seasons, underlining the role of the oceanic state for long-term ocean subsurface memory and ENSO predictability.

A representation of the RD oscillator mechanism is made through the descriptive phase space of an ENSO temperature metric, such as mean Niño-3 SST anomalies, versus the WWV

(Fig. 1.13). In the linear theory of the RD oscillator, the trajectory in this phase space is represented by an ellipse (see figure 2 of Timmermann et al. (2018)). Despite mainly irregular orbits and a positive skewness in eastern tropical Pacific SST anomalies (Fig. 1.13b), some trajectories appear more deterministic resembling a recharge-discharge oscillator: during the onset of strong El Niño events, a slow discharge of the heat content begins from maximum positive Z20 towards large positive SST anomalies. Then Z20 starts to strongly decrease just a few months before the SST anomalies peak, then leading to neutral and negative values of SST anomalies. It should be noted that this asymmetric feature of the RD oscillator with two types of decrease of the heat content, first slow then sharp when SST anomalies increase towards its peaks (Fig. 1.13a), may be explained by a non-linear facilitator favouring the development of strong El Niño events, subject of this paragraph 1.2.2 (see following paragraphs).

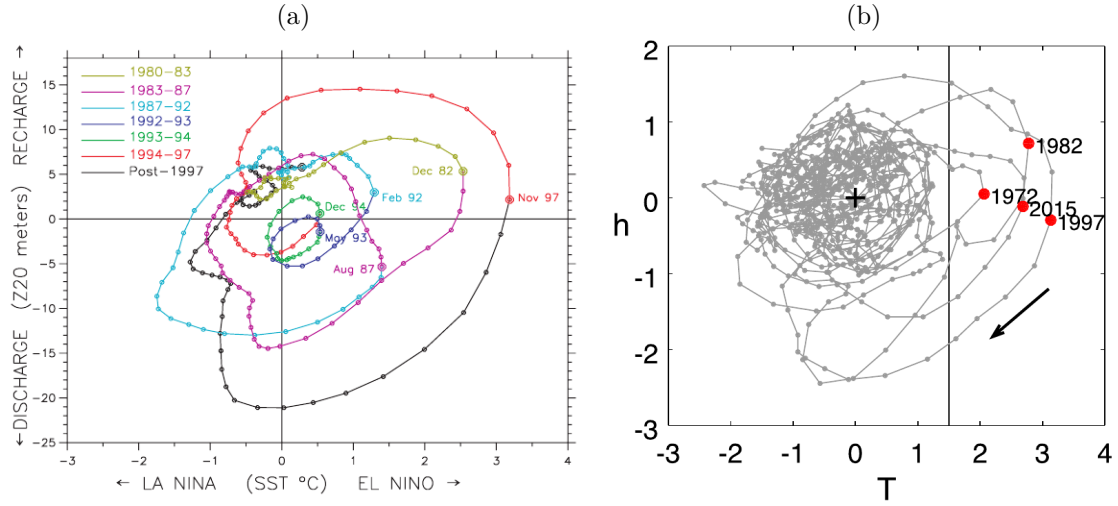

Figure 1.13 – Monthly evolution of ENSO in SST-Z20 (or h) phase space. The El Niño SST proxy is the Niño-3 SST anomalies index. The proxy of the heat content (Z20 or h) is the depth anomaly of the 20 °C isotherm averaged over the equatorial band (5°S-5°N, 120°E-80°W (Fig. 1.13b) and 130°E-80°W (Fig. 1.13a)). In Figure 1.13a, the SST data come from the NOAA Climate Prediction Center, Z20 is computed from the Australian Bureau of Meteorology Research Center (BMRC) gridded subsurface temperatures. The line color changes at the peak of each El Niño SST maximum, which is also shown as a large dot, and its date is labeled. The final point is May 2002, noted with a large black dot. In Figure 1.13b, the observation data correspond to the ERSST v3b dataset (1950-2016) for SST, a combination of SODA 2.2.4 (1950-1979) and GODAS (1980-2016) for Z20. The data are smoothed with a 1-2-1 filter. The cross indicates the origin, the line corresponds to SST = 1.5 °C, and the arrow indicates the direction of the evolution of the strong El Niño events. Figure 1.13a is reprinted from Kessler (2002), Figure 1.13b is reprinted from Takahashi et al. (2018)

However, after the discharge of the heat content, a pause may be marked in a weakly recharged state (Kessler, 2002). The recharge phase lasts longer and is less intense (Fig. 1.13). The pause can last up to two years, far longer than the ocean dynamic memory of the region. The cyclic view, with El Niño events following La Niña events, is rarely observed because of the weaker accumulation of oceanic memory during La Niña, insufficient for a transition to El Niño (An et al., 2005b). Moreover, the precursor role of the heat content is not systematic and seems to have decreased to one season over the last decades (McPhaden, 2012; Lu et al., 2017).

The underlying processes contributing to the WWV is still unclear. In the initial RD oscillator paradigm (Jin, 1997a), the slower oceanic feedback at the origin of the cyclic variation of the equatorial heat content is related to the Sverdrup balance. In this theory, the recharge oscillation relies on the non-equilibrium between the zonal-mean equatorial thermocline depth and wind stress. The anomalous easterly (westerly) wind stress during La Niña (El Niño) induces a slow recharge (discharge) of warm water through meridional transport converging towards the equatorial band (diverging poleward). Bosc and Delcroix (2008)

suggested that meridional transport variability was mainly due to Rossby waves dynamics. As they propagate, the Rossby waves modify the thermocline depth as well as the sea-level, generating anomalies of meridional currents that induce the recharge (or discharge) of the equatorial band in warm waters before (or during) an El Niño event. Clarke (2010) argued that the WWV mode is not due to a dominant meridional divergence driven by the wind, as suggested by Jin (1997a,b) because meridional and zonal divergence approximately cancel each other. More recently, Lu et al. (2017) showed that WWV changes are as much regulated by meridional convergence as by zonal transport from western boundaries, which leads by about 4-5 months the meridional convergence. The authors argued also that the strong western boundary transport suggests an off-equatorial forcing.

These uncertainties raise questions about the effectiveness of WWV as a predictor. Bunge and Clarke (2014) suggested that the change in the predictor role of the WWV index was linked to the decadal variability of the oceanic background state. After 1998 and before 1973, the equatorial Pacific is characterised by mean La Niña-like conditions, inducing a westward displacement of the anomalous wind forcing. This westward displacement of the zonal wind forcing leads to a westward displacement of the tilt mode, which increases the tilt mode contribution to the WWV. The WWV index is then no longer a good predictor of ENSO because it contains not only a non-equilibrium mode variability (second EOF mode, WWV mode) but also the tilt mode variability (first EOF mode) after 1998. Conversely, the second EOF mode amplitude decrease is suggested to be due to large-scale linear dynamics and a more in phase reflection of energy from the western boundary due to the westward shift of the zonal wind forcing, which generates a lower-amplitude non-equilibrium mode variability (Clarke, 2010; Fedorov, 2010).

Neske and McGregor (2018) showed recently by decomposing the WWV into its instantaneous and adjusted responses that roughly half of the WWV variability is dominated by the instantaneous response and is thus only as predictable as the winds that drive this component, raising questions about the self-sustained cycle view of ENSO. The adjusted response is due to the effect of Rossby waves, excited by Westerly Wind Bursts (WWBs, also called Westerly Winds Events or WWEs) more than two months earlier and reflected at the western boundary. This WWV contribution is consistent with the oscillators theories (Suarez and Schopf, 1988; Battisti and Hirst, 1989; Jin, 1997a,b). The instantaneous response is related to WWV changes due to Ekman transports induced by WWBs. Neske and McGregor (2018) showed that the balance between the two types of WWV contribution changed between the pre and post-2000 periods. For the pre-2000 period, both contributions are important while the instantaneous contribution is dominant after 2000. It means that the instantaneous WWV recharge, associated with westerly wind bursts, is largely responsible for the pre-El Niño event recharge since 2000. It is consistent with the increase of the influence of the tilt-mode showed by Bunge and Clarke (2014) and with the decrease of the predictability of ENSO after 2000 (Lu et al., 2017). In that case, the oscillatory nature of ENSO is reduced as the weaker adjusted WWV changes are overpowered by the instantaneous contribution.

The questioning of oscillator theories is further supported by the asymmetric WWV contribution between El Niño and La Niña events. The recharge process prior to an El Niño event is dominated by the instantaneous contribution while the discharge process accompanying an La Niña event appears to be dominated by the adjusted contribution (Neske and McGregor, 2018). It is consistent with Kessler (2002) who showed that ENSO oscillatory behaviour can pause for a longer time in a weakly recharged La Niña state (see Fig. 1.13). In this case, the reinvigoration of ENSO would be due to the instantaneous WWV response. Moreover, the fact that the pre-conditioning oceanic state, with warm water build-up in the equatorial Pacific, may arise from WWBs in a short term rather than be slowly charged years before an El Niño event (McGregor et al., 2016; Neske and McGregor, 2018), could explain the equatorial WWV changes during the weak 2014-15 El Niño event. A rapid increase of the WWV occurred in the first few months of 2014, concomitantly with observed strong WWBs,

which differs from the view of a slow build-up. Chen et al. (2015a) observed in the same way that the 2014 spring conditions of the equatorial heat content and WWBs suggested that a super El Niño was unlikely to take place. When strong El Niño events are preceded by a large build-up of heat content in winter (January-February), WWBs in March-April favour coupled interactions between modulated WWBs and SST background state (see paragraph 1.2.2.2), which can lead to extreme El Niño events. Note however that Takahashi and Dewitte (2016) recently suggested that a high heat content in winter is not a necessary condition for strong El Niño events to occur, in contrast to results from Lai et al. (2015) and Puy et al. (2017) among others.

More recently, Izumo et al. (2018) showed that WWV variations are dominated by the fast downwelling Kelvin wave contribution in response to zonal wind anomalies during the preceding 3 months, in agreement with McGregor et al. (2016) and Neske and McGregor (2018). It means that the forced Rossby wave contribution to WWV is relatively weak in March-April-May and the spring WWV contains more information from wind variations of the last few months than of the last year. Therefore the WWV in this season does not generally reflect the influence of the previous phase of the ENSO cycle, which is consistent with the findings of Chen et al. (2015a) for the 2014-2015 event. They argued that the long-term memory could be better understood by taking into account the heat content in the western Pacific, which is dominated by the forced Rossby waves. A better oceanic predictor of ENSO at 10-18 months lead times is then the WWV_W (120°E-155°W). They further suggested that an extended index to the southern Pacific, where off-equatorial Rossby waves propagation are slower, may be an even better index (notably in previous fall before ENSO onset) to fully integrate the wind information and capture the slower long-term recharge related to the recharge oscillator theory (Clarke, 2010).

Using WWV_W as a predictor, Planton et al. (2018) showed that La Niña events are more predictable than El Niño events. They argued that the asymmetry between recharged and discharged states, with La Niña events that can last two years while it is rarely the case for El Niño events, is not the sole source of the increased predictability of La Niña events. The enhanced predictability is suggested to be linked with the larger negative heat content anomalies ahead of La Niña events (see Figure 1.13) and a more unstable and more stochastic ocean-atmosphere system during El Niño. Indeed, despite the deterministic control of WWBs and ocean state interaction (see paragraph 1.2.2.2), WWBs have a sufficiently strong stochastic component to yield a broad range of El Niño amplitudes starting from the same initial state in boreal fall (Puy et al., 2017). Moreover, WWBs can have very different values for a given El Niño amplitude (see also paragraph 1.2.3.2) that may lead to a weaker El Niño predictability. This result is consistent with findings of Dommenget et al. (2013) who argued that strong El Niño events are mostly wind driven and less predictable and strong La Niña events are mostly thermocline depth driven and better predictable.

1.2.2.2 Multiplicative atmospheric noise

Numerous studies suggest that ENSO irregularities may be partly explained by the high frequency atmospheric variability (Kessler and Kleeman, 2000; Lengaigne et al., 2004; Eisenman et al., 2005; Hu et al., 2014). It would play a role of "spark" in the establishment and evolution of temperature anomalies in the equatorial Pacific Ocean, which would present favourable conditions acting as a "fuel" according to the metaphor of Mike McPhaden (ENSO conference 2018[5]).

Atmospheric forcing, such as westerly wind bursts, occurs over time-scales of few days. Because the decorrelation time-scale of this high frequency atmospheric variability is much shorter than that of ENSO, its spectral signature appears approximately like that of a white noise, capable of acting on the slow component of the system (the ocean). In that case, the

[5]http://www.ensoconference2018.org/

noise is an added external forcing to the system. If we take into account the modulation of the atmospheric noise by ENSO and more specifically by the background state, the noise becomes a multiplicative atmospheric noise. In that case, initial subsurface ocean conditions could modulate the role of stochastic wind forcing in producing asymmetry and diversity. These distinctions are discussed below (see also Levine et al. (2016)).

A large part of the high-frequency atmospheric variability occurs in the form of WWBs, characterised by sporadic but strong surface wind anomalies that persist for a few days to a few weeks (2-40 days) and develop in the western Pacific, usually west of the eastern edge of the Warm Pool (Vecchi and Harrison, 2000; Eisenman et al., 2005; Seiki and Takayabu, 2007; Puy et al., 2016a). They occur over warm water ($> 28\,°C$) associated with enhanced convection, preferentially around the boreal winter season. Their probability of occurrence significantly increases during active periods of intra-seasonal tropical variability, such as the Madden–Julian Oscillation (MJO) and Convectively-coupled Rossby Waves (CRW) (Seiki and Takayabu, 2007; Puy et al., 2016a; Gushchina and Dewitte, 2019). Also, there is the possibility of WWBs to be triggered by pair of Tropical Cyclones (TC), highlighting a two-ways feedbacks between TC activity and ENSO (Lian et al., 2018a). Moreover, Puy et al. (2016a) showed that WWBs are modulated by the intra-seasonal atmospheric variability. WWBs associated with MJO active phase tend to have a larger zonal extension and last longer than those associated with Rossby waves and are therefore likely to have a greater impact on the ocean.

WWBs have two effects on ocean dynamics. Their related wind stress anomalies induce a meridional surface water convergence towards the equator, which deepens the thermocline, exiting a strong wind-forced downwelling Kelvin waves propagating eastward. The deepening of the thermocline during the wave propagation limits the exchange of cold waters between the deep ocean and the surface, causing the warming of the SST in the central and eastern equatorial Pacific. WWBs also generate equatorial surface currents anomalies, which advect warm water eastward, extending the eastern edge of the Warm Pool (Picaut et al., 1997).

The role of WWBs in the onset and development of the particularly strong 1997-98 El Niño event was widely studied, arguing that westerly wind events in late 1996 and the first half of 1997 played a crucial role in the onset and development of the event (McPhaden (1999); Boulanger and Menkes (1999); Lengaigne et al. (2002, 2003) among others). The first reversal of the trade winds in winter 1996-97 led to warming in central Pacific, then a second episode of westerly wind event in March 1997 led to warming in the far eastern Pacific. The second event in March 1997 is one of the most intense measured to date, in terms of intensity (up to 0.2 N/m^2), fetch (more than 30° longitude), and duration (about a month, from mid-February to mid-March) (Lengaigne et al., 2003). Similar frequent WWBs were observed during the development of strong El Niño events in the boreal winters of 1982 and 2015 (Wyrtki, 1985; Hu and Fedorov, 2017).

Because of their short time-scale, they were initially treated as an external (additive, see definition above) stochastic forcing to explain the irregularity of ENSO given the deterministic physics of the oscillator (Penland and Sardeshmukh, 1995; Moore and Kleeman, 1999). However, observational studies have shown that WWBs are more frequent prior and during an El Niño event (Delcroix et al., 1993; Harrison and Vecchi, 1997; McPhaden, 1999), suggesting that WWBs that force ENSO, may depend to some extent on the ENSO background state. Modelling studies support these observational findings, showing that WWBs are significantly more likely to occur when the Warm Pool is extended eastward, beyond the dateline (Eisenman et al., 2005; Puy et al., 2016a). Lengaigne et al. (2003) analysed the impacts of the ocean response to the WWBs onto the atmosphere, using an Atmospheric General Circulation Model (AGCM). They confirmed that the eastward displacement of the Warm Pool initially induced by WWBs promoted the occurrence of subsequent WWBs in the following months (previous results from Vecchi and Harrison (2000)). The characteristics of the later WWBs are controlled both by the eastward extension of the Warm Pool and by the SST

gradients established in the far western Pacific, where WWBs induced a cooling (Lengaigne et al., 2003), and their location is dependent on the eastern edge of the Warm Pool (Hayashi and Watanabe, 2017).

The mechanism is as follows: the warming generated by the wind-forced downwelling Kelvin waves in the central to eastern Pacific decreases the zonal SST gradient. The subsequent eastward displacement of the Warm Pool induces a weakening of the trade winds in the central to eastern Pacific and a reduction of the equatorial upwelling, which both further increase the initial SST warming. In parallel, the eastward displacement of the warmest water from the western to the central Pacific induces an eastward shift of convection that consequently promotes the occurrence of further frequent and intense WWBs in the following months. These events reinforce the initial warming in the eastern Pacific through the generation of additional Kelvin waves. Air-sea coupled interaction between WWBs and anomalous warming in the central Pacific constitutes thus a positive feedback for the development of an El Niño event.

Eisenman et al. (2005) and Gebbie et al. (2007), using respectively an intermediate complexity coupled model and an hybrid coupled model, showed that considering WWBs as modulated (semi-stochastic) results in an ENSO amplitude twice as large as in a scenario with purely stochastic WWBs with the same amplitude and average frequency, as they generate only a weak oceanic response. If the ocean background state affects the probability of occurrence of WWBs, then they cannot just be considered as purely stochastic (additive) events but also state dependent (multiplicative). They suggested considering WWBs as an internal part of the coupled ENSO system, being partially stochastic and partially affected by the large-scale ENSO dynamics, rather than being completely external to ENSO. Puy et al. (2017) confirmed that numerous and strong WWBs favour the development of a strong El Niño event, with a particular emphasis on summer/fall WWBs occurrence increasing the probability for an extreme El Niño. Modulated WWBs are more effective at triggering El Niño than if they were randomly distributed, which is roughly equivalent to enhancing the ocean-atmosphere coupling coefficient (Eisenman et al., 2005). In addition to the crucial role that WWBs play in the triggering and development of the warm phase of ENSO, they are also involved in the irregularity of ENSO, in terms of timing (Gebbie et al., 2007; Jin et al., 2007) or strength (Lengaigne et al., 2004; Eisenman et al., 2005; Gebbie et al., 2007), favouring the El Niño - La Niña asymmetry. They affect El Niño but not La Niña due to their unidirectional nature, reinforcing asymmetric feature between El Niño and La Niña events with extreme El Niño events stronger than extreme La Niña events. Jin et al. (2007), using a RD oscillator, and Chen et al. (2015a), using a model of intermediate complexity, confirmed that the modulation of WWBs by the oceanic background state is responsible for the aperiodicity of ENSO and asymmetry in the predictability of the onsets. This enhancement of the intra-seasonal variability of surface winds induces a deterministic response of the atmosphere to the SST, allowing for an increased predictability.

Multiple WWBs, and especially WWBs around June, appear thus particularly important for the onset and development of strong El Niño events. Conversely, their absence, particularly in the preceding spring from April to June, is likely to have contributed to the aborted development of the expected 2014-15 El Niño event, significantly limiting the growth of the event (Menkes et al., 2014). Despite favourable oceanic conditions for the occurrence of WWBs, similar to those preceding the 1997 El Niño, they did not occur and only a weak El Niño occurred in 2014 (Puy et al., 2017). Moreover, not all WWBs during favourable oceanic conditions give rise to an oceanic response sufficient to significantly influence ENSO. Lengaigne et al. (2004) conducted a sensitivity study of the triggering of El Niño events by WWBs in a coupled ocean-atmosphere model and showed that despite oceanic favourable conditions, the same WWBs can lead to different oceanic response, ranging from strong El Niño to neutral conditions. They suggested that the diversity between the members was due to the internal atmospheric variability during and following the inserted WWB in the model.

Puy et al. (2017), using ensemble simulations, further showed that despite favourable oceanic conditions, the WWBs activity in their favoured spring/summer season, when the Warm Pool extends abnormally to the east, is subject to variation responsible for the large spread of the ensemble members' response. The stochastic part of WWBs leads to an intrinsic limitation of the predictability of the magnitude or even occurrence of El Niño events. Takahashi and Dewitte (2016) showed also that a "strong enough" westerly wind stress anomaly in the central Pacific in late boreal summer is a necessary condition for the development of a strong El Niño in the following winter, which could make the statistics of El Niño regime (strong versus moderate) very sensitive to the characteristics of the stochastic forcing.

The fast varying WWBs - slow ocean background interaction is not deterministic, but probabilistic, leaving an important role to the stochasticity of the atmosphere in the evolution of El Niño (Puy et al., 2017). This strong sensitivity of the coupled response to WWBs may therefore point to inherent limits in El Niño predictability, as the high frequency wind variability over the Warm Pool region remains largely unpredictable.

Finally, the deterministic part of WWBs strongly depends on and in turn affects the low-frequency development of El Niño. However, the stochastic part of the modulated WWBs makes this deterministic interaction only probabilistic. Another feature of the interaction between the WWBs and the ocean background state is that the latter does not response the same way to WWBs. This is discussed in paragraph 1.2.3.2. Lastly, the positive feedback loop between the large-scale SST field (i.e. the Warm Pool eastward extension) and the numbers and magnitude of WWBs can be viewed as an intra-seasonal component of the Bjerknes feedback, which will be discussed in the following paragraph 1.2.2.3.

1.2.2.3 Non linear response of the tropical convection

The Bjerknes feedback is at the heart of the mechanism of SST anomalies amplification in the equatorial Pacific. It can be understood as a deterministic, large-scale coupling between wind stress and SST anomalies. It has been clearly demonstrated in the recent literature that when ocean background state is favourable, the El Niño development phase favoured the occurrence of WWBs intra-seasonal component involved in the Bjerknes feedback (Lengaigne et al., 2004; Eisenman et al., 2005; Gebbie et al., 2007). The conditions for setting up the Bjerknes feedback can thus play a major role in the development of strong El Niño events.

Observations show non-linear relationship between tropical sea surface temperature and precipitation on climate time-scales, since the SST must exceed a threshold for deep convection to occur. This critical value may vary between 26 and 29 °C depending on the criteria for convection and types of data, the values of 27.5-28 °C being often retained (Graham and Barnett, 1987; Johnson and Xie, 2010; Jauregui and Takahashi, 2018). Therefore oceanic regions of active convection such as the Warm Pool depend on the underlying value of SST (Gadgil et al., 1984) and once the SST threshold of 28 °C is crossed, deep convection can take place.

This non-linear feature induces a distinct behaviour between the western and the eastern Pacific. Due to the zonal asymmetry of the climatological SST, even small deviations of the SST from its climatological value can excite large rainfall deviations on the periphery of the west Pacific Warm Pool region, whereas positive anomalies of significant amplitude are required to induce convection within the east equatorial Pacific Cold Tongue. On the other hand, negative SST anomalies in the Cold Tongue region have no further effect on the normally dry conditions, leading to appreciable non-linearity between the effects of El Niño and La Niña on tropical rainfall. Thus, rainfall anomalies associated with El Niño events are located east of the dateline, and west of the dateline during La Niña events (Hoerling et al., 1997). Due to this non-linear threshold convection, the maximum inter-annual variability of rainfall over the equatorial Pacific is shifted several thousand kilometres west of the maximum inter-annual variability of SST (Deser and Wallace, 1990). Clarke et al. (2007) also highlighted the role of the threshold for triggering deep atmospheric convection (SST around 28 °C) in

the RD oscillator theory because of the induced differences in the coupled dynamics between the western and the eastern Pacific.

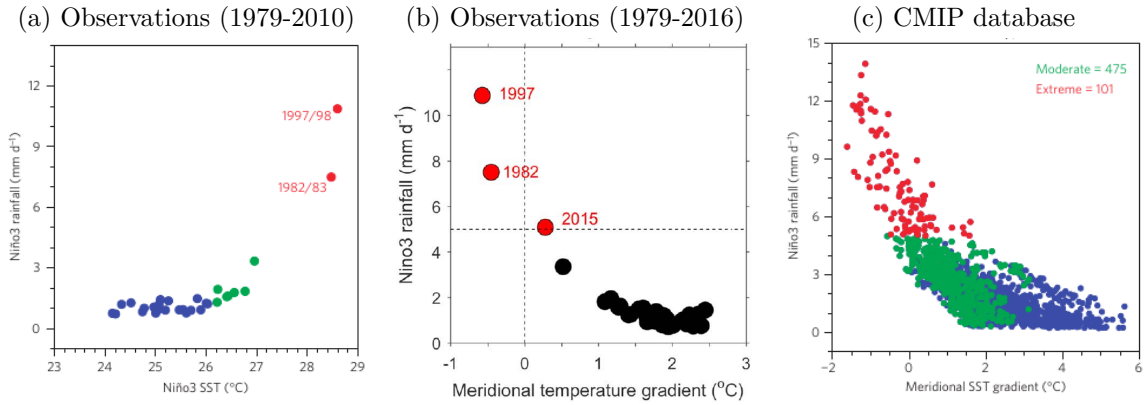

Figure 1.14 – Relationship of eastern equatorial Pacific (Niño-3 area) December-January-February (DJF) total rainfall with (Fig. 1.14a) DJF Niño-3 SST and (Fig. 1.14b and 1.14c) meridional SST gradients in the Niño-3 longitude range. The meridional SST gradient is defined as the average SST over the off-equatorial region (5°N-10°N, 150°W-90°W) minus the average over the equatorial region (2.5°S-2.5°N, 150°W-90°W). Figure 1.14a (Figure 1.14b) corresponds to observations over 1979-2010 (1979-2016), figure 1.14c corresponds to control simulations of 9 CMIP3 and 11 CMIP5 selected models. In figures 1.14a and 1.14c, extreme El Niño (defined as events for which austral summer rainfall is greater than 5 mm per day), moderate El Niño (defined as events with SST anomalies greater than 0.5 standard deviation over the corresponding period (since 1979 in Fig. 1.14a,) that are not extreme El Niño events), and La Niña and neutral events, are indicated by red, green and blue dots respectively. During extreme El Niño, the meridional SST gradient diminishes, or reverses, shifting the ITCZ to the eastern equatorial Pacific (Fig. 1.14b and 1.14c). In figure 1.14c, the number of moderate El Niño and extreme El Niño events is shown. The figures are reprinted from Cai et al. (2014, 2017).

Non-linearities in atmospheric deep convection have also been used to directly define extreme events, whether cold or warm (Cai et al., 2014, 2015a,b, 2017). During El Niño, precipitation anomalies in the eastern tropical Pacific are facilitated by the southward shift of the ITCZ due to the reorganisation of the large-scale atmospheric circulation (Rasmusson and Carpenter, 1982). Confirming the non-linear relationship between SST and precipitation anomalies in the eastern Pacific (Lengaigne and Vecchi, 2010), Cai et al. (2014) showed in models from the Coupled Model Intercomparison Project (CMIP) phases 3 and 5 (see paragraph 2.1.2 for more information on models) that the pronounced shift of the convective zone, facilitated by the weakening of meridional SST gradient in the eastern Pacific (Fig. 1.14b and 1.14c), induced a non-linear relationship between SST and rainfall anomalies (Fig. 1.14a), characterising distinctly extreme El Niño.

Rainfall in the Niño-3 region is then a correct indicator of extreme El Niño events, whether in observations or CGCMs. Similar to the previous study of Lengaigne and Vecchi (2010), Cai et al. (2015a, 2014, 2017) defined extreme El Niño events when the boreal winter rainfall in the Niño-3 region is beyond an arbitrary threshold of 5 mm/day. They then used this definition, with the same rainfall threshold, to estimate changes in extreme El Niño statistics with global warming as we will see in paragraph 1.4.2.1.

However, Johnson and Xie (2010) showed that the convective threshold of SST in the convective region is not absolute and varies with respect to the mean climate (e.g. the temperature of the free troposphere). Williams and Patricola (2018) raised the question to what extent rainfalls in the eastern Pacific, indicative of deep convection, reflect the dynamics of ENSO or the increase in column water vapour with warming when analysing ENSO rain-based statistics in future scenarios. They developed thus an ENSO Longitude Index (ELI) based on the non-linear, threshold-like response of deep convection to SST, which takes into account the seasonal changes in the SST as well as changes in climatological SST and its

seasonal cycle with global warming (see paragraph 1.4.2.2). This study confirmed the strong relationship between ENSO and the non-linear response of deep convection to SST anomalies.

The Bjerknes feedback involves westerly winds stress anomalies that may be driven by an anomalous zonal SST gradient (Bjerknes, 1969) but also from this anomalous deep atmospheric convection in the western to central equatorial Pacific (Clarke, 1994, 2014), which may induce non-linearities in the Bjerknes feedback. Kang and Kug (2002) suggested that the non-linear El Niño / la Niña response to wind stress anomalies, which is associated with the different spatial distributions of convection anomalies during the two ENSO phases, plays an important role in the formation of the asymmetries amplitudes and durations. The relatively weak SST anomalies during La Niña are related to the westward shift of wind stress anomalies by about 10-15° longitude. The SST anomalies over the equatorial Pacific become weaker as the zonal wind stress shifts to the west. Takahashi and Dewitte (2016) showed in observations that the convective and wind stress responses to SST warming in the eastern Pacific (the E-index) correspond, which supports the conclusion that the non-linearity in the Bjerknes feedback emerges from the triggering of deep convection. Takahashi and Dewitte (2016) further suggested that the westerly wind stress response was a function of the E-index amplitude, the zonal wind response to low E-index being mainly a response to zonal SST gradients whereas the zonal wind response to high E-index may be mainly a non-linear and localised east of the dateline response to convection. Different studies highlighted that the Bjerknes feedback is non-linear and that this non-linearity may be responsible for ENSO asymmetry. Note that this non-linear response being an intrinsic part of the thermodynamic control on deep convection, the non-linear response of the wind stress is also dependent on the equatorial SST anomalies position.

Frauen and Dommenget (2010) argued that while the asymmetry of ENSO is often attributed to oceanic processes, the non-linear and seasonal varying atmospheric feedback can also play a significant role in this asymmetry. The asymmetry between eastern Pacific SST anomalies during El Niño and La Niña can be explained by non-linearities in the zonal winds response to equal-strength but opposite SST anomalies (Fig. 1.15a). Dommenget et al. (2013) reinforced this results showing that the non-linearities of ENSO associated with the non-linear response of the zonal winds are also reflected in its spatial pattern and sequencing evolution. The sequencing asymmetry involves the tendency of warm events to be followed by cold events more readily than vice-versa. They extended the analysis to coupled models of the CMIP3 database, in addition to the same hybrid model of Frauen and Dommenget (2010). They suggested that the spatial differences associated with the EP and CP El Niño types (see paragraph 1.1.2) are at least partially related to these non-linearities. Indeed, strong El Niño events are shifted to the east while strong La Niña events are shifted to the central Pacific. Weak or moderate El Niño events are more shifted to the central Pacific than weak La Niña events. Therefore, strong (weak) El Niño events are mostly EP (CP) El Niños. These spatial pattern and amplitude asymmetries arise from the non-linear response of the zonal wind in the central Pacific to SST. The zonal wind stress is a function of both the amplitude and location of the SST in the central Pacific: it responds stronger and further east to positive SST anomalies, as observed by Kang and Kug (2002). This non-linear response of the wind stress supports the eastward shifted El Niño pattern. Dommenget et al. (2013) also qualitatively analysed the second element of the Bjerknes feedback, the thermocline depth sensibility to zonal wind. The fact that strong La Niña events tend to follow an El Niño event could suggest that the strong La Niña events are triggered partially by the ocean state set by the preceding El Niño event. No such ocean state may exist for strong El Niño events, which in turn would suggest that strong El Niño events might be forced by random atmospheric forcing. They suggested that strong El Niños are forced more strongly by zonal wind than by thermocline depth, which makes them less predictable, while strong La Niñas, preceded by El Niño events, are mostly thermocline depth driven and thus better predictable.

Concomitantly, Choi et al. (2013b) confirmed the non-linear relationship between zonal

wind and SST anomalies using a delayed-oscillator conceptual model, modified such that wind stress anomalies depend more strongly on SST anomalies. The strengthening of the air-sea feedback produces larger El Niño events that overshoot more rapidly into the opposite phase than La Niña events do. It should be noted that the sequencing asymmetry can be obtained only if there is stochastic external forcing included in the delayed-oscillator model. They also noted the importance of the realistic simulation by CGCMs of the spatial pattern of the wind stress. Bias in its representation, whether in mean location or meridional extent, could favour a symmetric ENSO evolution. They finally suggested that the non-linearities in atmospheric convection are a source of the stronger wind stress response sensitivity during warm events.

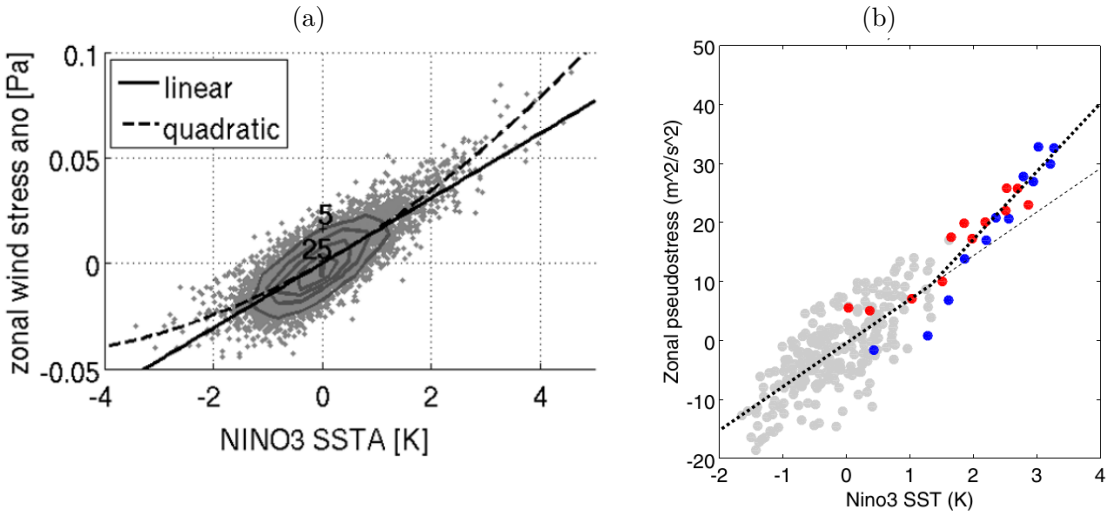

Figure 1.15 – Non-linearities in the Bjerknes feedback: interaction between zonal winds and SSTA. (Fig. 1.15a) Scatterplot of central Pacific zonal wind stress anomalies (6°S-6°N, 160°E-140°W) and Niño-3 SSTA with linear (solid line) and quadratic (dashed line) regression. The contour interval is 5.0 K/Pa. Figure reprinted from Frauen and Dommenget (2010). (Fig. 1.15b) Scatterplot of central Pacific (180°W-140°W, 5°S-5°N) pseudostress (estimated from monthly Tropical Atmosphere Ocean (TAO) wind speed and zonal wind data (McPhaden et al., 1998)) and Niño-3 SSTA (ERSST v3b, see paragraph 2.1.1). The piecewise linear regression fit (ARE-SLab from Jekabsons (2013)) yields a threshold SST of Tc=1.33 K and a nonlinear enhancement of 56 %. Blue and red dots correspond to July-June of 1997-98 and 2015-16, respectively. Figure reprinted from Takahashi et al. (2018).

The studies are mostly oriented towards explaining the asymmetrical features of ENSO (magnitude, aperiodicity, phase transition, pattern spatial) rather than focusing on the onset phase of strong El Niño events, although it is now recognised that they are subject to strong non-linear processes (Santoso et al., 2017). Unlike previous studies, Takahashi and Dewitte (2016) were interested in the possible bi-modality of El Niño events (and not statistical asymmetrical features of ENSO) that non-linearities could explain. Using the E and C indices (Takahashi et al., 2011; Dommenget et al., 2013), which differentiate strong warm events from moderate warm or cold events, they suggested that two distinct regimes of El Niño events exist (see also Figure 1.6b). Even if the relatively short period of observation does not allow to reject statistically the null hypothesis of a uni-modal distribution, the use of a CGCM suggested that non-linearities in the Bjerknes feedback lead to the existence of two separate dynamical regimes. Strong El Niño regime is triggered beyond a positive threshold in SST anomalies (Fig. 1.15b). Once the normally cold waters of the eastern tropical Pacific are warm enough to cause significant rainfall, the growing El Niño switches into a faster mechanism: the Walker circulation dramatically shifts to the eastern Pacific and the physical processes that lead to the growth of El Niño strengthen even more beyond this threshold (by a factor of 3). Recently, Takahashi et al. (2018) showed that a RD oscillator model in which is implemented a non-linear mechanism is able to reproduce the two El Niño regimes. They suggested that the sustained low-frequency component of the stochastic forcing plays

a key role for the onset of strong El Niño events (when SST anomalies are greater than the threshold), at least as important as the precursor positive heat content anomaly (Fig. 1.16).

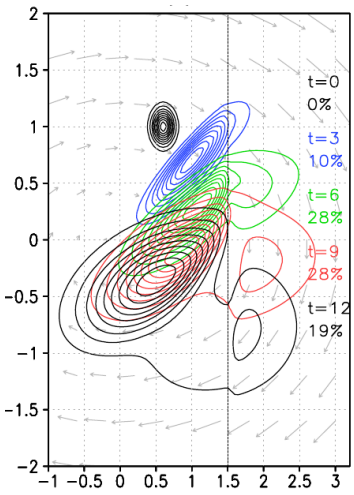

Figure 1.16 – Evolution of the joint T-h (or Z20) PDFs for an ensemble iniitially centred at T=0.6, h=1.0 (black line) after 3 (blue), 6 (green), 9 (red), and 12 (black) months from the solution of the Fokker–Planck equation for the nonlinear RD model. For visualization purposes, the PDFs were normalised by their peak value and contoured at 0.1–0.9 with an interval of 0.1. The probability that T is greater than the threshold 1.5 °C is indicated for each time as %. Reprinted from Takahashi et al. (2018).

Takahashi and Dewitte (2016) suggested that this non-linear relationship is instrumental in determining the El Niño regime. The westerly wind stress anomalies in the central Pacific in late boreal summer influence SST anomalies in the eastern Pacific the following winter. It should be noted that these studies do not take into account the time-evolution of the wind stress forcing, whether in terms of eastward shift or meridional extension whereas these features are suggested to play a significant role in the response of the feedback. A refinement of the method could lead to a better understanding of the link between the intra-seasonal variability of WWBs and the Bjerknes feedback.

Dewitte and Takahashi (2017) further investigated the developing phase of the 1972-73 and 2015-16 El Niño events, categorised respectively as moderate EP El Niño events, and not as strong EP El Niño events. They showed that their developing phase was marked by equatorial easterlies in the eastern Pacific (east of 130°W) in September, which prevented the SST anomalies growth of the events. These easterlies are connected to off-equatorial southerly winds in the far eastern Pacific, in response to the coastal SST warming off Peru, which develops in the previous spring (see the air-sea mode of the developing Bjerknes feedback in paragraph 1.2.3.3). The possible origins of these positive SST anomalies along the Peruvian coast are discussed in their study, suggesting among other candidates the South Pacific Meridional Mode (see Zhang et al. (2014) and paragraph 1.2.3.3) even if it operates at larger scale than the far eastern Pacific. Thus, during moderate EP El Niño events (contrary to extreme EP El Niño events), the appearance of easterlies in the far eastern Pacific (20°S-20°N, 130°W-80°W) in September acts to damp the growth of SST anomalies in the eastern Pacific. Interestingly, Hameed et al. (2018) suggested similarly that differences between strong EP El Niño and moderate El Niño may be explained by easterly winds in the far eastern Pacific (15°S-15°N, 120°W-80°W). They argued however that the damping easterlies arise from ENSO itself, coming from atmospheric Kelvin waves that develop at the eastern edge of the ENSO-induced convective anomalies (Gill, 1980). They further suggested that an extreme El Niño develops thanks to interaction with the positive phase of the Indian Ocean Dipole (IOD, Saji and Yamagata (2003)) and the weak but persistent westerly winds modulated by the IOD. Further investigations are needed to determine the possible mechanisms of the far eastern Pacific easterly winds variability in fall, whether ENSO-induced or stochastic,

as well as to diagnose if and which counter-acting forcing is needed for a strong El Niño to develop.

1.2.2.4 Non linear oceanic processes

An asymmetry between El Niño and La Niña also exists in the direction of zonal phase propagation: extreme El Niño events, in particular the 1982-1983 and 1997-98 El Niño, propagate eastward whereas moderate (CP) El Niño and La Niña events propagate westward (McPhaden and Zhang, 2009; Santoso et al., 2013; Boucharel et al., 2013). The direction of propagation of SST anomalies comes from a competition between the 3 main positive feedbacks (Neelin et al., 1998) Typical mechanisms associated with propagating SST variability include competition between surface-layer feedbacks and the thermocline feedback (TCF). The surface-layer feedbacks include the zonal advective feedback (ZAF) and the upwelling feedback (also called Ekman (pumping) feedback) that is the reduction of the upwelling due to reduced Ekman pumping as the trade winds weaken. They tend to reinforce the initial warming and shift it to the west through anomalies of zonal current and upwelling respectively. In the thermocline feedback, on the other hand, the thermocline slope tends to balance the wind stress, resulting in a deeper thermocline to the east of the original SST anomaly. This creates warm subsurface temperature anomalies carried to the surface via the mean upwelling, reinforcing the original anomalies eastward. These processes can establish propagation of SST anomalies in either direction: eastward if the thermocline feedback dominates, westward otherwise, due to the different centres of action of these two feedbacks. The role of the thermocline feedback is preponderant in the eastern Pacific (An and Jin, 2001) as stressed in the delayed oscillator (Suarez and Schopf, 1988; Battisti and Hirst, 1989) and the recharge-discharge theories (Jin, 1997a,b) whereas the zonal advective feedback is a key process in the central Pacific (Picaut et al., 1996; Vialard et al., 2001) but also in the eastern Pacific (Jin and An, 1999).

It should be noted that these two propagation directions could be facilitated by the alternating background state (Trenberth, 1990; Fedorov and Philander, 2000; An and Wang, 2000; Dewitte, 2000; Boucharel et al., 2009; Wang and Ren, 2017). However, one limitation of this view is that the background state does not affect La Niña events and it is unclear whether marked eastward propagation affects other events than extreme El Niño. Numerous El Niño events may rather undergo stationary growth (Neelin et al., 1998; Boucharel et al., 2013). The competition between oceanic feedbacks can play a role in the diversity of El Niño spatial patterns as we see in paragraph 1.2.3.1.

Focusing more specifically on the difference in propagation direction of extreme El Niño events compared to other warm moderate or cold events, Santoso et al. (2013) showed that the interplay between ENSO-related current anomalies and climatological currents determines how the equatorial Pacific circulation influences the zonal propagation of SST anomalies (Fig. 1.17). ENSO-related current anomalies has an opposite effect depending on the type of event. Easterly current anomalies, stronger than the average westward current, lead to a reversed flow during extreme El Niño events, leading to a dominant eastward propagation. For moderate El Niño events, eastward current anomalies are very small compared to the westward climatological current and thus the total current remains westward. The same occurs during La Niña events. The direction of propagation being the result of the balance between the westward mean current and the eastward ENSO-induced current anomalies, a change in ENSO intensity or in the mean current can therefore influence the propagation asymmetry.

Another oceanic process often invoked to be responsible for ENSO asymmetry is the term of non-linear temperature advection of anomalous temperature by anomalous current, called the "Non-linear Dynamical Heating" (NDH, see paragraph 2.3.1.4). Jin et al. (2003a) found that the NDH is positive for both the cold and warm ENSO phases. It enhances the extreme El Niño amplitude and weakens the amplitude of the subsequent La Niña, resulting in the asymmetry in the magnitude of warm/cold events. An and Jin (2004) showed that the

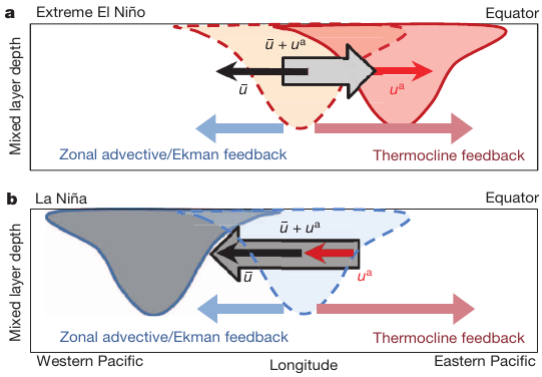

Figure 1.17 – Schematic of competing effects of oceanic processes on zonal propagation direction during ENSO events. (a) During extreme El Niño events, zonal currents in the equatorial Pacific (large grey arrow) have the effect of shifting the initial warm surface anomalies (dashed red patch) eastwards, because the current anomaly u^a (red arrow) is eastward and exceeds the strength of the westward background current $\overline{u}$ (black arrow). This effect counters westward propagation induced by the zonal advective and Ekman pumping feedbacks (blue arrow) and enhances eastward propagation induced by the thermocline feedback (pink arrow). (b) During La Niña events, the zonal currents are prominently westward because the current anomaly always enhances the westward mean current. This weakens the thermocline feedback effect and enhances westward propagation as induced by the other two dynamical feedbacks. Reprinted from Santoso et al. (2013).

NDH warming is induced by the eastward propagation of the extreme El Niño events, which provide a favourable phase relationship between temperature and current. During westward-propagating El Niño events, the phase relationships between zonal temperature gradient and current and between the surface and subsurface temperature anomalies prevents the NDH-induced warming. An et al. (2005a) confirmed a strong relationship between intensity and propagating feature of ENSO: strong (weak) ENSO events move eastward (westward). However, An et al. (2005a) and Zhang and Sun (2014), analysing respectively the CMIP3 and CMIP5 database, showed that the majority of CGCMs underestimates ENSO asymmetry.

Conversely, Liang et al. (2017) questioned the role of NDH in the growth of extreme El Niño events. They showed that non-linear oceanic advection does not guarantee the amplitude asymmetry between El Niño and La Niña in CMIP5 models. Takahashi and Dewitte (2016) showed that oceanic non-linear advection is not essential for the onset of strong El Niño events in reanalysis datasets and a CMIP3 CGCM. The NDH makes a contribution later on, by delaying the decay of the strong event. However, the estimation of NDH is complicated by the limited subsurface observations and their integration in theoretical models required possibly taking into account other processes such as wave dynamics (Takahashi and Dewitte, 2016).

Others non-linearities in oceanic processes may impact ENSO asymmetries, such as the non-linear rectification of Tropical Instability Waves (TIW) onto the mean state, more active during La Niña events (Vialard et al., 2001; An, 2009; Boucharel and Jin, 2020), the non-linear interaction between wind-forced downwelling Kevin waves and dynamical fronts located at the eastern edge of the Warm Pool (Boulanger et al., 2001), the vertical mixing in the oceanic mixed layer more effective during El Niño events.

1.2.3 Spatial asymmetry

Numerous studies have focused on the physical processes underlying the distinct characteristics of Central Pacific (CP) and Eastern Pacific (EP) El Niño events (Ashok et al., 2007; Kao and Yu, 2009; Kug et al., 2009, 2010; Capotondi, 2013).

EP El Niño events tend to involve basin-wide surface wind and subsurface ocean variations and a strong relaxation of the equatorial thermocline zonal tilt. They are characterised

by a prominent role of the thermocline feedback and a large eastward shift of the tropical convection. CP El Niño events tend to appear, develop and decay in situ (i.e. events relatively stationary), with surface winds, SST and subsurface temperature anomalies confined in the central Pacific. They are associated with a stronger role of the zonal advective feedback and a weaker role of the thermocline tilt variation, a stronger thermal damping during the decay phase, a stronger locally atmospheric convective response and they are more susceptible to be disrupted by wind noise. Whereas the dynamics of EP El Niño events are mainly related to thermocline variations, CP El Niño events are likely to be more influenced by the zonal advective feedback and atmospheric forcing (Kao and Yu, 2009; Kug et al., 2009).

ENSO diversity is likely to arise from the noise forcing as well as from the delicate balance between positive and negative ocean-atmosphere feedbacks that act to enhance or suppress the growth of SST anomalies. Several mechanisms have been suggested to explain ENSO spatial diversity, such as:

- differences in the interaction between SST and thermocline according to the longitudinal location of the warming, leading to a predominance of either the thermocline or zonal advective feedback (Kug et al., 2009; Yeh et al., 2009a; Kug et al., 2010; Ren and Jin, 2013);
- differences in WWBs location and intensity and in their timing with favourable oceanic conditions (Hu et al., 2012, 2014; Lai et al., 2015), which may lead to their modulation by the oceanic mean state (Chen et al., 2015a; Hayashi and Watanabe, 2017);
- various off-equator atmospheric forcing, such as the North and South Pacific Meridional Modes (Chiang and Vimont, 2004; Zhang et al., 2014; Stuecker, 2018), forcing from the north-eastern sub-tropical sea level pressure (Yu et al., 2010a; Yu and Kim, 2011), Asian-Australian monsoons forcing variations able to excite the CP El Niño type (Yu et al., 2009) or trans-basin climate variations (Chikamoto et al., 2015);
- the seasonal-phase locking of the central Pacific processes (Yu and Kao, 2007) and the dependence of the onset time of each type of El Niño to the timing of the mechanisms that trigger El Niño events (Kao and Yu, 2009);
- the South Pacific booster (Hong et al., 2014);
- Tropical Instability Waves (An, 2008; Holmes et al., 2018).

I explore here more particularly the first two mentioned mechanisms and some of the suggested off-equator precursors, knowing that ENSO diversity arises certainly from a combination of different mechanisms, which may change according to the event.

1.2.3.1 Role of oceanic feedbacks

In the canonical view of ENSO evolving from the balance between the positive Bjerknes feedback and negative feedback through oscillatory theories (see paragraph 1.2.1), SST and thermocline depth variations play an important role. SST anomalies are the manifestation of an El Niño event, while thermocline depth anomalies mark the onset and ending of an El Niño event. Thermocline variations are a key mechanism in the development of El Niño events, particularly in the eastern tropical Pacific where changes in the thermocline depth have more effects on SST than in the western Pacific because of the shallower thermocline (An and Jin, 2001; Jin et al., 2006). The deepening of the thermocline has the effect of suppressing exchanges between the surface and subsurface, which reduces surface cooling in the eastern Pacific. Conversely, zonal advection is a key process in the development of ENSO-related SST anomalies in the central and western Pacific due to the large zonal temperature gradient near the eastern edge of the Warm Pool. Abellán et al. (2017b) showed that the zonal advective feedback is the main heating term during the development phase of the three strong El Niño events in the central Pacific (Niño-3.4 region), although meridional and vertical advection could be significant, particularly during the last event.

Zelle et al. (2004) showed that the relationships between fluctuations of the thermocline depth and SST warming occur via two different pathways: the “upwelling pathway” and the

"wind coupling pathway", each associated with different time scales. The upwelling pathway is more important in the eastern Pacific (220°E-270°E): the temperature anomalies caused by thermocline depth anomalies are vertically advected to the surface by a combination of upwelling and vertical mixing. The temperature anomalies appear at the surface two weeks to two months later. Because of the deeper thermocline in the central Pacific, the upwelling pathway is much smaller there. Conversely, the wind coupling pathway is more efficient in the central Pacific (170°E-220°E): a thermocline depth anomaly in the central Pacific travels eastward through Kelvin waves, causing SST anomalies in the eastern Pacific. Arguing that these SST anomalies cause an eastward shift of the atmospheric convection region, they induce zonal wind anomalies in the central Pacific. The anomalous westerly winds drive anomalous eastward zonal advection across the temperature gradient of the eastern edge of the Warm Pool shifted in the central Pacific, thereby causing positive SST anomalies in the central Pacific. The anomalous zonal winds also heats up the surface waters directly through reduced evaporative cooling and reduced Ekman pumping, diminishing the upwelling of colder subsurface waters. Contrary to the upwelling pathway, a remote coupling through wave dynamics and an atmospheric response is required. This pathway is non-local: it makes an excursion to the eastern Pacific where the upwelling pathway acts. The temperature anomalies in the central Pacific appear at the surface two to twelve months after thermocline depth anomalies. The wind coupling pathway is less efficient in the eastern Pacific because the zonal wind shows little response to anomalous SST there and the zonal surface temperature gradient is weaker.

Finally, the thermocline feedback and vertical advection processes mostly operate in the eastern Pacific where the thermocline is shallow, whereas, in the western to central Pacific, SST is the closest to the deep atmospheric convection threshold, and hence more prone to induce an atmospheric response.

In the last ten years, many studies have focused more precisely on the oceanic dynamical processes associated with CP and EP El Niño events to better understand ENSO diversity and determine whether ENSO flavours are dynamically distinct. Because of the different preferential feedback centres of action, the thermocline feedbacks play a key role in the development and decay of EP events while the zonal advective feedback is a key process during CP events (Kug et al., 2009; Capotondi, 2013; Choi et al., 2011; Ren and Jin, 2013). This distinction between EP and CP events is confirmed by diagnostic results from climate models that can relatively realistically reproduce the two types of El Niño (Kug et al., 2010; Capotondi, 2013). However, the feedbacks contribution in the different phases of each El Niño types differs according to the studies. Kug et al. (2010) and Capotondi (2013) showed that ZAF is also an active term in the eastern Pacific during the development of an EP El Niño event, even if its contribution is half that of the TCF and of the same order of magnitude that the upwelling feedback's. Kug et al. (2010) suggested that, rather than the ZAF, the surface heat flux were responsible for the decay of the CP El Niño events. Kug et al. (2009) concluded that the Ekman pumping feedback plays a minor role in both types of El Niño events. Ren and Jin (2013) argued that TCF and ZAF contribute jointly to the development of both types of El Niño events, whereas ZAF provides the main negative contribution to the phase transitions, contrary to Kug et al. (2010). Fedorov et al. (2015) argued that TCF is also important in the development of CP El Niño events although thermocline depth variations are weaker. These differences in the contribution of each oceanic feedbacks come from the difficulty of measuring them in observational datasets, from the intrinsic model biases (see paragraph 2.3.1.4) and also from the different feedbacks' definitions used by these studies (see paragraph 2.1.2.2).

Associated with the strong influence of the thermocline feedback on SST anomalies in the eastern Pacific, numerous studies using observations and reanalysis datasets (Kug et al., 2009; Singh and Delcroix, 2013; Lai et al., 2015) or CGCMs (Kug et al., 2010; Capotondi, 2013) suggested that the oceanic heat content recharge-discharge process only applies to EP

El Niño events. In particular, central Pacific SST anomalies appear first on the surface, then extend down to a shallow layer of 100 m, over the thermocline (150-200 m), indicating that surface warming is not induced by subsurface dynamics (Kao and Yu, 2009; Yu et al., 2010b; Choi et al., 2011). Moreover, warm CP El Niño events are not followed by a cold event, normally induced by the discharge process (Yu and Kao, 2007; Kao and Yu, 2009; Kug et al., 2010). The prominent ocean dynamical processes differ with the location of the El Niño event, with the thermocline anomalies and the recharge-discharge processes becoming progressively weaker as the peaks of the events move further west. However, the previous results from CGCMs are likely biased by the westward shift of the regions in which the heat budget is calculated, reinforcing the weak signal of the RD oscillator. Capotondi (2013) showed that, for CP El Niño, the recharge-discharge processes still occur but with weaker evolution, while for CP-m El Niño events, defined by shifting westward Niño indices, they become absent. By removing the decadal variability of EP El Niño before contrasting the two ENSO regimes, Ren and Jin (2013) indicated that both EP and CP El Niño events undergo the same recharge-discharge oscillator mechanism, though CP El Niño has reduced feedback processes.

Ren and Jin (2011, 2013) connected the two El Niño types with the two leading ENSO-like coupled modes co-existing in the tropical Pacific under current climate conditions: the low-frequency quasi-quadriennal (QQ) mode and the higher-frequency quasi-biennial (QB) mode (Bejarano and Jin, 2008). These two modes first emerge from the suggested existence of a near-annual coupled mode (Jin et al., 2003b) in addition to the slow 2-7-yr cycles of ENSO. Two similar ENSO-like modes, a low-frequency remote mode in the eastern Pacific that is triggered by the wind stress in the western-central Pacific and a fast local SST mode in the central Pacific, which is controlled by local winds and ocean currents, were also noted by Fedorov and Philander (2000, 2001), whose findings can be further tracked back to some earlier theoretical ENSO studies (Neelin and Jin, 1993) (see paragraph 1.2.1.3). Fedorov and Philander (2000, 2001) showed thus that a change in the background conditions of thermocline depth and surface winds in the tropical Pacific may change ENSO properties, switching from a slow (period of 5 years) thermocline mode to the fast (period de 2-3 years) SST mode associated with zonal advective feedback and stronger in the central Pacific. The approach between the previous studies and that of Bejarano and Jin (2008) differ highly in that previous studies focused only on one leading mode, suggesting that its nature could change smoothly, from a recharge-discharge mode to a fast SST mode, according to the parameters of the background state. Bejarano and Jin (2008) showed that two (linear) coupled modes, independent and unstable, coexist in a modified Zebiak and Cane (ZC) intermediate model under climate conditions that resemble those of the present climate. That means that two types of El Niño events can co-occur in some ENSO regimes, which supports at least one type of unstable ENSO modes. More recently, Xie and Jin (2018) with a modified atmospheric component in the modified ZC model of Bejarano and Jin (2008) showed that these two modes can co-exist within a broad range of mean states and are sensitive to changes in the mean state. Unlike previous studies, they are interested in determining the mean state conditions favouring the dominance of one mode over the other (Fig. 1.18). The QQ mode (EP ENSO-like mode) is more prominent when the mean thermocline is deep and the trade winds are weak. It is dynamically controlled by the thermocline feedback, overcoming damping effects during the development of an El Niño event. The vertical movements of the thermocline that produce the dominant effect on the SST are determined by the ocean mass adjustment to the winds in the equatorial region. The QQ mode resembles a recharge-discharge mode, with positive SST anomalies in the eastern Pacific. It has a typical period between 3.5 and 8 years. The QB mode (CP ENSO-like mode) is dominant when the mean thermocline is shallow and the trade winds are strong. It is governed by the zonal advective feedback during the phase transition, while the role of the thermocline feedback is mainly to overcome the negative feedback of the damping terms. The QB mode with the maximum SST anomalies

centred more toward the central Pacific has a period between 1.5 and 3 years. The ZAF provides the primary negative contribution for phase transitions of both modes. Capotondi and Sardeshmukh (2015) using a linear inverse modelling framework suggested also that the initial subsurface conditions of the thermocline depth along the equator determine the El Niño type: a deeper (shallower) thermocline in the eastern Pacific and a shallower (deeper) thermocline in the central Pacific are conducive to EP El Niño type. However, it is quite at odds with the results from Yu and Kim (2010) who suggested that CP El Niño events could occur with different oceanic subsurface state (recharge, discharge or neutral thermocline state) and that this state at the peak phase of the event can be a potential predictor of its transition phase (EP warming, EP cooling (abrupt termination) or symmetric decay with respect to the growth).

Anyway, the ocean subsurface background state most definitely plays a role in ENSO diversity. The stability analyses are intended to determine the conditions that favour the dominant mode(s) and the induced changes in these modes. A change in the mean state of wind field and thermocline depth can thus determine which dynamical state the evolution El Niño mode would follow. Numerous studies argued therefore that changes in the background conditions have contributed to change in El Niño properties at different past periods, such as the late 1970s (Fedorov and Philander, 2001; Ren and Jin, 2013) or around 2000s (Thual et al., 2013; Wang and Ren, 2017). These different sensitivities to the background state are discussed in paragraph 1.3.2. Changes in ENSO properties due to changes in the background state lead to changes in oceanic feedback contributions, which can modify the direction of propagation (Neelin and Jin, 1993).

Xie and Jin (2018) argued that the instabilities of the two leading ENSO-like modes are essential to ENSO diversity. The spatial diversity is indeed generated in part by the different oscillation frequencies of the two modes but also by external excitation processes. Both modes operating not far away from their zero growth rate (that is their criticality, see figure 1.18c, lower left) in current background states, they can be easily excited by other processes.

Because CP El Niño events are not fully described by oceanic subsurface dynamics, numerous studies already emphasised the role of air-sea interactions and dynamical or thermodynamical processes in the ocean mixed layer in the growth and decay of CP El Niño events (Kao and Yu, 2009; Choi et al., 2011; Lai et al., 2015). The central Pacific is indeed a critical region for thermodynamical air-sea coupling processes, due to the movements of the equatorial edge of the Warm Pool (Picaut et al., 2001; Maes et al., 2004), which makes SST anomalies more sensitive to air-sea interactions than to interactions with the thermocline depth. The ocean mixed-layer thermodynamical and dynamical processes affect both heat fluxes and the WWBs, which are themselves controlled by convective processes. The studies which emphasised the role of atmospheric forcing in the CP El Niño dynamics often suggested that the initial establishment of the equatorial SST anomalies is forced by atmospheric forcing and that the ocean (local) advection processes are important only after the central Pacific warming onset to amplify SST anomalies (Yu et al., 2010a). Kug et al. (2010) and Dewitte et al. (2012) showed that the decay phase of CP El Niño is mainly due to a thermal damping process and not to a discharge process, since the warm event is generally not followed by a cold one. For all these differences, the CP El Niño events have been suggested to be more stochastic than oscillatory.

It should be however noted that the common bias of CGCMs such as the too weak winds response to SST anomalies and the too cold Cold Tongue could lead to an unrealistic balance between ENSO mechanisms and errors that cancel each others out, or in other words good ENSO statistics for the wrong reasons (Kim and Jin, 2011; DiNezio et al., 2012; Bayr et al., 2018b).

We discuss in the following paragraphs two mechanisms proposed to explain the triggering or reinforcing of CP El Niño events: the role of the westerly wind bursts and the associated recharged-discharged oceanic state (paragraph 1.2.3.2), the thermodynamic processes and

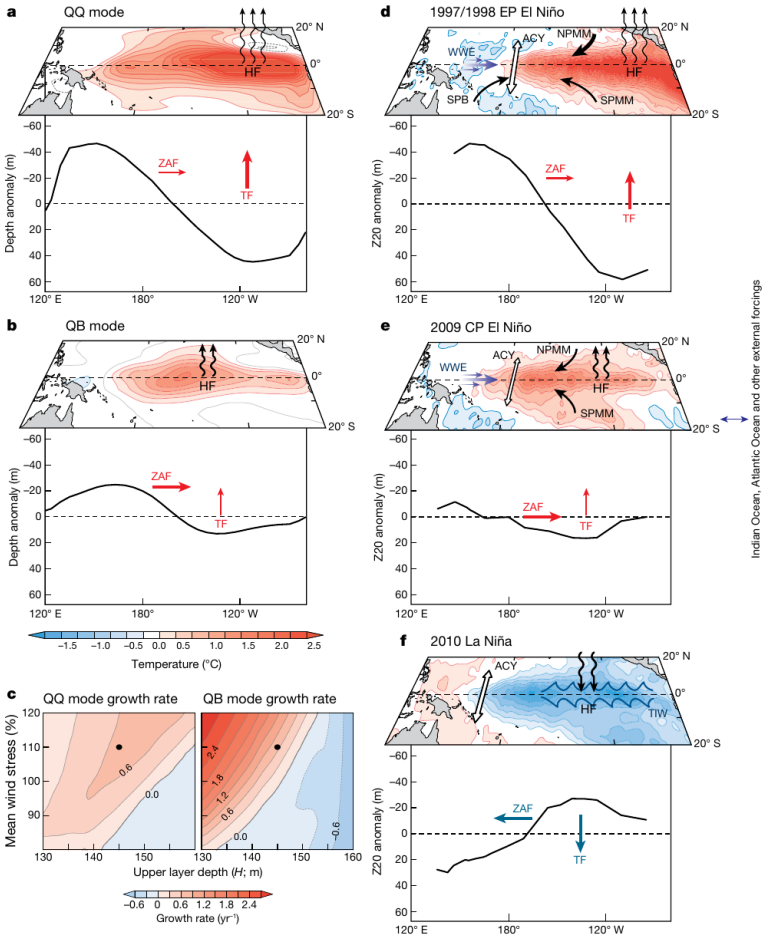

Figure 1.18 – (a, b) Leading two Eigen-modes of tropical Pacific SSTA and equatorial thermocline depth anomalies (averaged between 5°S-5°N) with periods of about 4 years (quasi-quadriennal (QQ) mode) and about 2 years (quasi-biennial (QB) mode), calculated from an intermediate ENSO model (Xie and Jin, 2018). The differences in longitudinal location of the centre in SSTA and thermocline anomalies are largely due to the different roles of the zonal advective feedback (ZAF) and thermocline feedback (TCF). (c) Growth rates of the two Eigen-modes as a function of the mean thermocline depth (H) and the mean strength of equatorial trade winds relative to climatological conditions. Black dots mark the mean state for the modes displayed in figures a and b. (d, e, f) Patterns of SSTA (HadISST v1.1 dataset) and equatorial 20 °C thermocline depth anomalies (Tropical Atmosphere Ocean (TAO)/ Triangle Trans-Ocean Buoy Network (TRITON) data) for typical EP (1997-98), CP (2009-10) El Niño and La Niña (2010-11) events (November-January). The main non-linear excitation and cross-scale interaction mechanisms are schematically represented: annual cycle (ACY), WWEs, South Pacific booster (SPB), North and South Pacific meridional modes (NPMM and SPMM, respectively) and tropical instability waves (TIW). The solid red, eastward (blue, westward) arrows represent the ZAF and the red, upward (blue, downward) arrows denote the TCF for El Niño (La Niña) conditions. The relative sizes and different zonal positions of the arrows indicate qualitatively the strength and areas of strong feedback efficiency. Curly upward (downward) arrows denote damping net surface heat flux (HF) feedback. Reprinted from Timmermann et al. (2018), adapted from Xie and Jin (2018).

some of the suggested off-equator precursors (paragraph 1.2.3.3).

1.2.3.2 Multiplicative atmospheric forcing

Puy et al. (2017) noticed that even if the dynamical subsurface ocean (i.e. thermocline) response to WWBs follows relatively well the equatorial waves theory (Schopf and Harrison, 1983), the SST response presents a large spread for a same WWBs forcing, depending on the mean state. Yet the spatial structures of SST anomalies are essential for determining the atmospheric response to ENSO. This affects in turn the structure of atmospheric stochastic forcing. Numerous studies showed that the response of the ocean to WWBs depends on its background state and so of the timing of the WWBs relative to the recharge-discharge state of the equatorial Pacific heat content (Fedorov, 2002; Lengaigne et al., 2004; Hu et al., 2014; Fedorov et al., 2015; Capotondi and Sardeshmukh, 2015; Lai et al., 2015). A westerly wind event is much more likely to trigger an EP El Niño event if the Pacific heat content is recharged than when it is in a neutral or discharged state. Lai et al. (2015) suggested that the recharged state is particularly important in the western Pacific for the strong continuous westerly anomalies to initiate the triggering of an EP El Niño event and to sustain the eastward propagation of Kelvin waves to the eastern Pacific. A moderate El Niño event, localised preferentially in the central Pacific, may occur for a recharged state in the absence of WWBs or for a neutral state with WWBs (Hu et al., 2014; Fedorov et al., 2015; Lai et al., 2015). The initial recharge state in the western Pacific controls the response of the system to atmospheric perturbations. However, even slight differences in the initial conditions can change the situation, leading to the development of weaker events (Fedorov et al., 2015). The exact same WWB can thus induce a variety of events ranging from extreme EP events to weak CP events or lead to no warming at all, depending on the ocean initial state at the moment of the wind burst.

Chen et al. (2015a) further investigated the role of WWBs in ENSO diversity, including CP, moderate EP and extreme EP El Niño events. They suggested that WWBs may behave as two types of triggers: they may produce EP El Niño events in the eastern Pacific through the combined effect of Kelvin waves (that deepens the thermocline in the central-to-eastern Pacific and favours the thermocline feedback) and the advection of warm water (displacing the edge of the Warm Pool eastward). When the integrated WWB intensity and the upper ocean heat content are both very high, and particularly when WWBs cross the dateline (see also paragraph 1.2.2.2), SST anomalies in the eastern equatorial Pacific are largely enhanced by the local thermocline feedback to generate an extreme EP El Niño. When the oceanic background state is not favourable for the RD process, they may generate CP El Niño through advection processes alone with WWBs confined to the western Pacific. WWBs would thus destabilise the regular ENSO oscillation, which then alternates alone between canonical El Niño events and La Niña events. The magnitude and the type of an El Niño event depend then on the interplay between the WWBs and the upper ocean heat content.

More recently, Hayashi and Watanabe (2017) used an ocean-atmosphere coupled model of intermediate complexity, including a prescribed annual cycle and state-dependent stochastic noise that mimics WWBs. Conducting experiments with additive versus state-dependent noise, they showed that both experiments contribute to the occurrence of the two types of El Niño. However, the state dependence of the stochastic noise guarantees the existence of CP El Niño events, regardless the efficiency of the thermocline feedback since the increased likelihood of WWBs occurrence at the eastern edge of the Warm Pool results in a positive feedback in the central Pacific (Fig. 1.19). When considering additive WWBs (b in Fig. 1.19), the zonal advection due to WWBs (thick dashed arrow) simultaneously excites the central Pacific warming accompanied by the atmospheric response to SST. Then the zonal advective feedback induces CP El Niño. The additive WWBs may also act to trigger EP El Niño through the downwelling Kelvin waves (thick bold arrow), which propagate to the eastern Pacific within a few months. The system favours EP El Niño events when the thermocline feedback, effective

in the eastern Pacific is large enough. When the WWBs are state dependent (c in Fig. 1.19), the positive central Pacific (Niño-4) SST anomalies increase the probability of occurrence of WWBs (thick grey arrow), enhancing the zonal advective feedback in the western-central Pacific to generate CP El Niño events. Gushchina and Dewitte (2012) previously argued that intraseasonal tropical variability tends to trigger EP El Niño events, with enhanced MJO and equatorial Rossby waves activity during spring-summer before the peak, while it tends to contribute to the persistence of CP El Niño events with enhanced activity mainly during the mature and decaying phases.

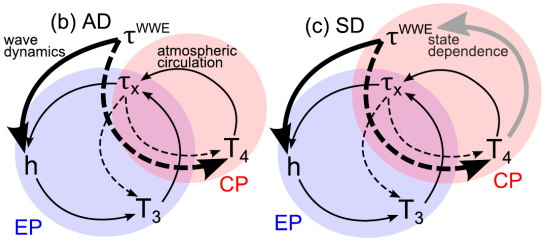

Figure 1.19 – Main ENSO feedbacks taking into account the spatial diversity. τ_x, h and T indicate the zonal wind stress associated with ENSO, thermocline depth and SST anomalies respectively. T_3 and T_4 are the SST anomalies in the Niño-3 and Niño-4 region respectively. τ^{WWE} indicates the wind stress associated with (b) additive and (c) state-dependent WWBs. AD refers to additive noise experiment, SD to state-dependent noise experiment. Circles with blue (red) shadings represent the feedbacks to produce EP (CP) El Niño events. All the dashed arrows indicate the zonal advection. Thick black solid and dashed arrows in (b),(c) indicate the roles of τ^{WWE}, and a thick grey arrow in (c) represent the state dependence. The figure is reprinted from Hayashi and Watanabe (2017), updated from Zelle et al. (2004)

Lai et al. (2015) showed in observations that both an ocean recharged state and WWBs are necessary for the development of El Niño events, whether they are CP or EP types. The two parameters contribute differently for each flavour: for EP El Niño events, an ocean recharged state and strong WWBs are required while different CP El Niño events can occur either when the western Pacific is moderately recharged with only moderate WWBs or when the western Pacific is strongly (weakly) recharged but with a weak (strong) WWB. Both parameters being required for an El Niño event to develop, they considered the CP and EP El Niño as the end members of the El Niño continuum (see paragraph 1.1.2.4).

Consequently, the observed El Niño diversity, including the occurrence of extreme events (see paragraph 1.2.2.2), depends conjointly on the stochastic atmospheric processes and their state-dependence, as well as on the recharged state of the ocean, which modulates El Niño properties within a broad continuum. The occurrence of extreme El Niño events involves further uncertainty associated with chaotic atmospheric dynamics (paragraph 1.2.2.2).

Hu et al. (2014) suggested the existence of a threshold in the metric they used beyond which the behaviour of the coupled system is different. The metric is related to ocean energetics via the Available Potential Energy (APE) characterising the tropical thermocline. When the APE anomalies are stronger than this threshold, an EP El Niño may develop whereas for weaker anomalies, a CP warming occurs. The transition between the two types of events is actually gradual and involves a strengthening of the thermocline feedback that gives rise to greater APE anomalies. Even if Hu et al. (2014) analysed EP versus CP warming, this bursting behaviour seems to be comparable with the behaviour of the Bjerknes feedback related to the onset of extreme El Niño events (see paragraph 1.2.2.3). Interestingly, Hu et al. (2014) imposed a wind stress anomaly that matches the WWB observed in February-March 1997 during the extreme observed El Niño event with a recharged state. Their EP El Niño event is therefore an extreme El Niño events. It could be interesting to test the sensitivity of the coupled system in the same configuration but for a moderate EP El Niño event to determine if the threshold in the APE metric, characterising the tropical thermocline, exist for all EP El Niño events or for extreme El Niño events only.

WWBs may be caused by tropical drivers, such as the MJO or CRW (see paragraph 1.2.2.2) or the Asian winter monsoon or by extra-tropical drivers, such as the North Pacific Oscillation (NPO) wintertime or the Pacific Meridional Mode (PMM) (see following paragraph 1.2.3.3). However, such remote influences appear to be mediated primarily by how they project onto wind variations in the equatorial Pacific.

1.2.3.3 Off-equator atmospheric precursors

Off-equator atmospheric variability may also play a role in the onset of ENSO and may also be involved in ENSO diversity. Numerous studies noticed that CP El Niño events are often associated with SST anomalies in subtropical regions, with for instance anomalous warming extending from the central Pacific to Baja California (Ashok et al., 2007; Kao and Yu, 2009), although such warming was also observed before the extreme El Niño event of 1997-98 (Yu and Paek, 2015). Yu et al. (2010a) suggested that given the lagged correlation between central Pacific and off Baja California SST anomalies (several months), the warming off Baja California may serve as a trigger for the development of CP El Niño events. The SST anomalies persist several months and extend south-westward, reaching the equatorial Pacific when the El Niño event begins to grow.

Several studies (Vimont et al., 2003; Yu and Kim, 2011) suggested that the initial warming outside Baja California is forced by atmospheric fluctuations via surface heat fluxes, particularly those associated with the North Pacific Oscillation (NPO), the dominant dominant mode of atmospheric variability in the north Pacific in terms of large-scale SLP signature (Rogers, 1981). The NPO is characterised by out-of-phase variations in SLP between subtropics and higher latitudes (Fig. 1.20a). When the wintertime NPO exhibits negative anomalies in its southern lobe, it is suggested to be able to trigger an El Niño event during the following winter via the Seasonal Foot printing Mechanism (SFM) (Vimont et al., 2003). The weakened trade winds over the central and eastern sub-tropical Pacific reduce the upward surface net heat flux, which causes SST warming. The winter footprint on SST via changes in wind-induced latent heat flux, persists over the subtropical northern Pacific (0-20°N) into the spring via thermodynamic air-sea interaction, often called wind-evaporation-SST (WES) feedback (Xie and Philander, 1994) and, in turn, forces a pattern of atmospheric circulation anomalies including summer westerly wind stress anomalies along the equatorial western Pacific. Wind anomalies induced by the convection tend indeed to be located to the south-west of the initial subtropical SST anomalies (Xie and Philander, 1994), where new positive SST anomalies can be formed through a reduction in wind evaporation. The wind anomalies, when in the deep tropics, would subsequently act as a trigger for ENSO by weakening the Walker circulation. This mechanism of the SFM via the WES feedback offers a way to explain how the subtropical SST anomalies can be sustained from boreal winter, when the extratropical atmospheric variability (the NPO in this example) is the most active, to the following spring or summer and subsequently excites El Niño events. However, the definition of the NPO index is crucial in the connection between the winter NPO and the subsequent winter El Niño (Chen and Wu, 2018). In particular, the NPO index should be defined over the appropriate subtropical North Pacific region, extending to near-equatorial regions but not extending too far north.

It has been also noted that the SST anomalies pattern of the subtropical precursor of a (preferentially CP) El Niño event (characterised by positive SST anomalies extending from the equatorial central Pacific to the north-eastern subtropical Pacific) strongly resembles the Pacific Meridional Mode (PMM), the leading coupled atmosphere-ocean (surface wind-SST) mode of variability in the subtropical Pacific (Chiang and Vimont, 2004; Chang et al., 2007). This strong coupling between SST and surface winds can be explained by the WES feedback mechanism. The PMM is characterised by an anomalous north-south SST gradient coupled to an anomalous latitudinal shift of the ITCZ toward the warmer hemisphere (Fig. 1.20b). Anomalous south-westerly winds extend from the equatorial dateline to the Baja Peninsula. Anomalies are maximized in boreal spring with SST anomalies lagging wind anomalies by

approximately one month because of the slower SST response to peak mid-latitude atmospheric variability in boreal winter (Chiang and Vimont, 2004; Chang et al., 2007). Unlike ENSO, the PMM does not require ocean dynamics for its existence and instead evolves via the WES feedback and is thought to be energised through the SFM by stochastic atmospheric forcing in the mid-latitudes (Chiang and Vimont, 2004; Di Lorenzo et al., 2015; Thomas and Vimont, 2016).

(a) North Pacific Oscillation (b) Pacific Meridional Mode

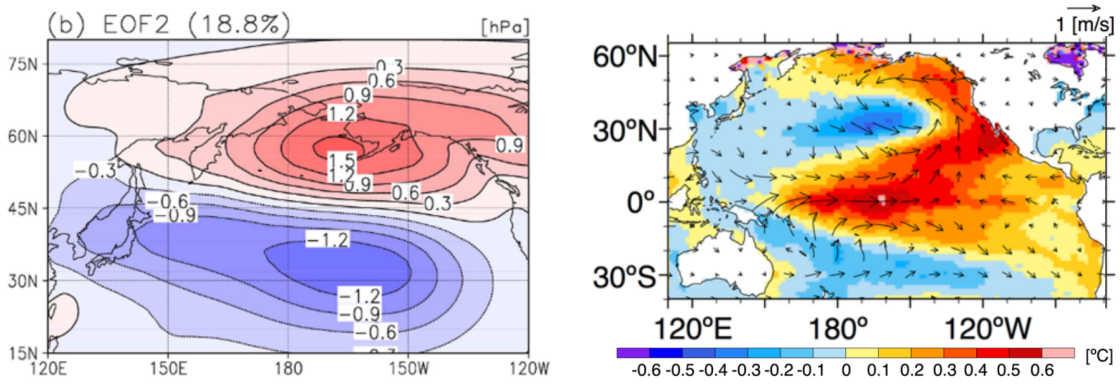

Figure 1.20 – 1.20a Second EOF mode of D(-1)JFM(0) Sea Level Pressure (SLP) anomalies over the North Pacific (15°N-80°N, 120°E-120°W). The SLP are from the 20Crv2 dataset (December 1871 to November 2012). The figure is reprinted from Shin and An (2018)). 1.20b Instantaneous SST (°C, data from HadISST v1 over the period 1948-2016) and surface wind (m/s, data from NCEP v1 over the period 1948-2016) regression patterns for the anomalous normalized PMM index. The figure is reprinted and adapted from Stuecker (2018)).

Several studies showed that the positive phase of the NPMM can excite central Pacific ENSO variability, operating as an effective conduit through which the north Pacific variability, particularly the NPO, triggers ENSO (Chang et al., 2007; Yu et al., 2010a; Larson and Kirtman, 2014; Yu and Paek, 2015; Thomas and Vimont, 2016). A significant number of El Niño events, mostly CP El Niño events, are preceded by a distinctive SST warming and southwesterly wind anomalies in the vicinity of the ITCZ during the boreal spring, representative of the NPMM (Chang et al., 2007). The arrival of the subtropical Pacific precursor in the equatorial central Pacific could trigger local air-sea interactions that intensify local SST anomalies into a CP El Niño event via surface heat fluxes (Yu et al., 2010a) or the wind-induced surface ocean advection (Kug et al., 2009). The generation of CP El Niño events is directly related to the mixed-layer dynamics forced by subtropical Pacific precursors, and not to the thermocline variations.

However, the PMM-ENSO relationship and more generally the low-frequency atmosphere-ocean coupled variability mode acting as a subtropical precursor of ENSO, is not yet clearly understood. Chen et al. (2013) showed that a positive wintertime NPO is not sufficient to trigger an El Niño event. They suggested that a positive phase of the Arctic Oscillation in spring is required for a SST warming to occur in the following winter. Shin and An (2018) showed in turn that when either the NPO or PMM occur alone, El Niño events are rarely triggered. But they found that when the NPO and PMM occur simultaneously during spring, an El Niño event is favoured during the following winter. However, these studies (Chen et al., 2013; Shin and An, 2018) do not differentiate EP from CP El Niño. Thomas and Vimont (2016) argued that PMM-ENSO relationship may present large spread between individual El Niño events and suggested that natural variability has important implications for the predictability of ENSO through the PMM. Larson and Kirtman (2014) showed, using a forecast model ensemble, that positive PMM events are a useful predictor of EP El Niño events in both observations and model forecasts with some skill, yet less skill than for CP El Niño events. Recently, Stuecker (2018) suggested that PMM and CP El Niño events cannot

be considered as two dynamically independent climate modes. Indeed, CP ENSO and PMM have close instantaneous relationship in the observations both on inter-annual and decadal time-scales, suggesting a strong coupling and fast positive feedback (the missing piece that remains to be found) between the two climate phenomena. He also showed that hardly any correlation exists between the EP ENSO index and the PMM.

The PMM is often studied in the northern hemisphere and referred to as the North Pacific Meridional Mode (NPMM) (Chiang and Vimont, 2004), but some studies highlighted a similar meridional mode in the South Pacific (SPMM) (Hong et al., 2014; Zhang et al., 2014; Larson et al., 2018). The associated off-equatorial southeast trade winds variability alters latent heat fluxes and SST and initiates a WES feedback that propagates signals north-westward into the tropics. Larson et al. (2018) suggested that the SPMM could modulate ENSO amplitude, by modulating the heat flux damping through fluctuations in the south-easterly trade winds intensity in the south-east Pacific. Min et al. (2017) suggested that the SPMM mainly favours the development of EP El Niño warming, whereas the NPMM mainly favours the development of CP El Niño warming.

Dewitte and Takahashi (2017) investigated the differences between the developments of moderate EP and moderate CP El Niño events. In the far eastern Pacific in the boreal summer preceding the winter peak, moderate EP El Niño events are characterised by significant warm anomalies, while moderate CP El Niño events are characterised by weak positive SST anomalies (even potentially slightly negative). They emphasised the major role of air-sea interactions in the eastern Pacific for the distinct development of these two types of events. The air-sea mode, assimilated to a developing seasonal Bjerknes feedback, is associated with a positive (negative) phase which consists in warm (weak warm or cold) SST anomalies along the coast of Peru in boreal spring that extends up to 130°W in summer and a low-level atmospheric response west of 130°W accompanied by westerly (easterly) winds in July-August before the winter peak of the EP (CP) El Niño event. Thus, the development of moderate EP El Niño events differs from the one of moderate CP El Niño events by an eastern air-sea mode of the developing Bjerknes feedback, which further induces equatorial downwelling Kelvin waves.

It should be noted that the relationship between the subtropical atmospheric modes of variability and (CP) ENSO is likely to be sensitive to low-frequency variations of the mean state. For instance, the SLP and SST variations associated with the NPO can excite SST variability in the tropical central Pacific especially after 1990 (Yu et al., 2012; Yeh et al., 2015).

1.3 Multi-scale interactions

As seen previously, the ENSO framework involves a multitude of time-scales, from intra-seasonal (few weeks) to inter-decadal. The notion of scale interaction in fact describes the two-ways feedbacks between small spatial and high-temporal scales and large spatial scale of low-frequency variability (seasonal to multi-annual) of the climate system. These interactions are an additional part of ENSO complexity (Timmermann et al., 2018) and the main ones are reviewed in the following.

1.3.1 Seasonal phase-locking

El Niño events tend to initiate in boreal spring, develop in summer and fall, reach their maximum amplitude in the later boreal fall or early boreal winter and then rapidly decay in the following end of winter or spring (Rasmusson and Carpenter, 1982). This "seasonal phase-locking" modifies the seasonality of the ocean-atmosphere coupled system stability, which favours the development of ENSO-like anomalies mainly in periods of strong instabilities.

SST anomalies will generally appear in the boreal spring, when the eastern Pacific is warmest, making the convection process even more sensitive to temperature changes. They

will then be able to grow in summer, when the equatorial upwelling is strong, making the surface temperature more sensitive to disturbances of the thermocline (among others vertical processes). The strength of the Walker circulation changes the stability of the seasonal cycle. Deep convection in the western Pacific, for example, peaks during the boreal spring, while the zonal surface temperature gradient peaks in September. The Cold Tongue annual cycle modulates the strength of the ocean-atmosphere coupled feedback, especially the Bjerknes feedback in the eastern Pacific. The anomalous warming will peak in winter as the coupling between the ocean and the atmosphere decreases (Zebiak and Cane, 1987) and the trade winds become stronger. This also leads to marked seasonal contrasts in ENSO climate impacts and predictability, especially via the reduced persistence of equatorial Pacific SST anomalies during boreal spring. ENSO loses its periodicity due to interaction with the seasonal cycle, which is a source of ENSO irregularity. Frauen and Dommenget (2010) showed in a numerical experiment that the seasonality of ENSO amplitude changes can be attributed to the seasonally varying sensitivity of the atmospheric response to SST anomalies. The seasonal cycle of the non-linear coupling between zonal wind stress and SST and between net heat flux and SST, influences the temporal evolution of ENSO amplitude by acting seasonally on the SST damping.

The seasonal forcing also forces the termination of events. One of the suggested mechanisms for strong El Niño events termination involves in particular the southerly shift of westerly wind anomalies from symmetric about the equator to the southern hemisphere during boreal winter (Harrison and Vecchi, 1999; Lengaigne et al., 2006; Vecchi and Harrison, 2006). Harrison and Vecchi (1999) first suggested that the shoaling thermocline that leads to the El Niño decay in the eastern Pacific could be explained by a direct seasonally varying wind-forced process without invoking any wave reflection as a negative feedback (Suarez and Schopf, 1988; Battisti and Hirst, 1989). This direct wind-forced response is carried out by an abrupt southward shift of the central Pacific westerly winds, which are not longer able to strongly force the oceanic equatorial waveguide, leading to an intense shoaling of the thermocline in the eastern Pacific. This constrains a rapid El Niño demise in the following months (spring). Indeed, prior to the meridional shift, the westerly zonal wind anomalies along the equator are responsible for maintaining the deep eastern equatorial thermocline (Harrison and Vecchi, 1999; Vecchi and Harrison, 2003, 2006). Lengaigne et al. (2006) suggested that the southward displacement of the winds is driven by the southward displacement of the warm water in the central Pacific in winter in response to the seasonal evolution of solar insolation, shifted south of the equator during boreal winter. This termination mechanism was observed for the 1997-98 (Vecchi and Harrison, 2006) and 2002-03 El Niño events (Vecchi and Harrison, 2003). McGregor et al. (2012) demonstrated that the southward shift of westerly winds that leads to the rapid decay of El Niño events is also related to seasonal development (DJF/MAM) of the South Pacific Convergence Zone (SPCZ) due to the seasonal evolution of solar insolation. They also showed that the southward shift of wind stress anomalies during the mature phase of El Niño in winter causes the asymmetric discharge of the equatorial heat content and plays a significant role in the rapid decay of the event, which strongly accelerate the termination of large El Niño events associated with the Sverdrup-transport induced discharge.

It should be noted that the termination of moderate El Niño events appears much less sensitive to the southward shift of the westerly winds in winter (Lengaigne et al., 2006; Zhang et al., 2015a; Karamperidou et al., 2015), even if the system is still preconditioned (shallow thermocline) for rapid event termination in both cases (Lengaigne and Vecchi, 2010). For moderate El Niño events, the thermocline shoaling caused by the decrease of equatorial westerly wind anomalies, even if less pronounced, may still transfer the coupled system into an unstable state in spring. This makes the eastern Pacific very sensitive to wind perturbations and allows a rapid surge of cold upwelled SST in spring and leads to La Niña conditions in the following months (Lengaigne et al., 2006). In other cases, weaker subseasonal easterly

activity combined with a slightly deeper thermocline allows the coupled system to maintain warm conditions until the following summer.

Lengaigne et al. (2006) however showed that even with a fixed solar insolation, El Niño events may eventually decay, implying that other mechanisms contribute to terminate the events. In particular, negative feedback of oscillator models (the delayed action oscillator or the recharge-discharge mechanism) play also a role both in the termination of events and in the warm-cold phase transition, by their memory effect. Recently, Abellán et al. (2017a) highlighted that in addition to the south wind-shift, the magnitude and zonal extent of the wind changes that accompany this south wind shift also drive changes in WWV and prime the ENSO system for termination. They suggested that more processes are likely to be involved in the spring termination of ENSO events, such as the seasonally changing cloud feedbacks (Dommenget and Yu, 2016).

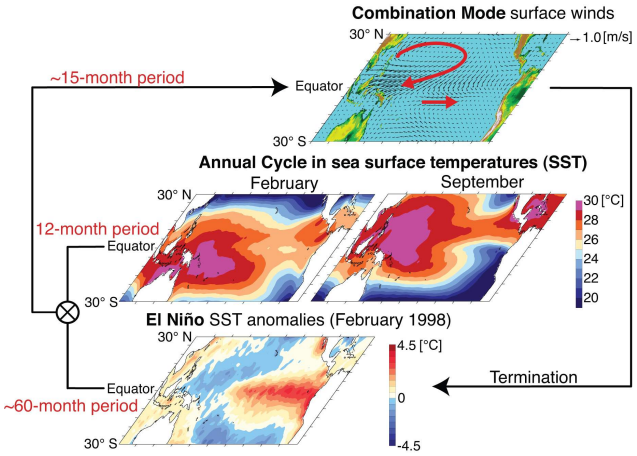

Figure 1.21 – The annual cycle (Tone 1) together with ENSO (Tone 2) generate the unusual surface wind pattern in the western Pacific, that is the Combination Tone. Reprinted from the personal page of M.F. Stuecker[6]

Finally, a large fraction of the tropical Pacific variability is explained by the annual cycle. As the coupled system of the equatorial Pacific is partly non-linear, the interaction between one (or more) inter-annual mode and the annual mode can generate a subharmonic frequency locking. Jin et al. (1994) and Tziperman et al. (1994) found in simplified and intermediate complex model that the non-linear interaction between ENSO and the eastern Pacific annual cycle is able to generate new time-scales and explain ENSO irregularity. These new time-scales include combinations of the annual and ENSO frequencies. Stuecker et al. (2013) further investigated the non-linear interaction between western Pacific seasonal cycle and inter-annual ENSO variability in observations and GCM simulations. They showed that the non-linear atmospheric response to this interaction gives rise to a near-annual combination mode (C-mode) with periods of 9-10 months and 15-18 months (Fig. 1.21). The atmospheric C-mode over the Pacific Warm Pool is associated with the seasonally modulated termination process of strong El Niño events through the DJF/MAM weakening of winds south of equator. This leads to the southward shift of El Niño-related wind anomalies (McGregor et al., 2012) and accelerates the termination of the event by generating eastward propagating upwelling Kelvin waves and a northward heat discharge. The C-mode operating only for strong El Niño events, and not for La Niña or weak El Niño, it is one reason why strong El Niño events are shorter than La Niña events.

1.3.2 ENSO modulation

ENSO properties (amplitude, frequency, spatial distribution) vary over decadal to multi-decadal time scales. This ENSO modulation can lead to a confused detection of anthropogenic

[6] http://www2.hawaii.edu/~stuecker/publications.html

influence on short-term climate measurements (Fig. 1.22): to what extent is the observed modulation of ENSO the cause or consequence of anthropogenic changes or intrinsic multi-decadal changes in the background state of the equatorial Pacific?

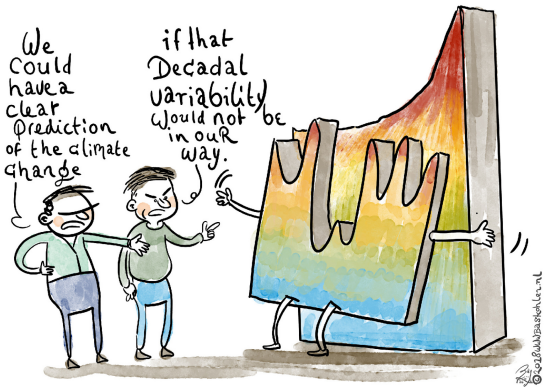

Figure 1.22 – Decadal variability drawn by Bas Kohler[7], who attended the 4th ECCWO Symposium[8] 2018.

The observational records are too short to sufficiently constrain multi-year variability (Wittenberg, 2009) and to quantify all the possible sources of the decadal modulation of ENSO characteristics. Different sources of the modulation have been suggested, including stochastic origin, internal variability in the tropical Pacific, extra-tropical atmospheric or oceanic teleconnections or external forcing.

An interannual process without inter-event memory can occasionally produce very long time periods in between El Niño events, resulting in an apparent low-frequency modulation of ENSO. Wittenberg (2009) showed for instance from statistical tests that multi-decadal spontaneous modulation of ENSO can happen stochastically from the inter-annual ENSO time scales and its seasonal phase-locking.

The low-frequency modulation of ENSO may also internally emerge, in the absence of any variation in external forcing. This has been confirmed by numerical simulations (Wittenberg, 2009; Newman et al., 2011; Stevenson, 2012). ENSO decadal modulation can be described by an internal process of the tropical Pacific climate system without invoking any extra-tropical influences, and conceived through the coupled instabilities approach, in which the prescribed mean state induces ENSO characteristics (see paragraph 1.3.2.1). A disturbance in the subtle balance of dominant dynamical feedbacks can destabilise the climate and change ENSO stability (Fedorov and Philander, 2000; Bejarano and Jin, 2008). Changes in external forcing, such as orbital forcing, also induce changes in ENSO properties at longer time-scales, as shown in paleo-proxies records and modelling of the climate of the past (see paragraph 1.3.2.2).

In turn, the intrinsic modulation of ENSO can affect the multi-decadal mean state through a positive feedback between ENSO and decadal climate modes (paragraph 1.3.2.3). In particular, the internal non-linearities of the tropical coupled system dynamics, such as the asymmetry between El Niño and La Niña, can modify the mean state through internal rectification processes (Timmermann and Jin, 2002; Jin et al., 2003a; Rodgers et al., 2004; Schopf and Burgman, 2006). This might be attributable to a two-way feedback between the climate state and ENSO. While ENSO induces tropical Pacific decadal variability through a non-linear rectification effect, the climate state provides favourable conditions for a specific regime of ENSO (Choi et al., 2009).

ENSO modulation is apprehended through many different characteristics, such as its variability (whose common metric is the standard deviation), its spatial diversity (whose common metric is the ratio EP/CP El Niño events) or its direction of propagation. It is still

[7] www.baskohler.nl, www.bocadillo.fr

[8] https://meetings.pices.int/meetings/international/2018/climate-change/Background

unclear if there is a relationship between these different parameters, even if ENSO intensity seems to be enhanced during periods with more frequent occurrence of EP El Niño events. In the following paragraphs, the low-frequency variability of the ENSO SSTA indices as well as the frequency of occurrence of the two ENSO regimes are regularly used as a metric to determine climate shifts.

An issue directly stemming from the modulation of ENSO is the definition of El Niño and La Niña events in relation to an average value. For instance, Fedorov and Philander (2001) showed the different interpretations of the tropical Pacific inter-annual variability when the reference value is no longer the mean temperature over the recent past period but the slowly undulating decadal fluctuation (Fig. 1.23).

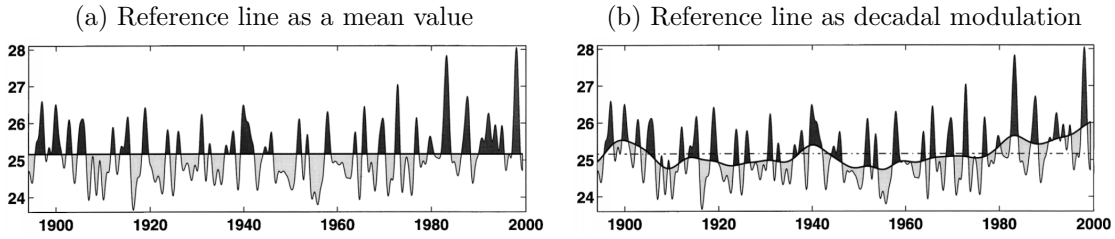

Figure 1.23 – Interannual oscillations of SST (°C) in the eastern equatorial Pacific (5°S-5°N, 80-120°W) relative to (1.23a) a time-averaged temperature for the dataset and (1.23b) the low-frequency interdecadal changes. Two different low-pass filters have been applied to the data with the cut-off frequencies of approximately 0.9 and 0.09/yr. The darker (lighter) part indicates the warm (cold) period that can lead to El Niño (La Niña) events. The figure is reprinted from Fedorov and Philander (2001)

The past evolution of the ENSO modulation is essential to understand the evolution to come. However, the analysis is made complicated by the intrinsic definition of ENSO with respect to a fluctuating mean state as well as by the difficult decorrelation of the causes of these low-frequency variations, whether they are internal or external to the climate system.

1.3.2.1 (Past) changes in the background state

Climate shifts correspond to somewhat abrupt decadal modulations of the characteristics of the tropical Pacific background state. Numerous studies highlighted a climate shift that occurred in 1976-1977 (Trenberth, 1990) via changes in correlated relationship between central Pacific and eastern Pacific SSTA indices (Trenberth and Stepaniak, 2001; Ashok et al., 2007; Ren and Jin, 2011) and changes in the statistical moments of the distribution of Niño indices, such as the standard deviation or skewness (Kao and Yu, 2009), even if the statistical significance is low because of the brevity of the time series.

Manifestations of the shift include stronger EP El Niño after (Kao and Yu, 2009) along with more El Niño than La Niña events (Fedorov and Philander, 2000). The return period of El Niño events also seems to have changed, even if the change depends on studies: from 2 years to 4 years after the climate shift for EP El Niño events while no change for CP El Niño occurrence according to Kao and Yu (2009), from 3-4 years to 4-6 years for El Niño events (defined by the Niño-3.4 index) according to An and Wang (2000). Moreover, before (after) the 1976-77 climate shift, positive SST anomalies tend to be initiated in the eastern (central) equatorial Pacific and moved westward (eastward) into the central equatorial Pacific (from the central Pacific or developed concurrently in the central and eastern Pacific) (Rasmusson and Carpenter, 1982; Wang, 1995; An and Wang, 2000; Fedorov and Philander, 2000; Ren and Jin, 2011).

After this 1976-77 climate shift, the equatorial Pacific experienced an increase in vertical stratification (Moon, 2004) as well as an eastward shift of the westerly wind anomalies (An and Wang, 2000). An and Wang (2000); An and Jin (2000) suggested that after the 1976-77

climate shift, the background conditions were more favourable to the thermocline feedback than to the zonal advective feedback, which leads to the eastward propagation of ENSO modes and produces positive NDH, enhancing ENSO asymmetry and non-linearities (Jin et al., 2003a).

A more recent climate shift occurred around 2000 in ENSO properties, with more frequent CP El Niño observed after 2000 and an almost disappearance of EP El Niño events (Kumar and Hu, 2014; Wang and Ren, 2017). The variability of the SST in the central Pacific slightly increased but weakened significantly in the eastern Pacific after 2000 (Guan and McPhaden, 2016). The frequency of these more frequent CP El Niño events is in the quasi-biennial band and their amplitude is relatively moderate compared to that of EP El Niño events. After 2000, ENSO events occurred more frequently but became much weaker. The main directions of SST anomalies propagation seem to have turned from eastward to almost static (Wang and Ren, 2017). Ren and Jin (2013) suggested that the propagation of EP El Niño events may change, while CP El Niño events made almost no contribution to the eastward propagation. It should be however noted that it is still unclear to what extent such results are not only related to the occurrence of two strong El Niño events during the 1980s-1990s. Finally, this second climate shift is accompanied by a decrease in the leading relationship of WWV on Niño-3.4 SSTA index, decreasing ENSO predictability (see McPhaden (2012); Kumar and Hu (2014); Neske and McGregor (2018) and paragraph 1.2.2.1). Note that intraseasonal tropical variability, and, in particular, MJO and equatorial Rossby waves activities, may also have undergone decadal changes in ENSO flavours around the 2000s (Gushchina and Dewitte, 2019).

It should be noted that the increase in the frequency of occurrence of CP El Niño events may begin before the 2000 shift. Ashok et al. (2007) argued that CP El Niño events increased since the 1976-77 climate shift, by analysing separately the 1958-1978 and 1979-2004 periods. Yeh et al. (2009a) determined that the number of CP El Niño events increased noticeably after 1990 when analysing a 1854-2007 SST dataset. Although some have seen this recent increase in occurrence of CP El Niño events as a consequence of global warming (Yeh et al., 2009a), it seems that the current trend to more CP relative to EP El Niño events is consistent with natural variability (Newman et al., 2011; Yeh et al., 2011).

After the 2000 climate shift, the tropical Pacific mean state returned to a colder mean state than during the 1980s-1990s. Chung and Li (2013) found the mean state of the equatorial Pacific since the last regime change (1999 for them) characterised by enhanced trade winds and a significant cooling (warming) over tropical eastern (western) Pacific. The SST variability decreased in the eastern Pacific but increased in the central Pacific. The slope of the thermocline is sharper (McPhaden et al., 2011), although the change is weak. This background state appears more La Niña-like. However, this mean state change observed in the tropical Pacific this last decades is opposite to what one would expect to produce more frequent CP El Niño events (McPhaden et al., 2011). They suggested that the natural decadal variations of El Niño projected onto changes in the background state because of the asymmetric spatial patterns of CP and EP El Niño events (see paragraph 1.3.2.3). By contrasting periods favouring CP El Niño from periods favouring EP El Niño events in a CGCM, Choi et al. (2011) suggested that CP El Niño events tend to occur more often when the zonal mean SST gradient is stronger due to an enhancement of the trade winds in the eastern Pacific similarly to the observed background state since 2000. They showed that during these periods of high-CP El Niño activity, even if the mean thermocline is deeper, primarily over the western-to-central Pacific, the vertical stratification is more unstable in the central Pacific. This leads to intensified ZAF, which promotes an increased generation of CP El Niño events. Guan and McPhaden (2016) showed that the TCF experienced a prominent (slight) reduction from 1980-1999 to the 2000s in the eastern (central) Pacific (Niño-3 versus Niño-4 regions) while the ZAF were less affected. It seems that changes in the mean state leads to an imbalance between the two main oceanic feedbacks, favouring or disfavouring the

TCF in particular. Confirming the importance of TCF, Boucharel et al. (2015) found that the TCF and the dynamical damping account for most of the multidecadal ENSO variance in the equatorial Pacific.

The changes in ENSO features (frequency, direction of propagation) associated with the background state change from 1960-1970s to 1980-1990s appear consistent with the coupled instabilities theory, in which the prescribed mean state allows the growth of ENSO-associated anomalies (see paragraph 1.2.1.3). Ren and Jin (2013) suggested from the coupled instabilities theory approach (see paragraph 1.2.3.1) that EP El Niño, which corresponds to the QQ mode of Bejarano and Jin (2008), has been enhanced, and CP El Niño, which corresponds to the QB mode, occurred more frequently during the period 1980-2000. Xie and Jin (2018) further investigated changes in the QQ and QB modes related to changes in the background state and showed that a background state resembling the 1980-1990s (deeper mean thermocline and weaker mean trade winds) favoured the dominance of the QQ mode. This is consistent with previous results from Fedorov and Philander (2001) and a background state resembling the La Niña-like mean state after 2000 with slightly stronger trade winds and a shallower mean thermocline, which favours the dominance of the QB mode (CP El Niño events). Wang and Ren (2017) suggested that the weakening of the mean trade winds may induce a weaken QQ mode after 2000 while the QB mode remains active and even became dominant. Thus, the slow-varying background state of the tropical Pacific is likely to control the preferred occurrence between CP and EP El Niño events generating the spatio-temporal complexity of ENSO. Choi et al. (2011) and Boucharel et al. (2011) showed a strong negative correlation between the low-frequency occurrence of CP and EP El Niño events in a CGCM, suggesting a possible relationship between the mean state and El Niño flavour.

In the coupled instabilities theory, there is no asymmetry between El Niño and La Niña in either anomaly amplitude or phase propagation, because of the linear dynamics invoked. However, while the direction of propagation of EP El Niño events may have changed during the climate shifts, the westward direction of La Niña SST anomalies propagation remained the same after the 1976-77 climate shift (McPhaden and Zhang, 2009). The El Niño - La Niña asymmetry as well as changes in SST variability at different longitudes suggest that the examination of changes in ENSO properties should not use a single index at a fixed location but must take into account the spatial asymmetry of ENSO anomalies.

The decadal changes in the mean state result in changes in the relative importance of the two main oceanic feedbacks, the thermocline and zonal advective feedbacks, in different tropical Pacific regions, which may compensate each other. The linear stability theory does not take into account different longitudinal behaviours. Boucharel et al. (2015) developed a method providing local information of dynamical feedbacks over all the tropical Pacific and showed that the eastern Pacific displayed a decrease of the thermocline feedback and the dynamical damping since 2000 while the western Pacific displayed an intensification. Lübbecke and McPhaden (2014) linked this weakening of the TCF in Niño-3 region to a reduced thermocline slope associated with a weak response of the wind stress to eastern Pacific SST anomalies. On the other hand, Dewitte et al. (2013) showed that the stronger equatorial stratification after the 1976-77 shift favoured the thermocline feedback (TCF) in the western-central Pacific. The increase of the vertical stratification allows for a more effective influence of the thermocline depth variations on the mixed-layer variability in the central Pacific. According to this study, the ZAF show decadal modulation east of the dateline. The main oceanic feedbacks may experience different decadal changes according to the region of the equatorial Pacific, leading to a different balance between them, which can favour different El Niño regime.

Contrasting the regions where changes in oceanic feedback may be different appears to be determinant in the selection of the favoured El Niño type. However, the coupled instabilities theory emphasised the role of the mean thermocline depth, as a proxy of the vertical stratification along the equator. Observations and oceanic reanalysis reveal a small change in the

mean thermocline depth at decadal-to-interdecadal time scales. Conversely, changes in stratification that affect both the intensity and sharpness of the thermocline, as well as changes in the slope of the thermocline, can be far more pronounced. For instance, a slight flattening of the thermocline, as experienced after the 1970s, is associated with an increased stratification in the central equatorial Pacific. Moreover, a deeper thermocline in the eastern Pacific, due to a flattened equatorial thermocline, is expected to reduce ENSO activity due to a weakened Walker circulation and reduced ocean-atmosphere coupling (Zebiak and Cane, 1987; Meehl et al., 2001). However, CGCMs and conceptual models (Rodgers et al., 2004; Cibot et al., 2005; Choi et al., 2009; Thual et al., 2011) provide counter-intuitive relationship between thermocline depth variation and low-frequency ENSO mode. Dewitte et al. (2007) suggested that a flatten thermocline may be associated with stronger ENSO modulation through different longitudinal contributions of the baroclinic modes derived from the equatorial wave dynamics. The suggested tropical mechanism involves the non-linear rectifying effect (see paragraph 1.3.2.3). But changes in the thermocline depth favouring CP El Niño events are not consistent between studies. Yeh et al. (2009a) and Xie and Jin (2018) suggested that a shallower thermocline (in the central Pacific) favours CP El Niño events when Choi et al. (2011) and Wang and Ren (2017) argued that it comes from a deeper thermocline in the western-to-central Pacific.

Finally, the separation in two distinct periods of ENSO modulation is not so clear. Ashok et al. (2007) and Yeh et al. (2009a) underlined recently that the number of CP El Niño events increased, compared to previous period even if the periods are not the same (1958-1978 for Ashok et al. (2007), 1854-1990 for Yeh et al. (2009a)). Moreover, the CP and EP distinction is dependant on the diagnostic method used (see paragraph 1.1.2). The direction of propagation is another ENSO property lacking a clear definition. Whereas Santoso et al. (2013) considered that strong El Niño events propagate eastward, Wang (1995) suggested that not only the 1982-83 strong El Niño events but also the 1986-87 and 1991 began with an anomalous warming in the central Pacific before the coastal warming off Ecuador. McPhaden and Zhang (2009) with a longer time-series suggested that all El Niño events since 1980 (2 strong El Niño and 6 weak-to-moderate El Niño events) showed clear eastward propagation. They further argued that the suggested westward propagation of SST anomalies during the termination phase of the weak-to-moderate El Niño composite is an artefact of the tendency for La Niña to follow El Niño since La Niña events are associated with not only unusually cold SST in the eastern basin but unusually warm SST in the far western Pacific. Rather than number of events or direction of propagation, other indicators such as regional variability (central versus eastern SST anomalies) or main modes of variability (PC time-series) seems to be more reliable to differentiate ENSO modulation.

Periods of climate shifts were extensively studied since the development of reliable observations. But interestingly, combined existence of CP and EP El Niño events has been shown during the last millennium (Stevenson et al., 2017) and can go back to the mid-Holocene (Karamperidou et al., 2015).

1.3.2.2 Changes in external forcing

Changes in external forcing play also a role in the slow-varying changes of ENSO properties. Past climate are characterised by different Earth's orbital parameters while present and future climates mainly undergo the influence of changes in radiative forcing due to anthropic activities such as greenhouse gas (GHG) and aerosols emissions. Volcanic eruptions provide also strong climate control on a large spatial scale, even if at shorter time scales (Khodri et al., 2017). It was for instance the greatest climate control during the pre-industrial period (Stevenson et al., 2017).

At larger time-scale, the impact of orbital forcing on ENSO amplitude may be investigated through paleo-proxies and past climate simulations. Karamperidou et al. (2015) showed that changes in tropical Pacific seasonal cycle (SST and winds) due to orbital forcing changes

during the mid-Holocene lead to changes in timing and duration especially for EP El Niño events. They were less frequent, with a lower variance and tended to develop more slowly and decay faster, with a shift of the seasonality. Few changes in CP El Niño events appeared although a slight increase in their occurrence frequency as observed. They argued that changes in EP El Niño events properties are linked to changes in the western Pacific winds seasonal cycle, which remotely controlled the eastern Pacific during ENSO development. In the western Pacific, a weakening of the trade winds in early boreal spring in the mid-Holocene initiates an anomalous downwelling annual Kelvin wave, which reaches the eastern Pacific during the ENSO development season, weakens the upper ocean stratification, and results in reduced ENSO upwelling feedback. The correct representation of forcing in the CGCMs is therefore crucial.

Stevenson et al. (2017) analysed the more recent period of the last-millennium (850-2005) through model simulations with a longer duration than the time scales of ENSO internal variability (Wittenberg, 2009; Stevenson et al., 2010; Stevenson, 2012). Thanks to different forcing scenarios (GHG, ozone and aerosols, volcanic, land use and land cover, orbital changes and solar irradiance), they investigated the impact of each forcing separately, as well as the combined impact ("full forcing"). The major controls on mean climate are greenhouse gas-driven warming and tropospheric ozone/aerosol-driven cooling during the twentieth century, and volcanic eruptions during the pre-industrial period. Since the beginning of the industrial period ($\sim$ 1850), GHG emissions are responsible of an increase in Pacific temperatures characterised by a stronger warming in the eastern equatorial Pacific than in the western, associated with a weakening of the Walker circulation (see paragraph 1.4.1). On the contrary, the effect of ozone and aerosols leads to an overall cooling across the tropics and, in particular in the equatorial Pacific, accompanied by a strengthening of the trade winds. These effects cancel each other out on the Pacific, but some warming due to GHG persists, mostly on the Warm Pool and in the south-east tropics. They conclude that changes in ENSO amplitude, computed as the 20-year running SST anomalies variance in the Niño-3.4 region, between the post-industrial period and the last millennium are close to the detectability threshold, suggesting that the changes in the twentieth century forcing have not yet played a substantial role. When analysing paleo-climate reconstructions, a recent ENSO amplitude strengthening is emphasised. For instance, McGregor et al. (2013) suggested that the ENSO variance (Niño-3.4) for any 30 year period during the interval 1590-1880 was considerably lower than that observed during 1979-2009. (Liu et al., 2017) using reconstructions (based on oxygen isotopes) established that the variability of Niño-4 SST increased from 1190 to 2007. However, the estimation of past ENSO variability through paleo-proxies shows uncertainties due to proxy resolution (from seasonally to centennially resolved) and spatial sparsity. Karamperidou et al. (2015) pointed out that the spatial diversity of ENSO, and therefore the location of the proxy records, needs to be taken into account when analysing ENSO variance.

1.3.2.3 Rectification onto the mean state

Although many studies questioned how changes in mean state may affect ENSO variability, the opposite question, how changes in ENSO can affect long-term changes in the tropical Pacific climate, has also been the subject of many studies.

Decadal modulation of ENSO is partly explained by the source of irregularities described in paragraph 1.2.2. Timmermann et al. (2003) and An and Jin (2004) related the El Niño-La Niña asymmetry to the intrinsic non-linearities of the tropical Pacific coupled system via the NDH (see Jin et al. (2003a) and paragraph 1.2.2.4). This dynamical relationship between decadal modulation of ENSO, asymmetry and NDH, is based on the decadal changes in the mean climate state, which may produce favourable conditions for the thermocline feedback rather than the zonal advection feedback, resulting in the eastward spread of ENSO-related atmospheric and oceanic variables (Jin et al., 2003a; An and Jin, 2004). This eastward propagation of the ENSO mode more easily produces a positive NDH, which results in the El

Niño-La Niña asymmetry. Whatever the phase of the ENSO cycle, this term is indeed always positive, which implies an increased warming in the El Niño period (pushing the positive anomaly to increase) as well as a cooling damping in the La Niña period (preventing the negative anomaly to grow too much). In this way, this reinforces the mean state control on ENSO asymmetry (Fig. 1.24). On decadal time scales, the heat balance is not zero since there remains a residual coming from the compensation between warm and cold events (positive NDH), causing an additional warming potentially having an effect on the mean state itself (Jin et al., 2003a; Rodgers et al., 2004; Choi et al., 2009). Jin et al. (2003a) have shown that at least half of the observed warming of the tropical Pacific in recent decades is due to NDH warming.

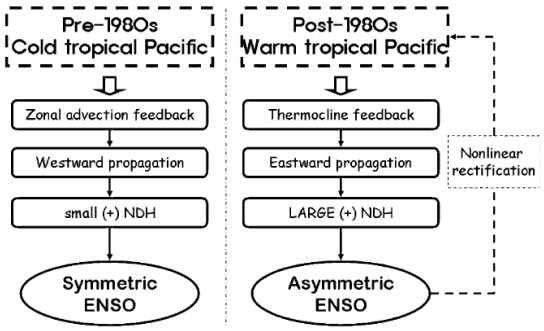

Figure 1.24 – Schematic diagram of suggested cause and effect for the interdecadal changes in ENSO asymmetry. The figure is reprinted from An (2009).

Other aspects of the El Niño-La Niña asymmetry show in their respective mean intensity (stronger SST anomalies during El Niño events) and spatial centre of action (a larger westward extension of negative SST anomalies during La Niña events). The mean spatial pattern associated with the residual (that is the sum) of the composite El Niño and La Niña pattern looks like a zonal dipole along the equator, warm in the east and cold in the west during ENSO-active periods. Interestingly, these residuals of incomplete compensation between the two types of ENSO events are similar to the spatial pattern associated with the decadal changes in SST, that is the Tropical Pacific Decadal Variability (TPDV) (Rodgers et al., 2004; Cibot et al., 2005; Choi et al., 2009). These studies have thus suggested that these residuals induced by ENSO asymmetry can rectify into background conditions and lead to the slow variability of the tropical Pacific. Decadal changes in the tropical Pacific (TPDV) emerge at least in part from the non-linear rectified effect of ENSO onto the mean state, by transferring energy from high frequencies variability to low frequencies through non-linear processes. Moreover, this TPDV mode is strongly correlated to ENSO decadal modulation, so that periods of high ENSO activity are characterised by a flattening of the equatorial thermocline associated with a deepening of the thermocline and a warming of subsurface waters in the eastern Pacific (Rodgers et al., 2004; Cibot et al., 2005). It is a counter-intuitive result because this particular spatial pattern of the mean state should accompany a reduced activity of ENSO (Zebiak and Cane, 1987; Meehl et al., 2001). This therefore questions the commonly accepted assumption that the low-frequency modulations of ENSO are due to decadal changes in the mean state. Conversely, it suggests that the decadal background state (TPDV) associated with periods of high ENSO activity can be interpreted as the residual of ENSO asymmetry. Because this pattern spatial is also similar to TPDV, the decadal modulation of ENSO induces the mean state associated with the dominant decadal mode of variability.

Choi et al. (2009) further suggested that the warming (cooling) of the ocean surface can cause an increase (decrease) in the variability of ENSO whereas the deepening (shoaling) of the thermocline can cause a suppression (an increase) in the variability of ENSO. In other words, the high variability of ENSO is mainly due to changes in the mean SST, whereas, as

expected, the average thermocline plays a role in suppressing ENSO activity. It provides a reasonable answer to the counter-intuitive mean state associated with high ENSO activity in these studies. Choi et al. (2013a) suggested that the strength of this feedback depends on ENSO variability in CGCMs. The tropical Pacific decadal oscillation is likely to be an intrinsic mode of the tropical Pacific that affects and is influenced by ENSO at the same time. There is a positive feedback with the mean SST and a negative feedback with the mean thermocline depth that destabilise the tropical Pacific decadal oscillation (Fig. 1.25).

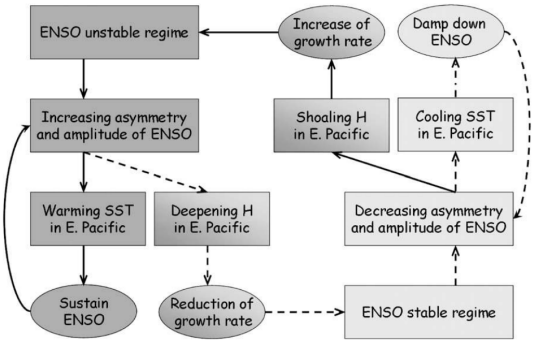

Figure 1.25 – Schematic diagram showing the interactive two-ways feedbacks mechanism of decadal variability in the tropical Pacific. The figure is reprinted from Choi et al. (2009).

It should be noted however that the TPDV mode is often the second mode of decadal variability found in most of the CGCMs used in these studies (Cibot et al., 2005; Choi et al., 2013a). It could be explained by the simulated frequency of El Niño events too high (quasi-biennial), which would be imprinted too strongly in the decadal variability of the tropical Pacific compared to observations.

Asymmetry between warm EP and CP El Niño events can also result in changes in the mean state. Because CP El Niño events have a short period of return and tend not to be followed by a La Niña event, their occurrence may modulate the climate mean state in the tropical Pacific, by an accumulative warming (Kug et al., 2009; McPhaden et al., 2011). It may be the case of the recent warm periods of 1990-1995 and 2001-2006. Lee and McPhaden (2010) suggested that the warming trend of the Warm Pool SST in the central Pacific over the period 1980-2010 is primarily a result of more intense CP El Niño events rather than a warming of the mean SST, even if the observed period is too short for the results to be statistically significant.

The low-frequency variability and the forcing changes such as the global warming can thus strongly overlap and the decorrelation of their signals, if possible, is a crucial remaining challenge for the climate community (see next section 1.4).

1.4 Global warming

The Earth's climate is changing, more drastically than it could have due to only internal variability (see paragraph 1.3.2). The main radiative forcing today comes from anthropogenic greenhouse gases, with the most telling indicator being the concentration of CO_2 in the atmosphere. The global mean CO_2 concentration exceeded 400 ppm in 2016, highest level ever achieved in 800,000 years. As a consequence, the last four years are the warmest years recorded since 1880[9] and 16 of the 17 warmest years have occurred since 2000[10].

To determine the response of the climate system to global warming, simulations of the climate system are used under different scenarios of future radiative forcing. Some projected changes of the mean state with global warming are common to a large number of models (see

[9] https://climate.copernicus.eu
[10] https://www.ncdc.noaa.gov/

paragraph 1.4.1). However, CGCMs projections may underestimate long-term warming, due in particular to the underestimation of the polar amplification, by a factor of two (Fischer et al., 2018).

Due to complex and numerous feedbacks, there is no consensus on the response of ENSO feedback to global warming, neither on the response of ENSO diversity to global warming. Changes in the mean state due to global warming may induce changes in ENSO statistics (see paragraph 1.4.2.1) and thermodynamical and dynamical processes (see paragraph 1.4.2.2), which may be different to changes due to internal low-frequency variability (see paragraph 1.3.2.1). Important questions, with many socio-economic issues, are thus still open:

- Has global warming already affected ENSO?
- To what extent do recent observed changes in ENSO result from anthropogenic forcing or intrinsic multi-decadal fluctuations of the climate system?
- How will global warming impact ENSO in the future?

Understanding if and how El Niño characteristics will evolve in a warming world is a major issue because it causes extreme weather conditions around the world.

1.4.1 Changes in the mean state

Some projected changes in the tropical Pacific mean state under global warming scenarios appear to be robust features among CGCMs (CMIP3 and CMIP5 databases):

- the Walker circulation is projected to weaken (Vecchi et al., 2006; Vecchi and Soden, 2007). This feature is contrary to what has been observed in recent decades (see paragraph 1.3.2.1);
- the equatorial Pacific is projected to warm faster than the off-equatorial Pacific (Collins et al., 2010), the east equatorial Pacific and the maritime continent faster than the central equatorial Pacific (Xie et al., 2010), the surface faster than the subsurface;
- the equatorial Pacific mean rainfall is likely to increase, following a warmer-gets-wetter pattern (Xie et al., 2010; Chadwick et al., 2013; Xie et al., 2015).

It should be noted that these climate change features are those that occur during El Niño events. An ENSO analogy is thus often invoked for interpreting tropical Pacific climate change. The east-west asymmetry that can result from a change in forcing can be amplified in the same way as the initial disturbance leading to an El Niño (or La Niña) event, through the different coupled feedbacks. This would then lead to an altered mean state of the tropical Pacific resembling an El Niño or La Niña event. For instance, recent observed changes in the tropical Pacific are referred to as a La Niña-like state (see paragraph 1.3.2.1) and future projected state of the tropical Pacific is often referred to as an El Niño-like state. However, subsurface temperature projected changes are not consistent with an El Niño-like state.

The Walker circulation is projected to weaken (Vecchi and Soden, 2007; Chung et al., 2019), which will decrease the strength of the trade winds and thus alter the thermal structure and ocean circulation of the tropical Pacific (DiNezio et al., 2009; Santoso et al., 2013). This will in particular promote a slower equatorial circulation (Vecchi et al., 2006; Vecchi and Soden, 2007; DiNezio et al., 2009) and a weakening of the equatorial upwelling (DiNezio et al., 2009; Dewitte et al., 2013). At inter-annual time scales, the weakened mean trade winds lead to a flattening of the thermocline (Philip and van Oldenborgh, 2006; Vecchi and Soden, 2007; Yeh et al., 2009a), a reduction of the cold water upwelling in the eastern Pacific, a relative warming of the eastern Pacific SST compared to the western SST, and in turn an even stronger weakening of the trade winds through the Bjerknes feedback.

The equatorial thermocline become shallower and sharper in all CGCMs projections (Vecchi and Soden, 2007; Yeh et al., 2009a; DiNezio et al., 2009). The increased vertical stratification due to the global warming is likely not only over the eastern Pacific (except the

(a) Current tropical Pacific mean state

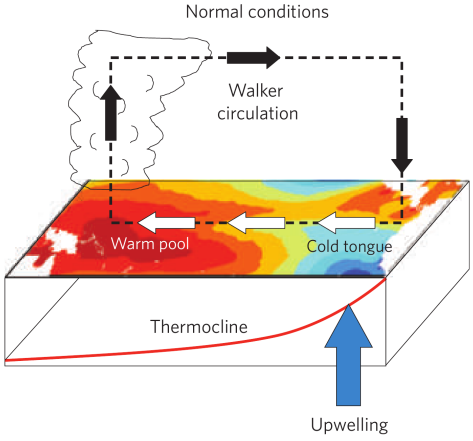

(b) Flattening and shallowing of the mean thermocline

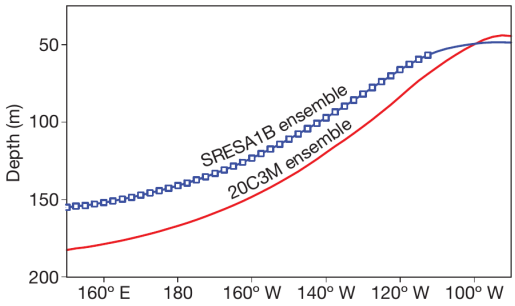

(c) Projected changes in the mean state

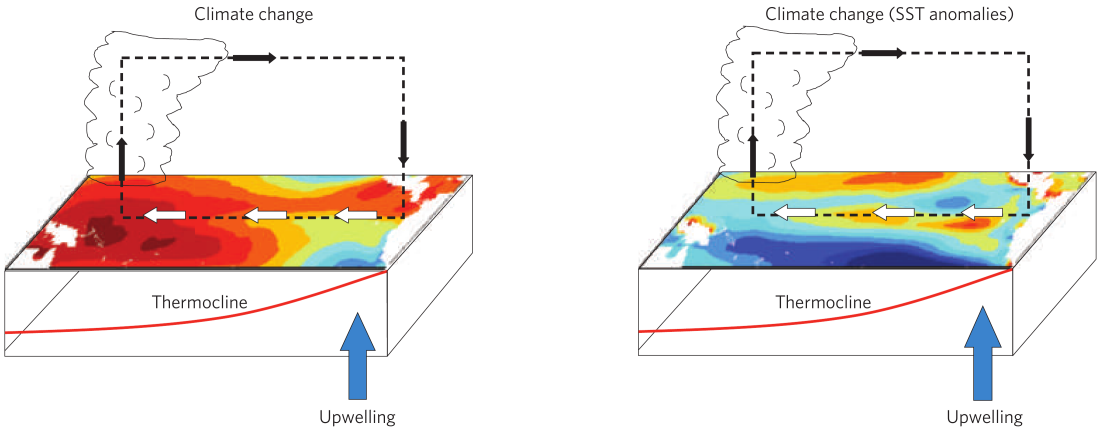

Figure 1.26 – Projected changes in the mean state under global warming. (1.26a) Mean current climate conditions in the tropical Pacific, indicating SST, surface wind stress and associated Walker circulation (white and black arrows), the mean position of deep convection and the mean upwelling (blue arrow) and position of the mean thermocline. (1.26b) Ensemble mean thermocline depth for (red line) the twentieth century (20C3M) and (red line) the Special Report for Emission Scenario A1B climate change projection applied to CMIP3 models (SRESA1B). (1.26c) The projected mean climate conditions under climate change. The trade winds weaken (narrow white arrows), the thermocline flattens and shoals, the upwelling is reduced (narrow blue arrow) although the mean vertical temperature gradient is increased and SST (shown as anomalies with respect to the mean tropical-wide warming on the right) increase more on the equator than off. It should be noted that SST anomalies are expressed with respect to the basin averaged temperature change, so that blue colours indicate a warming smaller than the basin mean, not a cooling, red colours indicate more warming than in average in the rest of the basin. Figures 1.26a, 1.26c are reprinted from Collins et al. (2010), figure 1.26b is reprinted from Yeh et al. (2009a).

far eastern Pacific) but also over the whole equatorial Pacific. This is due to a dynamical adjustment to the decrease of equatorial trade winds (Vecchi and Soden, 2007) as well as the tendency of surface waters to warm up faster than the deep ocean (Vecchi and Soden, 2007; DiNezio et al., 2009). Changes in thermocline depth in the eastern Pacific are thus affected by two compensating processes: the rise of the mean thermocline tends to reduce its depth in the eastern Pacific but a weakening of the equatorial tilt of the thermocline tends to deepen it in the western Pacific. The resulting thermocline depth in the eastern Pacific leads to opposite ENSO feedbacks (Collins et al. (2010), see paragraph 1.4.2.2) but depends on the CGCM.

SST will warm faster at the equator than in off-equatorial regions because the weaker Walker circulation will lead to a slowdown in the horizontal ocean circulation and a reduction in thermal flow divergence in the equatorial Pacific. Consequently, less heat content will be transferred poleward (Vecchi and Soden, 2007; DiNezio et al., 2009). This enhanced equatorial warming is also associated with a weaker evaporation damping on the equator (Xie et al., 2010).

Another robust feature of the CGCMs ensemble-mean prediction is the increase of the mean rainfall over the central and eastern equatorial Pacific. This change in mean tropical rainfall is related to the atmospheric circulation (Chadwick et al., 2013), which in turn is closely related to changes in mean SST spatial patterns. The weakening of the zonal and meridional SST gradient, due to the different warming rates in different tropical Pacific regions, favours a shift in convective areas. Slight changes in SST will facilitate the convection whereas strong current gradients, barriers of convection, require stronger changes (Cai et al., 2014).

However, these projections are to be nuanced because the projected changes in SST and rainfall occur in a region where CGCMs display known and persistent climate biases such as the double ITCZ and the Cold Tongue cold bias (see also paragraph 2.1.2.2). The shared common biases of the simulated tropical Pacific mean state by CGCMs reflect some common deficiencies in the models. This may potentially interact with the warming effect from GHG forcing, and may produce unrealistic climate change patterns that interfere with model projections (Collins et al., 2010). The simulation of tropical rainfall is not realistic even in the current climate, with in particular a tendency by CGCMs to simulate a double ITCZ, which makes projected changes highly uncertain (Ma and Xie, 2013). The Cold Tongue bias, which consists in a Cold Tongue region too cold and that extends too far to the west, may be of the same order of magnitude as the projected climate change signal in some models (DiNezio et al., 2010). Moreover, despite the relatively robust projection of a reduction in the mean sea-level pressure (SLP) gradient across the equatorial Pacific (Vecchi et al., 2006), the weakening of the zonal SST gradient is not systematically simulated (Vecchi and Soden, 2007; Yeh et al., 2012). Changes in the east-west SST gradient under global warming are also poorly related to the climatological thermocline depth in CGCMs (Li et al., 2016). The relationship between SST, thermocline and trade winds may become less strong than that resulting from the current Bjerknes feedback. This is in contrast to El Niño events, when the thermocline response is heavily dominated by a less tilted thermocline. The unexpected response of SSTA zonal gradient seems to be due to the excessive Cold Tongue bias in CGCMs, which induces an excessive projected SST warming in the western Pacific (Li et al., 2016; Ying et al., 2019). Thus, the projected SST tropical Pacific warming pattern should be closer to an El Niño-like pattern when correcting the Cold Tongue bias.

1.4.2 Changes in ENSO characteristics in a warmer climate

1.4.2.1 Changes in ENSO statistics

Projected atmospheric and oceanic mean state changes in the tropical Pacific are likely to alter the amplitude, frequency, seasonal timing or spatial patterns of ENSO. However, some

of the projected changes in the tropical Pacific mean state due to global warming are not subject to inter-model consensus, and conversely, some robust projected changes may actually be due to recurrent and common model biases. As a result of these limitations, there is no inter-model consensus on the evolution of ENSO amplitude and frequency (DiNezio et al., 2012; Bellenger et al., 2014). When analysing the evolution of the statistics of traditional ENSO indices, such as the Niño-3 index or the ONI, there is no consensus on changes in ENSO variability, neither with global warming, nor over the last century with the increase of GHG (Collins et al., 2010). For instance, even if all CMIP5 models simulate a mean warming in the Niño-3.4 region, its variability shows a wide spread among CGCMs (Fig. 1.27). More models simulate a weakening of ENSO amplitude but when the model does simulate a strengthening of the ENSO amplitude, this increase is more important.

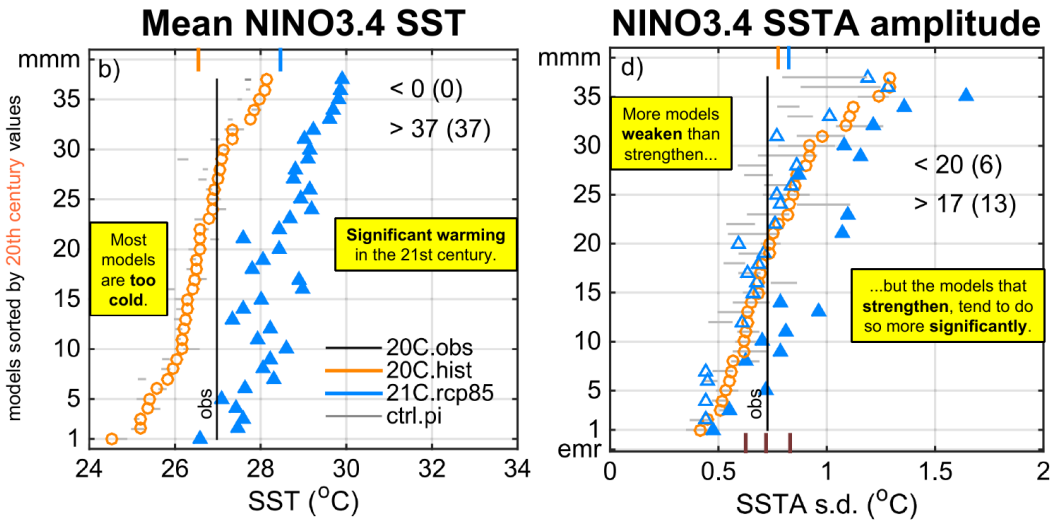

Figure 1.27 – Comparison of (left) Niño-3.4 mean state and (right) ENSO amplitude in current and future climates. The 37 CMIP5 models are sorted according to the 100-yr averaged Niño-3.4 SST (SSTA standard deviation in the figure on the right) in the twentieth century (20C, historical runs, 1900-1999). The black vertical line marks the 20C observation value. The multi-model mean (MMM) is shown at the top, with 20C in orange and 21C (the twenty-first century, RCP8.5 scenario, 2000-2099) in blue. Pre-industrial control simulations of each model are divided into 100-yr sliding epochs to calculate the 100-yr averaged SST and the 2.5th-97.5th percentile of the distribution are shown as grey horizontal lines. The number of models with decreased (<) or increased (>) change is indicated. The number in the brackets is the count for significant changes out of the range given by the control run. In addition, in the figure on the right, the 21C results with an increased (decreased) change are shown filled (unfilled). The figures are reprinted from Chen et al. (2017a).

When selecting models that are able to simulate non-linear processes associated with extreme El Niño events, only 12 over 21 models project an increase in ENSO amplitude in the Niño-3 region and only 12 over 21 generate an increased frequency of extreme (precipitation) El Niño events (Cai et al., 2015a).

Projected changes in El Niño intensity are also heavily model dependent (Guilyardi et al., 2009b; Kim and Yu, 2012; Bellenger et al., 2014; Chen et al., 2017b) and not significantly distinguishable from natural modulation (Stevenson, 2012; Chen et al., 2017a; Zheng et al., 2018). This uncertainty is mainly due to the inter-model uncertainty in the spatial pattern of tropical Pacific surface warming (Zheng et al., 2016), simulating a pattern that can go from an El-Niño-like to a La Niña-like warming pattern. Models projecting an enhanced (reduced) mean warming in the eastern equatorial Pacific project an increased (decreased) ENSO amplitude (Zheng et al., 2016). These differences in projected patterns are mainly due to the common Cold Tongue bias and correcting this bias favours an El Niño-like mean warming pattern (Li et al., 2016; Ying et al., 2019). This suggests a probable increase in ENSO-related SST variance under global warming.

Chen et al. (2017b) suggested that the divergence in projections of El Niño amplitude changes comes from the simulation of the climatological mean Pacific subtropical cells (STC). They induce changes in the anomalous thermocline response to wind forcing through perturbations of the meridional structure of ENSO. This bias leads to a westward shift of ENSO variability as well as a meridionally constrained structure. That means that such simulated spatial patterns are subject to caution, whereas the phenomenon is usually defined from departure from the mean state in fixed equatorial Pacific regions, such as Niño-3 or Niño-3.4.

Changes in ENSO diversity are also subject to many uncertainties. Kim and Yu (2012) showed that CMIP5 models better simulate the observed spatial patterns of the two types of ENSO than CMIP3 models, with a smaller inter-model intensity spread. By using the "KY" method (see paragraph 1.1.2.2) and selecting CMIP5 models that simulate well the observed ENSO diversity, they showed that the intensity of CP ENSO steadily increases from the pre-industrial (PI) to the RCP4.5 simulations (see Taylor et al. (2012) and paragraph 2.1.2) through historical simulations (current climate), while the intensity of EP ENSO increases from the PI to the historical simulations and then decreases in the RCP4.5 projections. The CP-to-EP ENSO intensity ratio, as a result, is almost the same in the pre-industrial and historical simulations but increases in the RCP4.5 simulations. It is consistent with results of Yeh et al. (2009a), who suggested that the proportion of CP El Niño events would increase compared to EP El Niño events from historical to RCP8.5 climate in 11 CMIP3 models. Using the linear instabilities coupled theory in the most likely future mean state of the tropical Pacific (i.e. weaker trade winds, weaker Cold Tongue, and shallower thermocline), Xie and Jin (2018) determined that the CP ENSO activity is projected to increase.

However, the proliferation of indices used to define each kind of El Niño events (see paragraph 1.1.2.2) has led to somewhat contradictory projected changes in ENSO statistics. In contrast to the results previously presented, Cai et al. (2014, 2015a, 2017) suggested that the frequency of occurrence of extreme precipitation El Niño events, associated with anomalous precipitation in the eastern Pacific, would increase with global warming (see next paragraph). Wang et al. (2017) showed that the occurrence frequency of extreme precipitation El Niño events (defined as Cai et al. (2014)) will continue to increase even after stabilising the warming at 1.5 °C, which is the aspirational target of the Paris Agreement and the Special Report on Global Warming of 1.5 °C (SR15) of Intergovernmental Panel on Climate Change (IPCC). They argued that the extreme precipitation El Niño occurrence frequency would continue to increase up to a century after the warming stabilisation. A deepening of the thermocline after the stabilisation would result in a faster warming of the eastern equatorial Pacific than the off-equatorial regions. Recently, Williams and Patricola (2018), using also a convection proxy, projected that extreme El Niño, Modoki El Niño and La Niña events would all become more frequent in the future climate, whereas the tropical Pacific would experience less neutral conditions. Santoso et al. (2013) and Chen et al. (2017a) suggested that global warming will favour more eastward propagating El Niño events, which is a feature presently mostly associated with strong El Niño events. The increase in extreme El Niño events is in turn conducive to an increase in the frequency of La Niña events due to a discharged thermocline that favours the influence of cold subsurface waters in the central Pacific, preferential region of La Niña events.

These different projection studies however are not based on the same definitions of El Niño and it is difficult to estimate whether there is a correspondence between their results. Moreover, another difficulty is the lack of consensus among CGCMs on the response of ENSO feedbacks to global warming.

1.4.2.2 Changes in ENSO dynamics

Mean state changes (especially the SST zonal gradient, namely the El Niño or La Niña-like warming pattern) may induce opposite changes in ENSO amplitude, which may explain the weak agreement in projected changes of ENSO variability among CGCMs. Changes in mean

state can lead to a different balance between damping or amplifying processes (Philip and van Oldenborgh, 2006) and, possibly, to wrong compensation between them (Collins et al., 2010). Moreover, the two regimes of El Niño are likely to have different sensitivity to changes in mean state. Changes in ENSO-related feedbacks are thus not only linked to changes in the mean state but also to changes in ENSO-related anomalies. In addition to the delicate balance of the ENSO feedback loop, the diversity in models sensitivity to global warming makes it difficult to identify which parameter, characterising changes in the mean state, is critical. Models biases, both in the simulated mean state and ENSO atmospheric feedbacks, such as the wind-SST (atmospheric part of the Bjerknes feedback) or the heat flux-SST feedbacks, can lead to unrealistic errors compensations (Bayr et al. (2018b), see also paragraph 2.1.2.2). However, some assumptions can be made using theoretical and numerical simulations that account for some of the robust changes in the tropical Pacific background.

The different projected changes of the thermocline characteristics, most notably its shoaling, sharpening and flattening, can have different effects on ENSO activity. An et al. (2008) even suggest that changes in the vertical temperature gradient is more influential on ENSO than changes in the mean surface temperature. The coupled instabilities models of Fedorov and Philander (2000) and Bejarano and Jin (2008) indicate that a shallower mean thermocline may lead to an increase in ENSO variability. However, these theories do not take into account regional disparities between the central and eastern Pacific. The dynamics of extreme El Niño events, which project mainly onto the eastern Pacific, are different from that of moderate events (Santoso et al., 2013; Cai et al., 2014; Capotondi et al., 2015) and their response to global warming must therefore be studied separately.

A shallower mean thermocline is due to a rise in the central Pacific and a slight deepening in the eastern Pacific under global warming scenarios (Fig. 1.26b). It is consistent with the weakening of the Walker circulation (Vecchi et al., 2006). A shallower thermocline is more sensitive to wind variations and enhances ocean-atmosphere interactions in the mixed layer (Philip and van Oldenborgh, 2006), which may perturb ENSO dynamics. SST become more sensitive to variability of the thermocline depth, which is likely to destabilise the balance of the two main ENSO oceanic feedbacks, the thermocline and the zonal advective feedback. A shallow thermocline tends to favour the ZAF in the central Pacific, which favours CP El Niño events (Kug et al., 2009). Moreover, a shallower thermocline in the central Pacific tends to reinforce SST anomalies induced by vertical advection there, because vertical movements of isotherms through the thermocline may influence SST variability more easily (Dewitte et al., 2013). A sharper thermocline may also enhance the zonal subsurface temperature gradient, which would increase the subsurface zonal advection and thus would increase the ENSO amplitude (DiNezio et al., 2012).

Similarly, a flattening of the thermocline tends to enhance the ZAF in the central Pacific and decrease the TCF in the eastern Pacific, which may promote a westward shift of the ENSO-induced warming (Yeh et al., 2009a).

Changes in the thermocline depth in the east of the equatorial Pacific could also affect the characteristics of El Niño. In the current climate, the mean upwelling in the eastern Pacific, associated with the mean subsurface zonal advection, acts to reinforce the climatological zonal and vertical temperature gradients. This tends to weaken anomalous SST warming in this region. Both the mean upwelling and advection are projected to decrease in CGCMs under global warming because of the weakening of the trade winds (Vecchi et al., 2006). This could favour an increase in ENSO activity in the eastern Pacific (Collins et al., 2010). However, a weaker mean upwelling ($\overline{w}$) may produce a weaker thermocline feedback in the eastern equatorial Pacific, and thus decrease EP El Niño variability (DiNezio et al., 2012). A shallower thermocline depth in the eastern Pacific (which is not the case if the thermocline flatten with a slight deepening in the eastern Pacific), would be more influential on SST variability (Philip and van Oldenborgh, 2006) and therefore favour an increase of ENSO variability in the eastern Pacific.

Another likely impact of global warming is the increase in ENSO-related rainfall variability in the central and eastern tropical Pacific (Power et al., 2013). The more frequent establishment of atmospheric convection in the eastern equatorial Pacific is induced by the decrease or even reversal of the meridional and zonal SST gradients (Cai et al., 2014, 2015a, 2017), rather than by localized warming that exceeds the convective threshold (which is likely to increase with the mean SST (Johnson and Xie, 2010)). They argued that because of the faster SST warming in the eastern tropical Pacific and the associated decrease in the meridional gradient, the ITCZ is likely to move more often southward and induce ENSO precipitation in the eastern Pacific. The ITCZ southward shift and the increase in extreme rainfall in the eastern Pacific are two features associated with extreme El Niño events. This mechanism will induce a doubling in occurrence frequency of extreme precipitation El Niño events, defined in terms of eastern equatorial rainfall pattern, under the global warming RCP8.5 scenario. However, Cai et al. (2017) and Williams and Patricola (2018) pointed out that it is unclear to what extent rain-based indices reflect changes in ENSO variability dynamics or changes in mean state due to the increase in column water vapour. Cai et al. (2017) decomposed the rainfall time-series trends in Niño-3.4 and argued that the increased frequency in occurrence of extreme precipitation El Niño events account for 50 % of the increase in mean rainfall. They confirmed, analysing the upward atmospheric vertical velocity, another proxy for deep convection less subject to an arbitrary threshold than rainfall, that the greater warming in the eastern equatorial Pacific than surrounding regions (Xie et al., 2010) would make convection easier to establish in the normally cold and dry Niño-3 region, even without SST changes (Cai et al., 2014). Williams and Patricola (2018) showed, using a method taking into account the increase in the convective threshold under global warming, that both CP and extreme EP El Niño frequency should simultaneously increase. This is because both the central and eastern Pacific SST shift closer to the convective threshold (Johnson and Xie, 2010). However, we should keep in mind that these results are directly related to the projected tropical Pacific warming pattern, which is sensitive to common model bias, although the Cold Tongue bias rectification seems to favour warming in the eastern Pacific and thus facilitate ENSO rainfall.

Another robust change in the projected mean state among CGCMs is the weakening of the westward equatorial mean currents, which can even lead to currents reversals (Vecchi et al., 2006; Santoso et al., 2013). Santoso et al. (2013) suggested that this is a determining factor for the future increase (up to a doubling) of El Niño events that propagate eastward whatever their magnitude. The eastward propagation is a current feature of extreme El Niño events, contrary to moderate El Niño and La Niña events. However, when analysing observed eastward propagating El Niño events after 1976, especially the two extreme El Niño events of 1982-83 and 1997-98, the propagation direction is partly due to the weakening of the westward mean currents and partly due to eastward current anomalies, strong enough to reverse the mean current. In future climate simulated by 40 CMIP3 and CMIP5 models, Santoso et al. (2013) showed that eastward propagating El Niño events are mainly associated with the projected mean currents weakening. This facilitates the current reversal and increases the probability of eastward propagating El Niño events of any intensity, and not only of high magnitude as in present situation. When they are associated in addition with a currents reversal (45 %), El Niño events are mainly (85 %) of large magnitude, often even higher than in historical climate.

Balance between atmospheric feedbacks (Rädel et al., 2016) or climatological mean Pacific subtropical cells (STC) (Chen et al., 2015b, 2017b) have also been suggested to explain the wide ENSO amplitude spread among models. For instance, Rädel et al. (2016) suggested that the response of ENSO amplitude to climate change will in part be determined by a balance between increasing cloud longwave feedback and a possible reduction in the area covered by upper-level clouds, known to strengthen the Bjerknes feedback.

As discussed in paragraph 1.4.1, model uncertainties in ENSO amplitude changes are related to the tropical Pacific warming pattern (Zheng et al., 2016; Li et al., 2017): El Niño

(La Niña)-like warming reduces (increases) the mean SST barrier to the tropical convection threshold (Johnson and Xie, 2010) in the eastern Pacific, reinforcing (weakening) the convection feedback on ENSO and reinforcing (suppressing) the ENSO SST variability via the Bjerknes feedback. The diversity of warming patterns in CGCMs is related to the Cold Tongue bias, which may modify ENSO dynamics by inducing biases in both oceanic and atmospheric feedbacks and inducing error compensation (Guilyardi et al., 2009a; DiNezio et al., 2012; Kim et al., 2014; Bayr et al., 2018a,b). The Cold Tongue bias shifts the rising branch of the Walker circulation too far to the west (by up to 30° in CMIP5 models), resulting in an underestimation of two important ENSO atmospheric feedbacks, the atmospheric component of the Bjerknes feedback (wind-SST feedback) and the heat flux-SST feedback (Bayr et al., 2018a). It leads to erroneous convective response during ENSO, which becomes driven by an anomalous positive shortwave radiation feedback rather than the realistic wind-SST feedback (Bayr et al., 2018b).

Additionally to the large diversity of ENSO projected changes by CGCMs summarized above, the natural ENSO variability also hinders our understanding of the effect of global warming on ENSO properties (Stevenson, 2012; Zheng et al., 2018). Uncertainties in ENSO amplitude due to internal variability are indeed of the same order of magnitude as those due to anthropogenic forcing (Zheng et al., 2018).

Synthesis

ENSO impacts

ENSO affects weather events, ecosystems, agriculture and fisheries worldwide through atmospheric and oceanic teleconnections. The impacts of the Eastern Pacific El Niño events include a monsoon disturbance, severe droughts and forest fires in Indonesia, India and north-eastern Australia in the boreal summer, winter floods and landslides in Ecuador, Peru and the south-western United States, an interruption of favourable conditions for industrial anchovy fishing off the Peruvian coast and a potentially devastating bleaching of the tropical Pacific coral (Goddard and Dilley, 2005; McPhaden et al., 2006). As an example, the 1997-98 strong El Niño event inflicted costs of approximately $33 billions in the world.

The impacts of ENSO are likely to change in intensity with global warming. Weaker El Niño events could produce increased impacts in terms of regional temperature extremes (heat waves) and wildfire frequency, mainly due to changes in land-atmosphere feedbacks (Fasullo et al., 2018).

Canonical ENSO

- Simplified view of ENSO

ENSO is a disruption of the tropical Pacific mean state. In average, the sea surface temperatures (SST) in the western tropical Pacific are among the warmest in the world (greater than 28 °C), while SST in the eastern Pacific are 4 to 10 °C colder. The "Warm Pool" in the west is maintained by the trade winds that blow from east to west along the equator. Above these warm SST, atmospheric deep convection can develop, generating heavy rainfall over "the Maritime continent", the western tropical Pacific and the eastern Indian Ocean. In the eastern Pacific, the trade winds drive coastal and equatorial upwelling of deep cold water that cools the surface and forms the "Cold Tongue". The thermocline, the sharp boundary separating warm upper waters from cold deeper waters, is close to the surface in the eastern Pacific, which favours the transport of cold water to the surface and deep in the western Pacific. This wind-driven zonal SST contrast results in higher pressure in the east than in the west, which reinforces the trade winds. The tropical Pacific mean state is thus maintained by an ocean-atmosphere coupled positive loop, between winds, SST and thermocline depth, called the Bjerknes feedback. Colder SST in the eastern Pacific than in the western Pacific drive stronger easterly winds due to the zonal pressure gradient. The easterly winds, in turn, reinforce the upwelling of cold waters, by shoaling the thermocline close to the surface; surface waters in the eastern Pacific become even colder and so on.

ENSO anomalies can grow thanks to the SST-wind Bjerknes feedback. Suppose to start with an anomalous warming in the eastern Pacific, due to a depressed thermocline for instance. The zonal SST contrast decreases, so does the pressure gradient, which leads to a weakening of the trade winds. The upwelling of cold water is therefore reduced and the thermocline in the eastern Pacific subsequently deepens, which reinforces the SST warming. Thus, during El Niño (La Niña) events, anomalous westerly (stronger easterly) winds in the western-to-central equatorial Pacific and positive (negative) SST anomalies in the eastern equatorial Pacific reinforce each other. The transition from the warm El Niño to the cold La Niña phase requires a delayed negative feedback, which has been suggested to come from an ocean dynamical adjustment, i.e. the restoring force of the unstable ENSO ocean-atmosphere coupled interaction. These negative feedbacks include the widely accepted recharge-discharge (RD) paradigm.

Synthesis

The key variable is the thermocline depth, whose wind-driven variations are not as perfectly in phase with the winds as they are with SST changes. The delayed oceanic subsurface adjustment to the winds acts to discharge (recharge during La Niña events) the equatorial upper heat content, i.e. the amount of warm water above the thermocline, and eventually terminates the ENSO event. The upper heat content could provide thus the memory of the oscillation between the warm and cold phases of ENSO.

At first approximation, the ENSO ocean dynamics is linear, while the surface layer air-sea coupled processes that determine the SST variability are quite non-linear. The main structuring theories of ENSO were built in stages:

* Sir Gilbert Walker defined the Southern Oscillation in 1923;
* Bjerknes (1969) described the air-sea coupled feedback at play in the tropical Pacific and defined ENSO as a tropical Pacific-scale phenomenon;
* Wyrtki (1975) showed that El Niño needs a recharge of heat content in the western Pacific, or in other terms a "build-up" of warm water, to onset;
* Zebiak and Cane (1987) and Jin (1997a,b) took up the previous ideas and turned them into equations and models.

However, this self-sustained oscillator view of ENSO, with the oceanic heat content as the system's memory, has been challenged by recent studies (Takahashi and Dewitte, 2016; Neske and McGregor, 2018). Moreover, it does not explain the initiation phase of ENSO events, nor the diversity of their spatial structures, nor the irregularity of their temporal evolutions.

- A lot of feedbacks

The dynamics of ENSO involves a lot of feedbacks, making the picture rather complicated. In addition to the atmospheric component of the Bjerknes air-sea coupled feedback (between SST and winds), oceanic feedbacks are involved through the thermocline depth variations:

* the zonal advective feedback (ZAF): advection of mean temperature by anomalous zonal currents;
* the thermocline feedback (TCF): vertical advection of anomalous warm subsurface waters by the mean upwelling;
* the Ekman or upwelling feedback: vertical advection of mean ocean temperature by anomalous upwelling.

Thermodynamic feedbacks are also invoked in ENSO dynamics, such as the atmospheric seasonal-phase locking feedback (Lengaigne et al., 2006), the thermal damping by net surface heat flux (negative feedback), the cloud radiative feedback, which may be positive or negative feedback depending on the nature of clouds (Rädel et al., 2016), among others.

Synthesis

ENSO diversity

ENSO diversity refers to the spatial and temporal diversity among El Niño events. The two main classifications used in this thesis are:

* the **Central Pacific** (CP) and **Eastern Pacific** (EP) **El Niño events**, differentiated by the location of anomalous SST warming (Kao and Yu, 2009; Kug et al., 2009; Yeh et al., 2009b);
* the **strong** and **moderate El Niño events**, differentiated by the intensity of the SST warming in the eastern Pacific, a region of high variability (Takahashi et al., 2011).

The spatial diversity is related to the amplitude and flavour of the event: while CP El Niño events are exclusively moderate or weak, strong El Niño events are only EP El Niños. However, EP El Niño events can be both moderate and strong (Dewitte and Takahashi, 2017).

- Spatial diversity

In addition to their distinct SSTA warming centres, EP and CP El Niño events are commonly distinguished from different characteristics.

* EP El Niño events display a stronger SSTA warming, basin-wide thermocline and surface winds variations, with phase reversal signatures and discharges of heat content as described by ENSO waves theories (Suarez and Schopf, 1988; Jin, 1997a),
* CP El Niño events tend to appear, develop and decay in situ (i.e. events relatively stationary), with surface winds, SST and subsurface temperature anomalies confined in the central Pacific.

Different mechanisms have been suggested to explain ENSO spatial diversity, including:

* the distinct roles of the oceanic processes: the TCF play a key role in the development and decay of EP events while the ZAF is a key process during CP events (Kug et al., 2009; Capotondi, 2013; Choi et al., 2011; Ren and Jin, 2013). The thermocline depth variations and the recharge-discharge processes could become progressively weaker as the SSTA peaks of the events move further west;
* a balance between the recharged state of the equatorial Pacific and the modulated WWBs, which could trigger CP or EP El Niño events following the values of these two parameters, and which could thus create the continuum of El Niño diversity (Chen et al., 2015a; Lai et al., 2015);
* the key role of the atmospheric forcing in the CP El Niño onset, via the sensitivity of the central Pacific mixed-layer dynamics to sub-tropical precursors, such as the North Pacific Oscillation (NPO) or the Pacific Meridional Mode (PMM) (Vimont et al., 2003; Chang et al., 2007; Yu and Paek, 2015; Thomas and Vimont, 2016);
* the role of air-sea interactions in the eastern Pacific, assimilated to a developing seasonal Bjerknes feedback mode, which could trigger moderate EP El Niño events in boreal summer (Dewitte and Takahashi, 2017).

These two flavours of El Niño events could be connected to the "T-mode" and "SST-mode" (Fedorov and Philander, 2001) or "quasi-quadriennal" and "quasi-biennal" modes (Bejarano and Jin, 2008; Xie and Jin, 2018), highlighting the role of the tropical Pacific background state in ENSO flavours.

Synthesis

- Intensity diversity

Non-linear processes have been suggested as essential in the development of strong EP El Niño events (Santoso et al., 2017), including:

  * Coupled interactions between modulated WWBs and SST (Puy et al., 2016b) could be an important trigger of strong El Niño. The key role of the WWBs has been highlighted in the development of strong El Niños, whether in March-April (Boulanger and Menkes, 1999; Lengaigne et al., 2002; Chen et al., 2015a) or in summer/fall (Takahashi and Dewitte, 2016; Puy et al., 2017). Hameed et al. (2018) suggested that the westerly winds that counter the easterlies are favoured by the positive phase of the Indian Oscillation Dipole (IOD). The majority of studies considers that an associated high recharged state in winter is required for a strong El Niño event to develop, but it may not be a necessary condition (Takahashi and Dewitte, 2016). The modulation of the WWBs response by the tropical Pacific mean state depends on both the WWBs characteristics and the structure of the underlying ocean. However, the stochastic part of the modulated WWBs may cancel El Niño growth, making the phenomenon only probabilistic (Puy et al., 2017). Moreover, the presence of WWBs in the central Pacific in late summer and early fall seems crucial in the development of an EP El Niño into a strong El Niño event, as they counter the easterly winds in the far eastern Pacific. The origin of the latter are suggested to be due to ENSO itself (Hameed et al., 2018), or to a SST warming off the Peruvian coast, which could be linked to the SPMM for instance (Dewitte and Takahashi, 2017).
  * Non-linearities in the Bjerknes feedback could explain the evolution of an EP El Niño event into a strong El Niño event (Dommenget et al., 2013; Takahashi and Dewitte, 2016; Takahashi et al., 2018). When the eastern Pacific SST warming reaches a threshold, the Bjerknes feedback is amplified and accelerate the warming. The reasons why the eastern Pacific is able to reach this unusually high warming are still investigated. Note that non-linearities in the SST-wind feedback may be induced by the non-linear response of the tropical atmospheric convection to SST (Cai et al., 2014).
  * Non-linear oceanic processes, such as the Non-linear Dynamical Heating (NDH) (An and Jin, 2004; An et al., 2005a), have also been suggested to trigger strong El Niño events, although recent studies questioned the role of NDH in the growth of strong El Niño events (Takahashi and Dewitte, 2016; Liang et al., 2017). Subtle balance between oceanic feedbacks, especially between TCF and ZAF, may also play a role in the development into a strong El Niño event and also dictate the direction of propagation of the event (Neelin et al., 1998; Santoso et al., 2013).

Synthesis

Low-frequency Pacific variability

ENSO properties (amplitude, frequency, spatial distribution) vary over decadal to multi-decadal time scales. Different sources of the modulation have been suggested, including stochastic origin, internal variability in the tropical Pacific, extra-tropical atmospheric or oceanic teleconnections, or external forcing.

The low-frequency modulation of ENSO may emerge from internal processes of the tropical Pacific climate system, in the absence of any variation in external forcing. ENSO decadal modulation can then be conceived through the coupled instabilities approach, in which the prescribed mean state induces ENSO characteristics (Fedorov and Philander, 2000; Bejarano and Jin, 2008).

In turn, the intrinsic modulation of ENSO can affect the multi-decadal mean state through a positive feedback between ENSO and decadal climate modes. In particular, the internal non-linearities of the tropical coupled system dynamics, such as the asymmetry between El Niño and La Niña, can modify the mean state through internal rectification processes (Timmermann and Jin, 2002; Jin et al., 2003a; Rodgers et al., 2004; Schopf and Burgman, 2006).

This ENSO modulation can lead to a confused detection of anthropogenic influence on short-term climate measurements: to what extent is the observed modulation of ENSO the cause or consequence of anthropogenic changes or intrinsic multi-decadal changes in the background state of the equatorial Pacific?

Internal variability appears to be a crucial component of the uncertainties of climate projections since, for instance, the spread among models of the ENSO amplitude changes due to the internal variability is comparable to the spread of the projected ENSO amplitude changes with global warming (Zheng et al., 2018).

Synthesis

Changes in a warmer climate

The climate is changing: the atmospheric concentration of CO_2, powerful greenhouse gas, has exceeded 400 ppm. As a result, the last four years have been the warmest years on record since 1880 and 16 of the 17 warmest years have occurred since 2000. The global warming of surface temperature alters ocean temperatures as well as large-scale atmospheric and oceanic circulations.

- Changes in the tropical Pacific mean state

There is a strong consensus among CGCMs on some projected changes of the mean state under global warming scenarios. In particular, the Walker circulation is projected to weaken (Vecchi and Soden, 2007), which will decrease the strength of the trade winds and thus alter the thermal structure and ocean circulation in the tropical Pacific (DiNezio et al., 2009; Santoso et al., 2013). The equatorial thermocline is projected to become shallower and sharper (Vecchi and Soden, 2007; Yeh et al., 2009a). The equatorial Pacific is projected to warm faster than the off-equatorial Pacific (Collins et al., 2010) and the east equatorial Pacific and the maritime continent faster than the central equatorial Pacific (Xie et al., 2010). The warming pattern is projected to be more "El Niño-like", even if uncertainties remain due to the strong biases exhibited by the models and their inability to simulate the current La Niña-like pattern.

- Changes in ENSO

The questions of whether global warming has already affected ENSO and how global warming will affect ENSO in the future are still open. There is no inter-models consensus on the evolution of ENSO amplitude and frequency based on the statistics of traditional ENSO indices (Collins et al., 2010; Bellenger et al., 2014). Projected changes in El Niño intensity are also heavily model dependent (Guilyardi et al., 2009b; Kim and Yu, 2012; Bellenger et al., 2014; Chen et al., 2017b) and not significantly distinguishable from natural modulation (Stevenson, 2012; Chen et al., 2017a; Zheng et al., 2018). Uncertainties on the future of ENSO mainly come from model biases and especially from the spread among models in the projection of the spatial pattern of tropical Pacific surface warming (Zheng et al., 2016). However, some features associated with extreme El Niño events in current climate have higher and robust probability of occurrence in the future climate, such as the zonal direction of propagation (Santoso et al., 2013) or the extreme ENSO-induced precipitation events (Cai et al., 2014). Although these studies are heading towards a mechanistic understanding of ENSO's sensitivity to climate change, they are hindered by the difficulties associated with the high spread among models (i.e. relatively weak consensus).

Chapter 2

Data and methods

Contents

2.1 Data description

ENSO is the main mode of variability in the tropical Pacific. It has been observed that this inter-annual phenomenon has a return period of between 2 and 7 years, governed by multi-scale processes ranging from unpredictable high frequency variability to low-frequency modulation through seasonal time scales. Past studies have shown that ENSO is modulated at low frequency, inter-decadal to inter-centennial time scales, which induces changes in intrinsic ENSO statistics when analysing shorter periods (Wittenberg, 2009; Stevenson et al., 2010; Stevenson, 2012). This long-term modulated variability can not be clearly distinguished in the too short instrumental records compared to the time-scale of ENSO variability. As an evidence, ENSO analysis in observations, especially when taking the period with a better reliability of measurements, since 1950, is tantamount to reviewing ENSO statistics with only a few recorded events and rare strong El Niño events. It is thus difficult to characterise ENSO diversity and to understand associated dynamics with high statistical confidence through only observation datasets. Paleo-climate proxy data provide an alternative to reconstruct ENSO variability in past climates. Paleo ENSO records showed that ENSO has been around for at least millennia (Lu et al., 2018). Paleo-proxies are either direct proxies of ENSO (such as coral and mollusc records) or indirect proxies from remote regions impacting by ENSO (the proxies are then lake sediment, tree ring, speleothem). Paleo-proxies provide indirect measure of atmospheric or oceanic temperature, often through the analysis of the oxygen isotope ratio ($\delta^{18}O/\delta^{16}O$). However, they are scattered and punctual and inconsistencies among the data or large uncertainties in the measurement lead to coupling the paleo-proxies analysis with past climate simulations (Karamperidou et al., 2015).

Thus, in a complementary way to observations sparsity (paragraph 2.1.1), long climate simulations (see paragraph 2.1.2) are used to provide information on internal variability and to estimate changes in a warmer climate. However, although models are the main tools for estimating the potential impact of climate change on ENSO, they are subject to systematic biases (paragraph 2.1.2.2) and uncertainties about their ability to simulate features and mechanisms specific to ENSO (paragraph 2.1.4). It results in confidence in models projections at the "medium" level according to the Intergovernmental Panel on Climate Change (IPCC) report (paragraph 2.1.2.1). In this thesis, we use a Coupled General Circulation Model (CGCM), CESM-LE, which provides a long simulation without anthropogenic forcings as well as multiple realisations of the climate, over the 1920-2100 period with a combination of both natural and anthropogenic climate forcings (paragraph 2.1.3). The realism of ENSO in the CESM-LE simulations is confronted with observations (paragraph 2.1.4).

2.1.1 Observations and Reanalysis

Different datasets of observations or reanalysis are used to analyse the efficiency of the general coupled model to reproduce the climate system and to estimate whether the simulation of the internal climate variability spread simulated by the members of CESM-LE includes the observed climate trajectory. Observation datasets are derived from satellite or in-situ measurements while reanalysis are a combination of dynamical models and assimilation of all the observations available at the time the analysis is performed, to reproduce the recent past climate system.

Note that we have chosen as the start date the year 1950 because it has been shown that before this date, which corresponds to the improvement of the spatial and temporal coverage of the Sea Surface Temperature (SST) data, the reconstructed data may have been altered by the interpolation method (Deser et al., 2010; Ray and Giese, 2012).

HadISST v1.1

We employ the Met Office Hadley Centre's Sea Ice and Sea Surface Temperature version 1.1 (HadISST v1.1) dataset (Rayner, 2003). The dataset is provided by the Met Office Hadley

Centre, from their Web site at https://www.metoffice.gov.uk/hadobs/hadisst/. This monthly average sea surface temperature dataset comes from the Met Office Marine Data Bank (MDB), consisting mainly of in-situ measurements of ship tracks up to 1996, and from data received through the Global Telecommunications System (GTS) since 1982. SST from the International Comprehensive Ocean-Atmosphere Data Set (ICOADS) have been used through 1997 to enhance MDB data coverage. Since 1998, the NCEP-GTS is used. The reconstruction of SST uses a reduced-space optimal interpolation method.

It has been recently shown that the HadISST v1.1 dataset presents numerous problems among which a lower variability of the global SST than in the OISST dataset (Optimum Interpolation Sea Surface Temperature, an observation dataset developed by the NOAA (Banzon et al., 2016)), a large zonal discontinuity of SST at the dateline which might limit the spatial gradients analysis and additional zonal discontinuities at intervals of 2° of longitude which makes the dataset inadequate to study spatial derivatives of SST [1]. Moreover, a misrepresentation of the equatorial Pacific trend over the observed period (1900-2010), cooling rather than warming (Deser et al., 2010), could alter results due to the interpolation method. Despite these known limitations, we use this commonly used dataset, in addition to the one below, to improve the robustness of the results presented.

The dataset has a resolution grid of 1° latitude-longitude. We use the period from January 1950 to December 2017.

ERSST v3b

The National Oceanic and Atmospheric Administration (NOAA) Extended Reconstructed Sea Surface Temperature version 3b (ERSST v3b) dataset is also used (Smith et al., 2008). The dataset is provided by the NOAA/OAR/ESRL PSD, Boulder, Colorado, USA, from their Web site at https://www.esrl.noaa.gov/psd/.

The monthly average sea surface temperature dataset comes from the ICOADS up to 2007, which includes buoy and ship observations, and from the NCEP-GTS since 2007. Satellite SST data are not used, unlike version 3 described in Smith et al. (2008), because they led to the appearance of residual cold biases. The reconstruction of the SST uses improved statistical methods to fill in missing data due to sparse in-situ data. The statistical methods is well explained on the Web site https://climatedataguide.ucar.edu/climate-data/ in the tab ERSST v3 and v3b, Expert Guidance. Unlike the HadISST dataset, the ERSST dataset takes into account changes in SST measurement practices over time.

The dataset has a resolution grid of 2° latitude-longitude. We also use the period from January 1950 to December 2017.

GPCP v2.3

The precipitation comes from the Global Precipitation Climatology Project (GPCP) Monthly Analysis Product version 2.3 (Adler et al., 2003). The monthly dataset is available at http://eagle1.umd.edu/GPCP_CDR/Monthly_Data/. The precipitation dataset is composed from rain gauges stations over land, radars and satellites data over land and ocean. It combines indirect measurements through satellites which measure brightness temperature of clouds converted to rain rate, and radars which measure energy reflected by clouds and rain drops, with direct but sparse and localised measurements of rain gauges. The lack of direct measurement over ocean which does not allow validation of satellite estimates induces systematic errors.

The dataset has a resolution grid of 2.5° latitude-longitude. We use the period from January 1979 (beginning of the dataset) to December 2017.

SODA v2.2.4

We use also the Simple Ocean Data Assimilation (SODA) reanalysis version 2.2.4 (Carton

[1] http://ir.librairy.oregonstate.edu/concern/defaults/kw52j9632

and Giese, 2008). SODA v2.2.4 is forced by 20CRv2 winds dataset (Compo et al., 2011) and constrained by assimilation, via an optimal interpolation scheme, of all available observed temperatures and salinities. The reanalysis variables are ocean temperature, salinity, horizontal and vertical ocean velocities, sea level and wind stress. The reanalysis dataset uses POP model as ocean component, the same component as the CESM-LE (see paragraph 2.1.3).

The reanalysis dataset has a resolution grid of 0.5° latitude-longitude and 40 vertical levels. We use the period from January 1950 to December 2010 (end of the dataset).

2.1.2 Coupled General Circulation models

Before focusing on the model used in this thesis (CESM-LE), we present succinctly the global climate models, their purpose, their general components and their limits.

2.1.2.1 CGCMs, CMIP and IPCC

Climate models are used in different configurations for different purposes: to access to the past climate, to investigate the behaviour of particular systems, to improve theory by comparing for instance the impacts of different configurations on the simulated dynamics, to forecast weather, to project changes under various greenhouse gases (GHGs) scenarios, among many other purposes. They are also used in addition to observations that have limitations in terms of spatial and temporal density. For instance few in-situ observations are available in oceans, especially in subsurface (Fig. 2.1). The development of the ARGO floats (Roemmich and Owens, 2000) leads to a significant increase in the spatial and depth repartition of measures, but their recent development does not provide for now a long-timeserie of records.

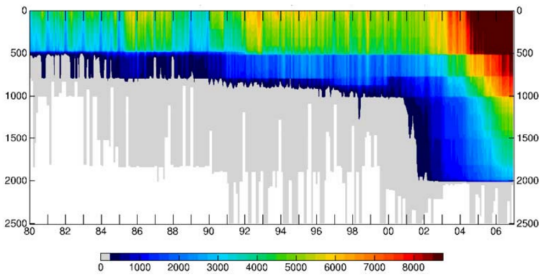

Figure 2.1 – Number of temperature observations in global ocean versus depth. The temperature measures come from XBTs, fixed moorings (such as TAO (Pacific) or PIRATA (Atlantic) programs) and ARGO floats. The figure is reprinted from Hurrell et al. (2009).

Modelling the Earth climate system requires the development of a numerical code to solve physical, thermo-dynamical, chemical, and biogeochemical equations of the system. Several steps are needed to construct the model:

- identification of the relevant processes;
- theory;
- simplification of the theory (elimination of unnecessary processes);
- discretisation of the equations, consisting in cutting the space in meshes and the time in elementary steps;
- parameterisation of unresolved processes;
- implementation as computer code.

The different steps lead intrinsically to uncertainties in the representation of the system. The discretisation of the equations and the parameterisation of the sub-grid or sub-time scale processes are the two main steps where assumptions and choices of the configuration lead to a large range of behaviours between models and to numerical errors.

These choices are also dictated by the objectives of the modelling and different types of simulations are used depending on the purpose:

- **Forecasts**: they can be retrospective (or hind-cast) or weather forecasts. Hind-casts are used in the past, to determine if the model performs well or not. They are representations seeking to reproduce the state of the climate system as close as possible as it has been observed. Weather forecasts correspond to the simulations used to predict future weather, up to two weeks. These simulations use data assimilation.
- **Climate predictions**: this kind of simulations predict the average future climate changes, on time scales that can go from the season to the next decade.
- **Climate projections**: climate projections are used to gain access to the Earth's climate over long periods of time (decades up to centuries). They require hypothesis or reconstructions of external forcings, such as orbital forcings (in particular for paleoclimate or last millennium simulations) or green-house gases scenarios (for future projections of the Earth's climate under global warming). They use coupled climate system models. I mainly use this kind of simulations in my thesis work.

A Coupled General Circulation Model (CGCM) is composed of several components describing the evolution of different spheres of the earth climate system such as the atmosphere, the ocean, the biosphere, the ice sphere. The main improvement in the last generation of CGCMs, called Earth System Model (ESM) is the introduction of an interactive carbon cycle component (Flato, 2011). This improvement was motivated by the impact of the terrestrial and oceanic ecosystems in the modifications of the carbon cycle with global warming (Friedlingstein et al., 2006). The main components of each kind of coupled model are:

- Physical climate system: atmosphere, ocean, cryosphere, land surface and exchange processes of energy, water and momentum (definition of the World Climate Research Program);
- Earth System: Physical climate system + aerosols + biogeochemical cycles + terrestrials and marine biology + atmospheric chemistry.

These CGCMs have been particularly developed in the framework of the Intergovernmental Panel on Climate Change (IPCC), an international initiative to raise awareness of climate change that began in 1988. IPCC was created by the United Nations Environment Programme (UN Environment) and the World Meteorological Organization (WMO). The objective is to establish reliable projections of changes in the climate system due to human activities. The human activities are changing the composition of the atmosphere in particular, the spheres of the climate system in general. Some of these modifications have direct (greenhouse gases emissions) or indirect (atmospheric chemical reactions) impact on the Earth's energy balance through radiative forcings changes and therefore are factors of climate change.

The Earth's energy is balanced between the solar incoming radiation, source of power of the climate system, and the outgoing radiation (Fig. 2.2a). However, beyond natural variations (see paragraph 2.1.2.3 for the natural modulation of the solar radiation for instance), changes in the incoming short-waves radiation may occur from changes in clouds or aerosols while changes in the outgoing radiation may emerge from changes in the Earth's temperature (surface or atmosphere). Radiative forcing is defined as the propensity of these factors to conserve solar energy on Earth or to send it back into space. For instance, greenhouse gases present positive radiative forcing because they contribute to warm the atmosphere by sending back to the Earth the long-wave radiation emitted by the Earth. Conversely, some aerosols are likely to have negative radiative forcing by preventing solar radiation from reaching the Earth's surface and low atmosphere, reflecting them to space. Figure 2.2a shows the different energy fluxes and the impact of different factors on them.

Climate feedbacks need to be taken into account in this balance (Fig. 2.2b). Climate change can induce changes in various biogeochemical cycles (in particular water and carbon cycles) that can reinforce (positive feedbacks) or mitigate (negative feedbacks) the expected warming. As an example of positive feedback, the relationship between warming the atmosphere and increasing its water vapour content further amplifies the initial warming. Another

example of positive feedback is related to ice melting, in response to high latitudes warming, which induces a decrease in surface albedo which decreases the proportion of radiation reflected by the surface, increasing the absorbed portion of radiation and the warming. Clouds and aerosols feedbacks may be positive or negative, affecting both solar radiation and long-waves radiation emitted from surface. They are widely responsible for the large inter-model uncertainties in the projected changes due to the climate change. Figure 2.2b shows the different climate feedbacks and their estimated contribution sign.

(a) Radiative forcings

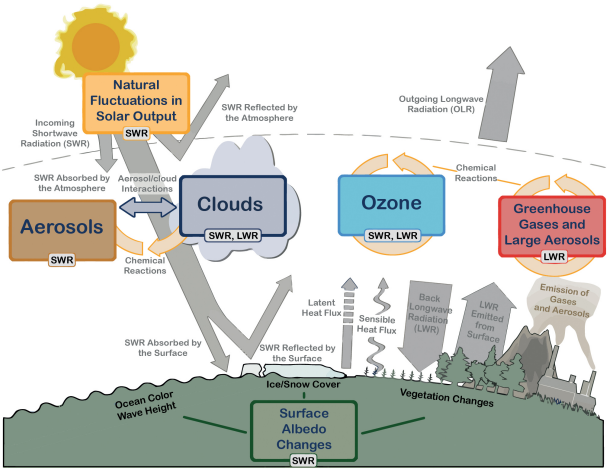

(b) Climate feedbacks

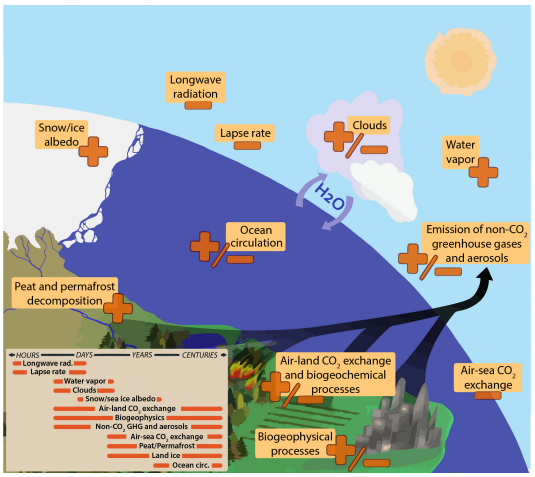

Figure 2.2 – (2.2a) Radiative balance between incoming solar short-wave radiation (SWR) and outgoing long-wave radiation (OLR). Ozone and aerosols, emitted mostly by human activities, absorb, scatter and reflect SWR. Clouds whose properties may be modified by anthropogenic aerosols, have different possible interactions with SWR and LWR. Finally, anthropogenic GHGs change outgoing long-wave radiation by absorbing long-wave radiation (LWR) emitted from the surface. (2.2b) Climate feedbacks relative to the GHGs increase. The figures are reprinted from the fifth Assessment Report (AR5) of the IPCC.

The IPCC is currently in its Sixth Assessment cycle, the Fifth Assessment Report (AR5) was released in 2014. Most of the results of the IPCC working group I are based on studies using CGCMs to project future climate changes and related impacts according to different scenarios. In particular, a collaborative climate modelling process, coordinated by the World Climate Research Programme (WCRP), has emerged through the Coupled Model Intercomparison Project (CMIP) since 1995. The last released set of CGCMs, CMIP5 (Taylor et al., 2012), used in the preparation of the AR5, provides a multi-model ensemble for:

- examining whether the models realistically simulate the recent past;
- providing two time scales of projections of the future climate: near term (out to about 2035) and long term (out to 2100);
- determining the mechanisms responsible for differences in model projections in particular in poorly understood feedbacks such as those involving clouds and the carbon cycle. The underlying issue is to understand why similarly forced models produce a such range of climate responses.

The AR5 adopted 4 scenarios of GHGs concentration of long-term (century time scale) integrations to simulate future climate. They are named Representative Concentration Pathway (RCP) with a value corresponding to the radiative forcing in the year 2100 relative to pre-industrial: +2.6, +4.5, +6.0 and +8.5 (W/m^2) (Meinshausen et al., 2011). We use simulations forced with the RCP8.5 scenario in the thesis.

All 4 scenarios are possible depending on how much GHGs are emitted in the years to come. However, since 2000, the trajectories of several markers (global temperature, sea level rise, Arctic sea-ice extent among others) follow those of the RCP8.5 scenario, which projects a global average temperature increase of 3.7 °C (2.6 to 4.8 °C). The global temperature have

already increased by 1.1 °C compared to the pre-industrial level. 2015, 2016, 2017, 2018 were the warmest years since 1850 and the pre-industrial period. The CO_2 atmospheric concentration reaches 400 ppm in average, a concentration never reached in 2.2 million years.

During the 2015 United Nations Climate Change Conference in Paris (COP21), the Paris Agreement has been adopted, setting a long-term goal of holding the increase in global mean temperature well below 2 °C above pre-industrial levels, pursuing efforts to limit the temperature increase to 1.5 °C. A recent IPCC Special Report on Global Warming of 1.5 °C above pre-industrial levels (SR15), released in October 2018, assessed climate risks of two scenarios of global warming, +2.0 °C compared to +1.5 °C. They showed that every half of degree of warming matters, amplifying risks on human societies through an increase in extreme events such as heating waves, droughts, cyclones and tropical storms, floods. While the commitments made by states under the Paris Agreement to reduce emissions are not sufficient to limit global warming to 2 °C, and even less to 1.5 °C, the SR15 concludes that it is essential to engage in a profound ecological transition of our societies in the next decade, through de-carbonisation of the key sectors of energy, transport and agriculture.

CGCMs are therefore powerful tools used in future climate projections. In the thesis, we investigate ENSO in the Large Ensemble of CESM. In comparison of CESM-LE, we use the SST field of one model of the previous CMIP3 database: the Geophysical Fluid Dynamics Laboratory Climate Model version 2.1 (GFDL CM2.1) (Delworth et al., 2006; Wittenberg et al., 2006). We use the long-term (500 years) PI-control simulation of GFDL CM2.1, which offers the possibility to establish statistical significances of ENSO properties to compare with those in CESM-LE.

The choice of this model is motivated by the fact that it simulates consistently main features of the tropical Pacific and ENSO (Guilyardi, 2006; van Oldenborgh et al., 2005; Wittenberg et al., 2006). Moreover, the GFDL CM2.1 is one of the few models simulating realistically the diversity of ENSO (Ham and Kug, 2012; Yu and Kim, 2013; Capotondi et al., 2015) exhibiting in particular a bimodal distribution of the SST variability accounting for extreme El Niño events (Takahashi et al., 2011). The GFDL CM2.1 is then widely used to investigate different features of ENSO, such as dynamics processes associated with the two spatial flavours of El Niño (Kug et al., 2010) or still the ENSO's flavours modulation with the mean state (Choi et al., 2011). Finally, Takahashi et al. (2011); Takahashi and Dewitte (2016) and Dewitte and Takahashi (2017) investigated how realistically the model simulates the ENSO diversity through strong and moderate El Niño events regimes. The thesis work is based on the same approach of strong and moderate El Niño events but in CESM-LE.

2.1.2.2 Models' biases

The presence of biases in a model suggests that at least one mechanism is poorly simulated, which may impact future projections. Their evaluation is required to take them into account when interpreting results.

The major source of diversity between simulated surface temperature in CGCMs comes from the simulation of clouds, atmospheric convection, and oceanic mixing (Bellenger et al., 2014). In particular, the representation of clouds and their response to SST, which can lead to atmospheric convection and change wind circulation, is of paramount importance in the realistic simulation of the climate system and its modes of variability, including ENSO (Lloyd et al., 2009, 2011, 2012; Bayr et al., 2018b). However, resolving convection processes requires a resolution of 1 km while it is 100 km in CMIP5 models.

When focusing on the tropical Pacific, common and known biases affect the mean state and natural variability, especially in ENSO key areas of the Tropical Pacific: the western region (the "Warm Pool") and the eastern region (where the thermocline influence is important). The main biases of the current mean state in the tropical Pacific are:

- an equatorial Cold Tongue too intense (too cool) and extending too westward;

- a double Inter-Tropical Convergence Zone (ITCZ);
- a bias in eastern Pacific SST off Equator and Peru, in the upwelling region.

The Cold Tongue bias is suggested to be due to a misrepresentation of the air-sea interactions via too strong zonal currents as well as excessive oceanic upwelling, related to too strong simulated zonal winds (Zheng et al., 2012; Vannière et al., 2013; Li and Xie, 2014). It results in deficient precipitation and surface easterly wind biases in the western half of the Pacific (Li and Xie, 2014). The equatorial Pacific Cold Tongue bias leads also to the underestimation of two important atmospheric feedbacks in ENSO dynamics: the positive (amplifying) wind-SST feedback and the negative (damping) net heat flux-SST feedback, both dependent on SST (Lloyd et al., 2011; Bayr et al., 2018a). During El Niño (La Niña) events, the convective response to SST warming in the western-to-central Pacific induces an eastward (westward) shift of the rising branch of the Walker circulation. The displacement of the atmospheric deep convection leads to ENSO zonal wind-SST and heat flux feedbacks. However, the Cold Tongue bias shifts the rising branch of the Walker circulation (see paragraph 1.1.1) westward by up to 30°, which results in a weak convective response during ENSO events. Bayr et al. (2018a) showed that the two important ENSO feedbacks are mainly related to the SST mean state rather than to differences in model parameterisation. The representation of the mean state is all the more crucial because the biases can partly compensate and still simulate realistic ENSO amplitude (Lloyd et al., 2009; Bellenger et al., 2014; Bayr et al., 2018b).

The double ITCZ bias refers to excessive precipitation in the southern tropical Pacific, corresponding to a simulated symmetric counterpart of the north ITCZ (see paragraph 1.1.1). It induces warmer SST, weaker easterly, and stronger meridional wind divergences away from the equator relative to observations (Zhang et al., 2015b). The double ITCZ bias invokes global processes. Hwang and Frierson (2013) showed that cloud biases outside the tropical band contribute to the double ITCZ bias because tropical precipitation moves to the hemisphere that receives the most heat, from sun or ocean. Li and Xie (2014) suggested that the double ITCZ bias is linked to an excessive solar radiation in the southern hemisphere Pacific resulting from insufficient cloud radiative forcings.

The region of the far eastern equatorial Pacific (off Equator and Peru) is also particularly biased in CGCMs (Richter, 2015; Zuidema et al., 2016). The coastal upwelling is not adequately simulated, as are cloud coverage and feedbacks, making SST too warm compared to observations. This bias has long been associated with a lack of low clouds due to SST errors, but the errors seem to come only from the atmospheric component (Zuidema et al., 2016). Exarchou et al. (2018) showed in a complementary way in the tropical Atlantic that the warm SST bias is due to an excessive solar absorption in the ocean mixed layer, which can be linked to the unrealistically low cloud cover, but it may also be due to the lack of simulation of the biological productivity variability in the ocean. However, Takahashi and Dewitte (2016) and Dewitte and Takahashi (2017) showed that it is a key region in the growth of El Niño event and in its differentiation between moderate and strong events.

A realistic simulation of the background state is therefore essential to the projection of the climate system responses to global warming (Fedorov and Philander (2000), see also paragraph 1.4.1). The Cold Tongue bias and the double ITCZ remain large in CMIP5 models and explain more than three-fourths of inter-models spread in the tropical Pacific precipitation pattern (Li and Xie, 2014). And differences in simulated mean-state SST between models are suggested to provide spread in ENSO simulation in current climate models (Bayr et al., 2018a). Karamperidou et al. (2017) showed also that the representation of ENSO oceanic nonlinearities is a key element to correctly apprehend the physical processes linked to ENSO and may affect the tropical Pacific response to external forcing. It should be noted however that the CMIP5 generation of CGCMs has improved the representation of the tropical Pacific mean state (mean zonal SST gradient), in particular due to the increased latitudes resolution leading to a more realistic simulation of the equatorial upwelling even if there is no improvement in the resolution of the double ITCZ bias in CMIP5 compared to CMIP3 database (Zhang et al.,

2015b).

The ENSO simulation presents large spread between models and in particular:

- the ENSO amplitude shows large inter-models discrepancy;
- the dominant period of ENSO is between 2-3 years instead of 3-8 years in observations;
- the ENSO SST anomalies (SSTA) have a meridional structure too narrow and extending too westward;
- the seasonal phase locking of ENSO is weakly represented in models.

It has been shown that the improvement of the Cold Tongue improves other characteristics of ENSO, whose variability extend too far to the west (Bellenger et al., 2014). Xiang et al. (2012) showed that the Cold Tongue bias drastically reduces the thermocline feedback in the eastern Pacific, whose equilibrium with the zonal advective feedback ultimately leads to divergent changes in ENSO amplitude simulated by the CMIP5 models (Chen et al., 2017b). An excessive Cold Tongue bias also leads to a weak seasonal phase-locking by reducing the Ekman and thermocline feedbacks in late boreal fall and early winter (Wengel et al., 2018). The associated shallow thermocline may induce the too short dominant period of ENSO that leads to increased inter-annual variability (Meehl et al., 2001). The short dominant period of ENSO could also be enhanced through the biases of the simulated seasonal cycle (upwelling, zonal current and SST), which leads to the enhancement of a fast coupled mode that interacts with the ENSO mode (Dewitte et al., 2007). Biases in the mean surface circulation lead to biases in the advection terms which modifies the mode of privileged variability of the equatorial Pacific. An enhanced (diminished) contribution of the zonal advective feedback is associated with the prevalence of the fast surface-driven (slow recharge-oscillator) ENSO mode (Jin and Neelin, 1993; Neelin et al., 1998) and a trend toward a cooler (warmer) mean state in the western to central equatorial Pacific (Belmadani et al., 2010).

The weak atmospheric response to SSTA patterns may also alter ENSO dynamics. Its enhancement in models leads to improving the ENSO seasonal phase locking and the asymmetry El Niño-La Niña (Bayr et al., 2018a). Abellán et al. (2017a) showed that most CMIP5 models realistically reproduce the southward shift of the westerly winds in winter, improving the winter peak of ENSO, even if the seasonal synchronisation is still underestimated. The atmospheric mean state biases impact likewise the ability of a model to simulate the two types of ENSO flavours. Ham and Kug (2012) showed that it is directly linked to the sensitivity of the atmospheric response to distinct SSTA patterns, which can be relatively weak due to climatological dry and cold biases in the equatorial central Pacific. Li et al. (2017) suggested that integrating the radiative effects of precipitating ice in models would also improve the simulated life-cycle of Central Pacific (CP) El Niño events. Because of the models' systematic biases, there are too many extreme events in models. Conversely, Graham et al. (2017) showed that due to the Cold Tongue bias, CGCMs tend to simulate fake El Niño events, double peaking in the tropical band. Finally, a limited number of climate models is able to simulate the statistics of the two types of ENSO events even if the ENSO diversity is better simulated in CMIP5 than CMIP3 models (Kim and Yu, 2012; Ham and Kug, 2012).

CGCMs are then powerful and useful tools to examine ENSO dynamics and interactions between global warming and ENSO, but their biases must be taken into consideration when interpreting results (see paragraph 1.4.2). It is likely that the CGCMs capture behaviours similar to reality but also non-realistic behaviours (Graham et al., 2017). Moreover, inter-comparison CMIP studies hypothesised that the "true" value is the multi-model ensemble mean. However, the value may be obtained for wrong reasons, altering the search for underlying processes, as shown by Kim (2011) (analysing the CMIP3 database) and Bayr et al. (2018b) (analysing the CMIP5 database) among others. Most models with a too weak winds response to SSTA have effects on thermocline variability, zonal advection and thermal damping, which may indeed lead to errors that cancel each other, simulating good ENSO statistics for the wrong reasons.

2.1.2.3 Estimation of the internal variability

In addition to projections of the future climate, CGCMs provide access to the internal variability of the simulated climate system. The variability of the system can be decomposed into two components: forced (natural or anthropogenic) variability and internal (natural) variability. The natural (other than anthropogenic) variability is the sum of:

- the variability due to external forcings such as solar radiation that modulates the radiative budget. It is called external or forced variability;
- and the variability due to internal mechanisms linked to exchanges of energy, mass and movement, within or between the different spheres of the climate system (atmosphere, ocean, cryosphere, biosphere). It is called internal or intrinsic variability.

The main natural forcings affecting the (forced) variability of the system are the modulation of the solar radiation at short time-scales (day and seasonal cycles), the volcanic eruptions modifying incoming short-wave radiation, the decadal modulation of the solar radiation through sunspots (period of 11 years), and the variations of the astronomical parameters of the Earth (eccentricity, obliquity and precession) due to interplanetary gravitational interactions (Milankovitch cycle).

The internal variability comes from intrinsic mechanisms of each climate components (in particular from the unstable nature of the atmosphere and ocean components) as well as from interactions between the different components of the system. They can generate irregular fluctuations and quasi-periodic cycles. The internal variability may indeed be organised around preferential structures, characterising modes of variability with different time-scales (and space-scales) such as intra-seasonal variability (Madden-Julian Oscillation, MJO), inter-annual variability (ENSO), decadal variability (Pacific Decadal Oscillation, PDO), etc. These modes of internal variability interact with each other (for instance ENSO and the PDO, see paragraph 1.3.2) and are also modulated by external forcings.

Detection and attribution of changes in climate require the understanding and assessment of the natural variability of the climate system. Thanks to CGCMs simulations, internal variability may be assessed through two different approaches.

The first method is based on PI-control simulations, which are long-term simulations with only natural forcings, without anthropogenic forcings. Variability in such simulations is induced by variations that the system is capable to generate itself, without variability in external forcings. Different possible states that the climate system can take spontaneously are described when they are integrated over a long time enough. The simulation provides thus a reliable estimate of the internal variability of the climate system, before industrial period.

The second approach relies on multiple realisations of a simulation, whose initial conditions are slightly perturbed. The dispersion of the different trajectories simulated by each member of the ensemble simulations corresponds to the internal variability of the climate system, caused mostly by the non-linear nature of the climate dynamics. This method is based on the theory of Lorenz (Lorenz, 1963) who highlighted the chaotic nature of the climate system and demonstrated sensitivity to the initial conditions of a deterministic chaotic system through its attractor.

These two methods are not equivalent. Ensemble simulations allow a statistical description based on the realisation of independent events. PI-control simulation approach requires to make certain assumptions on the properties of the system. In particular, we consider that internal variability without anthropogenic forcing is similar to that with anthropogenic forcing when studying the internal variability observed in the near past. In that case, internal variability and anthropogenic forcing do not interact. The equivalence between the two methods also requires the assumption of the ergodicity of the system, that is, the mean value of a statistically computed quantity over time is equal to the mean over the statistical ensemble of a very large number of measurements. It means that temporal and ensemble statistics are asymptotically equivalent.

In this thesis, we use both methods to access to the internal variability of the simulated climate system: a long-term pre-industrial control simulation (1801 years) and a large ensemble of simulations of the historical and future climate system computed from a single model, CESM1. In the first case, the variability of the climate system, used to establish if it is not enough on its own to explain the detected changes, integrates only the internal variability since the natural external forcings are constant. In the second case, the variability of the system comes from both internal and external forcings, including anthropogenic forcings of the 20th century.

Many studies use the CMIP multi-model ensemble to evaluate changes in the climate system due to changes in external forcings and more particularly in radiative forcing induced by human activities. However, this method requires the assumption that differences in physics modelling between models (equations, discretisation, parameterisation, spatial and temporal resolution) cause very low dispersion compared to the dispersion due to the variability of the system. Another approach to counter the latter assumption is to discriminate models that poorly simulate main features of the studied phenomenon. It is common to choose a subset of CGCMs that reproduce a particular feature of ENSO. In that case, the method requires the assumption that the CGCMs subset simulates a more reliable ENSO than the multi-model ensemble mean. The difficulty is then to define the "bad" representation of the ENSO feature, which can be biased by the result that we are looking for. The robustness of the results when only few models of the ensemble remain can also be reduced.

The development of large ensemble of simulations (in addition to CESM-LE, the Canadian Earth System Model Large Ensembles (CanESM2) (Kirchmeier-Young et al., 2016), and the Max Planck Institute for Meteorology (MPI-M) Grand Ensemble (MPI-GE) (Bittner et al., 2016), publicly available from the end of 2018 for instance) is very promising and can only lead to an improved understanding of the variability of the climate system. They provide unambiguous characterisations of the simulated internal variability in a changing climate without being confounded by different model configurations.

2.1.3 CESM-LE project

2.1.3.1 Presentation

The model used in this study is the Community Earth System Model Large Ensemble (CESM-LE) Project developed by the National Center for Atmospheric Research (NCAR) (Kay et al., 2015). The data are available on-line on `www.earthsystemgrid.org`. We acknowledge the CESM Large Ensemble Community Project and NSF/CISL/Yellowstone for providing model outputs and supercomputing resources needed for a such ensemble simulations.

The CESM-LE project provides multiple realisations (42 members in the historical forcing conditions and 40 members of future projection with the RCP8.5 scenario) of simulation of climate trajectories over the period 1920-2100. The model components and the external radiative forcing (historical up to 2005 and RCP8.5 thereafter) are the same for all realisations, but with small atmospheric or oceanic initialisation differences. The spread between members is thus considered to be solely due to the internal variability of the climate system (see paragraph 2.1.2.3). It is therefore an indispensable tool for studying climate change taking into account the internal climate variability, which can be differentiated from model errors thanks to the ensemble (Kay et al., 2015).

All the simulations use the Community Earth System Model, version 1 (CESM1), coupling the Community Atmosphere Model version 5.2 (CAM5.2) atmosphere component (Hurrell et al., 2013), the Los Alamos National Laboratory (LANL) Parallel Ocean Program version 2 (POP) ocean component (Smith et al., 2010), the Community Land model version 4 (CLM4) land component (Oleson et al., 2010; Lawrence et al., 2011) and the LANL Community Ice CodE (CICE4) sea ice component (Hunke and Lipscomb, 2010) (Fig. 2.3). CESM1 simulations are all fully coupled. All components of the model are approximately 1° horizontal

resolution.

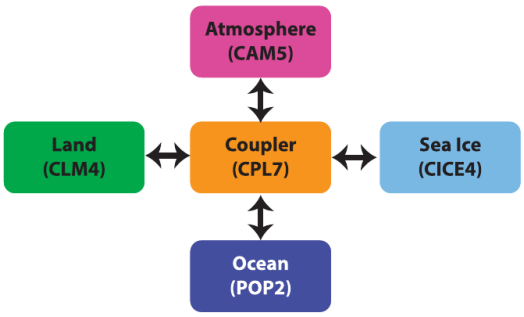

Figure 2.3 – CESM-LE component models. Reprinted from Kay et al. (2015).

Different kind of simulations are provided and used in the thesis:

PI-control run : a 1801 years long simulation of the pre-industrial earth climate system. The radiative forcing conditions are the reconstructed conditions of 1850, fixed in time along the simulation. The initial conditions of the ocean come from a succession of previous long runs corresponding to a long spin-up, which allows to reach the radiative balance through an adjustment of the Top Of the Atmosphere (TOA) balance ($\sim 0\,\mathrm{W/m^2}$) by tuning parameters. This first step is required also to reach quasi-equilibrium in particular of the slow ocean component (deep ocean). Then using the tuning parameters, the simulation is restarted with initialisation conditions from the World Ocean Atlas, often referred to as the Levitus climatology, based on current observations (Levitus, 1983).

Historical runs : 42 simulations of the recent past (1850-2005). The external forcing used comes from time-varying historical observations and estimations and includes greenhouse gases concentrations, volcanic eruptions, and solar variability for the main contributions (Lamarque et al., 2010). The ensemble members of historical simulations are initialised with different conditions:

- member 1: starts on 1850, is initialised with the conditions of a randomly selected date of the control run (1 January 402);
- member 2: starts on 1920, is initialised with the January 1, 1920 conditions of the member 1 and started with 1-day lagged ocean temperatures;
- members 3-35 and 101-107: start on 1920. The slightly different initial atmospheric state was created by a random disturbance of the air temperature field of the member 1. Perturbations occur at the level of round-off errors, which creates differences in initial global atmospheric temperatures less than one-trillion of a degree (order of $10^{-14}\,\mathrm{K}$).

RCP8.5 runs : 40 simulations under the RCP8.5 scenario of the CMIP5 design protocol (see paragraph 2.1.2.1 and Taylor et al. (2012)).

Ensemble members 1-35 were completed at NCAR, ensemble members 101-107 were completed at the University of Toronto. It is a possibility that the difference of computing platform for the last members may introduce numerical errors among members that in that case would be added to the internal variability of the climate system.

The CESM1 is the next generation of earth system models of the Community Climate System Model (CCSM) developed by NCAR. The main differences and additional capabilities between the previous model version, CCSM4 (Gent et al., 2011), and CESM1(CAM5) used in the large ensemble project are the following:

- the parameterisation of diabatic processes and aerosols properties has been improved in the new atmospheric component CAM5, released with CESM1. New schemes were

developed or updated for clouds processes, aerosol formation and removal, radiative properties of aerosols and cloud particles, radiative transfer, and convection and turbulence. In particular, it makes it possible to simulate interactions between aerosols and clouds and their combined radiative impacts. Thus both direct and indirect effects of aerosols are taken into account and the impact of anthropogenic aerosols emissions on the radiative forcing of climate by clouds may be assessed;

- a biogeochemical module, based on the nutrient-phytoplankton-zooplankton-detritus scheme, is integrated as well as an interactive carbon and nitrogen cycle, fully prognostic;
- an upper atmosphere component, the Whole Atmosphere Community Climate Model (WACCM), is integrated in CAM dynamics and physics;
- an atmospheric chemistry module, CAM-CHEM, is used;
- and a completely new land ice component is included.

It should be noted that tuning of simulations is performed on PI-control and historical simulations allowing modifications of the sea ice albedo, which controls the mean Arctic sea ice thickness, and parameterisations of the clouds, which controls the radiation balance at the top of the atmosphere (Gent et al., 2011). For more details, the reader can refer to Kay et al. (2015) and Meehl et al. (2013).

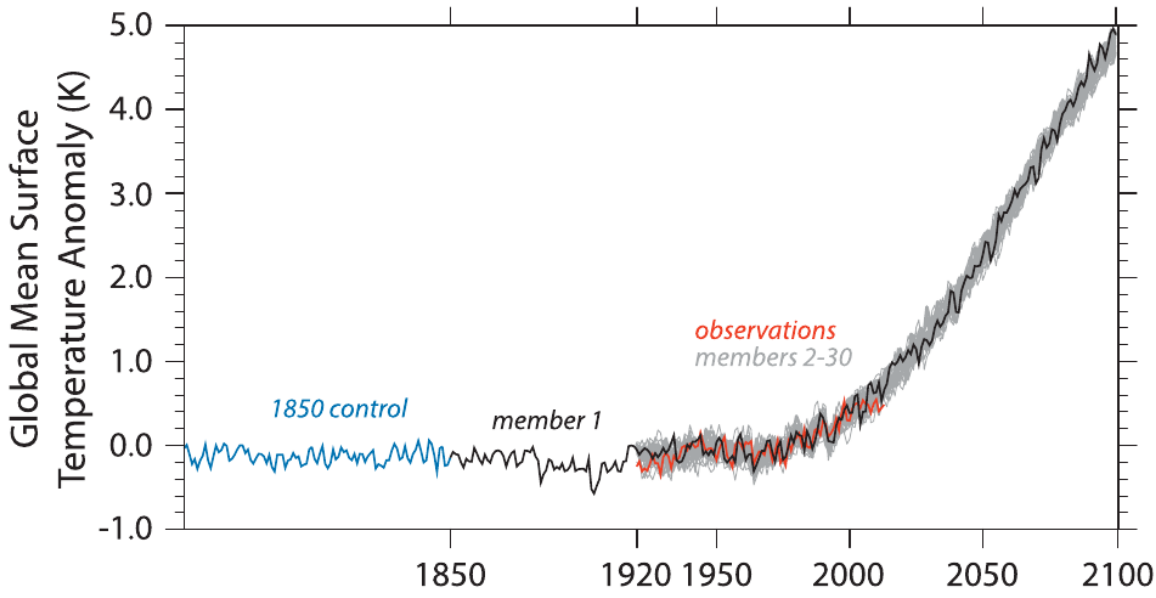

Figure 2.4 – Global surface temperature anomalies (1961-1990 base period) for the PI-control simulation (blue line), individual ensemble members of historical and RCP8.5 simulations (the member one in black line, the other members in grey lines) and observations (red line) from HadCRUT4 (Morice et al., 2012). Reprinted from Kay et al. (2015).

The ensemble begins in 1920, date from which are initialised with slightly differences 41 members with historical forcing conditions (all except member one). The large ensemble can be used for instance to evaluate changes in the global surface temperature from the pre-industrial period to future under the RCP8.5 forcings (Fig. 2.4). The increase in temperature is estimated to 5 °C by the year 2100 (ensemble mean value) with a spread due to the internal variability (inter-member spread) equal to 0.4 °C. Note also that the observed temperature timeserie is included in the spread of the historical members of CESM-LE.

Another advantage of a large ensemble of climate simulations is its ability to generate many realisations that allow for a robust sampling of the internal climate variability simulated by the model. We have thus access to a large number of El Niño events occurring during each period. The spread over a long-term period for the PI-control simulation is indicative of the internal variability of the climate system, whereas the spread over the different members of

historical and RCP8.5 simulations is indicative of the total transient variability (with internal and external variability).

We document in the paragraph 2.1.4 the ability of CESM-LE to simulate the tropical Pacific and the ENSO phenomenon, focus of the thesis.

2.1.3.2 Ocean component: POP model

The oceanic model incorporated in CESM-LE is the Parallel Ocean Program (POP) (Smith et al., 2010). POP is a fixed volume ocean model.

(a) Dipole POP grid

(b) Plan representation

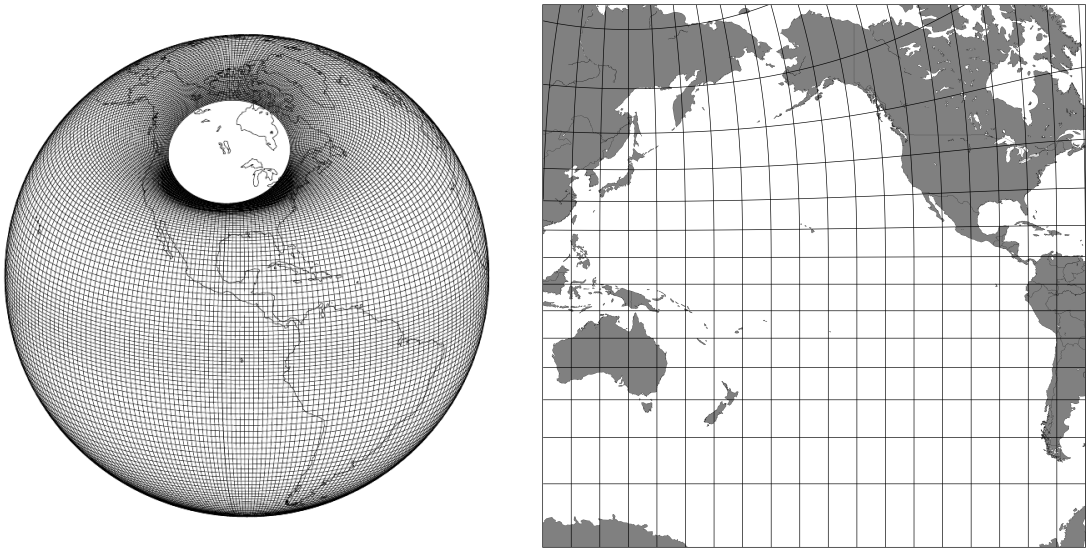

Figure 2.5 – Representation of the Arakawa B-grid used by POP ocean model. 2.5a shows the orthogonal curvilinear mesh-grid with the displaced pole (reprinted from Smith et al. (2010)). 2.5b shows the projection of the mesh-grid over the Pacific ocean onto plan coordinate.

The POP grid is an orthogonal curvilinear grid with displaced pole. In the Northern Hemisphere, the pole is displaced into land masses (Fig. 2.5a) in order to avoid merge meridians into a point of convergence, called the "North Pole singularity" over the oceans. The meshes are regular in the southern hemisphere, on a Mercator polar grid and they smoothly get distorted in the northern hemisphere, from the Equator. The horizontal resolution is 1° longitude-latitude with a lower meridional grid spacing when approaching the equator ($\sim$ 0.25°) to more accurately resolve the equatorial dynamical processes. POP model is a level z-coordinate model that uses 60 non-uniform vertical levels, whose thickness is relatively thin in surface layers (10 m) and increases with depth (250 m at the bottom of the ocean). The vertical resolution is enhanced in the upper levels to improve SST in the main upwelling regions including the equatorial Pacific upwelling. Gent et al. (2011) showed that in the previous version of the model (CCSM4), the tightening of the vertical resolution together with improvements in the atmospheric component of the model (CAM) helped to improve the spatial and temporal characteristics of ENSO.

The boundary conditions do not permit flux for tracers (zero tracer gradient normal to boundaries) and velocities are zero at the borders. The fluxes of momentum, heat and freshwater are applied as surface boundary conditions to vertical mixing terms. These turbulent fluxes of the near surface atmospheric state are parameterised by bulk formulae, including a feedback of the state of the ocean surface onto the fluxes (Large and Yeager, 2009).

More information on the ocean model physical processes and parameterisations can be found in Danabasoglu et al. (2012). We are interested in the tropical Pacific, between 35°S and 35°N. We will focus on the 10°S-10°N band to characterise El Niño diversity (see chapter 3) and on the equatorial band (2°S-2°N) to assess the oceanic processes involved in the El Niño

evolution (see in particular chapter 5).

2.1.4 Modelling ENSO

The objective of the paragraph is to investigate whether CESM-LE simulates realistically ENSO and the tropical Pacific. We invite the reader to refer to Meehl et al. (2013); Park et al. (2014) and Kay et al. (2015) for detailed climate change projections over the globe simulated in CESM1(CAM5).

Several recent studies have documented the ability of CESM1 or the previous version, CCSM4, to simulate the tropical Pacific and the variability associated with ENSO (Gent et al., 2011; Deser et al., 2012; Hurrell et al., 2013; Zhang et al., 2017). The bias of the double Inter-Tropical Convergence Zone (ITCZ) remains in CESM1 as well as an excessive tropical water cycle (Hurrell et al., 2013). The Cold Tongue bias in CESM1 has been shown to be related to the convective momentum transport parameterisation (Woelfle et al., 2018). Despite the remaining mean-state biases, the simulation of ENSO has been improved from CCSM4 to CESM1, with in particular a larger range of frequency of events, with a more realistic 3-6 years period even if the model still overestimates the magnitude of ENSO (Hurrell et al., 2013). The asymmetry of ENSO, with a longer duration of La Niña compared to El Niño is also simulated (Deser et al., 2012). However, Zhang et al. (2017) showed that CCSM4 and CESM1 underestimate observed ENSO asymmetry, mainly because of an overestimation of the cold SST anomalies during La Niña phase. This is directly linked to atmosphere components of the models (CAM4 and CAM5 respectively) which simulate a stronger time mean zonal wind than observed.

We use different datasets of observations (see paragraph 2.1.1): HadISST v1.1 (1950-2017) and ERSST v3b (1950-2017), and reanalysis: SODA v2.2.4 (1950-2010), to compare the observed variability of the tropical Pacific and the main features of ENSO with that modelled by CESM-LE and GFDL CM2.1. The three datasets of SST observations, HadISST v1.1, ERSST v3b and SODA v2.2.4, allow an estimation of uncertainties due to products construction methods and measure errors. The two PI-control simulations of CESM-LE and GFDL CM2.1 are used to compare simulated climates and highlight possible errors compensation. GFDL CM2.1, even if it is a CGCM of the previous CMIP3 generation, was chosen because it has already been studied using the method of El Niño events detection that we use and it simulates realistically main features of ENSO (see paragraph 2.1.2).

For each dataset, the anomalies data are the departure from the mean climatology over the entire timeserie and are linearly detrended at each grid point (see paragraph 2.2.2.1).

2.1.4.1 Seasonal cycle

The simulation of the seasonal cycle of the equatorial Pacific SST (2°S-2°N) is evaluated in the models. The SST seasonal cycle is of prime importance in the dynamics of ENSO. El Niño phases are locked on the seasonal cycle, they commonly start in the boreal spring when the eastern Pacific SST are warmer (Fig 2.6a, 2.6b and 2.6c), develop in summer when the air-sea coupling is stronger, reach their amplitude maximum in winter and vanish in the following spring after the trade winds have strengthened. Some seasons are more conducive than others to El Niño development and the seasonal cycle also constrains the termination of events. The reader is invited to refer to the paragraph 1.3.1 for more information.

Many studies showed that CGCMs do not simulate realistically the seasonal phase locking of El Niño (Bellenger et al., 2014; Chen et al., 2017a). The PI-control simulations of CESM and GFDL CM2.1 reproduce a seasonal cycle with alternation of warm and cold SST in spring and fall in the eastern Pacific but with different bias. In both cases, the Cold Tongue bias leads to a westward shift of the climatological Warm Pool, materialized by the 28 °C isotherm. The westward shift is more pronounced for GFDL CM2.1 (Fig. 2.6d) than for CESM-LE (Fig. 2.6e). As a consequence, the Warm Pool is colder in CGCMs.

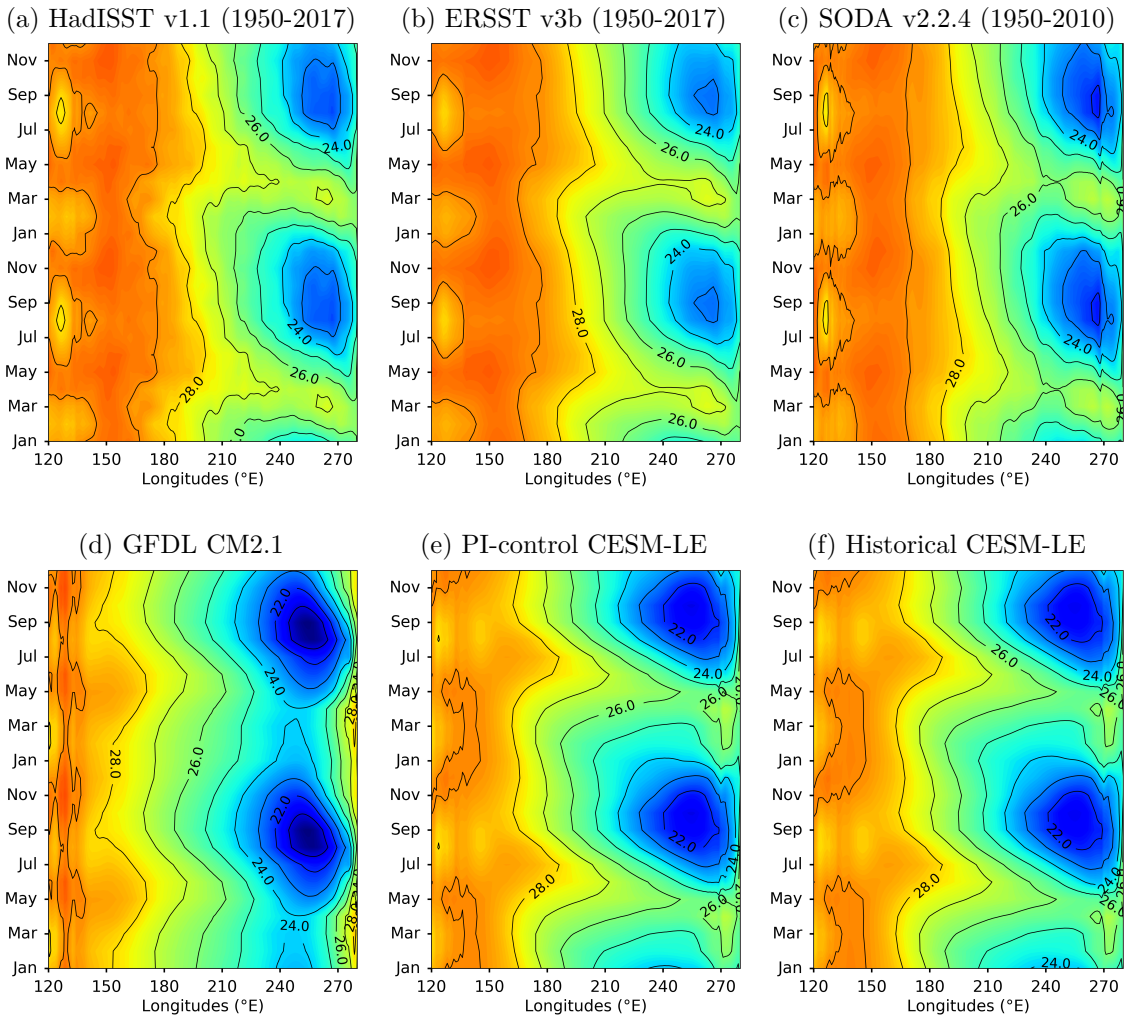

Figure 2.6 – Longitudes-time evolutions of the seasonal cycle of equatorial Pacific SST (2°S-2°N) for (Fig 2.6a) HadISST v1.1 (1950-2017), (Fig 2.6b) ERSST v3b (1950-2017), (Fig 2.6c) SODA v2.2.4 (1950-2010), (Fig 2.6d) the PI-control simulation of GFDL CM2.1 (500 years), (Fig 2.6e) the PI-control simulation of CESM-LE (1801 years) and (Fig. 2.6f) the ensemble-mean of the historical simulations of CESM-LE (42 members).

GFDL CM2.1 PI-control simulation has a seasonal cycle too cold and weak in the eastern Pacific, with small differences in amplitude between warm (spring) and cold (fall) seasons in the eastern Pacific (3.8 °C at 250°E). The Cold Tongue bias is less pronounced in CESM-LE, the colder SST are above 21 °C (around 20 °C in GFDL CM2.1) and the difference between spring and fall seasons is ∼ 4.8 °C, both values are only 1 °C colder than in observations. However, in observations, the maximal signature of the cold water of the upwelling is located more at the east of the equatorial Pacific, close to 270°E. The smaller difference in temperatures between warm and cold seasons in GFDL CM2.1 decreases the strength of the ENSO seasonal phase locking. Wengel et al. (2018) showed indeed that an excessive Cold Tongue in CGCMs leads to weak seasonal phase-locking by reducing the Ekman and thermocline feedbacks in late boreal fall and early boreal winter.

At last, a warm bias of GFDL CM2.1 along the coast of South America, diagnosed by Wittenberg et al. (2006), is also highlighted in Figure 2.6d, while it is less pronounced in CESM-LE.

2.1.4.2 Variability of the tropical Pacific surface temperatures

ENSO is the most important source of natural variability on inter-annual time-scales in the tropical Pacific (see paragraph 1.1).

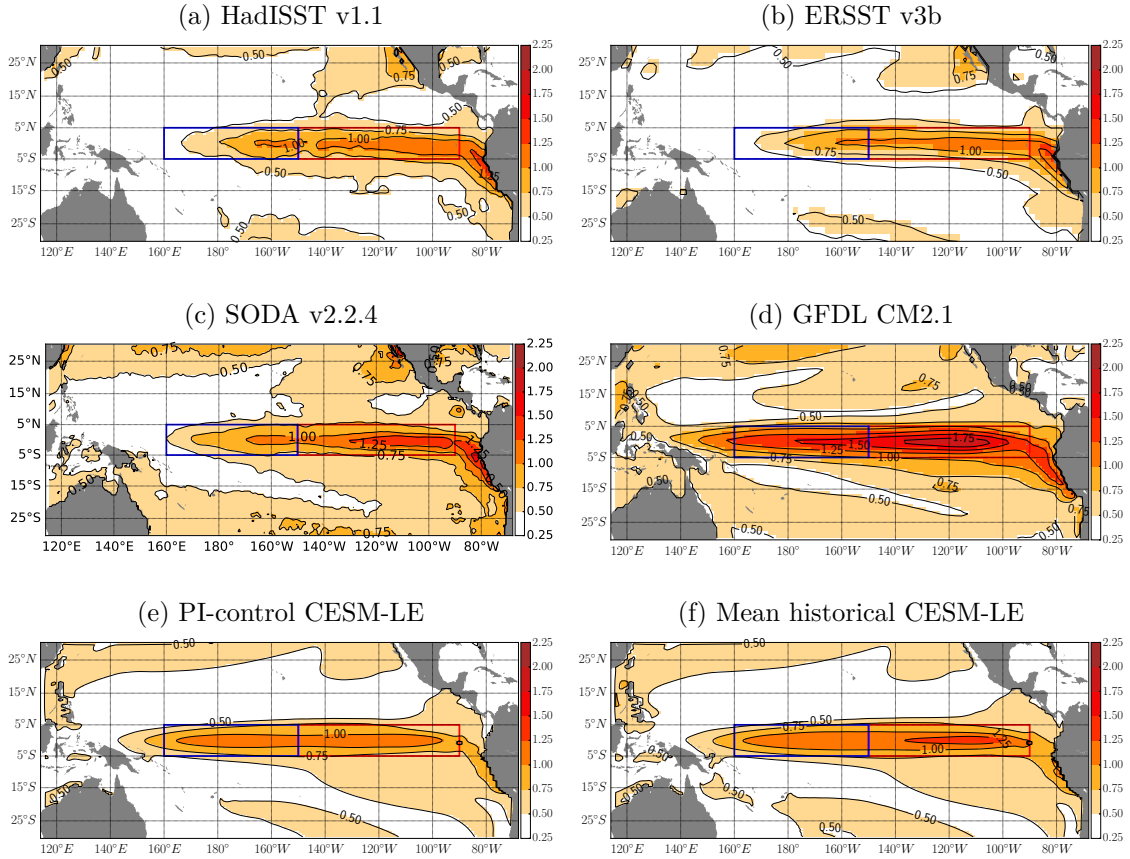

Figure 2.7 – Spatial patterns of the inter-annual SSTA variability (standard deviation) of the tropical Pacific (30°S-30°N) for (2.7a) HadISST v1.1 (1950-2017), (2.7b) ERSST v3b (1950-2017), (2.7c) SODA v2.2.4 (1950-2010), (2.7d) the PI-control simulation of GFDL CM2.1 (500 years), (2.7e) the PI-control simulation of CESM-LE (1801 years) and (2.7f) the ensemble mean of historical simulations of CESM-LE (1 member over 1850-2005 and 41 members over 1920-2005). The boxes represent the Niño-3 (blue) and Niño-4 (red) regions respectively. The data are linearly detrended and the annual cycle is removed.

The spatial pattern of the observed inter-annual variability (Fig. 2.7a, 2.7b and 2.7c) has maximum values, around 1.25 °C, located along the coast of Ecuador and Peru. This warming

is less developed in ERSST v3b which has a coarser resolution (2° latitude-longitude). The intensity of this coast warming is not so pronounced in CESM-LE with a maximum value less that 1 °C. GFDL CM2.1 reproduces this warming at the South American coast, but the amplitude in the eastern Pacific is much larger than observed, with maximum values above 1.75 °C. The SODA v2.2.4 reanalysis shows SST standard deviations larger in the eastern Pacific than the observed datasets and a slightly westward shift of the zonal extension, probably due to the combination of dynamical model in the observations. As a reminder, the model used in SODA reanalysis is the POP model (Smith et al., 2010), the ocean component of CESM-LE.

The strong variability region are shifted westward in both models compared to observation patterns. It is particularly the case in GFDL CM2.1, where large inter-annual SSTA are simulated all along the equator, in a lesser extent in CESM-LE. The westward extension of the tropical Pacific variability, linked to the westward extension of the Cold Tongue, is a common and well documented feature of CGCMs (see paragraph 2.1.2.2 and Wittenberg et al. (2006); Capotondi et al. (2006); Bellenger et al. (2014) among others). Another common CGCM bias visible in the figures is the too high variability of the equatorial Pacific, especially in GFDL CM2.1.

The inter-annual variability of the tropical Pacific is also assessed by an Empirical Orthogonal Functions (EOF, see paragraph 2.2.2.2) analysis applied to the SSTA (10°S-10°N). While the first mode resembles the canonical El Niño event (Ashok et al., 2007), the second mode tends to capture the spatial asymmetry between the canonical El Niño and La Niña events (Hoerling et al., 1997; Rodgers et al., 2004). Figure 2.8 shows the first two EOF modes for each dataset over the same period as for Figure 2.7.

Once again, the westward extension bias of the Cold Tongue appears in the model modes, as well as the detachment from the South American coast of the mode 1 warming. Wittenberg et al. (2006) noted that the tropical Pacific SST variability is shifted by 20°-30° westward compared to the observed spatial pattern. Here the localisation of the mean 28 °C isotherm, an indicator of the Warm Pool (materialized by the black lines in Fig. 2.8), is shifted westward, of 25° for the CESM PI-control simulation and 35° for the GFDL CM2.1 simulation. Another feature bias to note is the weak meridional extension of the variability, confined to the equator in the CGCMs.

The first two modes of the EOF analysis account for most of the variability in the tropical Pacific (Table 2.1). Except for SODA v2.2.4, the variance explained by the first two modes exceeds 75 % for each dataset. Note that the reduced period available for SODA compared to ERSST or HadISST does not explain the smaller variance, since when determining the variance explained by the two first modes of HadISST over the same period 1950-2010, it is equal to 78.8 %. The variance explained by the first two modes is slightly smaller for the CESM-LE PI-control simulations than for the historical ones, whose value is close to the observed value. When considering the internal variability of the simulated historical climate system, which is accessed by the different members of the large ensemble (indicated in Table 2.1 is the standard deviation associated with the variance values of each member, see following paragraph), the observed variance of HadISST v1.1 dataset is not included in the internal variability but the first mode of the ERSST v3b dataset is.

2.1.4.3 Variability of the equatorial Pacific subsurface temperatures

In the same way as for the SST, an EOF analysis is performed on the equatorial (5°S-5°N) subsurface temperatures anomalies, from the surface to 200 m depth (Fig. 2.9).

Even if the integration time differs between the three datasets (SODA v2.2.4 reanalysis, PI-control and historical simulations of CESM-LE), the two leading simulated modes have patterns similar to those observed. However, a longitude shift of 10° to the west of the positive surface temperature anomalies is found in both simulated modes, as a consequence of the common cold tongue bias of CGCMs (see paragraph 2.1.2.2). The 20°C mean isotherm

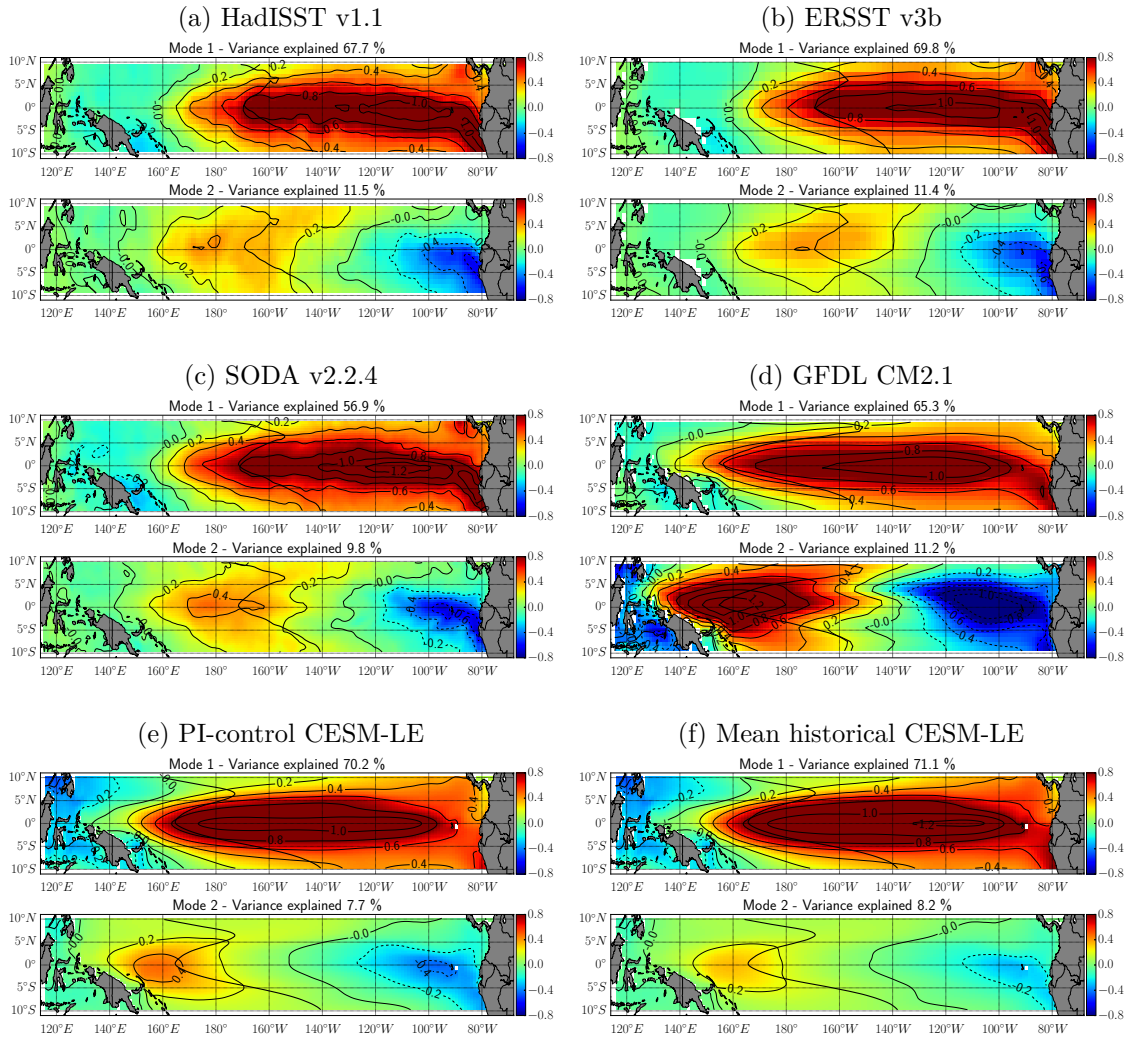

Figure 2.8 – First two modes of the EOF analysis of the tropical Pacific SSTA (10°S-10°N) of (2.8a) HadISST v1.1 (1950-2017), (2.8b) ERSST v3b (1950-2017), (2.8c) SODA v2.2.4 (1950-2010), (2.8d) the PI-control simulation of GFDL CM2.1 (500 years), (2.8e) the PI-control simulation of CESM-LE (1801 years) and (2.8f) the ensemble mean of historical simulations of CESM-LE (1 member over 1850-2005, 41 members over 1920-2005).

EOF modes	Mode 1	Mode 2	Total variance explained
HadISST v1.1	67.7 %	11.5 %	79.2 %
ERSST v3b	69.8 %	11.4 %	81.2 %
SODA v2.2.4	56.9 %	9.8 %	66.7 %
GFDL CM1.2 PI-control	65.3 %	11.2 %	76.5 %
CESM-LE PI-control	70.2 %	7.7 %	77.9 %
CESM-LE historical	71.1 % ±1.8	8.2 % ±1.0	79.4 %

Table 2.1 – Variance explained by the two first modes of the EOF analysis of the tropical Pacific SSTA (10°S-10°N) of HadISST v1.1 (1950-2017), ERSST v3b (1950-2017), SODA v2.2.4 (1950-2010), the PI-control simulation of GFDL CM2.1 (500 years), the PI-control simulation of CESM-LE (1801 years) and the ensemble mean of historical simulations of CESM-LE (1 member over 1850-2005, 41 members over 1920-2005). The errors associated with the CESM-LE historical values correspond to the spread of the corresponding standard deviation computed for each member of the ensemble.

(black lines), a proxy of the depth of the thermocline, is realistically simulated by CESM-LE, even if the slope of the thermocline in the east Pacific is more pronounced than in observations. Consistently with previous studies (Kumar and Hu, 2014; Choi et al., 2013a), the subsurface temperature variations are mainly localised along the thermocline. These two patterns reveal the well known modes of subsurface ENSO variability: the "Tilt" mode (the first leading mode of each dataset, left column of Figure 2.9) and the "Warm Water Volume" (WWV) mode (the second leading mode of each dataset, right column of Figure 2.9) of the recharge-discharge oscilllator paradigm (see Jin (1997a); Clarke (2010); Meinen and McPhaden (2000) and paragraphs 1.2.1.2 and 1.2.2.1).

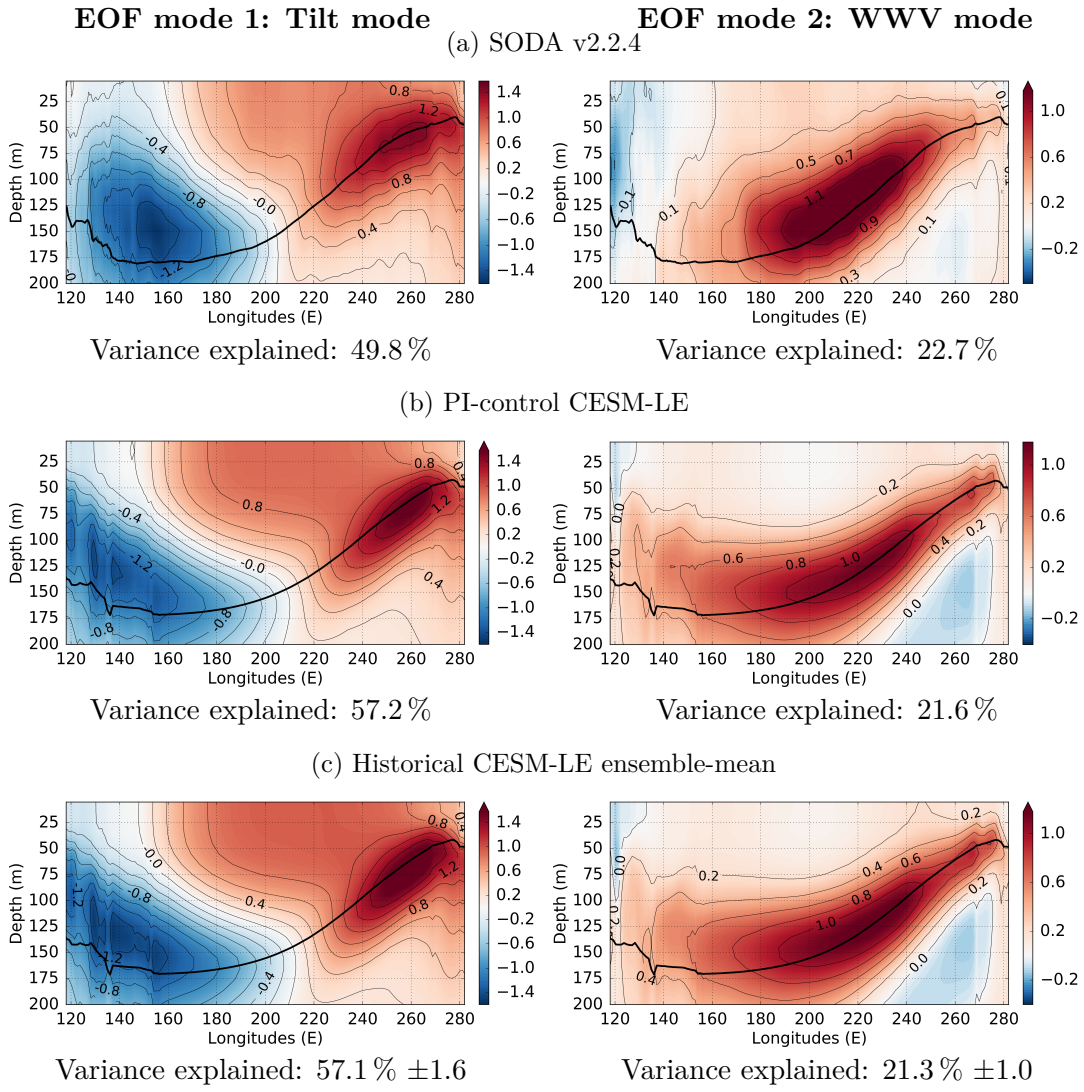

Figure 2.9 – Spatial patterns of the two leading modes (left: mode 1 and right: mode 2) of the EOF analyse of the equatorial subsurface temperature anomalies averaged between 5°S-5°N for (2.9a) SODA v2.2.4 reanalysis (1950-2010), (2.9b) PI-control CESM-LE simulation (1801 years) and (2.9c) the ensemble-mean of CESM-LE historical simulations (1850-2005 for 1 member, 1920-2005 otherwise). In black lines are the respective mean 20 °C isotherm, a proxy of the thermocline. The variance explained by each mode are indicated below the corresponding panel. The annual cycle is removed and the data are linearly detrended.

The tilt mode shows a vertical dipole structure with opposite temperatures between the eastern and western equatorial Pacific, and surface warming extending from the eastern Pacific. Note that the tilt mode patterns are consistent with those of Kumar and Hu (2014) using two other observation datasets (the global ocean data assimilation system (GODAS) and the tropical atmosphere ocean (TAO) project) in the equatorial Pacific (5°S-°N) (see their

Figure 1). The magnitude of the variability explained by the simulated tilt modes is slightly larger than the observed one in the positive center of high variability in the eastern Pacific and slightly smaller, further west and shallower in the negative center in the western Pacific (see also the total variances in Figure 2.9). Compared to the 6 CMIP3 models analysed by Choi et al. (2013a), the spatial patterns of the simulated tilt mode of CESM-LE are similar to that of the GFDL CM2.0 and GFDL CM2.1 models (see their Figure 2, left column).

The tilt mode corresponds to the instantly adjustment of the thermocline to zonal wind stress forcing in the western-to-central tropical Pacific, via Kelvin waves propagation. It is associated with variations in thermocline depth, with the deepening (raising) of the thermocline in the eastern equatorial Pacific during El Niño (La Niña) events in response to zonal wind stress. It is confirmed by the lag-correlation of the principal component (PC) time-series associated with the tilt mode and the first mode of the tropical SSTA EOF analysis (see paragraph 2.1.4.2) or the Niño-3.4 SSTA index, which are ENSO proxies. The tilt mode is highly correlated to ENSO indices whether in the SODA reanalysis dataset (correlation coefficient equal to 0.91 with both ENSO indices, significant at 99 % confidence level with a lag of one month) or in the PI-control simulation of CESM-LE (correlation coefficient equal to 0.97 with both ENSO indices, significant at 99 % confidence level with 0 lag). This mode is thus related with El Niño characteristics during its mature phase (Meinen and McPhaden, 2000; Choi et al., 2013a). It is also consistent with the spatial pattern of the regression of the equatorial Pacific SST anomalies (10°N-10°S) onto the principal component of the tilt mode (Fig. 2.10, top panels). The SST pattern spatial associated with the the tilt mode is similar to that of El Niño, represented through the first mode of the SSTA EOF analysis of the equatorial Pacific (10°S-10°N, see Figure 2.8 in paragraph 2.1.4.2). The pattern correlation coefficient is equal to 0.99 for the SODA reanalysis dataset and 1 for the PI-control simulation of CESM-LE.

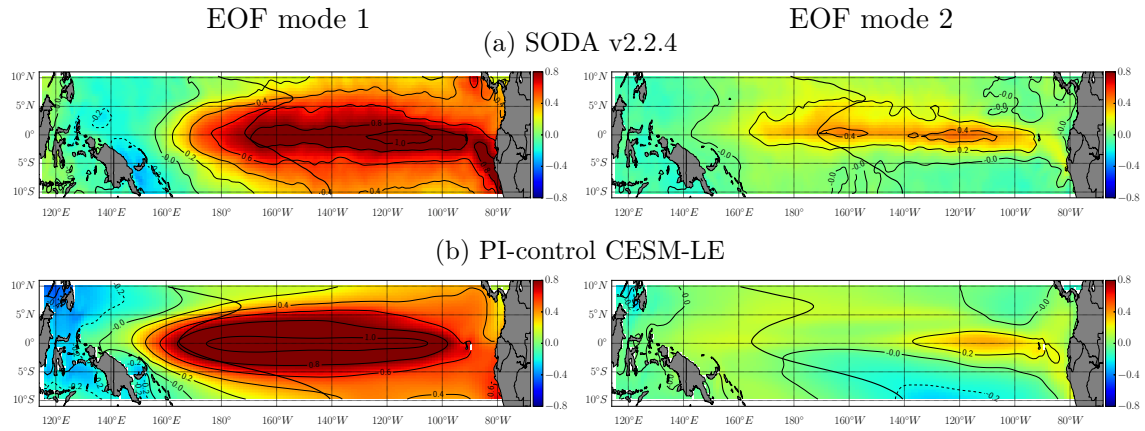

Figure 2.10 – Regressed spatial patterns of the equatorial SSTA onto the (left) first and (right) second leading modes of the EOF analyse of the equatorial subsurface temperature anomalies averaged between 5°S-5°N for (2.10a) SODA v2.2.4 reanalysis (1950-2010) and (2.10b) PI-control CESM-LE simulation (1801 years). The first mode is associated with the tilt mode and the second leading mode with the WWV mode. In black lines are the respective mean 28 °C isotherm, a proxy of the warm pool. The annual cycle is removed and the data are linearly detrended.

The "WWV" shows a basin-wide structure and is associated with variations in warm water volume. It is more representative of the delayed adjustment of the ocean to wind stress curl. Its simulated magnitude is lower than the observed one (see right column of Figure 2.9 and the associated total variances). The positive simulated variability spans the entire width of the Pacific, becoming shallower to the west of the dateline, which is not observed. This westward bias induces the appearance of two eccentric centres of low surface warming, around 160°E and 250°E that can be found in the regressed map of the SSTA onto this mode (Fig 2.10b). A more pronounced upwelling of cold water is simulated in the east

up to 50 m deep, which induces an inlet of cold water in the south-east in the associated regressed map. The bias in the simulation of the WWV mode in CESM-LE leads to poor spatial correlations with El Niño patterns (0.28 for CESM-LE PI-control simulation against 0.66 in SODA v2.2.4 dataset).

The WWV mode usually leads ENSO SSTA by 6-9 months (Kessler, 2002). However, numerous studies highlighted a shift in the lag-correlation between the WWV mode and ENSO SSTA that occurred around 2000s (McPhaden, 2012; Kumar and Hu, 2014; Hu et al., 2017). When analysing the WWV mode through the WWV index (volume of warm water with temperature greater than 20 °C integrated along the equatorial Pacific), McPhaden (2012) showed that WWV's lead over ENSO SSTA decreased from 2-3 seasons during the 1980s and 1990s to one season in the 2000s. The decrease in duration of lead correlation of WWV over ENSO is confirmed by Hu et al. (2017) with longer time-series of observations. Kumar and Hu (2014) and Hu et al. (2017) showed that this change is accompanied by an increase in the frequency of both WWV and ENSO, due to a westward shift of the Bjerknes feedback centre of action.

(a) SODA v2.2.4 for the 1950-2010 period

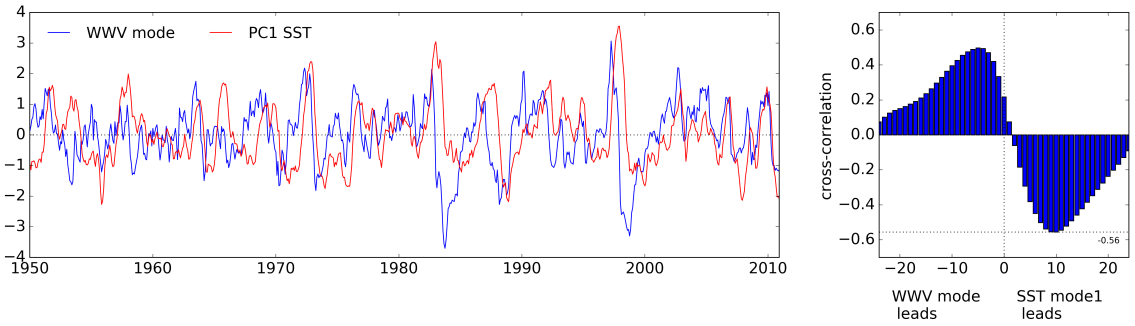

(b) SODA v2.2.4 for the 1979-1999 period

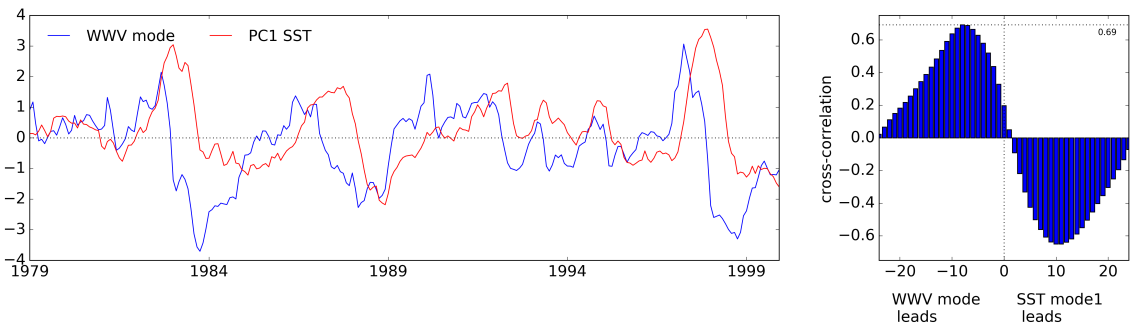

Figure 2.11 – (Left panels) Time-series of (blue) WWV mode and (red) ENSO index defined as the first principal component (PC) of the EOF analysis of SSTA equatorial Pacific (10°S-10°N) in SODA v2.2.1 reanalysis dataset for different periods: (2.11a) 1950-2010 period and (2.11b) 1979-1999 period. (Right panels) The lag-correlation coefficients between the two indices for the corresponding periods.

When analysing the lead-lag correlation between the WWV and ENSO modes in SODA v2.2.4, this feature of shift in 2000 is found even if the time-series ends in 2010 (Fig. 2.11). For the entire 1950-2010 period, the maximum absolute correlation ($c = -0.65$) occurred when the ENSO SSTA mode leads the WWV mode by 10 months. For the limited period 1979-1999, the maximum absolution correlation ($c = 0.69$) occurred when the WWV mode leads the ENSO mode by 8 months. Note that no change in lead-lag correlation occurred between the tilt mode and ENSO SSTA mode in SODA v2.2.4 dataset. The CESM-LE simulations show lead-lag correlations similar to those observed over the entire period (and similar to those between the WWV and tilt modes, due to the almost simultaneous nature of the tilt and ENSO modes). The lead (lag) of the ENSO mode over the WWV mode corresponds to the peak phase of El Niño followed (preceded) by a discharge (recharge) of heat content

(whose WWV is a proxy) in the equatorial Pacific, and conversely for La Niña.

(a) SODA v2.2.4

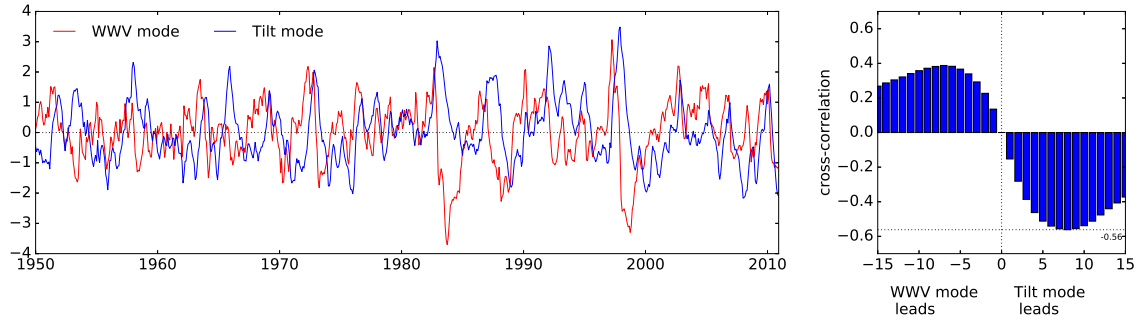

(b) WWV and tilt modes lag-correlations

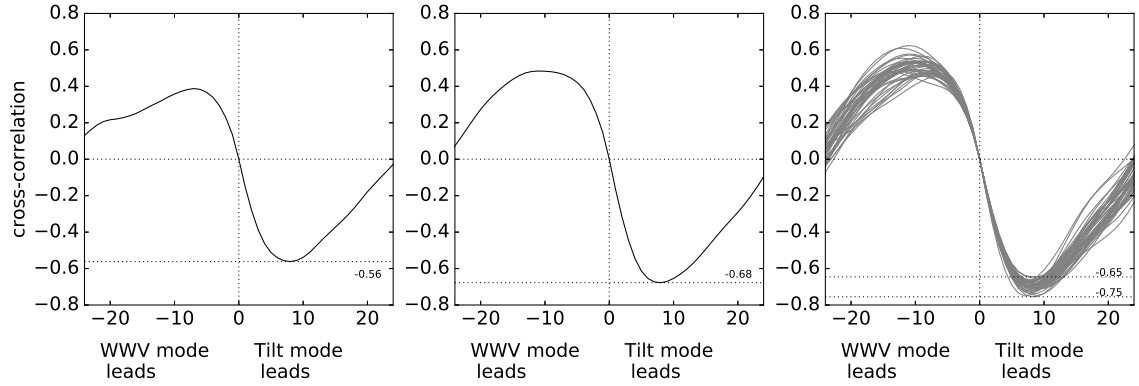

Figure 2.12 – (2.12a) (Left) The tilt mode (blue) and the Warm Water Volume (WWV) mode (red) defined from the leading principal components (PC) of the EOF analysis of the subsurface temperature anomalies averaged between 5°S-5°N for SODA v2.2.4 reanalysis (1950-2010). (Right) Cross-correlation between the two PC showing a maximum of absolute correlation ($c = -0.56$) with a lag of WWV over tilt mode of 8 months. The positive correlation (c=0.39) occurs when the WWV mode leads the tilt mode by 7 months. (2.12b) Cross-correlation between the WWV mode and the tilt mode for (left) SODA v2.2.4, (middle) CESM-LE PI-control simulation and (right) CESM-LE historical simulations. The maximum absolute correlation is higher for CESM-LE simulation ($c \sim -0.70$) with lags between 7 and 9 months depending on the historical member (8 months for the PI-control simulation). The positive correlation in PI-control simulation occurred for a lead of the WWV over the tilt mode by 7 months (c=0.52).

It was verified that the PC time-series of the tilt and WWV modes are in quadrature (Fig. 2.12) in a similar way to WWV and ENSO modes (Fig. 2.11 for SODA 2.2.4 dataset). This quadrature leads to the oscillatory feature of ENSO as described above. It is consistent with Kumar and Hu (2014) (see their Figure 3d). The simulated correlations occurred with the same lead-lag durations, but the strength of the correlations is higher than in the reanalysis dataset.

2.1.4.4 Variability of ENSO

The ENSO amplitude is often measured through the Niño-3 SSTA standard deviation (Guilyardi et al., 2009b; Bellenger et al., 2014; Chen et al., 2017b). Bellenger et al. (2014) showed that the CMIP5 and CMIP3 ensemble-mean values of ENSO amplitude is comparable to observations, but the spread of ENSO amplitudes is reduced by half in the CMIP5 database compared to the CMIP3 database, although models still tend to overestimate ENSO variability. According to Gent et al. (2011); Deser et al. (2012) and Hurrell et al. (2013), CESM1(CAM5) correctly simulates some intrinsic characteristics of ENSO, such as a more realistic 3-6 years period, but overestimates its magnitude compared to observations. To take into account the westward bias of the Cold Tongue in the CGCMs, we not only compute the Niño-3 but also

the Niño-3.4 standard deviation (Table 2.2).

We compute the spread of the internal variability associated with the value of ENSO amplitudes. As explained in paragraph 2.1.2.3, two types of natural variability are estimated:

- from the PI-control simulations: these simulations are long enough to provide a large range of variability of the climate system, only due to low-frequency changes. This internal variability corresponds to climate with constant external forcing and without anthropogenic influence, that is variations generated by the climate system itself. We calculate the variability associated with periods of duration similar to the observations.
- from the ensemble simulations: thanks to the different members, differing in only very small change of the initial atmospheric conditions, we estimate the internal variability through the spread of the different climate trajectories followed by each member of the ensemble. This internal variability is subject to changes of the climate system due to changes in external forcings.

Even if these two definitions of the internal variability are not equivalent, it gives an order of magnitude of the different states that the climate system can take.

SSTA standard deviation	Niño-3	Niño-34
HadISST v1.1	0.86	0.83
ERSST v3b	0.87	0.84
SODA v2.2.4	0.89	0.84
GFDL CM1.2 PI-control	1.25 ± 0.15	1.25 ± 0.15
CESM-LE PI-control	0.84 ± 0.07	0.90 ± 0.08
CESM-LE historical	0.95 ± 0.08	0.99 ± 0.08

Table 2.2 – ENSO amplitudes derived from the standard deviations of the Niño-3 and Niño-3.4 indices. The errors associated with the PI-control values correspond to the spread (standard deviation) of the standard deviation of the concerned index computed for overlapping 68 years period, taken every 50 years. The 68 years duration has been chosen as the duration of the observations dataset. The errors associated with the CESM-LE historical values correspond to the spread of the corresponding standard deviation computed for each member of the ensemble.

The ENSO amplitudes in the Niño-3 region in CESM PI-control simulation, computed from periods of same length than the observed one (68 years), are close to the observed values, the latter being included in the internal variability of the simulated pre-industrial climate. However, the ENSO amplitudes in the Niño-3.4 region tend to be slightly too high in the PI-control simulation. The amplitudes of ENSO variability in CESM-LE increase from Niño-3 to Niño-3.4 regions, while it is the opposite trend in observations. This is due to the westward Cold Tongue bias, shifting the variability westward and decreasing it along the South American coast (see figures 2.7 and 2.8), associated with the trend of CGCMs to overestimate ENSO variability. The bias of overestimating ENSO amplitudes appear clearly in historical simulations with ENSO amplitudes in Niño-3.4 region whose associated internal variability no longer includes observations. This overestimating bias is more pronounced in GFDL CM2.1 whose internal spread never includes observation values.

Another important feature of ENSO is the seasonal phase locking, that we investigate through the climatological variance of the Niño-3, Niño-4, E and C indices (Fig. 2.13). Zheng et al. (2018) showed that the monthly ENSO amplitudes in the Niño-3 region simulated by the historical members of CESM-LE are overestimated compared to those observed, in particular from January to April and from July to September. The magnitude of Niño-3 ENSO amplitudes being less pronounced in the CESM PI-control simulation than in historical simulations, the Niño-3 climatological variance of the latter is very close to the observed one. The winter peak is slightly weaker and the month of least variability is the month of May in CESM-LE when it is earlier, in March-April in observations. The Niño-3 climatological

variance of GFDL CM2.1 is not so well simulated, as it was highlighted by Wittenberg et al. (2006); Guilyardi (2006) and Bellenger et al. (2014). The quasi-inverse seasonal cycle of the variability in Niño-3 simulated by GFDL CM2.1 is consistent with Chen et al. (2017a) who showed a more important probability of occurrence of Eastern Pacific (EP) El Niño in early summer (July-August) than in winter (January-February). This bias is likely related to the semi-annual cycle of the convection and currents mean state, which is associated with the double ITCZ bias and the seasonal reversal of the meridional SST gradient and winds in the eastern Pacific (Wittenberg et al., 2006).

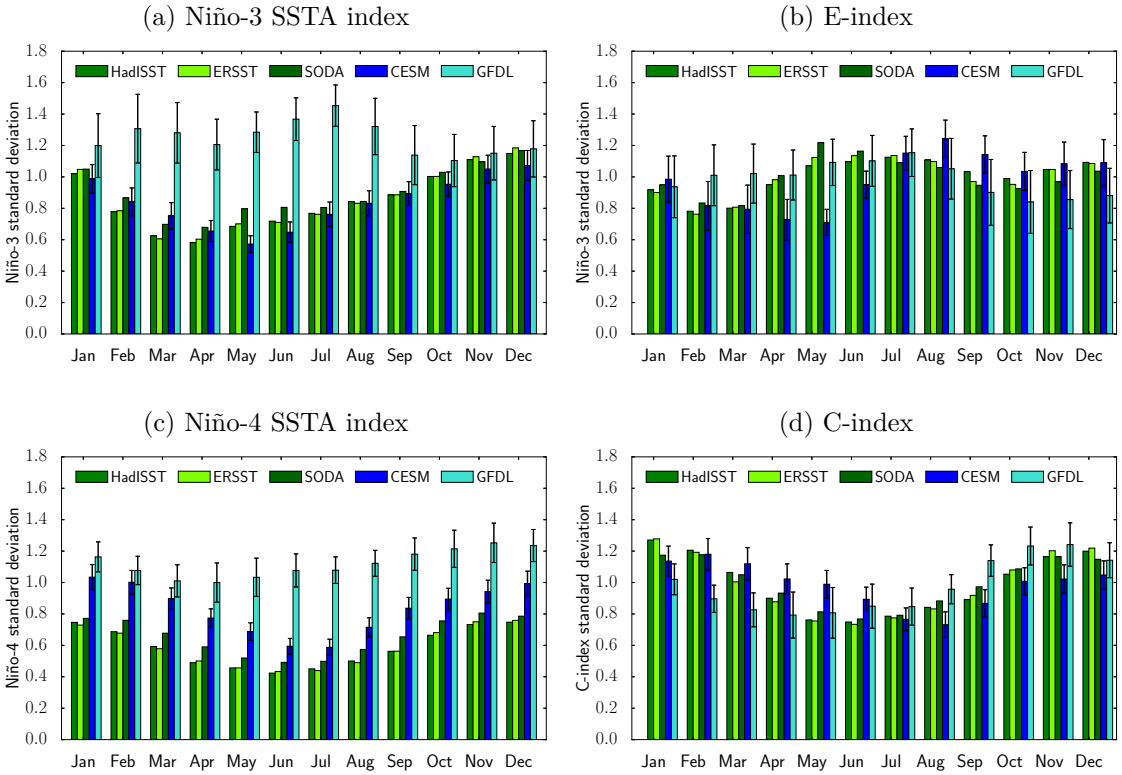

Figure 2.13 – Monthly evolution of the variability of (Fig 2.13a) Niño-3 SSTA index, (Fig 2.13b) E-index, (Fig 2.13c) Niño-4 SSTA index and (Fig 2.13d) C-index for the observed datasets (over 68 years) and for the PI-control simulation of (dark blue) CESM-LE and (turquoise) GFDL CM2.1. The error bars in the PI-control values correspond to the different values of the Niño-3 variability computed for overlapping 68 years period, taken every 50 years. The 68 years duration has been chosen as the duration of the observations datasets. The SST anomalies indices are analysed after removing the climatological monthly means and the linear trend from the data.

When moving westward, to the Niño-4 region, the variabilities of the PI-control simulations present more differences with the observed variability, since the latter decreases rapidly towards the west when the simulated variabilities remain stable (Fig. 2.13c compared to Fig. 2.13a). Interestingly, the climatological variance of GFDL CM2.1 changes and becomes similar to the observation cycle with a more pronounced peak in winter and a decrease in variability in March-April. It reinforces the idea that the SSTA variability in the eastern Pacific in some CGCMs, as GFDL CM2.1, is altered by the misrepresentation of the seasonal cycle of a SST forcing such as meridional winds in the eastern Pacific (Wittenberg et al., 2006).

The climatological variances of the normalised E and C indices have also time offsets (Fig. 2.13b and 2.13d). The observed E index variability has two main period of peak: a long period with higher variability from late spring to early fall and a shorter period in November-December. The CESM-LE E-index variability shows a pronounced peak in July-August-September and a second increase in November-December. The summer peak is off by 1-2 months. Consequently, the period of low variability, in February-March in observations,

occurs in April-May in CESM-LE PI-control simulation. Conversely, the GFDL CM2.1 E-index variance has a winter peak shifted in early spring (February-March) with surprisingly its period of low variability in October-November. The E-index is an indicator of strong EP El Niño events which it was shown that the trigger was linked to the Bjerknes feedback (Takahashi and Dewitte, 2016), air-sea coupling feedback whose strength is modulated by the annual cycle. The climatological C-index variability is composed of two main season, with larger variability in winter and weaker variability in summer. The simulated C-index variability showed time-lag with observations, leading (lagging) of two months for GFDL CM2.1 (CESM-LE). These variabilities are strongly linked to the simulation of ENSO dynamics and more precisely of strong El Niño dynamics and will be further investigated in this thesis.

2.1.4.5 ENSO non linearities

The representation of the non-linearities associated with ENSO is decisive in the representation of ENSO feedbacks in the CGCMs (Karamperidou et al., 2017). Following Dommenget et al. (2013), they suggested a metric of ENSO non-linearities, the leading coefficient α of the polynomial regression of the shape of the climate system in the phase space of the two leading principal components of the EOF analysis, PC1-PC2, for the mean December-January-February (DJF) values (Fig. 2.14). α is thus expressed as $PC2 = \alpha \cdot PC1^2 + b \cdot PC1 + c$. The value of the α coefficient gives an indication on the shape of the non-linear relationship between the two main modes of variability in the tropical Pacific.

The values of α obtained from the PI-control run ($\alpha = -0.35 \pm 0.07$) or from the set of historical members of CESM-LE ($\alpha = -0.37 \pm 0.08$) are close to the observed value obtained in the HadISST dataset (1950-2017) ($\alpha = -0.39$) or in the ERSST dataset (1950-2017) ($\alpha = -0.37$) and their spread includes the observed value. However, it should be noted that the value of the α coefficient is dependant on the chosen period and more particularly on the number of years (months) retained for the calculation. Karamperidou et al. (2017) found an α coefficient equal to -0.29 ± 0.03 with the same observations dataset HadISST v1.1 but using a period of 139 years. Cai et al. (2018), using 5 different datasets over different periods covering from 1948 to 2015 found an α value equal to -0.31.

The GFDL CM2.1 shape of the non-linearities in DJF is slightly different from the observed ones, with in particular a tightening toward high values in PC1 which leads to high absolute values of α. The computed value of α being largely dependant of the number of data available, we computed the range of the internal variability on the PI-control simulations for periods of same length than the observed ones (67 winters). Whereas the dispersion associated with the CESM-LE model includes the observed values, whether it is the variability associated with the low frequency variations (Fig. 2.14e where the standard deviation of the possible α values is indicated) or that associated with the large ensemble (Fig. 2.14f), the range of the internal variability of the α values of GFDL CM2.1 is still slightly higher than the observed values.

Despite these differences, both models, CESM-LE and GFDL CM2.1 are included in the group of models with strong nonlinearities (group A) of Karamperidou et al. (2017), a necessary condition for the simulation of fundamental ENSO feedbacks. The models are both able to reproduce the PC1/PC2 relationship, indicative of ENSO non-linearities in the system. In the PC1-PC2 phase space, when localising points associated with El Niño events, strong El Niños are deported towards the end of the boomerang shape, towards high values of PC1 whereas moderate El Niños are localised in the inflexion zone of the boomerang. Takahashi et al. (2011) suggested to rotate the axes to obtain a new basis with a more physical meaning, tracing the signature of strong and moderate El Niño events. The E and C indices thus obtained are used in the rest of this thesis work to define strong and moderate El Niño events.

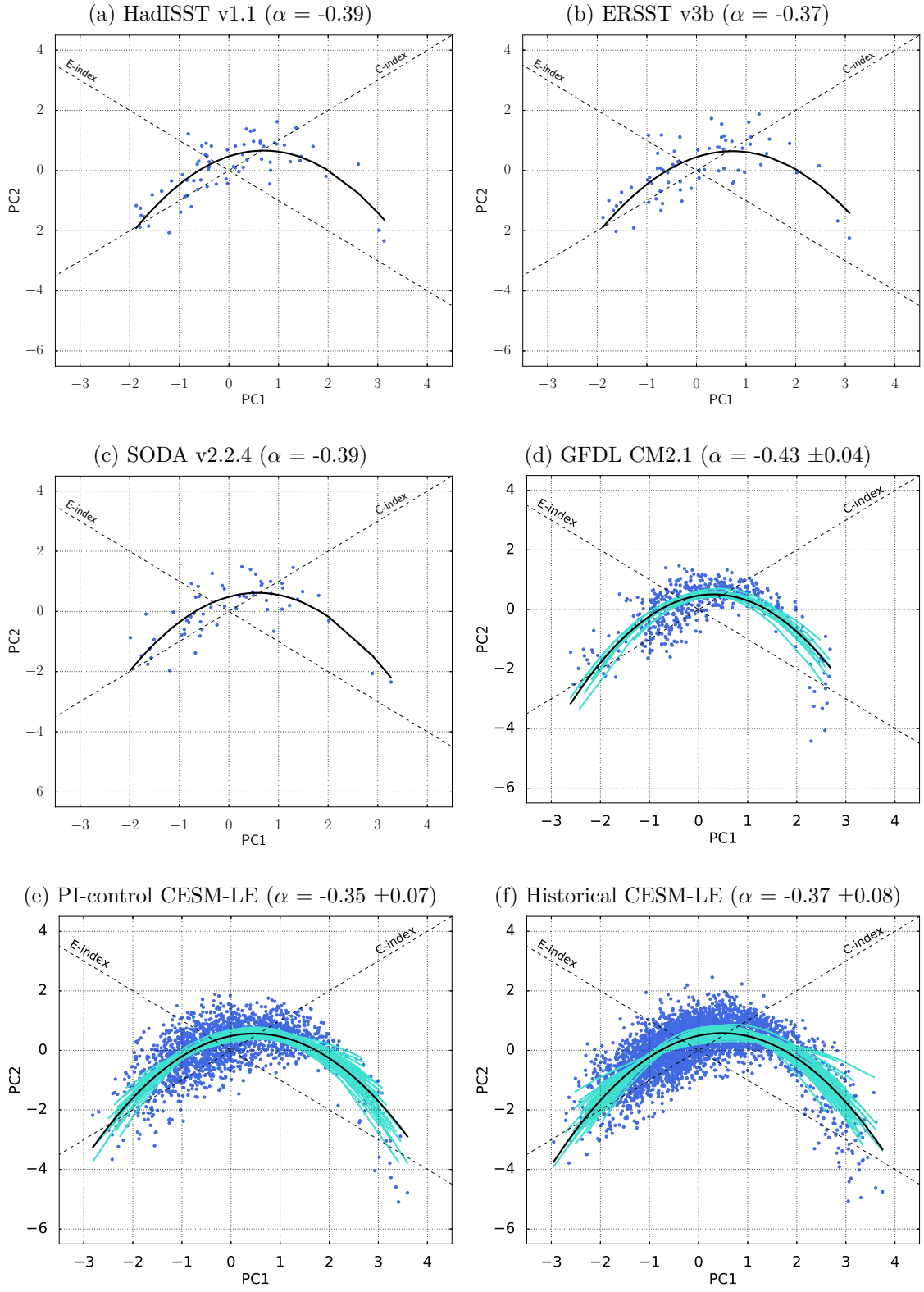

Figure 2.14 – December-February (DJF) mean first and second scaled principal components (PC1 and PC2) of the EOF analysis of the tropical Pacific SSTA (10°S-10°N) of (2.14a) HadISST v1.1 (1950-2017), (2.14b) ERSST v3b (1950-2017), (2.14c) SODA v2.2.4 (1950-2010), (2.14d) the PI-control simulation of GFDL CM2.1 (500 years), (2.14e) the PI-control simulation of CESM-LE (1801 years) and (2.14f) the ensemble mean of historical simulations of CESM-LE (42 members). Black lines represent the (ensemble-mean for historical simulations) fitted polynomial regression used to measure the α coefficient. Blue lines in figures 2.14d and 2.14e represent the fitted polynomial regression for different periods of 86 years over the PI-control simulations (the duration is the same as the duration of 41 of the historical members of CESM-LE). Blue lines in figure 2.14f represent the fitted polynomial regression for each historical member of CESM-LE. The principal components are normalised by their respective standard deviation to have a unit variance.

2.2 Methodological tools

We describe here the different data analysis tools used in this thesis. The study of the different physical variables involved in ENSO requires statistical transformations and post-processing to be interpreted. Different methodological tools are applied to prepare, transform and interpret data. Some of these tools are classified as supervised machine learning tasks, such as the regression, some are classified as unsupervised such as the Empirical Orthogonal Functions or the clustering.

2.2.1 Descriptive statistics

Statistics are based on the notion of (discrete) random variable. To characterise datasets, we analyse the probabilities of distribution of the random variable studied. The distribution of a variable is a function that associates a frequency of occurrence with each possible values of the series. It is called the probability density function (PDF). The PDF is often normally distributed for climate variables. It is not the case of precipitation which has a skewed distribution We study therefore the model, or population, from the analysis of the data described by this model, by using different characteristics of the random variable and its probability distribution.

2.2.1.1 Moments of a probability distribution

Moments are statistical tools characterising the shape of the considered variable probability distribution. In the thesis, we mainly use the first three moments: the mean (first moment), the variance (second central moment) and the skewness (third standardised moment). They are expressed as:

$$Mean = \frac{1}{N}\sum_{i=1}^{N} x_i$$

$$Standard\ deviation = \sqrt{\frac{1}{N-1}\sum_{i=1}^{N}(x_i - mean)^2} = std$$

$$Skewness = \frac{1}{N}\sum_{i=1}^{N}\frac{(x_i - mean)^3}{std^3}$$

The standard deviation (std), that is the square root of the variance, is often used to describe the deviation from the mean of a data sample, which is one measure of the dispersion. The skewness describes the asymmetry of the distribution, i.e. it quantifies whether the distribution tail, left or right, is long or short, thick or thin. If the distribution is symmetric, the skewness is equal to 0. If the distribution spreads to the left (right) with a longer tail on the negative (positive) side of the mean, the skewness is negative (positive).

The statistical moments of the "weather distribution" are likely to change with global warming (Fig. 2.15), which can lead to modify the likelihood of the occurrence of extreme weather events. By shifting the mean of a climate variable whose the PDF is normally distributed, such as surface temperatures for instance, what was defined as extreme positive (negative) events in historical climate become more (less) frequent. These changes are non-linear: a small change in the mean value can result in large changes in the probability of occurrence of extreme events. Changes in the variability of the variable can complicate the projected changes in the probability of occurrence of weather events. Changes in mean, variance and the symmetry of the distribution (skewness) may occur concomitantly and modify in different ways the frequency of occurrence of extreme events.

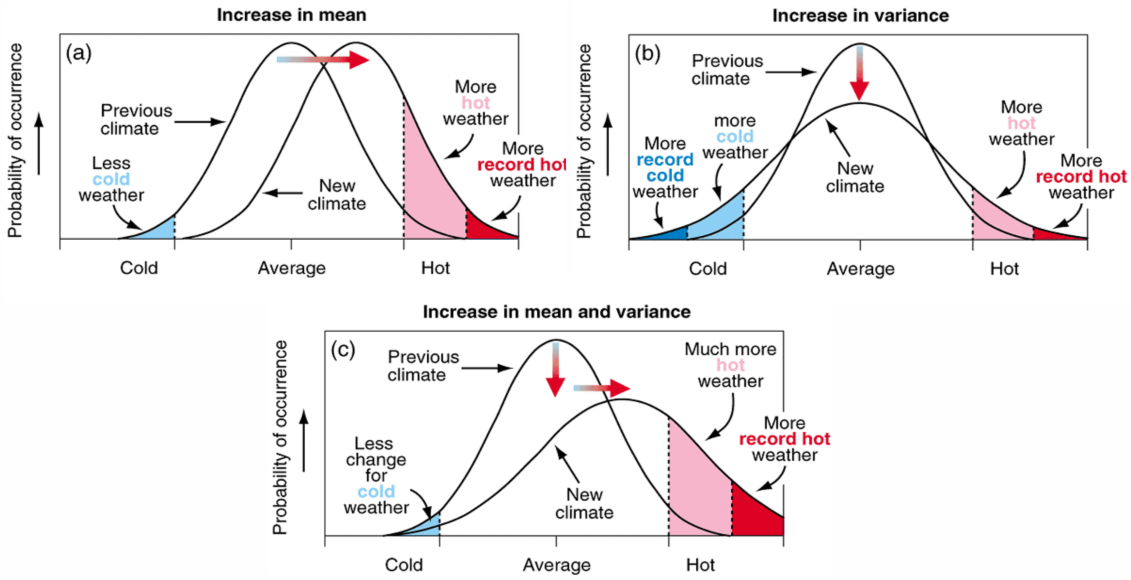

Figure 2.15 – Schematic representations of the PDF of a normally distributed climate variable such as temperatures. Shaded areas correspond to the probability of occurrence of extreme events, that is events in the tails of the distribution, that occur infrequently. Changes in the probability of occurrence of extreme events are affected by changes (a) in the mean, (b) in the variance, and (c) in both the mean and the variance. The figure is reprinted from IPCC Third Assessment Report (AR3, see https://www.ipcc.ch/report/ar3/wg1/the-climate-system-an-overview/).

2.2.1.2 Quantiles of a probability distribution

The quantile q of a data set is the value that divides this data into two parts:

- above of this value (to the right in the PDF representation), there are q% of data,
- below of the value (to the left), there are (100 - q)% of data.

The quantile is equivalent to the cumulative frequency of the distribution. Quantiles are used to estimate the confidence interval associated with significance tests (see paragraph 2.2.4).

Quantiles are also used as another measure of the dispersion of the data, by the Interquartile range (IQR). The IQR is defined as the difference between the 75th and 25th percentiles.

2.2.1.3 Kernel density estimation of a probability distribution

The probability density function of the data in the E-C indices phase space (2D) is estimated through a kernel density estimation (KDE). The estimation of the PDF of the E and C indices is made in Chapter 3 in the analysis of the bi-modality of the El Niño events. The main advantage of this method is that it is non-parametric, not assuming any distribution underlying the data. This choice is made because the E and C indices do not have a strict Gaussian distribution. In particular, the E-index (C-index) has a positive (negative) skewness.

The KDE is a neighbour-based approach. It calculates a kernel function centred in each data and this kernel function then extends symmetrically to cover the neighbours of the data. The width of the extension is determined by the bandwidth of the kernel function. The total probability density function is then estimated as the sum of the kernel functions on each data. The bandwidth is thus a smoothing parameter whose choice is decisive. A window width that is too small will favour local spikes in densities while a too large window width will smooth the entire distribution. We compared different bandwidths, estimated by methods such as Scott or Silverman methods and which may be optimised by cross-validating under the assumption of maximum likelihood or least squares. A Gaussian kernel is chosen.

2.2.2 Pre-processing and data transformation

2.2.2.1 Calculation of anomalies

Preliminary processing of the time series consists in removal of known signals prior to analysis so they will not confound the interpretation of the results. It can be view as a "pre-whitening" step. This supposes to know what is the signal that one wants to withdraw. In our case, ENSO is a phenomenon described as a departure from the mean state. The mean state, as well as the trend of global warming have to be removed before processing the data.

Seasonal cycle

The first step is thus to remove the mean state, more particularly the monthly mean state or annual cycle. When specified as anomalies, it means that data are deseasonalised, that is the annual cycle is removed in each grid point. The annual cycle is considered constant over the entire studied period unless otherwise mentioned. The entire periods are thus the PI-control duration (1801 years), the historical period of simulation (1850-2005 for the first member of CESM-LE, 1920-2005 for the other members), the RCP8.5 period of simulation (2006-2100) and the observed period when analysing observations dataset (1950-2017). When comparing with the method of detrend of Cai et al. (2018) in the paragraph 3.4, the considered period is the first 100 years of the concatenated historical and RCP8.5 simulations.

Therefore, a constant annual cycle is removed, even if the mean state is not a stationary state (see paragraph 1.3.2) and can be modulated by low-frequency fluctuations or climate shifts (Boucharel et al., 2009). We make the assumption that the seasonal cycle is an additive signal de-correlated to the rest of the variations.

Global change trend

To detrend the data and remove in particular the long-term trend due to global warming, the linear monthly trend at each grid point is removed. It is done using the least squares method to estimate the growth rate of the fitted straight line, by minimising the sum of the squared errors between the data and the fitted line.

In the paragraph 3.4, we compare this detrend method with two others. The first compared method considers a quadratic trend due to global warming, applied to the concatenated historical and RCP8.5 periods. The second compared method consists in removing the mean surface state of the tropical Pacific (30°S-30°N) at each time step. This method, called relative SST anomalies, is used by Khodri et al. (2017) using tropical Pacific (20°S-20°N) mean over the 5 years preceding the volcanic event they are studying.

One of the characteristics of the first two methods is to consider that global warming trend is not the same everywhere (in each grid point), which is consistent with an El Niño-like warming pattern even if there is no consensus in the global climate models (see paragraph 1.4.1). Conversely, the last method considers that the climate change trend is the same over the equatorial Pacific.

2.2.2.2 EOF analysis

Empirical Orthogonal Functions (EOF), also called Principal Component Analysis (PCA), are widely used in Earth sciences. It is a mathematical method for unsupervised reduction in dimensionality of the data. The technique determines the dominant spatial patterns of variability of geophysical fields, the time variation associated with each pattern and a measure of their relative importance.

The dataset is analysed as a 2D-field, in our case with dimensions of (space, time). The technique consists in a statistical decomposition of the 2D-field into a sum of spatial ($\vec{e}$) and

temporal (PC) modes such as:

$$\vec{X} = \sum_{i=1}^{k} \mathrm{PC}_i \cdot \vec{e}_i$$

The $\vec{e}$ vectors correspond to the spatial structures (x, y) that can account for the temporal variations of X(x, y, t). The PC(t) time-series are the respective contributions of the corresponding spatial structure to the spatial variation of X at each time-step. It gives the temporal variation of the amplitude of each corresponding EOF pattern. Often, only a small number of modes captures almost all the variance within the original dataset. This feature makes EOF analysis an effective tool for compressing multi-dimensional datasets.

The main assumption of the EOF analysis is that the modes are orthogonal. The orthogonal constrain in space (time) means that there is no spatial (simultaneous temporal) correlation between any two EOFs (PCs).

Mathematically, the EOF analysis is an eigenvalue problem and the EOF spatial patterns are found by computing the eigenvalues and eigenvectors of the (spatially weighted) anomaly covariance matrix of the dataset (X). The eigenvalues of the covariance matrix (often referred to as λ_i) explain the fraction of the data variance along each of the new axes represented by the eigenvectors $\vec{e}_i$. The PC time-series are then determined by projecting the corresponding eigenvector onto the anomalies dataset. In the thesis, we use an equivalent method of the Singular Value Decomposition (SVD) (Björnsson and Venegas, 1997). In this case, the singular values are the square roots of non-zero eigenvalues of the covariance matrix.

The PC time series are scaled to have unit variance (without units). The EOF spatial patterns obtained are dimensionless unit vectors and show (only) the map of the variance. To have access to the actual amplitude of the data (in physical units), the EOF spatial pattern are multiplied by square root of the corresponding eigenvalue.

Note that we took into account the weighted area matrix to compensate for grid spacing in the geophysical dataset (Baldwin et al., 2009).

In the thesis, this EOF analysis is used to determine the main variability modes of the tropical and the equatorial Pacific and is the basis for the El Niño events detection (see paragraph 3 for more details) and for the low-frequency variability modes of the equatorial Pacific (see paragraph 4). Note that for the El Niño events detection, the two first principal component (PC) time-series are linearly combined, equivalent to perform rotation of these two PC. This results in a new set of orthogonal time-series (called E and C indices), but the eigenvectors associated with each of the new time-series may no longer be orthogonal. The E and C indices are expressed as:

$$E = \frac{(PC1 - PC2)}{\sqrt{2}}$$
$$C = \frac{(PC1 + PC2)}{\sqrt{2}}$$

where the PC1 and PC2 are the normalised principal components of the first two EOF modes of SST anomalies in the tropical Pacific (10°S-10°N) (see paragraph 2.1.4.2 for the EOF analysis and 3.2.2 for the E and C modes). An El Niño event can be described as an appropriate weighted superposition of these two modes. The associated spatial patterns of the E and C indices are the regression of the E and C time series onto the dataset (see paragraph 2.2.3.3). The resulting map has amplitude in the physical units of the dataset. This method can be applied to other variables, as done in paragraph 5.3.4.1 with the zonal wind stress dataset.

The main limitations of the EOF analysis is that the main modes obtained may not correspond to physical variability modes (Dommenget and Latif, 2002) and that the EOF spatial patterns may be domain dependent.

The reader is advised to refer to Chapter 13 of Storch and Zwiers (1999) for more information and detailed equations of the EOF analysis, and Björnsson and Venegas (1997) for

more information on correspondence between the EOF analysis via the covariance matrix of the data field and the SVD of the data field.

The Python package "eofs" is used for the computation of the EOF (see Dawson (2016) and https://ajdawson.github.io/eofs/).

2.2.2.3 Clustering classification

Cluster analysis is a statistical technique that groups objects with similar characteristics in the same group or cluster. Objects in the same cluster are more similar to each other, according to the imposed criteria, than to those in other clusters. Due to their characteristics, data-clustering methods have been widely used in the analysis of ENSO flavours. Singh et al. (2011) and Kao and Yu (2009) used an (agglomerative) hierarchical clustering, Johnson (2013) and Li et al. (2015) used a self-organizing map (SOM) analysis, which is an unsupervised neural network method, Chen et al. (2015a) used a fuzzy clustering analysis and Takahashi et al. (2011) used a k-mean clustering analysis. It is the latter method that we use to study the density function associated with the E and C indices (see paragraph 3.2.2.2).

The k-mean analysis is a vector-based cluster analysis. It separates data in k groups of equal variance, tending to define cluster of comparable spatial extent. Each cluster is described by the mean of the data in the cluster, called the centroid. After initialisation and choice of k groups in the data, the k-mean algorithm determines the associated centroids. Then it will assign each data to its nearest centroid, then recalculate associated centroids and repeat these steps until the centroids do not change significantly. Note that the k-mean analysis may converge to a local minimum, depending on the initialisation. To avoid this, the computation is done several times.

The k-mean analysis requires to pre-specify the number of clusters, k (see Pham et al. (2005) for methods for selecting the number of clusters). We used k=2 following Takahashi and Dewitte (2016) and verified by other methods that this value was appropriate. In particular, we used a silhouette analysis which determines the distance between the resulting clusters, for k ranging from 2 to 7. We also used the mean shift clustering, a centroid-based method which determine the modes (the maxima) in a smooth density of data.

2.2.2.4 Wavelet analysis

One of the goal of wavelets analysis is to provide and conserve informations about the time varying amplitude at different frequencies of the signal. It describes time-series not only in frequency (as the Fourier transform method) but also in time, which is particularly interesting when the signal is not stationary. In the thesis, the wavelet transform analysis is used in Chapter 4 to determine the main time-scales of ENSO variability over long periods to highlight its low-frequency modulation.

The wavelet transform method steps are described in Torrence and Compo (1998). The Morlet wavelet function is used and the wavelet transform is made in Fourier space. The analysed time-series are padded with enough zeros to prevent wrap-around effects from the end to the beginning of the time-series.

The wavelet analysis has been rectified as suggested by Liu et al. (2007). They showed that the method described by Torrence and Compo (1998) has a bias that favours low frequencies and does not allow a comparison of the peaks between the different wavelet scales because the energy is not comparable. The energy must thus be divided by the scale associated with it to compensate the bias.

The resulting wavelet power spectrum is expressed in variance^2 units.

The Python script of Evgeniya Predybaylo, based on Torrence and Compo (1998) method, is used to calculate the wavelet transform but with bias correction added. The script is available at http://atoc.colorado.edu/research/wavelets/.

2.2.3 Models

2.2.3.1 Regression and piecewise linear regression

The simple regression is a model for predicting a linear relationship between one explained variable Y (the dependent variable or the response) and an explanatory variable X (the independent variable or the predictor). The linear model is expressed as:

$$Y = aX + b$$

where a is the slope and b is the intercept.

If we have n realisations of the explained variable Y and the explanatory variable X, the model is expressed as:

$$y_i = ax_i + b + \epsilon_i$$

with ϵ_i the error term. The error term corresponds to the differences between the true value of Y and the predicted/estimated value of Y ($\hat{Y}$).

In a regression model, the errors tend to be minimised by finding the "line of best fit". In the thesis, the coefficients a and b are estimated using the ordinary least squares criterion that is the fitted line minimizes the sum of squares residual (SSR).

$$SSR = \sum_{i=1}^{N}(y_i - \hat{y}_i)^2$$

where $\hat{y}_i$ is the model prediction and y_i is the observed result.

The most common way to evaluate how the model fits the data is to calculate the R-squared coefficient, R^2. The R^2 coefficient is defined as the ratio between the variance explained by the regression (Sum of squares explained, SSE) and the total variance (Sum of squares total, SST), in the case of a univariate linear regression (because SST = SSE + SSR).

$$R^2 = \frac{SSE}{SST} = 1 - \frac{SSR}{SST} = 1 - \frac{\sum_{i=1}^{N}(y_i - \hat{y}_i)^2}{\sum_{i=1}^{N}(y_i - \bar{y})^2}$$

with $\bar{y} = \frac{1}{n}\sum_{i=1}^{N} y_i$ the mean of Y.

R^2 varies between 0 and 1, with values close to 1 indicating a good predictive power of the model because it means that more variance is explained by the model. Note that the R^2 increases every time a new feature is added to the model, selecting the model with the highest R^2 does not necessarily mean choosing the best linear model. An alternative approach is to use the adjusted R^2 which increases only if the new term improves the model more than would be expected by chance and can also decrease with poor quality predictors.

We also use a piecewise linear regression in the thesis (see Chapter 5). It fits the data with continuous piecewise linear functions. The optimal location for line segments is estimated via a differential evolution and by minimising the sum of the square of the residuals. The Python package "pwlf" is used for the computation of the piecewise linear regressions (see https://jekel.me/piecewise_linear_fit_py/).

A regression model indicates a tendency for two indices to co-vary and is related to the correlation coefficient.

2.2.3.2 Correlation and spatial pattern correlation

Correlation is a statistical tool which measures the tendency of two variables X and Y to co-vary. Correlation does not predict the evolution of Y relative to X as the linear regression but gives intensity of the relationship between the two variables. It does not distinguish between

dependent and independent variables. Correlation coefficient depends on the dispersion of the different data around the regression line. In addition to using correlation as an indicator of the intensity of a linear relationship between two variables, correlation is also used to determine the tendency of two time series to vary similarly at the same time step. In that case, it is referred as Pearson's correlation coefficient.

The linear correlation coefficient of Pearson is the covariance of the two variables divided by the product of their standard deviations:

$$\begin{aligned} r_{x,y} &= \frac{cov(X,Y)}{\sigma_x \sigma_y} \\ &= \frac{\sum_{i=1}^{N} \frac{1}{N}(x_i - \bar{x})(y_i - \bar{y})}{\sqrt{\frac{1}{N}\sum_{i=1}^{N}(x_i - \bar{x})^2}\sqrt{\frac{1}{N}\sum_{i=1}^{N}(y_i - \bar{y})^2}} \end{aligned}$$

The values of the correlation coefficient are between -1 (total negative correlation) and 1 (total positive correlation). When equal to 0, there is no correlation between the two variables.

The link between linear regression and correlation appears through the expressions of the correlation coefficient and the slope of the regression. The slope of the linear regression is:

$$\begin{aligned} a &= \frac{\sum_{i=1}^{N}(x_i - \bar{x})(y_i - \bar{y})}{\sum_{i=1}^{N}(x_i - \bar{x})^2} \\ &= \frac{cov(X,Y)}{\sigma_x^2} \end{aligned}$$

Finally, $a = r_{(x,y)}\frac{\sigma_y}{\sigma_x}$. The linear correlation coefficient is the standardized slope of a simple linear regression.

The spatial pattern correlation coefficient corresponds to the Pearson product-moment coefficient between two variables at corresponding locations on two different maps. It is used in Chapter 4 to establish correlation between different modes of variability of the equatorial Pacific. The method has some limitations, including the fact that it applies to global patterns and are insensitive to local variations (Long and Robertson, 2018).

2.2.3.3 Bi-linear regression

As mentioned in paragraph 2.2.2.2, multiple linear regression is also used to estimate spatial patterns associated with time series. In particular, the spatial pattern associated with the E and C indices is determined by a bi-linear regression at each location, that is a linear regression to multiple input variables (the two indices) onto a 3-D field (SST for instance). In the case of the E and C indices regressed onto the detrended monthly SST anomalies, the bi-linear regression is expressed as:

$$\text{SSTA(x, y, t)} = \alpha(x,y) \cdot \text{E(t)} + \beta(x,y) \cdot \text{C(t)} + \text{constant} + \text{residuals}$$

$\alpha(x,y)$ is the spatial pattern corresponding to the E-mode, $\beta(x,y)$ corresponds to the spatial pattern associated with the C-index. It is therefore used to determine the associated SSTA spatial patterns of the E and C modes (see paragraph 3.2.2). The resulting map has amplitude in the physical units of the dataset. This method is also applied to zonal wind stress fields in paragraph 5.3.4.1.

2.2.4 Significance of the results

Statistical tests are used to verify the validity of a hypothesis in order to extrapolate the results obtained from a sample to an global population. A null hypothesis is formulated in such a way as to correspond to a postulate that one is only willing to reject with a high degree of certainty. A hypothesis test is therefore a kind of demonstration by the opposite of what we are trying to prove. For example, when analysing how changes in a variable due to global warming are significant, the variable is compared between the historical climate (sample x1) and the future climate (sample x2). The null hypothesis is that there is not significant difference between the samples, via for instance the mean of the samples: the null hypothesis is "The two means of the samples are identical". The statistical test determines the probability that the null hypothesis is true. If the null hypothesis cannot be rejected, no conclusion can be drawn from the samples concerned, as the probability that the distribution (means) is due to chance is high. Otherwise, differences between the means of the two samples are statistically significant. Note that the test does not make any assumptions about the equality of the distribution shapes of the two samples.

The conclusion adopted (whether or not the null hypothesis is rejected) is established with a certain probability of error. The p-value represents the probability of making a mistake on the rejection of this hypothesis: a low value of the p-value indicates that the hypothesis is rejected with a high certainty, while a high value indicates that the hypothesis probably cannot be rejected. A result is then said to be statistically significant when the p-value is less than a probability threshold of rejecting the null hypothesis when it is true. The probability threshold is generally equal to 0.05 (5 %) but may vary in the thesis up to 0.01 (1 %). The result is statistically significant at 95 % (99 %) confidence level. Note that the p-value is also used to validate the regression and correlations described above. The null hypothesis is then written "the linear trend is null" or "the correlation is null". If the p-value of a regression is less than the probability threshold, then the null hypothesis is rejected and the trend obtained by regression is considered significantly different from zero.

There are two main categories of tests: parametric tests and non-parametric tests. Parametric tests require that the form of the distribution of the studied variable be specified. This may be a normal distribution, which is the general case when dealing with large samples or the majority of climate variables such as temperatures. Non-parametric tests apply when it is not possible to make an assumption about the distribution of the variable. They do not refer to a particular distribution and can therefore be applied to small samples. They are theoretically less powerful than parametric tests on large samples but much more accurate on small samples. Note that for precipitation datasets, it is not possible to apply parametric tests. For instance, comparing the ensemble-means of each climate, historical and future, requires a non-parametric test.

2.2.4.1 Student's T-test

Student's T-test is a parametric method, it requires that the statistical distribution of the two samples be known. For instance, we compare the means μ_1 and μ_2 of the samples x1 and x2 of the historical and future climate respectively. The samples also have n_1 and n_2 elements and variances equal to σ_1 and σ_2 respectively. In these conditions, corresponding to the Welch's test, the t statistic to test whether the means are different is defined as:

$$t = \frac{\mu_1 - \mu_2}{\sqrt{\frac{\sigma_1}{n_1} + \frac{\sigma_2}{n_2}}}$$

The two means are significantly different if $|t|$ is greater than 1.96 for a statistical significance threshold equal to 0.05.

2.2.4.2 Bootstrap test

Bootstrap test is a non-parametric method. Consider the derived quantity to compare is the difference between the ensemble-means of each climate, historical and RCP8.5, with respectively 42 and 40 members in each set. The different steps of the method are as follows:

- take a random sample with replacement, of the same length as the initial sample (42 (40) elements for historical (RCP8.5) set) but which may contain the same element several times,
- calculate the difference between the average of this new set of RCP8.5 means minus the average of the new set of historical means. It is the (first) derived quantity,
- repeat the draw n times,
- the probability distribution function obtained from the n derived quantities, called the (empirical) bootstrap distribution, is used to calculate a confidence interval to test the hypothesis. For instance the 2.5 % and 97.5 % ranking from the probability distribution function indicate the 95 % confidence level. If zero is included in the interval, the means of the two samples are not significantly different and the null hypothesis can not be rejected. Instead of a confidence interval, the empirical variance of the bootstrap distribution can be used to estimate the standard error of the derived quantity.

Instead of construct the bootstrap distribution associated with the difference of the means of the two samples, a comparison between the bootstrap distributions of each sample can be performed. This methods needs to use at least n=1000 bootstrap samples and requires that the bootstrap distribution be symmetric and centred on the original sample parameter (Efron, 1982). In the thesis, we use n=10,000.

2.2.4.3 Wilcoxon test

Wilcoxon rank-sum test, also called Mann-Whitney U-test, is a non-parametric method (Wilcoxon, 1945; Mann and Whitney, 1947). The test estimates the distribution of the rank of two samples to determine whether the means of the distributions are the same. The procedure classifies the sample values from the smallest to the largest, ranging from rank 1 (the smallest observation) to rank $(n_1 + n_2)$. The test statistic is then given by:

$$U_1 = R_1 + \frac{n_1(n_1+1)}{2}$$
$$U_2 = R_2 + \frac{n_2(n_2+1)}{2}$$

where R_i is the sum of the ranks in sample i.

For large samples, U_i is approximately normally distributed. In this case, a standardized value of the test statistic is defined as:

$$z = \frac{U_i - \mu_i}{\sigma_i}$$

where μ_i and σ_i are the mean and standard deviation of U_i and for i=1:

$$\mu_1 = \frac{n_1 n_2}{2}$$
$$\sigma_1 = \frac{\sqrt{n_1 n_2 (n_1 + n_2 + 1)}}{12}$$

z is the same regardless of the U used.

Note that the choice of the non-parametric method does not lead to significant change in the significance of the results.

2.3 Heat budget computation and validation

2.3.1 Oceanic mixed layer thermodynamics

2.3.1.1 General temperature equations

Ocean dynamics are described in the POP model by the 3-D primitive equations of Navier-Stokes for a "thin" fluid using the hydrostatic and Boussinesq approximations. The Boussinesq approximation allows to consider the density as constant, except in pressure.

The temperature equation, when using the Boussinesq approximation, is:

$$\frac{DT}{Dt} = \underbrace{\frac{\partial T}{\partial t}}_{a} + \underbrace{\vec{u} \cdot \nabla T}_{b} = \underbrace{A_H \nabla_H^2 T}_{c} + \underbrace{\frac{\partial}{\partial z}\left(A_V(z)\frac{\partial T}{\partial z}\right)}_{d} + \underbrace{Q_{net}}_{e} \tag{2.1}$$

where:

- T is the 4D-potential temperature (K);
- $\vec{u}$ the 4D-velocity field (m/s);
- A_H the horizontal thermal diffusivity (m^2/s), assumed to be spatially constant;
- A_V the vertical thermal diffusivity (m^2/s);
- Q_{net} the effective net ocean-atmosphere heat flux (K/s).

The term a of the equation is the rate of change of temperature. The term b is the 3D-advection of heat, the terms c and d are respectively the horizontal and vertical diffusion of heat and the term e corresponds to the atmospheric forcing.

2.3.1.2 Within the oceanic surface layer

We are interested in oceanic processes at play in the oceanic mixed layer, which is defined as the surface layer where variables such as temperature, salinity and density are vertically homogeneous. This oceanic boundary layer constitutes the coupling zone with the atmosphere where turbulent processes are important because of the exchange of energy (e.g heat flux), mass (e.g evaporation and precipitation) and momentum (e.g wind stress) with the atmosphere (its boundary layer).

For reasons of simplification of calculations of the heat budget, we consider a fixed depth of the mixed layer, which allows to neglect the entrainment process of heat into the mixed layer, due to the tendency term of the mixed layer depth. Estimating a temporally varying mixed layer heat budget is complex especially because it requires the estimation of the entrained and detrained water of the mixed layer, whose volume changes concomitantly.

We assume that the temperature is vertically homogeneous over the fixed-depth layer. The heat budget of the oceanic layer is obtained by integrating vertically the temperature equation from the bottom of the layer (-h) to the surface. Moreover, we consider that the horizontal mixing and the vertical turbulent heat flux terms are negligible. Under these assumptions, the heat budget equation becomes:

$$\frac{1}{h}\int_{-h}^{0} \frac{\partial T}{\partial t} \mathrm{d}z \;=\; \frac{1}{h}\int_{-h}^{0} \left(-u\,\frac{\partial T}{\partial x} - v\,\frac{\partial T}{\partial y} - w\,\frac{\partial T}{\partial z}\right) \mathrm{d}z \;+ Q_{net} \;+ R$$

The writing of the equation is simplified:

$$\left[\frac{\partial T}{\partial t}\right] = -\left[u\,\frac{\partial T}{\partial x}\right] - \left[v\,\frac{\partial T}{\partial y}\right] - \left[w\,\frac{\partial T}{\partial z}\right] + Q_{net} + R \tag{2.2}$$

with

- $\left[*\right] = \frac{1}{h}\int_{-h}^{0} * \,\mathrm{d}z$;
- h is the fixed depth of the surface layer (m);

- u, v and w are the 4-D scalar components of the zonal, meridional and vertical currents respectively (m/s).

The horizontal mixing and the vertical diffusion of heat (terms c and d of the equation 2.1) are neglected in the study and included in the residuals R term. The residuals term includes also the short-wave fluxes of heat out of the base of the mixed layer (see paragraph below), the change in temperature associated with the freshwater flux, the sub-grid scale and sub-monthly time scale contributions including the impact of tropical instability waves and numerical errors due in particular to the off-line calculation of the heat budget and to the numerical diffusion associated with the finite difference approximation in solving equations (see paragraph 2.3.2).

It has been verified that the temperature is vertically homogeneous within the surface layer, even if some differences may occur in the eastern Pacific due to the shallow thermocline.

Note that a linearised, implicit free-surface formulation is used for the barotropic mode in CESM1 simulations, but will be neglected in our budget, as well as surface freshwater fluxes. These latter are treated in POP model as virtual salt fluxes, using a constant reference salinity, which leads to a constant net ocean volume (but not ocean mass).

2.3.1.3 Net surface heat flux

The net ocean-atmosphere heat flux, Q_{net} of the equation 2.2 includes surface heat fluxes (SHF) and penetrating short-wave radiation (SWR). It can be expressed as:

$$Q_{net} = \frac{Q_s}{\rho_0 \, C_p \, h} \tag{2.3}$$

with

- ρ the sea-water reference density (kg/m^3);
- c_p the specific heat content (J/(kg $\cdot$ K));
- and h the depth of the oceanic layer (m).

The density of the sea water is assumed to be constant at 1026 kg/m^3, the specific heat content is fixed at 3996 J/(kg $\cdot$ K), which are the values used in CESM-LE simulations.

The surface heat flux Q_s is composed of the short-wave solar radiation, the outgoing long-wave radiation, the latent heat flux and the sensible heat flux.

We use the SHF variable of the CESM-LE (W/m^2), corresponding to the "total surface heat flux including SW" according to the model description. This variable is provided in monthly data, directly interpolated on the ocean grid of POP model. It is a prognostic output variable of the atmospheric model. Carlos Conejero, a Ph.D. student colleague from Legos, verified that this variable corresponded, at least up to the mid-latitudes, to the sum of the short-wave radiation (Q_{SW}), long-wave radiation (Q_{LW}), latent heat flux (Q_{LH}) and sensible heat flux (Q_{SH}) also provided by the NCAR Website.

The POP model uses a parameterisation to determine the penetrative solar irradiance heat flux at depth h. It is parameterised by a Jerlov type I water hypothesis applied to open ocean: a fraction of the solar radiation reaches the depth z such as $f_{SW} = c * \exp\left(\frac{z}{depth1}\right) + (1-c) * \exp\left(\frac{z}{depth2}\right)$ with 0.58 <= c <= 0.78. We neglect this term in our heat budget, considering that no solar heat flux escapes through the base of the surface layer. Similarly, we do not take into account the attenuation of heat flux by other processes, such as absorption by chlorophyll.

2.3.1.4 Reynolds decomposition

To analyse the different physical processes, we decompose the equation between the mean and the eddy terms by a Reynolds decomposition that is a linearisation of the equation 2.2 around a mean state at equilibrium. Each advection terms are decomposed into the advection

of mean temperature by anomalous current, the advection of anomalous temperature by mean current and the advection of anomalous temperature by anomalous current. The anomalous temperature tendency is then expressed as:

$$\begin{aligned}\left[\frac{\partial T^{'}}{\partial t}\right] &= -\left[u\,\frac{\partial T}{\partial x}\right]^{'} - \left[v\,\frac{\partial T}{\partial y}\right]^{'} - \left[w\,\frac{\partial T}{\partial z}\right]^{'} + \frac{Q^{'}_{net}}{\rho_0\,C_p\,h} + R^{'} \\ &= \underbrace{\left[-\bar{u}\,\frac{\partial T^{'}}{\partial x} - \bar{v}\,\frac{\partial T^{'}}{\partial y}\right]}_{a} - \underbrace{\left[\overline{w}\,\frac{\partial T^{'}}{\partial z}\right]}_{b} - \underbrace{\left[u^{'}\,\frac{\partial \overline{T}}{\partial x}\right]}_{c} - \underbrace{\left[v^{'}\,\frac{\partial \overline{T}}{\partial y}\right]}_{d} \\ &\quad - \underbrace{\left[w^{'}\,\frac{\partial \overline{T}}{\partial z}\right]}_{e} - \underbrace{\left[u^{'}\,\frac{\partial T^{'}}{\partial x} + v^{'}\,\frac{\partial T^{'}}{\partial y}\right] - \left[w^{'}\,\frac{\partial T^{'}}{\partial z}\right]}_{f} + \underbrace{\frac{Q^{'}_{net}}{\rho_0\,C_p\,h}}_{g} + \underbrace{R^{'}}_{h} \\ &= MHD + TCF + ZAF + MAF + UPW + NDH + Q + R\end{aligned} \tag{2.4}$$

where the over-bar notation represents the climatological monthly mean and the prime denotes the inter-annual anomalous quantity. Square brackets indicate vertical integration over the surface layer, whose depth is set at 80 m.

The heat equation is then composed by different feedbacks:

- a : the anomalous temperature advection by the mean horizontal currents, referred as the mean horizontal dynamic heating term (MHD) (Guan and McPhaden, 2016);
- b : the vertical anomalous temperature advection by the mean vertical velocity, referred as the thermocline feedback (TCF);
- c : the mean temperature advection by the anomalous zonal current referred as the zonal advective feedback (ZAF);
- d : the mean temperature advection by the anomalous meridional current (MAF);
- e : the mean temperature advection by the anomalous vertical current, referred as the upwelling feedback (UPW);
- f : the non-linear terms are referred as the non-linear dynamical heating (NDH) (Jin et al., 2003a; Ren and Jin, 2013; An and Jin, 2004);
- g : the surface heat flux term referred as the thermodynamical damping (TD) (Ren and Jin, 2013; Guan and McPhaden, 2016).

The main feedbacks involved in the dynamics of ENSO are the zonal advective feedback and the thermocline feedback (An and Jin, 2000, 2001; Fedorov and Philander, 2001), to which we can add a term of damping feedback (Jin and Neelin, 1993; Neelin et al., 1998). The zonal advective feedback accounts for the zonal heat advection by anomalous zonal current in a mean zonal gradient of temperature, which is the case at the scale of the equatorial Pacific, with warmer water in the western Pacific than in the eastern Pacific. The thermocline feedback accounts for vertical heat advection of temperature anomalies by the mean upwelling, where temperature anomalies are related to thermocline vertical displacements. The thermocline feedback can be defined by decomposing the mean upwelling feedback in an approximation (Jin and Neelin, 1993; Ren and Jin, 2013):

$$-\,\overline{w}\,\frac{\partial T^{'}}{\partial z} = \overline{w}\,\frac{T^{'}_{sub}}{H} - \overline{w}\,\frac{T^{'}}{H} \tag{2.5}$$

where H is the effective mean mixed layer depth for the vertical advection and the subscript "sub" denotes a subsurface-layer immediately below the mixed layer.

Note that the different feedback definitions and names may vary depending on the studies. Takahashi and Dewitte (2016) group the terms of MHD, ZAF and MAF to obtain the horizontal linear advection and the terms of TCF and UPW to obtain the vertical linear advection. Their non linear dynamical heating term (NDH) removes the seasonality of

the non-linear advection by adding $\left[\overline{u' \frac{\partial T'}{\partial x}} + \overline{v' \frac{\partial T'}{\partial y}} + \overline{w' \frac{\partial T'}{\partial z}}\right]$ to our NDH term. Guan and McPhaden (2016) defines the Ekman feedback as our upwelling feedback while Ren and Jin (2013) defined the Ekman pumping feedback as $\left[-v' \frac{\partial \overline{T}}{\partial y} - w' \frac{\partial \overline{T}}{\partial z}\right]$.

2.3.2 Discretisation on the model grid

The heat budget was calculated off-line from monthly outputs, on the native grid of CESM-LE. We use the centred second-order finite differences scheme for advective derivation and a leap-frog time stepping for temporal derivation as described in paragraph 2.3.2.2.

2.3.2.1 POP model grid

The ocean POP model (Smith et al., 2010) utilizes a staggered grid. A staggered grid defines scalar variables (temperature, pressure, density, etc..) in the centre of the control volumes (named T-cells here) whereas vector variables (velocity e.g.) are located at the cell faces or cell corners. The main advantage of a staggered grid is that it allows to represent the wave propagation and to maintain the conservation properties. It prevents the decoupling of pressure and velocity, which can lead otherwise to discretisation errors and to checker-board patterns in the results.

The staggered grid of the POP model is an Arakawa B-grid (Arakawa and Lamb, 1977), that is the horizontal velocities are defined at the north-east corners of the T-cells. On Figure 2.16, the T-cells are illustrated by the solid lines, the U-cells by the dashed lines. The indexing for points (i,j) is increasing eastward and northward respectively. For the same (i,j) indices, a vector lies on the centre of the U-cells located on the north-east (upper right) of the centre of the T-cells where the scalar stands.

The main advantage of B-grid is that because the horizontal velocities are on the same grid point, the calculation of the zonal ($\vec{u}$) and meridional ($\vec{v}$) velocities contribution to the Coriolis force is easy at a given point, unlike the common Arakawa C-grid for example, for which this calculation requires the interpolation of the horizontal components of the velocity. This interpolation can be particularly problematic when the eddies are on the scale of the grid, resulting to spurious vertical velocities.

(a) Lengths of cells (b) Lengths between variables

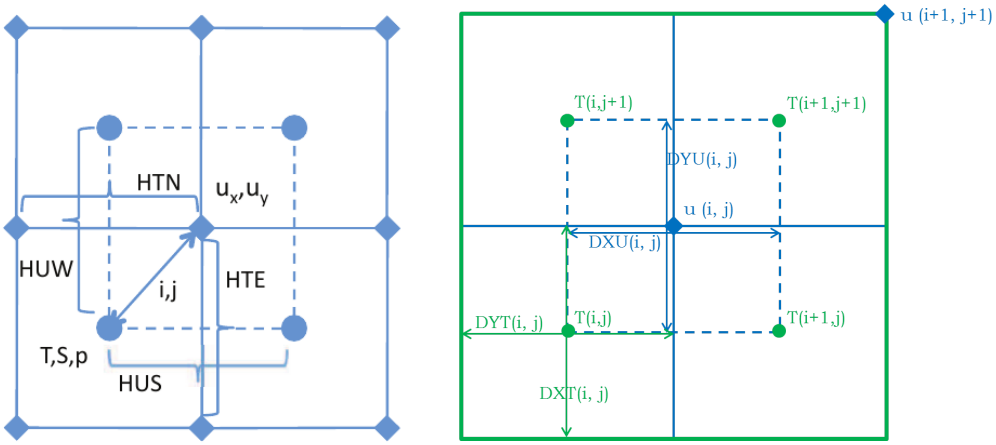

Figure 2.16 – Representation of the Arakawa B-grid used by POP ocean model (from Smith et al. (2010)) indicating scalars (T) and velocities (U, V) grid points, (2.16a) lengths of cells and (2.16b) lengths between variables used in the numerical scheme (see paragraph 2.3.2.3). The figure 2.16a is reprinted from Smith et al. (2010) and the figure 2.16b was drawn by Estelle Carréric.

The vertical grid uses a level-coordinate system. This kind of vertical coordinates allows a good resolution of the oceanic surface layers and, thus, of the air-sea interactions. However,

the staircase representation of the topography can generate irregularities in the bottom of the ocean and the numerical non-convergence of the solutions. The k-index in the vertical dimension is increasing with depth (Fig. 2.17b). The vertical grid is also a staggered grid (Lorenz grid) where the vertical velocity components are located on the top face of the T-grid (Fig. 2.17a). The vertical grid of POP model is composed of 60 levels with a decreasing resolution going towards the bottom of the ocean, from 10 m in the first 155 m to 250 m.

(a) staggered cube (b) Vertical staggered grid

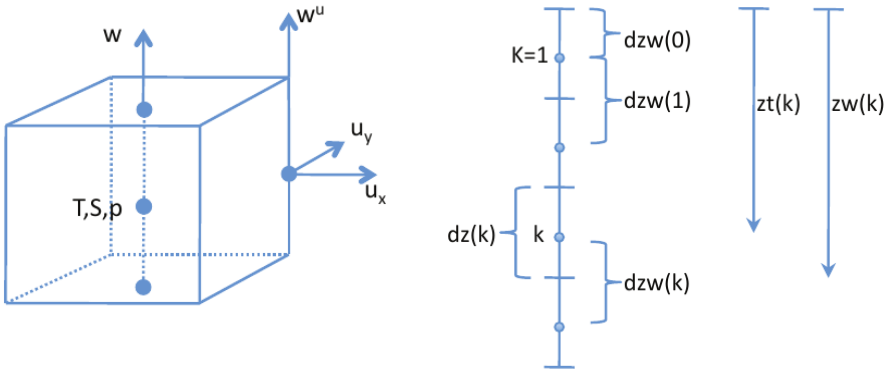

Figure 2.17 – Representation of the vertical staggered grid (Reprinted from Smith et al. (2010))

More information on the ocean model can be found in the POP reference manual (Smith et al., 2010). The manual of MOM model, whose grid is also an Arakawa B-grid, has been also very useful to understand the intrinsic characteristics of the grid and discrete equations associated with, because the numerical formalism and assumptions related are particularly well described (Griffies et al., 2004, 2010).

2.3.2.2 Temperature equations formalism

When running a simulation, the POP model can be used with different advection schemes: the centred scheme, the third-order upwind advection scheme and the flux-limited Lax-Wendroff algorithm. To calculate the heat budget off-line, we use the centred second-order finite differences scheme. The time derivative is approximated using a leap-frog time stepping. Thus, when the temperature tendency is computed between the time levels n-1 and n+1, the advective terms are calculated at the time level n.

We consider that the changes in tracer concentration associated with the freshwater flux and the changes in volume of the surface layer due to undulations of the free surface are negligible. The discrete temperature transport equations are then written in the POP model formalism as:

$$\frac{T^{n+1} - T^{n-1}}{2\Delta t} = -\mathcal{L}_T(T^n) + \mathcal{D}_H(T^{n-1}) + \mathcal{D}_V(T^{n+1}) + \mathcal{S} \tag{2.6}$$

where $\mathcal{L}_T$ is the advection operator in T-cells, $\mathcal{D}_{H,V}$ are the diffusion operators in the horizontal and vertical directions and $\mathcal{S}$ are the source terms.

This equation is partly that used to calculate the temperature field at each time step in the model, without our simplifying assumptions. The discretisation of each term of this equation is described in the following paragraphs considering the centred second-order scheme.

Temporal derivative term : using a leapfrog scheme (second order), the discretisation becomes :

$$\frac{\partial T}{\partial t}(n,i,j,k) = \frac{T(n+1,i,j,k) - T(n-1,i,j,k)}{2\Delta t(n)} \tag{2.7}$$

where Δt is the time-step. We assume that there is no change in volume of the surface layer due to undulations of the free surface.

Advection term : In general coordinates and using the standard second-order centred advection scheme, the advection operator for the temperature tracer is given by (cf. equation 3.14 in Smith et al. (2010)):

$$\mathcal{L}_T(T) = \frac{1}{\Delta_y}\delta_x\left[\overline{\left(\overline{\Delta_y u_x}^{\,y}\right)}^{\,xy}\overline{T}^{x}\right] + \frac{1}{\Delta_x}\delta_y\left[\overline{\left(\overline{\Delta_x u_y}^{\,x}\right)}^{\,xy}\overline{T}^{y}\right] + \delta_z(w\overline{T}^{z}) \tag{2.8}$$

- The factors Δ_x and Δ_y inside the difference operators (δ_x and δ_y) are located at U-points and correspond to DXU and DYU respectively (see Fig. 2.16b).
- The factors Δ_y^T and Δ_x^T outside the difference operators are located at T-points.
- The difference operators and the average operators are defined by (cf. equations 3.4 and 3.5 in Smith et al. (2010)):

$$\begin{cases} \dfrac{\partial\varphi}{\partial x} = \dfrac{\varphi(x+\frac{\Delta_x}{2}) - \varphi(x-\frac{\Delta_x}{2})}{\Delta_x} \\ \overline{\varphi}^{x} = \dfrac{\varphi(x+\frac{\Delta_x}{2}) + \varphi(x-\frac{\Delta_x}{2})}{2} \end{cases}$$

  with similar definitions in the y and z directions. These formulas apply for uniform grid spacing, which is not the case of the POP B-grid. For a uniform grid, if φ is a tracer located at T-points, then $\varphi(x+\frac{\Delta_x}{2})$ is located on the east face of the T-cell. For the POP B-grid, the definitions should be adapted such that the variables lie at T- or U-cell centres as appropriate.

Thereby, regarding the horizontal advection terms, the mass fluxes $\overline{\Delta_y u_x}^{\,y}$ and $\overline{\Delta_x u_y}^{\,x}$ as well as the temperature fields $\overline{T}^{x}$ and $\overline{T}^{y}$ are located on the lateral faces of the T-cells. The zonal advection term can thus be expressed at each time step by:

$$\begin{aligned} ADV_x(i,j,k) = & \frac{1}{\Delta_y}\,\delta_x\left[\overline{\Delta_y u_x}^{\,y}\overline{T}^{x}\right] \\ = & \frac{\partial[u_e(i,j,k)\,T_e(i,j,k)]}{\partial x} \\ = & \frac{u_e(i,j,k)\,T_e(i,j,k) - u_w(i,j,k)\,T_w(i,j,k)}{DXT(i,j)} \\ = & \frac{u_e(i,j,k)\,T_e(i,j,k) - u_e(i-1,j,k)\,T_e(i-1,j,k)}{DXT(i,j)} \end{aligned} \tag{2.9}$$

with

$$\begin{cases} u_e(i,j,k) = \dfrac{u(i,j,k)\,DYU(i,j,k) + u(i,j-1,k)\,DYU(i,j-1,k)}{2\,DYT(i,j,k)} \\ u_w(i,j,k) = u_e(i-1,j,k) \\ T_e(i,j,k) = \dfrac{T(i+1,j,k) + T(i,j,k)}{2} \\ T_w(i,j,k) = T_e(i-1,j,k) \end{cases}$$

u_e is the velocity in the x-grid direction centred on the east face of the T-cells. The definition is similar in the y-grid direction.

The vertical advection term includes the vertical velocity which is calculated by integrating the continuity equation ($L(1) = 0$) from the surface down to level k. The continuity equation gives (equation 3.7 in Smith et al. (2010)):

$$\frac{\partial w}{\partial z} = -\frac{1}{\Delta_y^T}\,\delta_x(\overline{\Delta_y^U u_x}^{\,y}) - \frac{1}{\Delta_x^T}\,\delta_y(\overline{\Delta_x^U u_y}^{\,x}) = -\nabla\vec{u} \tag{2.10}$$

The divergence is located at T-points. The vertical velocity is thus calculated by:

$$w(k+1) = -w(k) + \frac{dz_w}{2 \cdot TAREA(i,j)} \Big[u_x(i,j)DYU(i,j) + u_x(i,j\text{-}1)DYU(i,j\text{-}1) - u_x(i\text{-}1,j)DYU(i\text{-}1,j) - u_x(i\text{-}1,j\text{-}1)DYU(i\text{-}1,j\text{-}1) \Big] \quad (2.11)$$

with $w_{(k=0)} = 0$ at the surface when we neglect the evolution of the free surface over time.

Note that because a time-step was missing in the vertical velocity field for one historical member of the CESM-LE (number 033), we compute the vertical velocity for that member through this equation. The other non-missing time-steps being equal to our calculation, this reinforces our understanding of the formalism of the POP model.

The vertical advection term becomes:

$$\begin{aligned} ADV_z(i,j,k) = & \frac{\partial[w(i,j,k)\,T(i,j,k)]}{\partial z} \\ = & \frac{w_{top}(i,j,k)\,T_{top}(i,j,k) - w_{bottom}(i,j,k)\,T_{bottom}(i,j,k)}{\partial z} \\ = & \frac{w_{top}(i,j,k)\,T_{top}(i,j,k) - w_{bottom}(i,j,k)\,T_{bottom}(i,j,k)}{\partial z} \\ = & \frac{w(i,j,k)\,T_{top}(i,j,k) - w(i,j,k+1)\,T_{top}(i,j,k+1)}{\partial z} \end{aligned} \quad (2.12)$$

with $T_{top} = \frac{T_{k-1}+T_k}{2}$

Finally, the 3D-advection of tracers expressed by finite-difference scheme is:

$$ADV(i,j,k) = -\frac{u_e\,T_e - u_w\,T_w}{DXT} - \frac{v_n\,T_n - v_s\,T_s}{DYT} - \frac{w(k)\,T_T - w(k+1)\,T_B}{dz} \quad (2.13)$$

(see equation 6.1 in Smith et al. (2010) without the third-order upwind advection scheme in temperature).

The fluxes of heat and freshwater are applied in the numerical scheme of POP model as surface boundary conditions to vertical mixing terms (term d in equation 2.1 and terms $\mathcal{D}_{H,V}$ in equation 2.6). We neglect the freshwater and vertical mixing terms in our heat budget calculation, the heat fluxes are included in the S term of equation 2.6.

2.3.2.3 Discretisation of our advection terms

The previous paragraph describes the temperature advection formalism when using the continuity hypothesis to express the advection of the tracer (equation 2.8). Then the advection terms are calculated using the product rule. This formalism is used to calculate the temperature field at each time step in POP model.

However, in our case, we want to have access to each advection term individually. We can not used the continuity hypothesis to express the advection operator. We want to compute in each direction the fluxes across cell faces, that is the product of the advective velocity by the associated gradient of temperature at each cell. To do that, we need to calculate the advective velocity components on the corresponding face of the tracer cells, which requires, on the B-grid, averaging the prognostic B-grid horizontal velocity components. We compute the horizontal components of the advection velocity on the centres of T-cells, in order to have the horizontal advective components at the same grid point. We re-write our different advection terms in the POP formalism:

Zonal advection term :

$$u(i,j,k)\frac{\partial T(i,j,k)}{\partial x} = u_{centre}(i,j,k)\cdot\frac{\partial T_e(i,j,k)}{\partial x} = \frac{u_{e(i-1)}HUS_{(i-1)}+u_{e(i)}HUS_{(i)}}{2\cdot DXT_{(i)}}\cdot\frac{T_{e(i)}-T_{e(i-1)}}{DXT_{(i)}} \tag{2.14}$$

where u_{centre} is the zonal velocity at the centre of the T-cell, u_e and T_e are respectively the zonal velocity and the temperature in the middle of the east T-cell face:

$$\begin{cases} u_e(i,j,k) = \dfrac{u(i,j-1,k)DYU(i,j-1,k)+u(i,j,k)DYU(i,j,k)}{2\cdot HTE(i,j,k)} \\ T_e(i,j,k) = \dfrac{T(i+1,j,k)+T(i,j,k)}{2} \end{cases}$$

Meridional advection term

$$v(i,j,k)\frac{\partial T(i,j,k)}{\partial y} = v_{centre}(i,j,k)\cdot\frac{\partial T_n(i,j,k)}{\partial y} = \frac{v_{n(j-1)}HUW_{(j-1)}+v_{n(j)}HUW_{(j)}}{2\cdot DYT_{(j)}}\cdot\frac{T_{n(j)}-T_{n(j-1)}}{DYT_{(j)}} \tag{2.15}$$

where v_{centre} is the meridional velocity at the centre of the T-cell, v_n and T_n are respectively the meridional velocity and the temperature in the middle of the north T-cell face:

$$\begin{cases} v_n(i,j,k) = \dfrac{v(i-1,j,k)DXU(i-1,j,k)+v(i,j,k)DXU(i,j,k)}{2\cdot HTN(i,j,k)} \\ T_n(i,j,k) = \dfrac{T(i,j+1,k)+T(i,j,k)}{2} \end{cases}$$

Vertical advection term

$$w(i,j,k)\frac{\partial T(i,j,k)}{\partial z} = w(i,j,k)\cdot\frac{T_{(i,j,k-1)}-T_{(i,j,k)}}{dzw_{(k-1)}} \tag{2.16}$$

with dzw the thickness of layer associated with the vertical velocity grid.

It should be noted that different checks were made at each step of computation. It has been verified that the sum of the three Reynolds decomposition terms of the advection tendency in each direction is equal to the corresponding advection tendency. It means that the contribution of the $\left[\overline{u_i'\frac{\partial T'}{\partial x_i}}\right]$ component in each direction is very weak, that is the seasonality of the non-linear vertical advection is small.

It has also been verified that the different terms of the heat budget were corresponding to the heat budget calculated on-line directly by the model. Indeed, a variable, named ADVT, is available directly on the NCAR Website and corresponds to the vertically integrated temperature advection tendency. Our integrated temperature tendency along the entire water column is comparable to this variable even if there are locally pronounced differences, especially in the eastern Pacific.

2.3.3 Projection onto the E and C modes

The different tendency terms of the SST equation (see equation 2.4) are then projected onto each of the spatial patterns of the E and C modes following the method developed by Takahashi and Dewitte (2016). First, the heat budget within the surface layer is computed by vertically integrating the anomalous temperature equation from the bottom of the layer,

fixed at 80 m, to the surface. We project the resulting terms onto the spatial patterns of the first two normalised EOF modes of the equatorial Pacific (2°S-2°N). The resulting time-series are then linearly combined according to the definition of the E and C indices.

For instance, the projection of the heating rate onto the E mode is calculated as:

$$\langle \frac{\partial T'}{\partial t} \mid E \rangle = \frac{1}{N_x N_y} \int_{120°E}^{290°E} \int_{2°S}^{2°N} \left(\frac{\partial T'}{\partial t}(x,y,t) \cdot E(x,y) \right) \mathrm{d}x\mathrm{d}y \tag{2.17}$$

This gives us the contribution of each term of the heat budget to the two main rotated modes of variability of the equatorial Pacific, the E and C modes. The method is equivalent to the average of the tendency terms over the main influence regions of the E and C patterns.

This method has the advantage of estimating objectively the region of influence of the different feedbacks, compared to the method where tendency terms are averaged over the classical Niño-4 and Niño-3 regions, or modified versions of them to take into account mean state biases in the CGCMs (Kug et al., 2010; Capotondi, 2013; Stevenson et al., 2017). Moreover, the E and C patterns of the future climate can be modified compared to the present climate (see chapter 5). Our method take into account changes that may take place in the location of the main centres of action of the two types of El Niño events.

Finally, we take into account amplitude changes in the E and C modes with global warming by scaling the RCP8.5 heat budget terms by the projection coefficient of the RCP8.5 E and C patterns on their counterparts of the historical run. The scaling coefficients are equal to 1.18 (±10 %) for both E and C modes over 2°S-2°N. Changes in the heat budget due to global warming are analysed in chapter 5.

2.3.4 Validation of the heat budget

2.3.4.1 Comparison with observations

We compare a strong El Niño event chosen randomly in the PI-control simulation with an observed strong El Niño event. Firstly, we present the time-longitude evolution of different variables during the simulated El Niño event. The different variables are averaged along the equator, between 2°S and 2°N.

(a) SST anomalies

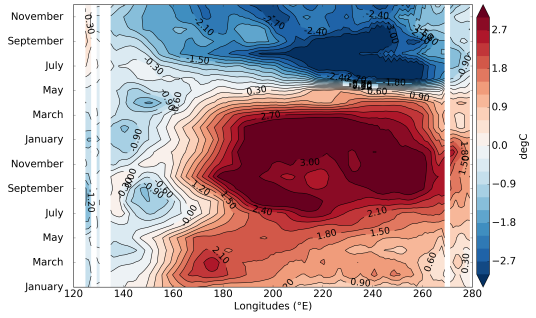

(b) TAUX anomalies

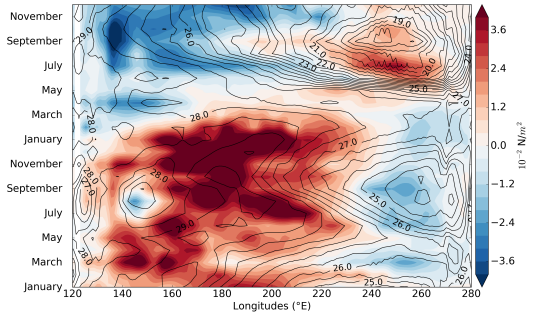

Figure 2.18 – Time-longitude sections of the equatorial (2°S-2°N) for a strong El Niño event in the CESM-LE PI-control simulation. The shadings represent the evolution of (2.18a) the SSTA (°C) and (2.18b) the anomalous zonal wind stress (10^{-2} N/m^2) respectively. The contours in figure 2.18b represent the evolution of the SST, with intervals every 0.5 °C.

The PI-control El Niño event is classified as strong El Niño (see chapter 3), meaning that the anomalous warming is strongly expressed in the E-mode of variability of the tropical Pacific. The SST anomalies (Fig. 2.18a) are stronger in the eastern Pacific during the mature phase of the event (NDJ) than in the central Pacific. These anomalies are directly linked to the anomalous surface zonal wind stress (Fig. 2.18b) during the mature phase of the event, through the Bjerknes feedback : the zonal SST gradient reinforces the westerly winds through

the zonal sea level pressure gradient and in turn the zonal wind stress enhances the zonal SST gradient. SSTA (Fig. 2.18a) and zonal wind stress anomalies (Fig. 2.18b) time-longitude patterns are comparable to those of L'Heureux et al. (2017) who make a comparative analysis of the last three strong El Niño events observed (see their figures 2 and 4 respectively).

We compare the evolution of the total heating rate during this event to that observed during the strong El Niño event of 1997-1998. The reanalysis dataset used is SODA v2.2.4 (see paragraph 2.1). The total heating rate is integrated over the surface layer, whose depth is fixed at 80 m and averaged along the equator, between 2°S-2°N.

(a) A PI-control strong El Niño event

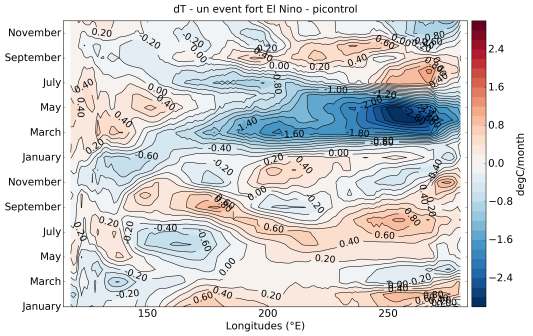

(b) El Niño 1997-1998 (SODA v2.2.4)

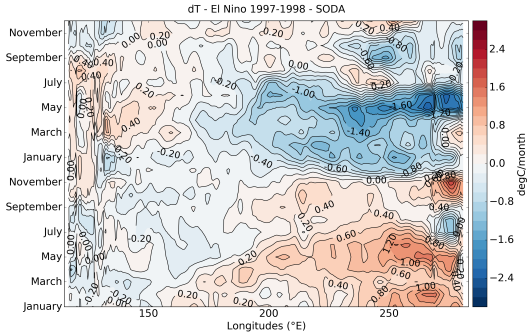

Figure 2.19 – Comparison of the total heating rate of (2.19a) a strong El Niño event of the CESM-LE PI-control simulation and (2.19b) the 1997-98 strong El Niño event in SODA v2.2.4 (°C/month). The tendency term is averaged along the equator between 2°S-2°N and integrated on the fixed-depth surface layer equal to 80 m.

Even if the maxima values are greater for the CESM-LE event than for the observed 1997-98 El Niño, the spatial evolution of the heating rate is similar. In the eastern equatorial Pacific, the CESM-LE El Niño event presents an alternation of positive and negative anomalies temperature tendency during the developing phase of the Niño event, which is not so pronounced in the observed event. The boreal summer peak spreads further west, with more intensity and quicker during the CESM-LE event than the observed one. The westward shift is observed, but later and weaker (around 180°W in November). The negative temperature tendency during the decay phase is more abrupt and pronounced in the CESM-LE event than in the observed event. The cooling rate is also extending more to the west. Finally, the decaying phase occurs later, starting between January and February while for the observed event, the negative anomalies begin in November. However, some of these features are likely due to inter-event variability. CESM-LE seems to simulate realistically the evolution of El Niño despite an extension further west, a stronger amplitude and a faster phase of decay.

We compare also different tendency terms of our heat budget calculated during strong El Niño events of the CESM-LE historical simulations with those of the three observed strong El Niño events analysed by Abellán et al. (2017b) (Fig. 2.20). They computed the heat budget in the Niño-3.4 region (170°W-120°W and 5°S-5°N) and over a fixed mixed layer of depth 50 m. Our tendency terms are integrated over a fixed mixed layer of depth 80 m.

We present only the year before the winter peak for our composites. Thus, only the months of January(Y0) to December(Y0) of Figure 2.20a are compared to Figure 2.20b. It should be noted that Abellán et al. (2017b) applied a three-month running mean filter on their terms. Interestingly, the different terms of the CESM-LE historical composite are very similar to those of the observed one. The total heating rate has a greater peak, around 0.5 °C per month, while those observed reach 0.4 °C per month, but the values of the observed events are smoothed by the applied filter. However, the 1997-98 El Niño has a temporal evolution of its heating rate, with a period of peak when the heating rate is greater than 0.2 °C/month from January(Y0) to October(Y0), that is outside the 95 percentiles of the simulated strong

(a) Observed tendency terms (b) Historical ensemble mean tendency terms

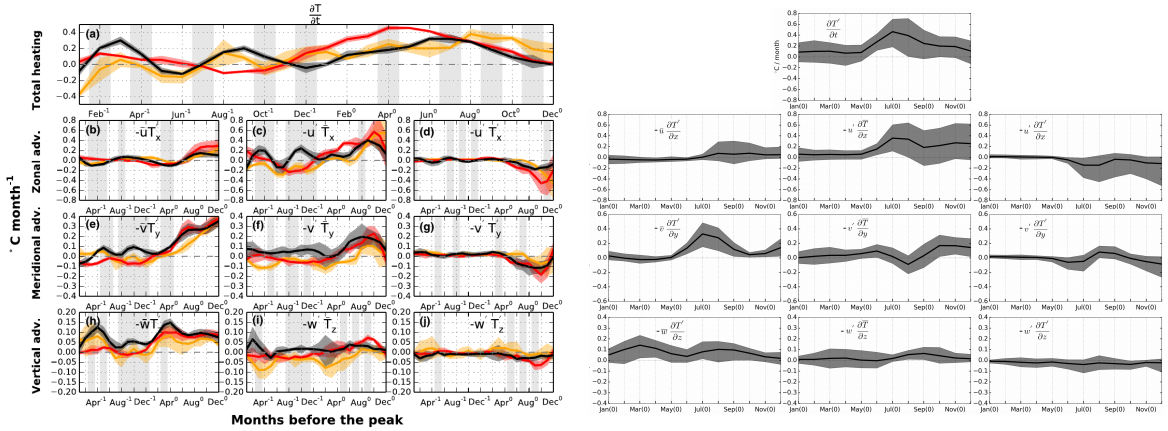

Figure 2.20 – Time evolution of the heat budget tendency terms of (2.20a) the three observed El Niño events and (2.20b) the historical ensemble-mean strong El Niño events in the Niño-3.4 region (°C/month). Figure 2.20a is the figure 9 of Abellán et al. (2017b). Black line is the 2015-16 El Niño, red line is the 1997-98 El Niño and yellow line is the 1982-83 El Niño. The shading corresponds to the standard deviation between the three datasets they used (GODAS, PEODAS and ORA-S4). The temporal evolution over 24-month prior to the event peaks is shown. In figure 2.20b, the temporal evolution over 12-month prior to the event peaks is shown. Thus, only the months of January(Y0) to December(Y0) of Figure 2.20a are compared to Figure 2.20b. The shading corresponds to the 5th and 95th percentiles between the events of the historical strong composite.

El Niño composite. The simulated strong El Niño composite is similar to the two other strong El Niño events that are included in the spread of the composite.

The two main zonal advective terms, the mean zonal dynamic heating term and the zonal advective feedback, present lower amplitudes in November and December than the 1997-98 and 1982-83 events. These terms would play a less important role during the mature phase of the event, but this may come from the cold tongue bias of the model. The prominent role of the zonal advection in the central Pacific could be shifted westward in the model. The mean meridional dynamic heating term, however, does not follow the same evolution as for the observed events with a decrease at the end of the summer while it increases throughout the year in observations. The others two meridional terms present similar amplitudes and evolutions. The vertical advection terms present higher amplitudes in the simulated strong El Niño composite (see the different plot scale), but show similar temporal evolution.

Finally, considering the preceding comparison, the heat balance during the strong El Niño events seems to be simulated realistically by the model.

2.3.4.2 Comparison with previous projected heat budget onto the E mode

Takahashi and Dewitte (2016) projected the heat budget of the two strong El Niño events observed (1982-82 and 1997-98) as well as strong El Niño events simulated in GFDL CM2.1 onto their respective E mode. We reprint their figure 6 and compare it to the same diagnosis applied to the strong El Niño events of the historical members of CESM-LE (Fig. 2.21).

Both periods have similar feedback contributions in observations, GFDL CM2.1 PI-control simulation or CESM-LE historical simulations, with, however, reinforced contributions of linear vertical advection and weaker contributions of linear zonal advection in CESM-LE simulations. The spread associated with the inter-events ensemble is more pronounced in CESM-LE, providing contributions that can be opposed for the same period (particularly for the period 1, see the NDH and ADVXY terms) according to the event.

(a) Drakkar and GFDL CM2.1 - First period

(b) Historical CESM-LE

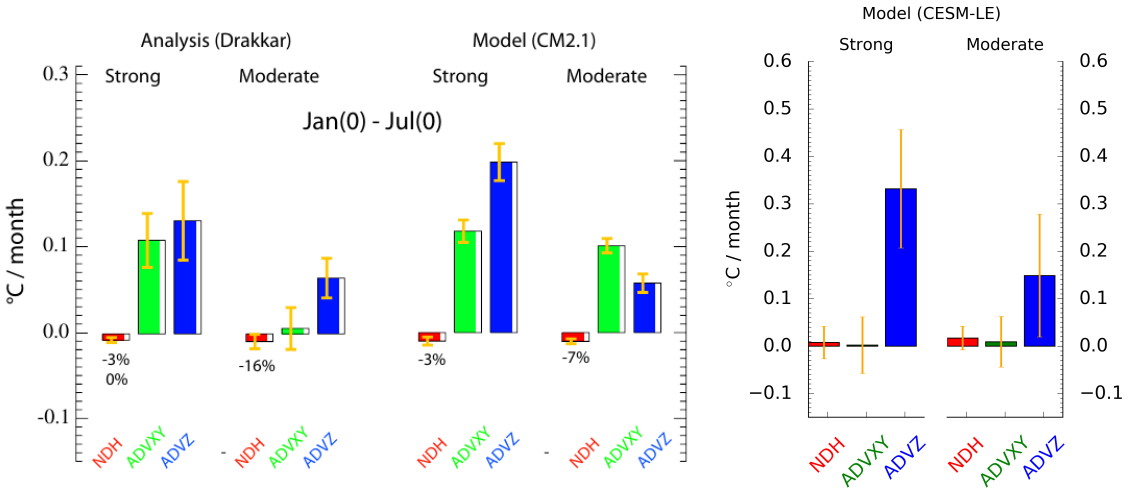

(c) Drakkar and GFDL CM2.1 - Second period

(d) Historical CESM-LE

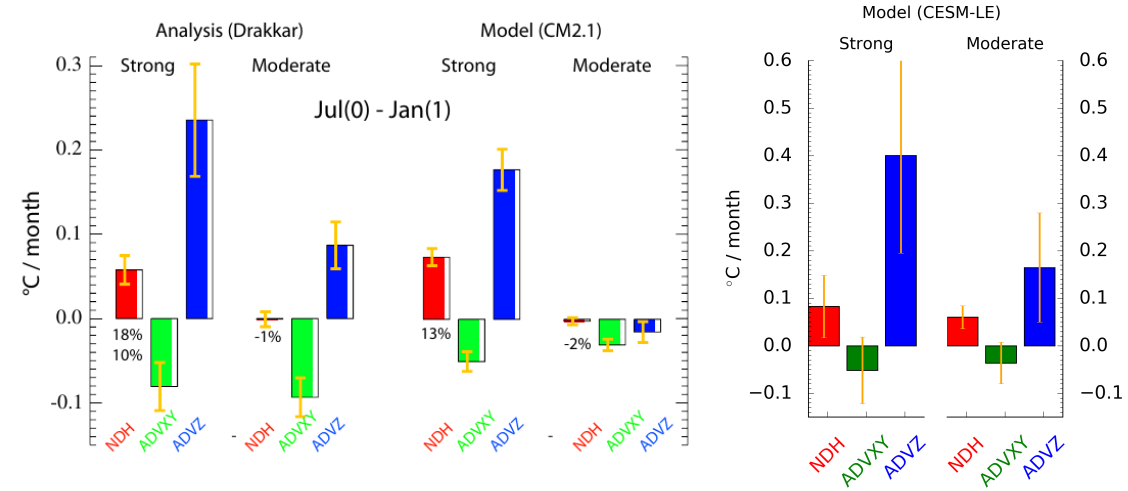

Figure 2.21 – Oceanic advective contributions to the rate of SST change in E (top, Fig. 2.21a and 2.21b) from January(Y0) to July(Y0) and (bottom, Fig. 2.21c and 2.21d) from July(Y0) to January(Y1) of strong and moderate El Niño events in (left) Drakkar, (middle) GFDL CM2.1 and (right) CESM-LE. Unit is °C/month. The red bar accounts for the non-linear dynamical heating (NDH) whereas the green and blue bars represents the horizontal and vertical linear advection respectively. The orange vertical segment provides the inter-events standard error on the advection terms (14 moderate and 2 strong events for Drakkar). Note the different scales. Figures 2.21a and 2.21c are reprinted from Takahashi and Dewitte (2016).

2.3.4.3 Limitations of our heat budget calculation

Our calculation of the tendency terms of the SST equation in CESM-LE simulations has limitations that must be kept in mind when interpreting the results.

First of all, the budget is not closed because, in addition to numerical errors, contributions are not calculated, such as:

- which can lead to poor estimates of the first order: the assumption of the fixed depth of the mixed layer (see paragraph 2.3.1.2);
- which can lead to poor estimates of the second order : the vertical turbulent heat flux (term d of equation 2.1);
- which can lead to poor estimates of the third order, the horizontal turbulent mixing (term c of equation 2.1);
- which can lead to poor estimates of the fourth order, the penetration of the heat flow under the mixed layer (see paragraph 2.3.1.3).

The main limitation of our heat budget comes from the fixed depth of the mixed layer. We chose this hypothesis for simplification of calculations because it allows to neglect the entrainment process of heat into the mixed layer (see paragraph 2.3.1.2). Numerous studies used the same assumptions (e.g. Kug et al. (2010); Capotondi (2013)).

Another issue in the time-varying mixed layer depth is the choice of the definition of the mixed layer, which can lead to important differences between estimated depths. Indeed, different methods are valid but not equivalent. The most common method consists in defining the depth of the mixed layer such that the temperature is 0.2 to 1 °C colder than the sea surface temperature. Another definition of the mixed layer is used in CESM-LE simulations: following Large et al. (1997), the mixed layer depth is defined as the shallowest layer k1 where the local buoyancy gradient is equal to the maximum value of the buoyancy gradient between the surface and the depth k within the water column. This definition leads to a deeper mixed layer than the first definition. This definition is used for instance in the calculation of the heat budget by Stevenson et al. (2017), using simulations of the Last Millennium Ensemble (LME) Project (Otto-Bliesner et al., 2016). They found in particular that the main contributions in the heat budget of the El Niño events in the fixed regions of Niño-3m (2.5°S-2.5°N, 190-250°E) and Niño-4m (2.5°S-2.5°N, 140-190°E) are from the zonal advective feedback (ZAF) and the upwelling feedback, for the latter to the detriment of the thermocline feedback. They argued that the deeper depths of the mixed layer estimated by the Large et al. (1997)'s method tend to damp the thermocline feedback. This sensitivity of the advection terms highlights the difficulty of comparing ENSO heat budget studies with each other, whereas integration depths differ.

A method of intermediate complexity to improve the consideration of the effects of the varying depth of the mixed layer is to use a longitude-varying depth, contrasting the deeper (shallower) mixed layer in the western (eastern) Pacific, rather than a time-varying depth. The zonal contrast in the equatorial Pacific mixed layer depths is likely to impact the results of the different terms of the heat budget, especially the vertical advection terms. Taking into account a stepped or linearly varying depth from west to east may facilitate the physical interpretation of the heat budget by approximating the effective heat transfer between the deep and the surface layers.

Lastly, the off-line calculation of the heat budget from monthly outputs is likely to influence results by adding numerical approximations.

Synthesis

- CESM-LE project

The CESM Large Ensemble (CESM-LE) Project (Kay et al., 2015) is a set of climate model simulations developed by NCAR (Colorado, USA) and available on-line on www.earthsystemgrid.org (see paragraph 2.1.3). We use three different scenarios of fully coupled simulations: 1) the Pre-industrial (PI-control) scenario aggregating 1801 years, 2) the historical scenario (1920-2005) aggregating 42 members for a total of 3682 years and 3) the RCP8.5 radiative forcing scenario (2006-2100) aggregating 40 members for a total of 3800 years of simulated climate system.

The important number of realisations of the same climate system is particularly interesting to study climate phenomena that can follow different trajectories solely because of internal variability. It is an indispensable tool to apprehend a climate phenomenon such as ENSO, which presents strong natural and low-frequency modulations in its intrinsic behaviour (Wittenberg, 2009; Stevenson, 2012). Zheng et al. (2018) showed that at least 15 members of a simulations ensemble are required to differentiate the effects of climate change from those of internal variability on ENSO.

- ENSO modelling by CESM-LE

We confirmed that CESM1, the CGCM used in the CESM-LE project, simulates realistically the variability of the tropical Pacific even if common CGCMs biases remain, especially the cold tongue bias and the double ITCZ (see paragraph 2.1.4). The simulation of the SST seasonal cycle is close to observations despite a westward shift of the cold tongue. This is all the more interesting because ENSO is particularly linked to the SST seasonal cycle (see paragraph 1.3.1). The simulation of ENSO by CESM-LE shows larger variability than observed, more confined equatorially (that is the meridional extension of El Niño is too small) and extending too far westward in the Pacific. Overall some intrinsic characteristics of ENSO are realistically simulated, such as a realistic 3-6 years period and a seasonality of its variance close to the observed one. The model has also skill in simulating ENSO diversity and non-linearities (Stevenson et al., 2017; Dewitte and Takahashi, 2017). These results give us confidence in the use of CESM-LE as a test-bed to better understand the mechanisms and sensitivity of ENSO diversity (chapter 3) to the Pacific mean state (chapter 4) or to climate change (chapter 5).

- Thermodynamical and dynamical oceanic processes

A heat budget of the mixed layer is performed to diagnose oceanic processes during El Niño events, in the framework of ENSO diversity and possible changes due to global warming. We perform the heat budget with a fixed depth of integration of the oceanic mixed layer, which can cause limitations in physical interpretation that we have to take into account in physical interpretations. Considering a longitude-varying depth could lead to a better closure of the heat budget and is a possible way of improving the results of this part of the thesis.

Synthesis

- Data quantities challenging

Modelling the climate system is directly related to the numerical development. Especially, the simulation of a growing number of processes involving different scale mechanisms requires the use of increasingly fine resolutions that make numerical simulations more and more expensive in terms of computation time and storage capacity (Fig. 2.22). Just for the CESM-LE, considering PI-control, historical and RCP8.5 simulations, about 1650 gigabytes are needed to download associated files with one 4D variable, such as the vertical velocity (for all ensemble members). In total about 6.5 terabytes had to be downloaded, a quantity of data that must then be processed.

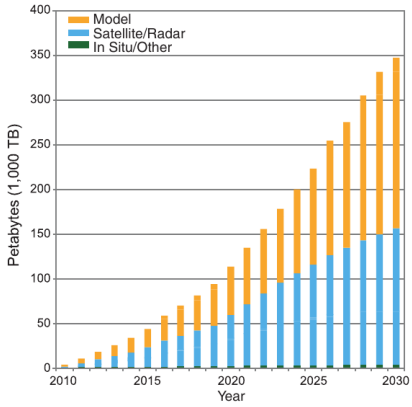

Figure 2.22 – Projected climate data volume, coming from models (yellow), remotely sensed data (blue) and in situ measurements and past proxy (green). Reprinted from Overpeck et al. (2011)

- Tools

The post-processing of the large ensemble is thus challenging, if only because of the large amount of data. However, the data scientist community is getting organized and is developing more and more tools to facilitate this post-processing. In particular, when using the Python programming language, many packages are available that continue to develop to facilitate the exploitation of geoscience data. The majority of these geoscience packages uses the SciPy Stack ecosystem (`https://www.scipy.org/`), which provides the core packages NumPy (`http://www.numpy.org/`), SciPy library (`https://docs.scipy.org/doc/scipy/reference/`), Matplotlib (`https://matplotlib.org/`) and pandas (`http://pandas.pydata.org/`), that I used a lot.

An interesting and powerful package, which has developed particularly from the end of my first year of thesis, is the xarray library (see Hoyer and Hamman (2017) and `http://xarray.pydata.org`). It makes it easy to manipulate georeferenced, labelled multi-dimensional arrays. The first interest is that dimensions, coordinates and attributes of netCDF files are understood as such to compose an object on which functions can be directly and easily applied. Another interest is the rapid development of integrated functions adapted to the post-processing of geoscience data. Finally, it is possible to integrate Dask with xarray, which supports parallel computations and streaming computation. Dask allows to make calculations on datasets which do not fit into memory, by "chunking" the matrix into many small pieces.

Synthesis

Despite its complexity, xarray remains intuitive to use, fun and accessible. In addition, many projects related to xarray continue to develop. I used for instance the packages: "eofs" for the computation of the EOF (see Dawson (2016) and https://ajdawson.github.io/eofs/), "pwlf" for the computation of the piecewise linear regressions (see https://jekel.me/), "oocgcm" for inspiration and transcription on the B-grid of the POP model (https://oocgcm.readthedocs.io/en/latest/), "marc cesm" project for optimisation of the management of CESM files (https://github.com/darothen/experiment) among others.

I also used the statsmodels (https://www.statsmodels.org) and scikit-learn (https://scikit-learn.org) packages, dedicated to statistics and machine learning.

Finally, an interactive computational environment has also matured during my Ph.D. and drastically changed the way I code: the Jupyter Notebook (https://ipython.org/notebook.html), whose ancestor was Ipython. Without the prior or concomitant development of all these Python packages, my Ph.D. would not have been the same.

Chapter 3

Characterising ENSO diversity

Contents

3.1 Preamble

Over the past two decades has emerged the question of defining the spatial diversity of ENSO (see paragraph 1.1.2). This issue is essential to project the evolution of ENSO, whose diversity leads to different meteorological impacts and different rectification effects on the mean state (see Chapter 1).

We focus in this chapter on two main methods commonly used in literature to characterise ENSO diversity.

The first method is the one proposed by Takahashi et al. (2011) (see paragraph 3.2.2). Using an EOF analysis of the tropical Pacific SSTA, they linearly combined the principal components (PC) time-series associated with the two first modes of variability. The new orthogonal base obtained highlights strong El Niño events by projecting them positively onto one of the new axes, while moderate El Niño events and La Niñas project on the other axis. The method is supported by the non-linear behaviour of the Bjerknes feedback: extreme Eastern Pacific (EP) El Niño events are reflected in an enhancement of the Bjerknes feedback, when the SST anomaly exceeds a threshold ($\sim +2\,°C$) in the far eastern Pacific (e.g. as measured by the E index) (Takahashi and Dewitte, 2016; Takahashi et al., 2018). In the simulations of the GFDL CM2.1 CMIP3 model, (Takahashi and Dewitte, 2016) showed that the threshold may be approached by a k-mean cluster analysis in the E and C phase space, highlighted by the apparent bi-modality of the simulated ENSO system. However, this bi-modality is not so well defined in CESM-LE and we test the sensitivity of the k-mean analysis to the period of the data trained (paragraph 3.2.2.2) as well as the sensitivity of the clustering to a fixed threshold (paragraph 3.2.2.3).

The second method (see paragraph 3.2.3) is a commonly used method using SSTA indices in historical Niño regions to separate Central Pacific (CP) and EP El Niño events (Kug et al., 2009; Yeh et al., 2009a; Capotondi, 2013; Stevenson et al., 2017). This method was chosen because it is widely used, whether for the investigation of dynamic processes (Kug et al., 2009, 2010; Capotondi, 2013; Stevenson et al., 2017), for the analysis of the ENSO's flavours modulation with the mean state (Choi et al., 2011) or for the analysis of changes in ENSO statistics with global warming (Yeh et al., 2009a). A EP (CP) El Niño is defined when the mean SST anomalies (SSTA) over the Niño-3 region (5°S-5°N, 210°-270°E) is greater (lower) than the SSTA mean in Niño-4 region (5°S-5°N, 160°-210°E). Due to the common Cold Tongue bias of the CGCMs, recent studies have used regions shifted 20° to the west (Kug et al., 2010; Capotondi, 2013; Stevenson et al., 2017), which increases the risk of integrating the so-called double peaked El Niño events that CGCMs unrealistically simulate (Graham et al., 2017). A comparative analysis of both regions in El Niño definition is presented in paragraph 3.2.3.3. The sensitivity of this definition of El Niño diversity to the choice of the winter season is also analysed (see paragraph 3.2.3.2). Note that by abuse of language and because many studies have taken up these terms independently of the method used, the EP (CP) El Niño events are called Cold Tongue (CT) (Warm Pool, WP) El Niño events in an equivalent way.

These two methods are not equivalent by nature: whereas the CP/EP method investigates the ENSO diversity through the position of the anomalous warming, whatever its intensity, the strong/moderate method has an approach focused on the intensity of warming through the E-index. However, the spatial patterns associated with the strong/moderate methods project variability mainly in eastern Pacific and central Pacific respectively, which can get closer to the method of detection by spatial position directly.

The objective of the chapter is thus to analyse strong/moderate El Niño events comparatively to CP/EP El Niño events to assess their intrinsic characteristics and evaluate their robustness and correspondence.

3.2 Robustness of definitions

The objective of this section is to investigate the sensitivity of both methods to various parameters depending on the intrinsic characterisations of each method.

After presenting corresponding metrics used, different tests are applied:

- for the strong/moderate classification, the sensitivity to the categorization method (cluster analysis) and to the index threshold is tested,
- for the EP/CP classification, the sensitivity to the season and to the region considered is tested.

Regarding the ENSO statistics, it should be noted that counting El Niño events is often computed by year (Kug et al., 2010; Choi et al., 2011; Cai et al., 2014; Stevenson et al., 2017). Another method is to consider each period above the threshold during at least 3 consecutive seasons (ONI definition) or 5 consecutive months as a single event, whatever its duration. In observation datasets, the warm event from 1986 to 1988 occurs during two consecutive winters without the indices failing below the threshold, regardless of the dataset or definition used (Fig. 3.1). The last event of 2014-2015 occurs also during two consecutive winters in the HadISST dataset according to the ONI definition. These two observed examples show the difficulty of defining El Niño events from a threshold exceeded for more than one season. How to count El Niño events is not well established, but is of first importance when projecting changes in ENSO diversity statistics with global warming (Yeh et al., 2009a; Cai et al., 2014). The two different methods can cause differences in estimating the frequency of occurrence of El Niños, but also in estimating the proportion of strong/moderate or EP/CP events.

For consistency with previous studies, we use the method based on detection of El Niño events per year when regarding frequencies of occurrence of events defined from the ONI index (EP/CP method). But, with the strong/moderate method, we use a detection of events per warm period. Indeed, this method does not require an event peak in winter to define an El Niño event and it allows the event to reach its peak in any season, unlike the ONI method which is based on a peak in winter. Counting the event per year when defining El Niño events with the strong/moderate method is tricky and would require to cut arbitrarily the calendar year before applying the cluster analysis.

When comparing El Niño composites, we use the method based on detection by warm periods. The 12-month El Niño event that is then selected is the 12-month period that includes the maximum index value of the entire initial warm period. Although it reduces the number of events in the El Niño composite, this method provides a better representation of the strong events on which we focus afterwards.

3.2.1 El Niño: an anomaly compared to the mean state

The two studied methods each use two different indices, recognising that at least two degrees of freedom are needed to reflect ENSO diversity (Trenberth and Stepaniak, 2001; Yeh et al., 2009a; Takahashi et al., 2011; Ren and Jin, 2011). But, as a first step, before classifying the two types of events, an El Niño event must be defined. The CP/EP method is more inclined to use the Oceanic Niño Index (ONI), defined by the 3 months running mean of the SST anomalies in the Niño-3.4 region (5°S-5°N, 120°-170°W). In that case, an El Niño (La Niña) event is defined when the ONI is higher (lower) or equal to +0.5 °C (−0.5 °C) over at least **five** consecutive overlapping seasons (definition of the NOAA Climate Prediction Center). The strong/moderate method defined an El Niño event based on the PC1 timeserie: an El Niño event is defined when the value of the first principal component of the Empirical Orthogonal Function (EOF, see paragraph 2.2.2.2) analysis of the tropical Pacific SSTA (10°S-10°N) exceeds its 75th percentile over at least 5 consecutive months.

The definition based on PC1 is comparable to the definition based on ONI in particular because the PC1 is strongly correlated with the ONI index (Table 3.1). The correlation

coefficients are computed as a Pearson correlation coefficients and it has been verified that all p-values associated are negligible.

	HadISST v1.1	ERSST v3b	SODA v2.2.4	GFDL CM1.2 PI-control	CESM-LE PI-control
Correlation coefficient	0.964	0.963	0.967	0.985 ± 0.002	0.990 ± 0.001

Table 3.1 – Pearson correlation coefficient between the ONI and PC1 indices. The observations correlation coefficients are determined over all the dataset (1950-2017 for HadISST v1.1 and ERSST v3b, 1950-2010 for SODA v2.2.4). The correlation coefficients for the PI-control simulations are computed over all the dataset and over 68-yr periods which do not overlap. The mean of the 68-yr correlation coefficients is equal to the all dataset correlation coefficient to an accuracy of 10^{-4}. The associated errors correspond to the standard deviation of the 68-yr correlation coefficients. The duration of 68-yr has been chosen because it is that of observation datasets.

A comparison of the two methods of El Niño definition is made on observation datasets (Fig. 3.1). It has been verified that all the periods considered as an El Niño event at least by one of the two datasets are cited in Trenberth (1997) analysing 1950-1997 SSTA using a base period climatology from 1950 to 1979 and are referenced by NOAA Climate Prediction Center or still in the El Niño composite of Timmermann et al. (2018) (see their Figure 1).

First of all, it should be noted that the definition based on ONI does not characterise the same El Niño events in the two observations datasets with the same base period (orange marks, top in figure 3.1). One event occurring during the winter of 1953 is spotted in the ERSST v3b dataset, but not in the HadISST v1.1 dataset. This event, referenced by NOAA[1], is one of the events constituting the canonical El Niño composite of Rasmusson and Carpenter (1982). It is also quoted by Wyrtki (1975) who catalogues it as a small event. Conversely, another event is spotted in the HadISST v1.1 dataset, but not in the ERSST v3b dataset, the event occurring during the winter of 2006. It is also an event referenced by NOAA and cited in some studies (Kao and Yu, 2009; Yeh et al., 2009a; Lee and McPhaden, 2010; Singh et al., 2011). Interestingly, this event can be classified as either a CP warm event (Kao and Yu, 2009) or a EP event (Yeh et al., 2009a). We will see in paragraph 3.2.3 the difficulties posed by this classification. These differences between datasets are mainly due to the duration of the events. Often the events are not defined because the criterion is reached less than 5 consecutive periods.

A better correspondence is found with the definition based on PC1 (red marks, bottom in figure 3.1): the main difference between the two datasets is the duration of the events, which in particular leads to the separation of the 1968-1969 warm period into two individual events in ERSST v3b. However, this split into two events is also done with the definition based on ONI. The definition based on PC1 may be less sensitive to the dataset.

We investigate the correspondence between the two methods, relative to the declared El Niño events. In both datasets, the PC1 definition does not see the event occurring during the winter of 1977, following the warm event of 1976, nor the event of winter 2004. Conversely, the PC1 definition defines two warm events, in 1979 and 1993. Only the 1993 event is not catalogued as a warm event by NOAA. The three periods (1976-1980, 1990-1995, 2002-2005) concerned by these definition differences are prolonged warm periods when warm events are likely to occur every year or two. These warm periods have been apprehended in different ways previously. First of all, it should be noted that for each event of these warm periods, the other index that does not see the event is close to the definition criterion. Trenberth (1997) showed in the same way that considering the 1990-95 period as one long El Niño event or three consecutive events depended on the choice of the SSTA index threshold. Fedorov and Philander (2000) modified the El Niño perception of this warm period by showing that

[1] http://origin.cpc.ncep.noaa.gov/products/analysis_monitoring/ensostuff/ONI_v5.php

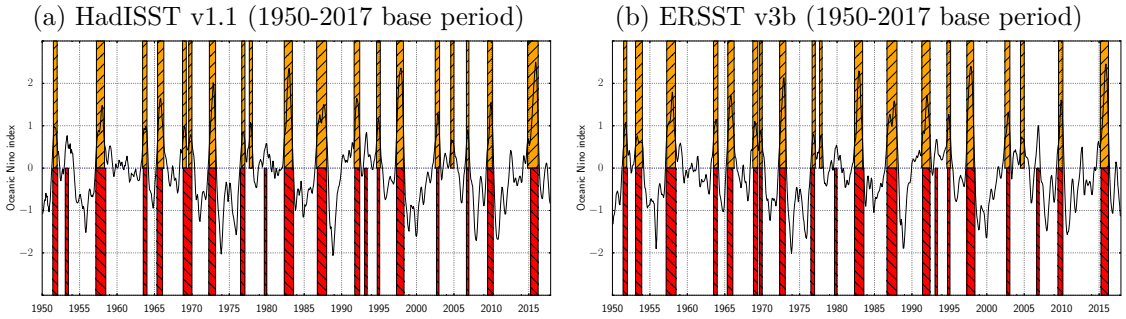

Figure 3.1 – ONI timeseries (°C) for (3.1a) HadISST v1.1 (1950-2015) and (3.1b) ERSST v3b (1950-2015). El Niño events obtained by the ONI definition are marked in orange and hatched (when the ONI is over 0.5 °C during at least 5 consecutive overlapping seasons) and the periods corresponding to El Niño events obtained by the PC1 definition are superimposed in red (when the PC1 is over its 75th percentile during at least 5 consecutive months).

this warm period could not be considered as an exceptionally long event if one considered SST departure from decadal fluctuations rather than mean climatology. In that case, this warm period represents the persistence of warm background conditions rather than a chain of moderate El Niño events or a long El Niño event. Finally, Kessler (2002) mentioned the period of the early 1990s as exceptional because these El Niño events (1993 and 1994-95) which follow each other closely have small amplitudes and do not last long. He suggested that these El Niño events do not need initiating warm water recharge in the western Pacific to be trigger. These different results highlighted the diversity of flavours of El Niño events and its closed relationship with decadal modulation of the background state, which is still an open issue and is the backdrop to these thesis work.

Finally, the difference between methods and between datasets is mainly due to the duration criterion imposed to define an El Niño events. However, these dataset-sensitive El Niño events have low amplitude and/or duration, which does not affect the statistics of strong events as defined by Takahashi et al. (2011) of primary interest in our study.

In the CESM PI-control simulation, according to the two definitions, there are 375 El Niño events defined by the PC1 and 371 El Niño events defined by the ONI over the 1801 years of simulation. Among them, 16 El Niño events are defined by the ONI, but not by the PC1, and 20 El Niño events are defined by the PC1, but not by the ONI index. This is mainly due to a long event based on the ONI definition being split into two PC1 definition events. And some short events defined by the ONI are not seen by the PC1 index (11 events), and conversely (6 events). These classification differences due to the definition tend to cancel each other and it represents 1 % of total differences. The same exercise is reproduced in GFDL CM2.1 PI-control simulation. There are 96 El Niño events defined by the PC1 and 118 El Niño events defined by the ONI over the 500 years of simulation. The difference comes from small El Niño events defined by the ONI index and not by the PC1.

So it must be kept in mind that these differences could affect statistics when looking at the correspondence between moderate El Niño events and CP/EP El Niño events defined by the two methods used in this chapter.

3.2.2 Strong and moderate El Niños

3.2.2.1 The metrics

Recent studies have suggested that the diversity of El Niño can be interpreted as resulting from the existence of two distinct dynamical regimes (Takahashi et al., 2011; Takahashi and Dewitte, 2016; Takahashi et al., 2018), a regime encompassing La Niña events and moderate El Niño events with a centre of action in the central Pacific, and the other regime

associated with extreme Eastern Pacific El Niño events. Building on this recent progresses to characterise ENSO diversity, we use the E and C indices defined by Takahashi et al. (2011) as $E = (PC1 - PC2)/\sqrt{2}$ and $C = (PC1 + PC2)/\sqrt{2}$ where the PC1 and PC2 are the normalised principal components of the first two EOF modes of SST anomalies in the tropical Pacific (10°S-10°N) (see paragraph 2.1.4.2 and Figure 2.8 for the corresponding EOF spatial patterns). The E and C indices are thus linearly uncorrelated by construction. The E and C indices describe two variability modes of the equatorial Pacific, statistically independent but linked together by the non-linearities of the Pacific coupled system (Takahashi et al., 2011; Dommenget et al., 2013; Karamperidou et al., 2017).

A multiple linear regression of the SSTA onto these indices (see paragraph 2.2.3.3) is used to determine the spatial SSTA patterns associated with each index (Fig. 3.2). The E-pattern explains most of the variability in the eastern Pacific and is related to strong warm events, the C-pattern explains the variability in the central Pacific and is related to cold and moderate warm events. The evolution of an El Niño event is a combination of these two modes (Takahashi et al., 2011), the E and C indices allowing the characterisation of the El Niño spatial type (EP versus CP) and its amplitude (strong versus moderate) (Takahashi and Dewitte, 2016; Dewitte and Takahashi, 2017).

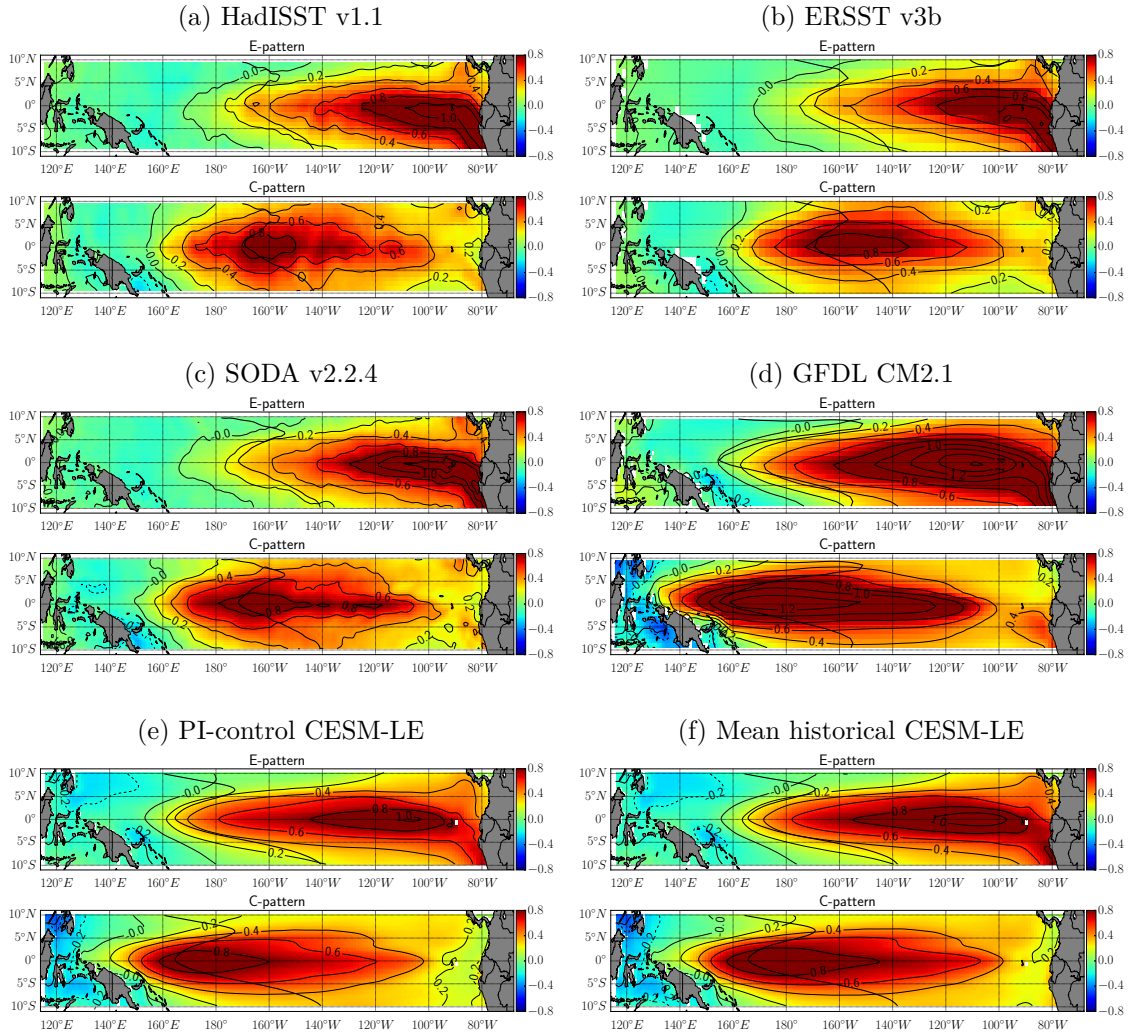

Figure 3.2 – Maps (°C) of linear regressions of SSTA onto the E (top) and C (bottom) indices for (3.2a) HadISST v1.1 (1950-2017), (3.2b) ERSST v3b (1950-2017), (3.2c) SODA v2.2.4 (1950-2010), (3.2d) the PI-control simulation of GFDL CM2.1 (500 years), (3.2e) the PI-control simulation of CESM-LE (1801 years) and (3.2f) the ensemble-mean of historical simulations of CESM-LE (42 members). The SST are linearly detrended over all the time period. Also shown is the corresponding 28 °C isotherm.

In the E-mode, the peak of warm SST anomalies is located east of 120°W. In observations, the warm peak of SSTA extends from the coast of Peru-Ecuador to 110°W, while it is not so linked to the South-American coast in CESM-LE, where it is located further west. As described in paragraph 2.1.2.2, we can thus note the westward bias of the Cold Tongue and the more constrained along the equator warming region in the CGCMs. CESM-LE and GFDL CM2.1 simulate the center of the patterns displaced to the west compared to observations by 20° and 30° for the E and C patterns respectively, which is comparable to the CMIP5 ensemble (cf. Figure 1 of Matveeva et al. (2018)). This bias in CGCMs is often bypassed in previous studies by shifting Niño regions 20° westward in order to classify El Niño diversity (Kug et al., 2010; Capotondi, 2013; Stevenson et al., 2017). The associated results are discussed in paragraph 3.2.3.3. The use of the E and C indices, which integrate the whole tropical Pacific band, allows us to overcome this issue.

These E and C patterns can be compared to patterns of variability associated with the Central Pacific (CP) and Eastern Pacific (EP) warming established by Kao and Yu (2009) on observations (HadISST). They used an EOF analysis associated with a linear regression of the tropical Pacific SSTA (their figure 3). Interestingly, even if the period of observations is not the same, the patterns are very similar with an extension of the eastern warming region to the dateline in the EP pattern and a region of maximum warming centred on the dateline in the CP pattern.

Thanks to this central and eastern tropical Pacific variability patterns, we distinguish El Niño diversity. Following Takahashi et al. (2011), moderate and strong El Niño events are classified using the time-series associated to the PC1 and the E-index. Firstly, an El Niño event is defined when the PC1 value is greater than or equal to its 75 percentile over at least 5 consecutive months. This method makes it possible not to assume that El Niño peaks can be identified in one single season (usually in boreal winter in previous studies). Secondly, regarding the classification in terms of amplitude, based on the analysis of observations and a long-term CGCM simulation (GFDL CM2.1), Takahashi and Dewitte (2016) suggested that moderate events may be defined as those for which the E index does not exceed 1.5-1.8 °C which corresponds to the threshold for which there is a sudden enhancement of the Bjerknes feedback in the eastern Pacific. In the E and C indices phase space, strong El Niño events will thus project on the high positive values along the E index axis, while moderate El Niño events will get closer to high values of the C-index axis.

When we analyse observations and reanalysis classification in the E and C indices phase space (Fig. 3.3a, 3.3b and 3.3c), two historical strong El Niño events emerge from the pattern: 1982-1983 and 1997-98 El Niños. These two strongest events recorded have been widely studied, used as extreme events framework in the literature (McPhaden, 1999; Vialard et al., 2001; Kug et al., 2009; Cai et al., 2014; Takahashi and Dewitte, 2016). Takahashi and Dewitte (2016) showed that these two strong El Niño events were associated with non-linearities in the Bjerknes feedback favouring an increase in the growth rate of these events. Interestingly, the last strong event of 2015-2016, even if it is often compared to the 1982-83 and 1997-98 strong events because of its strong signal in the Niño3.4 index (L'Heureux et al., 2017; Abellán et al., 2017b), is not so distinguishable from other strong (but not very strong) El Niños, such as the 1951 and 1957 events for instance. This event has been shown to be different in terms of induced impacts, such as precipitation anomalies in Northern Peru L'Heureux et al. (2017). Dewitte and Takahashi (2017) showed that for this event and the strong event of 1972-73, the 28 °C isotherm, a proxy of the Warm Pool, did not extend so far east as for the two preceding extreme El Niño events. They classify them as moderate Eastern Pacific (EP) events rather than strong events. This moderate classification of the two latter events is further highlight when analysing the temporal evolution of their E and C indices before the December month (Fig. 3.4). While strong events project strongly along the E axis (1982-83 and 1997-98 events), the events of 1972-73 and 2015-16 have lower E values (half) and stronger C values. The moderate El Niño event of 2009-10, typical CP El Niño events with

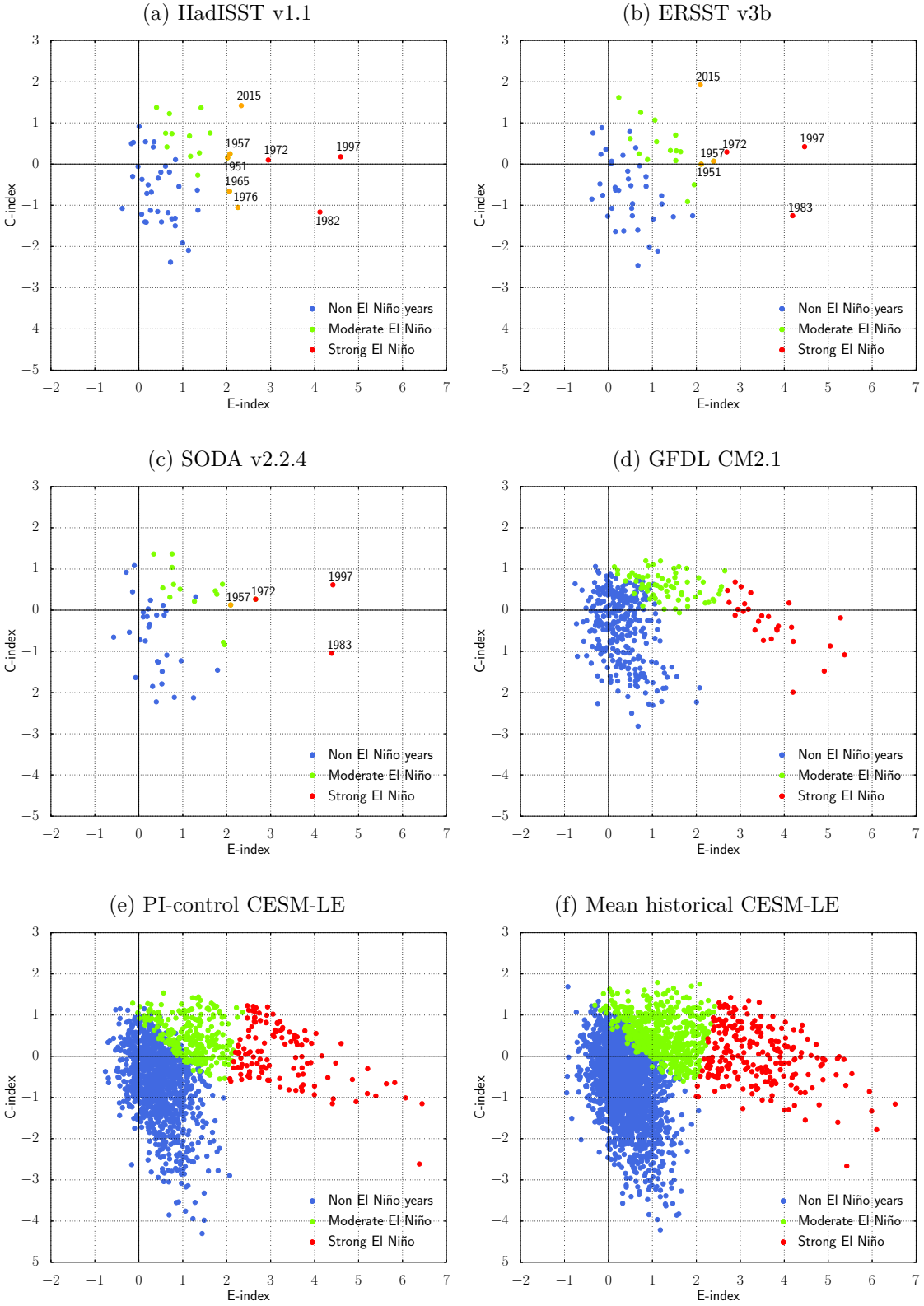

Figure 3.3 – K-mean cluster analysis on the E-peak of El Niño events for (3.3a) HadISST v1.1 (1950-2017), (3.3b) ERSST v3b (1950-2017), (3.3c) SODA v2.2.4 (1950-2010), (3.3d) the PI-control simulation of GFDL CM2.1 (500 years), (3.3e) the PI-control simulation of CESM-LE (1801 years) and (3.3f) the ensemble of historical simulations of CESM-LE (42 members). The k-mean analysis classifies (red) strong and (green) moderate El Niño events. In blue are shown non-El Niño years (which are therefore not used in the k-mean analysis). In orange for observations and reanalysis are shown mixed El Niño events, whose E-peak is close to the threshold.

a high peak in the Niño-4 region (Lee and McPhaden, 2010) shows a development with low E values and strong C values. These differences in the evolution of moderate El Niño events can be related to the EP and CP events classification, the signature in E makes it possible to differentiate moderate events that develop exclusively in the central Pacific from moderate events that also have warming in the eastern Pacific (Dewitte and Takahashi, 2017).

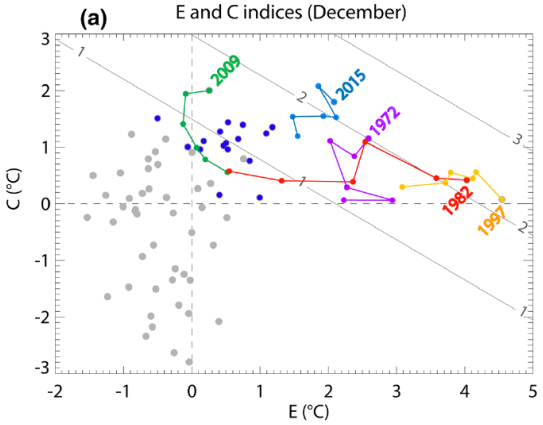

Figure 3.4 – E-C phase space for the month of Decembre. Blue dots correspond to El Niño years. Five El Niño events (1972, 1982, 1997, 2009 and 2015) are highlighted, with their evolution from July to December (last dot labeled with the year is the December value). The oblique gray lines are the iso-contours of the approximate Niño-3.4 index in the E and C space (Niño-3.4=0.47E+0.67C). Reprinted from Dewitte and Takahashi (2017).

In this thesis work, we adopt a similar approach than Takahashi et al. (2011), applying a k-mean cluster analysis (with k=2, see paragraph 2.2.2.3) for each dataset and for each period, present and future, including all members of CESM-LE simulations. The methodology is the following: a k-mean clustering is performed on the peak values of the E-index of each El Niño event of the PI-control simulation. As mentioned before, the considered peak of the event for the cluster analysis is not imposed to be in the winter season. Once the model is trained, it is applied over each period of simulations (Fig. 3.3). The values of the E-index which separate the two clusters are between 2 and 2.5 °C, except for the PI-control simulation of GFDL CM2.1 the limit being more close to 3 °C. This greater threshold value is due to the more important bias of GFDL CM2.1 simulating greater ENSO variability (see paragraph 2.1.2.2).

3.2.2.2 Sensitivity to the k-mean analysis

The k-mean analysis on the El Niño peaks in the E-C phase space, suggested by Takahashi and Dewitte (2016), is sustained by the bimodal probability distribution function apparent for the GFDL CM2.1 PI-control and 5-members historical simulations (see their figure 2). The bimodal distribution of the El Niño peaks in this space phase is less pronounced in CESM-LE PI-control and 42-members historical simulations than in GFDL CM2.1 (Fig 3.5 with dots corresponding to the red and green dots in figure 3.3). The PDF is estimated via a kernel density estimation (KDE, see paragraph 2.2.1.3). Different bandwidths have been tested. However, when investigating El Niño events through their E peaks (Fig. 3.5a), the probability distribution function exhibits a slight bimodality that we do not find when investigating El Niño events through their PC1 peaks as used by Takahashi and Dewitte (2016) (Fig. 3.5b). We recall here that we do not assume that the El Niño peak can be identified in one single season, the different peaks used in figure 3.5 are scattered throughout the calendar year, even if there are preferential peak seasons as we will see later (Chapter 5). Consequently to the distribution, the k-mean clustering gives different classification of El Niño events, as highlighted by the repartition of strong (red dots) and moderate (blue dots) in Figure 3.5.

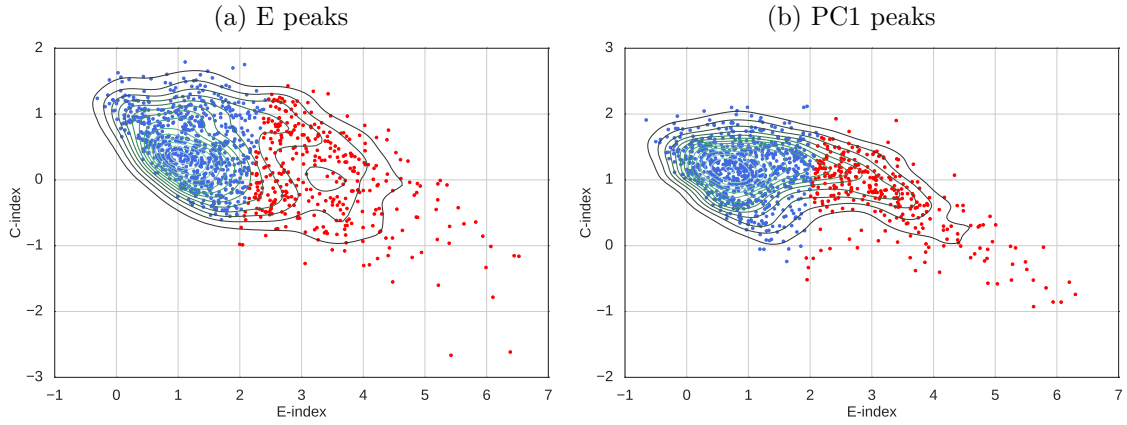

Figure 3.5 – El Niño peaks in the E-C phase space for the CESM-LE PI-control and historical (42 members) simulations. Blue (moderate El Niño) and red (strong El Niño) are identified through a k-mean (k=2) analysis. The probability distribution function (contours) is computed via a Kernel density estimation (KDE). A comparative analyse is done using the E peaks (3.5a) and the PC1 peaks (3.5b) of El Niño events.

Alongside that, the k-mean clustering can be used as a predictor or as a simple classifier. As a predictor, we train the k-mean clustering on the PI-control El Niño peaks and use it onto each ensemble of the historical and RCP8.5 El Niño peaks respectively. The underlying assumption is that the climate system on which the k-mean clustering is applied remains stable in terms of intrinsic features, that is the classification of strong and moderate El Niño events in our case. It could not be the case of the RCP8.5 climate. As a classifier, a new k-mean cluster is applied on each period of simulations. As a consequence, the k-mean analysis gives different classifications of the historical and RCP8.5 El Niño events. A comparative analysis of the different applications of the k-mean analysis (E-peaks versus PC1 peaks, predictor versus classifier) is done (Fig. 3.6 and Table 3.2).

Figure 3.6a shows the relative proportions of strong El Niño events according to the method used. Following Stevenson et al. (2017), the relative proportion is computed as the frequency of occurrence of strong El Niño events (number of strong El Niño per year) for the historical and RCP8.5 periods respectively and expressed as the relative difference to the PI-control simulation. Slight differences appear between methods. While the frequency of occurrence of strong El Niño events is lower in historical simulations than in PI-control simulation when applying the clustering onto the E-peaks (value lower than 0), the frequency of occurrence is slightly higher when applying onto the PC1 peaks. However, the result can be the opposite depending on the member, the interquartile range (IQR) associated with the frequency of occurrence of strong El Niño events of each member shows large spread. This spread is partly due to one of the intrinsic features of strong El Niño events, namely their modulation by low-frequency internal variability. Depending on the historical member, the number of strong El Niño events comes from 2 to 10 over the historical period (156 years for the member 1, 86 years otherwise), that is to say from simple to fivefold. With regard to RCP8.5 simulations, the frequency of occurrence of strong El Niño events increases compared to the PI-control simulation, whatever the method. The increase is statistically significant for all methods, according to a Wilcoxon test and a bootstrap test. Interestingly, the relative differences of moderate El Niño events differ little (no statistically significant change), whatever the k-mean method and whether in historical or in RCP8.5 simulations compared to PI-control simulation (Fig. 3.6b).

Figure 3.6c shows the relative occurrence ratio of strong El Niño events compared to moderate El Niño events according to the k-mean method used. Following Yeh et al. (2009a), the occurrence ratio is the ratio of the frequency of occurrence of strong events to that of moderate events. The different occurrence ratios are indicated in Table 3.2. Each ratio is

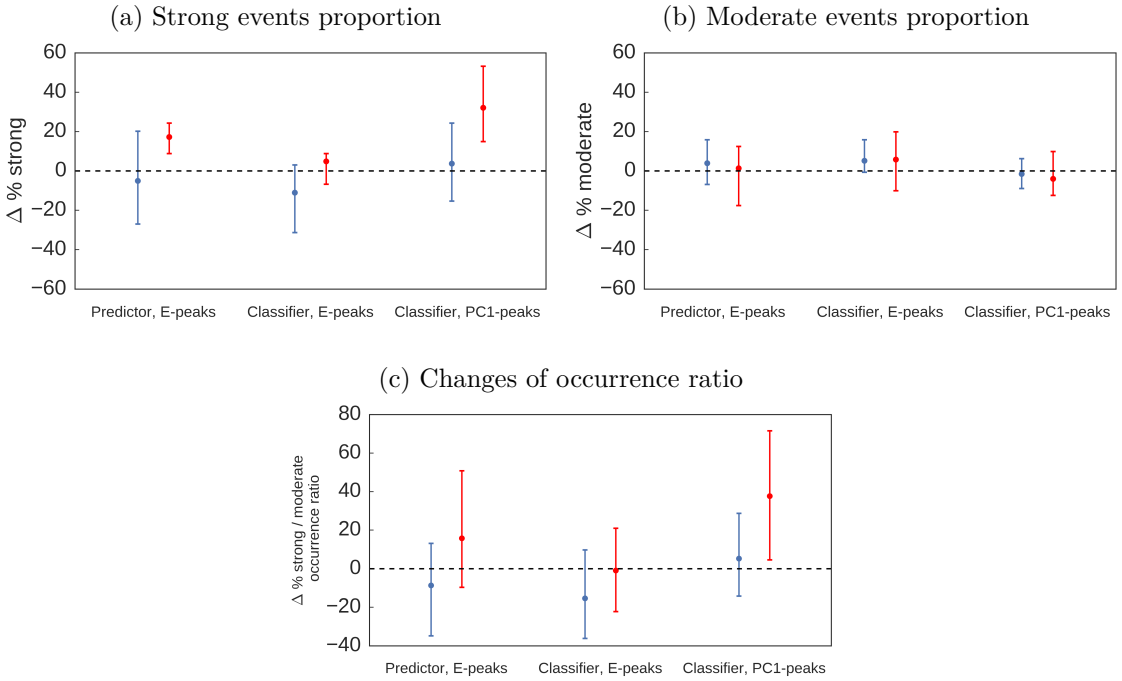

Figure 3.6 – Proportion of El Niño events according to the k-mean method in (blue) historical simulations and (red) RCP8.5 simulations. The k-mean methods are using the clustering as a predictor onto the E peaks (Predictor, E-peaks), using the clustering as a classifier onto the E peaks (Classifier, E-peaks) or using the clustering as a classifier onto the PC1 peaks of El Niño events (Classifier, PC1-peaks). Frequencies of occurrence of (Fig. 3.6a) strong and (Fig. 3.6b) moderate El Niño events expressed as difference relative to the PI-control simulation. The relative differences of frequencies of occurrence are computed following Stevenson et al. (2017). The associated occurrence fractions in the PI-control simulation are shown in Table 3.2. (Fig. 3.6c) Associated relative differences of strong / moderate El Niño occurrence ratios compared to the PI-control ratio. The occurrence ratios are computed following Yeh et al. (2009a). The error bars correspond to the inter-members spread estimated through the interquartile range.

then calculated relative to the PI-control simulation. The strong/moderate occurrence ratios in historical simulations are slightly similar regardless of the k-mean method (cf Table 3.2), but compared to the associated ratio in the PI-control simulation, the main difference appears between applying the cluster analysis to E or PC1 peaks. When considering E-peaks, the ratio is lower in historical simulations than in PI-control simulation, that is the proportion of strong El Niño events compared to moderate El Niño events is lower in historical simulations. More precisely, the frequency of occurrence of strong El Niño events slightly decreases and the frequency of occurrence of moderate El Niño events slightly increases in historical simulations for both methods. Conversely, the frequency of occurrence of strong El Niño events increases in historical simulation for the PC1 k-mean method. In RCP8.5, the ratio increases, which is mainly due to the increase in the frequency of occurrence of strong El Niño events. While in historical simulations the frequency of occurrence of strong events is more than half that of moderate events (around 0.40), it increases in RCP8.5 simulations so that the frequency of occurrence of moderate El Niños is only twice (or less than twice for the k-mean clustering as a predictor onto the E peaks) as important compared to the frequency of occurrence of strong El Niño events. For all method, the frequency of occurrence of strong El Niño events increases compared to that of moderate El Niño events in RCP8.5 simulations. Note, however, that the increase in RCP8.5 simulations only means a return to the value calculated for the pre-industrial period, after having experienced a decrease in the historical simulations, for the method of clustering as a classifier on the E peaks.

	PI-control			Historical					
	Strong	Mod.	Ratio	Strong	Mod.	Ratio	Strong	Mod.	Ratio
k-mean as a predictor onto E peaks	122	253	0.48	237	538	0.44	302	541	0.56
k-mean as a classifier onto E peaks	122	253	0.48	222	544	0.41	270	565	0.48
k-mean as a classifier onto PC1 peaks	99	276	0.36	210	556	0.38	276	559	0.49

Table 3.2 – Number of strong and moderate El Niño events in each period of simulation depending on the k-mean method. The number of events is calculated considering all the years of simulation available, that is 1801 years in PI-control simulation, 3682 years in historical simulations and 3800 years in RCP8.5 simulations.

Finally, whatever the k-mean method, there is some common features:

- the proportion of strong El Niño events increases in RCP8.5 simulations compared to the PI-control simulation (the increase is statistically significant for all methods),
- the proportion of moderate El Niño events remains stable in historical and RCP8.5 simulations compared to PI-control simulation (not statistically significant change),
- the frequency of occurrence of strong El Niño events increases compared to that of moderate El Niño events in RCP8.5 simulations, even if it remains twice as weak as that of moderate El Niño events.

3.2.2.3 Sensitivity to the threshold

Takahashi and Dewitte (2016) showed that the bi-modality in the E-C phase space of the El Niño peaks can be explained by the enhancement of the Bjerknes feedback when the SST anomalies exceed a threshold in the far eastern Pacific, that is as measured by the E index. The k-mean clustering analysis does not hypothesis that this threshold is a fixed value, rather a value of the E index which is a positive function of the C index. The function changes in

RCP8.5 climate (see Figure 3.5). For instance, when considering the mean value of the E threshold in the different k-mean methods, the historical (RCP8.5) threshold is included between 2 and 2.3 °C (1.7 and 2.4 °C). The decrease in the E peak in future climate may occur, meaning that the non-linear threshold of the SSTA warming is easier to be reached, facilitating the Bjerknes feedback in the eastern Pacific.

A sensitivity test to the threshold in E-index is conducted for the k-mean predictor method onto the E peaks. The different values tested are 1.9, 2.0 and 2.1.

As expected, the lower the threshold, the higher the proportion of strong events (Fig. 3.7). Lowering the threshold results in a statistically significant increase in the proportion of strong events compared to moderate events, with the frequency of occurrence of moderate El Niño events not changing significantly, either in historical or future simulations. The frequency of occurrence of strong El Niño events can reach a similar frequency occurrence than that of moderate El Niño events for some RCP8.5 members, for a threshold equal to 1.9 °C. Compared to the strong / moderate frequency of occurrence ratio in the PI-control simulation (Fig. 3.7b), the ratio is almost the same in historical simulations and increases in RCP8.5 simulations. Separation between strong and moderate is highly dependant on the threshold and more physical basis are needed particularly in the case the bimodal probability distribution function is not so well defined as in GFDL CM2.1. Takahashi and Dewitte (2016) suggested to analyse the relationship between the E-index and the wind stress could serve to determine the threshold. However, this threshold could vary in time due to background climate state (Johnson and Xie, 2010) (see also Chapter 5).

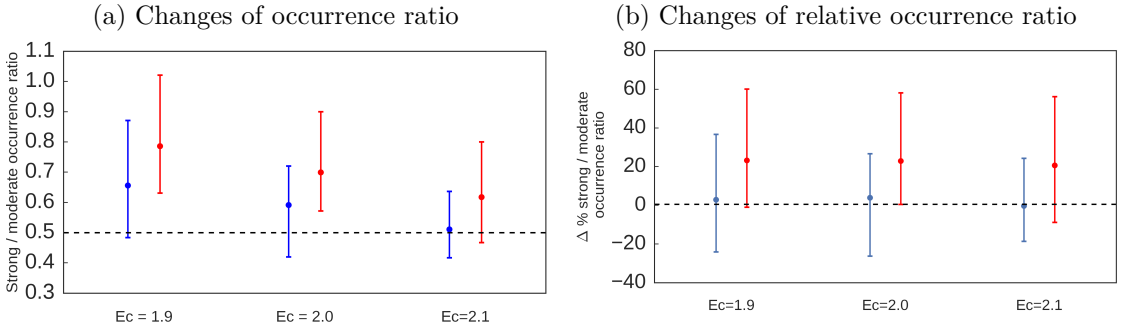

Figure 3.7 – (Fig. 3.7) Absolute and (Fig. 3.7b) relative strong/moderate El Niño occurrence ratio for different thresholds in the E-C phase space delimiting strong and moderate events. The threshold is applied onto the E-peaks of the El Niño events. The test is applied on the (blue) historical and (red) RCP8.5 simulations. The occurrence ratios are computed following Yeh et al. (2009a). The error bars correspond to the inter-members spread estimated through the interquartile range.

3.2.3 Eastern and Central Pacific El Niños

3.2.3.1 The metrics

Following Kug et al. (2010), we classified two types of El Niño based on their spatial patterns of SSTA. As mentioned before, we use equivalently both the denomination of Warm Pool (WP) and Central Pacific (CP) events for El Niño events whose variability is strong in the centre of the Pacific and the denomination of Cold Tongue (CT) and Eastern Pacific (EP) events for El Niño events whose variability is higher in the eastern Pacific. As a reminder, CP events are identified when Niño-4 index is greater than 0.5 °C and greater than Niño-3 index. EP events are identified when Niño-3 index is greater than 0.5 °C and greater than Niño-4 index. Niño-3 (Niño-4) index is defined as the averaged SST anomalies over 5°S-5°N, 150°-90°W (5°S-5°N, 160°E-150°W).

Kug et al. (2010) fixed the November-January period (NDJ) as the peak phase of El Niño events and used it to compare the mean Niño-3 and Niño-4 indices for classification. Ham and

Kug (2012) used the same definition but considering the December-February (DJF) season in CMIP3 CGCMs, as well did Yeh et al. (2009a) in observations (ERSST v2, 1854-2007). Capotondi (2013) used the same definition as Kug et al. (2010) but considering the January-March (JFM) season, in a CMIP3 CGCMs, the CCSM4 PI-control simulation, previous version of CESM1. In the paragraph 3.2.3.2, we analyse the sensitivity of ENSO statistics to the chosen season in observations and two CGCMs in order to estimate the dependence of the classification to the peak season.

Another point is that Kug et al. (2010) actually defined El Niño events from modified Niño indices. Because of the westward shift of the climatological Cold Tongue diagnosed in CGCMs and in the model they used (GFDL CM2.1), shifting ENSO variability to the west (Wittenberg et al., 2006), Kug et al. (2010) used Niño-3m and Niño-4m indices, defined on the areas shifted 20° westward compared to the historical Niño indices (Niño-3m: 5°S-5°N, 170°-110°W and Niño-4m: 5°S-5°N, 140°E-170°W). Capotondi (2013) used both regions, conventional and modified, to define El Niño events. They showed that ENSO repartition statistics presented large discrepancy between the GFDL CM2.1 PI-control simulation used (500 years) by Kug et al. (2010) and the CCSM4 PI-control simulation (500 years) they analysed, but also between the classification EP/CP with the conventional Niño regions or the modified ones using the same model, CCSM4. In the paragraph 3.2.3.3, we analyse the sensitivity of ENSO statistics to the 20° westward shift of the region in two different CGCMs with exactly the same season definition, in order to estimate the reliability on the westward shift of the Niño regions depending on the intrinsic bias of the CGCMs used.

It is unclear whether these different studies used a minimum duration threshold to define an event. In our case, we first define an El Niño event through the ONI definition (see paragraph 3.2.1). Once the event defined, the classification between WP (CP) or CT (EP) events is made from the different hypotheses described previously.

3.2.3.2 Sensitivity to the season

Many studies use different seasons to differentiate CP (or WP) and EP (or CT) El Niños. Table 3.3 shows the alternation of recorded El Niño events, depending on the peak season considered for two observation datasets. Choosing the NDJ season favours CT El Niños, while choosing the JFM season favours WP El Niños. The ratio of WP events to CT events is going from 24 % (27 %) to 62 % (53 %) in HadISST (ERSST) dataset, the number of WP events going from simple to more than double.

Only 4 historical events are characterised as Warm Pool El Niño events, whatever the dataset and the season considered: the 1968-1969, 1977-1978, 1994-1995 and 2004-2005. Interestingly, two of them (1977-1978 and 2004-2005) are events not detected by the PC1 definition, occurring during prolonged warm periods when warm events are likely to occur every year or two, which is also the case for the 1994-1995 event. The last three events are classified as Warm Pool El Niño events by Kug et al. (2009) starting their analysis from 1970 and using the mean September-February SSTA spatial pattern to classify historical El Niño events into three categories: WP El Niño, CT El Niño and mixed El Niño. Two others El Niños are classified as WP El Niños: the 1990-1991 event (not detected in the used dataset, Kug et al. (2009) used ERSST v2 from 1970 to 2005) and 2002-2003 event, included in a warm period. Timmermann et al. (2018) classified the El Niño events of 1968, 1994 and 2009 as CP events which are some of the consistent CP El Niño events throughout the dataset and the season.

Figure 3.8 shows the proportion among El Niño events of each type of events in PI-control simulations, according to the season of the SSTA peak considered and according to the two counting methods (see 3.2 the introduction). It should be noted that the sum of the proportions of WP and CT events are not equal to 100 % because there are some events (6 in CESM1 and 13 in GFDL CM2.1) that occur during the calendar year without reaching the month of January(+1). The mean value of Niño indices for the seasons NDJ, DJF or JFM

	HadISST			ERSST		
	NDJ	DJF	JFM	NDJ	DJF	JFM
1951	CT	CT	CT			
1953				CT	CT	CT
1957	CT	CT	WP	CT	CT	CT
1963	CT	CT	WP	CT	CT	WP
1965	CT	CT	WP	CT	CT	WP
1968	WP	WP	WP	WP	WP	WP
1969	CT	CT	WP	CT	CT	WP
1972	CT	CT	CT	CT	CT	CT
1976	CT	CT	CT	CT	CT	CT
1977	WP	WP	WP	WP	WP	WP
1982	CT	CT	CT	CT	CT	CT
1986	CT	CT	CT	CT	CT	CT
1987	CT	WP	WP	CT	CT	WP
1991	CT	CT	CT	CT	CT	CT
1994	WP	WP	WP	WP	WP	WP
1997	CT	CT	CT	CT	CT	CT
2002	CT	CT	WP	CT	CT	WP
2004	WP	WP	WP	WP	WP	WP
2006	CT	CT	WP			
2009	CT	CT	WP	WP	WP	WP
2014	WP	WP	WP			
2015	CT	CT	CT	CT	CT	CT

Table 3.3 – Classification of El Niño events between Warm Pool (WP) and Cold Tongue (CT) events in HadISST v1.1 (1950-2017) and ERSST v3b (1950-2017) according to the peak season considered.

is not calculated in this case and the events are therefore not classified.

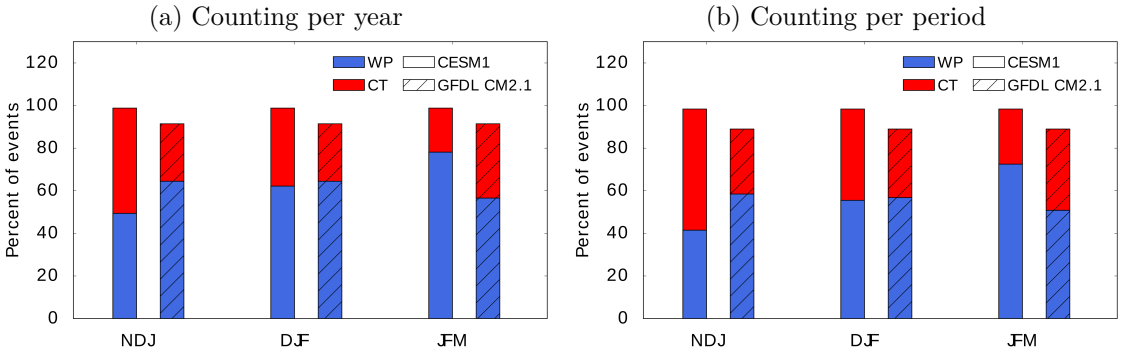

Figure 3.8 – Comparison of the proportion (percent) of WP (blue) and CT (red) El Niño events according to the considered season of the SSTA peak: November-January (NDJ), December-February (DJF) and January-March (JFM) for the PI-control simulation of CESM1 (1801 years) and GFDL CM2.1 (500 years, hatched). Fig 3.8a presents the proportion of each event when counting events per year, Fig 3.8b when counting events per period during which the criterion is met.

It appears that the choice of the season to look at the peak of ENSO is important and a lag of two months can alter the ratio of the two types of events, regardless of the counting method used. The ratio of WP to CT events can be from 0.5 (NDJ per year) to 3.8 (JFM per year) for CESM1 and from 1.62 (JFM per year) to 2.4 (NDJ per year) for GFDL CM2.1. In CESM1, the ratio may be inverted according to the season. The use of the method per period does not change the type of most frequent event following the season, even if it changes the value of the ratio by changing the number of events selected.

CESM1 PI-control simulation favours CT El Niño events when considered in NDJ season, while favours WP El Niños in JFM season. It is a feature also encountered in observations. Conversely, GFDM CM2.1 PI-control simulation tends to act in the opposite way, increasing the number of CT El Niño events in JFM season even if the proportion of WP events is always higher. The classification of CT/WP event by comparing the value of Niño-3 and Niño-4 indices is strongly dependent on the chosen season. Note, however, that the NDJ and DJF seasons show less important variability in GFDL CM2.1 PI-control and observations datasets than in CESM-LE.

Despite the sensitivity of the definition to the region or season, both CGCMs tend to simulate more WP events than CT events in contrast to previous studies. Stevenson et al. (2017) using the 850 control simulation of the CESM last millennium ensemble found a proportion of WP events equal to 31 % with the definition of Kug et al. (2010), 36 % with the definition of Kao and Yu (2009) and 44 % with the definition of Yeh et al. (2009a), that is less WP than CT events. However, these differences in results could come from the shifted Niño regions they used, at least in the case of the Kug et al. (2010) method (the westward shift is not mentioned for the two others methods Stevenson et al. (2017) used). Indeed, we will show in paragraph 3.2.3.3 that shifting westward the metrics boxes leads to a favoured classification of events in CT El Niño events.

We further analyse changes in CT/WP events occurrence ratio with global warming in CESM-LE (with the method based on periods). Changes in the frequency of occurrence of both CT (Fig. 3.9a) and WP (Fig. 3.9b) El Niño events in historical and RCP8.5 simulations compared to the PI-control simulation show large discrepancy depending on the choice of the peak season. The frequency of CT El Niño events may slightly decrease in RCP8.5 simulations compared to historical simulations (NDJ season) or strongly increase (JFM season). Only changes for the DJF season are not statistically significant. For all seasons, the frequency of occurrence of CT El Niño events increases compared to PI-control simulation. Conversely, the frequency of occurrence of WP El Niño events may slightly decrease in JFM (change not statistically significant) or strongly increase in DJF and NDJ (changes statistically signifi-

cant). The resulting changes in the occurrence ratio of CT / WP El Niño events (Fig. 3.9c) with global warming are contradictory depending on the considered season. The ratio is projected to decrease with global warming, even below the ratio of the PI-control simulation when considering the NDJ season, while it is projected to increase, until the proportion ratio of CT and WP El Niño events is inverted, when considering the JFM season.

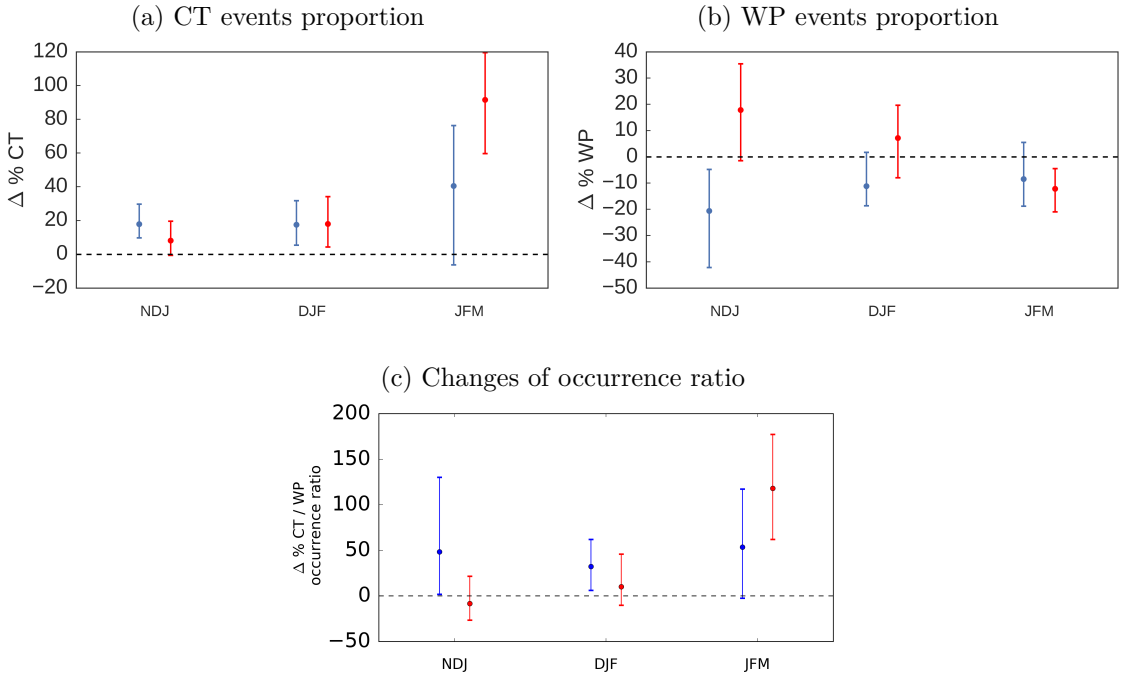

Figure 3.9 – Proportion of El Niño events according to the season of the peak in (blue) historical simulations and (red) RCP8.5 simulations. The considered seasons of El Niño peak are November to January (NDJ), December to February (DJF) and January to March (JFM). Frequencies of occurrence of (Fig. 3.9a) CT and (Fig. 3.9b) WP El Niño events expressed as difference relative to the PI-control simulation. The relative differences of frequencies of occurrence are computed following Stevenson et al. (2017). (Fig. 3.9c) Associated relative differences of CT / WP El Niño occurrence ratios compared to the PI-control ratio. The occurrence ratios are computed following Yeh et al. (2009a). The error bars correspond to the inter-members spread estimated through the interquartile range.

3.2.3.3 Sensitivity to the region

Another issue concerns the most appropriate regions of ENSO variability. Wittenberg et al. (2006) noted that the tropical Pacific SST variability is shifted by 20-30° westward in GFDL CM2.1 simulations compared to the observed spatial pattern. This common bias is due to the westward shift of the climatological Cold Tongue, shifting ENSO variability westward (see paragraphs 2.1.2.2 and 2.1.4). Kug et al. (2010) suggested to use modified Niño-3 and Niño-4 indices, defined on the areas 5°S-5°N, 170°-110°W and 5°S-5°N, 140°E-170°W respectively to characterise ENSO variability within the Cold Tongue bias. The modified regions are then the traditional regions displaced 20° to the west.

The variability in each Niño regions are compared between observations datasets, GFDL CM2.1 and CESM-LE simulations (Fig. 3.10a). GFDL CM2.1 tends to overestimate variability more than CESM-LE, as pointed out by Bellenger et al. (2014), and both tend to overestimate variability compared to that observed, with a discrepancy between simulated and observed values increasing when moving westward. It is less pronounced in CESM-LE than in GFDL CM2.1, consistent with the fact that the Cold Tongue bias is reduced by 30-40 % in CMIP5 models compared to CMIP3 models Bellenger et al. (2014). Although the bias is less pronounced in CESM-LE, we use both models to compare WP-CT classification methods (Fig. 3.10b).

Three different methods of counting are compared, both presented previously and a new one (called "Per DJF year") that allows to remain consistent with other studies because it is not clear whether they used a minimum duration threshold to define an El Niño event. Kug et al. (2010) found 121 WP-modified El Niños and 84 CT-modified El Niños with the same GFDL CM2.1 model. It is different from the number of events found by the first two methods. It has been verified that the differences come from the definition: they defined an event, whether CT or WP, when one of both mean winter Niño-3 or Niño-4 indices is greater than 0.5 °C, without taking into account a minimum duration for the definition of an event. Capotondi (2013) defined normal and modified El Niño events with conditions only on traditional Niño indices or with conditions only on modified Niño indices respectively. Each of these small variant definitions results in different numbers of selected events and therefore different proportions of CT and WP El Niños. The sensitivity test is applied for El Niño peaks defined during the DJF season (see paragraph 3.2.3.2). The first (second) column of Figure 3.10b can thus be directly compared to the second column (DJF) of Figure 3.8a (Figure 3.8b).

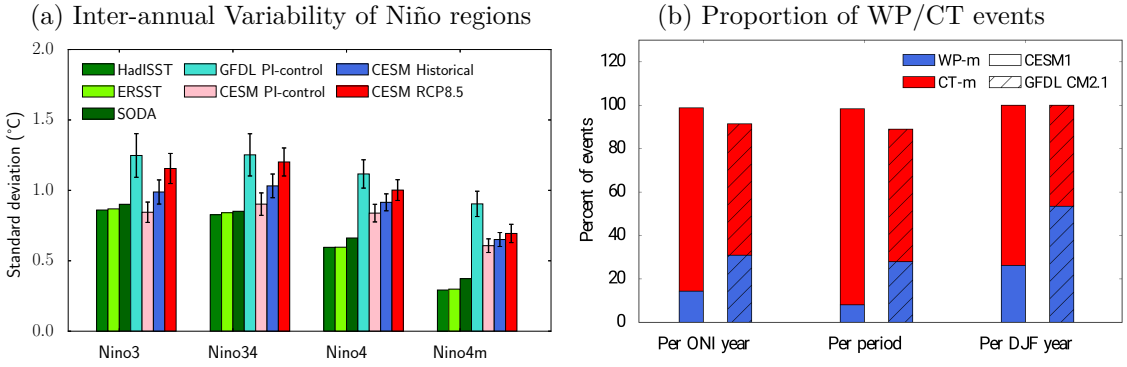

Figure 3.10 – (Fig. 3.10a) Inter-annual variability computed over different regions: Niño-3 (5°S-5°N, 150°-90°W), Niño-34 (5°S-5°N, 170°-120°W), Niño-4 (5°S-5°N, 160°E-150°W) and Niño-4m (5°S-5°N, 140°E-170°W). The variability is computed over period of 68 years, like the observations dataset duration, for the PI-control simulation of CESM-LE (pink), GFDL CM2.1 (turquoise), historical (blue) and RCP8.5 (red) simulations of CESM-LE. The error bars in the PI-control values correspond to the spread of overlapping 68-year periods, taken every 50 years, included in the duration of the simulation. The error bars in the historical and RCP8.5 simulations correspond to the spread between members. (Fig. 3.10b) Proportion (percent) of WP-m (blue) and CT-m (red) El Niño events defined in DJF from the modified regions Niño-3m (5°S-5°N, 170°-110°W) and Niño-4m, for the PI-control simulation of CESM (1801 years) and GFDL CM2.1 (500 years, hatched). Three different methods of counting are compared: per ONI year, per period during which the criterion is met or per DJF winter during which the criterion is met (regardless of duration).

Even if the choice of the method does not change which type of event is more frequent in CESM-LE, it does in GFDL CM2.1. It is the opposite sensitivity as in paragraph 3.2.3.2. Displacing Niño regions westward favours drastically CT(-m) El Niño events, few SSTA peaks occurring west to the dateline, even if the SSTA variability in this region is higher in CGCMs than in observations (Fig. 3.10a).

This artefact effect can, however, be masked by counting events in DJF season, without condition on duration, as used in many studies. Indeed, the definition of unconditional events over the duration of warming seems to capture more the inter-annual SSTA variability in the central to western Pacific than the variability of El Niño itself, since more WP(-m) El Niño events are detected. Counting per DJF year considers more warming events as El Niño events and the extra events are almost all WP(-m) El Niño events, which are then warming episodes normally not defined as El Niño events. These western warm events could be related to the "double peaked" bias El Niño events of which Graham et al. (2017) revealed the existence in CGCMs and which can be assimilated to WP El Niño events when compositing.

3.3 Correspondence of definitions

Due to the spatial variability expressed by the E and C modes, one might want to compare moderate El Niño events to Central Pacific events on one hand and strong El Niño events to Eastern Pacific events on the other hand. We investigate the relationship between strong/moderate and CP/EP El Niño events in terms of indices evolution and statistics in CESM-LE. Note that we use El Niño composites of the historical simulations in this paragraph.

3.3.1 Temporal evolution of the sea surface temperatures

Strong and moderate El Niño events show different temporal evolution of the E and C indices (Fig. 3.11a). Strong El Niño event has high values of the E-index during the development of the event, from a fast increase from April to August(0) (+2.8 °C per 4 months) to a decrease giving way to the development of an La Niña event in June-July(+1) (visible on the C index). The E index accounts for SST variability in the far eastern Pacific, where the thermocline is shallow and the thermocline feedback more intense than in the central equatorial Pacific. So, when a Kelvin wave is triggered during the development of ENSO (typically during Feb-April Y(0)), the SST increase in the far eastern Pacific, which projects on the E mode, then El Niño develops, which maintains an elevated E. In other words, the first part of the warming in E is due to the forced Kelvin wave acting as a trigger of ENSO, while the second part of the warming in E is more associated with the growing coupled mode. A strong discharge is then captured by the C-index, from June-July Y(1), corresponding to strong La Niña events following strong El Niño events. Moderate El Niño shows similar evolution but with lower positive magnitude of the E-index (3.2 times lower on average) and higher value of the C-index than the E-index from the end of the first year to the decay of the event. It indicates that the SSTA warming associated with the moderate El Niño composite is more pronounced in the central than in the eastern Pacific, corresponding more generally to the definition of CP El Niño event (Yeh et al., 2009a).

This spatial difference between strong and moderate El Niño events is observable on the temporal evolution of the conventional Niño-3 and Niño-4 indices (Fig. 3.11b). For strong (moderate) events, the magnitude of Niño-3 (Niño-4) index, describing the variability of the eastern (central) equatorial Pacific, is much larger (slightly more pronounced) than that of the Niño-4 (Niño-3) index. During strong events, the eastern Pacific experiences strong warming, which corresponds to the definition of EP-events. However, both Niño-3 and Niño-4 indices have similar magnitudes for moderate events, with a shift of 1-2 months in the peak of the Niño-4 index. The classification between CP and EP events for moderate events is thus very sensitive to the peak season in question (NDJ or DJF usually used) as showed in paragraph 3.2.3.2.

3.3.2 Correspondence between El Niño events

The proportion of strong and moderate El Niño events classified as EP or CP El Niño events is investigated. We use historical and RCP8.5 simulations. We compute the probability of occurrence of El Niño events per 10 years, probability over 40 simulated climates. It corresponds to the ensemble-sum of the number of events per 10 years for each year normalised by the number of members (Fig 3.12).

As expected, most of strong El Niño events, whatever in historical or RCP8.5 simulations, are classified as EP El Niños. 87 % and 89 % of strong El Niño events are EP El Niño events in historical and RCP8.5 simulations respectively. However, EP El Niño events are not all strong El Niño events. All strong El Niño have a SST warming in the eastern equatorial Pacific as expected by definition, but all events characterised by greater warming in the eastern than in the centre of the equatorial Pacific in boreal winter are not necessarily strong

(a) Temporal evolution of E and C indices

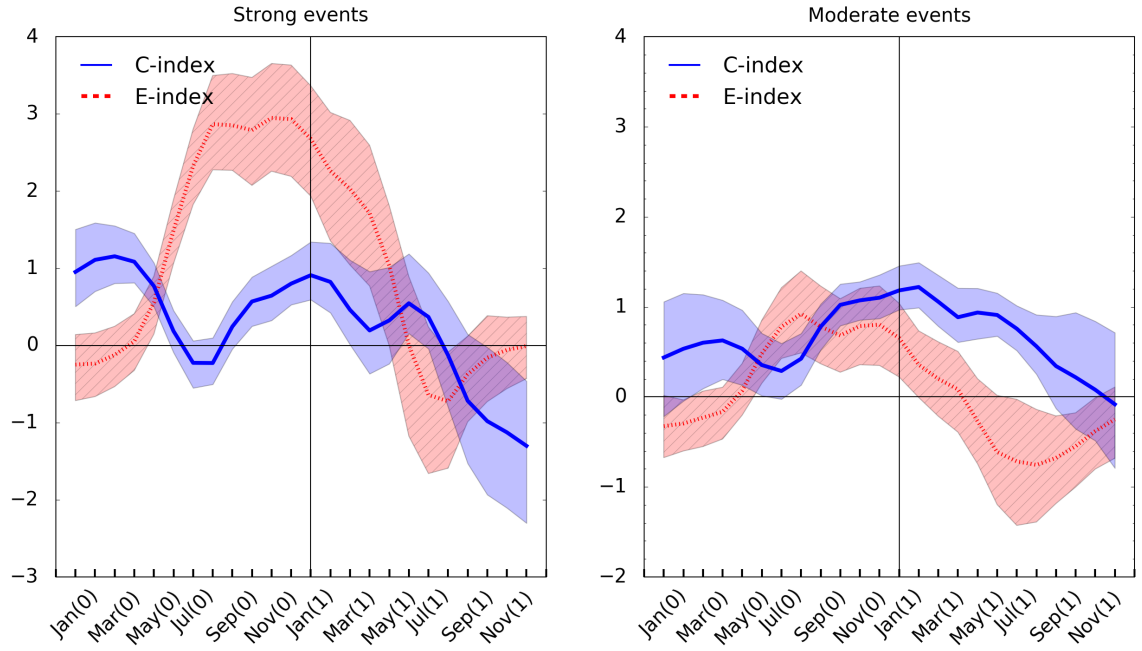

(b) Temporal evolution of Niño-3 and Niño-4 indices

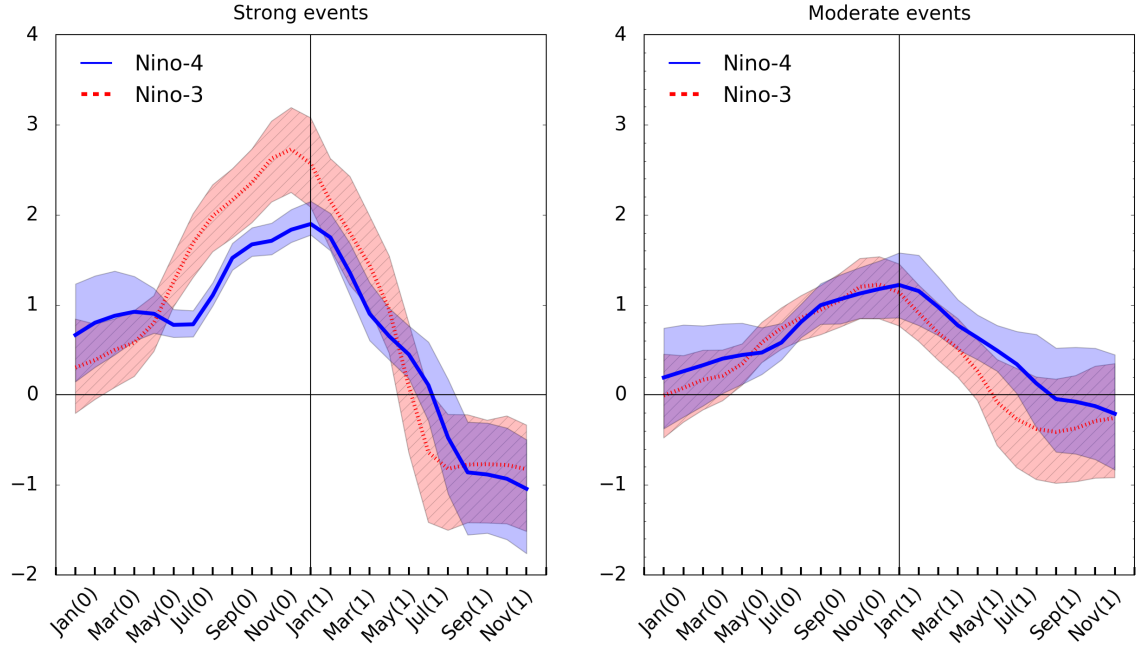

Figure 3.11 – Temporal evolution of CESM-LE historical strong (left) and moderate (right) El Niño events composite for (Fig. 3.11a) the E and C indices and (Fig. 3.11b)the Niño-3 and Niño-4 indices. The shading indicates the range of values between the 25 and 75 percentiles of the distribution of the composite.

events as defined by the E-index. It is consistent with Dewitte and Takahashi (2017), who showed that even if by definition strong El Niño events are preferentially EP events, this is not the opposite case of the moderate events. The latter may as well be moderate Eastern Pacific El Niño, having not passed the threshold of the Bjerknes feedback, counteracted by easterly winds in boreal fall before the winter peak.

Interestingly, the proportion of EP El Niño events being also classified as moderate El Niño events tends to decrease, from 35 % during the first 50 years of historical simulations to 20 % during the last 50 years of RCP8.5 simulations. Takahashi and Dewitte (2016) and Takahashi et al. (2018) suggested that strong El Niño events are EP El Niño events whose warming in the eastern Pacific reaches a threshold that enhances the Bjerknes feedback. The increased proportion of EP El Niño events being strong El Niño events with global warming could thus be related to an easier enhancement of the Bjerknes feedback. Several reasons may be invoked such as a change in the seasonal cycle of the Bjerknes feedback and the air-sea mode associated (Dewitte and Takahashi, 2017), disconnecting the enhancement from the easterly winds in September that come from the coastal SSTA off Peru. The threshold leading to the enhancement of the Bjerknes feedback may also become easier to reach in a warmer climate, favouring the EP El Niño events to become strong El Niño events.

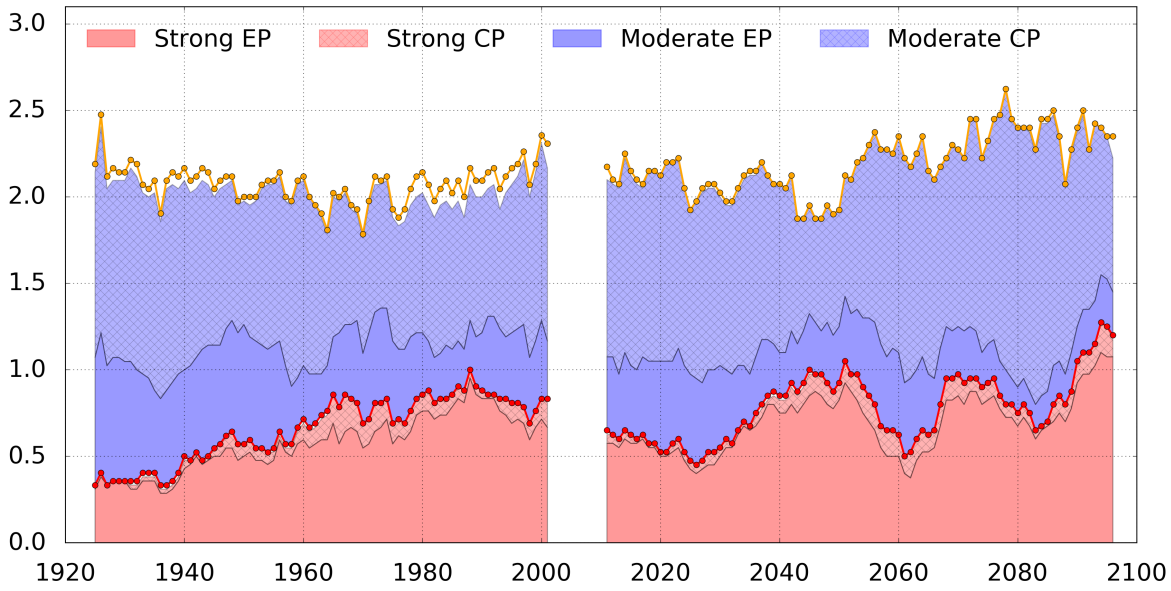

Figure 3.12 – Temporal evolution of the probability of occurrence of El Niño per 10 years of strong (red) and moderate (blue) El Niño and their proportion of being classified as EP (dark colors) or CP (light colors and hatched) El Niño events.

These changes in the characteristics of El Niño events with global warming are further investigated in Chapter 5.

3.4 Discussion: A coupled system in transition

One of the intrinsic complexities of ENSO definition is that this phenomenon is described in relation to a mean state. The question that arises is: **How to define the mean state in a climate that varies over time?**

ENSO characteristics, such as frequency and asymmetry, are modulated at low-frequency, which is related to changes in the mean state (see paragraph 1.3.2 and chapter 4). However, changes in mean state can result from the ENSO rectification effects, that is from residual effects of ENSO asymmetry (see paragraph 1.3.2.3 and Rodgers et al. (2004)). For instance, Lee and McPhaden (2010) argued that the warming trend of the Warm Pool SST in the

central Pacific over the period 1980-2010 is primarily a result of more intense CP El Niño events rather than a mean SST warming due to climate change.

This dependence of the ENSO definition on the mean state, and therefore on the chosen base-period, is all the more problematic as the mean state changes rapidly because due to strong external forcing, i.e. the increase in greenhouse gases. The main issue is on the trend of global warming due to climate change. **Is that possible to entirely separate the signal of global warming from the internal variability of the climate system? If so, how to remove this trend?**

Different methods have been suggested; we investigate in this paragraph three of them: removing a linear trend, removing a quadratic trend (Cai et al. (2018) for instance) or removing a relative SST signal (Zheng et al. (2016); Khodri et al. (2017) for instance).

The main method used in this thesis is to remove a linear trend. To calculate the EOF modes, that are used to define the E and C indices, and thus to define El Niño events, we consider separately the historical and RCP8.5 periods. For each period (and each member), we remove the mean annual cycle and we linearly detrend the SST before the EOF calculation.

Cai et al. (2018) removed the annual cycle of the first 100 years of the simulations, that is to say about the historical period, and quadratically detrended the entire period (concatenated historical and RCP8.5 simulations). In addition to the type of trend, the seasonal reference cycle is not the same as in the linear detrend method. Their underlying assumption is that the seasonal cycle do not change with global warming. Moreover, they applied the EOF analysis over the entire period, while we calculate the EOF over the historical and RCP8.5 periods separately.

In both methods, the strong underlying assumption is that the global warming is uncorrelated to internal variability but affects the frequency of the climate phenomenon. Internal variability is superimposed on global warming.

We will also test a different detrend method, which consists in removing the surface mean state of the tropical Pacific (30°S-30°N) at each time step. This method is used by Zheng et al. (2016); Khodri et al. (2017) and called relative SST anomalies. Unlike previous methods, the subtracted warming is the same (same shape and amplitude) throughout the studied region. The previous methods impose the shape of the trend, but allow the warming amplitude to be different at each point.

The climatological variances of the E-index obtained with the different methods are compared (Fig. 3.13). The linear method leads to greater amplitude of the variability as well as a larger inter-member spread. Conversely, the climatological variance of the E-index obtained with the relative SSTA method shows a seasonal cycle with less variations. Surprisingly, the E-index variance is weaker in RCP8.5 simulations than in historical simulations when applying the relative SSTA method, which corresponds to an opposite result to the other two methods. This result is explained by the intrinsic nature of the global warming trend considered. In the relative SSTA method, the subtracted warming trend is the same in the whole tropical Pacific, while in the other two methods, the subtracted warming trend is different in the different regions of the Pacific. In particular, the eastern tropical Pacific is projected to warm more rapidly than the western tropical Pacific and off-equator regions (see paragraph 5.3.1 and Fig. 5.3). The subtraction of these different trends has a distinct impact on the variability of the eastern Pacific in particular.

The monthly evolution of the climatological variance is similar between methods, even if the monthly rates of changes between historical and RCP8.5 differ. In historical climates, the E-index variance has a significant peak in summer (July-August-September), followed by a second smaller peak in winter (November-December). In RCP8.5 simulations, the peak in E-index variance in summer remains, can be strengthened, while the second peak is shifted to late winter, early spring (February-March-April, FMA). Whatever the method used to remove the warming due to climate change, the E-index variance increases the most in FMA and decreases the most (the relative SSTA method) or increases the least (the other two

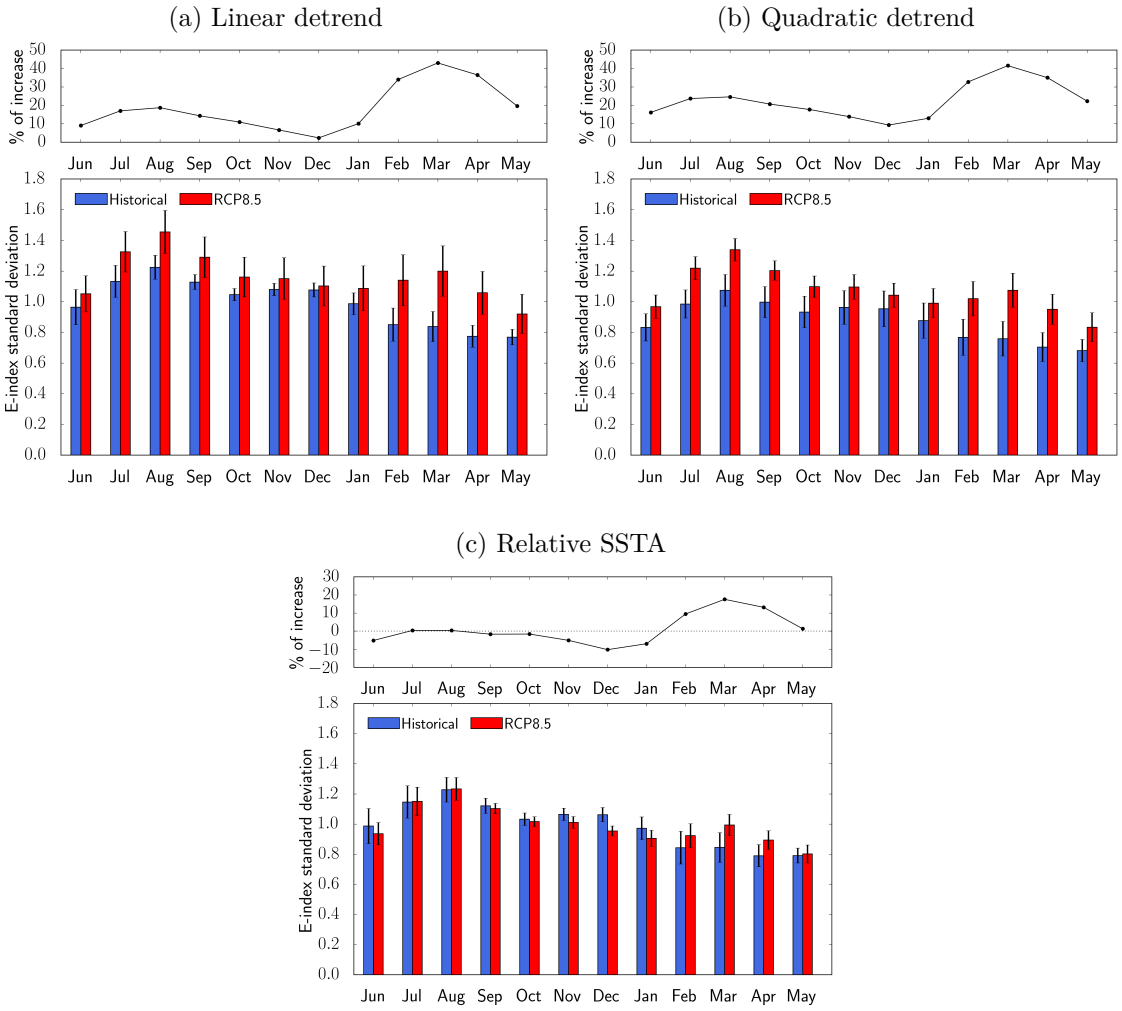

Figure 3.13 – Climatological variance of the E-index for historical (blue) and RCP8.5 simulations with (3.13a) the linear detrend method applied, (3.13b) the quadratic detrend method applied and (3.13c) the relative SSTA method applied on the SST of the tropical Pacific before the calculation of the E-index (10°S-10°N). See text for details on the different methods. The error bars correspond to the spread between the different members of each ensemble. The statistical significance of the changes between historical and RCP8.5 variances has been calculated from a Wilcoxon test and a bootstrap test. The changes are statistically significant at the 95 % level confidence, except for the months of November and December for the detrend methods and the months of May, June, July, August and September for the relative SSTA method.

methods) in December, in RCP8.5 climate compared to historical climate. The increase in FMA is statistically significant at the 95 % confidence level based on a Wilcoxon and a bootstrap test (see paragraph 2.2.4) for all methods. This feature is particularly interesting in the analysis of changes in ENSO statistics with global warming (see Chapter 5).

An important difference between the relative SSTA method and the other two methods is in the way the processes responsible for the warming trend are understood. In the first two methods, the temperature warming (linear or quadratic) is considered only due to climate change. However, the faster warming in the eastern tropical Pacific can also be induced by ENSO in a warmer climate (process change) or by ENSO low-frequency modulation (internal variability). The relative SSTA method leaves the possibility of a possible role of ENSO (and others processes) in the warming trend. The result of the climatological changes in the E-index variance indicates that, whatever the processes considered responsible for the SST warming, the FMA increase in the E-index variance is robust and due to global warming. Possible change in processes that could lead to enhanced warming in the eastern Pacific is not (only) involved. Note that the definition of El Niño events differ between methods, because they are defined from the mean state without the warming trend. It could be interesting to analyse the spatial pattern and evolution associated with El Niño events defined from the relative SST method. Impact of internal processes onto the warming trend in the eastern Pacific could thus be diagnosed.

Note that another method taking into account the warming pattern over a different spatial scale, like the relative SST method, is defined by Williams and Patricola (2018). Using the relationship between rainfall and SST warming in the tropical Pacific during El Niño events, they defined a SST-based index to estimate the longitude of the centre of action of the El Niño event. Their index tracks the zonal shift of the ascending branch of the Walker Circulation through the SST threshold associated with the atmospheric convection. To determine the SST threshold, they use the mean tropical SST over 5°S-5°N as a reference. The main advantage is that the index integrates changes in SST with climate change and does not require to define SST anomalies relative to an arbitrarily chosen climatology. This method is particularly suitable for precipitation that is not linearly impacted by climate change. As a perspective, it would be interesting to evaluate the relationship between their index of convective longitude and the E-index during historical climates, and whether this relationship changes with global warming. This could provide more insight into the non-linear relationship between SST and convection in the eastern Pacific (see chapter 5).

Synthesis and Perspectives

A lot of different paired indices have been suggested in recent studies to characterise ENSO diversity and its spatial diversity. However, numerous studies highlighted that ENSO definition is dependent on the metrics used (Singh et al., 2011; Stevenson et al., 2017). This raises the difficult consensus of El Niño definition. Two different methods with different approaches of ENSO are compared: the strong/moderate method highlights the ENSO amplitude in two spatial patterns of variability, whereas the EP/CP definition is based on the traditional SST indices in fixed regions.

- EP/CP method

The main advantage of this method is its simplicity, it only requires calculating the traditional indices Niño-3 and Niño-4 during winter. Past studies using CGCMs focused on Niño-3 or Niño-3.4, that is fixed regions, to define El Niño, hypothesising that the warming centre associated with El Niño was correctly simulated by CGCMs, or shifting the regions westward to take into account at least one common bias of CGCMs, the Cold Tongue bias. Graham et al. (2017) showed that the equatorial cold bias can lead to the existence in CMIP5 CGCMs of "double peaked" El Niño events that have never been observed. These "double peaked" events may be mistaken for a central El Niño event when composited. The impact of CGCM biases, particularly pronounced in the fixed regions used in this definition, limits the confidence that can be placed in the results obtained by this method. Moreover, the definition of El Niño events depends on the winter months selected. Lag of one month in the winter season changes the classification of El Niño events, also in observation datasets. It finally appears that the definition is hardly robust in either observations or models.

- Strong/moderate method

The main advantage of the method is its independence from fixed regions and, therefore, from model biases. Indeed, the classification of strong/moderate El Niño events from the amplitude of the first mode of variability of the tropical Pacific allows not to be constrained by the localisation of the warming. However, the bi-modality of the tropical Pacific variability, on which the definition of strong/moderate El Niño events of Takahashi et al. (2011) is based, does not appear clearly in CESM-LE. Takahashi and Dewitte (2016) showed that the ENSO regimes of strong and moderate events may be linked to non-linear processes in the Bjerknes feedback. But, the determination of a threshold distinguishing ENSO regimes is not yet well understood. Thus a variation of $\pm$ 5 % of the threshold leads to a variation of the number of strong El Niño events from 225 (-5.1 %) to 262 (10.5 %) for the historical simulations and from 271 (-10.3 %) to 322 (6.6 %) for the RCP8.5 simulations in CESM-LE. Overall, this method provids robust statistics in estimating ENSO amplitude changes with global warming in climate models (see Cai et al. (2018), Chapter 5 and Annexe A).

Synthesis and Perspectives

- ENSO and the mean state

Different issues arise from the definition of ENSO as a departure from the mean state. First is the definition of the mean state. The underlying problematic is to take into account the low-frequency variability (see paragraph 1.3.2). Fedorov and Philander (2001) showed that by defining the inter-annual oscillation of El Niño from a mean state that fluctuates on the decadal scales rather than from a time-averaged temperature of the past periods, the interpretation of an exceptionally long El Niño became a record of the persistence of warm background conditions. Kang and Kug (2002) suggested to define El Niño events as a departure from the mean state of non-ENSO years, because of the asymmetry between El Niño and La Niña events. Indeed, El Niño being larger than La Niña, the time mean state could be biased toward warmer conditions.

Once removed the low frequency variability, the second issue is the definition of the seasonal cycle. Should we consider a constant seasonal cycle over the period considered (entire periods of historical simulations up to 100 years, depending on the studies) or a seasonal cycle that varies with decadal fluctuations? The computation of anomalies with respect to the seasonal cycle is directly linked with the previous point. In this study, as in many studies, the seasonal cycle is considered stationary over the considered period (respectively historical and RCP8.5 in this study). However, beyond decadal fluctuations, this method makes the strong assumption that the climate system is stabilized, which is not the case for future simulations given the strong external forcing. Others methods could be to apply a filter, as for instance a 13-month Hanning filter, to remove any remaining seasonality (Singh et al., 2011) or to use complex empirical orthogonal functions to separate ENSO from the seasonal cycle and its spatiotemporal behaviour (Boucharel et al., 2013). Cai et al. (2018) removed a constant annual cycle, but of historical periods for the entire timeserie of historical and RCP8.5 period. In that case, the underlying assumption is that the seasonal cycle does not change with global warming. When analysing current observations, an usual method is to remove a 30-years running mean climatological SST, which takes into account a possible trend due to global warming. Note that in our comparative analysis of observations, we remove a constant annual cycle over the considered period.

Chapter 4

Low-frequency modulation of ENSO diversity

Contents

4.1 Preamble

ENSO properties (amplitude, frequency, spatial distribution) exhibit low-frequency variations, at decadal to multi-decadal time scales (Timmermann, 2003; Cibot et al., 2005). Different sources of modulation have been suggested, including stochastic origin, internal variability in the tropical Pacific, extra-tropical atmospheric or oceanic teleconnections, or external forcing (see paragraph 1.3.2).

The modulation of ENSO spatial diversity by the tropical Pacific mean state has also been highlighted. In particular, stronger zonal mean SST gradient and trade winds (i.e. La Niña-like SST pattern) are associated with a higher occurrence of CP El Niño events (McPhaden et al., 2011; Choi et al., 2011; Chung and Li, 2013). However, the mechanisms of the decadal modulation of ENSO and its flavour are still unclear.

Many studies argued that, in turn, ENSO non-linearities associated with El Niño-La Niña asymmetry can induce residuals, which modulate the tropical Pacific mean state through internal rectification processes (Timmermann and Jin, 2002; Jin et al., 2003a; Rodgers et al., 2004; Schopf and Burgman, 2006). This might be attributable to a two-way feedback between the climate state and ENSO. While ENSO induces tropical Pacific decadal variability through a non-linear rectification effect, the climate state provides favourable conditions for a specific regime of ENSO (Choi et al., 2009). As an example, the mean SST warming in the eastern Pacific develops with the intensification of ENSO activity periods and an enhanced El Niño-La Niña asymmetry.

Understanding the relationship between low-frequency ENSO modulation and the tropical Pacific mean state is crucial, especially in the context of global warming. ENSO modulation can, indeed, lead to a confused detection of the anthropogenic influence. As an example, Zheng et al. (2018) showed in CGCMs that the diversity of the ENSO amplitude changes due to the internal variability is comparable to the diversity of the projected ENSO amplitude changes with global warming.

In this chapter, we investigate the low-frequency modulation of ENSO diversity by the tropical Pacific internal variability, in the absence of any variation in external forcing. In that case, the internal variability of the system can emerge from the integration of atmospheric noise by a passive ocean through mixing layer processes (Clement et al., 2015), or from coupled interactions with the high-frequency variability of the atmosphere (see paragraph 2.1.2.3).

The relationship between the tropical Pacific mean state, ENSO modulation and ENSO diversity modulation has been widely investigated in the GFDL CM2.1 PI-control simulation (Kug et al., 2010; Choi et al., 2011, 2012, 2013a). Choi et al. (2011) argued that ENSO flavours depend on the background state in GFDL CM2.1. They showed that the the tropical Pacific decadal variability (TPDV) modulates periods of high-occurrence of CP or EP El Niño events. Choi et al. (2012) showed moreover that the decadal modulation of ENSO amplitude (through the definition of strong and weak-ENSO amplitude periods) and of ENSO spatial diversity (through the EP and CP El Niño events definition) are related in GFDL CM2.1. Strong EP El Niño and CP La Niña events occur more frequently during the period of high ENSO amplitude, while weak CP El Niño and EP La Niña events occur more frequently during the period of low ENSO amplitude. They argued that the residuals induced by ENSO asymmetry (El Niño-La Niña) can generate decadal variability in the tropical Pacific, since they resemble the first mode of the TPDV, especially during the mature phase of the decadal oscillation. The second mode of the TPDV would then be representative of the transition of the decadal oscillation phase. Finally, Choi et al. (2013a) showed in a set of CGCMs including GFDL CM2.1 that the strength of the relationship between the first mode of the TPDV and the ENSO residuals further intensifies the interactive feedback between the two processes.

We thus compare the behaviour of the long-term PI-control simulation of CESM-LE and GFDL CM2.1, in which the external forcing is fixed. These simulations are longer than the time scales of ENSO internal variability (Wittenberg, 2009; Stevenson, 2012).

After having determined the modes of low-frequency variability simulated in CESM-LE (paragraph 4.2), we will investigate the relationship between the different flavours of El Niño and the low-frequency variability of the tropical Pacific (paragraph 4.3). Central Pacific (CP) and Eastern Pacific (EP) El Niños on one side, strong and moderate El Niños on the other side are analysed (see paragraphs 1.1.2 and 3.2 for more details on ENSO flavours). ENSO modulation is therefore apprehended through its variability and its spatial diversity.

4.2 Low-frequency modulation of the tropical Pacific

4.2.1 Variability of tropical Pacific surface temperatures

4.2.1.1 Inter-annual variability

A wavelet analysis (see paragraph 2.2.2.4) is used to determine the main time-scales of ENSO variability. Wavelet analysis allows to visualise on the same graph the temporal (x-axis) and frequency (wavelet period in years on the y-axis) evolution of the variance of the ENSO index. Following Torrence and Compo (1998), a Morlet wavelet analysis is applied on the E (Fig. 4.1 and 4.3) and C (Fig. 4.2) indices. The wavelet analysis has been corrected as suggested by Liu et al. (2007). They showed that the initial method has a bias that favours low frequencies and does not allow a comparison of the peaks between the different wavelet scales because the energy is not comparable. This latter must be divided by the scale associated with it to compensate the bias.

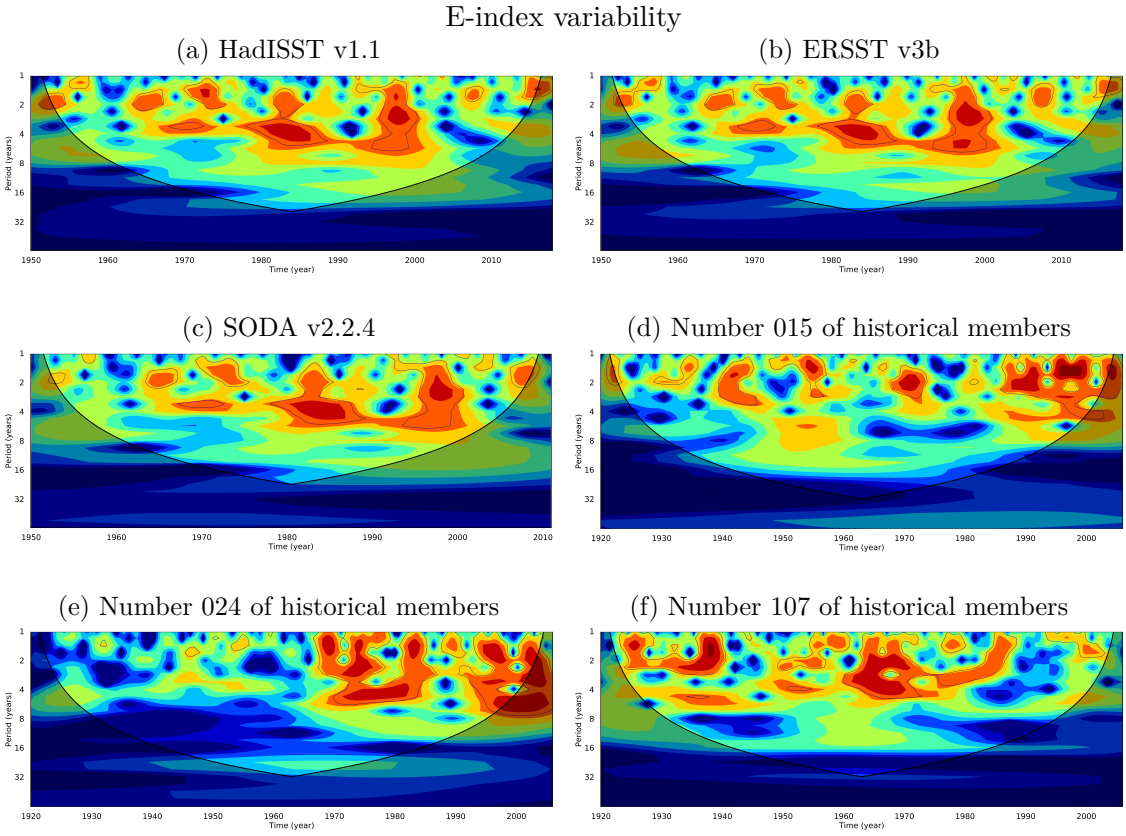

Figure 4.1 – Wavelet power spectrum using the Morlet wavelet of the E-index of (4.1a) HadISST v1.1 (1950-2017), (4.1b) ERSST v3b (1950-2017), (4.1c) SODA v2.2.4 (1950-2010) and (4.1d) member 15, (4.1e) member 24 and (4.1f) member 107 of CESM-LE historical simulations (1920-2005). The shaded contours are at normalised variance of 0.25, 0.5, 1, 2, 4, 8 and 16 ($°C^2$). The black contours enclose the 95 % significance regions of energy, when comparing to a red-noise background spectrum. Hatch indicates the cone of influence where zero-padding reduces the variance, that is where edge effects become important.

The observed wavelet power spectra of the E-index (Fig. 4.1a, 4.1b and 4.1c) and C-index (Fig. 4.2a, 4.2b and 4.2c) emphasize changes with time of the ENSO variability time-scales.

Periods of high oscillation frequency alternate with periods of lower frequency, such as, for the E-index, the 1960-1975 (2-4 years) and 1980-2000 (4-6 years) periods highlighted by An and Wang (2000). The change in oscillation frequency is concomitant with the 1976-77 climate shift that caused inter-decadal change in dominant EP-ENSO period (Kao and Yu, 2009). The period 1980-2000 of low frequency includes the strong (EP) El Niño events of 1982-1983 and 1997-1998, pointed out by strong E-index amplitudes. Conversely, the 2000s saw a decrease in the E-index variability, simultaneous with observed changes toward an amplified central Pacific variability period (Fig 4.2). This recent period of low activity in the eastern Pacific is comparable to the period 1950-1960, while the central Pacific has already experienced periods of similar oscillation frequency, but of lower intensity than the recent period. This feature can be related only to the internal variability of the climate system (Yeh et al., 2011) rather than to a response to the increasing greenhouse gases concentration (Yeh et al., 2009a).

The C-index wavelet power shows less variation in oscillation periods, between 2 and 5 years, than the E-index and no change occurred with the climatic shift of 1976-77, unlike the E-index, consistent with Kao and Yu (2009). Note that the amplitude of the C-index variance is less pronounced than that of the E-index in observations dataset (Fig. 4.2a, 4.2b, 4.2c).

Interestingly, historical runs of CESM-LE (Fig. 4.1d, 4.1e, 4.1f for the E-index, and Fig. 4.2d, 4.2e, 4.2f for the C-index) display a realistic simulation of the ENSO variability, with a range of variability (2-8 years) closer to that observed than the previous generation of CGCMs that tended to center the variability around 2 years (Meehl et al., 2001; Dewitte et al., 2007). However, the C-index variability is less realistically simulated, with in particular an oscillation period between 4–8 yr rather than between observed 2–4 yr (Fig. 4.2d, 4.2e, 4.2f).

Moreover, the simulated variability is not so regular as it used to be in CGCMs (see paragraph 2.1.2.2). Despite slightly stronger magnitudes, the alternation of periods of high and low activity and of different duration is realistically simulated. These periods can be relatively long, as is the case for the member 024 with a low activity period of 45 years in the eastern Pacific (Fig. 4.1e). A large spread of wavelet power spectra is observed among each historical member of CESM-LE. Note that periods of high C-index variability seem to be more concomitant with periods of high E-index variability than in observations.

Finally, EP and CP-ENSO experiment low-frequency modulation of their variability, with alternation of high and low activity period as well as changes in the preferential period of oscillation. It is consistent with results of Torrence and Compo (1998) on the reconstructed Niño-3 index since 1871. They highlighted an alternation of periods of several decades of high activity (1880-1920 and 1960-1990) and lower power (1920-1960).

This observed internal variability is the topic of the chapter. However, due to the length of the observation records, it is difficult to diagnose this low-frequency modulation (Wittenberg, 2009; Stevenson et al., 2010; Stevenson, 2012). Our analysis of the ENSO internal variability is therefore based on PI-control simulations of two long-term CGCMs, CESM-LE (1801 years) and GFDL CM2.1 (500 years) (see paragraph 2.1 for a description of the models).

Wittenberg (2009) showed that periods of low or high variability can last up to 100 years (their M3 and M4 periods for instance). The wavelet analysis of the PI-control E-index (Fig. 4.3) confirms this result with a low variability period of 100 years in GFDL CM2.1 around the year 500 and in CESM-LE around the year 1300 for instance.

GFDL CM2.1 simulates stronger magnitudes of variability than CESM-LE and observations, which is a known bias of CGCMs in general, of GFDL CM2.1 in particular (see paragraph 2.1.4.4). Morevoer, the bias in the shift towards higher oscillation periods (4–8 yr rather than observed 2–4 yr) of the C-index is also present in the CESM-LE PI-control

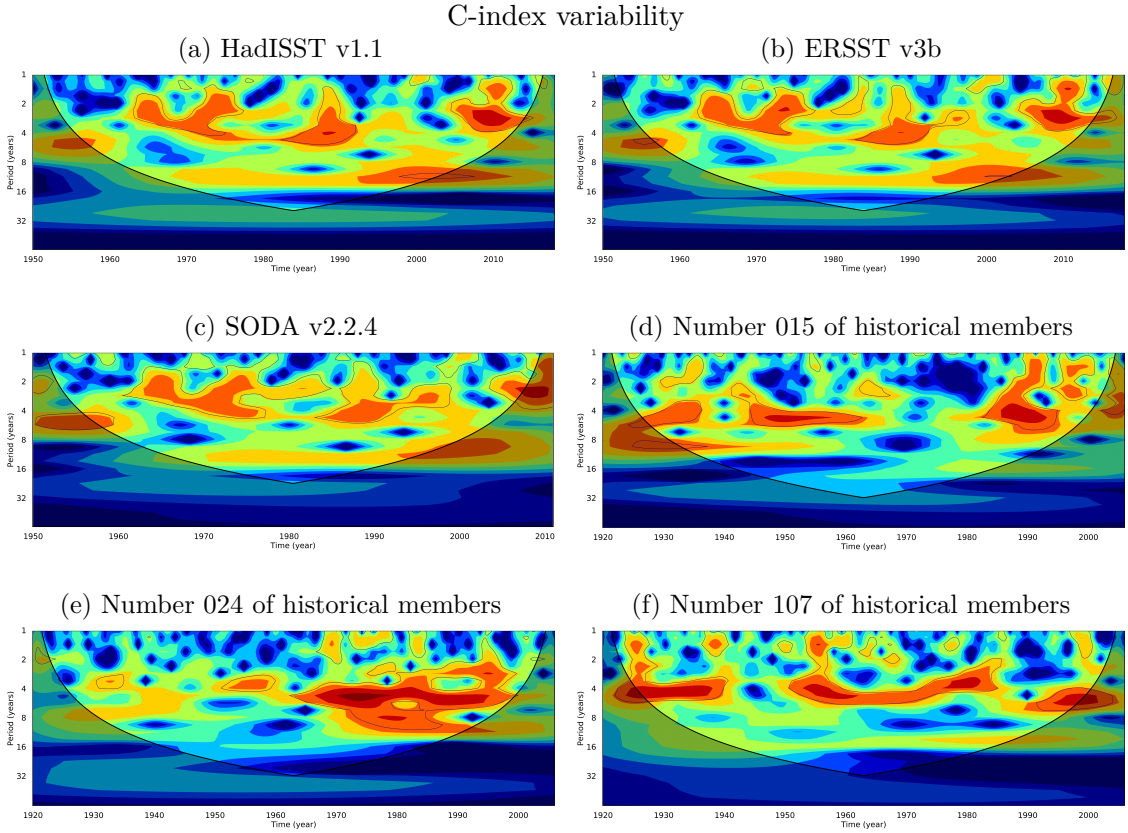

Figure 4.2 – Same as Fig. 4.1 but for the C-index.

simulation and, in a lesser extent, in the GFDL CM2.1 PI-control simulation (not shown).

Using reconstructed SST over the period 1871-1997, Torrence and Compo (1998) suggested that ENSO modulation, defined by the Niño-3 index variance, has a modulation period of 15 yr. Historical simulations of CESM-LE show lower-frequency modulations of the E-index but with disparity between members, ranging from 10-15 to around 30 years timescales for the E-index (Fig. 4.1d, 4.1e, 4.1f). The PI-control simulations of both models show a high power of the E and C indices in the band between 20-35 years. The low-frequency modulation of ENSO, based on the PI-control simulations of CESM-LE and GFDL CM2.1, is investigated in the following paragraph.

4.2.1.2 Low-frequency variability

Following Torrence and Webster (1999); Timmermann (2003); Cibot et al. (2005); Choi et al. (2009), we apply a wavelet analysis to the ENSO indices, in order to characterise the low-frequency modulation of ENSO amplitudes. We first analyse the global wavelet spectrum (that is the time-averaged wavelet spectrum), corrected according to Liu et al. (2007), of the E index (the diagnostic on the C index is not shown). The most powerful frequency band is determined, ranging from 1-8 to 2-16 years following the datasets. For clarity and consistency with previous studies, the frequency band between 2 and 8 years is used (Torrence and Compo, 1998).

We then calculate the inter-annual (2-8 years) wavelet variance of the E-index, called E-Var on the same way as Rodgers et al. (2004); Cibot et al. (2005). It corresponds to the scale-averaged wavelet power between periods of 2 and 8 years, that is the weighted sum of the wavelet power spectrum over scales from 2 to 8 years. The filtered time-series obtained is used to characterise the low-frequency modulation of the preferred ENSO time-scales (Torrence and Webster, 1999; Timmermann, 2003; Cibot et al., 2005). We finally derived the global wavelet spectrum of the rectified E-Var (Fig. 4.4). The same diagnosis is applied to the

(a) GFDL CM2.1 E-index

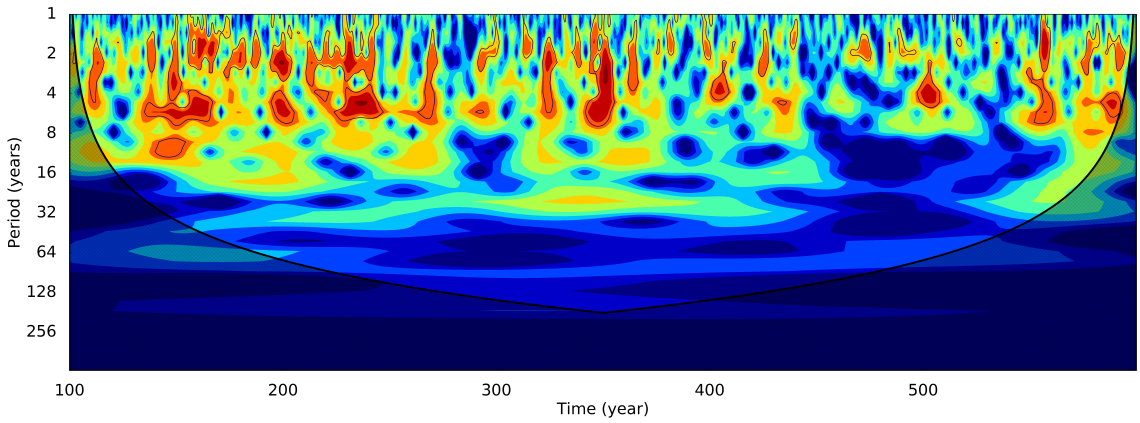

(b) PI-control CESM-LE E-index

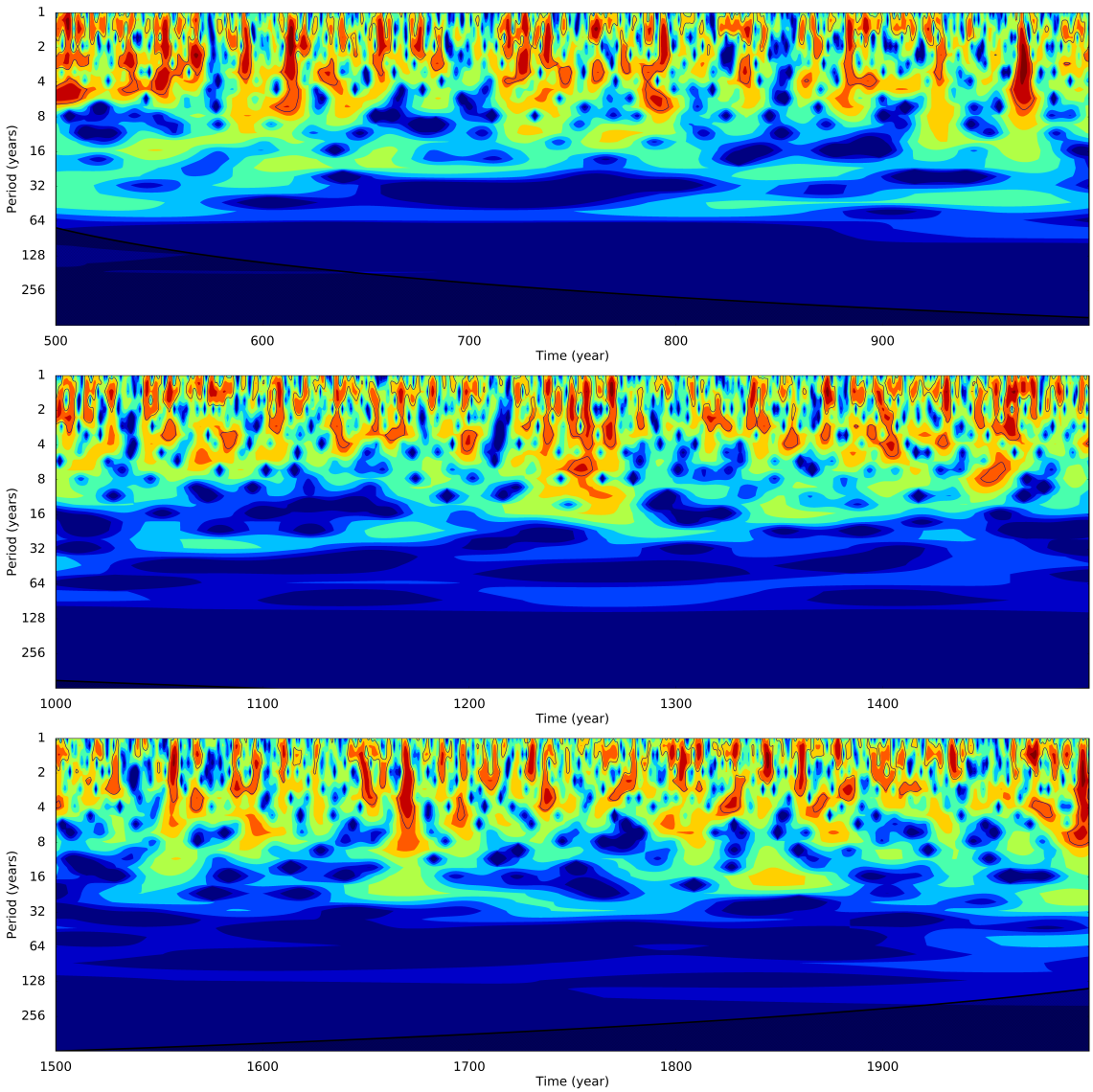

Figure 4.3 – Wavelets power spectrum, using the Morlet wavelet, of the E-index of (4.3a) GFDL CM2.1 PI-control simulation (500 years) and (4.3b) CESM-LE PI-control simulation (1801 years). The shaded contours are at normalised variance of 0.25, 0.5, 1, 2, 4, 8 and 16 ($°C^2$). The black contours enclose the 95 % significance regions of energy, when comparing to a red-noise background spectrum. Hatch indicates the cone of influence where zero-padding reduces the variance, that is where edge effects become important.

C-index.

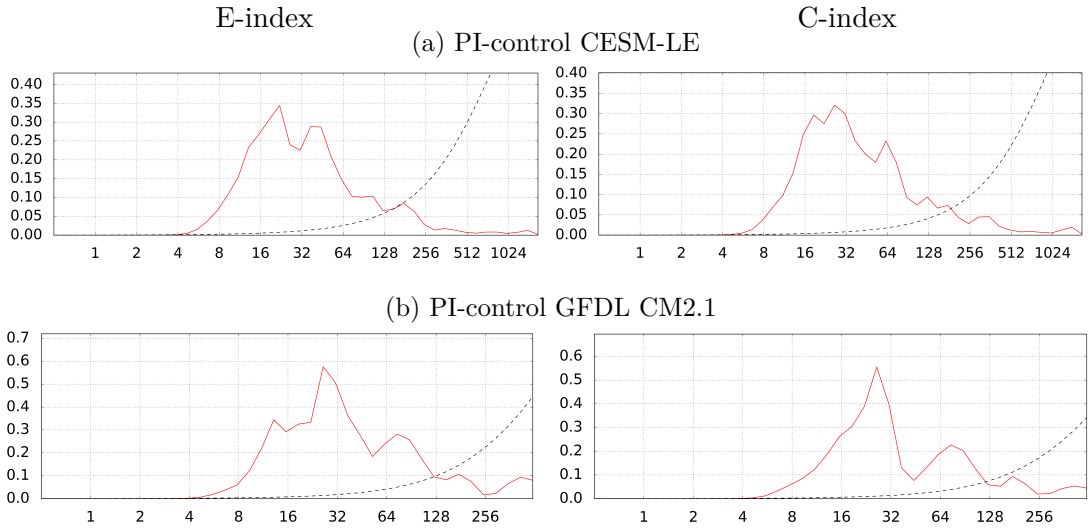

Figure 4.4 – Scaled global wavelets power of (left column) the E-Var index and (right column) the C-Var index of (4.4a) CESM-LE PI-control simulation (1801 years) and (4.4b) GFDL CM2.1 PI-control simulation (500 years). The scale is computed following the bias rectification of Liu et al. (2007).

Note that the GFDL-CM2.1 PI-control simulation has global spectrum peaks of larger amplitude than the CESM-LE PI-control simulation, due to the overestimation bias of ENSO amplitude (see paragraph 2.1.4.4).

The results indicate that the E-Var exhibits low frequency modulation at the dominant periods of 20-40 years for CESM-LE with two peaks around 22 and 37 years respectively, at the dominant periods of 20-30 years for GFDL CM2.1 with a main peak around 26 years. The C-Var index is modulated in the 25-35 years spectral band for CESM-LE, with peaks around 26 and 31 years and centred around 25 years for the GFDL CM2.1. It can also be noted that a smaller peak is present for the GFDL CM2.1 E-Var index, around 13 years, a period that is also found for the Niño-3 and Niño-4 indices in this model (not shown). Previous studies using Niño-3 modulation index suggested a low-modulation in the spectral band of 12-20 years (Torrence and Webster, 1999), 16-17 years (Timmermann, 2003), 10-20 years (Cibot et al., 2005) or still 16 years (Choi et al., 2009). The higher frequency of ENSO modulation could be explained by the length of the datasets used in these studies. As an example, Choi et al. (2012) showed that the spectral peak of their decadal ENSO amplitude index is around 29 years in the GFDL CM2.1 PI-control simulation. Their decadal ENSO amplitude index is calculated in the same way by a wavelet analysis from the modified Niño-3.4 SSTA index (5°S-5°N, 140°E-110°W). By analysing the modulation of the E-Var index in CESM-LE historical simulations (minimum duration of 86 years), a preferential spectral band around 16 years is found, which confirms the need for a long-term simulation to access the ENSO low-frequency modulation (Wittenberg, 2009).

Finally, the 2-8 years variance of E and C indices show decadal modulation around 30 years. A 31 yr window of modulation will subsequently be used to study inter-decadal changes in variance of ENSO and its relationship with the mean state.

4.2.2 Variability of equatorial Pacific subsurface temperatures

The tropical Pacific decadal variability (TPDV) is investigated through the slow varying modes of vertical stratification in the tropical Pacific (Choi et al., 2013a). To calculate the TPDV modes in the CESM-LE PI-control simulation, we apply a 31 yr running-mean filter on subsurface temperature anomalies, averaged between 5°S-5°N, before performing an EOF analysis (Fig. 4.5). The 31 yr running mean filter was chosen from the results on the decadal

modulation of ENSO (see previous paragraph 4.2.1.2).

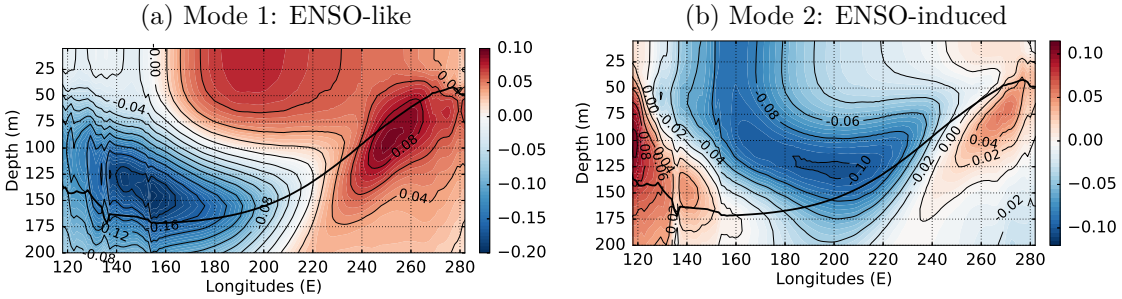

Figure 4.5 – Spatial patterns of the two leading modes of the EOF analyse of the decadal equatorial subsurface temperature anomalies averaged between 5°S-5°N for CESM-LE PI-control simulation. The decadal equatorial subsurface temperature anomalies, de-seasoned and linearly detrended, are computed by applying a 31 yr running-mean filter. In black line is the mean 20 °C isotherm, a proxy of the thermocline. The mode 1 (4.5a) is called ENSO-like mode of the tropical Pacific decadal variability (TPDV), the mode 2 (4.5b) is the ENSO-induced TPDV mode.

Several studies showed that one of the two leading mode of the TPDV is related to the decadal ENSO modulation and thus called the ENSO-induced TPDV mode (Timmermann, 2003; Dewitte et al., 2009). In CGCMs, this ENSO-induced mode can be either the first or the second mode of variability of the EOF analysis (Choi et al., 2013a). To determine which mode corresponds to the ENSO-induced TPDV in the CESM-LE PI-control simulation, the correlation between the associated PC time-series and a decadal modulation index of ENSO amplitude is calculated. The EOF mode that yields the highest temporal correlation between its PC time-series and the ENSO decadal modulation index is classified as the ENSO-induced TPDV.

The ENSO variability modulation index is defined as the 31 yr sliding standard deviation of Niño-3.4 SSTA index. In CESM-LE, the ENSO-induced (ENSO-like) TPDV mode is the second (first) mode of the CESM-LE PI-control simulation and has a correlation equal to 0.71 (0.44) with ENSO modulation index, statistically significant at 99 % confidence level. The correlation between ENSO amplitude modulation and the TPDV ENSO-induced mode in GFDL CM2.1 is equal to 0.94, with the ENSO amplitude modulation index defined from a 20 yr sliding standard deviation of Niño-3m (Choi et al., 2012). It should be noted that, in CESM PI-control simulation, the ENSO-induced TPDV mode is not only correlated with the ENSO modulation defined from the Niño-3.4 SSTA index but also with different SSTA modulation indices all along the central to eastern Pacific (Table 4.1).

	ENSO-like	ENSO-induced
31-yr run-std E-index	0.34	0.62
31-yr run-std Niño-3	0.39	0.74
31-yr run-std Niño-34	0.44	0.71
31-yr run-std Niño-4	0.49	0.66
31-yr run-std Niño-4m	0.37	0.69
31-yr run-std C-index	0.38	0.63

Table 4.1 – Correlation coefficients between indices of ENSO modulation and the two leading modes of the decadal subsurface temperature variability for the PI-control CESM-LE simulation. The correlations are statistically significant at 99 % confidence level.

The ENSO-induced TPDV mode is characterised by an east-west dipole along the equator. Its spatial pattern resemble the ENSO-induced pattern of GFDL CM2.1 PI-control simulation (see Figure 5 of Choi et al. (2011) or Figure 8b of Choi et al. (2012) using a 20 yr running-mean filter on the equatorial subsurface temperatures and Figure 2c middle column of Choi et al. (2013a) using a 10 yr running-mean filter). Several studies showed that this decadal mode

could be induced by the rectification effect of ENSO due to the residual of the asymmetry between El Niño and La Niña onto the mean SST (Timmermann, 2003; Rodgers et al., 2004; Cibot et al., 2005; Schopf and Burgman, 2006; Choi et al., 2012).

The spatial pattern associated with the ENSO-like TPDV mode presents a similar vertical structure than the so-called tilt mode of ENSO (Fig. 2.9). The pattern correlation between these two vertical structures is 0,96, statistically significant at 99 % confidence level (the centred correlation is equal to 0.90 statistically significant at 99 %). The center of the anomalies of ENSO-like TPDV is located further west than for the ENSO mode, which is similar to the results of Choi et al. (2013a) using the CMIP5 database. The ENSO-like TPDV has a weak temporal correlation with the ENSO decadal modulation, despite their similar spatial structure (Table 4.1). This result is coherent with previous studies (Yeh and Kirtman, 2004; Dewitte et al., 2009; Choi et al., 2013a).

A regression of the tropical Pacific SST anomalies onto the principal component of each TPDV mode is performed (Fig. 4.6). The SST anomalies associated with the ENSO-induced mode present a west-east dipole along the equator, directly linked to the ENSO-induced TPDV temperatures profile (Bottom panel of Fig. 4.6). These results are consistent with Choi et al. (2009, 2011, 2013a). Note, however, that the negative anomalies expand more eastward than for the GFDL CM2.1 PI-control simulation with a 10 yr running-mean filter (Figure 3c of Choi et al. (2013a)) and, to a lesser extent with a 20 yr running-mean filter (Figure 9a of Choi et al. (2012)). The SST anomalies associated with the ENSO-like mode extend off-equator, in particular southward, while most of the variability in ENSO mode is constrained along the equator in the CESM-LE.

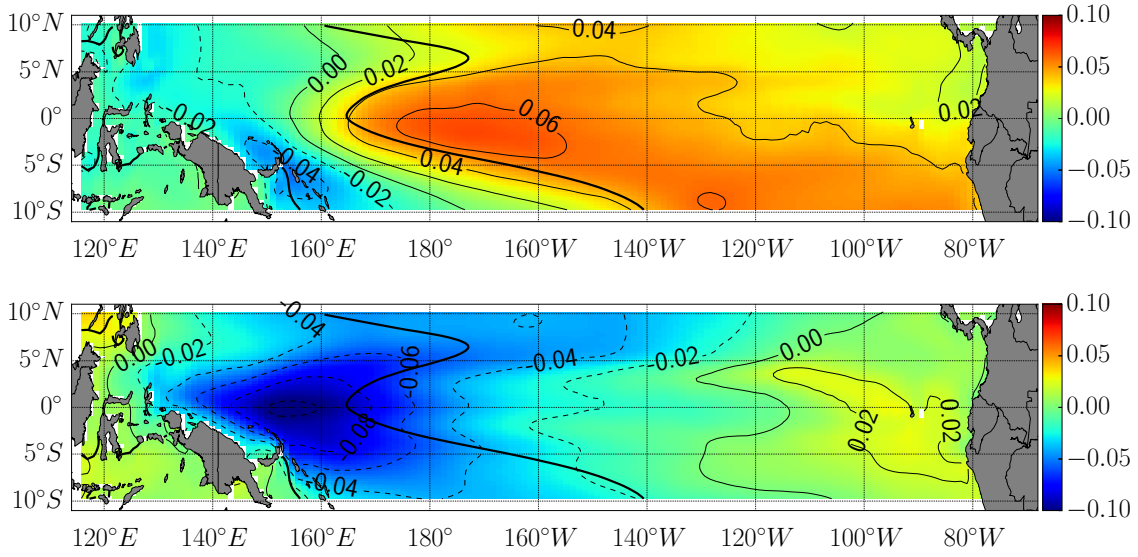

Figure 4.6 – Regressed spatial patterns of the equatorial SSTA onto the (top) ENSO-like and (bottom) ENSO-induced TPDV modes. The TPDV modes are defined from an EOF analyse of the decadal equatorial subsurface temperature anomalies averaged between 5°S-5°N for the CESM-LE PI-control simulation (1801 years). The black line is the mean 28 °C isotherm, a proxy of the warm pool. The decadal equatorial subsurface temperature anomalies, de-seasoned and linearly detrended, are computed by applying a 31 yr running-mean filter.

The ENSO-like mode explains 56.6 % of the total decadal variance and the ENSO-induced mode 23.4 % in the CESM-LE PI-control simulation. It is consistent with the SST TPDV modes of Zheng et al. (2018), applying a 11 yr low-passed filter onto the SSTA. However, the variance explained by these two modes is highly dependant on the CGCM used, the leading mode may not be the same (Choi et al., 2013a). The leading modes of TPDV are thus swapped in CESM-LE compared to GFDL CM2.1, which is mainly used in the compared studies. Whether with a 10 yr or a 20 yr running-mean filter, the first mode in GFDL CM2.1 is the ENSO-induced mode explaining 59 % of the total variance (Choi et al., 2011, 2013a), the

second mode is the ENSO-like mode explaining 22 % of the total variance (Choi et al., 2013a). The difference of explained variances by the two leading modes of subsurface equatorial temperatures variability between CGCMs could induce a different dynamical relationship of ENSO with the mean state. This issue is discussed in more detail in the Synthesis and Perspectives paragraph.

4.3 Relationship between ENSO and mean state

We analyse the possible relationship between the occurrence frequency of the different types of El Niño events and the mean state of the tropical Pacific. The occurrence frequency is defined by counting each El Niño events during the 31 yr sliding periods, following the methods of Kug et al. (2010); Choi et al. (2011). Note that an El Niño event is defined as long as the threshold of the corresponding index (ONI for EP/CP events or PC1 for strong/moderate events) is exceeded and not per winter where the threshold is exceeded as in previous studies (see paragraph 3.2).

4.3.1 Eastern and Central Pacific El Niños

We define Eastern Pacific (EP) and Central Pacific (CP) El Niño events through the definition described in the paragraph 3.2.3 and using DJF mean SSTA indices .

The low-frequency occurrence of EP and CP events shows decadal variations, larger for CP events than for EP events for both models, CESM-LE and GFDL CM2.1 (Fig. 4.7). The correlation between the occurrence frequencies of the two types of events is equal to -0.58 for both models. These negative correlations are consistent with Choi et al. (2011), who found a correlation equal to -0.65 for the GFDL CM2.1 PI-control simulation using the modified SSTA indices, due to the westward Cold Tongue bias. There is an inverse relationship between the EP and CP El Niño occurrences on decadal time scales. Choi et al. (2011) suggested that this inverse relationship is induced by change in the mean state.

Kug et al. (2010) showed that the occurrence frequency of CP-modified El Niño events is correlated (0.70) with the low-frequency mean Niño-4m SSTA index (5°S-5°N, 140°E-170°W) in GFDL CM2.1 PI-control simulation. They used a window of 20 yr to establish the slow-varying indices and analysed the CP El Niño events and the mean state in the modified Niño-4 region, that is shifted of 20° longitude to the west to take into account the westward Cold Tongue bias of GFDL CM2.1. They suggested that this relationship between CP-m occurrence frequency and the warmer state of the tropical decadal variability could be related to either non-linear rectification effect (Timmermann, 2003; Rodgers et al., 2004; An et al., 2005a; An, 2009) or the mean state providing favourable conditions for the occurrence frequency of CP El Niño events.

The same diagnostic is applied using the PI-control simulations of CESM-LE and GFDL CM2.1. The diagnostic is repeated for the occurrence frequency of EP El Niño events. The correlation coefficients with different ENSO modulation indices are calculated (Table 4.2).

The link between number of flavours of El Niño events and SST mean state in the associated region of main variability (Niño-4 region for CP El Niño and Niño-3 region for EP El Niño) is much less pronounced in CESM-LE than in GFDL CM2.1. EP El Niño occurrence frequency is positively correlated at the slow-varying mean SSTA in the eastern Pacific, but the correlation is particularly low with the Niño-3 SSTA index. Surprisingly, EP El Niño occurrence frequency is more correlated with the E-index than with traditional ENSO indices by which the event is defined. The correlation quickly decreases when moving westward towards the Niño3.4 region.

The occurrence frequency of CP El Niño events is linked to the mean state in the western-to-central tropical Pacific in both models (see also Figure 4.8). However, the relationship is more pronounced and more spread westward in GFDL CM2.1 than in CESM-LE.

(a) CESM-LE PI-control simulation ($c = -0.58$)

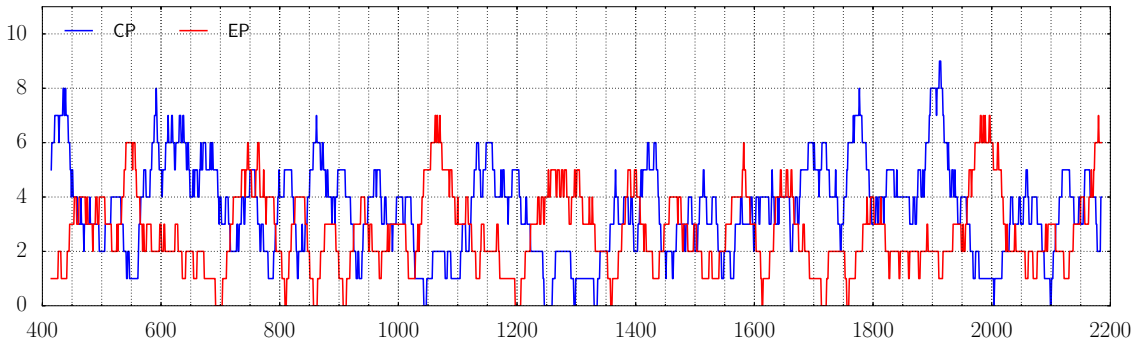

(b) GFDL CM2.1 PI-control simulation ($c = -0.58$)

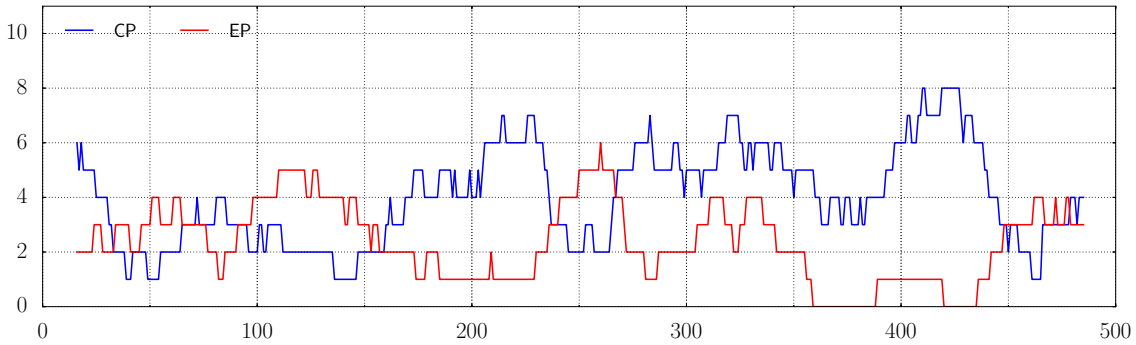

Figure 4.7 – Occurrence frequency of EP (red) and CP (blue) El Niño events over 31 yr sliding periods for the PI-control simulations of (4.7a) CESM-LE (1801 years) and (4.7b) GFDL CM2.1 (500 years). The EP and CP El Niño events are defined by the ONI index and classified by comparing Niño-3 and Niño-4 SSTA indices.

	CESM-LE	GFDL CM2.1
	CP El Niño frequency	
31-yr run-mean Niño-34	0.38	0.38
31-yr run-mean Niño-4	0.54	0.70
31-yr run-mean Niño-4m	0.42	0.65
31-yr run-mean C-index	0.52	0.63
	EP El Niño frequency	
31-yr run-mean E-index	0.44	0.71
31-yr run-mean Niño-3	0.14	0.54
31-yr run-mean Niño-34	-0.01*	0.06*

Table 4.2 – Correlation coefficients between decadal modulation SSTA indices and occurrence frequency of CP and EP El Niño events over 31 yr sliding periods, for the PI-control simulations of CESM-LE and GFDL CM2.1. The correlations are statistically significant at 99 % confidence level except for *.

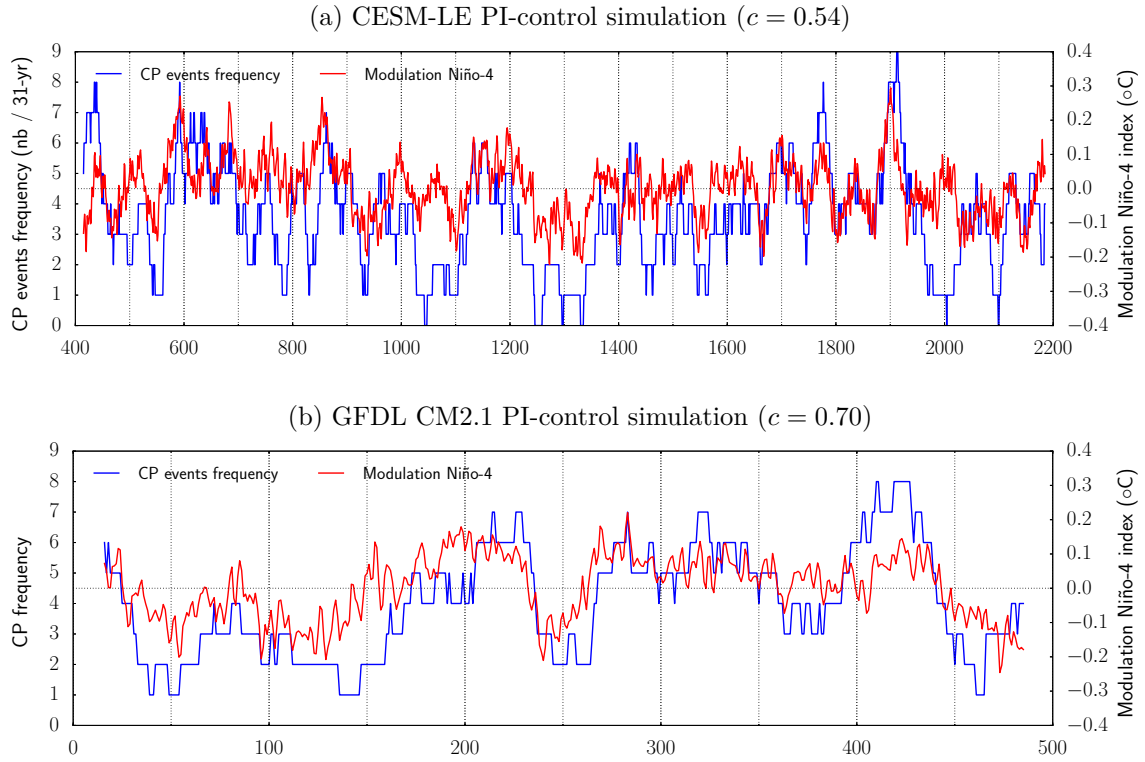

Figure 4.8 – Frequency of occurrence of CP (blue) El Niño events over a 31 yr sliding period and the 31 yr running mean Niño-4 SSTA index for (4.8a) the PI-control simulation of CESM-LE (1801 years) and (4.8b) the PI-control simulation of GFDL CM2.1 (500 years). The corresponding correlation coefficient is indicated and statistically significant at 99 % confidence level.

We investigate the same way the relationship between the occurrence frequencies of El Niño events and the subsurface temperature mean state. The subsurface slow-varying states are characterised by the TPDV modes (see paragraph 4.2.2). Choi et al. (2011) showed that the number of occurrences of CP-modified events is correlated with the ENSO-induced TPDV mode (-0.64 statistically significant at the 99 % confidence level) in the GFDL CM2.1 PI-control simulation.

The relationship between the frequency of occurrence of CP events and the ENSO-induced TPDV mode is not so pronounced in CESM-LE than in GFDL CM2.1 (Fig. 4.9). Surprisingly, the frequency of occurrence of CP events is even more linked to the ENSO-like TPDV mode.

One of the difficulty of the diagnostic is the way to count El Niño events. When counting CP events per year (and not per period as presented in figure 4.9), the correlation coefficient with the ENSO-induced mode goes up to -0.56. And when counting all El Niño events (CP and EP) per year, the correlation coefficient reaches -0.64. It seems that more than a relationship between the occurrence frequency CP El Niño events and the ENSO-induced TPDV mode, it could be a relationship between the low-frequency variability of the tropical Pacific and the ENSO-induced TPDV mode (Table 4.1). It is consistent with the higher correlations when counting all El Niño years, since then the occurrence frequency tends to approach the ENSO amplitude variability. This interaction requires further investigations in CESM-LE.

4.3.2 Strong and moderate El Niños

The same analysis is performed but for strong and moderate events, defined as in paragraph 3.2.2. The correlation between the frequencies of the two types of events is equal to -0.50 for CESM-LE, to -0.69 for GFDL CM2.1 (Fig. 4.10). The correlation is negative, showing an inverse relationship between the number of moderate and strong El Niño occurrences on

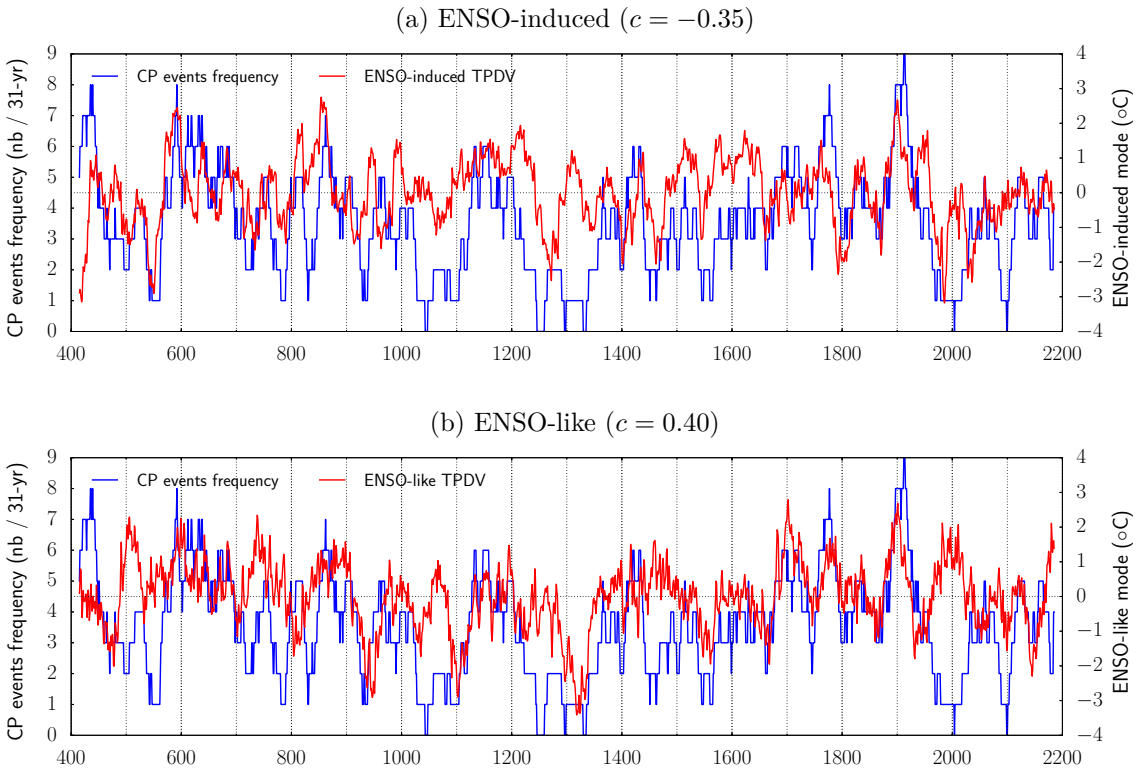

Figure 4.9 – Frequency of occurrence of CP (blue) El Niño events over a 31 yr sliding period and the PC timeserie associated with (4.9a) the ENSO-induced mode and (4.9b) the ENSO-like mode for the PI-control simulation of CESM-LE (1801 years).

decadal time scales. This is consistent with previous results comparing EP and CP El Niño occurrence frequencies. Note that the decadal modulation frequency is larger for moderate events than for strong events.

	CESM-LE	GFDL CM2.1
	Moderate El Niño frequency	
31-yr run-mean Niño-4	0.42	0.51
31-yr run-mean Niño-4m	0.50	0.51
31-yr run-mean C-index	0.51	0.48
	Strong El Niño frequency	
31-yr run-mean E-index	0.63	0.62
31-yr run-mean Niño-3	0.32	0.54
31-yr run-mean Niño-34	0.20	0.23

Table 4.3 – Temporal correlation coefficients between decadal modulation SSTA indices and the frequency of occurrence of strong and moderate El Niño events over 31 yr periods, for the PI-control simulations of CESM-LE and GFDL CM2.1. The correlations are statistically significant at 99 % confidence level.

The correlations between the number of strong and moderate events over 31 years and the slow-varying mean SSTA indices are computed in the same way as for EP and CP events (Table 4.3). There is a positive relationship between the low-frequency occurrence of moderate events and the mean state of the central tropical Pacific, but less pronounced than for the low-frequency occurrence of CP El Niño events, in particular in GFDL CM2.1. Moderate El Niño events tend to be more CP El Niño than EP El Niño events in CESM-LE (see paragraph 3.3.2). However, the physical process associated with each kind of events may not be the same, explaining the difference in relationship.

(a) CESM-LE PI-control simulation ($c = -0.50$)

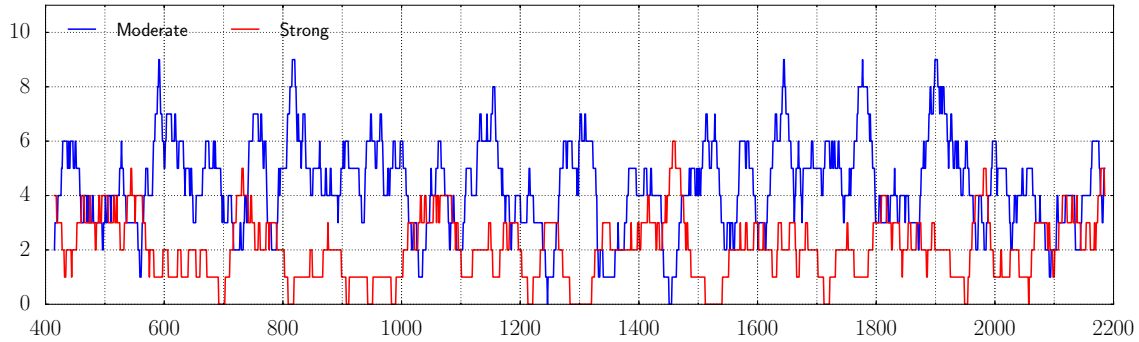

(b) GFDL CM2.1 PI-control simulation ($c = -0.69$)

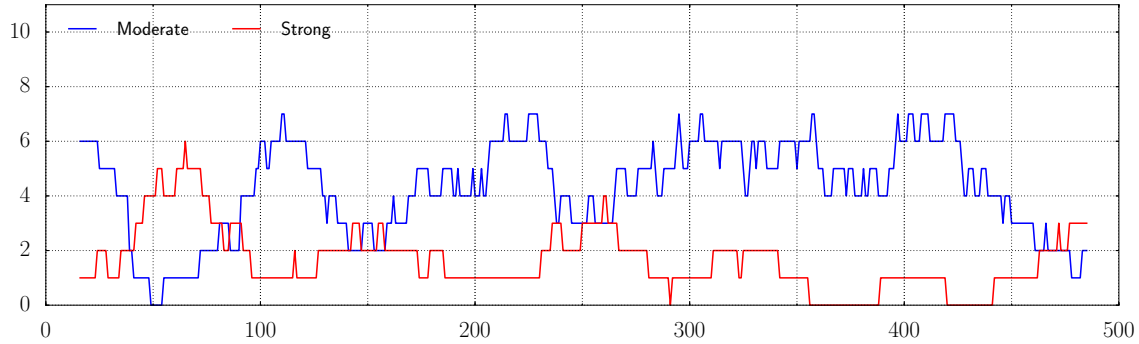

Figure 4.10 – Frequency of occurrence of strong (red) and moderate (blue) El Niño events defined by the normalised PC1 time-series and by the E-index over a 31 yr sliding period for the PI-control simulation of (4.10a) CESM-LE (1801 years) and (4.10b) GFDL CM2.1 (500 years).

The relationship between moderate El Niños occurrence frequency and the ENSO-induced TPDV mode is slightly more pronounced than with CP El Niños. The correlation coefficient is equal to -0.42, statistically significant at 99 % level.

Synthesis and Perspectives

- TPDV modes

The tropical Pacific decadal variability modes in the PI-control simulation of CESM-LE behave in the same way as previous results using different models. The ENSO-induced mode is correlated with low-frequency ENSO modulation, while the pattern of the ENSO-like mode is similar to the spatial pattern of El Niño.

However, in CESM-LE as in others CGCMs (Choi et al., 2013a), the ENSO-induced mode is the second mode of main variability of the equatorial Pacific, which is not the case in previous studies (Rodgers et al., 2004; Cibot et al., 2005). This different characteristics of the tropical Pacific variability could arise from the too strong and too regular variability simulated by previous models. ENSO residuals may act too strongly in these models with respect to observations and this may be sufficient to induce the dominant decadal mode of the model. This question is beyond the scope of this study but deserves further investigation and should be kept in mind as it may reveal different low-frequency dynamic processes depending on the CGCMs. In particular, Choi et al. (2012) suggested that the ENSO-like mode corresponds to the phase transition of the decadal oscillation. The ENSO-induced mode would be a positive feedback with ENSO modulation, reinforcing itself when the amplitude of ENSO modulation increases and being active during the mature phase of the decadal oscillation. The ENSO-like mode would be a negative feedback that leads the phase change of the decadal oscillation. However, the variance explained by the two modes in CESM-LE does not seem to be consistent with this interpretation. Choi et al. (2013a) suggested that the variance of each mode depends on the strength of the two-ways feedback between the residuals of ENSO asymmetry and the ENSO-induced mode. The higher the variance explained by the ENSO-induced mode, the stronger the two-ways feedback and the higher the ENSO amplitude variability. This relationship therefore appears to be highly subject to ENSO amplitude biases in CGCMs (see paragraph 2.1.2.2) and requires further studies, especially in CESM-LE. An interesting diagnosis could thus to analyse the relationship between ENSO asymmetry residuals and TPDV in CESM-LE and extend this diagnosis to historical simulations, which could highlight the mechanism at work through inter-member variability.

Synthesis and Perspectives

- TPDV modes and ENSO modulation

Kug et al. (2010) and Choi et al. (2012) showed in the GFDL CM2.1 PI-control simulation that the low-frequency modulation of CP El Niño (through the slow-varying occurrence frequency) is highly correlated with the slow-varying SST mean state of the central Pacific and the ENSO-induced TPDV mode (correlation coefficients equal to 0.70 and -0.64 respectively). These relationships are much less pronounced in the CESM-LE PI-control simulation. In GFDL CM2.1, this relationship induces a direct link between the mean vertical stratification and ENSO. Low-frequency changes in stratification lead to a direct change in the dynamics and then, indirectly, to the associated thermodynamic processes in GFDL CM2.1. In CESM-LE, the link between the mean vertical stratification and ENSO variability seems to be more complicated and needs further investigations.

In CESM, the ENSO-induced TPDV mode appears correlated with the low-frequency variability of the tropical Pacific, rather than with the occurrence frequency of CP El Niño events. This distinct feature may arise from a model bias in the simulation of the TPDV modes, and, in particular, in the ENSO-induced mode. Indeed, in addition to explaining a lower variance, the mode also spreads further over the central Pacific, with positive anomalies confined in the eastern Pacific. This bias is particularly visible on the regressed spatial pattern onto the SST. Further investigations, particularly on the spatial patterns associated with the residuals due to El Niño-La Niña asymmetry, are needed. Indeed, the relationship between the TPDV and the two-way feedback on ENSO variability, through the non-linear rectification effects, could explain the distinct features between the TPDV and ENSO.

Zheng et al. (2018) showed that the TPDV is related to the CESM-LE inter-member spread of the SST warming by 2100, under the sustained RCP8.5 scenario. They suggested that the two-ways feedback between TPDV and ENSO modulation trough ENSO rectification effects leads to uncertainties on the SST warming rate and on ENSO amplitudes under global warming. Given this strong contribution of internal variability to projected changes, the mechanisms linking ENSO and TPDV in CESM-LE require further study. In particular, understanding why the spatial pattern of the ENSO-induced mode seems to shift eastward when descending into low frequency variability could be the key linking the different characteristics observed in CESM.

Finally, Choi et al. (2011) and Choi et al. (2012) used the modified Niño SSTA indices to define El Niño flavours and their definition of El Niño and La Niña events has criteria only during the winter season, without condition of duration of the event (see paragraph 3.2.3). The definition of ENSO diversity is an issue when analysing relationship between the mean state and ENSO flavours.

Chapter 5

ENSO diversity and global warming

Contents

5.1 Preamble

One of the debated issue is to predict changes in El Niño features, such as amplitude or diversity, with global warming (see paragraph 1.4.2). Most CMIP models project a deepening of the thermocline in the eastern Pacific in response to the weakening of the Walker circulation, which could reduce the effectiveness of the upwelling and thermocline feedbacks (DiNezio et al., 2012), and thus decrease ENSO amplitude. In the meantime, the projected intensification of the vertical stratification may strengthen the thermocline feedback, by increasing the sensitivity of SST anomalies to thermocline depth fluctuations (Zelle et al., 2004; Dewitte et al., 2013), and thus increase ENSO amplitude.

The two regimes of El Niño are also likely to have different sensitivity to changes in mean state. Changes in the background state of the tropical Pacific could favour CP El Niños, by flattening the thermocline in the central Pacific (Yeh et al., 2009a), or by preventing the growth of positive SSTA in the eastern tropical Pacific, due to a weakened Bjerknes feedback (Li et al., 2017). They could also favour extreme eastern El Niños, by promoting southward movement of the ITCZ (Cai et al., 2014), by shallowing the thermocline in the eastern Pacific (Philip and van Oldenborgh, 2006), or by weakening the westward mean equatorial currents (Santoso et al., 2013).

However, the dispersion of the ENSO response among the models does not allow to estimate significant trends in El Niño amplitude change. CGCMs have common biases in the tropical Pacific mean state simulation, which may lead to divergent model responses in ENSO simulation (see section 1.4 and paragraph 2.1.2.2). In particular, the inter-model uncertainty is mainly due to the different simulations of the tropical Pacific surface warming, simulations ranging from an El Niño-like to a La Niña-like warming pattern: models projecting an enhanced (reduced) mean warming in the eastern equatorial Pacific project increased (decreased) ENSO amplitude (Zheng et al., 2016). These differences in the projected patterns are mainly due to the common cold tongue bias of CGCMs. Correcting this bias favours El Niño-like mean warming pattern (Li et al., 2016; Ying et al., 2019). This result suggests a probable increase in ENSO-related SST variance under global warming.

It also suggests that, given the existing uncertainties about projected spatial patterns, it is hazardous to estimate ENSO magnitude changes based on fixed tropical Pacific regions, such as Niño-3 or Niño-3.4, subject to these biases. As highlighted in chapter 3, using the E and C indices defined by Takahashi et al. (2011) makes it possible to overcome this localised spatial constraint. In this chapter, we focus on strong El Niño events defined from a threshold on the E-index. The objectives of this chapter, whose main results are published in the journal *Climate Dynamics*, are:

- to diagnose changes associated with global warming in ENSO statistics simulated by CESM-LE,
- to document changes in ENSO mechanisms and feedback processes, to improve our mechanistic understanding of the impact of a warmer climate on ENSO.

5.2 Article submitted to *Climate Dynamics*

Given the socio-economic and meteorological impacts that can cause ENSO, the projection of its evolution with climate change presents strong challenges. In the following publication, changes in ENSO statistics with climate change are first analysed to diagnose the associated process changes. We focus on strong El Niño events defined by the E and C indices following the method of Takahashi et al. (2011).

This method has recently been used by Cai et al. (2018) (see Annexe 5.3.4.2). Using the E and C indices, they analysed ENSO variability at the action centres of the SST warming of each model, rather than at fixed regions (Fig. 5.1). They showed that the majority of the models simulates a robust and significant increase of the SST variability in these action

centres, whose longitude differ in each model. When the model simulates an increase in the E-index SST variance, it generally results in more occurrences of EP El Niño events for a given intensity. Analysing a set of models simulating realistically the non-linear character of ENSO (see paragraph 2.1.4.5), they argued that this increase in the variance of EP El Niño events is associated with the projected stronger vertical stratification in the central Pacific.

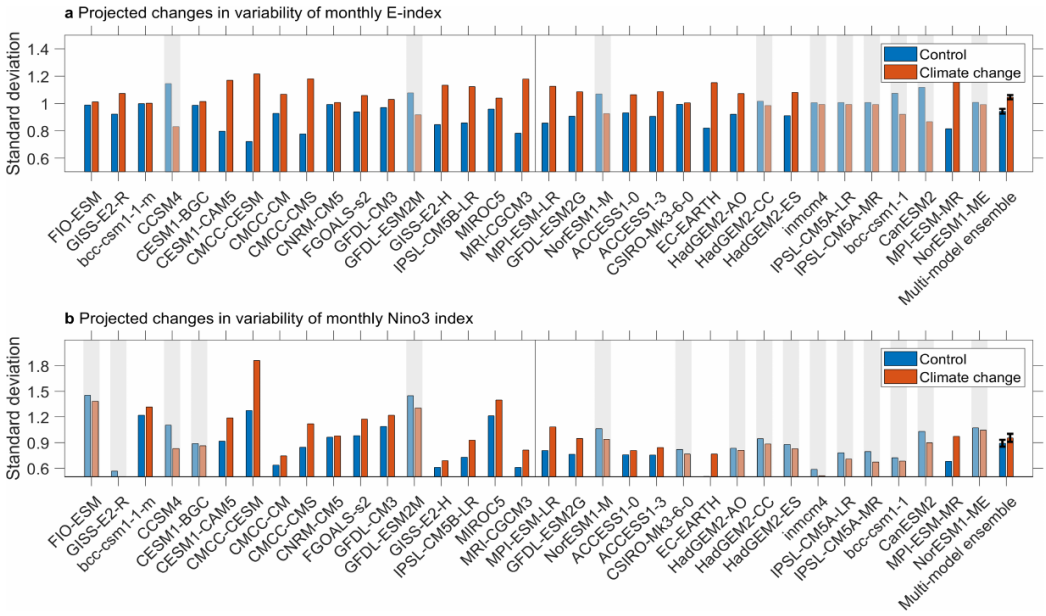

Figure 5.1 – (Top panel) Projected changes in E-index variance (standard deviation) between present-day (1900-1999, blue bars) and future (2000-2099, red bars) simulation periods. 24 of the 34 CMIP5 models show an increase in the E-index variance (models that simulate a decrease in E-index variance are greyed out). Note that the 17 CMIP5 models selected in the study because of their realistic representation of ENSO non-linearities are on the left part of the panels, to the left of the vertical gray line. 15 of the 17 selected models simulate an increase in the E-index variance. (Bottom panel) Same as on the top panel but for the Niño-3 SSTA index. The ensemble mean is shown on the far right of the two panels. Error bars correspond to the standard deviation of the bootstrap distribution, that is of 10,000 inter-realisations with replacement. The multi-model mean increase in the E-index variance (top panel) is statistically significant at more than the 95 % confidence level, which is not the case for the Niño-3 SSTA variance change (bottom panel). Reprinted from Cai et al. (2018).

CESM-LE also simulates this increase in EP Niño variability. We further investigate the E-index variance and show that its climatological variance is projected to change with global warming, in particular during the late winter, early spring (February-March-April, FMA hereafter). This change in the seasonal cycle of the SST variability in the action centres of EP El Niño warming is associated with an increased duration of strong EP El Niño events by two months in the warmer climate (see paragraph 5.3.2 for supplementary materials). This higher persistence of strong EP events is interpreted as resulting from both a stronger recharge process and a more effective thermocline feedback in the eastern equatorial Pacific, associated with the increased vertical stratification across the equatorial Pacific with global warming.

Moreover, we show that the increase in strong EP El Niño events peaking in FMA in the warmer climate explains one quarter of the increase in frequency of occurrence of extreme precipitation events defined as Cai et al. (2014) in the CESM model. And 34 % of the increase in extreme precipitation events are concomitant with weak to moderate El Niño events and thus associated with the warmer mean SST. We therefore argue that both the increase in mean SST in the eastern equatorial Pacific and the change in ENSO processes associated with differential warming between the surface and the subsurface (i.e. sharper mean thermocline) contribute to the increase in extreme precipitation events in a warmer climate in this model (see paragraph 5.3.3.2 for supplementary materials).

Change in strong Eastern Pacific El Niño events dynamics in the warming climate

Aude Carréric[1*], Boris Dewitte[1,2,3,4*], Wenju Cai[5,6], Antonietta Capotondi[7,8], Ken Takahashi[9], Sang-Wook Yeh[10], Guojian Wang[6] and Virginie Guémas[11]

[1] LEGOS, Université de Toulouse, CNES, CNRS, IRD, UPS, Toulouse, France

[2] Centro de Estudios Avanzados en Zonas Áridas (CEAZA), Coquimbo, Chile

[3] Facultad de Ciencias del Mar, Universidad Católica del Norte, Coquimbo, Chile

[4] Millennium Nucleus Ecology and Sustainable Management of Oceanic Island (ESMOI), Coquimbo, Chile

[5] Key Laboratory of Physical Oceanography, Institute for Advanced Ocean Studies, Ocean University of China and Qingdao National Laboratory for Marine Science and Technology, Qingdao, China

[6] Centre for Southern Hemisphere Oceans Research (CSHOR), CSIRO Oceans and Atmosphere, Hobart, Tasmania, Australia

[7] Cooperative Institute for Research in Environmental Science, University of Colorado, Boulder, CO, USA

[8] Physical Sciences Division, NOAA Earth System Research Laboratory, Boulder, CO, USA

[9] Servicio Nacional de Meteorología e Hidrología del Perú—SENAMHI, Lima, Peru

[10] Department of Marine Sciences and Convergent Technology, Hanyang University, Ansan, South Korea

[11] CNRM UMR 3589, Météo-France, CNRS, Toulouse, France

Submitted to Climate Dynamics (14/03/2019)

Revised (30/09/2019)

* Corresponding authors:

Boris Dewitte, email: boris.dewitte@ceaza.cl

Aude Carréric, email: aude.carreric@gmail.com

Abstract

While there is evidence that ENSO activity will increase in association with the increased vertical stratification due to global warming, the underlying mechanisms remain unclear. Here we investigate this issue using the simulations of the NCAR Community Earth System Model Large Ensemble (CESM-LE) Project focusing on strong El Niño events of the Eastern Pacific (EP) that can be associated to flooding in Northern and Central Peru. It is shown that, in the warmer climate, the duration of strong EP El Niño events peaking in boreal winter is extended by two months, which results in significantly more events peaking in February-March-April (FMA), the season when the climatological Inter-Tropical Convergence Zone is at its southernmost location. This larger persistence of strong EP events is interpreted as resulting from both a stronger recharge process and a more effective thermocline feedback in the eastern equatorial Pacific due to increased mean vertical stratification. A heat budget analysis reveals in particular that the reduction in seasonal upwelling rate is compensated by the increase in anomalous vertical temperature gradient within the surface layer, yielding an overall increase in the effectiveness of the thermocline feedback. In CESM-LE, the appearance of strong EP El Niño events peaking in FMA accounts for one-quarter of the increase in frequency of occurrence of ENSO-induced extreme precipitation events, while one-third results from weak-to-moderate El Niño events that triggers extreme precipitation events because of the warmer mean SST becoming closer to the convective threshold. In CESM-LE, both the increase in mean EP SST and the change in ENSO processes thus contribute to the increase in extreme precipitation events in the warmer climate.

Keywords: CESM-LE, extreme El Niño event, climate change, vertical stratification

1. Introduction

El Niño-Southern Oscillation (ENSO) is the most important mode of inter-annual variability in the tropical Pacific. By impacting meteorological conditions worldwide via atmospheric teleconnections (Ropelewski and Halpert, 1987; Yeh et al., 2018), it leads to dramatic societal and economics impacts (McPhaden et al., 2006). Understanding if and how El Niño characteristics will change with global warming has been a major concern since the first Coupled Model Intercomparison Projects in the 1990s (Meehl et al., 2000). While large progresses in our vision of the likely changes in ENSO statistics have been made in the recent decades (Yeh et al., 2009a; Power et al., 2013; Cai et al., 2014; 2015b), there are still many uncertainties in the mechanisms at play to explain the changes in statistics in the context of global warming, all the more so as models have persistent biases (e.g. westward shift in the center of action of El Niño (Zheng et al., 2012; Li and Xie, 2013), double Inter-Tropical Convergence Zone (ITCZ) syndrome (Hwang and Frierson, 2013; Li and Xie, 2013), warm bias in the far eastern Pacific (Richter, 2015)). These biases can in particular impact the realism of ENSO diversity in models (Ham and Kug, 2012; Karamperidou et al., 2017) by, for instance, influencing the evolution of Sea Surface Temperature (SST) anomalies during El Niño development (Santoso et al., 2013; Dewitte and Takahashi, 2017), favoring so-called double peaked El Niño events (Graham et al., 2017) or yielding compensating errors amongst the main ENSO feedbacks (Bayr et al., 2018). Since ENSO diversity is also a manifestation of the non-linearity of ENSO (Takahashi et al., 2011; Capotondi et al., 2015) that can impact mean state changes at low-frequency (Lee and McPhaden, 2010; McPhaden et al., 2011; Choi et al., 2012; Karamparidou et al., 2016), these biases are also likely influential on the way models simulate internal variability (Zheng et al., 2017). This has been a limitation to gain confidence in the projections of ENSO changes by these same models, but also to infer a clear mechanistic understanding of the sensitivity of ENSO to climate change.

So far, two broad views of the mechanisms at work in ENSO change due to global warming have been documented: 1) The projected faster warming of the eastern equatorial Pacific compared to that of the central Pacific will induce an easier eastward shift of the convection area from the central Pacific, through a weakening of westward mean equatorial currents associated with the reduction of the equatorial trade winds (Vecchi et al., 2006; Santoso et al., 2013); 2) The faster eastern equatorial Pacific surface warming due to climate change will reduce the meridional SST gradient in the eastern Pacific so that the ITCZ is likely to move more often southward, inducing an increase in the number of ENSO-induced extreme precipitation events in the eastern Pacific (Power et al., 2013; Cai et al., 2014, 2015b, 2017). Note that this applies to the warm phase of ENSO and not to the cold phase (La Niña) for which the faster warming of the Maritime continent in the Indonesian sector will tend to facilitate extreme La Niña events (Cai et al., 2015a).

Although these paradigms of the impact of climate change on ENSO provide useful guidance for analyzing and interpreting models, they present two main related caveats: first, they allow explaining the increase in ENSO-related

extreme precipitation events but do not address changes in ENSO statistics itself. In particular, the increase in extreme precipitation events does not necessarily require that El Niño events become stronger. This issue is nevertheless relevant considering the oceanographic consequences of strong El Niño events on the marine ecosystems in particular along the coast of Peru and Chile (Barber and Chavez, 1983; Carr et al., 2002). Second, in their principles, these paradigms only consider changes in surface processes (mixed-layer) although the latter are tightly linked to dynamical changes associated with thermocline processes. In particular, the differential warming between the surface oceanic layer and the thermocline under anthropogenic forcing yields a significant increase in vertical stratification across the equatorial Pacific (Yeh et al., 2009a; DiNezio et al., 2009; Capotondi et al., 2012) that can be influential on ENSO dynamics through a number of processes. Not only it modulates the way the wind stress forcing projects on the wave dynamics (Dewitte et al., 1999; 2009), influencing ENSO stability (Dewitte et al., 2007; Thual et al, 2013), but it also directly influences the so-called thermocline feedback, that is the sensitivity of SST to thermocline fluctuations (Zelle et al., 2004), a key process during Eastern Pacific (EP) El Niño events (Zebiak and Cane, 1987; An and Jin, 2001). The effect of changes in vertical stratification on ENSO dynamics in the context of global warming has been suggested in former studies (Yeh et al., 2009ab; 2010; DiNezio et al., 2009; Stevenson et al., 2017). Recently it has been shown that the variance of EP El Niño events increases in association with the stronger vertical stratification in the central Pacific in a set of models that realistically simulate the non-linear character of ENSO (Cai et al., 2018). While this study consolidates the confidence in climate change projections by showing a large inter-model consensus with regards to their sensitivity to changes in vertical stratification, the statistical approach somehow limits a clear understanding of the oceanic processes involved. It thus calls for advancing our mechanistic understanding of the sensitivity of EP El Niño events to changes in vertical stratification in the context of climate change. In particular, the main question that motivates the present work is: Through which processes are strong EP El Niño events favored in the warmer climate and how does their increase in frequency explain the increased occurrence of extreme precipitation events?

Here we take advantage of the simulations of the CESM-LE project (Kay et al., 2015) to investigate the mechanisms behind the sensitivity of ENSO statistics to mean state changes focusing on strong EP El Niño events that are those associated with extreme events (Takahashi et al., 2011; Takahashi and Dewitte, 2016, hereafter TD16). The CESM-LE project provides a large number of realizations of the same model, the NCAR Community Earth System Model (CESM), a Coupled General Circulation Model (CGCM) that accounts for ENSO diversity with some skill (Stevenson et al., 2017; Dewitte and Takahashi, 2017). The CESM model also simulates changes in mean SST pattern between the present climate (historical) and the climate corresponding to RCP8.5 future greenhouse gas emission scenarios (hereafter RCP8.5) comparable to those of the CMIP5 ensemble mean (Vecchi and Soden, 2007; Li et al., 2016), that is an El Niño-like pattern warming. Finally, this model also predicts an increase in ENSO-related extreme precipitation events in a warmer climate comparable to that of the CMIP5 ensemble (Cai et al., 2014), thus offering a

perfect test-bed for better understanding the relative influence of the gradual SST warming and the changes in ENSO dynamics on the statistics of extreme precipitation events.

The paper is organized as follows: after describing the data sets and the methods used in section 2, we document the changes in ENSO statistics due to global warming (section 3), highlighting changes in the seasonality of the number of events. Section 4 presents a heat budget analysis where changes in the composite evolution of the tendency terms associated with global warming are interpreted in the light of an analysis of change in the thermocline feedback in the model. Section 5 is a discussion followed by concluding remarks.

2. Data and Method

2.1. Data

We use long-term simulations of the NCAR Community Earth System Model Large Ensemble Project (CESM-LE) (Kay et al., 2015). The 42 and 40 members of the historical runs (1850-2005 for one member, 1920-2005 otherwise) and RCP8.5 runs (2006-2100) are respectively used here consisting in a total of 3682 and 3800 years, which allows estimating the spread between the members and thus confidence levels in the statistics (estimated by a Wilcoxon rank sum test in this study).

As defined by the CMIP5 design protocol (Taylor et al., 2012), the historical external forcing is composed of the observed atmospheric composition changes due to emissions of greenhouse gases and aerosols and the natural volcanic and orbital forcing. The RCP8.5 scenario corresponds to a "representative concentration pathways" (RCP) of high emissions of greenhouse gases, where the 8.5 label corresponds to an estimation of the radiative forcing (8.5 W/m²) at the end of the simulation that is the year 2100.

The simulations of the CESM-LE project use the Community Earth System Model, version 1 (CESM1) (Hurrell et al., 2013) coupling the Community Atmosphere Model version 5 (CAM5) atmosphere component (Meehl et al., 2013), the Los Alamos National Laboratory (LANL) Parallel Ocean Program version 2 (POP) ocean component (Smith et al., 2010), the Community Land model version 4 (CLM4) land component (Oleson et al., 2010) and the LANL Community Ice CodE (CICE4) sea ice component (Hunke and Lipscomb, 2010). All components of the model are approximately 1° horizontal resolution. The atmospheric component has 30 vertical levels, the oceanic component has 60 vertical layers. CESM1(CAM5) still presents some of the persistent biases of coupled models, such as a westward shift of the cold tongue, the double ITCZ and an excessive mean precipitation in the tropical Pacific (Hurrell et al., 2013). However, as its previous version CCSM4, CESM1(CAM5) correctly simulates some intrinsic characteristics of ENSO such as a realistic 3-6 years period but overestimates the magnitude compared to observations (Gent et al., 2011; Deser et al.,

2012; Hurrell et al., 2013). The seasonality of the ENSO variance is well represented despite the magnitude bias and a larger difference between winter and summer. It implies that the observed variance values are outside the simulated CESM-LE internal variability for certain months of the year (January to April) (Zheng et al., 2017). This model also accounts for many ENSO properties, in particular its diversity (Stevenson et al., 2017; Dewitte and Takahashi, 2017). Karamperidou et al. (2017) and Cai et al. (2018) showed the importance of ENSO non-linearities in the response of the tropical Pacific to global warming. The metric of non-linearity α defined by Karamperidou et al. (2017) and consisting in the leading coefficient of the parabolic approximation of the ENSO variability in the first and second principal components (PC) of SST anomalies in the tropical Pacific space, is used here as an integrated measure of diversity (see also Dommenget et al. (2013) for such an approach). It yields a value $\alpha = -0.37 \pm 0.08$ (±22%) for the CESM-LE historical run, which is close to the estimate from HadISST v1.1 observations (1950-2017) ($\alpha = -0.39$) and from some CMIP5 models (Karamperidou et al., 2017; Cai et al., 2018). In particular, the α value for the CESM ensemble is lower than the threshold value for α used in Cai et al. (2018) (i.e. $\alpha=-0.15$) to discriminate non-linear models. The CESM model has thus a non-linear behavior similar to that of the ensemble model used in Cai et al. (2018).

Stevenson et al. (2017) showed that the ENSO diversity in the CESM model is sensitive to various forms of external forcing using the Last Millennium Ensemble that contains many realizations of the 850–2005 period with differing combinations of forcing. In particular, anthropogenic changes in greenhouse gases and ozone/aerosol emissions can alter the persistence of EP and CP El Niño events, although forced changes in ENSO amplitude are generally small because of compensating effects between changes in oceanic processes. Here since we focus on the RCP8.5 scenario that corresponds to a significantly larger external forcing on the mean climate, we expect to identify more pronounced changes in ENSO processes, aided by our methodological approach to derive robust ENSO diversity changes in models (See section 2.2).

The HadISST v1.1 monthly average sea surface temperature dataset (Rayner, 2003) is used to estimate whether the representation of the internal climate variability spread simulated by the members of CESM-LE includes the observed contemporary climate trajectory. The dataset has a resolution grid of 1° latitude-longitude. We use the period from January 1950 to December 2017.

2.2. Definition of El Niño events and extreme precipitation events

a) El Niño events

Considering that at least two indices should be used in order to account for the different locations of SST anomalies peaks (Trenberth and Stepaniak, 2001; Takahashi et al., 2011; Ren and Jin, 2011; Dommenget et al., 2012), we use the E and C indices defined by Takahashi et al. (2011) as $E = (PC1 - PC2)/\sqrt{2}$ and $C = (PC1 + PC2)/\sqrt{2}$ where

the PC1 and PC2 are the normalized principal components of the first two empirical orthogonal function (EOF) modes of SST anomalies in the tropical Pacific (120°E-290°E; 10°S-10°N). The E and C indices are thus linearly uncorrelated by construction. They are calculated separately for the two different periods (historical versus RCP8.5). The SSTs are linearly detrended and the seasonal cycle is removed for each period and for each member independently, prior to carrying the EOF decomposition. A bilinear regression of the SST anomalies onto these indices is used to determine the SST anomalies spatial patterns associated with each index (Figure 1), indicating a relative good agreement between model and observations, although CESM simulates the center of the patterns displaced to the west compared to observations by 20° and 30° for the E and C patterns respectively. This westward bias of the SST variability is comparable to the CMIP5 ensemble (cf. Figure 1 of Matveeva et al. (2018)). Note also the cold tongue bias as evidenced by the position of the mean 28°C isotherm in Figure 1, that is shifted westward by 25°, a feature common to many other CGCMs (Wittenberg et al., 2006; Bellenger et al., 2014). These biases have been detrimental for comparing observations and models, particularly from historical ENSO indices, because the use of fixed regions (e.g. Niño-3) for averaging quantities results in differences that reflect this shift in variability and mean state rather than the actual dynamics of the system. For instance, Graham et al. (2017) showed that the recurrent CGCMs equatorial Cold Tongue bias can lead to the simulation of "fake" El Niño events that have never been observed, double peaking in the tropical band and called "double peaked" El Niño events. Using the conventional Niño regions to define El Niño diversity increases the risk of integrating so-called "double peaked" El Niño events and mistaking them as CP El Niños when compositing, although they have more commonalities with the observed EP El Niño events. We will thus follow the methodology of TD16 which projects tropical Pacific variability (and feedbacks) onto the E and C modes rather than fixed regions to avoid these limitations (see section 2.3.). Note that this method has proven to be skillful in showing a strong inter-model consensus on the SST variability of EP El Niño events despite differences in the details of El Niño simulation across models (Cai et al., 2018).

In order to diagnose changes in ENSO statistics between the present and future climates, we estimate the E and C modes for the two periods, the historical period (1920-2005) and the RCP8.5 period (2006-2100), which provides two sets of E and C modes (patterns and timeseries). The change in statistics is therefore reflected here in both the pattern and the temporal evolution of the modes. This is motivated by the fact that the ENSO pattern is changing between the present and future climate (Figure 2). The E and C indices have been normalized so that the patterns can be expressed in °C. In particular, there is a westward amplification (by 20°) of the E mode and an eastward amplification (by 35°) of the C mode in the warmer climate. In order to take into account these changes in the spatial patterns, the E and C indices of the RCP8.5 simulations are scaled by the projection of the associated spatial pattern on its counterpart of the historical runs. The scaling coefficients are equal to 1.16±10% (±0.12) for both E and C modes over 10°S-10°N. This allows comparing changes in the amplitude of the composite evolution of the E and C indices (Figure 3) and not just

changes in temporal evolution. Note that this method yields similar results than the one used in Cai et al. (2018), that does not consider change in spatial patterns of the E and C modes, but instead performs an EOF analysis of SST anomalies over the whole record (1920-2100). In particular, the increase in the variance of the E index in DJF from historical to RCP8.5 runs is 14% for our method and 18% for the Cai et al. (2018)'s method when considering the last 85 years of each period. The largest difference in methods is the dispersion amongst the members that is in general larger in the method used here. Despite these differences, we find that the increase in variance of the E index in DJF is significant at the 95% confidence level based on a Wilcoxon test for both methods. CESM simulates thus an increase in the DJF E-index variance in the future climate, regardless of the method, comparable to 17 models of the CMIP5 data base that account realistically for the non-linear behavior of ENSO (Cai et al., 2018).

El Niño events are defined from the PC1 derived from the analysis of the main mode of variability of the tropical Pacific by the EOF method. El Niño events are when the value of the PC1 exceeds its 75% percentile over at least 5 consecutive months, regardless of season. Our definition is slightly different from that of TD16 that seek for El Nino peaks over 2-year running mean time windows with a 1-2-1 filter applied to the PC1. We checked that both methods provide very comparable statistics by applying our definition to the GFDL CM2.1 PI-control simulation and comparing our results with that of TD16. In the meantime, it has been also verified that using the historical definition by the ONI index does not change ENSO statistics on the PI-control simulation of CESM. El Niño classes (strong versus moderate) are then defined based on the E index. When the E-index value reaches a threshold value (interpreted here as the value of SST anomalies in the far eastern Pacific needed for deep convection to be activated) a strong EP event takes place. This threshold is estimated from a *k-mean* cluster analysis (k=2) applied jointly to the E and C values during El Niño years and for the calendar month when the E-index is maximal. It yields two classes that correspond to moderate (either EP or CP) Niño events (cluster 1) and strong EP El Niño events (cluster 2). We find a threshold value of 2.2°C for the PI-control simulation (see also Dewitte and Takahashi (2017)). Note the PI-control and historical simulations of CESM do not exhibit a well-defined bimodal distribution in the (E, C) space conversely to the GFDL CM2.1 model (see TD16), so that the determination of this threshold value is somewhat subjective and certainly sensitive to the model biases. Nevertheless the model exhibits a clear non-linearity in the response of the wind stress to SST anomalies in the eastern Pacific (Figure S1 – Supplementary material). The cluster analysis applied to historical and RCP8.5 simulations yields threshold values similar to the PI-control value. Sensitivity tests to this threshold value (taking an error of 5%) indicate that results presented in this paper are not impacted significantly. For a variation of ±5% of the threshold, the number of strong El Niño events varies from 225 (-5.1%) to 262 (10.5%) for the historical simulations and from 271 (-10.3%) to 322 (6.6%) for the RCP8.5 simulations.

b) Extreme precipitation events

The definition follows that of Cai et al. (2014), that is based on the total DJF rainfall averaged over the Niño-3 region (150°W-90°W; 5°S-5°N). An extreme precipitation event is such that the rainfall index is above the threshold value of 5 mm/day. This definition was shown to be robust in accounting for changes in statistics of extreme events due to global warming despite the arbitrary choice of the threshold value in the warmer climate (Cai et al., 2017). Noteworthy, with such a definition, all extreme precipitation events are however not necessarily associated with a strong or weak to moderate El Niño event. In particular, extreme precipitation events are defined from a threshold value of the DJF Niño-3 rainfall index. In that case, when two consecutive winters are affected by the same episode of anomalous positive surface temperature, causing precipitation events in DJF, the same warm episode is counted as two "independent El Niño events". It thus allows two extreme precipitation events to take place from one year to another, while strong or weak-to-moderate El Niño events can last over more than one year (with the selected year corresponding to the maximum amplitude of the PC1 timeseries of the EOF analysis of SST anomalies). Nevertheless, with such a definition, 96% of the extreme precipitations events are concomitant with a strong El Niño event in the historical runs (Table 1). As will be seen, this percentage is reduced in the RCP8.5 runs (55%) due to both changes in the seasonality of strong El Niño events and the gradual warming of the eastern equatorial Pacific.

2.3. Heat budget

The equation of the SST change within the surface layer that is used for the heat budget is the following:

$$\left[\frac{\partial T'}{\partial t}\right] = -\left[u\frac{\partial T}{\partial x}\right]' - \left[v\frac{\partial T}{\partial y}\right]' - \left[w\frac{\partial T}{\partial z}\right]' + \frac{Q'_{net}}{\rho_0\, c_p\, h} + R' \qquad (1)$$

The prime denotes the monthly anomaly relative to the mean climatology. T is the 4D-potential temperature, u, v and w are respectively 4-D zonal, meridional and vertical currents. Square brackets indicate vertical integration over the surface layer, whose depth is set at 80m. The first three right hand side terms correspond respectively to the zonal, meridional and vertical advections. The term Q_{net} is the net ocean-atmosphere heat flux, including surface fluxes and penetrating short-wave radiation. The coefficients ρ_0 and Cp are respectively the sea-water reference density (kg/m^3) and the specific heat content (J/(kg.C)). The residual term R includes the short-wave fluxes of heat out of the base of the mixed layer, the change in temperature associated with the freshwater flux, the horizontal and vertical diffusion of heat, and errors associated with the off-line calculation and the use of monthly mean outputs. The method further follows TD16 that consists in projecting the tendency terms of the SST equation (Eq. 1) onto the spatial patterns of the first two normalized EOF modes of the equatorial Pacific (2ºS-2ºN). The resulting timeseries are then linearly combined

according to the definition of the E and C indices, which is convenient for infering how processes contribute to the rate of change of SST anomalies in the E and C equatorial regions (Figure 2). The projection of the heating rate onto the E mode is thus expressed as:

$$\left\langle \frac{\partial T'}{\partial t} \middle| E \right\rangle = \frac{1}{N_x N_y} \int_{120ºE}^{290ºE} \int_{2ºS}^{2ºN} \left(\frac{\partial T'}{\partial t}(x,y,t) \cdot E(x,y) \right) dxdy$$

This method has the advantage of objectively estimating the region of influence of the different feedbacks and their changes in a warmer climate, compared to the method where tendency terms are averaged over the classical Niño-4 (5°S-5°N, 160°E-210°E) and Niño-3 (5°S-5°N, 210°E-270°E) regions, or modified versions of them to take into account mean state biases in the CGCMs (Kug et al., 2010; Capotondi, 2013; Stevenson et al., 2017). Since the E and C patterns are modified in the future climate (see Figure 2 and section 2.2.a), ourmethod thus takes into account changes that may occur in the location of the main centers of the thermodynamical processes. To be able to compare the amplitude in the evolution of the tendency terms between the two climates, tendency terms for the RCP8.5 simulations are scaled by the projection coefficient of the RCP8.5 E and C patterns on their counterparts in the historical runs. The projection is done here over the domain (120°E-290°E; 2°S-2°N). The values of the scaling coefficient are equal to 1.18 (±10%) for both E and C modes over 2°S-2°N. The heat budget was calculated on the model native grid. The CESM uses the ocean POP model (Smith et al., 2010), which has a staggered Arakawa B-grid (Arakawa and Lamb, 1977). The centered second-order finite differences scheme and leap-frog time stepping were used for the calculation of the tendency terms following the model grid discretization.

3. Changes in Eastern Pacific El Niño events

3.1. Composite evolution

As a first step we present the composite evolution of the E and C indices during moderate and strong events in the two climates (Figure 3). It indicates that, in this model, strong (moderate) El Niño events are preferentially of EP (CP) types because strong (moderate) El Niño events have large (weak) values of the E index. The E index during strong El Niño event tends also to peak from Aug(Y0), which is counterintuitive if compared to other historical indices (e.g. NINO34). This can be understood as follows: The E index accounts for SST variability in the far eastern Pacific where the thermocline is shallow and the thermocline feedback more intense than in the central equatorial Pacific. So when a Kelvin wave is triggered during the development of ENSO (typically during Feb-April Y(0)), the SST increase in the far eastern Pacific a couple month later, which projects on the E mode, then El Niño develops, which maintains an

elevated E. In other words, the first part of the warming in E is due to the forced Kelvin wave acting as a trigger of ENSO, while the second part of the warming in E is associated with the growing coupled mode. The values of the C index are somewhat larger for moderate than for strong El Niños during the development phase. The C index has weaker positive values for strong El Niño events and can become negative during their decaying phase because strong El Niño events tend to be followed by La Niña events (DiNezio and Deser, 2014), which the C index accounts for. The evolution of the indices is comparable to observations (see Figure 4 of TD16) although the comparison is limited for strong El Niño events owing to their too few numbers in the observational record.

The striking feature of Figure 3 is that the temporal evolution and amplitude of the indices do not change much from the present to the future climate in particular during the developing and mature phases of the El Niño composite, even if there are time frames when amplitude changes are statistically significant according to a Wilcoxon rank sum test. However, strong EP El Niño events last significantly longer by 2 months in the RCP8.5 simulations peaking in March (Y1) instead of December (Y0), while the central Pacific cools earlier and more than in the present climate. This suggests changes in seasonality of some events. Moderate El Niño events exhibit in general weaker changes in their evolution and amplitude, although there is a similar increase in persistence of the E index than that of strong events.

3.2. Seasonal stratification

In order to get further insights into the changes in ENSO statistics, the changes in the numbers of strong and moderate EP El Niño events are stratified according to the month of their peak value of the E index. Figure 4 allows identifying periods in the calendar year (hereafter referred to as "seasons") when the number of events changes significantly from the historical to the RCP8.5 simulations. Considering periods in the calendar year when the number of events is above 15 events for 3 to 4 consecutive months in the RCP8.5 simulations, three "seasons" can be defined: Jul-Aug-Sep (JAS), Oct-Nov-Dec-Jan (ONDJ) and Feb-Mar-Apr (FMA) (see Table 1). The threshold value of 15 events is selected arbitrarily and corresponds to 2% of the total number of events.

The results indicate a drastic change in the seasonal distribution of the number of events between the two climates. The most important changes are for strong EP El Niño events, with a significant increase (+1315%) in the number of events peaking during FMA. This is also observed for moderate EP El Niño events but to a lesser extent (+92%). Such a change indicates that, while the mean amplitude of EP El Niño event is weakly impacted by global warming (Figure 3), this is not the case for the seasonal variance of the E index. This is evidenced in Figure 5 that shows the climatological variance of the E index for the two climates. There is a significant increase in the E index variance (at the 95% confidence level based on a Wilcoxon test) at almost all calendar months, more pronounced for the FMA season (+ 40% increase in variance). The large increase in variance of the E index in FMA is likely to translate in a larger number of

extreme precipitation events in the warmer climate because this corresponds to the season when the ITCZ has its southernmost position (Xie et al., 2018). In the CESM mode, the frequency of occurrence of extreme precipitation events (see definition in section 2.2) is projected to increase from 0.04 per 10 years (one event every 24.7 years) to 0.16 (one event every 6.4 years) on average over the last 50 years of the RCP8.5 simulations, which corresponds to a 3.9 fold increase of the number of extreme events at the end of the 21st century (+225% increase from the present to the future climates, Table 1). The CESM model thus projects more than a doubling of extreme precipitation events in the future climate, consistent with Cai et al. (2014). The CESM model exhibits however a more modest increase, from the present to the warmer climate, in the number of strong EP El Niño events than in the number of extreme precipitation events. In particular, the number of strong EP El Niño events (extreme precipitation events) increases from 237 (146) in the historical period to 302 (489) in the RCP8.5 period, which corresponds to an increase of their frequency of occurrence (in events/decade) of +18% from the present to the future climates (Table 1), so that the increase in strong EP El Niño events is much less that the increase in extreme precipitation events. This can be interpreted broadly as resulting from the fact that moderate EP El Niño events can yield extreme precipitation events in the warmer climate due to increased mean SST in the eastern equatorial Pacific (Cai et al., 2014), independently of whether or not the moderate EP El Niño events undergo a change in their dynamics. However, since the overall number of EP El Nino events has almost no change, the 18% increase in the frequency of strong EP El Nino events indicate that global warming may favor the "high-regime" of ENSO (TD16), suggesting that the increase in extreme precipitation events in the warmer climate does not solely results from the warming of the cold tongue (Cai et al., 2014). This will be further documented in the discussion section. In the following, we investigate the processes explaining the increased persistence of EP El Niño and the emergence of events peaking in FMA in the warmer climate, focusing on key ENSO oceanic processes sensitive to the increased vertical stratification, i.e. the thermocline feedback and the recharge of heat content.

4. ENSO processes and increased stratification

In this section, the focus is on the processes that could explain the increased variance and persistence of the E index in FMA. As mentioned in the introduction, the increase in vertical stratification is a salient feature of the climate change pattern on temperature in the ocean, which has implications for ENSO dynamics. Not only it modulates the thermocline feedback through changing the relationship between SST and thermocline depth fluctuations (Dewitte et al., 2013), but it can also influence the dynamical response of the ocean through the projection of momentum forcing on the wave dynamics (Philander, 1978; Dewitte, 2000), and thereby the ENSO stability (Yeh et al., 2010; Thual et al., 2011, 2013). Recently Cai et al. (2018) showed that changes in vertical stratification due to greenhouse warming are associated with the increase in variance of the EP El Niño events in an ensemble composed of models simulating ENSO

366 diversity/non-linearity similar to that of CESM (see section 2). We thus here use the CESM simulations to get insights
367 in the mechanisms at work for explaining the increased climatological variance in strong EP El Niño events.
368
369 **4.1. Recharge-discharge process**
370
371 Heat content along the equator is a precursor of ENSO and its primary source of predictability, which has been
372 conceptualized by the recharge-discharge oscillator model (Jin, 1997). Although large heat content anomalies are not
373 always necessary for strong EP El Niño to occur (TD16), it is worth diagnosing the recharge-discharge process in the
374 model, as it can explain to some extent the persistence of SST anomalies during ENSO. In the framework of the simple
375 recharge-discharge model (Jin, 1997), a stronger recharge would imply a longer lasting El Niño event once it has
376 developed. Figure 6 shows the strong El Niño composite evolution of estimates of the so-called tilt and warm water
377 volume (WWV) modes that depict the recharge discharge-discharge process (Clarke, 2010). The WWV mode is phase-
378 shifted (ahead by ~6 months) with the tilt mode that accounts for the quasi-instantaneous response of the eastern Pacific
379 thermocline to wind stress anomalies. It is clear from Figure 6a that the recharge process is increased in the warmer
380 climate (the mean over the period Jun(Y0)-Oct(Y0) increases from 0.55 m to 6.25 m between the two climates), while
381 the tilt mode amplitude also increases prior to the ENSO peak (Figure 6b). The tilt mode amplitude increase is
382 consistent with westerly winds projecting more on the ocean dynamics in the warmer climate due to the increased
383 stratification in the central Pacific (Figure 7) (Dewitte et al., 1999; Thual et al., 2011). Note that it was checked that the
384 zonal equatorial wind stress integrated from one side of the Pacific to the other (that represents an estimate of the tilt
385 mode which does take explicitly into account the change in stratification) during the EP El Niño events is not
386 significantly changed between the two climates (not shown) so that the increase in the amplitude of the tilt mode is not
387 the result of changes in the amplitude of wind stress forcing that contributes to the build-up of heat content, but instead
388 has to result from the fact that wind stress forcing projects more efficiently onto wave dynamics due to the increased
389 stratification. The increase lasts until Jan(Y1) so that the effect on SST anomalies could last until ~Mar(Y1) through the
390 thermocline feedback because of the delayed response of SST anomalies to thermocline fluctuations (Zelle et al., 2004;
391 see also section 4.2). Regarding the WWV mode, the change in amplitude in Jul(Y0)-Oct(Y0) from the present to the
392 future climate is certainly more difficult to interpret because of likely compensating effects amongst different processes
393 (Thual et al., 2011; Lengaigne et al., 2012; Izumo et al., 2018), the potential role of changes in off-equatorial high-
394 frequency winds (McGregor et al., 2016; Neske and McGregor, 2018) and other sources of external forcing (see section
395 5). However, the increase in amplitude of the WWV can be associated to a large extent with the increased occurrence of
396 the strong events peaking in FMA as evidenced by the composite of the WWV evolution with and without strong events
397 peaking in FMA (Figures 6c and 6d). The increase in amplitude of the WWV is statistically significant (at 95%

confidence level based on a Wilcoxon rank sum test) from Apr(Y0) to Jan(Y1) when considering the events peaking in FMA. The increase is statistically significant only from Jun(Y0) when El Niño events whose peak occurs in FMA are not considered. Note that the same diagnosis was done using the thermocline depth, i.e. the depth of the maximal vertical temperature gradient. While the change with global warming of the WWB amplitude prior to the ENSO peak (i.e. Jun(Y0)-Oct(Y0)) is less pronounced, it is statistically significant when considering strong El Niño events peaking in FMA (not shown). .

4.2. Mixed-layer processes

While the strengthened vertical stratification increases the effectiveness of momentum flux onto the wave dynamics (Dewitte et al., 1999), which tends to destabilize ENSO by increasing the coupling efficiency between the ocean and the atmosphere (Thual et al., 2011; 2013), the sensitivity of ENSO to changes in stratification also operates through changes in the mixed-layer processes. Owing to the shallow thermocline in the eastern Pacific, the main oceanic process there is the mean vertical advection of anomalous temperature ($-\overline{w}.\frac{\partial T'}{\partial z}$), often referred to as the thermocline feedback (An and Jin, 2001). Since changes in the thermocline feedback not only depend on changes in the magnitude of the seasonal upwelling rate ($\overline{w}$) but also on changes in the vertical gradient of anomalous temperature between the surface and the base of the mixed layer ($\frac{\partial T'}{\partial z}$), inferring its sensitivity to vertical stratification is not straightforward. In particular, increased stratification in the eastern Pacific may reduce the effectiveness of upwelling through flattening and tightening the isotherms, while it could increase the sensitivity of SST anomalies to thermocline fluctuations through enhancing mean vertical diffusivity (Zelle et al., 2004). Compensating effects are thus possible.

As a first step, we present the composite evolution during strong El Niño events in the eastern Pacific (E region) of the mixed-layer processes (tendency terms) for the present and future climates (Figure 8). For conciseness sake, we focus hereafter on the developing and peak phases, noting also that the residual term being relatively large during the decaying phase (Figure 8e), the interpretation of the results is not straightforward during that particular phase. As expected, total vertical advection exhibits the largest amplitude (Figure 8d). It was checked through a Reynolds decomposition of the tendency terms that the main contributor to total vertical advection is the thermocline feedback, with non-linear vertical advection and anomalous vertical advection of mean temperature ("upwelling feedback") only marginally contributing during the onset and peak phase of strong EP El Niño events (Figure S2 – Supplementary material) consistently with TD16. The residual term has a comparable contribution (cooling) than the thermal damping term, and can be interpreted as resulting from the reduced vertical diffusivity in the first 80m as the mixed-layer

deepens. The largest changes between the present and future climates are for vertical advection and thermal damping with a 71% increase (90% reduction) for the average over Apr(Y0)-Feb(Y1) for vertical advection (thermal damping) relatively to the value over the present climate (Figure 8f). Changes in these two opposite sign terms explain why the rate of SST change is hardly impacted from the present climate to the future climate. While the larger contribution of thermal damping is expected from the increase variance of the E index from the present to future climate, the increase in the magnitude of vertical advection is more difficult to interpret. 77% of this increase is associated with the contribution of climatological vertical advection of anomalous temperature (Figure S2), so that it can be interpreted as resulting from the combined effects of the weakening of the Walker circulation on the seasonal upwelling on the one hand (DiNezio et al., 2009; Dewitte et al., 2013; Chung et al., 2019) and of the increased stratification on the relationship between SST and thermocline anomalies on the other hand. Figures 9ab present estimates of the changes of these two quantities (i.e. upwelling rate and the slope of the linear relationship between SST and thermocline anomalies) between the two climates. The slope of the linear relationship between SST and thermocline anomalies is estimated for lag between -6 and 6 months and the maximum value is shown considering that temperature anomalies in the vicinity of the thermocline are transported to the surface by a combination of upwelling and vertical mixing, which introduces a delay in the time dependence of the local relation between SST and thermocline anomalies (Zelle et al., 2004). As expected, the climatological upwelling rate is reduced in the warmer climate (Figure 9a). The reduction is most important in boreal winter reaching -14% in March. The decrease is statistically significant at the 95% confidence level except for the month of October. On the other hand, the sensitivity of the SST to thermocline fluctuations is significantly increased in particular with a maximum relative increase in August (+ 100 %). On average over the year, the relationship between SST and thermocline fluctuations is increased by 46%. Such increase largely compensates for the decrease in climatological upwelling and yield an overall increase in the thermocline feedback as evidenced by Figure 9c that shows the change in climatological variance of the mean vertical advection of anomalous temperature between the present and the future climate. In particular, the relative increase in variance is maximum in May-June-July (+83%), which corresponds to the season when the tropical Pacific system becomes highly unstable (Stein et al., 2010) and is more susceptible to develop an El Niño event. As a summary, Figure 8f presents the averaged changes in amplitude of the tendency terms during the developing phase of strong EP El Niño events. The largest increase is for vertical advection (+71%), 77% of which is attributed to the thermocline feedback.

5. Discussions and concluding remarks

We have investigated the sensitivity of ENSO dynamics to mean state changes in a model that has skill in simulating ENSO diversity and non-linearity. We find that, in the CESM model, the persistence of strong EP events is

increased by 2 months so that the variance in SST anomalies in the eastern Pacific is significantly increased over the FMA season when the ITCZ is about to reach its southernmost position. Noteworthy a similar behavior is found in the CMIP5 ensemble (Figure 10), allowing to some extent to generalize the results obtained here from the CESM model.

While recent studies have shown that the number of extreme precipitation events associated with El Niño is projected to increase in the warmer climate (Cai et al., 2014; 2015b), the mechanisms by which this will take place remain unclear. Here we suggest that a portion of the increase in extreme precipitation events in the warmer climate is associated with the increase in the number of strong EP El Niño events, in particular those that peak in FMA, which corresponds to the season when climatological SST in the eastern Pacific is already high. Those events are thus strongly coupled to the ITCZ and do not necessarily require the anthropologically-forced mean SST warming trend in the eastern Pacific to yield extreme precipitation events. In order to estimate the proportion of extreme precipitation events that relates either to moderate or strong El Niño events, we consider the number of events over 10-year running windows among all simulation members (i.e. at least 400 years are considered for each chunk) and estimate the proportion of El Niño events (strong and moderate) compositing extreme precipitation events along historical and RCP8.5 periods (Figure 11). The increase (by 1315%) in the frequency of occurrence of strong EP El Niño events peaking in FMA explains 24% of the increase in the frequency of occurrence of extreme precipitation events in the CESM model. 9% and 21% of the increase in the frequency of occurrence of extreme precipitation events are explained by the frequency of occurrence of strong El Niño events peaking in ONDJ and JAS respectively (see section 3.2 for the definition of "seasons"). This sums to 54% of the increase in the frequency of occurrence of extreme precipitation events thus explained by the increase in the frequency of occurrence of strong El Niño events. Concomitantly, the increased proportion of extreme precipitation events associated with weak and moderate El Niño events (which represents an additional 0.43 events/decade of weak to moderate El Niño events that relates to an extreme precipitation events in the warmer climate) results in that 34% of the increase in extreme precipitation events are associated with moderate El Niño events and thus due to the warmer mean SST in the eastern equatorial Pacific. Note that in the present climate, there is almost no weak to moderate El Niño event (i.e. 0.003 events/decade) that relates to extreme precipitation events (versus 0.43 events/decades in the future climate). The remaining 12% of the increase in the frequency of occurrence of extreme precipitation events could not be explained by the occurrence of an El Niño event and thus corresponds to internal variability in precipitation in a warmer climate. Overall Figure 11 illustrates the influence of the number of events peaking in FMA on the change in extreme precipitation events in the warmer climate, although very few of these events (9) exist in the historical simulation. It indicates that changes in the statistics of extreme precipitation events cannot be solely attributed to changes in mean SST in the equatorial eastern Pacific i.e. the warmer mean SST becoming closer to the convective threshold, but also depend on changes in ENSO dynamics.

The "emergence" of strong EP El Niño peaking in FMA in the warmer climate is suggested to be associated with the increased vertical stratification across the equatorial Pacific, a salient feature of the climate change patterns in climate models (Yeh et al., 2009; DiNezio et al., 2009; Cai et al., 2018). Cai et al. (2018) showed in particular that the increased variance in Eastern Pacific SST anomalies is associated with the increase in vertical stratification. We suggest further that the increased persistence of EP El Nino events is resulting from both a stronger recharge process and a more effective thermocline feedback in the warming climate due to an increased vertical stratification. In particular, the sensitivity of SST anomalies in the far eastern Pacific to thermocline fluctuations is significantly increased in FMA and overwhelms the reduction in mean upwelling (Figure 9). The recharge process is also shown to be enhanced in the warmer climate, which can be interpreted as resulting from the increased stratification in the central-western Pacific where wind stress can be more efficiently projected onto the wave dynamics. Overall our study suggest that the influence of the increased ocean vertical stratification in a warmer climate on ENSO could be understood in terms of two main mechanisms involving mostly linear processes, i.e. 1) on the dynamical side, a stronger recharge process and an overall more energized wave dynamics, and 2) on the thermodynamical side, an increased thermocline feedback in the eastern Pacific. These processes work together to produce the increased persistence/variance in EP El Niño events in the warmer climate.

Of course, considering the coupled nature of ENSO, there are other potentially important processes that could be at play to explain the longer duration of strong EP El Niño events in the warmer climate and their changing seasonal stratification. In particular, non-linear oceanic processes are important for the strong El Niño regime (Jin et al., 2003) although non-linear advection, the main contributor to the oceanic non-linearities during ENSO, does not appear essential for the onset of strong EP El Niño events (TD16), a feature that is also observed here (Figure S2c). Nevertheless non-linear advection is increased by 120% from the present to the future climate, over Apr-May-Jun(Y1), the period over which it peaks in the E region, contributing to the longer persistence of warm anomalies during strong El Niño events. Determining if such increase is related to the increase in vertical stratification would deserve further investigation which is beyond the scope of the present study considering the likely interplay between the various non-linear processes. The other important non-linear processes for ENSO are those encapsulated in the Bjerknes feedback and are atmospheric processes by nature (Dommenget et al. 2013, TD16). While the details of the change in the characteristics of the Bjerknes feedback is beyond the scope of the present study, we note that, within the approximations of our methodological approach, the slopes of the piecewise linear relationship between the E index and the zonal wind stress in the eastern equatorial Pacific are weakly changed from the present to the future climate (See Figure S1). This suggests that the characteristics of the Bjerknes feedback are not fundamentally modified in this model from the present to the future climate, although the convective SST anomaly threshold appears to have changed consistently with Johnson and Xie (2010) that showed that it is not absolute and varies with the mean climate (e.g. the

temperature of the free troposphere). The other key ingredient for strong El Niño events to develop, that was not looked at here although it can non-linearly interact with the equatorial ENSO dynamics, is the nature of the changes in the external stochastic forcing that has multiple facets. While high-frequency stochastic forcing, in the form of Westerly Wind Bursts (WWBs), is expected to energize more wave dynamics in the warmer climate, it is not clear how its characteristics will change in the future (Bui and Maloney, 2018; Maloney et al., 2019). We note here that, in the CESM mode, the high-frequency (frequency > 90 days-1) variance of the equatorial zonal wind stress is increased from the present to the future climate (not shown), which could contribute to the stronger recharge process in the warmer climate for strong El Niño events (see Figure 6). This would deserve further investigation which is planned for future work. In particular, since there is more and more evidence that the low-frequency component of the external forcing to ENSO is certainly as important as the high-frequency component (Dommenget and Yu, 2017; Takahashi et al., 2018), such investigation will have to consider all aspects of the external forcing, including the North Pacific Meridional Mode (Chiang and Vimont, 2004) that is also suggested to become more energetic in the warmer climate in this model (Liguori and DiLorenzo, 2018).

Acknowledgements:

We acknowledge the CESM Large Ensemble Community Project for providing model outputs, which are available on https://www.earthsystemgrid.org. The CESM project is supported by the National Science Foundation and the Office of Science (BER) of the U.S. Department of Energy. B. Dewitte acknowledges supports from FONDECYT (projects 1171861 and 1190276) and the Agence Nationale de la Recherche (ANR, project ARISE).

References:

An, S.-I. and F.-F. Jin, 2001: Collective role of thermocline and zonal advective feedbacks in the ENSO mode. Journal of Climate, 14, 3421–3432.

Arakawa, A. and V. R. Lamb, 1977: Computational Design of the Basic Dynamical Processes of the UCLA General Circulation Model. Methods in Computational Physics: Advances in Research and Applications, J. Chang, ed., Elsevier, volume 17 of General Circulation Models of the Atmosphere, 173–265.

Barber, R. T. and F. P. Chavez, 1983: Biological Consequences of El Niño. Science, 222, 1203–1210, doi:10.1126/science.222.4629.1203.

Bayr, T., C. Wengel, M. Latif, D. Dommenget, J. Lübbecke, and W. Park, 2018: Error compensation of ENSO atmospheric feedbacks in climate models and its influence on simulated ENSO dynamics. Climate Dynamics, doi:10.1007/s00382-018-4575-7.

Bellenger, H., E. Guilyardi, J. Leloup, M. Lengaigne, and J. Vialard, 2014: ENSO representation in climate models: from CMIP3 to CMIP5. Climate Dynamics, 42, 1999–2018, doi:10.1007/s00382-013-1783-z.

Bui, H. X., and E. D. Maloney, 2018: Changes in Madden-Julian Oscillation precipitation and wind variance under global warming. Geophysical Research Letters, 45, 7148-7155.

Cai, W., S. Borlace, M. Lengaigne, P. van Rensch, M. Collins, G. Vecchi, A. Timmermann, A. Santoso, M. J. McPhaden, L. Wu, M. H. England, G. Wang, E. Guilyardi, and F.-F. Jin, 2014: Increasing frequency of extreme El Niño events due to greenhouse warming. Nature Climate Change, 4, 111–116.

Cai, W., A. Santoso, G. Wang, S.-W. Yeh, S.-I. An, K. M. Cobb, M. Collins, E. Guilyardi, F.-F. Jin, J.-S. Kug, M. Lengaigne, M. J. McPhaden, K. Takahashi, A. Timmermann, G. Vecchi, M. Watanabe, and L. Wu, 2015b: ENSO and greenhouse warming. Nature Climate Change, 5, 849–859, doi:10.1038/nclimate2743.

Cai, W., G. Wang, B. Dewitte, L. Wu, A. Santoso, K. Takahashi, Y. Yang, A. Carréric, and M. J. McPhaden, 2018: Increased variability of eastern Pacific El Niño under greenhouse warming. Nature, 564, 201–206, doi:10.1038/s41586-018-0776-9.

Cai, W., G. Wang, A. Santoso, X. Lin, and L. Wu, 2017: Definition of Extreme El Niño and Its Impact on Projected Increase in Extreme El Niño Frequency. Geophysical Research Letters, 44, doi:10.1002/2017GL075635.

Cai, W., G. Wang, A. Santoso, M. J. McPhaden, L. Wu, F.-F. Jin, A. Timmermann, M. Collins, G. Vecchi, M. Lengaigne, M. H. England, D. Dommenget, K. Takahashi, and E. Guilyardi, 2015a: Increased frequency of extreme La Niña events under greenhouse warming. Nature Climate Change, 5, 132–137, doi:10.1038/nclimate2492.

Capotondi, A., 2013: ENSO diversity in the NCAR CCSM4 climate model. Journal of Geophysical Research: Oceans, 118, 4755–4770, doi:10.1002/jgrc.20335.

576 Capotondi, A., M.A. Alexander, N. A. Bond, E. N. Curchitser, and J. D. Scott, 2012: Enhanced upper-ocean
577 stratification with climate change in the CMIP3 models. Journal of Geophysical Research, 117, C04031,
578 doi:10.1029/2011JC007409.
579 Capotondi, A., A. T. Wittenberg, M. Newman, E. Di Lorenzo, J.-Y. Yu, P. Braconnot, J. Cole, B. Dewitte, B. Giese, E.
580 Guilyardi, F.-F. Jin, K. Karnauskas, B. Kirtman, T. Lee, N. Schneider, Y. Xue, and S.-W. Yeh, 2015:
581 Understanding ENSO Diversity. Bulletin of the American Meteorological Society, 96, 921–938,
582 doi:10.1175/BAMS-D-13-00117.1.
583 Carr, M. E., Strub, P. T., Thomas, A. C., and Blanco, J. L., 2002: Evolution of 1996–1999 La Niña and El Niño
584 conditions off the western coast of South America: a remote sensing perspective. Journal of Geophysical Research,
585 107(C12), 3236, doi:10.1029/2001JC001183.
586 Chiang, J. C. H. and D. J. Vimont, 2004: Analogous Pacific and Atlantic Meridional Modes of Tropical Atmosphere–
587 Ocean Variability. Journal of Climate, 17, 4143–4158, doi:10.1175/JCLI4953.1.
588 Choi, J., S.-I. An, and S.-W. Yeh, 2012: Decadal amplitude modulation of two types of ENSO and its relationship with
589 the mean state. Climate Dynamics, 38, 2631–2644, doi:10.1007/s00382-011-1186-y.
590 Clarke, A.J., 2010: Analytical Theory for the Quasi-Steady and Low-Frequency Equatorial Ocean Response to Wind
591 Forcing: The “Tilt” and “Warm Water Volume” Modes. Journal of Physical Oceanography, 40, 121–137,
592 doi:10.1175/2009JPO4263.1.
593 Deser, C., A. S. Phillips, R. A. Tomas, Y. M. Okumura, M. A. Alexander, A. Capotondi, J. D. Scott, Y.-O. Kwon, and
594 M. Ohba, 2012: ENSO and Pacific Decadal Variability in the Community Climate System Model Version 4.
595 Journal of Climate, 25, 2622–2651, doi:10.1175/JCLI-D-11-00301.1.
596 Dewitte, B., 2000: Sensitivity of an Intermediate Ocean–Atmosphere Coupled Model of the Tropical Pacific to Its
597 Oceanic Vertical Structure. Journal of Climate, 13, 2363–2388, doi:10.1175/1520-
598 0442(2000)013<2363:SOAIOA>2.0.CO;2.
599 Dewitte, B., J. Choi, S.-I. An, and S. Thual, 2012: Vertical structure variability and equatorial waves during central
600 Pacific and eastern Pacific El Niños in a coupled general circulation model. Climate Dynamics, 38, 2275–2289,
601 doi:10.1007/s00382-011-1215-x.
602 Dewitte, B., C. Cibot, C. Périgaud, S.-I. An, and L. Terray, 2007: Interaction between Near-Annual and ENSO Modes
603 in a CGCM Simulation: Role of the Equatorial Background Mean State. Journal of Climate, 20, 1035–1052,
604 doi:10.1175/JCLI4060.1.
605 Dewitte B., G. Reverdin, C. Maes, 1999: Vertical structure of an OGCM simulation of the equatorial Pacific Ocean in
606 1985–1994. Journal of Physical Oceanography. 29(7), 1542–1570.

Dewitte, B. and K. Takahashi, 2017: Diversity of moderate El Niño events evolution: role of air–sea interactions in the eastern tropical Pacific. Climate Dynamics, doi:10.1007/s00382-017-4051-9.

Dewitte, B., S. Thual, S.-W. Yeh, S.-I. An, B.-K. Moon, and B. S. Giese, 2009: Low-Frequency Variability of Temperature in the Vicinity of the Equatorial Pacific Thermocline in SODA: Role of Equatorial Wave Dynamics and ENSO Asymmetry. Journal of Climate, 22, 5783–5795, doi:10.1175/2009JCLI2764.1.

DiNezio, P. N., A. C. Clement, G. A. Vecchi, B. J. Soden, B. P. Kirtman, and S. K. Lee, 2009: Climate response of the equatorial pacific to global warming. Journal of Climate, 22, 4873–4892, doi:10.1175/2009JCLI2982.1.

DiNezio, P. N. and C. Deser, 2014: Nonlinear Controls on the Persistence of La Niña. Journal of Climate, 27, 7335–7355, doi:10.1175/JCLI-D-14-00033.1.

Dommenget, D., T. Bayr, and C. Frauen, 2013: Analysis of the non-linearity in the pattern and time evolution of El Niño southern oscillation. Climate Dynamics, 40, 2825–2847, doi:10.1007/s00382-012-1475-0.

Dommenget, D. and Y. Yu, 2017: The effects of remote SST forcings on ENSO dynamics, variability and diversity. Climate Dynamics, 49, 2605–2624, doi:10.1007/s00382-016-3472-1.

Gent, P. R., G. Danabasoglu, L. J. Donner, M. M. Holland, E. C. Hunke, S. R. Jayne, D. M. Lawrence, R. B. Neale, P. J. Rasch, M. Vertenstein, P. H. Worley, Z.-L. Yang, and M. Zhang, 2011: The Community Climate System Model Version 4. Journal of Climate, 24, 4973–4991, doi:10.1175/2011JCLI4083.1.

Graham, F. S., A. T. Wittenberg, J. N. Brown, S. J. Marsland, and N. J. Holbrook, 2017: Understanding the double peaked El Niño in coupled GCMs. Climate Dynamics, 48, 2045–2063, doi:10.1007/s00382-016-3189-1.

Ham, Y.-G. and J.-S. Kug, 2012: How well do current climate models simulate two types of El Niño? Climate Dynamics, 39, 383–398, doi:10.1007/s00382-011-1157-3.

Hunke, E.C. and W. Lipscomb, 2010: CICE: the Los Alamos sea ice model documentation and software user's manual version 4.0 LA-CC-06-012. Tech. Rep. LA-CC-06-012.

Hurrell, J. W., M. M. Holland, P. R. Gent, S. Ghan, J. E. Kay, P. J. Kushner, J.-F. Lamarque, W. G. Large, D. Lawrence, K. Lindsay, W. H. Lipscomb, M. C. Long, N. Mahowald, D. R. Marsh, R. B. Neale, P. Rasch, S. Vavrus, M. Vertenstein, D. Bader, W. D. Collins, J. J. Hack, J. Kiehl, and S. Marshall, 2013: The Community Earth System Model: A Framework for Collaborative Research. Bulletin of the American Meteorological Society, 94, 1339–1360, doi:10.1175/BAMS-D-12-00121.1.

Hwang, Y.-T. and D. M. W. Frierson, 2013: Link between the double-Intertropical Convergence Zone problem and cloud biases over the Southern Ocean. PNAS, 201213302, doi:10.1073/pnas.1213302110.

637 Izumo, T., M. Lengaigne, J. Vialard, I. Suresh, and Y. Planton, 2018: On the physical interpretation of the lead relation
638 between Warm Water Volume and the El Niño Southern Oscillation. Climate Dynamics, doi:10.1007/s00382-018-
639 4313-1.
640 Jin, F.-F., 1997: An Equatorial Ocean Recharge Paradigm for ENSO. Part I: Conceptual Model. Journal of the
641 Atmospheric Sciences, 54, 811–829, doi:10.1175/1520-0469(1997)054<0811:AEORPF>2.0.CO;2.
642 Jin, F.-F., S.-I. An, A. Timmermann, and J. Zhao, 2003: Strong El Niño events and nonlinear dynamical heating.
643 Geophysical Research Letters, **30**, 20–1–20–1, doi:10.1029/2002GL016356.
644 Johnson, N. C. and S.-P. Xie, 2010: Changes in the sea surface temperature threshold for tropical convection. Nature
645 Geoscience, 3, 842–845, doi:10.1038/ngeo1008.
646 Karamperidou, C., F.-F. Jin, and J. L. Conroy, 2017: The importance of ENSO nonlinearities in tropical pacific
647 response to external forcing. Climate Dynamics, 49, 2695–2704, doi:10.1007/s00382-016-3475-y.
648 Kay, J. E., C. Deser, A. Phillips, A. Mai, C. Hannay, G. Strand, J. M. Arblaster, S. C. Bates, G. Danabasoglu, J.
649 Edwards, M. Holland, P. Kushner, J.-F. Lamarque, D. Lawrence, K. Lindsay, A. Middleton, E. Munoz, R. Neale,
650 K. Oleson, L. Polvani, and M. Vertenstein, 2015: The Community Earth System Model (CESM) Large Ensemble
651 Project: A Community Resource for Studying Climate Change in the Presence of Internal Climate Variability.
652 Bulletin of the American Meteorological Society, 96, 1333–1349, doi:10.1175/BAMS-D-13-00255.1.
653 Kug, J.-S., J. Choi, S.-I. An, F.-F. Jin, and A. T. Wittenberg, 2010: Warm Pool and Cold Tongue El Niño Events as
654 Simulated by the GFDL 2.1 Coupled GCM. Journal of Climate, 23, 1226–1239, doi:10.1175/2009JCLI3293.1.
655 Lee, T. and M. J. McPhaden, 2010: Increasing intensity of El Niño in the central-equatorial Pacific. Geophysical
656 Research Letters, 37, doi:10.1029/2010GL044007.
657 Lengaigne, M., U. Hausmann, G. Madec, C. Menkes, J. Vialard and J. M. Molines, 2012: Mechanisms controlling
658 warm water volume interannual variations in the equatorial Pacific: diabatic versus adiabatic processes. Climate
659 Dynamics, 38, 1031 – 1046, doi:10.1007/s00382-011-1051-z.
660 Li, G. and S.-P. Xie, 2013: Tropical Biases in CMIP5 Multimodel Ensemble: The Excessive Equatorial Pacific Cold
661 Tongue and Double ITCZ Problems. Journal of Climate, 27, 1765–1780, doi:10.1175/JCLI-D-13-00337.1.
662 Li, G., S.-P. Xie, Y. Du, and Y. Luo, 2016: Effects of excessive equatorial cold tongue bias on the projections of
663 tropical Pacific climate change. Part I: the warming pattern in CMIP5 multi-model ensemble. Climate Dynamics,
664 47, 3817–3831, doi:10.1007/s00382-016-3043-5.
665 Liguori, G. and E. Di Lorenzo, 2018: Meridional Modes and Increasing Pacific Decadal Variability Under
666 Anthropogenic Forcing. Geophysical Research Letters, 45, 983–991, doi:10.1002/2017GL076548.
667 Maloney, E. D., A. F. Adames, and H. X. Bui, 2019: Madden-Julian Oscillation Changes under Anthropogenic
668 Warming. Nature Climate Change, 9(1), 26-33, doi:10.1038/s41558-018-0331-6.

669 Matveeva, T., D. Gushchina, and B. Dewitte, 2018: The seasonal relationship between intraseasonal tropical variability
670 and ENSO in CMIP5. Geoscientific Model Development, 11, 2373–2392, doi:10.5194/gmd-11-2373-2018.
671 McGregor, S., A. Timmermann, F.-F. Jin and W. S. Kessler, 2016: Charging El Niño events with off-equatorial wind
672 bursts. Climate Dynamics, 47: 1111, doi:10.1007/s00382-015-2891-8.
673 McPhaden, M. J., T. Lee, and D. McClurg, 2011: El Niño and its relationship to changing background conditions in the
674 tropical Pacific Ocean. Geophysical Research Letters, 38, doi:10.1029/2011GL048275.
675 McPhaden, M. J., S. E. Zebiak, and M. H. Glantz, 2006: ENSO as an Integrating Concept in Earth Science. Science,
676 314, 1740–1745, doi:10.1126/science.1132588.
677 Meehl, G. A., G. J. Boer, C. Covey, M. Latif, and R. J. Stouffer, 2000: The Coupled Model Intercomparison Project
678 (CMIP). Bulletin of the American Meteorological Society, 81, 313-318.
679 Meehl, G. A., W. M. Washington, J. M. Arblaster, A. Hu, H. Teng, J. E. Kay, A. Gettelman, D. M. Lawrence, B. M.
680 Sanderson, and W. G. Strand, 2013: Climate Change Projections in CESM1(CAM5) Compared to CCSM4.
681 Journal of Climate, 26, 6287–6308, doi:10.1175/JCLI-D-12-00572.1.
682 Neske, S. and S. McGregor, 2018: Understanding the Warm Water Volume precursor of ENSO events and its
683 interdecadal variation, Geophysical Research Letters, 45, doi:10.1002/2017GL076439.
684 Oleson, W., M. Lawrence, B. Bonan, G. Flanner, E. Kluzek, J. Lawrence, S. Levis, C. Swenson, E. Thornton, A. Dai, M.
685 Decker, R. Dickinson, J. Feddema, L. Heald, F. Hoffman, J.-F. Lamarque, N. Mahowald, G.-Y. Niu, T. Qian, J.
686 Randerson, S. Running, K. Sakaguchi, A. Slater, R. Stockli, A. Wang, Z.-L. Yang, X. Zeng, and X. Zeng, 2010:
687 Technical Description of version 4.0 of the Community Land Model (CLM). doi:10.5065/D6FB50WZ.
688 Philander, S. G. H., 1978: Forced oceanic waves. Reviews of Geophysics, 16, 15-46, doi:10.1029/RG016i001p00015.
689 Power, S., F. Delage, C. Chung, G. Kociuba, and K. Keay, 2013: Robust twenty-first-century projections of El Niño and
690 related precipitation variability. Nature, 502, 541–545, doi:10.1038/nature12580.
691 Rayner, N. A., 2003: Global analyses of sea surface temperature, sea ice, and night marine air temperature since the late
692 nineteenth century. Journal of Geophysical Research, 108, 4407, doi:10.1029/2002JD002670.
693 Ren, H.-L. and F.-F. Jin, 2011: Niño indices for two types of ENSO. Geophysical Research Letters, 38,
694 doi:10.1029/2010GL046031.
695 Richter, I., 2015: Climate model biases in the eastern tropical oceans: causes, impacts and ways forward. Wiley
696 Interdisciplinary Reviews: Climate Change, 6, 345–358, doi:10.1002/wcc.338.
697 Ropelewski, C. F. and M. S. Halpert, 1987: Global and Regional Scale Precipitation Patterns Associated with the El
698 Niño/Southern Oscillation. Monthly Weather Review, 115, 1606–1626, doi:10.1175/1520-
699 0493(1987)115<1606:GARSPP>2.0.CO;2.

Santoso, A., S. McGregor, F.-F. Jin, W. Cai, M. H. England, S.-I. An, M. J. McPhaden, and E. Guilyardi, 2013: Late-twentieth-century emergence of the El Niño propagation asymmetry and future projections. Nature, 504, 126–130, doi:10.1038/nature12683.

Smith, R., P. Jones, B. Briegleb, F. Bryan, G. Danabasoglu, J. Dennis, J. Dukowicz, C. Eden, B. Fox-Kemper, P. Gent, and others, 2010: The parallel ocean program (POP) reference manual ocean component of the community climate system model (CCSM) and community earth system model (CESM). Los Alamos National Laboratory Tech. Rep. LAUR-10-01853, 141, 1–140.

Stein, K., N. Schneider, A. Timmermann, and F.-F. Jin, 2010: Seasonal Synchronization of ENSO Events in a Linear Stochastic Model. Journal of Climate, 23, 5629–5643, doi:10.1175/2010JCLI3292.1.

Stevenson, S., A. Capotondi, J. Fasullo, and B. Otto-Bliesner, 2017: Forced changes to twentieth century ENSO diversity in a last Millennium context. Climate Dynamics, 1–16, doi:10.1007/s00382-017-3573-5.

Takahashi, K. and B. Dewitte, 2016: Strong and moderate nonlinear El Niño regimes. Climate Dynamics, 46, 1627–1645, doi:10.1007/s00382-015-2665-3.

Takahashi, K., C. Karamperidou, and B. Dewitte, 2018: A theoretical model of strong and moderate El Niño regimes. Climate Dynamics, doi:10.1007/s00382-018-4100-z.

Takahashi, K., A. Montecinos, K. Goubanova, and B. Dewitte, 2011: ENSO regimes: Reinterpreting the canonical and Modoki El Niño. Geophysical Research Letters, 38, doi:10.1029/2011GL047364.

Taylor, K. E., R. J. Stouffer, and G. A. Meehl, 2012: An Overview of CMIP5 and the Experiment Design. Bulletin of the American Meteorological Society, 93, 485–498, doi:10.1175/BAMS-D-11-00094.1.

Thual, S., B. Dewitte, S.-I. An, and N. Ayoub, 2011: Sensitivity of ENSO to Stratification in a Recharge–Discharge Conceptual Model. Journal of Climate, 24, 4332–4349, doi:10.1175/2011JCLI4148.1.

Thual, S., B. Dewitte, S.-I. An, S. Illig, and N. Ayoub, 2013: Influence of Recent Stratification Changes on ENSO Stability in a Conceptual Model of the Equatorial Pacific. Journal of Climate, 26, 4790–4802, doi:10.1175/JCLI-D-12-00363.1.

Trenberth, K. E. and D. P. Stepaniak, 2001: Indices of el Niño evolution. Journal of Climate, 14, 1697–1701.

Vecchi, G. A. and D. E. Harrison, 2006: The Termination of the 1997–98 El Niño. Part I: Mechanisms of Oceanic Change. Journal of Climate, 19, 2633–2646, doi:10.1175/JCLI3776.1.

Vecchi, G. A. and B. J. Soden, 2007: Global Warming and the Weakening of the Tropical Circulation. Journal of Climate, 20, 4316–4340, doi:10.1175/JCLI4258.1.

Wittenberg, A. T., A. Rosati, N.-C. Lau, and J. J. Ploshay, 2006: GFDL's CM2 Global Coupled Climate Models. Part III: Tropical Pacific Climate and ENSO. Journal of Climate, 19, 698–722, doi:10.1175/JCLI3631.1.

Xie, S.-P., Q. Peng, Y. Kamae, X.-T. Zheng, H. Tokinaga, and D. Wang, 2018: Eastern Pacific ITCZ Dipole and ENSO Diversity. Journal of Climate, 31, 4449–4462, doi:10.1175/JCLI-D-17-0905.1.

Yeh, S.-W., W. Cai, S.-K. Min, M.J. McPhaden, D. Dommenget, B. Dewitte, M. Collins, K. Ashok, S.-I. An, B.-Y. Yim, and J.-S. Kug, 2018: ENSO atmospheric teleconnections and their response to greenhouse gas forcing. Reviews of Geophysics, 56, 185–206, doi:10.1002/2017RG000568.

Yeh, S.-W., B. Dewitte, B. Y. Yim, and Y. Noh, 2010: Role of the upper ocean structure in the response of ENSO-like SST variability to global warming. Climate Dynamics, 35, 355–369, doi:10.1007/s00382-010-0849-4.

Yeh, S.-W., J.-S. Kug, B. Dewitte, M.-H. Kwon, B. P. Kirtman, and F.-F. Jin, 2009a: El Niño in a changing climate. Nature, 461, 511–514, doi:10.1038/nature08316.

Yeh, S.-W., B. Y. Yim, Y. Noh, and B. Dewitte, 2009b: Changes in mixed layer depth under climate change projections in two CGCMs. Climate Dynamics, 33, 199–213, doi:10.1007/s00382-009-0530-y.

Zebiak, S. E. and M. A. Cane, 1987: A Model El Niño–Southern Oscillation. Monthly Weather Review, 115, 2262–2278, doi:10.1175/1520-0493(1987)115<2262:AMENO>2.0.CO;2.

Zelle, H., G. Appeldoorn, G. Burgers, and G. J. van Oldenborgh, 2004: The Relationship between Sea Surface Temperature and Thermocline Depth in the Eastern Equatorial Pacific. Journal of Physical Oceanography, 34, 643–655, doi:10.1175/2523.1.

Zheng, X.-T., C. Hui, and S.-W. Yeh, 2018: Response of ENSO amplitude to global warming in CESM large ensemble: uncertainty due to internal variability. Climate Dynamics, 50:4019, doi:10.1007/s00382-017-3859-7.

Zheng, Y., J.-L. Lin, and T. Shinoda, 2012: The equatorial Pacific cold tongue simulated by IPCC AR4 coupled GCMs: Upper ocean heat budget and feedback analysis. Journal of Geophysical Research, 117, C05024, doi:10.1029/2011JC007746.

	Historical (1920-2005)			RCP8.5 (2006-2100)			Increase rate of frequency from present to future climate
	Number of events	Frequency of occurrence (events/decade)	% of events concomitant with an extreme precipitation event/strong event	Number of events	Frequency of occurrence (events/decade)	% of events concomitant with an extreme precipitation event/strong event	
Number of strong events	237	0.65	59%	302	0.77	89%	+18.5 %
Number of moderate events	538	1.42	1% (5)	541	1.42	31% (167)	-0.1 %
Number of extreme precipitation events	146	0.39	96%	489	1.26	55%	+225.6 %
Number of strong events peaking in JAS	107	0.30	34%	137	0.35	78%	+16.5 %
Number of strong events peaking in ONDJ	120	0.33	79%	44	0.11	100%	-65.8 %
Number of strong events peaking in FMA	9	0.02	100%	120	0.31	99%	+1314.9 %

Table 1 Statistics in El Niño events and extreme precipitation events. 3682 (3800) years are considered for the historical (RCP8.5) runs. Note that the values of the frequency of occurrence have been rounded while the percentages in the text use the exact values.

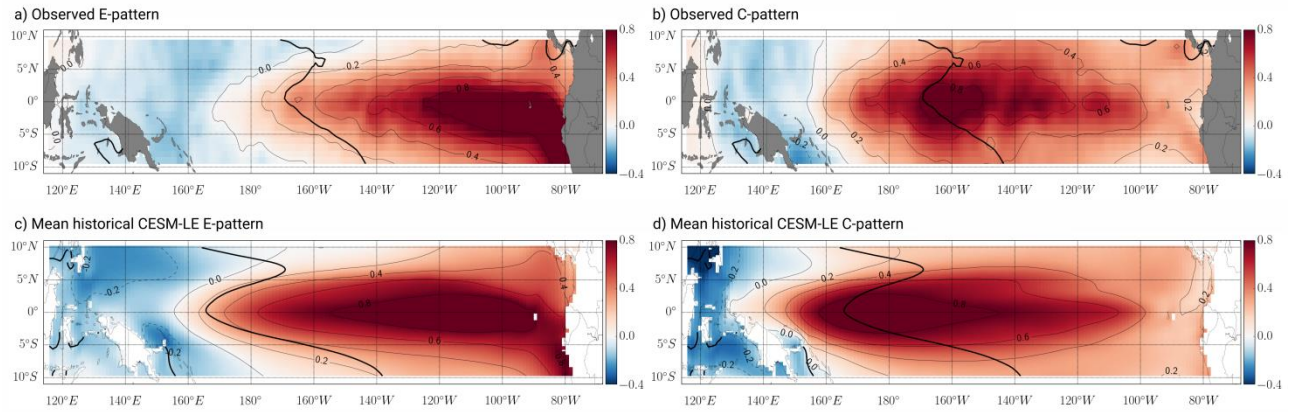

Figure 1: Linear regression coefficients (°C) of SST anomalies onto the E (a, c) and C (b, d) indices for (a, b) HadISST v1.1 (1950-2017) and (c, d) the ensemble mean of CESM-LE historical simulations (42 members). The E and C indices are defined from the two leading principal components of the EOF analysis of the SST anomalies in the tropical Pacific (115ºE-290ºE; 10ºS-10ºN). The SST anomalies are linearly detrended over each time period. Also shown is the mean position of the 28°C isotherm (thick black line).

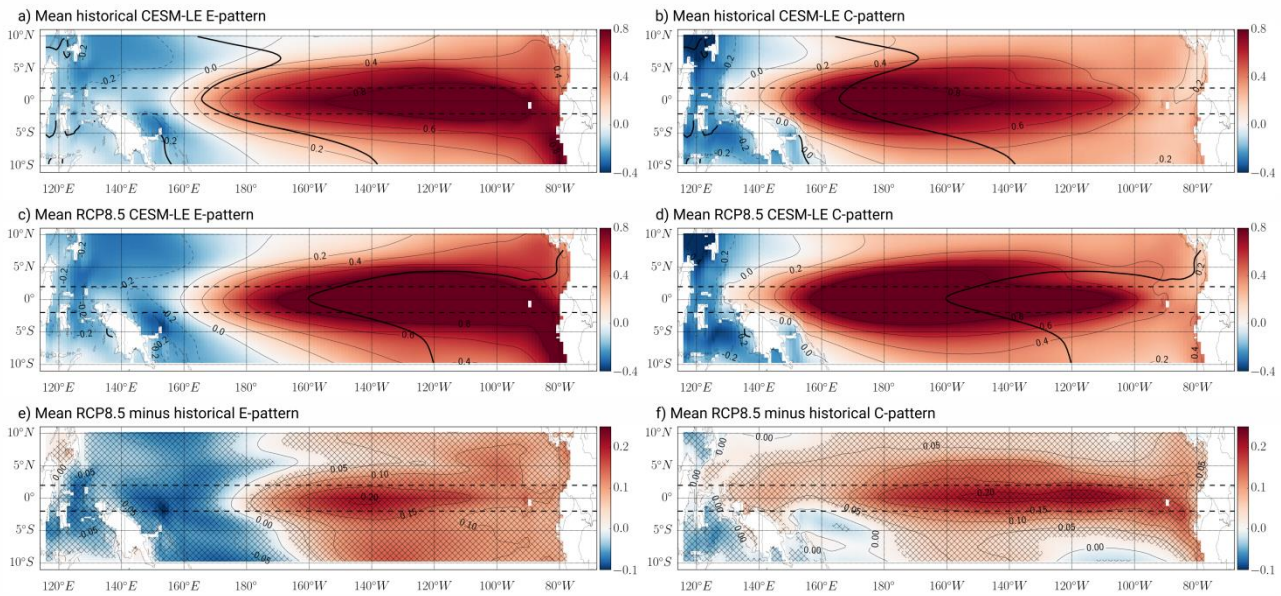

Figure 2: Ensemble mean of the linear regression coefficients (°C) of SST anomalies onto the E (left) and C (right) indices calculated for the historical runs (a, b), the RCP8.5 runs (c, d) and the differences between RCP8.5 and historical runs (e, f). The E and C indices are defined from the two leading principal components of the EOF analysis of the SST anomalies in the tropical Pacific (115ºE-290ºE; 10ºS-10ºN). The SST anomalies are linearly detrended over each time period. The 5% confidence intervals from a Wilcoxon rank-sum test is indicated by stippling. The stippling indicates where the values of the RCP8.5 runs are significantly larger (in absolute value) than that of the historical runs. Note the different scale of the colorbar on (e) and (f). In the dashed lines is indicated the 2°S-2°N region onto which the heat budget is projected.

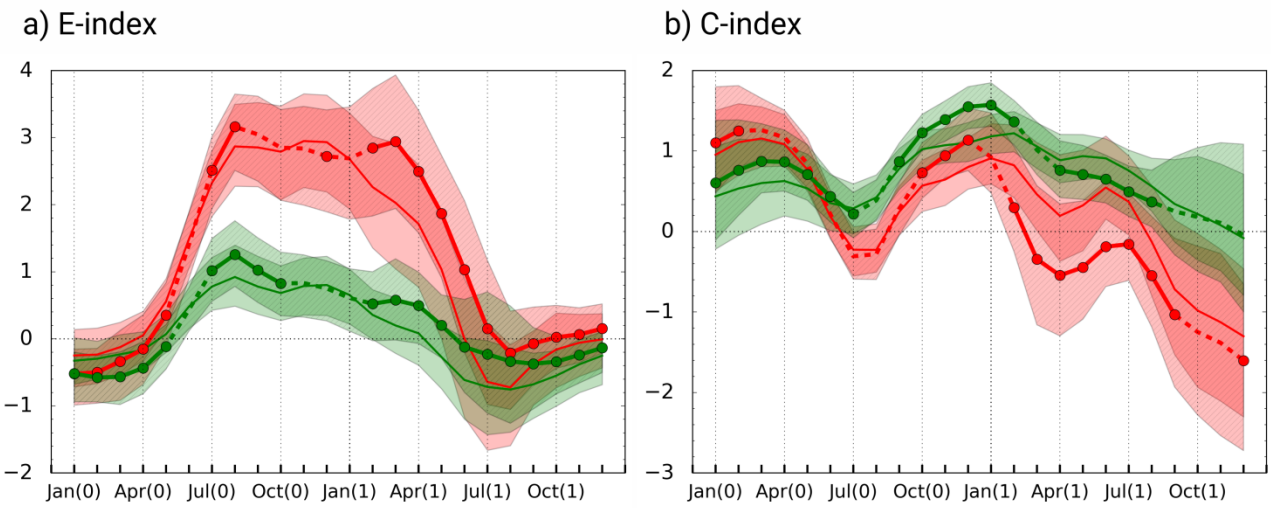

Figure 3: Composite evolution of (a) the E and (b) the C indices (115ºE-290ºE; 10ºS-10ºN) during strong (red) and moderate (green) El Niño events for (solid lines) historical and (lines with circles) RCP8.5 runs. The shading indicates the range of values between the 25th and 75th percentiles of the distribution. The portion of the curves in dashed line for the RCP8.5 composites indicates where the changes between historical and RCP8.5 are not significant at the 95% level according to a Wilcoxon rank sum test.

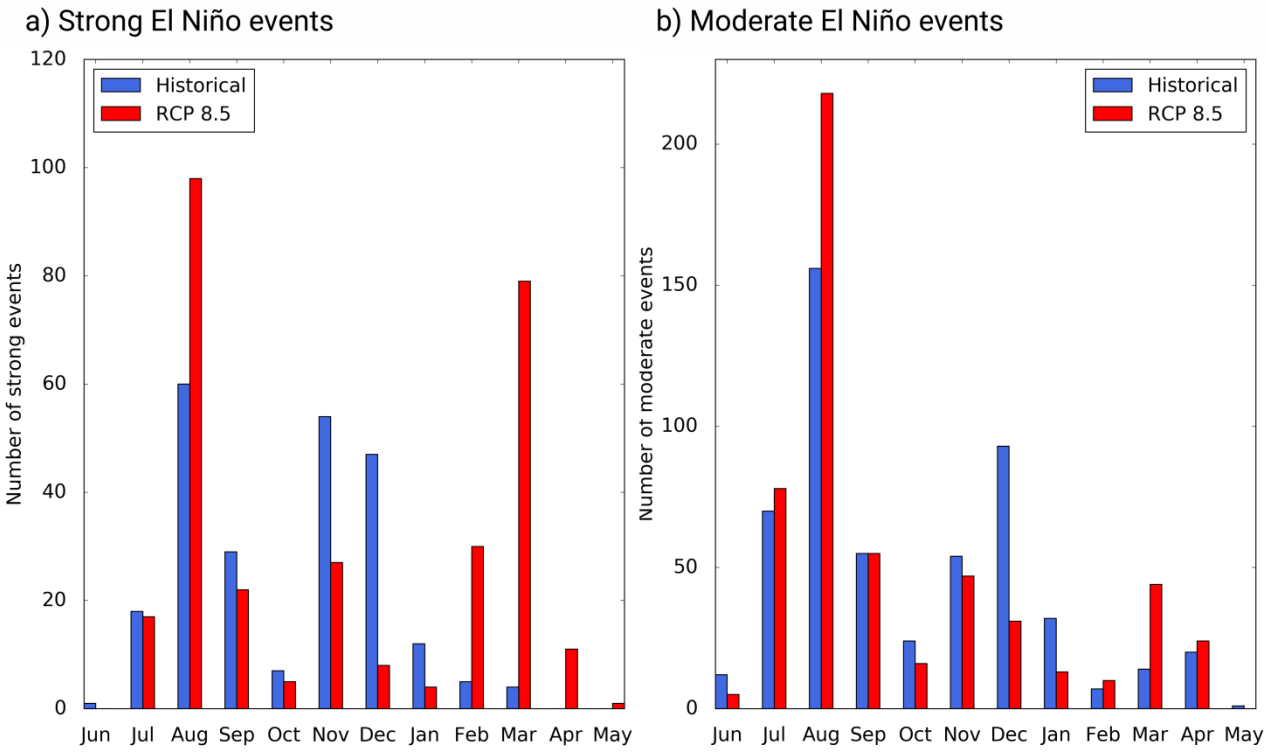

Figure 4: Number of (a) strong and (b) moderate El Niño events, defined from the E-index, as a function of the month in the calendar year when they peak (i.e. E index has maximum value) for (blue) historical and (red) RCP8.5 simulations. Note the different scale on the y-axis between (a) and (b).

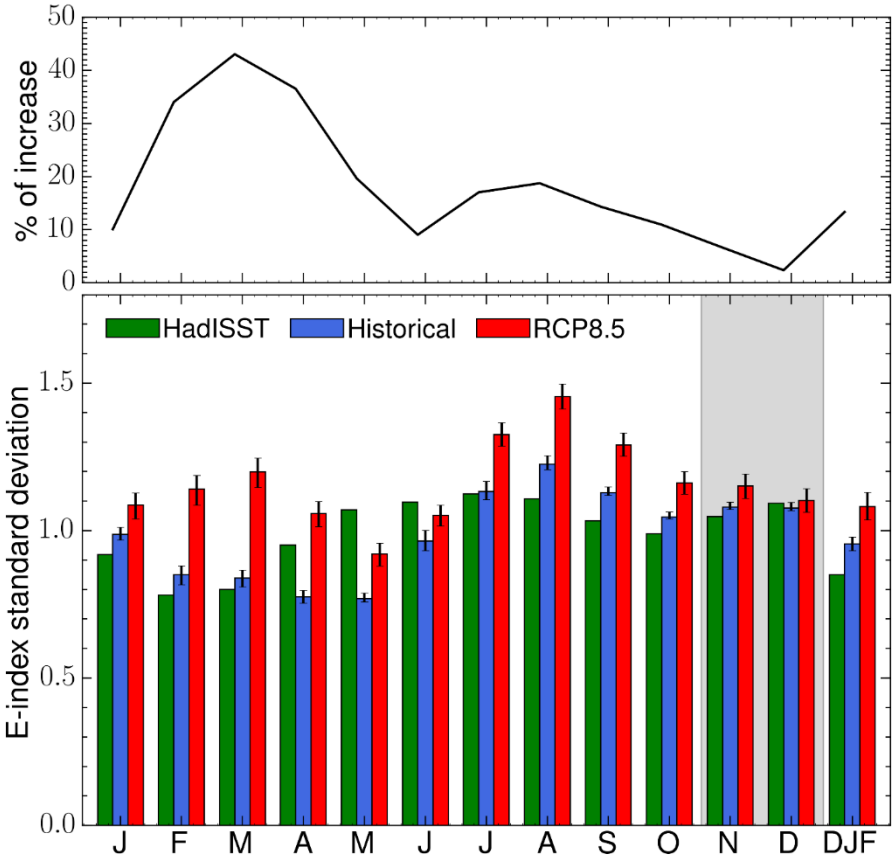

Figure 5: (Bottom panel) Climatological variance of the E index for (green) observations (1950-2017, 115ºE-290ºE; 10ºS-10ºN), (blue) the historical and (red) RCP8.5 simulations of CESM-LE. Error bars are inferred from the 95th and 5th percentiles of the distribution obtained by 10,000 realisations of randomly resampling the 40 (42) members and calculating their variance each time, any member being allowed to be selected again. (Top panel) Percentage of increase in variance from the historical to the RCP8.5 runs as a function of calendar month. The increase in variance between historical and RCP8.5 simulations is statistically significant at the 95% confidence level for all months except November and December (grey shading) according to Wilcoxon and bootstrap tests. The increase in variance associated with the DJF mean is provided on the left hand side of each panel. It is significant at the 95% confidence level.

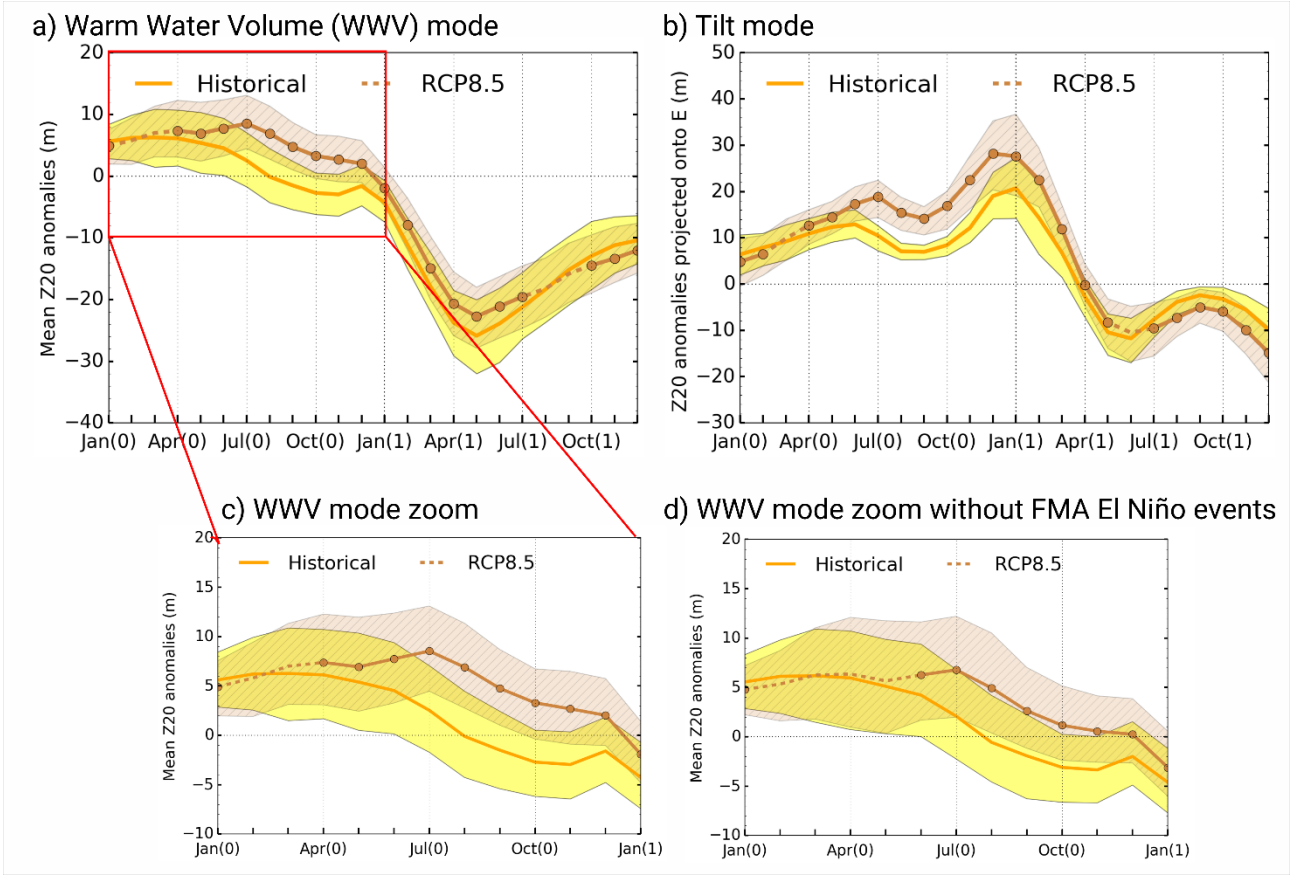

Figure 6: (Top panels) Composite evolution of (a) the Warm water volume (WWV) mode and (b) the tilt mode during strong El Niño events for the (solid yellow lines) historical and (brown lines with dots) RCP8.5 runs. The WWV mode corresponds to the mean 20°C isotherm depth (Z20) anomalies (m) averaged over the region (115°-290°E; 2°S-2°N). The tilt mode is estimated by projecting the 20°C isotherm depth (Z20) anomalies (m) onto the E mode pattern calculated over the domain (115°E-290°E; 2°S-2°N). The shading indicates the range of values between the 25th and 75th percentiles of the distribution of the members. The portions of the curves in dashed line for the RCP8.5 composites indicate when the changes between historical and RCP8.5 are not significant at 95% confidence level based on a Wilcoxon rank sum test. (Bottom panels) Composite evolution of Warm water volume (WWV) over Jan (Y0)-Jan(Y1) for (c) all the strong El Niño events, and (d) excluding the contribution of strong El Niño events peaking in FMA.

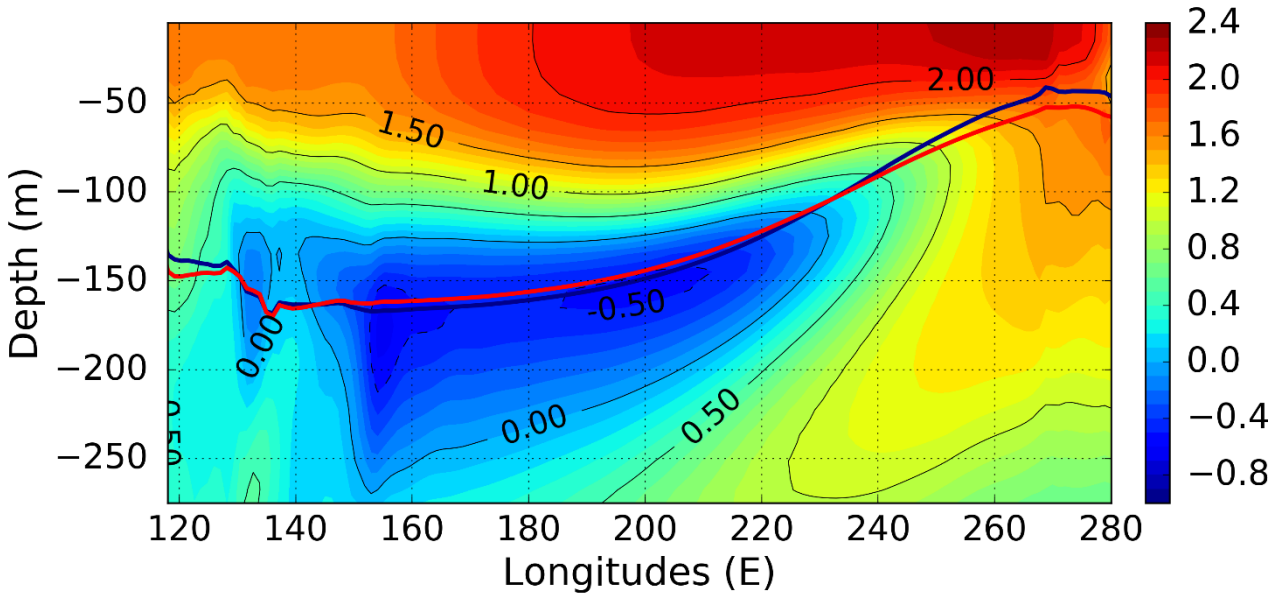

Figure 7: Mean differences of equatorial (2°S-2°N) temperature (in °C) between the RCP8.5 and historical simulations. The blue (red) line indicates the mean depth of the 20 °C isotherm for the historical (RCP8.5) simulations.

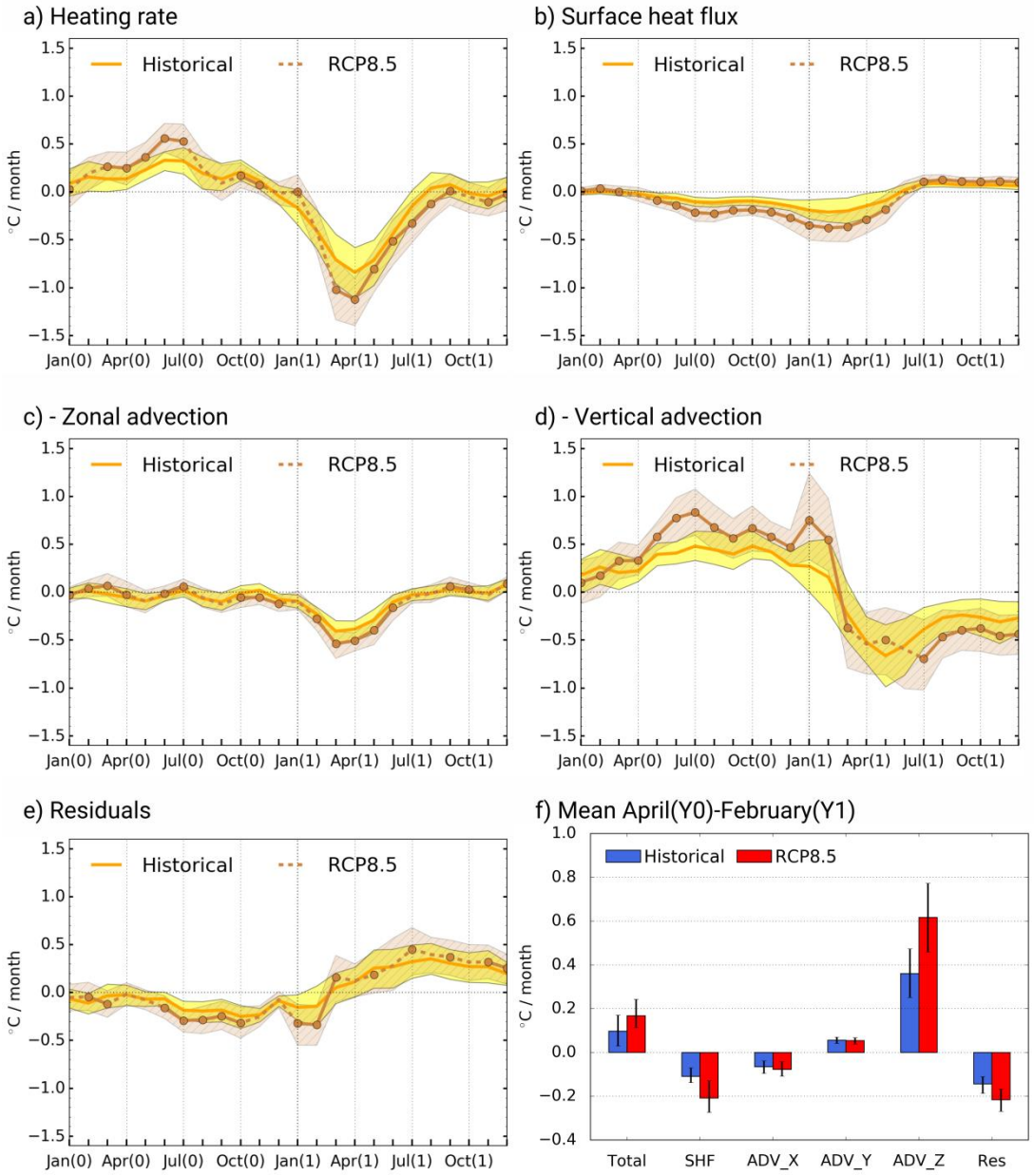

Figure 8: Heat budget projected onto the E mode: Composite evolution during strong El Niño events for (a) the total heating rate, (b) the surface net heat flux, (c) the zonal advection, (d) the vertical advection and (e) the residuals (i.e. difference between the rate of SST change and all tendency terms including meridional advection) for the (yellow) historical and (brown) RCP8.5 simulations. All terms are projected onto the E mode patterns (see the method section). The shading indicates the range of values between the 25th and 75th percentiles of the distribution of the members. The portions of the curves in dashed line for the RCP8.5 composites indicate when the changes between historical and RCP8.5 are not significant at 95% confidence level based on a Wilcoxon rank sum test. (f) Mean values over the period Apr (Y0)-Feb (Y1) of all the terms. Error bars are inferred from the 95th and 5th percentiles of the distribution obtained by randomly resampling the values of tendency terms of the 40 (42) members, any members being allowed to be selected again.

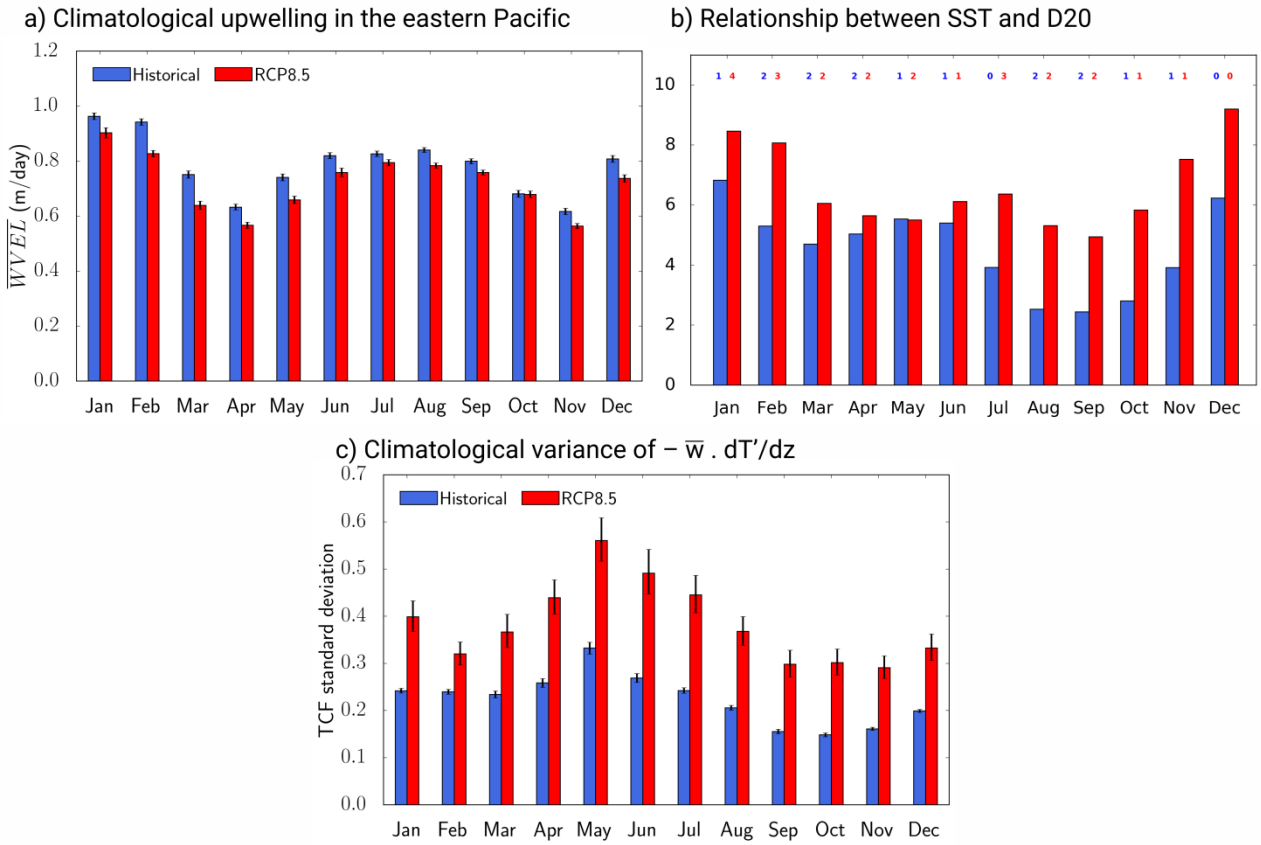

Figure 9: a) Changes in climatological mean upwelling in the eastern Pacific (Niño-3 region) for the (blue) historical and (red) RCP8.5 simulations (m/day). Error bars correspond to the inter-members spread (standard deviation). b) Changes in the maximum value of the slope of the lagged relationship between SST anomalies (E index) and the depth of the 20 °C isotherm (D20) anomalies in the eastern Pacific (projected onto the E mode) for the (blue) historical and (red) RCP8.5 simulations. The lag is indicated above the corresponding bars (positive value corresponds to D20 ahead SST). (c) Climatological variance of the thermocline feedback for the (blue) historical and (red) RCP8.5 simulations (°C/days). Error bars are inferred from the 95th and 5th percentiles of the distribution obtained by 10,000 realisations of randomly resampling the 40 (42) members and calculating their variance each time, any member being allowed to be selected again.

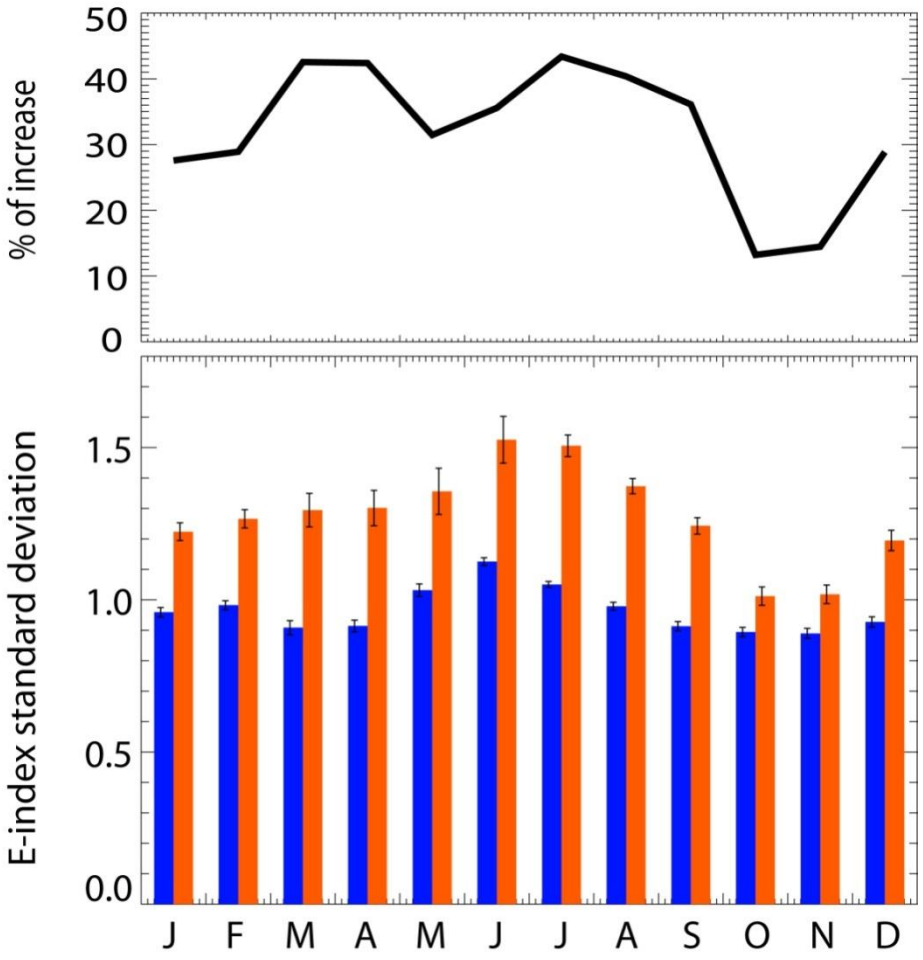

Figure 10: (Bottom panel) Climatological variance of the E-index for (blue) the historical and (red) RCP8.5 simulations of an ensemble of CMIP5 models. The ensemble corresponds to the 17 models used in Cai et al. (2018) that realistically represent the nonlinear Bjerknes feedback. Error bars are inferred from the standard deviation of 10,000 realisations obtained by randomly resampling the 17 models and calculating their variance each time, any models being allowed to be selected again. (Top panel) Percentage of increase in variance from the historical to the RCP8.5 runs as a function of calendar month.

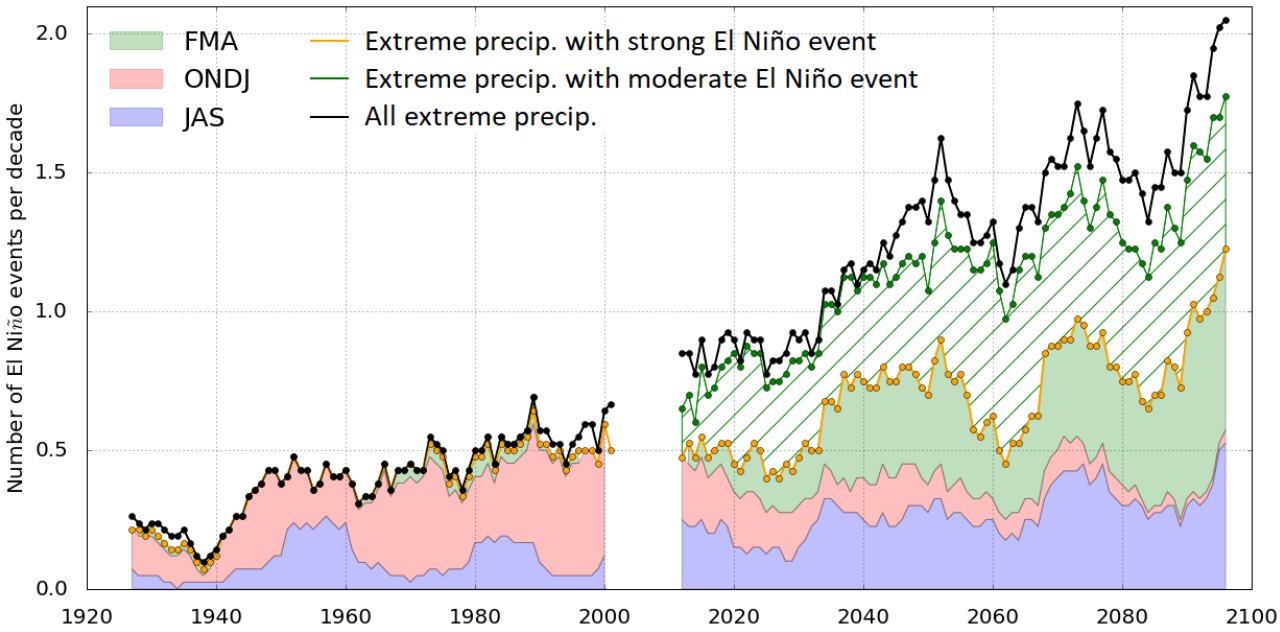

Figure 11: Number of extreme precipitation events over 10-year running windows that are concomitant with either strong or moderate El Niño events among the ensemble of the historical (1920-2005) and the RCP8.5 (2006-2100) simulations. Hatch indicates the proportion of moderate El Niño events while shading is for strong El Niño events. The colors refer to the seasons as defined in section 3.2: blue for JAS events, red for ONDJ events and green for FMA events. Note that there is a little share of extreme events that are not concomitant with either a moderate or a strong El Niño events (i.e. the green curve does not overlap the black curve), which is due to internal variability in precipitation (year of extreme precipitation event without an El Niño event).

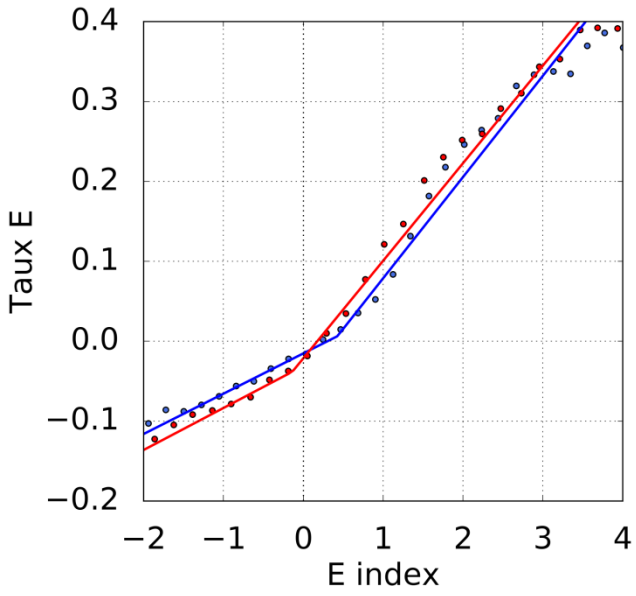

Figure S1: Changes in the non-linearity in the BJ feedback in CESM-LE. Response of monthly zonal wind stress anomalies (10^{-1} $N.m^{-2}$) at the location along the equator where the projection of the zonal wind stress onto the E mode (2°S-2°N) peaks for (blue) historical and (red) RCP8.5 simulations. 50 bins were defined on the maximum range of values of the index E in historical and RCP8.5 simulations respectively, and the median wind stress anomaly and E index are identified for each bin (circles). The method is similar to the one used in Cai et al. (2018) applied to the CMIP5 models except that a linear piecewise regression was carried out rather than two separate linear regressions for positive and negative median index values.

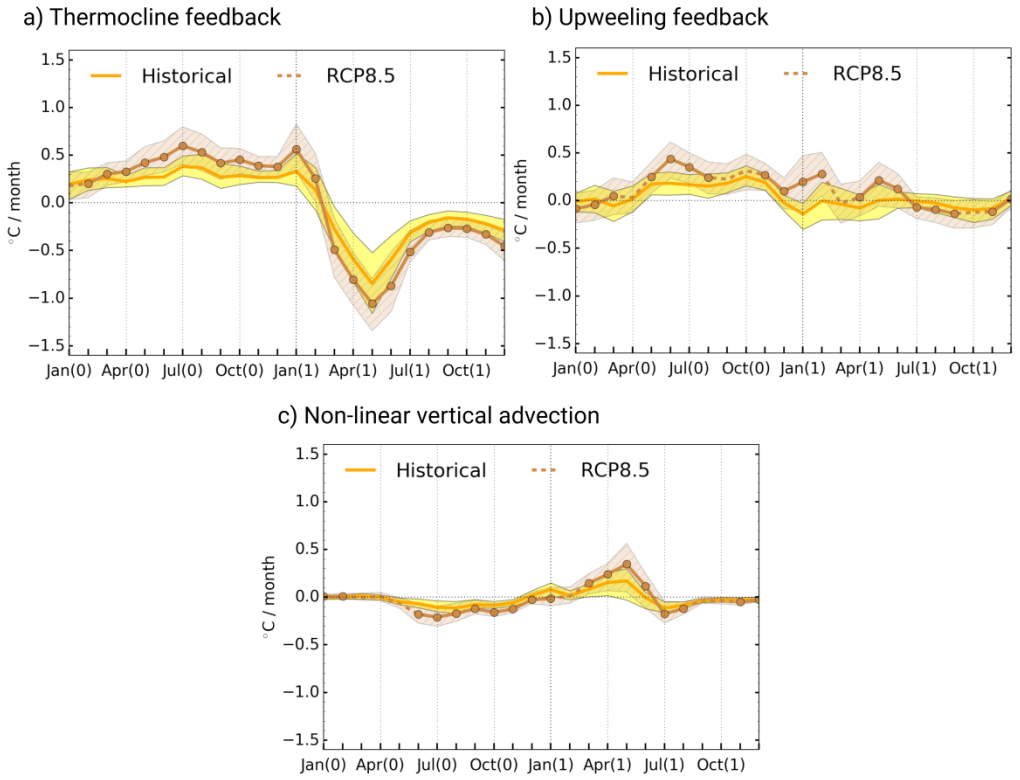

Figure S2: Reynolds decomposition of vertical advection. Composite evolution during strong El Niño events for (a) climatological vertical advection of anomalous temperature (thermocline feedback), (b) anomalous vertical advection of mean temperature (upwelling feedback), and (c) non-linear vertical advection for the (yellow) historical and (brown) RCP8.5 simulations. All terms are projected onto the E mode patterns (see the method section). The shading indicates the range of values between the 25th and 75th percentiles of the distribution of the members. The chunks of the curves in dashed line for the RCP8.5 composites indicate when the changes between historical and RCP8.5 are not significant at 95% confidence level based on a Wilcoxon rank sum test.

5.3 Supplementary materials

5.3.1 Changes in mean state under greenhouse gas forcing

Changes in ENSO statistics are intimately related to changes in the mean state of the tropical Pacific (see section 1.4 and paragraph 5.1). In particular, mean zonal SST gradient and mean vertical temperature gradient are of paramount importance in ENSO's dynamics, especially because the zonal advective feedback (ZAF) and the thermocline feedback (TCF) are explicitly dependent on each of them respectively. Their changes with global warming and changes in their interaction require special attention. In this paragraph, we focus thus on changes in surface temperatures and vertical profile of equator temperatures simulated by the model.

To estimate changes in SST due to global warming, we calculate the warming trend through a linear regression over the RCP8.5 period (2006-2100). We consider the RCP8.5 period as a whole because the increase in SST is very low before (1920-2005) and only really starts at the beginning of future simulations. It is the case whether in the Pacific between 35°S-35°N, or between 10°S-10°N, or between 5°S-5°N, whether on the entire width of the Pacific or in the Niño-3 or in the Niño-4 regions (Fig. 5.2).

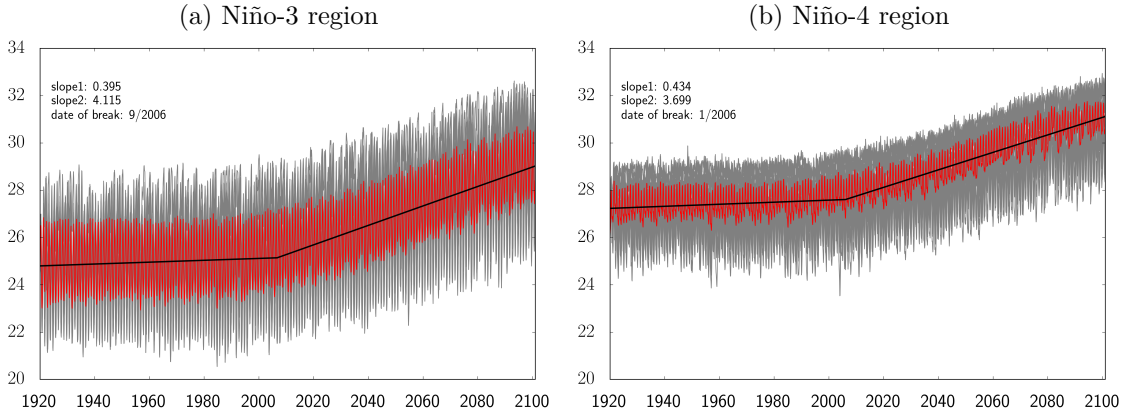

Figure 5.2 – Surface temperature for individual ensemble members of historical and RCP8.5 simulations (grey lines) and the ensemble mean (red line), averaged over (5.2a) Niño-3 region (5°S-5°N, 210°E-270°E) and (5.2b) Niño-4 region (5°S-5°N, 160°E-210°E). The slope 1 (slope 2) indicates the warming rate (°C/100 years) over the period before (after) the date break calculated via a piecewise linear regression.

For each region, the date from which temperature warming follows a new linear regression slope (according to a piecewise linear regression, see paragraph 2.2.3.1) is close to January 2006 (from November 2005 to September 2006 for the different regions included between 10°S and 10°N, and October 2007 when considering the Pacific between 35°S-35°N). Changes in the regression slope of global warming are almost immediate between 5°S-5°N. The warming rate over the historical period is in the order of 0.35 to 0.4 °C per century, while it reaches 10 times more over the period 2006-2100. Results are similar, even if slightly weaker, when calculating the warming trend via differences between the last 20 years in RCP8.5 (2080-2100) and the last 20 years in historical climate (1980-2000).

The CESM-LE ensemble mean warming pattern of the tropical Pacific is an "El Niño-like" pattern (Fig. 5.3) (Collins et al., 2010; Xie et al., 2010). The eastern Pacific is projected to warm faster than the western Pacific, which will decrease the zonal SST gradient in the tropical Pacific. Figure 5.2 shows consistently that the mean SST in Niño-3 at the end of future simulations reach values that are close to those of the future mean SST in Niño-4. The mean SST differences between Niño-4 and Niño-3 regions decrease from 2.5 °C to 2 °C. It is consistent with Zheng et al. (2018) who analysed the warming pattern simulated by each individual member of the CESM large ensemble (their figure 4). The eastern equatorial Pacific warms also faster than the off-equatorial regions, especially in the south Pacific. These

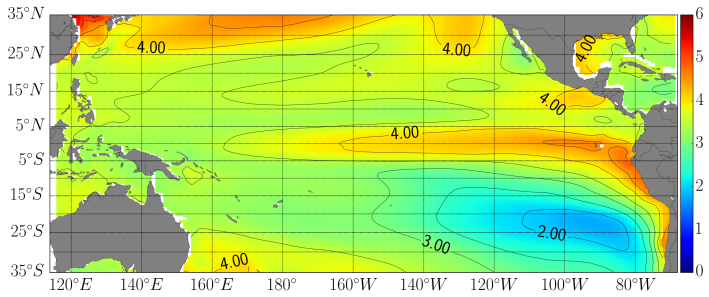

Figure 5.3 – CESM-LE ensemble mean warming rates of SST (°C/100 years) over the RCP8.5 period (2006-2100).

features of changes in mean state due to global warming, consistent with projected mean changes simulated by CMIP5 models (see paragraph 1.4.1), are likely to influence changes in ENSO statistics and dynamics (see paragraph 1.4.2).

Lian et al. (2018b) showed that especially the eastern equatorial Pacific has experienced a cooling over the historical period (1880-2015) in observation datasets, which is the opposite of the historical simulations. They argued that, in models, the atmospheric response to global warming, leading to an El Niño-like pattern through the weakening of Walker circulation, suppresses the oceanic response to global warming, which would lead to an La Niña-like pattern through an increase in vertical stratification and a strengthening of the zonal gradient of SST.

When analysing the warming trend observed in HadISST v1.1 over the period 1950-2005, the "La Niña-like" warming pattern is not so pronounced, nor is the "El Niño-like" warming pattern in the historical simulations of CESM-LE (Fig. 5.4a). The warming pattern of the ensemble mean of the CESM-LE historical simulations is also estimated (Fig. 5.4b). Although the warming rates are less pronounced in the simulation, and no cooling is simulated, there are common characteristics. The far eastern Pacific experiences a cooling, which is also simulated by CESM-LE. A large area, from the Baja California coast to the western-to-central equatorial Pacific, has warmed over this period. However, this area is divided in observations by a narrow band along the equatorial upwelling that seems to have strengthened, feature that is not simulated. The oceanic circulation in the tropical south Pacific and in the mid-latitudes north Pacific seems not to be realistically simulated in CESM-LE. The pattern of warming in the tropical south Pacific extends from the central to the eastern equatorial Pacific Pacific in observations while an inverted warming pattern that goes up to the Maritime Continent is simulated by CESM-LE. The mid-latitudes in the north Pacific has experienced a cooling that is not simulated.

However, these features of the mean warming pattern of CESM-LE in historical simulations should be taken with caution, given the disparity among members. While the warming pattern of member 019 (Fig. 5.4d) resembles the one observed, the pattern of member 003 (Fig. 5.4c) experiences a lower warming at the equator and in the south-eastern tropical Pacific. The two patterns show distinct warming trends, particularly off Baja California coast and in the equatorial Pacific. Note that in both case, the dynamics of the southern tropical Pacific is not well simulated. The majority of historical members simulates an El Niño-like warming. However, around a third of the historical members simulates less warming in the eastern equatorial Pacific than in the western equatorial Pacific and in the off-equator regions. These simulation failures, related to model biases, require further investigation to make future projections more reliable (Li et al., 2016; Ying et al., 2019; Lian et al., 2018b). Note, however, that despite the wide dispersion of patterns warming in the historical climate, the warming patterns projected into the future climate are very similar. Internal variability has very little impact on projected surface warming. This result is consistent with Zheng et al. (2018) (see their Figure 4).

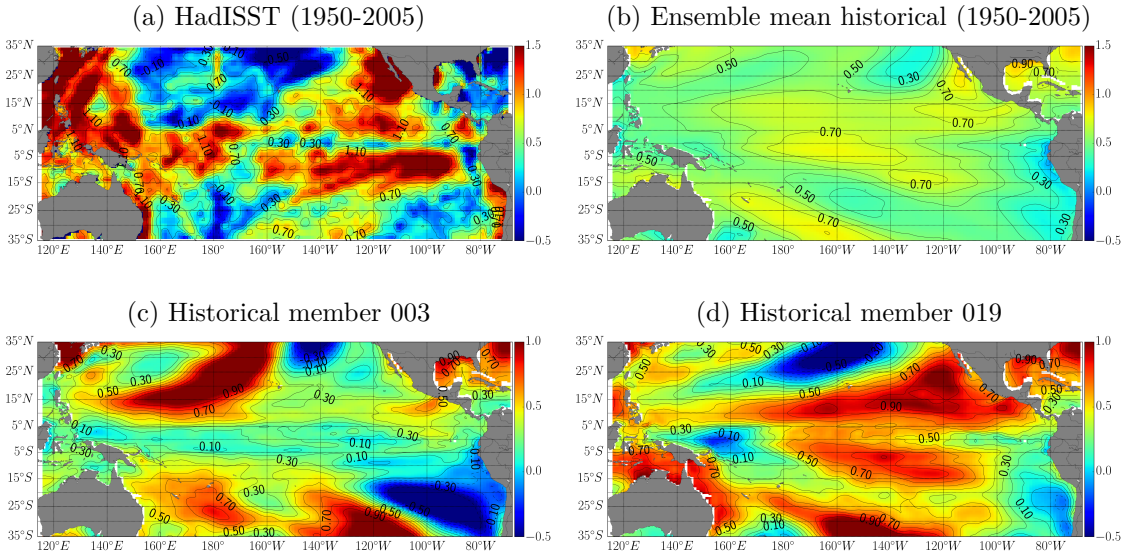

Figure 5.4 – Warming rates of SST (°C/100 years) over the historical period (1950-2005) for (5.4a) HadISST v1.1, (5.4b) the ensemble mean of CESM-LE historical simulations, (5.4c) the member 003 and (5.4d) the member 019 of CESM-LE historical simulations .

CESM-LE projects also an increase in the vertical stratification with global warming, due to the faster warming in surface (Fig. 5.5). The increased stratification leads to a flattened thermocline, defined by the depth of the maximum of the vertical temperature gradient (red lines in Figure 5.5), consistent with Vecchi and Soden (2007) and Yeh et al. (2009a). The thermocline flattens especially because it becomes shallower in the central Pacific. However, in the far eastern Pacific, east of 270°E, the thermocline depth does not change with global warming, unlike the depth of the 20 °C isotherm (Z20) (black lines in Figure 5.5). Even if Z20 is widely used as a proxy of the thermocline depth, Castaño Tierno et al. (2018) showed that both definitions give different results from estimated depths, whether in reanalysis dataset (SODA v2) or CMIP5 simulations. In reanalysis dataset, the thermocline depth is shallower in the far eastern Pacific and west of 160°W. This feature is even more pronounced in CMIP5 models. Moreover, the seasonal cycle of the thermocline depth especially in the eastern Pacific has much more pronounced variations than that of the Z20. These differences might be reinforced in the future climate and using the Z20 as a proxy for the thermocline depth can lead to misinterpretations of mean state and process changes (Yang and Wang, 2009; Castaño Tierno et al., 2018).

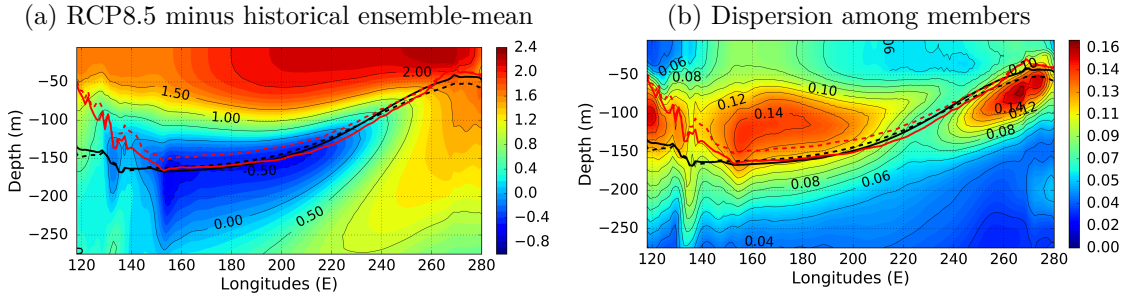

Figure 5.5 – Changes in vertical stratification in CESM-LE. (5.5a) Differences between ensemble-mean RCP8.5 minus historical equatorial (2°S-2°N) temperature anomalies (°C). (5.5b) Dispersion among the ensemble of the mean temperature difference (°C). Red lines indicate the ensemble-mean depth of the thermocline defined as the depth of the maximum value of the vertical temperature gradient. Black line are the ensemble-mean depth of the 20 °C isotherm. Solid lines are for the ensemble-mean of CESM-LE historical simulations and dashed lines are for the ensemble-mean of RCP8.5 simulations.

In the present work, the diagnostics of changes in oceanic processes are based on the anomalies of Z20, i.e. with its mean depth removed, so that we expect much less sensitivity to

the way the thermocline is calculated, because the processes that form the mean thermocline are distinct from those that produce thermocline fluctuations. The mean thermocline is, in particular, constrained by vertical mixing and the ventilation from the mid-latitudes (Wyrtki, 1961; Harper, 2000), while the thermocline inter-annual anomalies result mostly from the equatorial wave dynamics (Zebiak and Cane, 1987). Both types of processes have a different sensitivity to climate change.

5.3.2 The seasonally stratified El Niño events

In the submitted publication (see paragraph 5.2), we show that the E-index during El Niño events can peak at different seasons, preferably in winter (from October to January, ONDJ) and summer (from July to September, JAS). This feature leads to the classification of El Niño events according to the seasonal stratification of the E-peak:

- El Niño events whose the E-peak occurs between July and September, referred as JAS El Niño events and represented by the blue color thereafter,
- El Niño events whose the E-peak occurs in winter, between October and January, referred as ONDJ El Niño events (red color),
- and El Niño events whose the E-peak occurs at the end of the winter, early spring, referred as FMA El Niño events (green color).

The months of May and June are excluded of the seasonal stratification of the El Niño events, because few events are peaking during these months, whether in historical or RCP8.5 runs (see figure 4 of the paper).

All events show similar development (or not distinguishable significantly) of the E and C indices until August, with, in particular, an initial abrupt increase of the E-index from April to August of the developing year (year Y0), whatever in historical or RCP8.5 simulations (see also paragraph 3.3.1). In historical simulations (Fig. 5.6a and 5.6c), JAS El Niño events have an E-index which only decreases after a punctual peak in summer, first slowly until April of the next year and then more abruptly. In the same time, after the summer peak, the C-index is always positive and greater than for the others kind of events. ONDJ El Niño events present a more known evolution, with a positive E-peak centred in October-December. FMA El Niño events have grater magnitude in E-index than ONDJ El Niño events and the E-index continues to grow to reach a peak in February-March, then decay rapidly. The C-index is negative as of January.

Interestingly, in RCP8.5 simulations (Fig. 5.6b and 5.6d), JAS and ONDJ composite events do not show great differences in the evolution of the E or C indices. The main differences appear for the FMA El Niño composite, but it is also due to the fact that there are very few El Niño events in the historical FMA composite (9 events) and that these events are very strong in terms of magnitude. Thus, the RCP8.5 FMA El Niño composite is composed of more "normal" strong events.

Finally, El Niño events can have E-peaks that do not coincide with peaks on traditional SSTA indices, like PC1 or Niño-3.4 index. This is the case in historical situation and it will be amplified in future situation. Note that traditional ENSO indices, such as the Niño-3 index, have a projection on both the E and C indices. Niño-3 index can thus be expressed as Niño-3 = α E + β C. When the E-index peaks in summer during strong events, the C-index is negative at the same time (Fig. 5.6), so that the Niño-3 index cannot peak at that time, but instead peaks when the C-index peaks, i.e. in Dec Y(0) since the E-index remains almost constant between Aug and Dec Y(0). Thus, the events with E-peak in July-August-September correspond to events with peak in Niño-3 mainly in NDJF owing to the larger contribution of the C-index to Niño-3 as El Niño develops. The shift in seasonality of the E-peak during El Niño events does not occur when looking at other SST indices (PC1, Niño-4, Niño-3, Niño-34 SSTA indices), whose distributions remain centred in boreal winter (December-January), even if a weak peak appears for Niño-3 and Niño-34 SSTA indices in the future climate (not

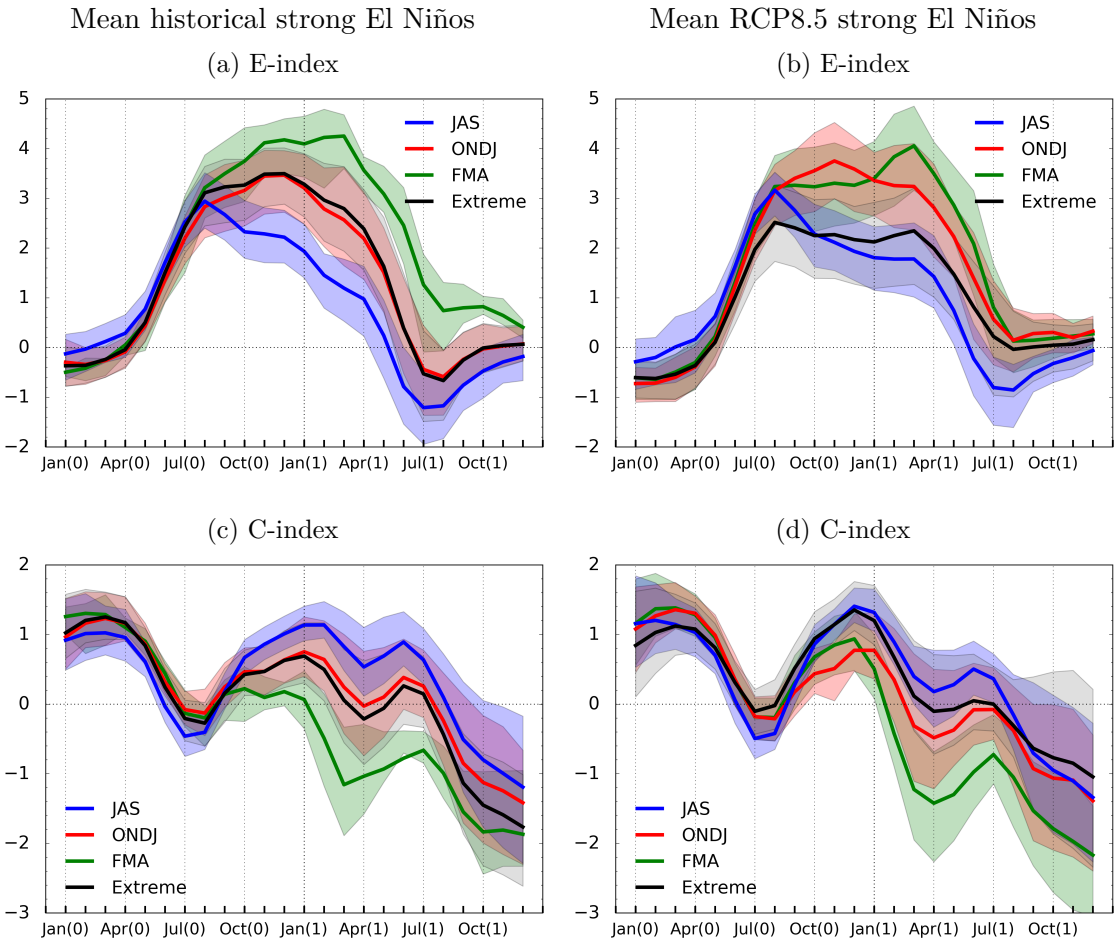

Figure 5.6 – Temporal evolution of (top) the E-index and (bottom) the C-index of strong El Niño events, for the composite events of (left) the 42-members of the historical simulation and (right) the 40-members of the RCP8.5 simulation. Composites consist of strong events whose E-peak occurs in (blue) July-August-September (JAS), (red) October-November-December-January (ONDJ), (green) in February-March-April (FMA). In black lines are the composite event according the definition of extreme events by Cai et al. (2014). The shadow corresponds to events of the strong regime between the 25th et 75th percentiles.

shown). Time-longitude evolutions of SSTA, zonal wind stress anomalies and precipitation for the different types of El Niño events are described in detail in Annexe 5.3.4.2.

The change in the El Niño E-peak season appears to be a robust feature of the future climate. The increase in the number of FMA El Niño events is associated with an increase in the E-index variance in FMA. We show that this increase in E-index variance is also simulated by a set of CMIP5 models that realistically represents the non-linear Bjerknes feedback (see Figure 10 of the paper, paragraph 5.2). Moreover, this increase in the E-index variance during FMA in CESM-LE is not dependent on the method used to remove the signal of the global SST warming (see section 3.4). Although the choice of the method affects the mean E-index variability and the rate of change of certain monthly E-index variances, this rate is positive whatever the method for the months of February to April. This means that, whatever the method, the variability in FMA increases significantly (at the 95 % confidence level) between historical and RCP8.5 simulations of CESM-LE.

Another interesting feature of changes in El Niño events in RCP8.5 simulations appears when comparing strong events with extreme events defined by Cai et al. (2014), referred as extreme precipitation events (black lines in Figure 5.6). Extreme precipitation El Niño events present an evolution of the E and C indices very similar to ONDJ strong El Niño events in historical simulations. However, in RCP8.5 simulations, extreme precipitation El Niño events present a lower amplitude than strong El Niño events. In fact, RCP8.5 extreme precipitation El Niño composite is also composed of El Niño events classified as moderate from E-index. The increase in extreme precipitation events corresponding to events that cause rainfall in the eastern Pacific during the boreal winter, it is interesting to understand how events associated with a warming, even moderate, of the SST projected on the E-index in summer cause rains in the eastern tropical Pacific in winter in RCP8.5 simulations. This interesting change in classification of extreme precipitation El Niño events is discussed in the publication (see paragraph 5.2) and in the paragraph 5.3.3.2.

This seasonal variation in the E-peak is also an observable feature (Fig. 5.7). The most commonly observed El Niño has a E-peak in winter (top panels). The strong El Niño events of 1997-98 and 2015-16 belong to this category. On the other hand, the strong El Niño event of 1982-83, although displayed with the winter events in Figure 5.7a, has its peak in June of the second year (June Y1). In addition to these strong El Niño events, some moderate El Niños, in 1994, 2002 and 2006, have also their peak in winter. However, their evolution differs from strong events: it is not a smooth and regular warming but a short, rapid and small amplitude warming. The strong El Niño event of 1972-73 is a summer event (JAS, Fig. 5.7b). Except this event, all JAS El Niño are moderate. This category has a large dispersion, particularly in the month of their peak, which can occur from May (1965, 1969) to September (1979, 1987). Another small category appears with El Niño events that follow each other from one year to the next, and that preferentially peak in the spring (Fig. 5.7c).

The peak on the E index can be translated into a maximum anomalous warming in one of the ENSO fixed regions (Niño-3 or Niño-3.4) and thus be diagnosed in previous studies. Thus Kessler (2002) mentioned that SSTA peaks occurred in others seasons than winter, such as August 1987, February 1992 and May 1993 for the corresponding El Niño events using NCEP/NOAA dataset. Neelin et al. (2000) showed that, even if most El Niño events have a maximum warming in winter, some events have a peak in fall or even in the spring season. They mentioned the local maximum in August of the 1972-73 El Niño event and the peak (in Niño-3 region) in September of the 1987 El Niño event.

5.3.3 Changes in ENSO statistics

5.3.3.1 Changes in frequency of occurrence

The frequency of occurrence of (total) El Niño events, whether defined by PC1 or ONI, is projected to slightly increase, but not dramatically (Table 5.1).

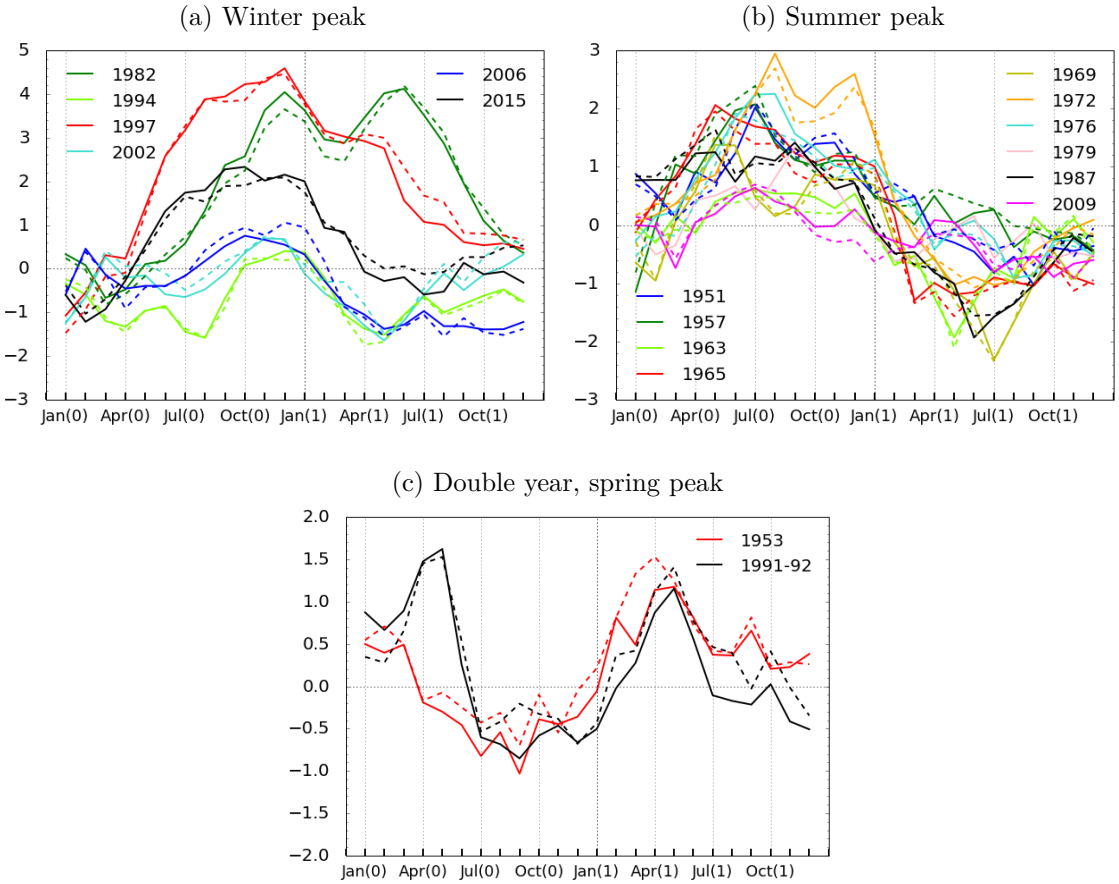

Figure 5.7 – Temporal evolution of the E-index during observed El Niño events. The solid lines correspond to the HadISST v1.1 dataset, the dashed lines to ERSST v3b.

	Historical		RCP8.5	
	Frequency	Return period	Frequency	Return period
PC1 El Niños	0.21	1 event/4.8 years	0.24	1 event/4.2 years
ONI El Niños	0.21	1 event/4.7 years	0.25	1 event/4.1 years

Table 5.1 – Changes in frequency of occurrence (and return period) of El Niño events. The frequency of occurrence in historical (RCP8.5) simulations are estimated over 1920-2005 (2051-2100, the last fifty years of simulation).

Note that the return periods of PC1 El Niños in historical simulations are close to those computed for the PI-control simulation with return periods of 1 event every 4.8, 14.8 and 7.1 years for all PC1, strong and moderate El Niños respectively. The PI-control simulation does not include anthropogenic forcing. Thus the frequency evolutions analysed during the RCP8.5 simulations and attributed to global warming does not seem to be apparent yet on average over the 86 years of historical simulations.

When focusing on strong and moderate events statistics (Table 5.2), it appears that the probability of occurrence of moderate El Niños will probably not change much in the future, and that of strong El Niños is likely to increase, multiplied by an ensemble-mean coefficient of 1.35.

The probabilities of frequency of occurrence of EP and CP El Niños, very close to each other in historical simulations (Table 5.2), are likely to evolve differently. In particular, the frequency of CP El Niños is projected to increase with global warming in CESM-LE simulations, consistent with the result of Yeh et al. (2009a) using a set a CMIP3 CGCMs. However, in PI-control simulation, the return periods of EP and CP El Niños are estimated to 1 event every 11.3 years and 1 event every 8.7 years respectively, while the return periods of ONI El Niño is estimated to 1 event every 4.9 years. It seems that the internal variability can play a significant role in the estimation of frequencies according to the period studied (Wittenberg, 2009).

Return period	Historical	RCP8.5
Strong El Niños	1 event/15.4 years	1 event/11.4 years
Moderate El Niños	1 event/6.9 years	1 event/6.8 years
EP El Niños	1 event/9.6 years	1 event/9.4 years
CP El Niños	1 event/9.9 years	1 event/7.6 years

Table 5.2 – Changes in frequency of occurrence (and return period) of El Niño events depending on its diversity. The frequency of occurrence in historical (RCP8.5) simulations are estimated over 1920-2005 (2051-2100, the last fifty years of simulation).

To further analyse changes in frequency of El Niño events during the 21st century, while taking into account the internal low-frequency variability, we compute the probability of occurrence of El Niño events per 10 years, that is the ensemble-sum of the number of events per 10 years for each year normalised by the number of members (Fig 5.8). The probabilities of occurrence in historical and RCP8.5 simulations are compared to the internal variability estimated from the PI-control simulation. The spread of the natural variability is estimated through a bootstrap test: 42 periods (same value as the number of historical members) of 100 years are taken randomly in 1801 years of the PI-control simulation. The sum of the numbers per 10 years of each type of El Niños along the 100 years is then normalised by the number of periods. The result obtained is a timeserie of 100 years of the probability of occurrence of each type of El Niño event, comparable to that obtained from the historical members. We repeat the calculation 5,000 times randomly and compute the 5th and the 95th percentiles in order to estimate the spread of the internal variability (dashed lines on figures 5.8a, 5.8b, 5.10a). The same exercise was performed using 40 periods as the number of RCP8.5 members, the number of members of climatic systems does not change the results, the differences being of the order of 10^{-3}. The number of members of the simulations is high enough to obtain a satisfactory significance of the climate system (Zheng et al., 2018).

Note first that the frequencies of occurrences of all PC1 or all ONI-based on definition El Niño events (Fig. 5.8, yellow lines) are very close to each other as well as in PI-control simulation, that is without anthropogenic forcing, and in historical simulations. The evolution of the number per 10 years of all PC1 or ONI based on definition El Niño has little dispersion with a maximum difference between the extreme values of the order of 0.50 event per 10 years ($\pm$0.25 event per 10 years around the mean value), except at the end of the RCP8.5 simulations when the values begin to come out, for several periods in a row, of the values

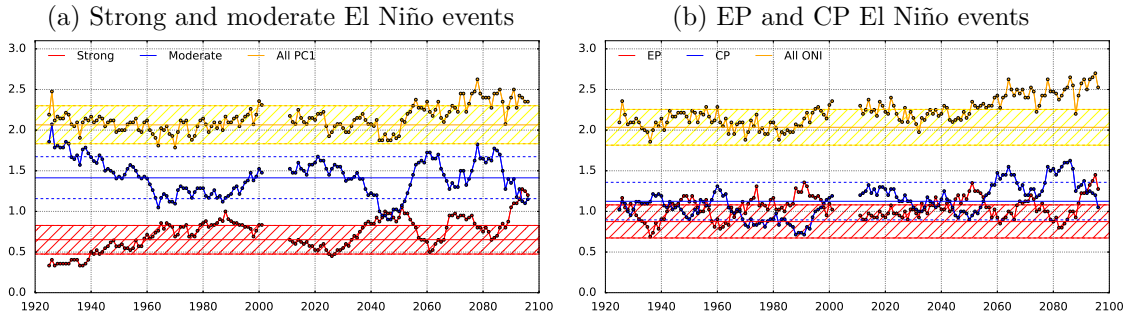

Figure 5.8 – Temporal evolution of the probability of occurrence of El Niño events per 10 years for (5.8a) El Niño events defined by the PC1 and (5.8b) El Niño events defined by the ONI (yellow line). On 5.8a appear also the numbers per 10 years of strong (red line) and moderate (blue line) El Niños while on 5.8b appear also the numbers per 10 years of EP (red line) and CP (blue line) El Niños defined in DJF. The dashed lines of each color represent the 5th and the 95th percentile values of probability of each event in the PI-control simulation determined from a 5,000 bootstrap draws using 42 periods of 100 years randomly taken in 1801 years of the PI-control simulation. The number of events is counted by considering periods definition.

that the system can take in PI-control simulation with internal variability.

The frequency of occurrence of the diversity of El Niño (strong and moderate (Fig. 5.8a) or EP and CP El Niño events (Fig. 5.8b presents larger spread in historical simulations. Their frequency could be more influenced by low-frequency variability, with a frequency of occurrence out of the PI-control spread, from 1925 to 1940 for the PC1-based on definition events (Fig. 5.8a) and from 1970 to 1995, and more particularly from 1985 to 1995, for the ONI-based on definition events (Fig. 5.8b). These low-frequency fluctuations lead to more or less long periods of alternation of the EP/CP ratio. A longer period of distribution of the EP/CP ratio is simulated, for example, at the end of the historical simulations. Surprisingly, this period of historical ensemble-mean low rate of CP compared to EP events occurs at the same time as the observed period categorised as being favourable to EP events (An and Wang, 2000; Kao and Yu, 2009). The new increase in CP events in the early 2000s can similarly be compared to the observed last decades favouring CP events (Wang and Ren, 2017). This resemblance of the low-frequency internal variability, simulated on average by the members, with the observations, requires further investigation in order to understand if it can be related, for instance, to a realistic representation of the low-frequency phases of the internal variability, or to a response to forcings, changing with GHG emissions, of the historical simulations.

At the end of the RCP8.5 simulations, from 2055, it is projected that the frequency of occurrences of El Niño events, whatever the diversity, will increase beyond the internal variability spread. A long period with more CP than EP events is projected, with a higher CP number than the internal variability spread of the system without anthropogenic forcing, which is consistent with results of Yeh et al. (2009a). Regarding strong and moderate evolution, although it seems that there are always more moderate than strong El Niño events in PI-control and historical simulations, it appears that it could be different with global warming due to the increasing number of strong events in particular.

5.3.3.2 Changes in the relationship between temperature and rainfall in the eastern Pacific

Changes in statistics of extreme precipitation El Niño events are compared to changes in strong El Niño statistics. Extreme precipitation El Niño events are defined as Cai et al. (2014, 2017), focusing on precipitation anomalies rather than SSTA.

Precipitation anomalies are induced during El Niño events in the eastern tropical Pacific due to the southward shift of the Inter-tropical Convergence Zone (ITCZ) (Rasmusson and

Carpenter, 1982). Based on the coupling between SST, atmospheric convection and circulation, Cai et al. (2014, 2017) defined extreme precipitation El Niño events when the boreal winter rainfall in the Niño-3 region is beyond an arbitrary threshold of 5 mm/day. Note that they defined El Niño events (normal and extreme) when the mean DJF Niño-3 SSTA index is greater than 0.5 times the standard deviation of the index during the control simulation. We use this method to define extreme precipitation El Niño events in CESM-LE. However, this method allows two events to follow from one year to the next, which is less often the case with the method based on the E and C indices, which follows the temporal evolution of the SSTA index: as long as the index has not dropped below the detection threshold, we consider this warm episode to be a single El Niño event. This explains the differences in the total number of El Niño events per simulation (see Fig.5.10).

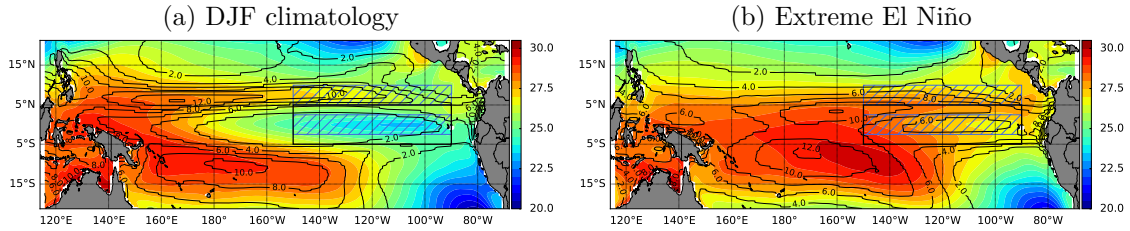

Figure 5.9 – CESM historical ensemble-mean spatial patterns of SSTA and precipitation of (5.9a) December-January-February (DJF) mean state and (5.9b) DJF extreme precipitation El Niño composite. Extreme El Niños are defined following Cai et al. (2014) from a rainfall threshold in the Niño-3 region (black box, 5°S-5°N, 210°-270°E)). The blue boxes materialise the regions used for the calculation of the SST meridional gradient.

Cai et al. (2014) analysed the non-linear relationship between the values of DJF Niño-3 SSTA and rainfall on one hand, and the values of DJF meridional SST gradient and Niño-3 rainfall on the other hand. The meridional SST gradient is defined as the mean DJF SST over the region 5°N-10°N, 210°-270°E (longitudes of Niño-3 region, top blue box on Fig. 5.9b) minus the mean DJF SST over the region 2.5°S-2.5°N, 210°-270°E (bottom blue box). In normal winter conditions (Fig. 5.9a), SST are colder in Niño-3 region due to the mean equatorial upwelling and there is few or no precipitation in this region, the Walker circulation bringing dry air down.

During strong El Niño events, an anomalous warming of the eastern tropical Pacific leads to an eastward shift of convection and an equatorward shift of the ITCZ. Exceptional rainfall then occurs in the usually dry region of the eastern equatorial Pacific (Fig. 5.9b). The rainfall anomalies follow, with a non-linear relationship, the increasing SST and the decreasing or even reversing SST meridional gradient, which is an indicator of the equatorward shift of the ITCZ (Cai et al., 2014). They concomitantly show that moderate events, with anomalous warming in the central Pacific, do no cause the same displacement of the ITCZ and therefore the same increase in rainfall or decrease in the meridional gradient in the Niño-3 region. They define thus extreme El Niño from a precipitation threshold of 5 mm/day.

In CESM-LE, the frequency of occurrence of extreme precipitation events is projected to increase from 0.04 (one event every 24.7 years) to 0.16 (one event every 6.4 years) in average of the last 50 years of RCP8.5 simulations, which corresponds to a 3.9 fold increase of the number of extreme events at the end of the 21st century. The CESM-LE model thus projects more than the doubling of extreme events projected in a set of CMIP3 and CMIP5 models (Cai et al., 2014).

An interesting feature of changes in El Niño statistics with global warming appears when analysing the number of seasonal types of strong and extreme El Niños and, therefore, the change of their frequency of occurrence between historical and RCP8.5 simulations (Fig. 5.10).

The frequency of occurrence of all strong El Niños increases from around 0.3 events per 10 year at the beginning of the historical simulations to around 1 per 10 years at the end of the RCP8.5 simulations (Fig. 5.10a, yellow lines). But, the increase is attributable to different

reasons according to the periods: until the end of the historical simulations, the increase is mainly due to the increase in the ONDJ strong El Niño events frequency (red lines), while it is mainly due to the increase of the FMA strong El Niño events frequency in the RCP8.5 simulations (green lines).

In historical simulations, the values of probability of occurrences of strong events per 10 years navigate around the values of the internal variability determined in the PI-control simulation (horizontal yellow dotted lines). But, in RCP8.5, a positive trend in the probability of occurrence of strong events results in values beyond the internal variability of the PI-control simulation. It is associated with a more pronounced positive trend in the probability of occurrence of FMA strong events, almost non-existent in historical and PI-control simulations. Conversely, the probability of occurrence of ONDJ strong events decreases drastically in RCP8.5 simulations, while they composed half of the events in historical and PI-control simulations.

(a) Strong and extreme El Niño

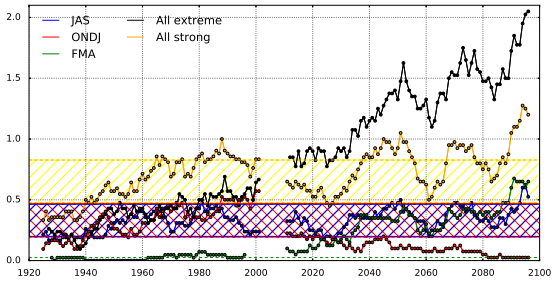

(b) Seasonal stratification of extreme El Niño

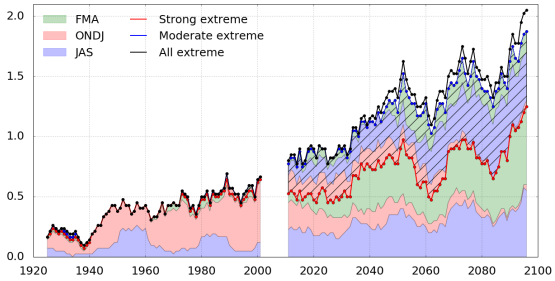

Figure 5.10 – (5.10a) Temporal evolution of the probability of occurrence of El Niño events per 10 years for (yellow line) strong, (black line) extreme precipitation and seasonal stratified El Niño events: (blue line) strong JAS, (red line) strong ONDJ and (green line) strong FMA El Niño events. The dashed lines of each color represent the 5th and the 95th percentile values of probability of each event in the PI-control simulation determined from a 5,000 bootstrap draws, using 42 periods of 100 years randomly taken in 1801 years of the PI-control simulation. (5.10b) Same as (5.10a) but for extreme precipitation El Niño events. The proportion of seasonal classification of strong and moderate El Niño events is indicated by coloured shadows: blue for JAS events, red for ONDJ events and green for FMA events. Hatch indicates proportion of moderate El Niño events. The number of events is counted by considering periods definition for strong events and by considering years as Cai et al. (2014) for extreme events. In RCP8.5, some extreme El Niño events are thus not classified as PC1 based on definition (26 events that is 5.3 %), mainly because they are included in the same PC1 based on definition El Niño periods (21 of 26 non classified events).

When comparing seasonal strong events with extreme precipitation events (Fig. 5.10a, black lines), it appears that, whereas, in historical simulations, the temporal evolution of the number every 10 years of extreme precipitation events is correlated with the number every 10 years of strong ONDJ El Niño events (0.82), it becomes strongly correlated with the number every 10 years of strong FMA El Niño events in RCP8.5 simulations (0.93).

Moreover, while extreme events are classified almost solely as strong events in historical simulations (only 3.4 % of extreme precipitation events (that is 5 events) are moderate El Niños), 34 % of extreme precipitation events in RCP8.5 simulations are classified as moderate El Niño according to the E-index (Fig. 5.10b).

It means that, according to the definition of extreme precipitation El Niño events, more El Niño events cause rain anomalies in the eastern Pacific with global warming, whatever its SST warming intensity. Cai et al. (2014, 2017) suggested that it is due to a facilitating equatorward shift of the ITCZ, due to a faster warming in the eastern equatorial Pacific and thus a decrease in SST meridional gradients. They showed furthermore that more extreme precipitation El Niños are associated with smaller SSTA with global warming compared to historical simulations and that there will be more convective episodes associated with more than 2 mm/d in the eastern Pacific. However, it is not clear whether the increase in the

frequency of occurrence of extreme precipitation El Niño events is due to the increasing eastern convective episodes due to a change in the mean state, or whether it is accompanied by an increase in strong El Niño events, one of the characteristics of which is the displacement of the ITCZ.

In the discussion of the paper (see paragraph 5.2), we show that the emergence of strong FMA El Niño events in the warmer climate explains one quarter of the increase in frequency of occurrence of extreme precipitation events in the CESM model. Concomitantly, 34 % of the increase in extreme precipitation events is associated with weak to moderate El Niño events. The increase in extreme precipitation events in a warmer climate is thus attributed not only to the increase in mean SST in the eastern equatorial Pacific, through the growing part of moderate El Niño events that contribute to ENSO precipitation events, but also to changes in ENSO characteristics, through the increase in strong El Niño events peaking in FMA, when the ITCZ is about to reach its southernmost position. Those events are thus strongly coupled to the ITCZ and do not necessarily require the anthropologically-forced mean SST warming trend in the eastern Pacific to yield extreme precipitation events. In CESM-LE, both the increase in mean SST in the eastern equatorial Pacific and the change in ENSO processes associated with the differential warming between the surface and the subsurface (i.e. sharper mean thermocline) thus contribute to the increase in extreme precipitation events in the warmer climate.

Another interesting feature, which requires further investigation, is the growing number of JAS El Niño events that are considered as extreme ENSO precipitation events in RCP8.5 simulations, half of which are classified as moderate events (Fig. 5.10b). Because extreme precipitation El Niño events cause rainfall in the eastern Pacific during the boreal winter, it will be interesting to understand how events, associated with a warming, even moderate, of the SST projected on the E-index in summer, cause rains in the eastern tropical Pacific in winter in RCP8.5 simulations.

An equivalent decomposition of EP and CP El Niño events is performed by matching each event to an event of seasonal stratification (JAS, ONDJ and FMA), whether strong or moderate events (Fig. 5.11).

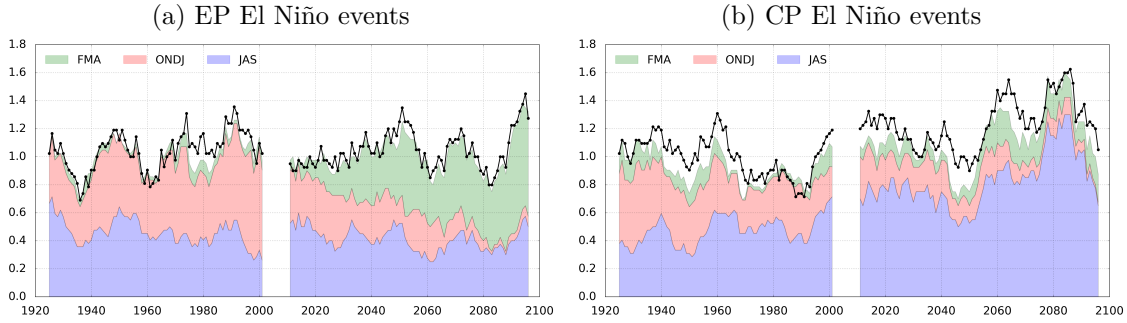

Figure 5.11 – Seasonal stratification of the temporal evolution of the probability of occurrence of El Niño events per 10 years for (5.11a) EP El Niño events and (5.11b) CP El Niño events. Seasonal stratification includes strong and moderate classification. In blue is the proportion of moderate and strong JAS El Niño events, in red the proportion of ONDJ El Niño events and in green the proportion of FMA El Niño events.

In historical simulations, EP El Niño are composed of JAS and ONDJ El Niño events, the proportion of one relative to the other being dependant of the period. In RCP8.5 simulations, the proportion of ONDJ El Niño events tend to be replaced by FMA El Niño, as the latter becomes more frequent with global warming. The proportion of ONDJ and FMA El Niño events in EP events is thus 52 % in historical simulations and 57 % in RCP8.5 simulations. No significant change appears regarding JAS El Niño events compositing EP El Niño events (44 % of EP El Niño events in historical simulations, 40 % in RCP8.5 simulations).

With global warming, CP El Niño events tend to become more often classified as JAS El Niño events, from 47 % in historical simulations to 67 % in RCP8.5 simulations, and even 70 % in the last fifty years of RCP8.5 simulations. It suggests that El Niño events that have a summer signature on the E index (JAS El Niño) tend to have more signal in the center of the equatorial Pacific during the next winter, which underlies a westward propagation of the heating zone. This requires further investigation.

5.3.4 Discussion: Focus on the processes that can explain the persistence of Niño events

5.3.4.1 Changes in the Bjerknes feedback

The strength of the Bjerknes feedback is assessed through the μ coefficient defined by Jin et al. (2006). It comes from the recharge-discharge linear equations and is expressed as the linear regression coefficient between zonal wind stress and SST:

$$[\tau_x] = \mu\,[SST] \tag{5.1}$$

with $[*]$ the spatial average. It is usually calculated from the average of zonal wind stress anomalies τ_x in the western-to-central Pacific, such as, for instance, in the Niño-4 region, and the average of SST anomalies in the eastern Pacific, such as in the Niño-3 region for example (Bellenger et al. (2014) for instance).

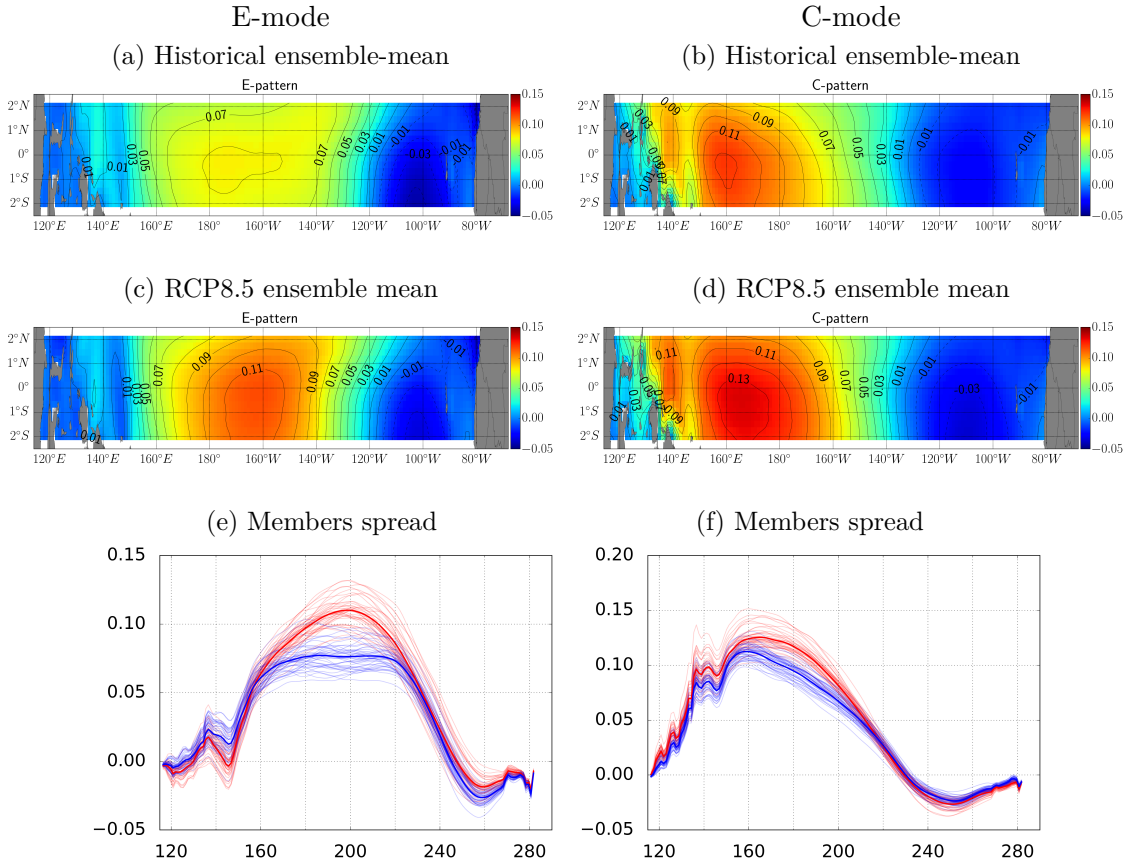

Figure 5.12 – Bi-linear regression of the zonal wind stress fields onto the (left column) E and (right column) C indices. (5.12a and 5.12b) Historical ensemble-mean zonal wind stress E and C modes respectively and (5.12c and 5.12d) RCP8.5 ensemble-mean zonal wind stress E and C modes (10^{-1} N/m^2). (5.12e and 5.12f) E and C zonal wind stress modes averaged over 2°S-2°N for (blue) historical and (red) RCP8.5 members. The maximum value of each profile is retained to determine the location of each centre of action, following the method of Cai et al. (2018).

To avoid being constrained by fixed regions, we use the method based on the E and C modes, used by Cai et al. (2018) We first calculate the E and C modes associated with the zonal wind stress through a bi-linear regression (see paragraph 2.2.3.3), in the same way as for determining the SST spatial patterns associated with E and C modes. The most important changes in the mean wind stress patterns with global warming are visible on the E-mode. In addition to an increase in intensity, the E-mode pattern will experience a tightening of its centres of action. This feature is found on the profiles along the equator for each member, with a larger peak and less dispersion in the location of these peaks between members (Fig. 5.12e).

The location of the E-peak of each member is retained to calculate the Bjerknes feedback, rather than using a mean value in a fixed region as it is usually calculated (Fig. 5.13a). A piecewise linear regression (see paragraph 2.2.3.1) is used to determine the optimum slope change points between each regression. As comparison test, the Bjerknes feedback has been also calculated for a fixed region (150°E-190°E, 5°S-5°N, Fig. 5.13b). The results, and in particular the values of the slope change points, are similar when using the zonal wind stress averaged between 5°S-5°N or its projection onto the E and C modes between 2°S-2°N.

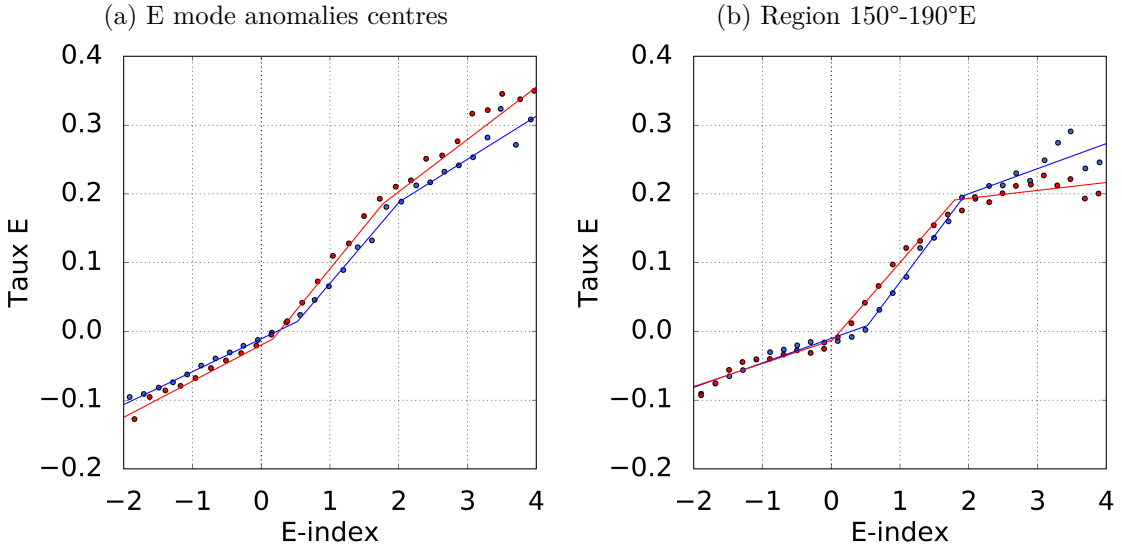

Figure 5.13 – Response of monthly zonal wind stress anomalies (10^{-1} N/m^2) to SST in the eastern Pacific (E-index averaged between 10°S-10°N) for (blue) historical and (red) RCP8.5 simulations. (5.13a) Zonal wind stress, averaged between 5°S-5°N, at the location along the equator where the regression of the zonal wind stress onto the E mode (2°S-2°N) peaks and (5.13b) zonal wind stress averaged in the western-to-central region 150°E-190°E, 5°S-5°N. 50 bins were defined on the maximum range of values of the E-index in historical and RCP8.5 simulations respectively, and the median wind stress anomaly and E-index are identified for each bin (circles). The method is similar to the one used in Cai et al. (2018) applied to the CMIP5 models, except that a linear piecewise regression was carried out here, rather than two separate linear regressions for positive and negative median index values.

The results are similar than those of Cai et al. (2018) when analysing CMIP5 models, with a distinct behaviour for negative and positive values of the E-index (see their figures S1e,f and S3e,f). The E values of the first slope change point are equal to 0.53 (0.55) in historical climate and 0.17 (0.11) in future climate, when considering the longitude of the center of action of the E-mode (150°E-190°E, 5°S-5°N region). For positive values of the E-index, the response of the zonal wind stress is amplified, reinforcing the strength of the Bjerknes feedback to warm the eastern Pacific. The characteristics of the Bjerknes feedback, as simulated by the model, change slightly with global warming.

However, in CESM-LE, the Bjerknes feedback shows another behaviour for higher E-values, with a decrease in the strength of the response, even if it remains higher than that for negative values of the E-index. The E-thresholds of the second slope change point are

equal to 2.01 (1.93) in historical climate and 1.77 (1.75) in future climate, when considering the longitude of the center of action of the E-mode (150°E-190°E, 5°S-5°N region). These threshold values approximate the thresholds used to distinguish strong El Niño events from moderate El Niño events. With a two-step behaviour, the non-linearities of the Bjerknes feedback in CESM-LE seem to act differently than in the GFDL CM2.1 model. Because this threshold value also intervenes in the bi-modality of the El Niño events in GFDL CM2.1, non-linearities of the Bjerknes feedback deserve further investigation and comparative analysis between models and observations.

5.3.4.2 Changes in the thermocline feedback

We investigated the role of thermocline feedback changes in the persistence of El Niño events with global warming.

The thermocline feedback amplifies the surface warming during an El Niño event by the thermocline deepening in the east equatorial Pacific: subsurface waters, warmer than in normal conditions, are then raised by the mean upwelling ($\overline{w}$). In first approximation, the TCF can be expressed by:

$$\left[\overline{w}\,\frac{\partial T'}{\partial z}\right]_{80m} = \left[\overline{w}\right]_{80m} * \, rms\left(\left[\frac{\partial T'}{\partial z}\right]_{80m}\right) \tag{5.2}$$

With global warming, vertical stratification is projected to intensify with steeper temperature gradients in the vicinity of the thermocline. The thermocline is also projected to be shallower (Yeh et al., 2009a) and flatter (Philip and van Oldenborgh, 2006; Vecchi and Soden, 2007).

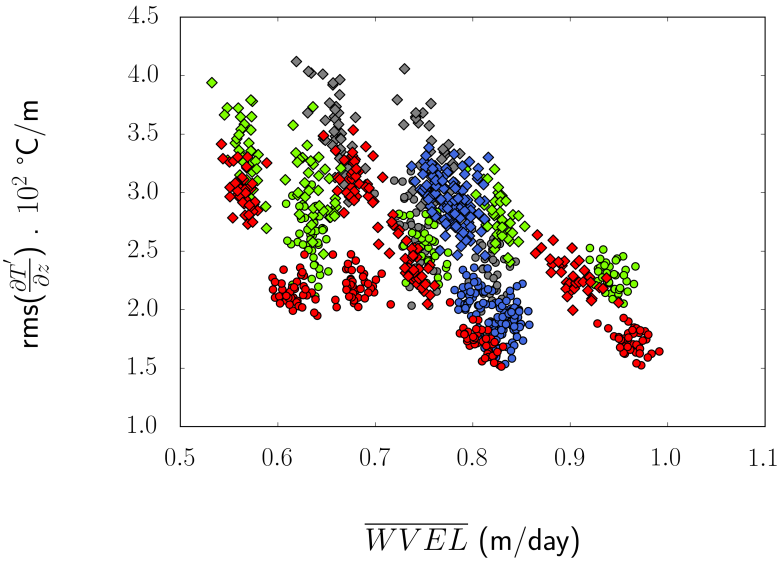

Figure 5.14 – Mean upwelling (m/day) plotted against the variability of the vertical temperature anomalies gradient (10^{-2} °C/m) in the eastern Pacific (Niño-3 region) for historical (dots) and RCP8.5 (diamonds) members and for seasons whose colours follow El Niño events stratification colours: blue for the months of January, October, November and December; green for the months of February, March and April; red for the months of July, August and September; and grey for the months of May and June.

In CESM-LE, although the flattening of the climatological isotherm 20 °C under global warming causes its deepening in the east of the equatorial Pacific, as proposed by Collins et al. (2010), the flattening of the climatological thermocline, defined as the location of the maximum in the vertical gradient of temperature, does not. The climatological thermocline tends to be shallower in the central Pacific but remains at similar depths in the east (Fig. 5.5). However, its variability increases in the east of the equatorial Pacific under global warming,

which is likely to enhance the thermocline feedback. The decrease of the mean upwelling is largely compensated by the increase in the variability of the vertical temperature gradient. It results in an overall increase in the thermocline feedback (see the publication in paragraph 5.2).

Monthly changes in each component of the thermocline feedback with global warming are highlighted in Figure 5.14. The decrease in mean upwelling is effective in any given month, but with a higher rate of decrease for the months of October to April (red and green, from dots to diamonds). The increase in the variability of the vertical temperature gradient is greater from October to January (red dots and diamonds). The monthly evolutions of the two components thus modulate the monthly evolution of the thermocline feedback (Figure 9c of the publication). However, understanding the mechanisms behind the change in the seasonal cycle of the two components needs further investigation. The increase in tropical Pacific vertical stratification and change in seasonal cycle of the thermocline depth must also be put in perspective with these seasonal cycle changes.

Synthesis and Perspectives

- Changes in ENSO statistics with global warming

In CESM-LE, the seasonality of the peak of the E-index during El Niño events is projected to change with global warming. Especially, the model projects the emergence of El Niño events peaking in February-March-April (FMA). Even if moderate El Niño events are also subject to this emergence of FMA events (+92 %), it is mostly strong El Niño events that are affected by this longer persistence (+1315 % in occurrence frequency). Conversely, strong El Niño events peaking between October and January (ONDJ events) experience a significant decrease.

- Changes in extreme precipitation El Niño events processes

CESM-LE simulates an increase of 3.9 in the frequency of occurrence of extreme precipitation El Niño events as defined by Cai et al. (2014). The changes in the statistics of extremes precipitation events cannot be solely attributed to changes in mean SST in the equatorial eastern Pacific, but also depends on changes in ENSO dynamics, in particular associated with the differential warming between the surface and the subsurface.

Because extreme precipitation El Niño events cause rainfall in the eastern Pacific during the boreal winter, it may be interesting to understand how events, associated with a warming, even moderate, of the SST projected on the E-index in summer, cause rains in the eastern tropical Pacific in winter in RCP8.5 simulations.

- These changes are associated with changes in vertical stratification

The increased stratification in the eastern Pacific with global warming reduces the efficiency of the upwelling by flattening and tightening the isotherms. On the other hand, the strengthened vertical stratification increases the sensitivity of SSTA to thermocline fluctuations by enhancing mean vertical diffusivity (Zelle et al., 2004). This increase largely compensates for the decrease in climatological upwelling and yields an overall increase in the thermocline feedback with global warming in CESM-LE. The increase in thermocline feedback with global warming is thus likely to play a key role in the persistence of El Niño events and the emergence of FMA El Niños.

- However, little confidence in simulating temperatures near the thermocline

There are significant persistent biases in mean temperatures in the vicinity of the thermocline, not only in CGCMs but also in reanalysis products (Xue et al., 2017). The TPOS2020 program, currently under discussion (Smith et al., 2019), could provide the observational strategy needed to improve oceanic model formulation (e.g. mixing parametrisations, resolution).

- Involved processes deserve further investigation

In addition to the thermocline feedback, other processes may play a role in the persistence of El Niño events, such as the non-linear dynamical heating, the non-linear processes encapsulated in the Bjerknes feedback (Dommenget et al., 2013; Takahashi and Dewitte, 2016), the external stochastic forcing and, in particular, the role of the Westerly Wind Bursts (WWBs). These different processes would deserve further investigation. For instance, the non-linear behaviour of the Bjerknes feedback is simulated differently in CESM-LE compared to GFDL CM2.1, which may impact the simulation of strong El Niño events and, therefore, their persistence.

Conclusions et Perspectives

Ce travail de thèse a porté sur la diversité des événements de l'Oscillation Australe El Niño ou ENSO (l'acronyme anglais pour El Niño-Southern Oscillation) et sur ses changements projetés avec le réchauffement climatique. La diversité des occurrences du phénomène ENSO a connu un regain d'attention ces dernières décennies du fait d'une augmentation du nombre d'événements El Niño qui ont présenté un réchauffement anormal des eaux de surface océaniques au centre du Pacifique tropical plutôt qu'à l'est, où le phénomène a généralement une plus forte signature en anomalies positives de températures des eaux de surface océaniques (SST pour Sea Surface Temperatures) (Ashok et al., 2007; Lee and McPhaden, 2010). Ces différences spatiales de réchauffement de la surface de l'océan pendant les événements El Niño sont déterminantes dans la réponse atmosphérique qu'elles entraînent autour du bassin Pacifique et les téléconnexions associées entre les tropiques et les moyennes latitudes (Weng et al., 2009). De subtiles variations des SST du Pacifique central peuvent avoir de forts impacts sur la localisation et l'intensité du dégagement de chaleur latente dans l'atmosphère, impactant alors la circulation atmosphérique globale. Ainsi, même s'ils présentent des extensions zonales de réchauffement de SST plus petites et des intensités plus faibles que les événements El Niño du Pacifique est, les événements El Niño du Pacifique central sont susceptibles d'induire une réponse atmosphérique et des téléconnexions extra-tropicales plus fortes (Weng et al., 2009). Il apparaît donc primordial de mieux comprendre les événements ENSO et leur diversité pour mieux les anticiper.

Dans un premier temps, j'ai évalué les caractéristiques de la diversité d'ENSO, et plus particulièrement celle des événements chauds, les événements El Niño (chapitre 3). J'ai pour cela comparé deux approches de caractérisation de cette diversité, en utilisant les simulations de contrôle de deux modèles couplés de climat, CESM-LE et GFDL CM2.1.

La première méthode de caractérisation de la diversité d'El Niño repose sur la distinction spatiale des centres d'actions du réchauffement des eaux de surface du Pacifique tropical pendant les événements El Niño (Kug et al., 2009; Kao and Yu, 2009; Yeh et al., 2009a). En particulier, cette méthode compare les intensités de réchauffement dans les régions historiques d'étude d'ENSO, à savoir la région Niño-3 à l'est (5°S-5°N, 210°E-270°E) et la région Niño-4 au centre (5°S-5°N, 160°E-210°E) du Pacifique tropical. Deux types d'événements El Niño sont ainsi classifiés, les événements El Niño dits "Central Pacific" (CP) et les événements dits "Eastern Pacific" (EP) (Kug et al., 2009). Les événements EP (CP) El Niño correspondent aux hivers El Niño pendant lesquels l'indice Niño-3 (Niño-4) est supérieur à l'indice Niño-4 (Niño-3) (et supérieur au seuil de détection des événements El Niño), c'est à dire lorsque le réchauffement anormal des eaux de surface est plus marqué à l'est (au centre) du Pacifique tropical.

Plusieurs études ont suggéré que les dynamiques associées à ces deux types d'événements étaient différentes, avec une dynamique déterministe expliquée par la théorie de l'oscillateur recharge-décharge (Jin, 1997a) pour les événements EP El Niño et une dynamique plus marquée par le forçage atmosphérique pour les CP El Niño (Kao and Yu, 2009; Kug et al., 2009). En effet, du fait des forts contrastes zonaux du Pacifique le long de l'équateur, que ce soient en termes de SST, de profondeur de thermocline ou encore de sensibilité à la convection

atmosphérique, le centre et l'est du Pacifique tropical sont susceptibles de favoriser des processus différents. En particulier, deux processus océaniques jouent un rôle primordial dans le développement des événements ENSO, les processus de thermocline et d'advection zonale. La position longitudinale de la zone de réchauffement anormale au début des événements El Niño entraîne une prédominance de l'un ou l'autre de ces processus. Dans le Pacifique équatorial oriental, l'approfondissement de la thermocline pendant le développement des événements El Niño diminue le refroidissement en surface en limitant les échanges entre la surface et la subsurface (Vialard et al., 2001). Plus particulièrement, l'advection verticale moyenne des anomalies de température de subsurface, processus appelé rétroaction de la thermocline (thermocline feedback en anglais, ou TCF), est accentuée dans le Pacifique oriental où les changements de profondeur de la thermocline ont plus d'effets sur les SST en raison d'une thermocline moyenne moins profonde que dans le Pacifique ouest et central (An and Jin, 2001; Jin et al., 2006). A l'inverse, les processus d'advection zonale sont primordiaux dans le Pacifique ouest et central (Picaut et al., 1996). En particulier, l'advection zonale du gradient de température par les anomalies de courants, appelée rétroaction de l'advection zonale (zonal advective feedback en anglais ou ZAF), est plus efficace dans le développement d'anomalies de SST liées à ENSO dans le Pacifique central en raison du gradient de température zonal important près du bord est de la Warm Pool. Les différences de températures des eaux de surface, entre l'est froid (la langue d'eau froide ou "Cold Tongue") et l'ouest chaud (la piscine d'eau chaude, ou "Warm Pool"), entraînent également une plus forte sensibilité du déclenchement de la convection atmosphérique au centre du Pacifique qu'à l'est, où de plus fortes anomalies de SST seront nécessaires.

La seconde méthode se base sur l'existence de deux modes principaux de variabilité du Pacifique tropical. Ces modes sont calculés par la méthode de décomposition orthogonale aux valeurs propres (Empirical Orthogonal Functions en anglais, ou EOF). Le centre d'action du premier mode de variabilité se situe à l'est, celui du second mode de variabilité se situe au centre du Pacifique tropical (Takahashi et al., 2011). Ces deux modes de variabilité conduisent à la définition de deux régimes El Niño, intrinsèquement liés aux non-linéarités du système couplé océan-atmosphère. Les événements chauds, dont la signature en SST s'imprime fortement à l'est, sont en effet ceux qui présentent les plus fortes intensités (Dommenget et al., 2013; Takahashi and Dewitte, 2016). Les deux régimes d'El Niño ainsi définis, les événements forts et les événements modérés, se distinguent par l'intensité du réchauffement des eaux de surface dans le Pacifique tropical est.

J'ai estimé la robustesse de ces deux définitions en les comparant dans des jeux de données d'observations et de simulations numériques du système climatique. Dans un premier temps, j'ai utilisé deux simulations du climat pré-industriel, c'est à dire sans forçage anthropique et avec un forçage externe constant. Ces simulations sont appelées simulations de contrôle pré-industriel, ou simulations "PI-control". Ce sont des simulations longues, qui permettent d'estimer la variabilité interne du système climatique sans interaction avec des changements des forçages externes. Les simulations PI-control sont celles des modèles couplés CESM1 (1801 années de simulation) et GFDL CM2.1 (500 ans). Dans un second temps, j'ai utilisé un large ensemble de simulations du climat en situation historique (42 membres, 1920-2005) et de projections climatiques sous le scénario d'émission soutenue de gaz à effet de serre, appelé scénario RCP8.5 (40 membres, 2006-2100). Ces simulations proviennent du modèle de climat couplé CESM Large Ensemble (CESM-LE) Project, développé par le National Center for Atmospheric Research (NCAR, Colorado, USA). Ce modèle simule de façon réaliste et satisfaisante la variabilité du Pacifique tropical et d'ENSO, même si certains biais connus et fréquents dans les modèles de climat couplés restent présents, comme le biais froid de la Cold Tongue ou encore la double zone de convergence inter-tropicale (ITCZ pour Inter-tropical convergence zone).

Plusieurs études ont montré que la définition des événements El Niño est fortement dépendante des indices utilisés et donc de la méthode utilisée (Singh et al., 2011; Stevenson

et al., 2017). Je montre qu'au sein d'une même méthode, la définition des événements El Niño est également dépendante de plusieurs paramètres spatiaux-temporels. En effet, la première méthode décrite précédemment, qui définit les événements El Niño à partir des régions fixes de variabilité observée du Pacifique tropical (les régions Niño-3 et Niño-4), est fortement dépendante de la saison hivernale considérée pour le pic de l'événement. Ainsi, pour un même jeu de données, qu'il soit d'observations ou de simulations de contrôle, la détection des événements El Niño CP ou EP diffère suivant que l'on utilise les mois de novembre à janvier (NDJ), de décembre à février (DJF) ou de janvier à mars (JFM) pour définir le pic de l'événement. Cette différence peut entraîner une inversion du ratio du nombre d'événements CP comparé au nombre d'événements EP El Niño. Cette sensibilité à la saison du pic peut s'expliquer par l'évolution spatiale et temporelle des événements El Niño, dont la direction de propagation zonale des eaux chaudes vient modifier les valeurs moyennes des SST entre novembre et mars. De plus, cette méthode de définition des événements El Niño à partir des régions fixes, Niño-3 et Niño-4, apparaît difficilement applicable aux modèles de climat global du fait de leurs biais récurrents. Ces biais sont particulièrement prononcés dans les régions utilisées pour définir ENSO, ce qui complique l'interprétation des processus physiques associés et limite fortement la confiance que l'on peut avoir en ces résultats.

La deuxième méthode, utilisant les indices associés aux deux principaux modes de variabilité du Pacifique tropical, permet de s'affranchir de cette spatialisation fixe des indices. Ces deux modes de variabilité sont décrits par les indices E et C, obtenus par une combinaison linéaire des séries temporelles, ou composantes principales, associées aux deux principaux modes de variabilité issus de l'analyse EOF. Le mode E explique la plus grande partie de la variabilité du Pacifique oriental et est associé plus spécifiquement aux événements El Niño forts, alors que le mode C a un centre d'action dans le Pacifique central et englobe les événements La Niña et les événements El Niño modérés. Cependant, la classification des événements El Niño en événements modérés ou forts est dépendante de la valeur du seuil retenu sur l'indice E pour différencier ces deux types d'événements. Takahashi and Dewitte (2016) ont fait valoir que ce seuil de séparation des deux régimes d'El Niño est directement lié à la rétroaction de Bjerknes. Au delà de ce seuil, les non-linéarités du système couplé océan-atmosphère du Pacifique tropical entraînent une forte amplification de la rétroaction de Bjerknes : une légère augmentation des SST dans le Pacifique oriental provoque alors une réponse accrue de la tension de vent zonal, ce qui amplifie le réchauffement initial dans cette région du Pacifique tropical. La rétroaction de Bjerknes apparaît ainsi non linéaire et fonction du réchauffement en surface dans le Pacifique tropical oriental. Takahashi and Dewitte (2016) et Takahashi et al. (2018) suggèrent que les événements El Niño forts sont des événements El Niño dont le réchauffement à l'est du Pacifique atteint ce seuil en SSTA, ce qui renforce la rétroaction de Bjerknes. Ce comportement non-linéaire est diagnostiqué dans le modèle GFDL CM2.1 à partir d'un seuil compris entre +1.5 et +2 °C d'anomalies de SST dans le Pacifique est. Il se matérialise par une bi-modalité de la distribution des événements El Niño dans l'espace des phases correspondant aux deux modes de variabilité du Pacifique tropical, c'est à dire dans l'espace des indices (E, C). Cependant, ce comportement bi-modal est peu marqué dans les simulations du modèle CESM-LE. L'estimation de ce seuil peut ainsi être considérée comme subjective dans notre étude. Une modification de ±5 % du seuil entraîne ainsi une variation du nombre d'événements El Niño forts comprise entre 225 (-5.1 %) et 262 (10.5 %) pour les simulations historiques et entre 271 (-10.3 %) et 322 (6.6 %) pour les simulations RCP8.5.

Néanmoins, le comportement non-linéaire de la rétroaction de Bjerknes est simulé par CESM-LE. Il est toutefois associé à des valeurs de l'indice E plus faibles (proches de 0 °C) que dans les observations ou dans la simulation de contrôle de GFDL CM2.1 (proches de 2 °C). Il semble également que le comportement non-linéaire de la rétroaction de Bjerknes s'effectue par paliers dans le modèle CESM-LE, avec un premier seuil, proche de 0 °C, qui entraîne une forte amplification de la rétroaction et un second seuil, proche de 2 °C, au delà duquel la rétroaction de Bjerknes est atténuée par rapport au premier seuil. Cette différence

de comportement entre les modèles CESM-LE et GFDL CM2.1 nécessite de plus amples investigations, qui pourraient être également effectuées sur l'ensemble des modèles de la phase 5 du projet d'inter-comparaison de modèles (CMIP5 pour Coupled Model Intercomparison Project) du Groupe d'experts intergouvernemental sur l'évolution du climat (GIEC). Il semblerait en effet que certains des modèles CMIP5 présentent un comportement moyen similaire à celui de CESM-LE, avec un seuil proche de E=0.5 °C et potentiellement un comportement plus faible au-delà de 1.5 °C (cf la figure S1e de Cai et al. (2018) pour l'ensemble des modèles CMIP5 ou leur Figure S3e pour les modèles sélectionnés du fait de leur simulation des non-linéarités associées à ENSO, qui affichent un seuil proche de E=0 °C).

J'ai ensuite comparé les deux méthodes entre elles. Les événements forts sont préférentiellement des événements EP El Niño que ce soit en simulations historiques (87 % des événements forts sont des EP El Niño) ou futures (89 % des événements forts), du fait de leur définition par l'indice E. C'est cohérent avec les observations et en particulier les événements extrêmes de 1982-83 et de 1997-98 (McPhaden and Yu, 1999), ainsi qu'avec les résultats de nombreuses études qui ont montré que les événements El Niño les plus forts en termes d'intensité se développent à l'est du Pacifique tropical (Takahashi et al., 2011; Chen et al., 2015a; Santoso et al., 2017). Cependant, tous les événements EP El Niño ne sont pas des événements forts. Ainsi, même si les événements modérés sont préférentiellement des événements CP El Niño, 33 % sont classifiés comme étant des EP El Niño dans les simulations historiques. Nous revenons par la suite sur le changement projeté de ces caractéristiques des événements El Niño avec le réchauffement climatique.

Dans un second temps, je me suis intéressée à l'impact que peut avoir la modulation basse-fréquence de l'état moyen du Pacifique tropical sur la diversité d'El Niño et aux rectifications possibles de la modulation d'ENSO sur l'état moyen (chapitre 4). Les mécanismes associés à la modulation basse-fréquence de la diversité d'ENSO sont encore mal compris. Plusieurs études ont suggéré que la diversité spatiale d'El Niño, définie par les événements EP et CP, était modulée à basse fréquence par l'état moyen, qu'elle pouvait en retour rectifier à travers les résidus d'ENSO dus à l'asymétrie entre les événements El Niño et La Niña (Choi et al., 2009, 2012).

Cependant, alors que la relation est forte entre le mode de variabilité basse-fréquence du Pacifique tropical (TPDV pour Tropical Pacific Decadal Variability), appelé ENSO-induced, et la fréquence d'occurrence des événements CP El Niño dans la simulation de contrôle du modèle GFDL CM2.1, elle n'est que faiblement diagnostiquée dans la simulation de contrôle de CESM.

Plusieurs sources d'incertitudes peuvent expliquer ces différents comportements de la variabilité interne simulée par les modèles. La première interrogation vient de la simulation de la variance du mode TPDV ENSO-induced. Dans le modèle CESM, le mode ENSO-induced est le second mode dominant de la variabilité décennale du Pacifique tropical, alors que c'est le principal mode de variabilité décennale dans le modèle GFDL CM2.1. Ce mode explique 59 % de la variance totale dans GFDL CM2.1 alors qu'il n'explique que 23 % de la variance totale dans CESM. Ces différences de variabilité peuvent ainsi entraîner des mécanismes différents d'interaction entre l'état moyen et la modulation basse-fréquence d'ENSO. En particulier, Choi et al. (2013a) ont suggéré que la variance de chacun des deux modes dépend de la force de la relation entre les résidus dus à l'asymétrie d'ENSO et le mode TPDV ENSO-induced. Dans leur mécanisme, plus la variance expliquée par le mode ENSO-induced est élevée, plus la rétroaction bidirectionnelle entre la modulation d'ENSO et l'état moyen (à travers les résidus non-linéaires d'ENSO) est forte, plus la variabilité de l'amplitude d'ENSO est élevée. Cependant, cette relation apparaît sujette aux biais récurrents des modèles de climat, en particulier du fait d'une amplitude régulièrement sur-estimée d'ENSO. Un diagnostic intéressant pourrait ainsi consister à analyser la relation entre les résidus d'ENSO et le mode TPDV ENSO-induced dans CESM-LE et d'étendre ce diagnostic aux simulations historiques, ce qui pourrait permettre d'appréhender le mécanisme à l'oeuvre à travers la

variabilité inter-membre.

La seconde incertitude vient de la simulation de la structure spatiale du mode ENSO-induced. Dans le modèle CESM, les anomalies négatives du mode ENSO-induced s'étendent plus loin dans le Pacifique central, confinant les anomalies positives dans le Pacifique oriental. Ce biais est particulièrement visible dans la structure spatiale des SST associées à ce mode. Il pourrait conduire à une modification de la relation entre le mode ENSO-induced et les résidus associés à l'asymétrie d'ENSO, puisque ces derniers sont plus susceptibles à l'inverse d'avoir une structure spatiale qui s'étend vers l'ouest compte tenu du biais, récurrent dans les modèles de climat, de la langue d'eau froide qui s'étend trop à l'ouest du Pacifique équatorial.

Zheng et al. (2018) ont montré que le mode TPDV ENSO-induced et la dispersion, entre les membres du grand ensemble CESM, du réchauffement simulé des SST à l'horizon 2100 sous le scénario RCP8.5 étaient fortement liés. Ils suggèrent ainsi que l'intéraction bi-directionnelle entre l'état moyen du Pacifique tropical et ENSO entraîne en particulier des incertitudes sur les taux de réchauffement des SST dus au changement climatique. Compte tenu de cette forte contribution de la variabilité interne sur les changements projetés et en particulier sur le changement d'amplitude d'ENSO, les mécanismes liant ENSO et le TPDV dans CESM-LE nécessitent de plus amples études.

Enfin, j'ai étudié les changements projetés des statistiques d'ENSO et des processus thermodynamiques associés au phénomène dans le contexte de réchauffement climatique (chapitre 5).

Dans un premier temps, je me suis intéressée aux changements de statistiques d'ENSO du fait du réchauffement climatique dans CESM-LE. Nous montrons que la variance des anomalies de SST dans le Pacifique tropical oriental (retranscrites par le mode E) augmente de façon significative (statistiquement significatif à 95 %) entre les simulations historiques et futures de CESM-LE. Cette augmentation est associée à une augmentation de la fréquence d'occurrence des événements El Niño forts, bien que cette augmentation soit modérée (+24 %) et non linéaire, soumise à de fortes variations basse fréquence. Ce résultat est cohérent avec les résultats obtenus à partir des modèles CMIP5 et publiés dans la revue Nature (Cai et al., 2018). Cet article est présenté en annexe 5.3.4.2. Cette augmentation de la variabilité du Pacifique tropical oriental est associée à l'augmentation de la stratification verticale du Pacifique central. Nous revenons par la suite sur les processus océaniques impliqués dans ce changement de statistiques d'ENSO.

De plus, nous montrons, par l'analyse du cycle saisonnier de la variabilité du mode E, que la variance de l'indice E augmente significativement pendant les mois de février, mars et avril (FMA) avec le réchauffement climatique. Cette augmentation significative est associée à une augmentation de la fréquence d'occurrence des événements forts EP El Niño qui culminent pendant cette saison FMA et à une augmentation de la durée moyenne des événements forts EP. Il est intéressant de noter que cette augmentation de la variance de l'indice E en FMA est indépendante de la méthode utilisée pour retirer la tendance imprimée sur les SST par le réchauffement climatique. J'ai en effet testé deux autres méthodes permettant de retirer le signal du changement climatique, en plus de la méthode de tendance linéaire. La deuxième méthode consiste à retirer une tendance quadratique en chaque point, la troisième méthode soustrait le réchauffement moyen calculé sur une plus grande région (méthode utilisée par Khodri et al. (2017)). Pour cette dernière méthode, la région du Pacifique tropical (30°S-30°N) a été considérée. Qu'elle que soit la méthode appliquée, la variance de l'indice E augmente de façon significative statistiquement en FMA, alors même que les changements de la variance de E peuvent être opposés suivant les méthodes pour les autres mois de l'année. Enfin, des résultats préliminaires conduits sur des modèles CMIP5 semblent confirmer cette augmentation de la variance des anomalies de SST dans le Pacifique équatorial oriental dans un climat plus chaud.

Un des résultats marquants de ces dernières années, concernant le changement de statistiques d'ENSO avec le réchauffement climatique, est l'augmentation projetée de la fréquence

d'occurrence des événements El Niño extrêmes en précipitation à l'est du Pacifique (Cai et al., 2014, 2015b, 2017). La fréquence d'occurrence de ces événements extrêmes en précipitation est susceptible de doubler avec le réchauffement climatique à l'horizon 2100 selon les modèles CMIP5 (Cai et al., 2014) et même quasi-quadrupler dans CESM-LE. Compte tenu des impacts météorologiques et socio-économiques de ce type d'événements extrêmes, nous avons cherché à mettre en relation cette augmentation des événements extrêmes en précipitation avec la persistance observée des événements forts EP El Niño. Nous montrons que l'émergence de ces événements forts EP El Niño qui ont leur pic de SST en FMA dans le climat futur explique un tiers (33 %) de l'augmentation de la fréquence d'occurrence des événements El Niño extrêmes en précipitation. En effet, la période FMA est celle pendant laquelle les SST dans le Pacifique oriental connaissent leur pic saisonnier et l'ITCZ est sur le point d'atteindre sa position la plus au sud (Xie et al., 2018), ce qui renforce le couplage entre El Niño et l'ITCZ et favorise les précipitations extrêmes. Du fait de ce fort couplage saisonnier entre les événements forts FMA El Niño et l'ITCZ, un réchauffement des eaux de surface dû au forçage anthropique n'est pas nécessaire pour produire des épisodes de précipitation extrêmes dans le Pacifique tropical est. Par ailleurs, 34 % de l'augmentation de la fréquence d'occurrence des événements El Niño extrêmes en précipitation est associée à des événements El Niño d'intensité faible à modérée, et donc associée au réchauffement global des SST. Nous montrons ainsi que dans le modèle CESM-LE, l'augmentation projetée des événements El Niño extrêmes en précipitation s'explique à la fois par l'augmentation des SST moyennes dans le Pacifique oriental et par les changements des processus d'ENSO associés au réchauffement plus fort en surface qu'en subsurface conduisant à une thermocline plus resserrée et une augmentation de la stratification verticale.

Ainsi, ces résultats réconcilient les travaux de recherche de la dernière décennie sur les changements de statistiques d'ENSO qui mettaient en exergue d'une part un manque de consensus entre les modèles de climat sur l'évolution projetée de la variabilité de l'amplitude d'ENSO dans le Pacifique oriental (région Niño-3 ou Niño-3.4) (Chen et al., 2017a) et, d'autre part, l'augmentation projetée de la fréquence d'occurrence des événements El Niño extrêmes en précipitation dans le Pacifique tropical oriental (Cai et al., 2014). L'analyse des événements El Niño par le mode E de variabilité dominante du Pacifique tropical oriental a montré que l'augmentation de la variance de l'indice E est significative statistiquement sur l'ensemble des modèles CMIP5. La fréquence d'occurrence des événements El Niño forts EP augmentera dans un climat plus chaud. Elle sera de plus accompagnée par une augmentation des événements El Niño qui auront leur pic en SST plus tard qu'en situation actuelle, en FMA plutôt qu'en NDJ. Cette augmentation explique en partie l'augmentation des événements de précipitation extrême dans le Pacifique tropical oriental.

L'analyse par le mode E permet de considérer le phénomène ENSO dans son ensemble, en conservant une continuité physique des processus dynamiques associés, ce que ne permet pas l'analyse d'ENSO par des régions fixes de variabilités (à savoir les régions Niño-3 et Niño-4). Cette méthode permet de prendre en compte de manière objective les centres d'action des événements ENSO par les modes E et C. Elle permet également de s'affranchir des biais des modèles dans la région du Pacifique tropical et en particulier du déplacement vers l'ouest de la Cold Tongue climatologique.

Dans un second temps, je me suis intéressée aux changements de processus thermodynamiques qui accompagnent et sont susceptibles d'expliquer les changements de statistiques d'ENSO en situation future. Nous proposons l'hypothèse selon laquelle la plus forte persistance des évènements EP El Niño et le décalage temporel dans leur pic de réchauffement proviennent d'un processus de recharge plus important et d'une rétroaction de la thermocline plus efficace dans le Pacifique est dans un climat plus chaud tel que simulé par CESM-LE. En particulier, l'analyse du bilan de chaleur dans la couche de mélange pendant les événements El Niño montre que la réduction de l'upwelling moyen du fait de l'augmentation de la stratification verticale du Pacifique est largement compensée par

l'augmentation du gradient vertical des anomalies de température au travers de la couche de mélange ce qui conduit à une augmentation de la rétroaction de la thermocline.

Une problématique à la généralisation des résultats vient de la précision des modèles de climat à simuler de manière réaliste l'état moyen du Pacifique tropical et les processus associés à ENSO. En particulier, l'affaiblissement du gradient zonal de SST n'est pas systématiquement simulé en situation future malgré l'affaiblissement projeté de la Circulation de Walker (Vecchi et al., 2006; Yeh et al., 2012). Le changement de ce gradient zonal de SST n'est que faiblement relié aux changements de profondeur de la thermocline (Li et al., 2016). La relation entre SST, profondeur de thermocline et alizés peut ainsi être plus faible que l'actuelle relation observée par la rétroaction de Bjerknes. Cela entraîne des processus en contradiction avec ceux en jeu pendant les événements El Niño pendant lesquels la réponse de la thermocline est fortement dominée par une moindre inclinaison le long de l'équateur. Ces changements contre-intuitifs peuvent provenir en particulier du biais récurrent des modèles de climat à simuler une Cold Tongue excessive, ce qui provoque un réchauffement projeté plus important dans le Pacifique ouest dans certains modèles de climat (Li et al., 2016; Ying et al., 2019). Lorsque ce biais de la Cold Tongue est corrigé dans les modèles de climat, le réchauffement projeté des températures de surface du Pacifique tropical ressemble à une structure de type El Niño. Cependant, l'impact de ce biais de l'état moyen sur les processus en jeu lors des événements ENSO actuels et futurs nécessite de plus amples investigations. De plus, le réchauffement projeté en subsurface est diversement simulé dans le Pacifique central dans la génération actuelle des modèles de climat (CMIP5). Compte tenu de l'importance des processus de thermocline dans le développement des événements El Niño, une amélioration des processus océaniques modélisés est nécessaire et peut passer par une optimisation des paramétrisations des processus de mélange et par une augmentation de la résolution des modèles. Enfin, la simulation des non-linéarités du système climatique du Pacifique tropical est primordiale dans la simulation de l'état moyen et des processus associés à ENSO (Boucharel et al., 2011; Karamperidou et al., 2017; Cai et al., 2018). En particulier, les modèles qui simulent de façon plus réaliste les non-linéarités associées à ENSO sont ceux qui retranscrivent le mieux la diversité d'ENSO, que ce soit en termes de structures spatiales ou d'amplitude.

La compréhension de ces différents processus associés à ENSO et à l'état moyen du Pacifique tropical pourra être améliorée dans un avenir proche grâce à :

- des observations renforcées (température, vent de surface, courant), en particulier du Pacifique est. Actuellement, le réseau d'observation du Pacifique tropical ne permet pas d'obtenir des résolutions verticales et horizontales suffisantes pour correctement analyser les non-linéarités des processus d'ENSO. Le développement d'un réseau d'observation amélioré du Pacifique tropical est en cours de discussion dans le cadre du programme TPOS2020 (Tropical Pacific Observing System for 2020, Smith et al. (2019) en cours de révision).
- une nouvelle génération de modèles couplés dans le cadre de la phase 6 du projet d'intercomparaison des modèles (CMIP6, Eyring et al. (2016)). La résolution plus importante des modèles ainsi qu'une paramétrisation différente des processus océaniques peuvent permettre d'améliorer :
  - d'une part, la simulation des non-linéarités et de l'asymétrie d'ENSO, sous-estimées de façon récurrente dans les modèles de climat,
  - d'autre part, la simulation des processus couplés océan-atmosphère en jeu dans les zones sujettes aux biais récurrents des modèles (le biais de la langue d'eau froide, la double ITCZ et la région de l'extrême est du Pacifique équatorial).

Alors que nous nous sommes concentrés sur l'impact des changements de la stratification verticale sur les processus liés à ENSO (le processus de recharge et la rétroaction de la thermocline), d'autre processus peuvent potentiellement intervenir sur la plus grande persistance

des événements El Niño mais également sur l'augmentation des événements forts El Niño en situation future :

- l'augmentation des températures moyennes du Pacifique tropical qui peut faciliter le dépassement du seuil de la rétroaction de Bjerknes, seuil qui est susceptible d'être modifié avec l'état moyen (Johnson and Xie, 2010),
- un changement du cycle saisonnier de la rétroaction de Bjerknes et du mode d'interactions océan-atmosphère associé dans la partie orientale du Pacifique tropical. Dewitte and Takahashi (2017) ont suggéré que les événements modérés El Niño se différencient des événements forts par l'émergence de coups de vent d'est en septembre dans l'extrême est du Pacifique. Ces coups de vents d'est contre-carreraient la rétroaction de Bjerknes dans le Pacifique est et empêcheraient l'événement EP El Niño de se développer en fort El Niño en limitant le réchauffement qui alors ne dépasserait pas le seuil requis. Un changement du cycle saisonnier de ce mode d'interactions air-mer avec le réchauffement climatique pourrait déconnecter l'émergence de ces coups de vent d'est de la croissance de l'événement El Niño. De plus amples investigations sont nécessaires pour déterminer en particulier si ces épisodes de vent d'est sont stochastiques ou induits par ENSO comme le suggèrent Hameed et al. (2018) et quel mécanisme se met en place pour les contrer lors de la croissance d'un événement fort El Niño.
- des changements du forçage stochastique externe, tel que les coups de vent d'ouest (WBWs pour Westerly Wind Bursts en anglais) qui interagissent non-linéairement avec l'océan de surface jusqu'à le moduler (Chen et al., 2015a; Hayashi and Watanabe, 2017). Les WWBs sont susceptibles de modifier les processus de recharge du Pacifique tropical lors des événements forts EP El Niño. Les WWBs font l'objet de nombreuses études récentes (Puy et al., 2016b, 2017), tout comme les processus de recharge (Neske and McGregor, 2018; Izumo et al., 2018). Leur interaction nécessite de plus amples diagnostiques, en particulier concernant les mécanismes déterministes en jeu dans les processus de modulation des WWBs par l'océan.

Deux régions sont donc au cœur des interactions océan-atmosphère en jeu lors des événements El Niño extrêmes. Le Pacifique tropical ouest est le centre d'action des coups de vents d'ouest qui apparaissent déterminants dans la croissance d'un événement El Niño fort, en particulier lorsqu'ils se produisent en été (Puy et al., 2017). Le Pacifique tropical oriental, voire extrême-oriental, en plus des fortes interactions entre la surface et la thermocline, est le siège des coups de vent d'est en été/automne qui sont à même de contrer le développement d'un événement fort El Niño. Cependant, ces régions font encore l'objet de biais récurrents dans leur simulation par les modèles couplés de climat.

Une autre interaction qui pourrait intervenir dans la persistance des événements forts El Niño avec le réchauffement climatique est celle entre les anomalies de courant liées à ENSO et les courants moyens. Santoso et al. (2013) ont montré que que les anomalies de courant liées à ENSO avaient des effets opposés suivant l'intensité de l'événement El Niño. En particulier, pendant les événements forts El Niño, les anomalies de courant d'est devenant supérieures au courant moyen d'ouest, elles conduisent à un renversement des courants pendant les événements forts, qui se propagent alors vers l'est du Pacifique tropical. Ils ont suggéré que la diminution projetée des courants zonaux moyens avec le réchauffement climatique (Vecchi et al., 2006) faciliterait la propagation vers l'est des événements El Niño. Un diagnostique préliminaire sur la direction de propagation des événements forts EP El Niño a été réalisé dans le modèle CESM en tenant compte de la saison du pic des SST dans le Pacifique est. La direction de propagation des événements est déterminée à partir de la pente du taux de chauffage nul, c'est à dire quand $dT/dt = 0$ dans un diagramme représentant l'évolution de l'événement El Niño à l'équateur. Les résultats préliminaires montrent que les événements forts EP El Niño sont plus susceptibles de se propager vers l'est dans un climat plus chaud qu'en situation actuelle, cohérent avec les résultats de Santoso et al. (2013) et que les événements forts EP FMA et ONDJ (Octobre-Janvier) El Niño sont plus susceptibles de se

propager vers l'est que les événements forts JAS (Juillet-Septembre) El Niño. Ces résultats pourraient confirmer le rôle renforcé de la rétroaction de la thermocline dans les événements forts FMA et ONDJ El Niño en situation future. Cependant, cette méthode est dépendante de la région en longitudes ou de la période du pic considérée et nécessite d'être affinée.

Enfin, la proportion d'événements EP modérés diminue dans un climat plus chaud, 24 % (33 %) des événements El Niño modérés étant des EP El Niño en situation future (actuelle). Takahashi and Dewitte (2016) et Takahashi et al. (2018) ont suggéré que les événements forts El Niño sont des événements EP dont le réchauffement dans le Pacifique oriental atteint un seuil qui renforce la rétroaction de Bjerknes. Ce changement peut être dû à une augmentation des événements EP El Niño qui deviennent des événements forts ou à une diminution des événements modérés qui deviennent des événements EP El Niño (préférentiellement des événements CP modérés). Dans le cas où les événements forts sont privilégiés, les mêmes processus que ceux qui peuvent favoriser l'augmentation des événements forts El Niño et leur persistance en FMA peuvent entrer en jeu. Dans le cas où les événements modérés CP El Niño sont privilégiés aux événements modérés EP El Niño, un changement du mode saisonnier d'interactions air-mer associé à la rétroaction de Bjerknes et qui intervient dans la différentiation des événements modérés El Niño EP et CP peut être invoqué (Dewitte and Takahashi, 2017). Cependant, Dewitte and Takahashi (2017) ont montré que deux modèles de climat, GFDL CM2.1 et CESM-LE, qui simulent de façon réaliste la diversité d'ENSO et les non-linéarités associées, ne reproduisent pas correctement les variations de SST lors de la phase de développement des événements modérés (Avril-Octobre) en particulier le long de la côte du Pérou. Cette région est en effet sujette à des biais importants dans les modèles de climat (Richter, 2015). Améliorer la représentation des interactions air-mer dans ces régions clés de la dynamique océanique près des côtes apparaît ainsi primordial dans la compréhension du développement de la diversité des événements El Niño.

Finalement, cette thèse, en étudiant l'évolution temporelle des événements El Niño, définis par leur intensité de réchauffement dans le Pacifique est plutôt que par leur différence spatiale, a permis de mettre en avant différents comportements d'El Niño et en particulier leur évolution saisonnière différente. Elle s'inscrit dans un contexte riche d'études qui ont amené à la différentiation de la dynamique associée aux événements El Niño extrêmes (Chen et al., 2015a; Takahashi and Dewitte, 2016; Santoso et al., 2017; Hameed et al., 2018; Takahashi et al., 2018; Abellán et al., 2017b). Il semble émerger une vision d'ENSO constitué d'un côté d'un continuum d'événements chauds faibles à modérés, dont la localisation spatiale s'étend du Pacifique central (CP El Niño) au Pacifique oriental (EP El Niño modéré) et qui représentent la norme plutôt que l'exception et d'un autre côté d'événements extrêmes intensifiés à l'est, fortement associés aux non-linéarités du système couplé océan-atmosphère. Certaines approches ajoutent un mode biennal fortement influencé par le forçage atmosphérique, se produisant localement dans le Pacifique central et ne donnant pas lieu au renversement de phase d'ENSO par les événements La Niña (Kao and Yu, 2009; Chen et al., 2015a). Ce dernier mode se confondrait, en termes de structures spatiales de SST et de températures de subsurface, avec les CP El Niño modérés, compliquant les diagnostics de processus associés.

L'analyse de l'évolution temporelle des EP El Niño et en particulier leur saison préférentielle de pic en SSTA peut permettre de mieux appréhender le phénomène ENSO dans son ensemble, en se détachant de la vision centrée sur les caractéristiques spatiales des événements El Niño.

Conclusions and Perspectives

This thesis work focused on the diversity of the El Niño-Southern Oscillation (ENSO) phenomenon and its projected changes with global warming. ENSO diversity has received renewed attention in recent decades due to an increase in the number of El Niño events with warming of surface waters in the central tropical Pacific rather than in the eastern Pacific, where the phenomenon generally has higher positive Sea Surface Temperatures (SST) (Ashok et al., 2007; Lee and McPhaden, 2010). These spatial differences in ocean surface warming during El Niño events are crucial to the atmospheric response they cause around the Pacific Ocean and the associated teleconnections between the tropics and mid-latitudes (Weng et al., 2009). Subtle variations in Central Pacific SST can have strong impacts on the location and intensity of latent heat release into the atmosphere, which impacts global atmospheric circulation. Thus, even if they have smaller SST warming zonal extensions and lower intensities than the El Niño events in the eastern Pacific, the El Niño events in the central Pacific are likely to induce a stronger atmospheric response and extra-tropical teleconnections (Weng et al., 2009). It is therefore essential to better understand ENSO events and their diversity in order to better anticipate them.

First, I assessed the characteristics of ENSO diversity, and more particularly that of warm events, El Niño events (chapter 3). To do this, I compared two approaches to characterise this diversity, using the control simulations of two Coupled General Circulation Models (CGCMs): CESM-LE and GFDL CM2.1.

The first method of characterising El Niño diversity is based on the spatial distinction of the action centres of SST warming in the tropical Pacific that can be observed between El Niño events (Kug et al., 2009; Kao and Yu, 2009; Yeh et al., 2009a). In particular, this method compares SST warming intensities in the ENSO historical regions, namely the Niño-3 region in the east (5°S-5°N, 210°E-270°E) and the Niño-4 region in the central tropical Pacific (5°S-5°N, 160°E-210°E). Two types of El Niño events are thus classified, "Central Pacific" (CP) and "Eastern Pacific" (EP) El Niño events (Kug et al., 2009). EP (CP) El Niño events correspond to El Niño winters during which the Niño-3 (Niño-4) SST anomalies index is higher than the Niño-4 (Niño-3) SST anomalies index (and higher than the detection threshold for El Niño events), i.e. when the anomalous warming of surface waters is more pronounced in the eastern (central) tropical Pacific. Several studies have suggested that the dynamics associated with these two types of events were different, with a deterministic dynamic explained by the theory of the recharge-discharge oscillator (Jin, 1997a) for EP El events Niño and a dynamic marked by atmospheric forcing for CP El Niño (Kao and Yu, 2009; Kug et al., 2009). Indeed, due to the strong zonal contrasts of the Pacific along the equator, whether in terms of SST, thermocline depth or sensitivity to atmospheric convection, the central and eastern Pacific are likely to favour different processes. In particular, two oceanic processes play a key role in the development of ENSO events, the thermocline and zonal advection processes. The longitudinal position of the anomalous warming area at the onset of El Niño events leads to a predominance of one or the other of these processes. In the eastern equatorial Pacific, the deepening of the thermocline during the development of El Niño events reduces surface cooling by limiting exchanges between the surface and the subsurface (Vialard et al., 2001) In particular, the mean vertical advection of subsurface temperature anomalies, a

process called thermocline feedback (TCF), is enhanced in the eastern Pacific where changes in thermocline depth have more effects on SST, due to a shallower mean thermocline, than in the western and central Pacific (An and Jin, 2001; Jin et al., 2006). On the other hand, zonal advection processes are essential in the western and central Pacific (Picaut et al., 1996). In particular, the zonal advection of the temperature gradient by current anomalies, a process called zonal advective feedback (ZAF), is more effective in the development of ENSO-related SST anomalies in the central Pacific due to the large zonal temperature gradient near the eastern edge of the Warm Pool. Differences in SST between the cold eastern Pacific, referred as to the "Cold Tongue", and the warm western Pacific, referred to as the "Warm Pool", also lead to a greater sensitivity of the deep atmospheric convection onset in the central Pacific than in the eastern Pacific, where stronger positive temperature anomalies will be required.

The second method is based on the existence of two main modes of variability in the tropical Pacific, calculated by the Empirical Orthogonal Functions (EOF) method. The centre of action of the first mode of variability is located in the eastern Pacific, that of the second mode of variability is located in the central Pacific (Takahashi et al., 2011). These two modes of variability lead to the definition of two El Niño regimes intrinsically linked to the non-linearities of the coupled ocean-atmosphere system (Dommenget et al., 2013; Takahashi and Dewitte, 2016). Warm El Niño events, whose SST signature is strongly printed in the eastern Pacific, are also those with the highest intensities. The two El Niño regimes defined by this methods, strong and moderate El Niño events, are distinguished by the intensity of surface water warming in the eastern Pacific.

I estimated the robustness of these two definitions by comparing them in observational datasets and numerical simulations of the climate system. First, I used two simulations of the pre-industrial (PI) climate, i. e. without anthropogenic forcing and with constant external forcing. These simulations are called PI-control simulations. These are long simulations that are an essential tool for analysing the internal variability of the climate system without interacting with changes in external forcings. The PI-control simulations are those of CESM1 (1801 years of simulation) and GFDL CM2.1 (500 years). In a second step, I used a large set of historical climate simulations (42 members, 1920-2005) and climate projections under the sustained greenhouse gas emission scenario, called the RCP8.5 scenario (40 members, 2006-2100). The simulations come from the CESM Large Ensemble (CESM-LE) Project, launched by the National Center for Atmospheric Research (NCAR, Colorado, USA) and intended for advancing understanding of internal climate variability and climate change. This coupled climate model realistically simulates the variability of the tropical Pacific and ENSO, although some known and frequent biases in CGCMs remain present, such as the cold bias of the Cold Tongue or the double inter-tropical convergence zone (ITCZ).

Several studies showed that the definition of El Niño events is highly dependent on the indices used and therefore on the method used (Singh et al., 2011; Stevenson et al., 2017). I show that within a same method, the definition of El Niño events is also dependent on several spatial-temporal parameters. Indeed, the first method described above, which defines El Niño events from the fixed regions of observed variability in the tropical Pacific (Niño-3 and Niño-4 regions), is highly dependent on the winter season considered for the peak of the event. Thus, for the same dataset, whether observations or control simulations, the detection of CP or EP El Niño events differs depending on whether the months of November to January (NDJ), December to February (DJF) or January to March (JFM) are used to define the event peak. This difference may result in an inversion of the ratio of the number of CP events compared to the number of EP El Niño events. This sensitivity to the peak season can be explained by the spatial and temporal evolution of El Niño events, whose zonal direction of warm water propagation changes the mean SST values between November and March. Moreover, this method of defining El Niño events from fixed regions (Niño-3 and Niño-4 regions) appears difficult to apply to CGCMs because of their recurring biases. These biases are particularly pronounced in the regions used to define ENSO, which complicates the interpretation of the

associated physical processes and severely limits the confidence that can be placed in these results.

The second method, using the indices associated with the two main modes of variability of the tropical Pacific, is not constrained by this fixed spatialization of the indices. These two modes of variability are described by the E and C indices, obtained by a linear combination of the time series, or principal components, associated with the two main modes of variability derived from the EOF analysis. Mode E explains most of the variability in the eastern Pacific and is more specifically associated with strong El Niño events, while mode C has a focus in the central Pacific and includes La Niña and moderate El Niño events. However, the classification of El Niño events as moderate or strong events depends on the threshold value used on the E index to differentiate between these two types of events. Takahashi and Dewitte (2016) argued that this threshold for separating the two El Niñoregimes is directly related to the Bjerknes feedback. Above this threshold, the non-linearities of the tropical Pacific coupled ocean-atmosphere system result in a strong amplification of the Bjerknes feedback. A slight increase in SST in the eastern Pacific then causes an enhanced response of zonal wind stress, which amplifies the initial warming in this tropical Pacific region. The Bjerknes feedback thus appears non-linear and function of surface warming in the eastern tropical Pacific. Takahashi and Dewitte (2016) and Takahashi et al. (2018) suggested that strong El Niño events are El Niño events whose warming in the eastern Pacific reaches this threshold in SSTA, thus reinforcing the Bjerknes feedback. This non-linear behaviour is diagnosed, in GFDL CM2.1, from a threshold between +1.5 and +2 °C in SST anomalies in the eastern Pacific. It is materialised by a bi-modality of the distribution of El Niño events in the phase space corresponding to the two modes of variability of the tropical Pacific, i.e. in the phase space of indices (E, C). However, this bi-modal behaviour is not very pronounced in the CESM-LE simulations. The estimation of this threshold can therefore be considered subjective in our study. A change of ±5 % of the threshold thus leads to a variation in the number of strong El Niño events between 225 (-5.1 %) and 262 (10.5 %) for historical simulations and between 271 (-10.3 %) and 322 (6.6 %) for RCP8.5 simulations.

Nevertheless, the non-linear behaviour of the Bjerknes feedback is simulated by CESM-LE. However, it is associated with lower E-index values (close to 0 °C) than in observations or in the control simulation of GFDL CM2.1 (close to 2 °C). It also appears that the non-linear behaviour of the Bjerknes feedback is carried out in stages in CESM-LE, with a first threshold, close to 0 °C, which results in a strong amplification of the feedback, and a second threshold, close to 2 °C, beyond which the Bjerknes feedback is reduced compared to the first threshold. This difference in behaviour between CESM-LE GFDL CM2.1 requires further investigation, which could also be carried out on all models in Phase 5 of the Coupled Model Intercomparison Project (CMIP5) of the Intergovernmental Panel on Climate Change (IPCC). It would indeed seem that some of the CMIP5 models have a mean behaviour similar to that of CESM-LE, with a threshold close to E=0.5 °C and potentially a lower behaviour beyond 1.5 °C (see Figure S1e of Cai et al. (2018) for all CMIP5 model database or their Figure S3e for selected models due to their ENSO non-linearities simulation, which have a threshold close to E=0 °C).

I then compared the two methods with each other. Strong events are preferably EP El Niño events, whether in historical simulations (87 % of strong events are EP El Niño events) or future simulations (89 % of strong events), due to their definition by the E index. This is consistent with the observations and in particular the extreme events of 1982-83 and 1997-98 (McPhaden and Yu, 1999), as well as with the results of numerous studies that showed that the most intense El Niño events develop in the eastern tropical Pacific (Takahashi et al., 2011; Chen et al., 2015a; Santoso et al., 2017). However, not all EP El Niño events are strong events. Thus, even if moderate events are preferentially CP El Niño events, 33 % are classified as EP El Niño events in historical simulations. We then return to the projected change in these El Niño flavours with global warming.

In a second step, I was interested in the impact that low-frequency modulation

of the tropical Pacific mean state can have on the diversity of El Niño and the influence of ENSO modulation on the mean state (chapter 4). The mechanisms associated with the low-frequency modulation of ENSO diversity are still poorly understood. Several studies suggested that the spatial diversity of El Niño, defined by the EP and CP events, is modulated at low frequency by the mean state, which it could in turn rectify through the ENSO residuals due to the asymmetry between El Niño and La Niña events (Choi et al., 2009, 2012).

However, while the relationship between the Tropical Pacific Decadal Variability (TPDV) mode, called ENSO-induced, and the frequency of occurrence of CP El Niño events, in the PI-control simulation of CM2.1 GFDL, is strong, it is only poorly diagnosed in the CESM PI-control simulation.

Several sources of uncertainty can explain these different behaviours of internal variability simulated by the models. The first issue comes from the simulation of the ENSO-induced mode variance. In CESM, the ENSO-induced mode is the second dominant mode of decadal variability in the tropical Pacific, while it is the main mode of decadal variability in GFDL CM2.1. This mode explains 59 % of the total variance in GFDL CM2.1 while it explains only 23 % of the total variance in CESM. These differences in variability can thus lead to different interaction between the mean state and ENSO low-frequency modulation. In particular, Choi et al. (2013a) suggested that the variance of each of the two modes depends on the strength of the relationship between the residuals due to ENSO asymmetry and the ENSO-induced TPDV mode. In their mechanism, the higher the variance explained by the ENSO-induced mode, the higher the bidirectional feedback between the ENSO modulation and the mean state (through the non-linear ENSO residuals), the higher the variability of the ENSO amplitude. However, this relationship appears to be subject to recurrent climate model biases, particularly the regularly overestimated amplitude of ENSO. An interesting diagnosis could therefore consist in analysing the relationship between ENSO asymmetry residuals and the TPDV ENSO-induced mode in CESM-LE, and extending this diagnosis to historical simulations, which could highlight the mechanism at work through inter-member variability.

The second uncertainty comes from the simulation of the ENSO-induced mode spatial pattern. In CESM, the negative anomalies of the ENSO-induced mode extend further into the central Pacific, confining the positive anomalies into the eastern Pacific. This bias is particularly visible in the regressed SST spatial pattern associated with this mode. It could lead to a change in the relationship between the ENSO-induced mode and the residuals associated with ENSO asymmetry, since the latter are more likely to have a spatial pattern that extends westward given the bias, recurrent in CGCMs, of the Cold Tongue that extends too far west of the equatorial Pacific.

Zheng et al. (2018) showed that the TPDV ENSO-induced mode and the dispersion, between the CESM-LE members, of the simulated SST warming by 2100 under the RCP8.5 scenario were strongly linked. They suggested that the two-ways feedback between the tropical Pacific mean state and ENSO leads in particular to uncertainties about the SST warming rates due to climate change. Given this strong contribution of internal variability to projected changes, and in particular to the change in ENSO amplitude, the mechanisms linking ENSO and TPDV in CESM-LE require further study.

Finally, I studied the projected changes in ENSO statistics and thermodynamic processes associated with the phenomenon in the context of global warming (chapter 5).

First, I was interested in the changes in ENSO statistics due to global warming in CESM-LE. We show that the variance of SST anomalies in the eastern tropical Pacific (transcribed by mode E) increases significantly (statistically significant at 95 % confidence level) between historical and future CESM-LE simulations. This increase is associated with an increase in the occurrence frequency of strong El Niño events, although this increase is moderate (+24 %) and non-linear, subject to pronounced low frequency variations. This

result is consistent with the results obtained from the CMIP5 models and published in the journal Nature (Cai et al., 2018). This article is presented in appendix 5.3.4.2. This increase in variability in the eastern tropical Pacific is associated with an increase in the vertical stratification of the central Pacific. We will return to the ocean processes involved in this change in ENSO statistics.

In addition, we show, by analysing the seasonal cycle of the variability of the mode E, that the E-index variance increases significantly during the months of February, March and April (FMA) with global warming. This significant increase is associated with an increase in the frequency of occurrence of strong EP El Niño events that peak during this FMA season, and an increase in the mean duration of strong EP El Niño events. It is interesting to note that this increase in the E-index variance in FMA is independent of the method used to remove the trend on SST due to global warming. I have indeed tested two other methods to remove the climate change trend, in addition to the linear detrend method. The second method consists of removing a quadratic trend at each point, the third method subtracts the mean warming calculated over a larger region, following Khodri et al. (2017). For the latter method, the tropical Pacific region (30°S-30°N) is considered. Regardless of the method applied, the E-index variance increases significantly statistically in FMA, while changes in the E-index variance can be opposed according to the methods for the other months of the year. Finally, preliminary results from CMIP5 models seem to confirm this increase in the SST anomalies variance in the eastern equatorial Pacific in a warmer climate.

One of the most significant results in recent years, regarding the change in ENSO statistics with global warming, is the projected increase in the occurrence frequency of El Niño extreme precipitation events in the eastern Pacific (Cai et al., 2014, 2015b, 2017). The frequency of occurrence of these extreme precipitation events is likely to double with global warming by 2100 according to CMIP5 models (Cai et al., 2014), and even almost quadruple in CESM-LE. Given the meteorological and socio-economic impacts of this type of extreme event, we have sought to relate this increase in precipitation extreme events to the observed persistence of strong events EP El Niño. We show that the emergence of these strong EP El Niño events that have their SST peak in FMA in the future climate explains a third (33 %) of the increase in the frequency of occurrence of extreme El Niño events in precipitation. Indeed, the FMA period is the period during which SST in the eastern Pacific experience their seasonal peak and the ITCZ is about to reach its southernmost position (Xie et al., 2018), which strengthens the coupling between El Niño and the ITCZ and promotes extreme precipitation. Because of this strong seasonal coupling between the strong FMA El Niño events and the ITCZ, a SST warming due to anthropogenic forcing is not required to produce extreme precipitation events in the eastern tropical Pacific. In addition, 34 % of the increase in the frequency of occurrence of extreme precipitation El Niño events is associated with weak to moderate El Niño events, and therefore associated with SST warming. We show that in CESM-LE, the projected increase in extreme precipitation El Niño events is explained both by the increase in mean SST in the eastern Pacific and by changes in ENSO processes associated with higher surface warming than subsurface warming leading to a sharper thermocline and an increased vertical stratification.

Thus, these results reconcile the research work of the last decade on ENSO statistical changes under global warming. On the one hand, many studies highlighted a lack of consensus between CGCMs on the projected evolution of ENSO amplitude variability in the eastern Pacific (Niño-3 or Niño-3.4 regions) (Guilyardi et al., 2009b; Bellenger et al., 2014; Chen et al., 2017a). On the other hand, the frequency of occurrence of extreme precipitation El Niño events in the eastern tropical Pacific are projected to increase in the future by the CMIP5 models (Cai et al., 2014, 2015a, 2017). The analysis of El Niño events by the mode E of dominant variability in the eastern tropical Pacific showed that the increase in the E-index variance is statistically significant across CMIP5 models. The frequency of occurrence of strong EP El Niño events will increase in a warmer climate. It will also be accompanied by

an increase in El Niño events, which will peak in SST later than in the current situation, in FMA rather than in NDJ. This increase partly explains the increase in extreme precipitation events in the eastern tropical Pacific.

The analysis of El Niño events by the mode E allows the ENSO phenomenon to be considered as a whole, while maintaining a physical continuity of the associated dynamic processes, which is not possible with the analysis of ENSO by fixed regions of variability (Niño-3 and Niño-4 regions). This method objectively takes into account the action centres of ENSO events by modes E and C. It also avoids model biases in the tropical Pacific region and, in particular, the westward shift of the climatological Cold Tongue.

Secondly, I was interested in the changes in thermodynamic processes that accompany and are likely to explain the changes in ENSO statistics in the future. We suggest that the greatest persistence of EP El Niño events and the time lag in their warming peak are due to a larger recharging process and more effective thermocline feedback in the eastern Pacific in a warmer climate as simulated by CESM-LE. In particular, the analysis of the mixed layer heat budget during the El Niño events shows that the reduction in mean upwelling, due to the increase in Pacific vertical stratification, is largely offset by the increase in the vertical gradient of temperature anomalies across the mixing layer, which leads to an overall increase in the thermocline feedback.

An issue in generalising the results comes from the accuracy of CGCMs to realistically simulate the tropical Pacific mean state and the processes associated with ENSO. In particular, the weakening of the SST zonal gradient is not systematically simulated in future simulations, despite the projected weakening of the Walker Circulation (Vecchi et al., 2006; Yeh et al., 2012). The change in the SST zonal gradient is only weakly related to changes in thermocline depth (Li et al., 2016). The relationship between SST, thermocline depth and trade winds may therefore be weaker than the current relationship observed by the Bjerknes feedback. This leads to processes in contrast to El Niño processes, when the thermocline response is strongly dominated by a lower inclination along the equator. These counter-intuitive changes may be due in particular to the recurrent bias of CGCMs to simulate excessive Cold Tongue, resulting in greater projected warming in the western Pacific in some models (Li et al., 2016; Ying et al., 2019). When this Cold Tongue bias is corrected in CGCMs, the projected tropical Pacific SST warming resembles an El Niño-like pattern. However, the impact of this mean state bias on the processes involved in current and future ENSO events requires further investigation. In addition, the projected subsurface warming is variously simulated in the Central Pacific in the CMIP5 models. Given the importance of thermocline processes in the development of El Niño events, an improvement of modelled oceanic processes is required and can be achieved by optimizing mixing process parameterizations and increasing model resolution. Finally, the simulation of the non-linearities of the tropical Pacific climate system is essential in the simulation of the mean state and processes associated with ENSO (Boucharel et al., 2011; Karamperidou et al., 2017; Cai et al., 2018). In particular, models that more realistically simulate the non-linearities associated with ENSO are those that best reflect ENSO diversity, both in terms of spatial patterns and amplitude.

The understanding of these different processes associated with ENSO and the tropical Pacific mean state can be improved in the near future through:

- increased observations (temperature, surface wind, current), particularly in the eastern Pacific. Currently, the tropical Pacific observation network does not provide sufficient vertical and horizontal resolutions to properly analyse the non-linearities of ENSO processes. The development of an improved observation network for the tropical Pacific is being discussed as part of the TPOS2020 programme (Tropical Pacific Observing System for 2020, Smith et al. (2019)).
- a new generation of coupled models as part of Phase 6 of the Model Intercomparison Project (CMIP6,Eyring et al. (2016)). The higher resolution of the CGCMs and a different parameterization of ocean processes can improve:

– on the one hand, the simulation of ENSO non-linearities and asymmetry, which are repeatedly underestimated in CGCMs,

– on the other hand, the simulation of coupled ocean-atmosphere processes at play in regions subject to recurrent model biases (the cold water tongue bias, the double ITCZ and the extreme eastern equatorial Pacific region).

While we focused on the impact of changes in vertical stratification on ENSO-related processes (the recharging process and thermocline feedback), other processes can potentially influence the greater persistence of El Niño events but also the increase in El Niño strong events in future situations:

- the increase in mean SST in the tropical Pacific that can facilitate exceeding the Bjerknes feedback threshold, which is subject to change with the mean state (Johnson and Xie, 2010),
- a change in the seasonal cycle of Bjerknes feedback and the associated ocean-atmosphere interaction pattern in the eastern tropical Pacific. Dewitte and Takahashi (2017) suggested that moderate EP El Niño events are distinguished from strong EP El Niño events by the emergence of easterly wind bursts in September in the far eastern Pacific. These easterly wind bursts would counter the Bjerknes feedback in the eastern Pacific and prevent the EP El Niño event from developing into a strong El Niño by limiting the warming that would then not exceed the required threshold. A change in the seasonal cycle of this mode of air-sea interactions with global warming could disconnect the emergence of these easterly wind bursts from the growth of the El Niño event. Further investigation is needed to determine in particular whether these easterly wind episodes are stochastic or induced by ENSO as suggested by Hameed et al. (2018), as well as to diagnose if and which counter-acting forcing is needed for a strong El Niño to develop.
- changes in external stochastic forcing, such as Westerly Wind Bursts (WWBs) that interact non-linearly with the surface ocean until they modulate it (Hayashi and Watanabe, 2017). WWBs are likely to alter the recharge processes in the tropical Pacific during strong EP El Niño events. WWBs are the subject of numerous recent studies (Puy et al., 2016b, 2017), as are recharge processes (Neske and McGregor, 2018; Izumo et al., 2018). Their interaction requires further diagnosis, in particular regarding the deterministic mechanisms at play in the ocean modulation processes of WWBs.

Two regions are therefore at the heart of the ocean-atmosphere interactions at play during extreme El Niño events. The western tropical Pacific is the centre of action for WWBs that appear to be decisive in the growth of a strong El Niño event, especially when they occur in summer (Puy et al., 2017). The eastern, even far eastern, tropical Pacific, in addition to the strong interactions between the surface and the thermocline, is the site of easterlies wind bursts in summer/fall that are able to counter the development of a strong El Niño event. However, these regions are still subject to recurrent biases in their simulation by CGCMs.

Another interaction that could be involved in the persistence of El Niño strong events with global warming is that between ENSO-related current anomalies and mean currents. Santoso et al. (2013) showed that ENSO-related current anomalies have opposite effects depending on the intensity of the El Niño event. In particular, during strong El Niño events, with the eastern current anomalies becoming greater than the western mean current, they lead to a reversal of currents during strong events, which then spread to the eastern tropical Pacific. They suggested that the projected decrease in mean zonal currents with global warming (Vecchi et al., 2006) would facilitate the eastward spread of El Niño events. A preliminary diagnosis on the direction of propagation of strong EP El Niño events was carried out in CESM, taking into account the season of the SST peak in the eastern Pacific. The direction of propagation of the events is determined from the slope of the zero heating rate, i.e. when $dT/dt = 0$ in a diagram representing the evolution of the event El Niño at the equator (Hovmuller diagram).

Preliminary results show that strong EP El Niño events are more likely to spread eastward in a warmer climate than in the current situation, consistent with the results of Santoso et al. (2013). Strong EP FMA and ONDJ (October-January) El Niño events are also more likely to spread eastward than strong JAS (July-September) El Niño events. These results could confirm the enhanced role of thermocline feedback in strong FMA and ONDJ El Niño events in future situations. However, this method is dependent on the longitudinal region or on the peak period considered and needs to be refined.

Finally, the proportion of moderate EP events decreases in a warmer climate, with 24 % (33 %) of moderate El Niño events being EP El Niño in future (current) situations. Takahashi and Dewitte (2016) and Takahashi et al. (2018) suggested that the strong El Niño events are EP events whose warming in the eastern Pacific reaches a threshold that reinforces the Bjerknes feedback. This change may be due to an increase in EP El Niño events that become strong events or a decrease in moderate events that become EP El Niño events (preferably moderate CP events). In the case where strong events are privileged, the same processes as those that can promote the increase of strong El Niño events and their persistence in FMA can come into play. In the case where moderate CP El Niño events are favoured over moderate EP El Niño events, a change in the seasonal mode of air-sea interactions associated with Bjerknes feedback, which is involved in the differentiation of moderate El Niño EP and CP events, can be invoked (Dewitte and Takahashi, 2017). However, Dewitte and Takahashi (2017) showed that the two climate models, GFDL CM2.1 and CESM-LE, which realistically simulate ENSO diversity and associated non-linearities, do not correctly reproduce SST variations during the development phase of moderate events (April-October), particularly along the Peruvian coast. This region is indeed subject to significant biases in CGCMs (Richter, 2015). Improving the representation of air-sea interactions in these key regions of ocean dynamics near the coast is therefore essential in understanding the development of the diversity of El Niño events.

This thesis, by investigating the temporal evolution of El Niño events, defined by their warming intensity rather than by their spatial difference, highlighted different El Niño behaviours and in particular their different seasonal evolution. It is part of a rich context of studies that led to the differentiation of the dynamics associated with extreme El Niño events (Chen et al., 2015a; Takahashi and Dewitte, 2016; Santoso et al., 2017; Hameed et al., 2018; Takahashi et al., 2018; Abellán et al., 2017b). There appears to be a vision of ENSO consisting of:

- a continuum of weak to moderate warm events, whose spatial location extends from the Central Pacific (CP El Niño) to the Eastern Pacific (moderate EP El Niño) and which represent the norm rather than the exception,
- intensified extreme events in the eastern Pacific, strongly associated with the non-linearities of the coupled ocean-atmosphere system.

Some approaches add a biennial mode strongly influenced by atmospheric forcing, occurring locally in the central Pacific and not leading to ENSO phase reversal of La Niña events (Kao and Yu, 2009; Chen et al., 2015a). The latter mode would merge, in terms of SST spatial patterns and subsurface temperatures, with the CP moderate El Niño, complicating the diagnosis of associated processes.

The analysis of the temporal evolution of the El Niño events, and in particular their preferential SSTA peak season, can provide a better understanding of the ENSO phenomenon as a whole, by moving away from the vision focused on the spatial characteristics of El Niño events.

Appendix A: Article published in Nature

ARTICLE

https://doi.org/10.1038/s41586-018-0776-9

Increased variability of eastern Pacific El Niño under greenhouse warming

Wenju Cai[1,2]*, Guojian Wang[1,2], Boris Dewitte[3,4,5,6], Lixin Wu[1]*, Agus Santoso[2,7], Ken Takahashi[8], Yun Yang[9], Aude Carréric[6] & Michael J. McPhaden[10]

The El Niño–Southern Oscillation (ENSO) is the dominant and most consequential climate variation on Earth, and is characterized by warming of equatorial Pacific sea surface temperatures (SSTs) during the El Niño phase and cooling during the La Niña phase. ENSO events tend to have a centre—corresponding to the location of the maximum SST anomaly—in either the central equatorial Pacific (5° S–5° N, 160° E–150° W) or the eastern equatorial Pacific (5° S–5° N, 150°–90° W); these two distinct types of ENSO event are referred to as the CP–ENSO and EP–ENSO regimes, respectively. How the ENSO may change under future greenhouse warming is unknown, owing to a lack of inter-model agreement over the response of SSTs in the eastern equatorial Pacific to such warming. Here we find a robust increase in future EP–ENSO SST variability among CMIP5 climate models that simulate the two distinct ENSO regimes. We show that the EP–ENSO SST anomaly pattern and its centre differ greatly from one model to another, and therefore cannot be well represented by a single SST 'index' at the observed centre. However, although the locations of the anomaly centres differ in each model, we find a robust increase in SST variability at each anomaly centre across the majority of models considered. This increase in variability is largely due to greenhouse-warming-induced intensification of upper-ocean stratification in the equatorial Pacific, which enhances ocean–atmosphere coupling. An increase in SST variance implies an increase in the number of 'strong' EP–El Niño events (corresponding to large SST anomalies) and associated extreme weather events.

Alternating between El Niño and La Niña events, the ENSO affects extreme weather events, ecosystems and agriculture around the world[1–7]. ENSO events vary greatly[8–15]: the EP-ENSO is associated with strong El Niño events and weak cold SST anomalies, and is characterized by the maximum SST anomaly (the SST anomaly centre) being located in the eastern equatorial Pacific (the 'Niño3' region: 5° S–5° N, 150°–90° W); the CP-ENSO is associated with strong or moderate La Niña events and modest El Niño events, and is characterized by the SST anomaly centre being located in the central equatorial Pacific (5° S–5° N, 160° E–150° W). EP-El Niño events are the strongest and most destructive El Niño events. During such events, SST warming in the Niño3 region leads to flooding in southwest USA, Ecuador and northeast Peru, and to droughts in regions that border the western Pacific[1,4]. In extreme cases, the disruption includes substantial loss of marine life in the eastern Pacific, mass bleaching of corals across the Pacific and beyond[2], and movement of the intertropical convergence zone[7] and of the South Pacific convergence zone towards the equator[5,16], inducing catastrophic floods and droughts across the Pacific region[5,7]. Because of these severe effects, determining how EP-El Niño SST variability responds to greenhouse warming is one of the most important issues in climate science. However, over several model generations, there has been no inter-model consensus on future variability using conventional ENSO indices[17–19].

This lack of consensus is despite inter-model agreement on the change in mean state and modest inter-model agreement on the response of CP-ENSO SST variability and on the change in certain characteristics of ENSO extremes. First, faster warming in the eastern equatorial Pacific than in the surrounding regions and in the equatorial Pacific than in the non-equatorial Pacific[20] facilitates an increased frequency of equatorward shifts of the convergence zones and increased rainfall variability, even if SST variability does not change[7,16,21]. The extreme shifts of the convergence zones occur during El Niño events, particularly during strong ones[5,7,16]. Second, El Niño events with eastward-propagating anomalies increase in frequency as a consequence of weakening Walker circulation[22]. Finally, there has been a focus on the response of CP-ENSO SST variability to greenhouse warming. Although the frequency of CP-El Niño events is projected to increase, the robustness of the increased frequency is debated[9,23–25]. On the other hand, a projected faster warming in the surface layer of the ocean than at depths enhances the role of the relatively cold subsurface water in the central Pacific in generating strong La Niña events, leading to an increased frequency of extreme La Niña events under greenhouse warming[26].

The response of EP-ENSO SST variability to greenhouse warming is even more uncertain, owing to the lack of inter-model consensus[17–19]. Previous examinations of this issue focused on SST variability at a fixed location, typically the Niño3 region[17,18]. This approach assumes that models simulate an EP-ENSO SST anomaly centre that can be represented by the Niño3 SST index, as is the case in observations. Here we show that the longitude of EP-ENSO SST anomaly centres differs greatly from one model to another, particularly when considering models that cannot simulate ENSO diversity. However, we also show that there is a robust increase across models in EP-El Niño SST variability at the anomaly centre of each model.

[1]Key Laboratory of Physical Oceanography, Institute for Advanced Ocean Studies, Ocean University of China and Qingdao National Laboratory for Marine Science and Technology, Qingdao, China. [2]Centre for Southern Hemisphere Oceans Research (CSHOR), CSIRO Oceans and Atmosphere, Hobart, Tasmania, Australia. [3]Centro de Estudios Avanzados en Zonas Áridas, Coquimbo, Chile. [4]Departamento de Biología, Facultad de Ciencias del Mar, Universidad Católica del Norte, Coquimbo, Chile. [5]Millennium Nucleus for Ecology and Sustainable Management of Oceanic Islands, Coquimbo, Chile. [6]Laboratoire d'Etudes en Géophysique et Océanographie Spatiales, Toulouse, France. [7]Australian Research Council Centre of Excellence for Climate Extremes, The University of New South Wales, Sydney, New South Wales, Australia. [8]Servicio Nacional de Meteorología e Hidrología del Perú—SENAMHI, Lima, Peru. [9]College of Global Change and Earth System Science, Beijing Normal University and University Corporation for Polar Research, Beijing, China. [10]NOAA/Pacific Marine Environmental Laboratory, Seattle, WA, USA. *e-mail: wenju.cai@csiro.au; lxwu@ouc.edu.cn

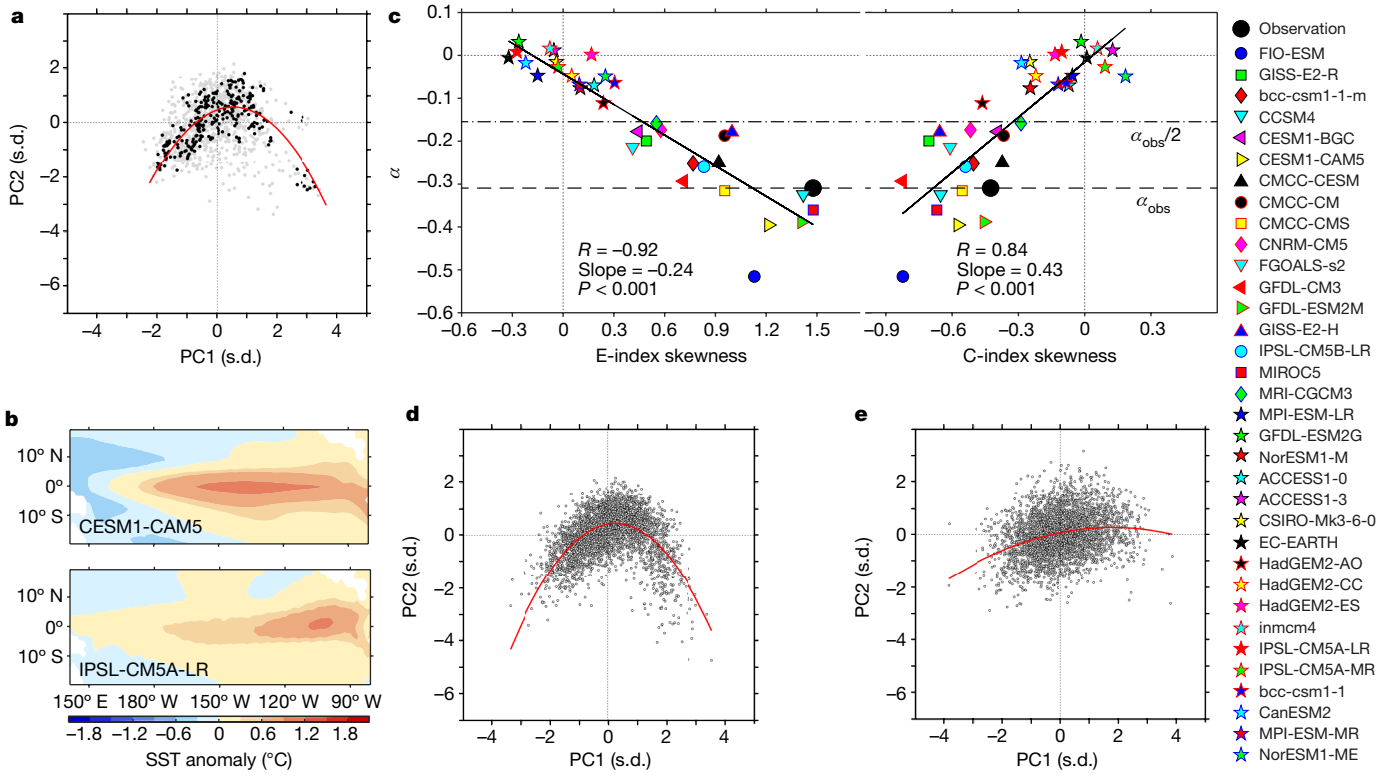

Fig. 1 | Identifying the EP-ENSO anomaly centre in observations and models. a, Nonlinear relationship between the first and second principal components (PC1 and PC2) of SST anomalies averaged over December–February (black dots; see also Extended Data Fig. 1) from five observational reanalysis products. Grey dots indicate monthly data. The nonlinearity is determined by fitting these monthly data with the quadratic function $PC2(t) = \alpha[PC1(t)]^2 + \beta PC1(t) + \gamma$. The red curve shows the same fit, but using the December–February average (black points). **b**, SST anomaly patterns associated with EP-ENSO in two models, highlighting the large difference in the longitude of EP-ENSO anomaly centres (132.25° W for CESM1-CAM5; 101.75° W for IPSL-CM5A-LR) that can occur between climate models. **c**, The parameter α determined using the monthly data versus the skewness of the E-index and C-index for all models analysed (symbols). This parameter is a measure of the contrast between the CP-ENSO and EP-ENSO and of the size of the skewness of the corresponding C-index and E-index. Models with greater $|\alpha|$ systematically produce larger negative skewness in the C-index and larger positive skewness in the E-index. The large black filled circles indicate the observed value α_{obs} (dashed line; the mean of the five observational reanalysis products). The 17 models that produce $|\alpha| < |\alpha_{obs}|/2$ (above the dash-dotted line) are denoted by stars and referred to as 'non-selected'; the other 17 models are shown using various symbols and correspond to the 17 models that we select for further analysis. Details of all models can be found in ref. [29]. The linear fits (solid lines) between α and the E-index or C-index are displayed together with the correlation coefficient R, slope and P value from the regression. **d**, **e**, Nonlinear relationship between the December–February-average principal components for the selected (**d**) and non-selected (**e**) models, with the red curves showing quadratic fits.

Distinguishing SST anomaly centres

At least two ENSO indices are required to distinguish between CP-ENSO and EP-ENSO SST anomaly centres[12,13]. As in previous studies, we use the first two principal modes of an empirical orthogonal function (EOF) analysis of monthly SST anomalies[12,13], with each EOF mode (EOF1 and EOF2) described by a principal spatial pattern, and a principal-component time series scaled to have a variance of unity (see Methods section 'Data, model outputs and EOF analysis'). We applied the EOF analysis to each of five reanalysis products, which we take as the observed SSTs. The positive EOF1 phase exhibits a warm-anomaly centre in the central eastern Pacific; the positive EOF2 phase exhibits a warm-anomaly centre in the central Pacific and a cool-anomaly centre in both the eastern and western parts of the basin[8] (Extended Data Fig. 1a, b). The SST anomaly pattern of an ENSO event is described by a combination of EOF1 and EOF2.

The two monthly principal-component time series display a nonlinear (quadratic[13]) relationship between the two principal modes (Fig. 1a): $PC2(t) = \alpha[PC1(t)]^2 + \beta PC1(t) + \gamma$. For the observations, obtained from multi-reanalysis products (see Methods section 'Data, model outputs and EOF analysis'), the mean value of α is −0.31, which is significantly different from zero at a confidence level of greater than 95%. An EP-ENSO event is described by an E-index[12], which is defined as $(PC1-PC2)/\sqrt{2}$ so that the associated warm-anomaly centre averaged over the season in which an EP-El Niño peaks (December–February) is in the eastern equatorial Pacific. The CP-ENSO regime is described by a C-index, defined as $(PC1+PC2)/\sqrt{2}$, which has a warm-anomaly centre in the central equatorial Pacific (Extended Data Fig. 1c, d). The skewness of the observed monthly E-index is 1.48, reflecting a greater amplitude of EP-El Niño events than of cold SST anomalies. By contrast, the skewness of the monthly C-index is −0.43, reflecting a stronger amplitude of CP-La Niña events than of CP-El Niño events.

Nonlinear dynamics generate skewness

The skewness of the C-index and E-index distributions encapsulates the asymmetry in their associated spatial patterns, and the physical processes responsible for ENSO diversity. Over the central Pacific, during a CP-El Niño event, eastward displacement of the atmospheric convection over the western Pacific warm pool is small, and zonal advection feedback dominates over other processes such as the thermocline feedback[10,11,13,14]. An extreme La Niña event occurs when the central equatorial Pacific thermocline is shallower than normal. This is often associated with the aftermath of an EP-El Niño heat discharge, during which Ekman pumping and nonlinear zonal advection are important, facilitating negative SST skewness[26]. Over the eastern equatorial Pacific, the formation of cool anomalies is curtailed by limited upward displacement of the climatological thermocline, which is already very close to the ocean surface. Instead, this climatological

setting of the thermocline favours thermocline deepening and thus the development of strong warm anomalies during EP-El Niño events, which also involve substantial eastward movement of atmospheric deep convection from the western Pacific warm pool to the eastern equatorial Pacific.

These processes in the eastern Pacific region are enhanced by nonlinear Bjerknes feedback, by which the response of zonal winds increases with positive SST anomalies, contributing to the positive SST skewness in the eastern equatorial Pacific[13,14]. We obtained the EP-El Niño and CP-El Niño SST anomaly pattern using a bi-linear regression of the quadratically de-trended December–February-average SST anomaly at each grid point onto the December–February-average E-index and C-index (Extended Data Fig. 1c, d), to focus on the peak ENSO season. The same was carried out for zonal wind stress anomalies (see Methods section 'Diagnosis of nonlinear Bjerknes feedback'), but using monthly data to take into account that winds are important before the peak season. We then took the time series at the associated wind-stress anomaly centre (the longitude of the maximum wind anomalies averaged over 5° S–5° N) to illustrate this nonlinear process. Wind-stress anomalies respond linearly to concurrent monthly SST anomalies in the CP-ENSO centre (Extended Data Fig. 1f). However, the response is nonlinear for EP-ENSO anomalies[13,14,27,28]: stronger for warm anomalies than for cold anomalies (Extended Data Fig. 1e). Enhanced westerly-wind anomalies induce a reduction in equatorial upwelling, an eastward tilting thermocline and westward upper-ocean currents, through Ekman pumping, zonal advection and, particularly, thermocline feedbacks, which promote further growth of eastern Pacific warm anomalies[14,27,28].

Skewness determines the anomaly centre

To identify the EP-ENSO anomaly centre in models, we conducted a similar analysis for 34 CMIP5 models. We applied EOF analysis to monthly SST anomalies, quadratically de-trended over the full period 1900–2099 (see Methods section 'Data, model outputs and EOF analysis'). These models were forced with historical anthropogenic and natural forcings until 2005, and the Intergovernmental Panel on Climate Change Representative Concentration Pathway (RCP) 8.5 future greenhouse gas concentration trajectory from 2006 onwards[29]. Although the multi-model average position of the EP-ENSO anomaly centre compares well with the observed position, the position of the anomaly centre differs from one model to another with a range of 61.5° in longitude (Extended Data Table 1), and the associated SST anomaly patterns could be very different (Fig. 1b). Our approach does not impose a fixed-location anomaly centre, in contrast to approaches that use the Niño3 index. This allows us to assess the response of the EP-ENSO SST simulated by each individual model.

By definition, the model-predicted SST anomaly centres associated with the C-index and E-index correspond to the maximum negative and positive skewness of these indices, respectively. Thus, identifying the CP-ENSO and EP-ENSO anomaly centre in a model is equivalent to locating the maximum negative and positive skewness, assuming that the model is able to generate skewness. An inter-model relationship shows that models with a larger $|\alpha|$ systematically produce greater positive skewness in the E-index (correlation of 0.92) and greater negative skewness in the C-index (correlation of 0.84; Fig. 1c). Thus, the parameter α connects the two skewness values and measures the diversity of the ENSO, which encapsulates the nonlinear Bjerknes feedback discussed above. The parameter α is also related to the response of zonal winds to eastern Pacific warm anomalies and to central Pacific cool anomalies (Extended Data Fig. 2). We therefore select models on the basis of their corresponding value of α.

The majority of models examined here simulate a value of $|\alpha|$ that is lower than the observed value, consistent with previous findings that many models struggle to simulate the two types of ENSO[30,31], and the observed α[32]. Only 17 models produce a value of $|\alpha|$ that is at least 50% of the observed value and generate a reasonable, nonlinear PC1–PC2 relationship (Fig. 1d; see Extended Data Fig. 3 for anomaly patterns and Extended Data Fig. 4 for the nonlinear relationship in some individual models). Excluding these 17 values, the next largest value of $|\alpha|$ is only 36% of the observed value. We therefore use only these 17 models to assess changes in EP-ENSO under greenhouse warming. The remaining 17 models (stars in Fig. 1c) generate small values of $|\alpha|$—with some values of α having the opposite sign in at least one centre compared to the observed value (Fig. 1c)—and consistently produce a far weaker nonlinear PC1–PC2 relationship (Fig. 1e), indicating a weaker or lack of nonlinear Bjerknes feedback (see Extended Data Fig. 5 for anomaly patterns and Extended Data Fig. 6 for the lack of a nonlinear relationship in some non-selected individual models). In these non-selected models, PC1 and PC2 are scattered without a well-defined relationship, which means that events with the same E-index can correspond to a combination of large PC1 and small PC2, or the other way around. As a result, the EP-El Niño anomaly pattern and the location of the anomaly centre vary substantially from one event to another, so it is difficult to assess the future change in variability.

Variability increases at the EP–ENSO centre

We compare the standard deviation (s.d.) of the E-index in the present-day control (1900–1999) and future climate change (2000–2099) periods, each of 100 years. 15 of the 17 selected models (88%) simulate an increased variance in the E-index in the future period (red bars Fig. 2a). The two models that generate reduced EP-El Niño variability (CCSM4[33] and GFDL-ESM2M) also produce reduced climatological rainfall in the equatorial eastern Pacific, in contrast to increased climatological rainfall in the ensemble average. However, it is not clear whether the reduced climatological rainfall is a consequence or a cause of the decreased EP-El Niño variability. The ensemble-mean increase in the standard deviation of EP-El Niño SST is 15%, which is significant at more than the 95% confidence level according to a bootstrap test (see Methods section 'Statistical significance test'; Extended Data Fig. 7a). The increase in variance translates to a 25% and 27% increase in occurrences of EP-El Niño events with an E-index of more than 0.75 s.d. and more than 1 s.d., respectively. For strong events (E-index $>$ 1.5 s.d.; Fig. 2b), the increase in frequency is 47%, although there is no inter-model consensus on changes in intensity. By contrast, for the non-selected models, there is no inter-model consensus on the change in variance, with only 9 of the 17 models (53%) producing an increase (Extended Data Fig. 8a).

Sensitivity to emission scenarios and to model generations suggests that 12 of the 15 selected CMIP5 models (80%) that are forced under RCP4.5 and five of the seven CMIP3 models (71%) forced under the A2 scenario and selected using the same value of α generate an increase in E-index variance (see Methods section 'Sensitivity to emission scenarios'). In addition, a sensitivity test of our finding to model selection reveals that, even when all 34 CMIP5 models under RCP8.5 are considered, there is still a reasonable inter-model consensus on the increased E-index variance, with 24 of the 34 models (71%) simulating an increase (Extended Data Fig. 8a). By contrast, in terms of Niño3 SST variance, only 18 of the 34 CMIP5 models (53%) produce an increase (Extended Data Fig. 8b). In the selected models, the inter-model consensus is further enhanced because the CP-ENSO and EP-ENSO regimes are more distinguishable, with the EP-ENSO anomaly pattern and centre better defined than in the non-selected models, as indicated by the large $|\alpha|$ and SST skewness values. As such, for the selected models, the longitudinal range of the EP-ENSO anomaly centre is reduced from 61.5° to 28.5° and the Niño3 SST anomaly becomes a reasonable index to represent EP-El Niño events. 12 of the 17 selected models (70.5%) produce an increased Niño3 SST variance. This is a reasonable inter-model consensus, although still lower than that using the E-index (Extended Data Fig. 8a, b).

Stratification change boosts dynamic coupling

We find that although there is an ensemble-mean increase in $|\alpha|$—which signifies the continuous separation of eastern and central Pacific

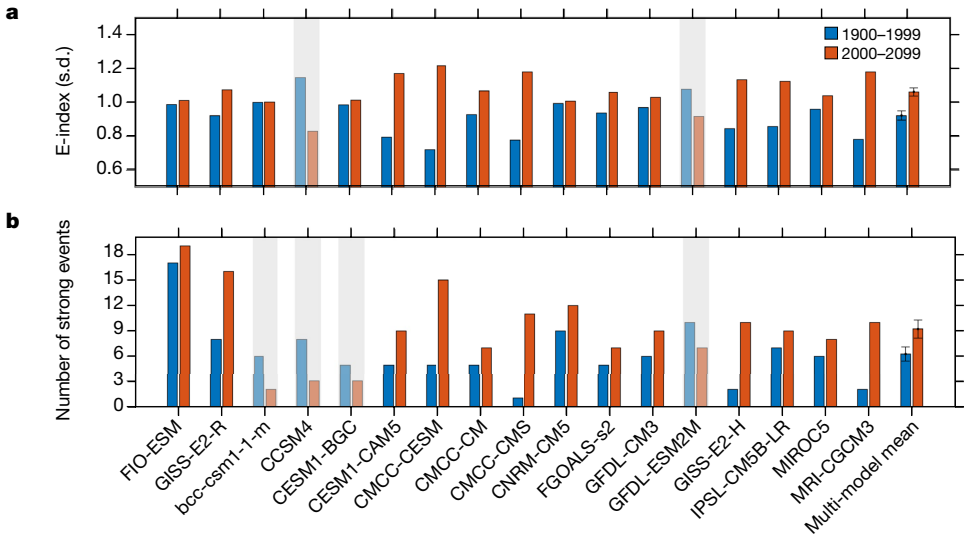

Fig. 2 | Projected increase in EP-ENSO variance. a, Comparison of the standard deviation of the E-index over the present-day (1900–1999) and future (2000–2099) 100-year periods in the 17 selected models. 15 of the 17 selected models (88%) simulate a greater variance in the E-index in the future period (red bars) than in the present-day period (blue bars); the two models that simulate a reduction in variance are greyed out. **b**, Number of strong EP-El Niño events (E-index $>$ 1.5 s.d.) that occurred in the two 100-year periods. The multi-model mean is also shown in **a** and **b**; error bars in the multi-model mean correspond to the 95% confidence interval. The differences between the present-day and future multi-model-mean E-index (s.d.) and between the present-day and future multi-model-mean number of strong events are statistically significant at more than the 95% confidence level. The increase in EP-ENSO SST variance (E-index variance) generally translates to more EP-El Niño events for a given E-index intensity.

centres—from the present-day to the future climate, the change is statistically insignificant and without an inter-model consensus. On the other hand, the change in mean climate is robust and can explain the increased EP-ENSO variance. For example, under greenhouse warming, the change in mean state includes faster warming in the eastern equatorial Pacific than in the surrounding regions[20] (Extended Data Fig. 9a). Although its direct effect on SST variability is already removed through the quadratic de-trending process, there is a statistically significant relationship between the intensity of the warming pattern and eastern Pacific variability (Extended Data Fig. 9b). The surface warming pattern, with stronger warming in the eastern equatorial Pacific than in the surrounding regions, contributes to the increased EP-El Niño variability by facilitating more frequent atmospheric convection in the region.

However, a greater contribution to this variability comes from increased vertical stratification of the upper equatorial Pacific Ocean (Fig. 3a, b). The increased vertical stratification is another robust feature of the change in mean state that is supported by a strong inter-model consensus[17,18]. To assess the effect of the increased stratification, we conduct a vertical mode decomposition of the mean Brunt Väisälä frequency profiles (see Methods section 'Wind projection coefficient') and determine the projection of the wind-stress forcing momentum onto the dominant ocean baroclinic modes[34,35] (the wind-projection coefficient), which measures the dynamical coupling between the atmosphere and the ocean at the wind anomaly centre[36–38]. The centre, determined by a bi-linear regression of quadratically de-trended monthly zonal wind anomalies onto the C-index and E-index, is located west of the SST anomaly centre (Extended Data Table 1). Because ENSO instability increases with wind–ocean coupling, stochastic forcing is more likely to trigger positive feedbacks for an El Niño event[38–42]. In all selected models, the coupling increases in the future climate (Fig. 3c). There is a strong inter-model consensus, and models with greater strengthening in vertical stratification at the wind anomaly centre systematically produce a greater increase in the coupling (Fig. 3d). Thus, the increased stratification enhances the EP-El Niño by increasing the dynamical coupling between the ocean and the atmosphere.

Additional analysis reveals that the dynamical coupling at the wind centre of the C-index increases from the present-day to the future climate by a similar amount, suggesting that the same mechanism operates for the CP-ENSO. This is indeed the case (see Methods section 'Response of central Pacific ENSO'). In particular, 11 of the 17 selected models (65%) generate an increased frequency of CP-El Niño, defined as when the magnitude of the C-index is greater than 1 s.d. The inter-model consensus is not as strong as for the EP-El Niño, perhaps in part because there is no faster warming in the central Pacific region to facilitate atmospheric convection and thus enhance SST variability, as there is for the EP-El Niño.

Summary

Our finding of a greenhouse-warming-induced increase in EP-El Niño SST variance is in contrast to previous findings of no consensus using the Niño3 SST index. Previous studies assumed that all models produce an anomaly pattern and centre that can be represented by the Niño3 index, as generally seen in observations. We show that the EP-ENSO pattern and its anomaly centre differ greatly from one model to another, and therefore cannot be represented by the spatially fixed Niño3 SST index. Further, the EP-El Niño SST anomaly centre is determined by the positive-skewness centre, which is governed by the associated nonlinear processes. Focusing on the different EP-El Niño anomaly centres for each model, there is an increase in EP-El Niño SST variance under greenhouse warming, with a strong inter-model consensus. The robust result arises from the use of process-based metrics representing the nonlinear Bjerknes feedback that underlies ENSO diversity. The increased SST variance stems from enhanced stratification of the upper equatorial Pacific Ocean under greenhouse warming, which enhances the wind–ocean coupling that is conducive to an increase in SST anomalies. With this projected increase, we should expect more extreme weather events associated with the EP-El Niño, with important implications for twenty-first-century climate, extreme weather and ecosystems.

Online content

Any methods, additional references, Nature Research reporting summaries, source data, statements of data availability and associated accession codes are available at https://doi.org/10.1038/s41586-018-0776-9.

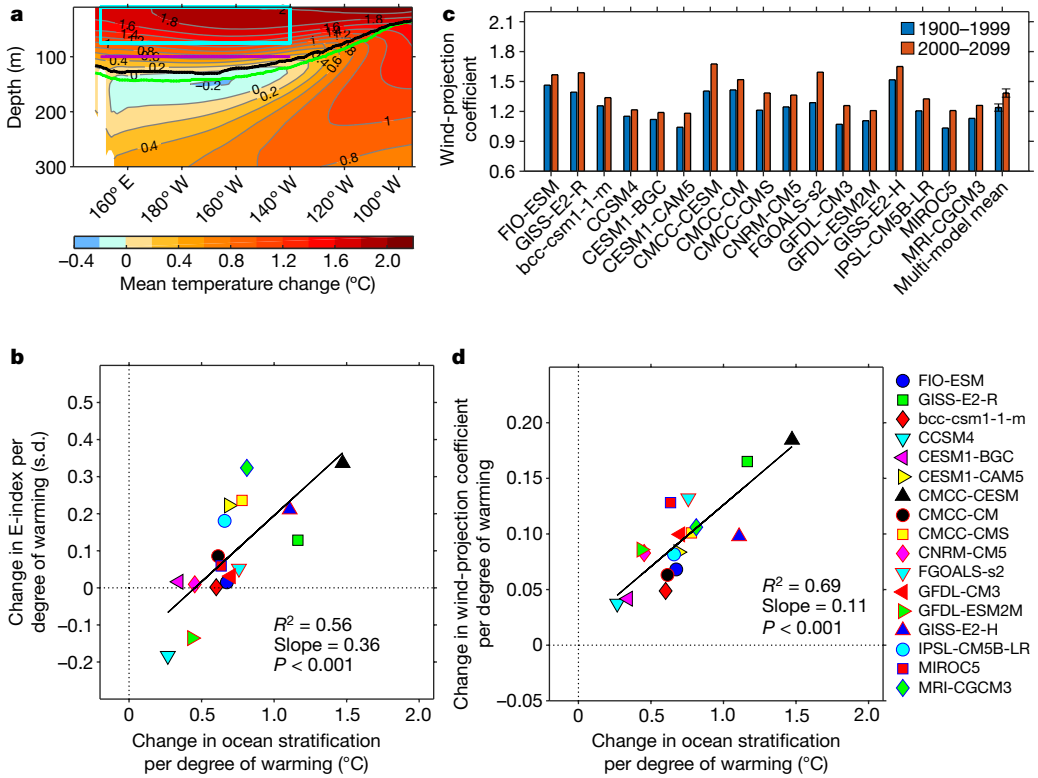

Fig. 3 | Mechanism for the projected increase in EP-ENSO variance. **a**, Multi-model-mean change in equatorial ocean temperature (the upper 300 m) between future (2000–2099) and present-day (1900–1999) climates (colour scale; values are also indicated on each contour). The present-day (green) and future (black) thermoclines are also shown. The stratification increases and the thermocline shallows under greenhouse warming. **b**, Statistically significant ($P < 0.001$) relationship between the change (between future and present-day climates) in ocean stratification and the change (between future and present-day climates) in E-index. The ocean stratification is calculated as the difference between the mean temperature over the upper 75 m (cyan box in **a**) and the temperature at 100 m (purple line in **a**), both averaged over the longitude range 150° E–140° W. To enhance the inter-model comparability, the changes are scaled by the increase in global-mean temperature over the present-day and future periods. Approximately 55% of the change in E-index variance is attributable to the change in ocean stratification, much more than is due to the faster surface warming in the eastern equatorial Pacific (Extended Data Fig. 9). **c**, Comparison of the wind–ocean coupling coefficients (wind-projection coefficients) in present-day and future climates. All models generate increased coupling in the future. ENSO instability increases with wind–ocean coupling. **d**, Statistically significant ($P < 0.001$) relationship between greenhouse-warming-induced changes in ocean stratification and in the wind–ocean coupling coefficient.

Received: 6 August; Accepted: 25 October 2018;
Published online 12 December 2018.

1. Ropelewski, C. F. & Halpert, M. S. Global and regional scale precipitation patterns associated with the El Niño/Southern Oscillation. *Mon. Weath. Rev.* **115**, 1606–1626 (1987).
2. Glynn, P. W. & DE Weerdt, W. H. Elimination of two reef-building hydrocorals following the 1982-83 El Niño warming event. *Science* **253**, 69–71 (1991).
3. Bove, M. C., O'Brien, J. J., Eisner, J. B., Landsea, C. W. & Niu, X. Effect of El Niño on US landfalling hurricanes, revisited. *Bull. Am. Meteorol. Soc.* **79**, 2477–2482 (1998).
4. McPhaden, M. J., Zebiak, S. E. & Glantz, M. H. ENSO as an integrating concept in earth science. *Science* **314**, 1740–1745 (2006).
5. Vincent, E. M. et al. Interannual variability of the South Pacific Convergence Zone and implications for tropical cyclone genesis. *Clim. Dyn.* **36**, 1881–1896 (2011).
6. Valle, C. A. et al. The impact of the 1982–1983 El Niño-Southern Oscillation on seabirds in the Galapagos Islands, Ecuador. *J. Geophys. Res.* **92**, 14437–14444 (1987).
7. Cai, W. et al. Increasing frequency of extreme El Niño events due to greenhouse warming. *Nat. Clim. Chang.* **4**, 111–116 (2014).
8. Ashok, K., Behera, S. K., Rao, S. A., Weng, H. & Yamagata, T. El Niño Modoki and its possible teleconnection. *J. Geophys. Res.* **112**, C11007 (2007).
9. Yeh, S.-W. et al. El Niño in a changing climate. *Nature* **461**, 511–514 (2009).
10. Kug, J.-S., Jin, F.-F. & An, S.-I. Two types of El Niño events: cold tongue El Niño and warm pool El Niño. *J. Clim.* **22**, 1499–1515 (2009).
11. Kao, H. Y. & Yu, J.-Y. Contrasting eastern-Pacific and central-Pacific types of ENSO. *J. Clim.* **22**, 615–632 (2009).
12. Takahashi, K., Montecinos, A., Goubanova, K. & Dewitte, B. ENSO regimes: reinterpreting the canonical and Modoki El Niño. *Geophys. Res. Lett.* **38**, L10704 (2011).
13. Dommenget, D., Bayr, T. & Frauen, C. Analysis of the non-linearity in the pattern and time evolution of El Niño Southern Oscillation. *Clim. Dyn.* **40**, 2825–2847 (2013).
14. Takahashi, K. & Dewitte, B. Strong and moderate nonlinear El Niño regimes. *Clim. Dyn.* **46**, 1627–1645 (2016).
15. Capotondi, A. et al. Understanding ENSO diversity. *Bull. Am. Meteorol. Soc.* **96**, 921–938 (2015).
16. Cai, W. et al. More extreme swings of the South Pacific convergence zone due to greenhouse warming. *Nature* **488**, 365–369 (2012).
17. Cai, W. et al. ENSO and Greenhouse warming. *Nat. Clim. Chang.* **5**, 849–859 (2015).
18. Collins, M. et al. The impact of global warming on the tropical Pacific Ocean and El Niño. *Nat. Geosci.* **3**, 391–397 (2010).
19. Watanabe, M. et al. Uncertainty in the ENSO amplitude change from the past to the future. *Geophys. Res. Lett.* **39**, L20703 (2012).
20. Xie, S.-P. et al. Global warming pattern formation: sea surface temperature and rainfall. *J. Clim.* **23**, 966–986 (2010).
21. Power, S., Delage, F., Chung, C., Kociuba, G. & Keay, K. Robust twenty-first-century projections of El Niño and related precipitation variability. *Nature* **502**, 541–545 (2013).
22. Santoso, A. et al. Late-twentieth-century emergence of the El Niño propagation asymmetry and future projections. *Nature* **504**, 126–130 (2013).
23. McPhaden, M. J., Lee, T. & McClurg, D. El Niño and its relationship to changing background conditions in the tropical Pacific. *Geophys. Res. Lett.* **38**, L15709 (2011).
24. Newman, M., Shin, S.-I. & Alexander, M. A. Natural variation in ENSO flavors. *Geophys. Res. Lett.* **38**, L14705 (2011).
25. Yeh, S.-W., Kirtman, B. P., Kug, J.-S., Park, W. & Latif, M. Natural variability of the central Pacific El Niño event on multi-centennial timescales. *Geophys. Res. Lett.* **38**, L02704 (2011).
26. Cai, W. et al. More frequent extreme La Niña events under greenhouse warming. *Nat. Clim. Chang.* **5**, 132–137 (2015).
27. Choi, K.-Y., Vecchi, G. A. & Wittenberg, A. T. ENSO transition, duration, and amplitude asymmetries: role of the nonlinear wind stress coupling in a conceptual model. *J. Clim.* **26**, 9462–9476 (2013).
28. Frauen, C. & Dommenget, D. El Niño and La Niña amplitude asymmetry caused by atmospheric feedbacks. *Geophys. Res. Lett.* **37**, L18801 (2010).

29. Taylor, K. E., Stouffer, R. J. & Meehl, G. A. An overview of CMIP5 and the experiment design. *Bull. Am. Meteorol. Soc.* **93**, 485–498 (2012).
30. Kim, S. T. & Yu, J.-Y. The two types of ENSO in CMIP5 models. *Geophys. Res. Lett.* **39**, L11704 (2012).
31. Ham, Y.-G. & Kug, J.-S. How well do current climate models simulate two types of El Nino? *Clim. Dyn.* **39**, 383–398 (2012).
32. Karamperidou, C., Jin, F.-F. & Conroy, J. L. The importance of ENSO nonlinearities in tropical Pacific response to external forcing. *Clim. Dyn.* **49**, 2695–2704 (2017).
33. Stevenson, S. et al. Will there be a significant change to El Niño in the twenty-first century? *J. Clim.* **25**, 2129–2145 (2012).
34. Cane, M. A. & Sarachik, E. S. The response of a linear baroclinic equatorial ocean to periodic forcing. *J. Mar. Res.* **39**, 651–693 (1981).
35. Zebiak, S. E. & Cane, M. A. A model El Niño–Southern Oscillation. *Mon. Weath. Rev.* **115**, 2262–2278 (1987).
36. Dewitte, B., Reverdin, G. & Maes, C. Vertical structure of an OGCM simulation of the equatorial Pacific Ocean in 1985–1994. *J. Phys. Oceanogr.* **29**, 1542–1570 (1999).
37. Dewitte, B. et al. Low frequency variability of temperature in the vicinity of the equatorial thermocline in SODA: role of equatorial wave dynamics and ENSO asymmetry. *J. Clim.* **22**, 5783–5795 (2009).
38. An, S.-I. & Jin, F.-F. Collective role of thermocline and zonal advective feedbacks in the ENSO mode. *J. Clim.* **14**, 3421–3432 (2001).
39. Thual, S., Dewitte, B., An, S.-I. & Ayoub, N. Sensitivity of ENSO to stratification in a recharge-discharge conceptual model. *J. Clim.* **4**, 4331–4348 (2011).
40. Thual, S., Dewitte, B., An, S.-I., Illig, S. & Ayoub, N. Influence of recent stratification changes on ENSO stability in a conceptual model of the equatorial Pacific. *J. Clim.* **26**, 4790–4802 (2013).
41. Gent, P. R. & Luyten, J. R. How much energy propagates vertically in the equatorial oceans? *J. Phys. Oceanogr.* **15**, 997–1007 (1985).
42. Kim, W. & Cai, W. The importance of the eastward zonal current for generating extreme El Niño. *Clim. Dyn.* **42**, 3005–3014 (2014).

Acknowledgements This work is supported by the Centre for Southern Hemisphere Oceans Research, a joint research centre between QNLM and CSIRO. W.C., G.W. and A.S. are also supported by the Earth Systems and Climate Change Hub of the Australian Government's National Environmental Science Program, and a CSIRO Office of Chief Executive Science Leader award. B.D. was supported by Fondecyt (grant number 1171861) and LEFE-GMMC. PMEL contribution number: 4817.

Reviewer information *Nature* thanks Y.-G. Ham and the other anonymous reviewer(s) for their contribution to the peer review of this work.

Author contributions W.C. conceived the study and wrote the initial manuscript in collaboration with L.W. and B.D. G.W. performed the model analysis and generated the final figures. B.D. analyses the dynamical coupling between the atmosphere and the ocean. A.S., B.D., K.T., A.C., Y.Y. and M.J.M. contributed to interpretation of the results, discussion of the associated dynamics and improvement of the paper.

Competing interests The authors declare no competing interests.

Additional information
Extended data is available for this paper at https://doi.org/10.1038/s41586-018-0776-9.
Reprints and permissions information is available at http://www.nature.com/reprints.
Correspondence and requests for materials should be addressed to W.C. or L.W.
Publisher's note: Springer Nature remains neutral with regard to jurisdictional claims in published maps and institutional affiliations.

METHODS

Data, model outputs and EOF analysis. We use five SST reanalysis products[43–47] to characterize ENSO diversity, and atmospheric circulation fields from the National Center for Environmental Prediction (NCEP) and the National Center for Atmospheric Research (NCAR) global reanalysis[48]. The five reanalysis products are: HadISST v1.1 (Hadley Centre Sea Ice and Sea Surface Temperature dataset version 1.1)[43] from 1948 to 2015; ERSST v5 (Extended Reconstructed Sea Surface Temperature version 5)[44] from 1948 to 2015; OISST v2 (NOAA Optimum Interpolation Sea Surface Temperature version 2)[45] from 1982 to 2015; ORA-s3 (ECMWF Ocean Analysis System: ORA-s3)[46] from 1959 to 2009; and ORA-s4 (ECMWF Ocean Analysis System: ORA-s4)[47] from 1958 to 2013. We use a multivariate signal-processing method referred to as EOF analysis[49] in an equatorial domain (15° S–15° N, 140° E–80° W) to de-convolve spatio-temporal variability into orthogonal modes, each described by a principal spatial pattern and an associated principal component (PC) time series. The PC time series is scaled to have a standard deviation of one. For the observational reanalysis products, EOF analysis is applied to monthly SST anomalies, referenced to their long-term mean. The CP-ENSO and EP-ENSO regimes were reconstructed using EOF1 and EOF2 such that their temporal variability can be described by a C-index ($(PC1+PC2)/\sqrt{2}$) and an E-index ($(PC1-PC2)/\sqrt{2}$), respectively. Each regime is associated with a suite of distinct processes that lead to the negative and positive skewness in the C-index and E-index, respectively, as discussed in the main text. This approach was applied to 34 CMIP5 coupled global climate models (CGCMs; Extended Data Table 1) forced with historical anthropogenic and natural forcings, and future greenhouse gases under the RCP8.5 scenario[29], covering the 200-year period 1900–2099. Monthly anomalies referenced to the climatology of the first 100 years were constructed and quadratically de-trended.

Diagnosis of nonlinear Bjerknes feedback. For each model, we obtained the associated zonal wind-stress anomaly pattern through the same bi-linear regression onto the monthly E-index and C-index to identify the location of the maximum anomaly associated with each index. We used monthly anomalies to obtain the associated wind-stress anomalies (to capture that the wind-stress response is important during the development phase), but for the SST anomaly pattern and centre we focused on the mature phase of December–February. The westerly anomaly centre is located to the west of the SST anomaly centre, consistent with the fact that the warm anomalies are a dynamic consequence of wind-induced eastward-propagating equatorial downwelling Kelvin waves (Extended Data Table 1). Quadratically de-trended monthly wind anomalies at the centre were plotted against the monthly C-index and E-index, using all samples from observations, the 17 selected models and the 17 non-selected models. Samples were binned at a C- or E-index interval of 0.25 s.d. to obtain median values for each bin (Extended Data Figs. 1e, f, 3e, f and 5e, f).

The nonlinear Bjerknes feedback is measured by a ratio of the regression slope for binned values with a positive C-index, or E-index, over the slope for a negative index. A greater ratio indicates strong nonlinear Bjerknes feedback. For the non-selected models, the wind response to SST anomalies associated with the C-index is essentially linear (ratio of 1.10; Extended Data Fig. 5f) and the response to SST anomalies associated with the E-index becomes moderately nonlinear (ratio of 1.69; Extended Data Fig. 5e). For the selected models, the corresponding ratios are 1.09 and 2.49 (Extended Data Fig. 3e, f); that is, there is a much stronger nonlinear response for the EP-ENSO regime. The response to SST anomalies associated with the E-index for the selected models is close to the observed value (2.42; Extended Data Fig. 1e). In other words, in the selected models the CP and EP regimes are far more distinguishable, and EP- and CP-ENSO anomaly centres are more clearly separated and better defined than in the non-selected models. This is reflected in the lack of, or weak, nonlinear relationship between PC1 and PC2 in the non-selected models, in which an EP-El Niño event is a combination of EOF1 and EOF2, which are uncorrelated, such that in a given model there is a strong inter-event diversity in the spatial pattern and the anomaly centre of the EP-El Niño.

Statistical significance test. We use a bootstrap method to examine whether the increased E-index variance is statistically significant. The 17 standard deviation values of the E-index in the present-day period from the 17 selected models are re-sampled randomly to construct 10,000 realizations of mean standard deviation over 17 models. In this random re-sampling process, any model is allowed to be selected again. The standard deviation of the 10,000 inter-realizations of mean standard deviation for the control period is 0.027. The same is carried out for the future period, and the standard deviation of the inter-realization is 0.024. The increased standard deviation in the future period is greater than the sum of these two standard deviation values, indicating statistical significance above the 95% confidence level (Extended Data Fig. 7a). Identical analyses for increased occurrences in EP-El Niño events with E-index > 1.5 s.d. and for increased wind-projection coefficients leads to the same conclusion (Extended Data Fig. 7b, c).

Sensitivity to emission scenarios. 32 CMIP5 models were forced under the RCP4.5 emission scenario and 15 were selected. 12 of the 15 selected models (80%) produced increased E-index variance. Using all models under this scenario, 20 of the 32 models (63%) generate an increase. The same conclusion is found when applying the same analysis and model-selection criterion on an ensemble of 16 CMIP3 models forced under the A2 emission scenario. Seven CMIP3 models were selected and five (71%) produce increased E-index variance.

Wind projection coefficient. From linear theory, the total amount of momentum flux associated with equatorial wave dynamics can be estimated by the zonal wind stress along the equator multiplied by a coefficient, referred to as the wind-projection coefficient P_n, which depends on the vertical stratification of the ocean[50]. This coefficient corresponds to the coupling efficiency between the ocean and the atmosphere associated with equatorial wave dynamics for a particular baroclinic mode n[34,35]. In a multi-mode context, the coefficients associated with the first three baroclinic modes allow us to characterize the mean thermocline shape (sharpness), depth and intensity[39–41]. These coefficients have been used to diagnose the long-term variability in vertical stratification along the equator associated with changes in ENSO amplitude in reanalysis products and CGCMs[36,51,52]. We calculate the wind-projection coefficients from climatological temperature and salinity profiles of the present-day and future climates[36], and calculate the following quantity for both periods for each of the models[53]:

$$P=\sum_{n=1}^{n=3}P_n=\sum_{n=1}^{n=3}\frac{150}{\int_{z=5{,}000\ \mathrm{m}}^{z=0}F_n^2(x_E,z)\mathrm{d}z}$$

Here F_n corresponds to the vertical mode structure and x_E is the location along the equator, where the salinity and temperature profile are considered. This location is taken as the centre of action of the zonal winds stress for the EP regime and corresponds to the maximum amplitude of the regressed patterns of the zonal wind stress associated with the EP regime (Extended Data Table 1). The factor of 150 is a normalizing coefficient (in metres), corresponding to the average thermocline depth in the equatorial CP. The larger the value of P, the sharper the mean thermocline and the larger the input of momentum flux into the baroclinic ocean response.

Warming pattern. CGCMs produce a warming pattern with faster warming in the equatorial EP than in the surrounding regions, with a strong inter-model consensus[17,18,20]. We calculated the warming in each model as the difference between the average over the future and present-day 100-year periods, and normalized it by the difference in the global-mean temperature (in units of warming per degree of global warming). We constructed a multi-model mean over the 17 selected models (Extended Data Fig. 9a) and then projected individual-model warming patterns onto the multi-model-mean warming pattern to obtain inter-model variations in the warming pattern. We examined the relationship between the inter-model warming pattern and change in the E-index (Extended Data Fig. 9b).

Response of central Pacific ENSO. Inter-model consensus on changes in monthly C-index variance is weaker compared to that of the monthly E-index, with 10 of the 17 selected models (59%) producing an increase. Without model selection, 19 of the 34 models (56%) produce an increase.

In terms of changes in the frequency of CP-El Niño events, defined as when the December–February-average C-index is greater than 1 s.d., 11 of the 17 selected models (65%) produce an increase. Without model selection, 24 of the 34 models (71%) produce an increase.

In terms of changes in the frequency of extreme La Niña events, defined as when the magnitude of the December–February-average C-index is greater than 1.75 s.d., 11 of the 17 selected models (65%) produce an increase. Without model selection, 24 of the 34 models (71%) produce an increase. Note that some of the 24 models that contribute to the increased frequency of extreme La Niña events are different from those that contribute to the increased frequency of CP-El Niño events.

Code availability. Codes used to calculate the EOF and α can be downloaded from https://drive.google.com/open?id=1d2R8wKpFNW-vMIfoJsbqIGPIBd9Z_8rj; codes for calculating the wind-projection coefficients using ocean salinity and temperature are available on request.

Data availability

Data related to this paper can be downloaded from the following: HadISST v1.1, https://www.esrl.noaa.gov/psd/data/gridded/data.hadsst.html; ERSST v5, https://www.ncdc.noaa.gov/data-access/marineocean-data/extended-reconstructed-sea-surface-temperature-ersst-v5; OISST v2, https://www.esrl.noaa.gov/psd/data/gridded/data.noaa.oisst.v2.html; ORA-s3, http://apdrc.soest.hawaii.edu/datadoc/ecmwf_oras3.php; ORA-s4, https://climatedataguide.ucar.edu/climate-data/oras4-ecmwf-ocean-reanalysis-and-derived-ocean-heat-content; and CMIP5 database, http://www.ipcc-data.org/sim/gcm_monthly/AR5/.

43. Rayner, N. A. et al. Global analyses of sea surface temperature, sea ice, and night marine air temperature since the late nineteenth century. *J. Geophys. Res.* **108**, 4407 (2003).

44. Huang, B. et al. Extended reconstructed sea surface temperature version 5 (ERSSTv5), upgrades, validations, and intercomparisons. *J. Clim*. **30**, 8179–8205 (2017).
45. Reynolds, R. W. et al. An improved in situ and satellite SST analysis for climate. *J. Clim*. **15**, 1609–1625 (2002).
46. Balmaseda, M. A., Vidard, A. & Anderson, D. L. T. The ECMWF ocean analysis system: ORA-S3. *Mon. Weath. Rev*. **136**, 3018–3034 (2008).
47. Balmaseda, M. A., Mogensen, K. & Weaver, A. T. Evaluation of the ECMWF ocean reanalysis system ORAS4. *Q. J. R. Meteorol. Soc*. **139**, 1132–1161 (2013).
48. Kalnay, E. et al. The NCEP/NCAR 40-year reanalysis project. *Bull. Am. Meteorol. Soc*. **77**, 437–472 (1996).
49. Lorenz, E. N. *Empirical Orthogonal Functions and Statistical Weather Prediction*. Statistical Forecast Project Report 1 (MIT Department of Meteorology, 1956).
50. Fjelstad, J. E. *Interne Wellen* (Cammermeyer in Komm., 1933).
51. Dewitte, B., Yeh, S.-W., Moon, B.-K., Cibot, C. & Terray, L. Rectification of the ENSO variability by interdecadal changes in the equatorial background mean state in a CGCM simulation. *J. Clim*. **20**, 2002–2021 (2007).
52. Yeh, S.-W., Dewitte, B., Yim, B. Y. & Noh, Y. Role of the upper ocean structure in the response of ENSO-like SST variability to global warming. *Clim. Dyn*. **35**, 355–369 (2010).
53. Blumenthal, M. B. & Cane, M. A. Accounting for parameter uncertainties in model verification: an illustration with tropical sea surface temperature. *J. Phys. Oceanogr*. **19**, 815–830 (1989).

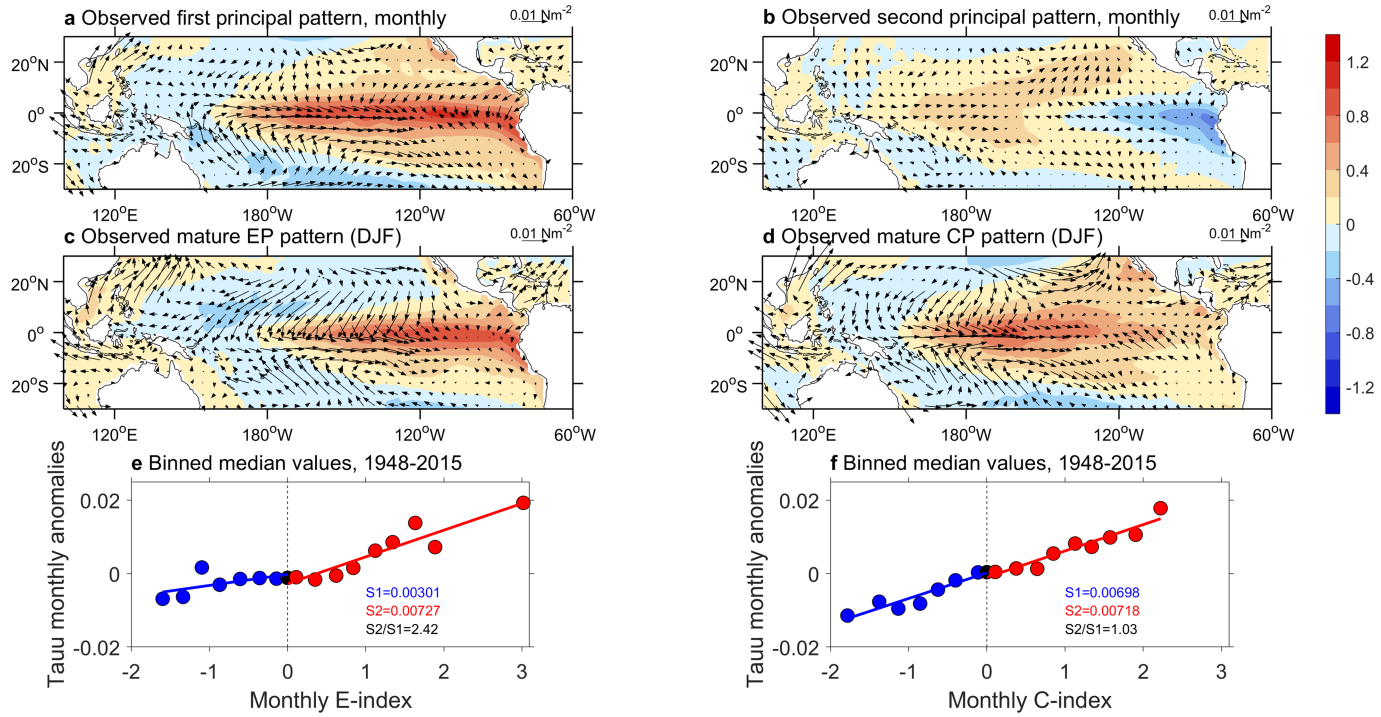

Extended Data Fig. 1 | Properties of the observed ENSO diversity, the associated CP and EP regimes, and the nonlinear Bjerknes feedback. **a**, **b**, The diversity means that the pattern of any ENSO event may be reconstructed by a combination of the first (**a**) and second (**b**) principal pattern from an EOF analysis on monthly SST anomalies (colour scale) and the associated wind-stress vectors (scale shown top right). The associated monthly PC time series are used to describe their evolution, and the CP- and EP-ENSO regimes by the C-index $((PC1 + PC2)/\sqrt{2})$ and E-index $((PC1 - PC2)/\sqrt{2})$, respectively. **c**, **d**, The anomaly pattern associated with the EP-ENSO (**c**) and CP-ENSO (**d**) for December–February (DJF), the season in which ENSO events typically mature. **e**, **f**, Response to the E-index (**e**) or C-index (**f**) of monthly zonal wind-stress (Tauu) anomalies (in units of N m^{-2}) at the anomaly centre (see Methods) associated with the E- or C-index, respectively. The monthly wind-stress anomalies were binned in 0.25-s.d. E- or C-index intervals, and the median wind-stress anomaly and index are identified for each bin (circles). A separate linear regression was carried out for positive (red) and negative (blue) median index values. The ratio of the slope for the positive indices (S2) over that for the negative indices (S1) is taken as an indication of the nonlinear Bjerknes feedback, which operates in the EP-ENSO.

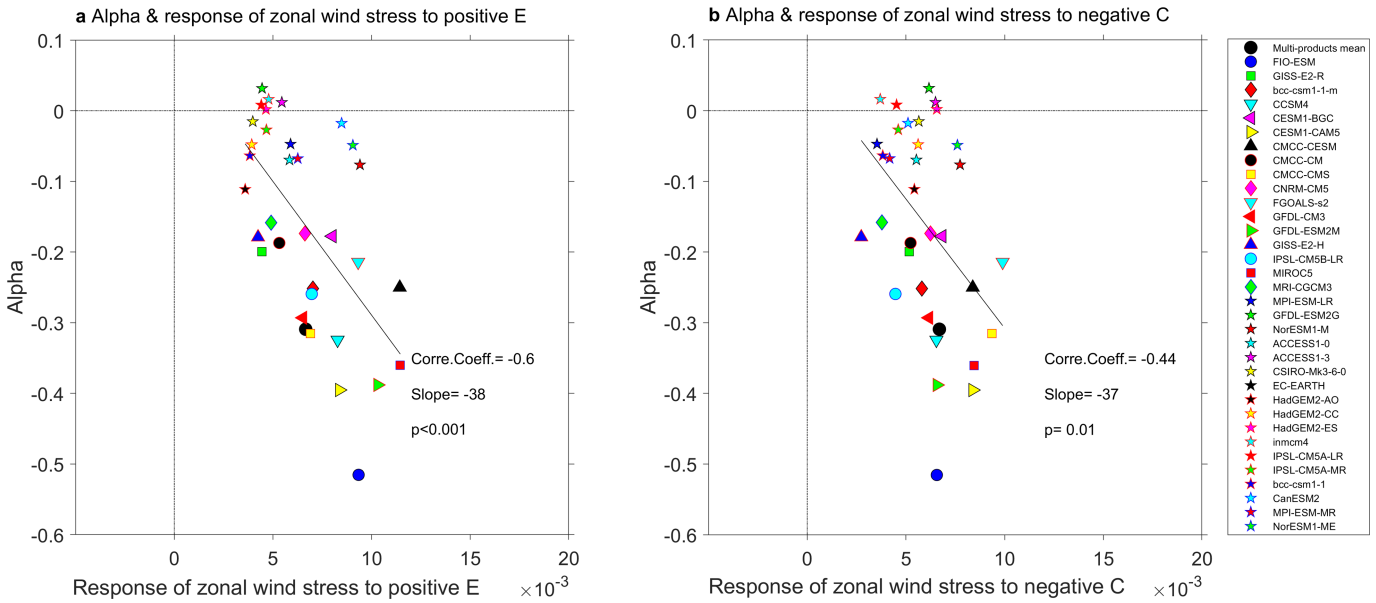

Extended Data Fig. 2 | Inter-model relationship between α and the zonal wind response to SST. a, Relationship between α and the response of monthly zonal wind anomalies to positive E-index values. Zonal wind anomalies are taken at the anomaly centre associated with the E-index. **b**, Relationship between α and the response of zonal wind anomalies to negative C-index values. Zonal wind anomalies are taken at the anomaly centre associated with the C-index.

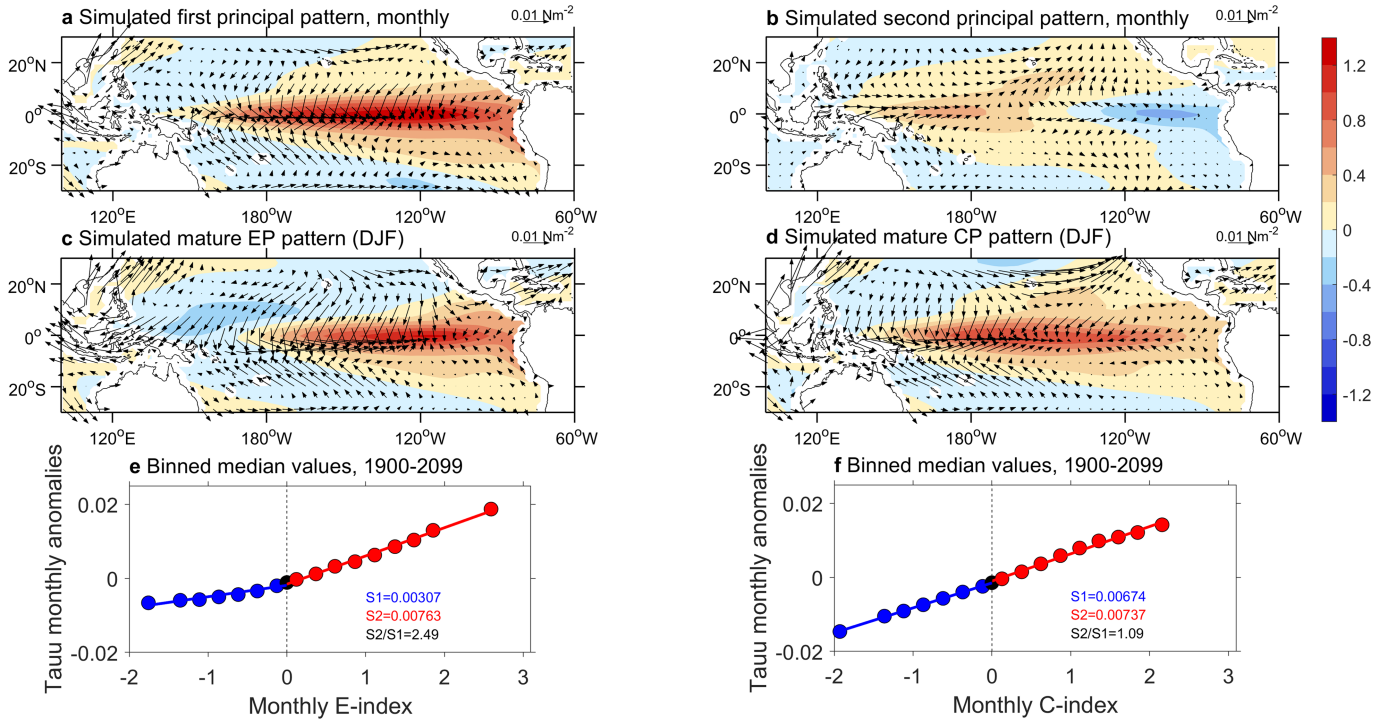

Extended Data Fig. 3 | Properties of the selected models in terms of ENSO diversity, the associated CP and EP regimes, and the nonlinear Bjerknes feedback. As in Extended Data Fig. 1, but for only the 17 selected models.

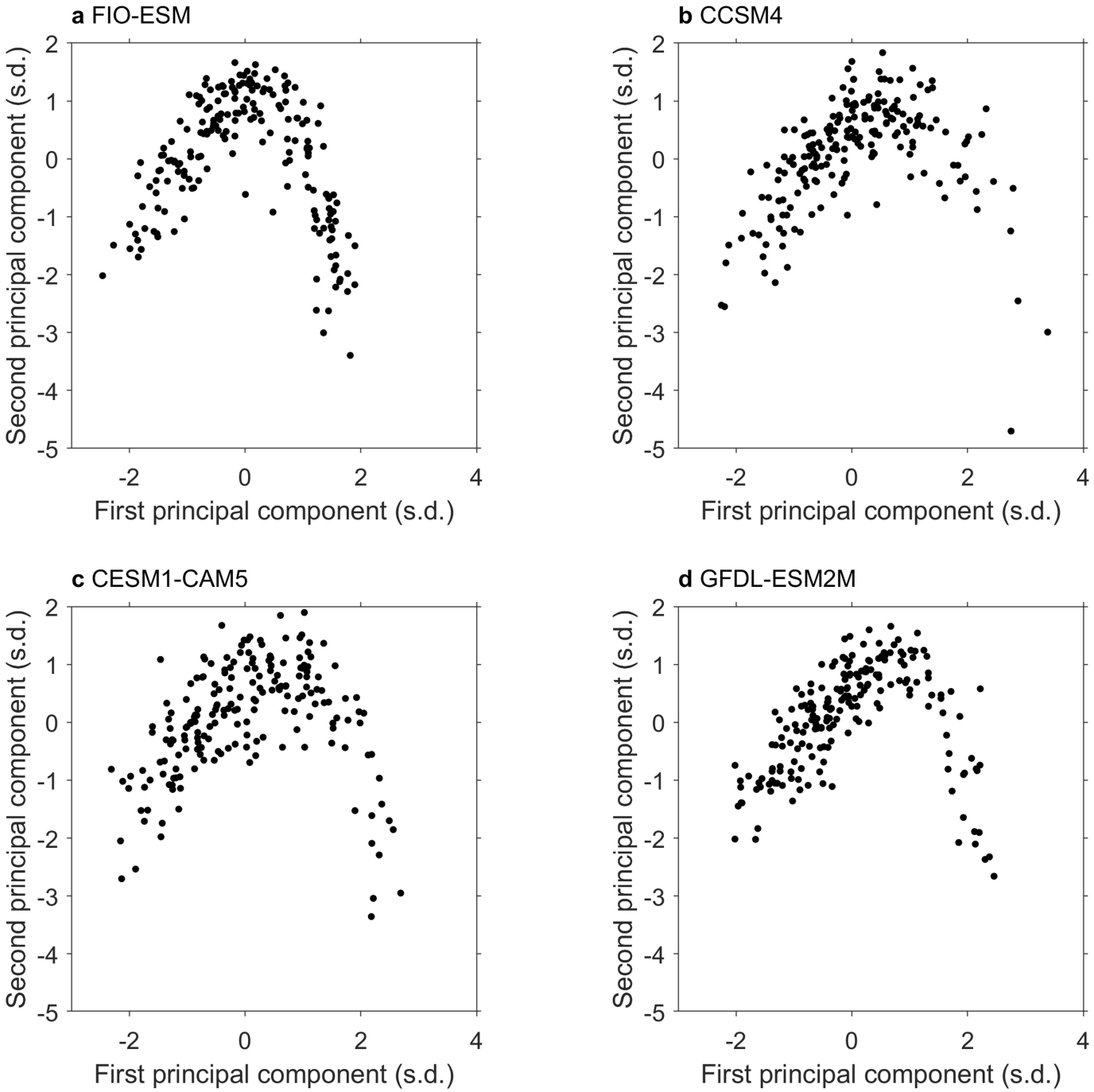

Extended Data Fig. 4 | Examples of the nonlinear relationship between the PC1 and PC2 time series in some selected models. a–d, December–February averages, with an apparent inverted V-shaped nonlinear relationship between PC1 and PC2 for FIO-ESM (**a**), CCSM4 (**b**), CESM1-CAM5 (**c**) and GFDL-ESM2M (**d**).

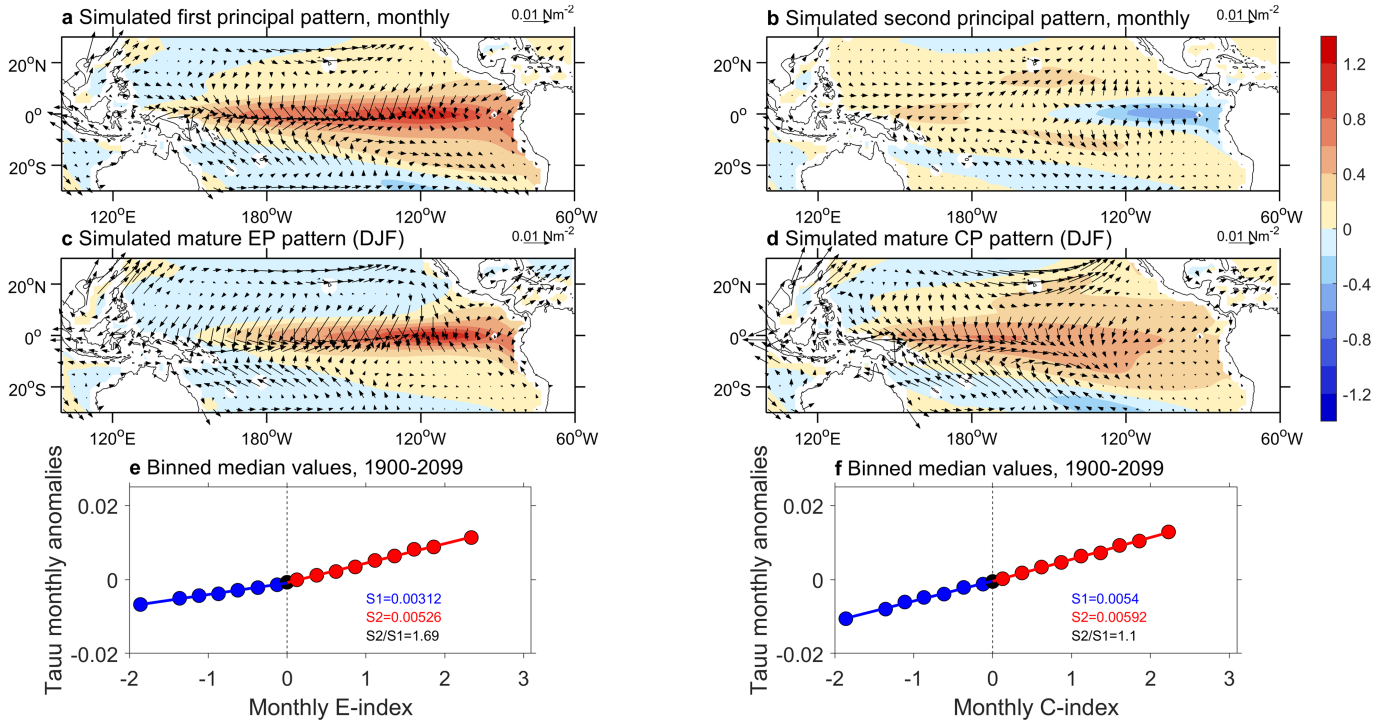

Extended Data Fig. 5 | Properties of the non-selected models in terms of ENSO diversity, the associated CP and EP regimes, and nonlinear Bjerknes feedback. As in Extended Data Fig. 3, but for only the 17 non-selected models. In this case, the nonlinear Bjerknes feedback is much weaker.

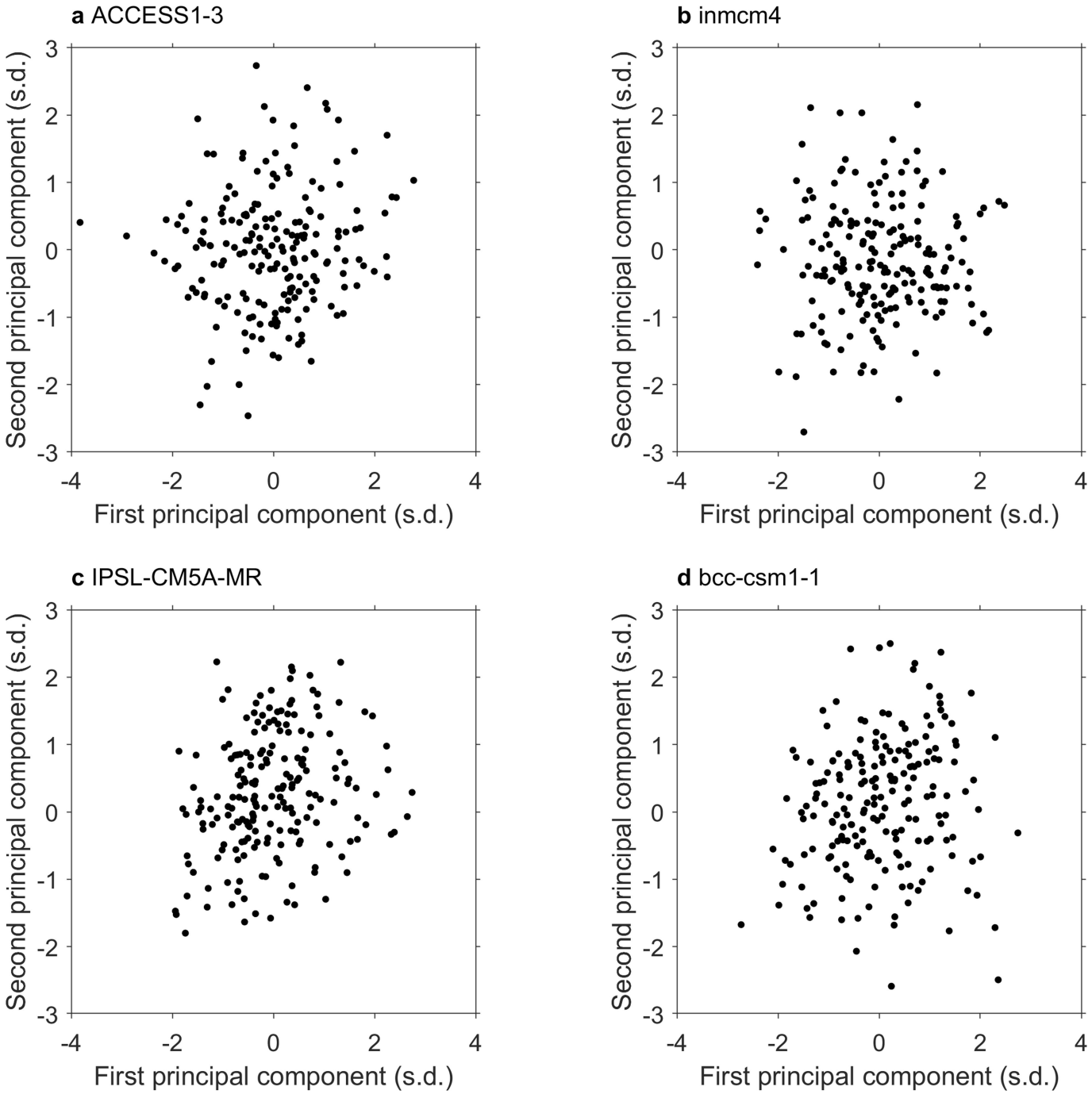

Extended Data Fig. 6 | Examples of the nonlinear relationship between the PC1 and PC2 time series in some non-selected models. **a**–**d**, December–February averages for ACCESS1-3 (**a**), inmcm4 (**b**), IPSL-CM5A-MR (**c**) and bcc-csm1-1 (**d**). In contrast to the selected models (Extended Data Fig. 4), these models display a weak or no nonlinear relationship between PC1 and PC2.

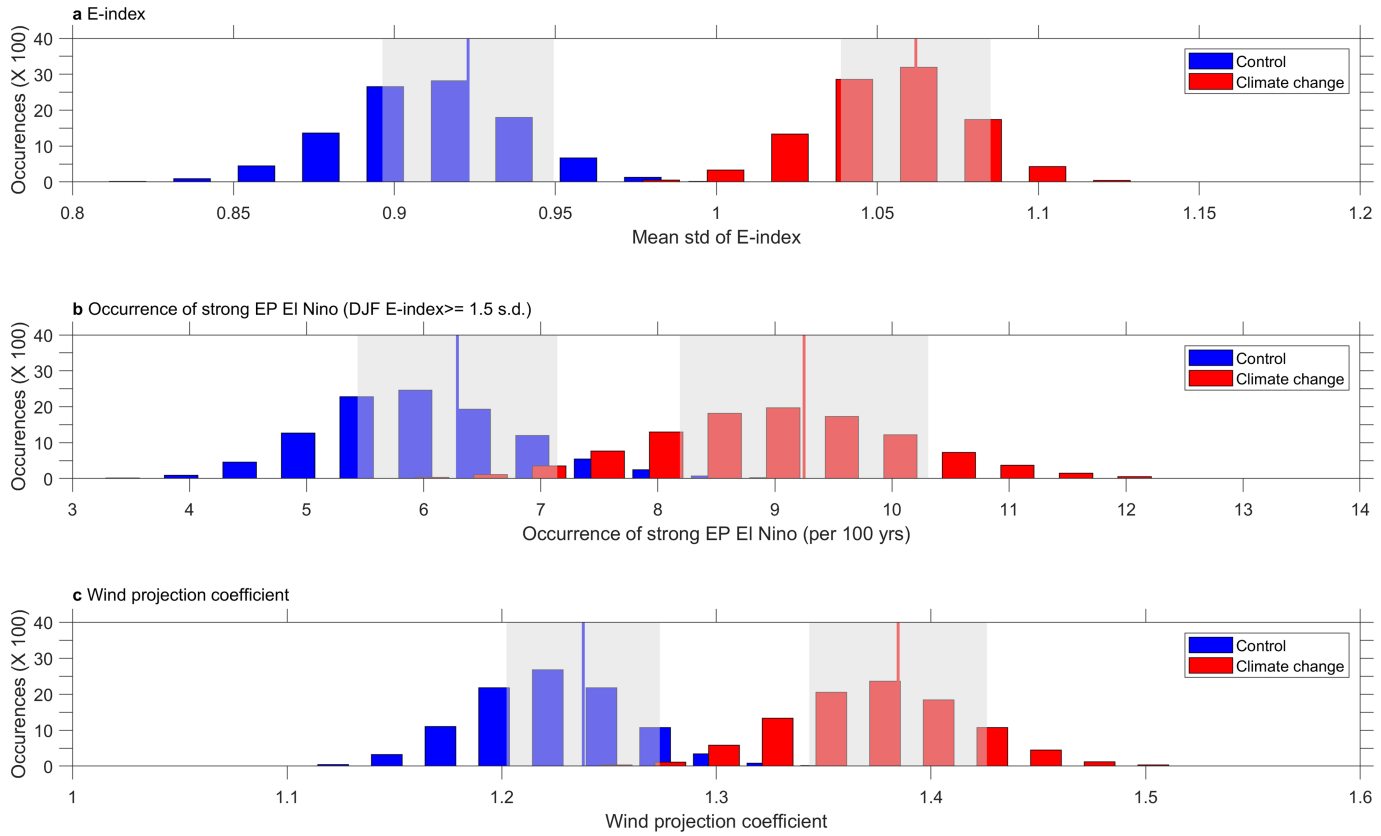

Extended Data Fig. 7 | Histograms of 10,000 realizations of a bootstrap method for the present-day (control) and future (climate change) periods. Each realization is averaged over 17 models, independently resampled randomly from the 17 selected models. The standard deviation of the 10,000 inter-realization is calculated for each period. **a**, For the E-index, the standard deviations are 0.0263 (blue) and 0.0234 (red) for the two periods. **b**, For occurrences with E-index > 1.5 s.d., the standard deviations are 0.87 (blue) and 1.06 (red) for the two periods. **c**, For the wind-projection coefficient, the standard deviations are 0.036 (blue) and 0.042 (red) for the two periods. The difference between the future and the present-day periods is greater than the sum of the two inter-realization standard deviation values (each indicated by half of the grey shaded region). The blue and red vertical lines indicate the mean values of 10,000 inter-realizations for the present-day and future periods, respectively.

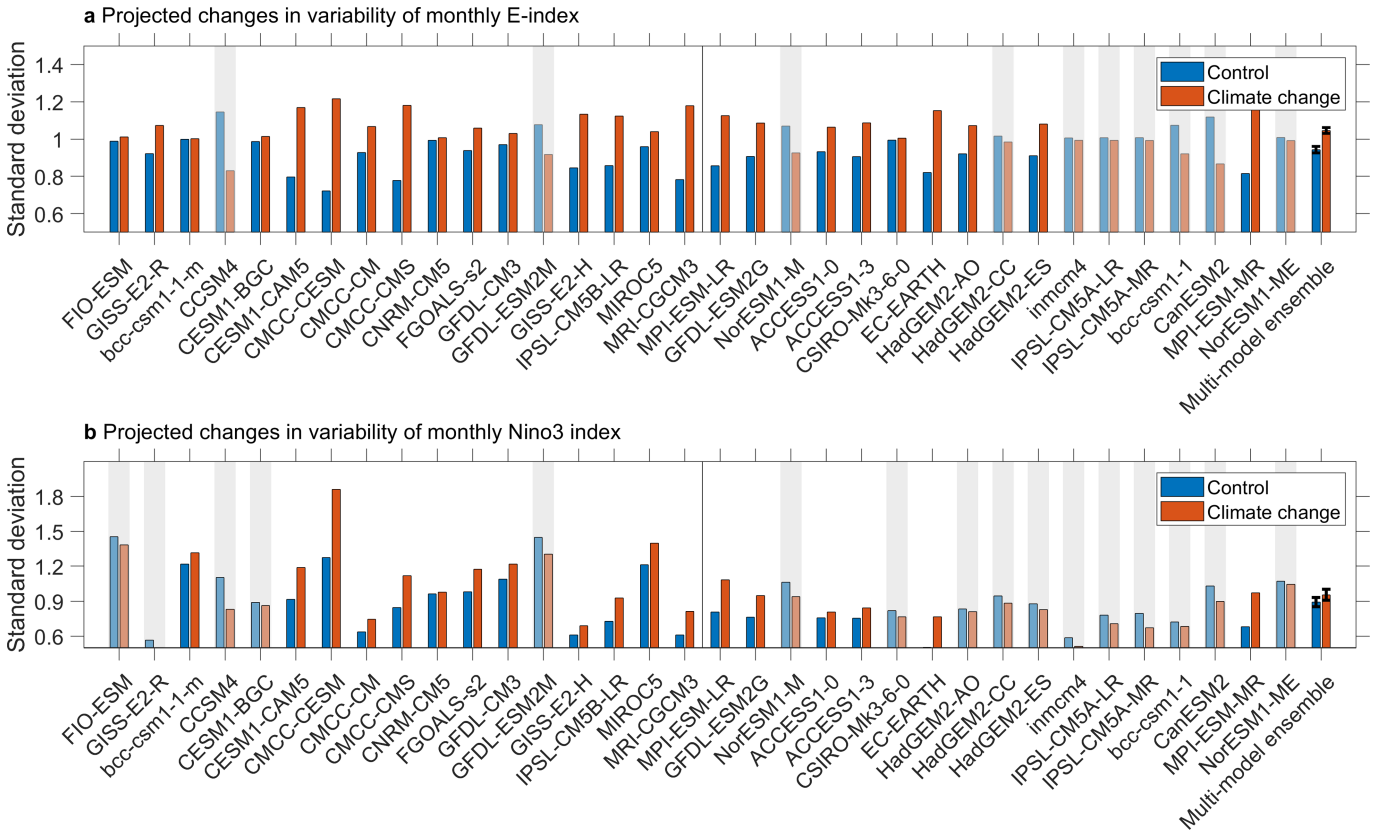

Extended Data Fig. 8 | Projected change in EP-ENSO variability using the E-index and the Niño3 SST index. a, Comparison of the standard deviation of the E-index in the present-day (1900–1999) and future (2000–2099) 100-year periods for all 34 models. 24 of the 34 models show an increase in variance (the other 10 are greyed out). **b**, The same as **a**, but for the Niño3 SST index. Error bars in the multi-model mean are calculated as the standard deviation of the 10,000 inter-realizations. The multi-model-mean change in the E-index variance (**a**) is statistically significant at more than the 95% confidence level, but that in the Niño3 SST index is not significant (**b**). The vertical line separates the selected (left) from the non-selected (right) models.

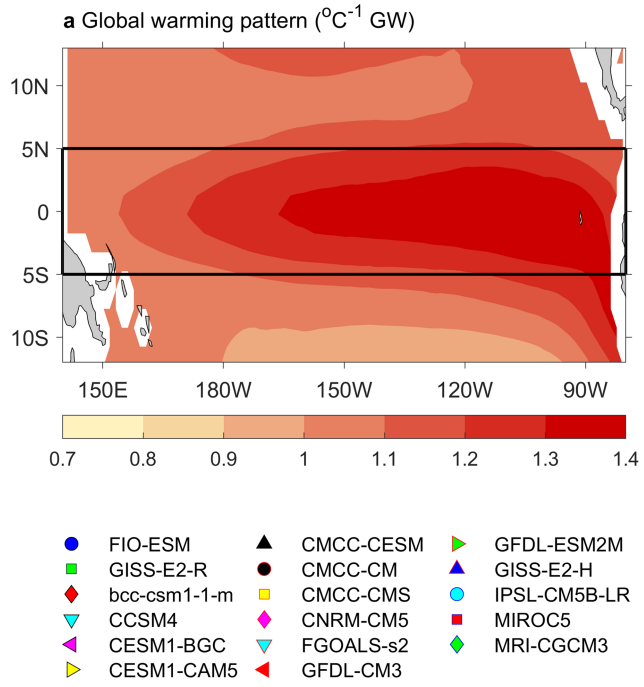

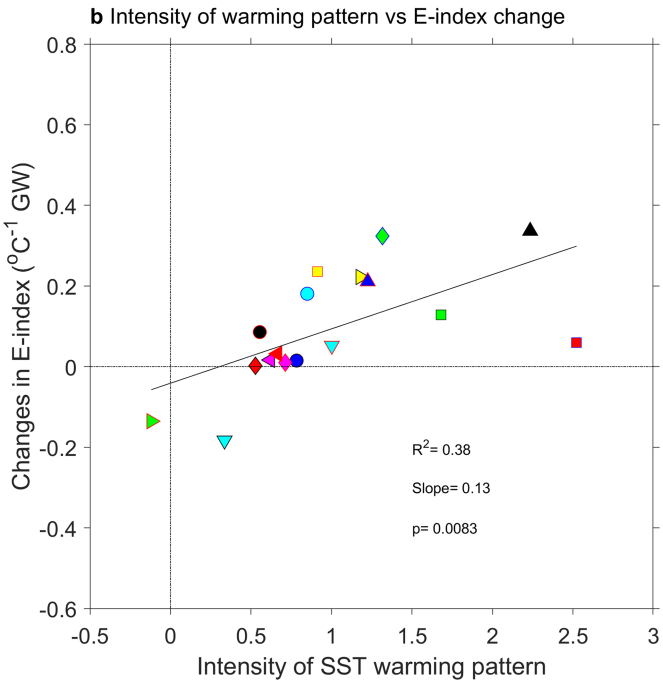

Extended Data Fig. 9 | Relationship between SST warming and change in E-index for selected models. a, Multi-model-mean warming pattern (in °C per °C of global warming (GW); colour scale). First, for each model we construct a warming pattern by calculating the difference between the average SST anomalies over the future (2000–2099) and present-day (1900–1999) periods. Second, we scale this difference by the increase in global-mean SST simulated by the model over the corresponding period. Finally, we take the mean of the scaled difference over all models to construct the multi-model-mean warming pattern. **b**, Inter-model relationship between the intensity of the SST warming pattern (**a**) and change in E-index, also scaled by the corresponding increase in global-mean SST in each model. The intensity of the scaled SST warming pattern for each model is obtained by regressing the scaled SST warming pattern for each model onto the scaled multi-model-mean SST warming pattern, using the region indicated by the black box in **a**. The inter-model relationship is statistically significant above the 95% confidence level, with the statistical properties shown.

Extended Data Table 1 | Details of the 34 models

	Models	Data available	EP (Tauu)	CP (Tauu)	EP (SST)	CP (SST)
1	FIO-ESM	sst,τx,τy,so,T	222.25	184.75	250.75	232.75
2	GISS-E2-R	sst,τx,τy,so,T	201.25	166.75	247.75	198.25
3	bcc-csm1-1-m	sst,τx,τy,so,T	196.75	178.75	243.25	225.25
4	CCSM4	sst,τx,τy,so,T	205.75	189.25	244.75	195.25
5	CESM1-BGC	sst,τx,τy,so,T	201.25	195.25	241.75	198.25
6	CESM1-CAM5	sst,τx,τy,so,T	193.75	142.75	223.75	175.75
7	CMCC-CESM	sst,τx,τy,so,T	220.75	172.75	234.25	187.75
8	CMCC-CM	sst,τx,τy,so,T	192.25	177.25	235.75	196.75
9	CMCC-CMS	sst,τx,τy,so,T	189.25	166.75	241.75	187.75
10	CNRM-CM5	sst,τx,τy,so,T	190.75	165.25	247.75	202.75
11	FGOALS-s2	sst,τx,τy,so,T	199.75	181.75	231.25	198.25
12	GFDL-CM3	sst,τx,τy,so,T	204.25	141.25	244.75	184.75
13	GFDL-ESM2M	sst,τx,τy,so,T	196.75	142.75	246.25	189.25
14	GISS-E2-H	sst,τx,τy,so,T	223.75	141.25	247.75	207.25
15	IPSL-CM5B-LR	sst,τx,τy,so,T	216.25	165.25	252.25	202.75
16	MIROC5	sst,τx,τy,so,T	204.25	142.75	237.25	175.75
17	MRI-CGCM3	sst,τx,τy,so,T	222.25	142.75	240.25	190.75
18	MPI-ESM-LR	sst,τx,τy,so,T	142.75	142.75	243.25	175.75
19	GFDL-ESM2G	sst,τx,τy,so,T	142.75	142.75	252.25	169.75
20	NorESM1-M	sst,τx,τy,so,T	205.75	193.75	252.25	199.75
21	ACCESS1-0	sst,τx,τy	232.75	171.25	246.25	234.25
22	ACCESS1-3	sst,τx,τy,so,T	222.25	165.25	253.75	228.25
23	CSIRO-Mk3-6-0	sst,τx,τy,so,T	178.75	141.25	196.75	159.25
24	EC-EARTH	sst, so,T	NaN	NaN	252.25	201.25
25	HadGEM2-AO	sst,τx,τy	228.25	174.25	241.75	229.75
26	HadGEM2-CC	sst,τx,τy	229.75	184.75	246.25	237.25
27	HadGEM2-ES	sst,τx,τy,so,T	229.75	192.25	244.75	234.25
28	inmcm4	sst,τx,τy	217.75	192.25	240.25	192.25
29	IPSL-CM5A-LR	sst,τx,τy,so,T	205.75	198.25	258.25	201.25
30	IPSL-CM5A-MR	sst,τx,τy,so,T	198.25	187.75	258.25	193.75
31	bcc-csm1-1	sst,τx,τy,so,T	210.25	183.25	240.25	234.25
32	CanESM2	sst,τx,τy	145.75	145.75	238.75	201.25
33	MPI-ESM-MR	sst,τx,τy,so,T	163.75	141.25	238.75	177.25
34	NorESM1-ME	sst,τx,τy,so,T	207.25	195.25	249.25	204.25

The final four columns show the longitudes (° E) of the monthly maximum zonal wind-stress (Tauu) anomalies and SST anomalies in the EP and CP patterns, averaged over 5° S–5° N, for the 34 CMIP5 CGCMs, each forced under greenhouse gas concentration scenario RCP8.5. The first 17 models listed produce a reasonably large $|\alpha|$ and a nonlinear PC1–PC2 relationship (Fig. 1c, d). The zonal wind-stress anomalies associated with the EP and CP patterns are obtained by regressing monthly anomalies onto the monthly E-index and C-index, respectively; the SST anomaly pattern and centre are identified in a similar manner, except using the December–February averages of the E and C indices and SST anomalies. 'sst', 'τx', 'τy', 'so' and 'T' in the third column indicate SST, zonal wind stress, meridional wind stress, ocean salinity and temperature that are available, respectively. The 17 non-selected models are shown in grey. 'NaN' indicates data not available.

Appendix B: Spatial features of seasonal El Niño

We analyse the spatial evolution of each kind of El Niño previously defined (see Chapter 3 and paragraph 5.3.2), for different climate variables: SST, precipitation and zonal wind stress.

Strong and moderate El Niños A comparison is made between the time-longitude SSTA evolutions of strong and moderate composites and between historical and RCP8.5 simulations (Fig. 15).

Historical strong El Niño events (Fig. 15a) are characterised by anomalous warming of the surface ocean more intense and more confined in the eastern part of the equatorial Pacific than moderate El Niño events (Fig. 15b). Strong El Niño composite starts in spring in the eastern equatorial Pacific and develops rapidly. A first SSTA peak occurs in autumn towards 250°E, then spreads westward (210°E) at the end of winter. Moderate El Niño composite event starts later, at the beginning of summer, and presents rapidly a first SSTA peak in the Niño-4 region (160°E-210°E). The second SSTA peak occurs at the beginning of winter and spreads westward to join the warming in the central Pacific. The anomalous peak warming in the Niño-3 region presents an important amplitude difference between both type of events (3.4 °C and 1.7 °C for the ensemble-mean of the strong events and moderate events respectively). The transition period differs between the two types of events with a decay beginning in the east and spreading slowly westward until the end of the next summer for moderate composite, while the decay is more abrupt and earlier in the central Pacific for strong composite.

The RCP8.5 composites of these two types of events are similar to the historical composites in terms of evolution, but with more pronounced intensities. The SSTA peak reaches 3.5 °C for strong composites and 2 °C for moderate composites and the maximal SSTA values are maintained longer. For moderate composites, the more pronounced SSTA are now located in the central Pacific during winter. The differences between RCP8.5 and historical moderate composites show a more intense warming in the central Pacific with global warming. Conversely, strong composites present a more rapid decay in the central Pacific. The differences between RCP8.5 and historical strong composites confirm this weaker extension towards the west, as well as a greater persistence in the east at the end of the event. The changes are significant at the 95 % of confidence level.

For the rest of this section, we focus on strong or extreme precipitation El Niño events.

Seasonal El Niño The differences of the temporal evolutions of the E and C indices, that led to the seasonal classification of El Niño events, are also found in the spatial evolution of the composites of strong seasonal El Niño events.

Figure 16 shows the longitude-monthly evolutions of SST anomalies averaged between 2°S-2°N for strong JAS (left column), ONDJ (middle column) and FMA (right column) El Niño composites in historical simulations (top), RCP8.5 simulations (middle row) and the difference between the RCP8.5 and the historical composites (bottom).

The ONDJ strong historical composite (Fig. 16a, middle column) looks like the strong historical composite (Fig 15a, left column), because they are slightly more numerous than the other types of events and their intensity is stronger than the strong JAS historical composite, which makes up the other important part of the strong composites. The latter (Fig. 16a, left column) has less persistence in the eastern Pacific at the end of the event, before it decays, than ONDJ composite and even less that FMA composite. The FMA strong historical composite (Fig. 16a, right column) shows SSTA intensity particularly pronounced compared to the others. However, the historical strong FMA El Niño composite is composed of only few events (9 events over 3682 historical years), that are particular strong events in terms of intensity. The historical composite thus has also stronger SST anomalies than the RCP8.5 composite (Fig. 16b, right column), which is composed of 119 events.

Regarding the RCP8.5 composites, JAS El Niño retains with lower intensities than the other two. ONDJ and FMA El Niño have similar evolutions in RCP8.5, except for the weakest

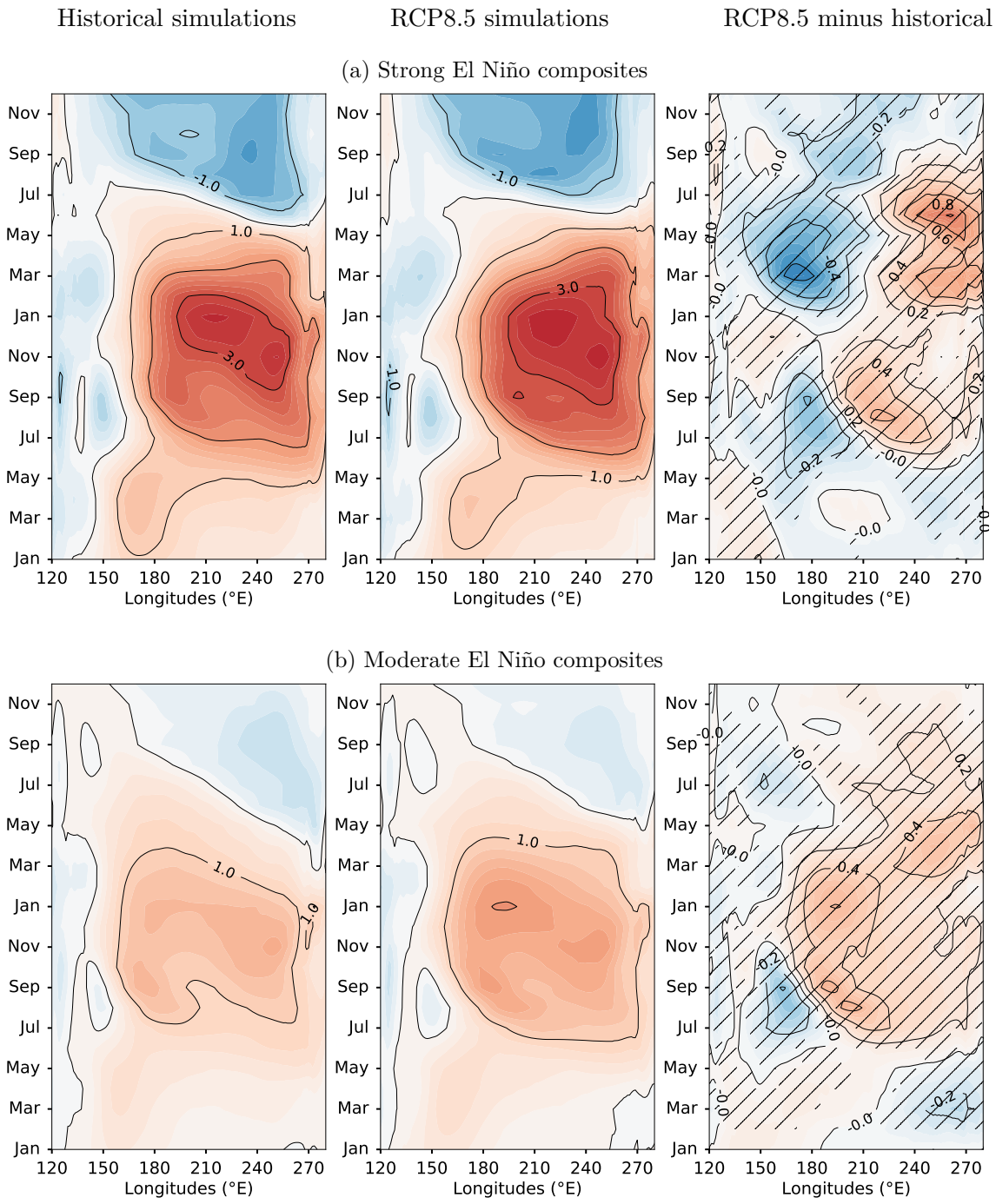

Figure 15 – Longitudes-time SSTA evolutions of (Fig. 15a) strong and (Fig. 15b) moderate El Niño composites for (left column) historical simulations, (middle column) RCP8.5 simulations and (right column) the difference between the RCP8.5 and historical composites. The stippling on the latter column indicates where the values of the ensemble of the RCP8.5 composites are significantly positively or negatively larger than that of the ensemble of the historical composites according to a Wilcoxon rank-sum test at 95 % confidence intervals. The SSTA are averaged between 2°S-2°N.

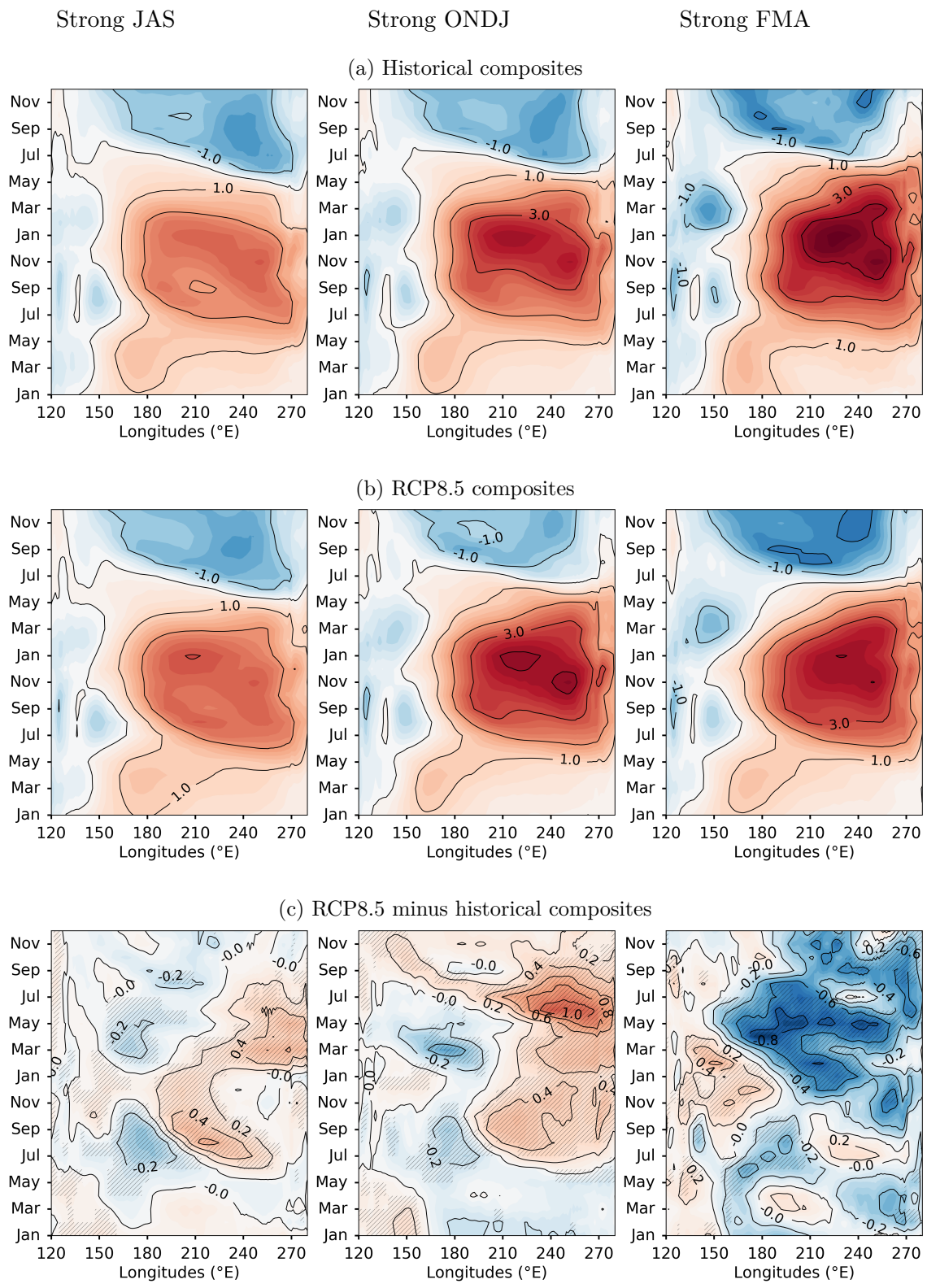

Figure 16 – Longitudes-time SSTA evolutions of strong (left column) JAS, (middle column) ONDJ and (right column) FMA El Niño composites for (16a) historical simulations, (16b) RCP8.5 simulations and (16c) the difference between the RCP8.5 and historical composites. The stippling on the latter row indicates where the values of the ensemble of the RCP8.5 composites are significantly positively or negatively larger than that of the ensemble of the historical composites according to a Wilcoxon rank-sum test at 95 % confidence intervals. The SSTA are averaged between 2°S-2°N.

persistence in the western-central Pacific at the end of the event for FMA El Niño composite.

Because there are only few FMA El Niño events in historical simulations and that they are particularly strong, in order not to artificially distort the conclusions, the comparative evolution of JAS and ONDJ El Niño events between historical and RCP8.5 composites is first analysed. In a second time, the comparative evolution of strong ONDJ and FMA El Niño events, only in RCP8.5 climate, is conducted.

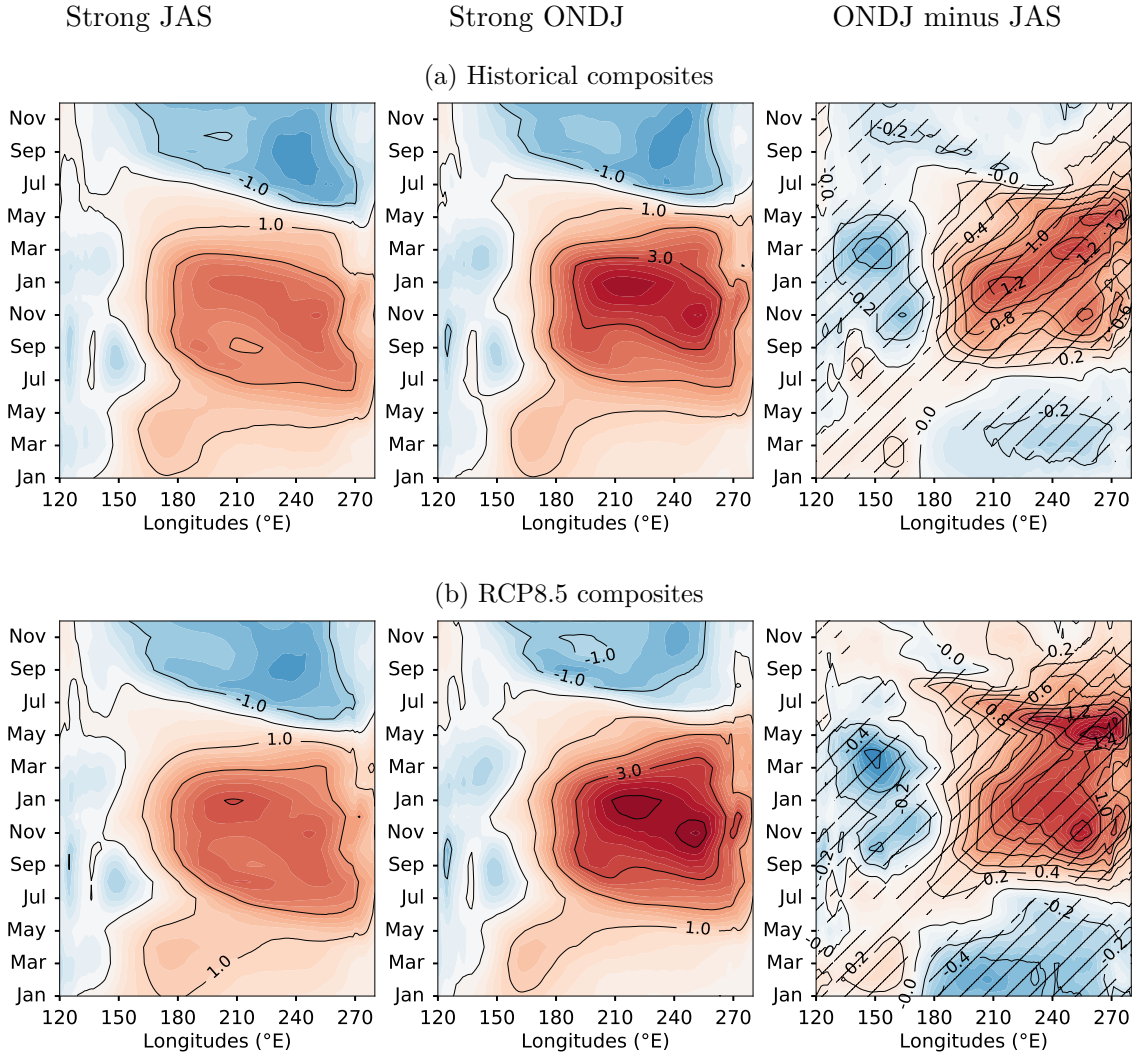

Figure 17 – Longitudes-time SSTA evolutions of strong (left column) JAS, (middle column) ONDJ El Niño and (right column) the difference between the strong ONDJ and JAS El Niño composites for (17a) historical simulations and (17b) RCP8.5 simulations. The stippling on the latter column indicates where the values of the ensemble of the ONDJ composites are significantly positively or negatively larger than that of the ensemble of the JAS composites according to a Wilcoxon rank-sum test at 95 % confidence intervals. The SSTA are averaged between 2°S-2°N.

Whether in historical or RCP8.5 simulations, the strong JAS El Niño composite exhibits less east-west contrast than the ONDJ composite. During the developing phase of the event, the ONDJ composite shows more pronounced warming in the eastern Pacific. The persistence of the warming in the eastern Pacific at the end of the event, also more pronounced for the ONDJ composite, is getting stronger in the future and spread more westward. Interestingly, the differences in the evolution between both events are more important than between the RCP8.5 and historical evolution of each event. Even if global warming will cause changes in the evolution of each of these composites, it appears that these changes will be less pronounced than those that already exist between these two types of events and that will be accentuated in the future.

When analysing the longitudes-time evolution of these JAS and ONDJ composites on other variables, precipitation (Fig. 19) and zonal wind stress (Fig. 20), we find these differences in behaviour between our two composites.

Precipitation is an important indicator of El Niño event, in particular of strong El Niño with warming in the eastern Pacific (Cai et al., 2014). The equatorial Pacific mean rainfall is likely to increase, following a warmer-gets-wetter pattern (Xie et al., 2010; Chadwick et al., 2013; Xie et al., 2015). CESM-LE projects also an increase in rainfall, which can be observed in the annual cycle of rainfall in the equatorial Pacific (Fig. 18). The increase in detrended annual cycle of rainfall occurs from January to June with a particularly pronounced increase in April-May.

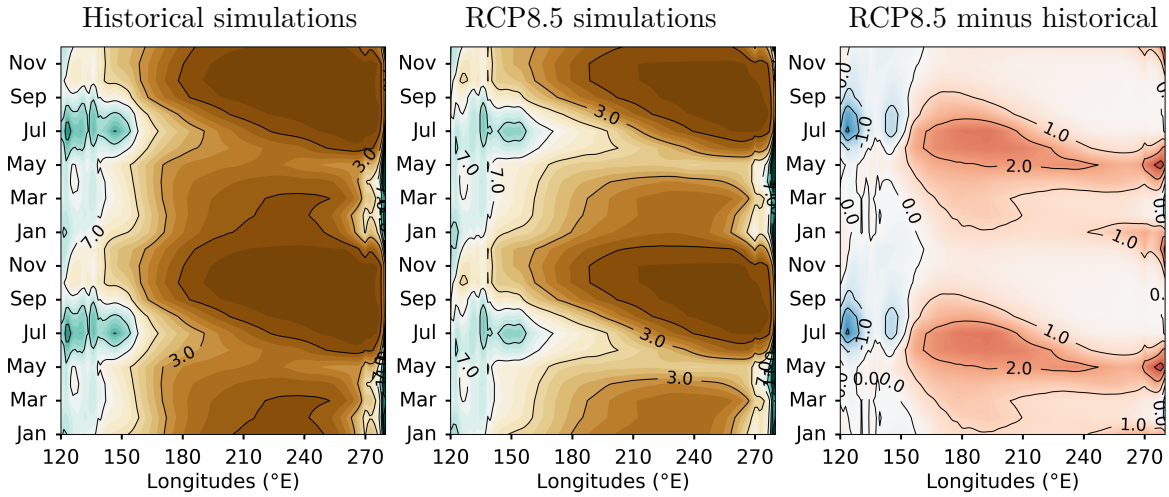

Figure 18 – Longitudes-time evolutions of (left) the historical ensemble-mean and (middle) the RCP8.5 ensemble-mean seasonal cycle of rainfall averaged between 2°S-2°N. The figure on the right represents the difference between the RCP8.5 and the historical sets.

Regarding detrended precipitation in historical simulations (Fig 19a), the strong JAS composite presents more precipitation than usual in the western Pacific during the developing phase of the event around the dateline. The precipitation maximum region is located around 170°E from January to March, when there is more rainfall than usual along the equator. The strong ONDJ composite is characterised by an important anomalous precipitation along the equator from December to May, with a eastward extension of the maximum rainfall. Differences between the two historical composites are thus particularly pronounced from December to May, east of the dateline.

The RCP8.5 JAS composite shows more pronounced eastward intrusion of important rainfall during the summer preceding of the developing year of the event (Fig. 19b, left column), facilitated by the more pronounced seasonal rainfall at this time. During the following winter, the JAS spatial pattern of rainfall looks like the spatial pattern of historical ONDJ composite, with similar intensities and the same intrusion to the east. For the ONDJ composite (Fig. 19b, right column), the same intensification occurs during the winter, to achieve rainfall greater than 7 mm / day all along the equator. Interestingly, the differences between RCP8.5 and historical composites have similar shapes with more rainfall during summer and winter. However, JAS differences composite has a more pronounced intensity and a more westward extension. Despite the increase in rainfall with global warming, the differences between ONDJ and JAS composites in RCP8.5 have similar shapes with a maximum difference in winter, even if this area is shifted eastward. Thus, the precipitation associated with ENSO seems to be shifted eastward with global warming, which could perturb the traditional vision that one has of the link precipitation - El Niño.

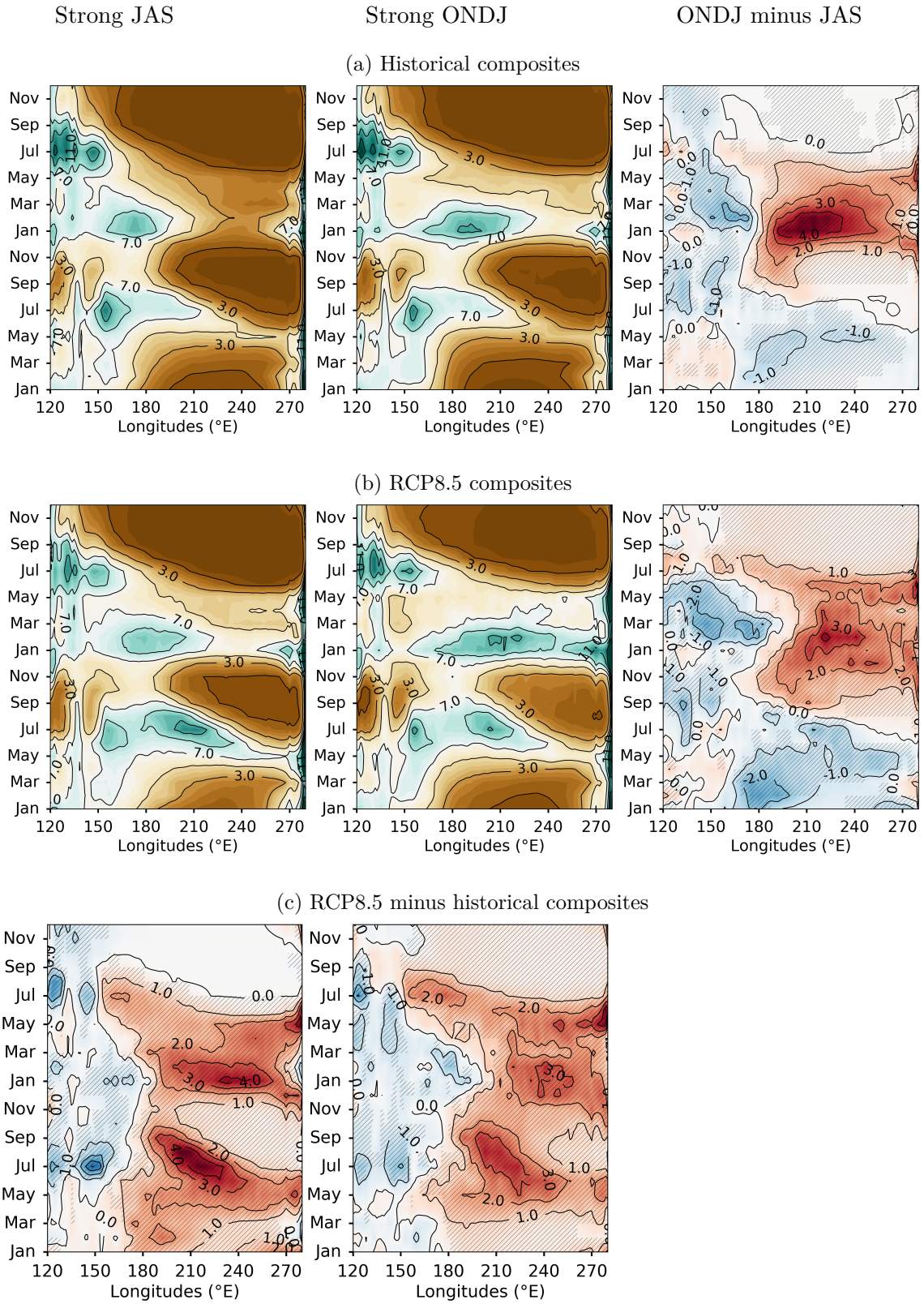

Figure 19 – Longitudes-time detrended precipitation evolutions of strong (left column) JAS, (middle column) ONDJ El Niño and (right column) the difference between the ONDJ and JAS strong El Niño composites for (19a) historical simulations, (19b) RCP8.5 simulations and (19c the difference between the RCP8.5 and historical composites. The stippling on the latter row indicates where the values of the ensemble of the RCP8.5 composites are significantly positively or negatively larger than that of the ensemble of the historical composites according to a Wilcoxon rank-sum test at 95 % confidence intervals. The stippling on the latter column indicates where the values of the ensemble of the ONDJ composites are significantly positively or negatively larger than that of the ensemble of the JAS composites according to a Wilcoxon rank-sum test at 95 % confidence intervals. The precipitations are averaged between 2°S-2°N.

The zonal wind stress is usually used as a precursor of El Niño, Westerly Wind Events (WWEs) often initiating strong El Niño through the initiation of equatorial downwelling Kelvin waves. Figure 20 shows the same comparison as for rainfall between JAS and ONDJ composite et their evolution with global warming.

Historical JAS composite presents several WWEs, beginning in boreal spring around 150°E, followed by several more intense episodes in summer with peaks around 210°E and 190° and in winter in the central Pacific. The RCP8.5 spatial evolution is similar but with an intensification of the WWEs during the summer around 200°E.

Historical ONDJ composite presents the same beginning than JAS composite. An intensification of the events occurs then but with a smaller eastern extension than for JAS composite during summer. The maximum values occur during the winter between 180-200°E. Once again, the RCP8.5 spatial evolution is similar than in historical simulations but with an intensification of the values and a maximum reached in December around 180°.

The differences between the RCP8.5 and historical composites of each kind of events are similar with in particular an intensification of the WWEs in the central Pacific during summer. Interestingly, the differences between the two types of events are greater than the difference for each composite between RCP8.5 and historical simulations. In particular, strong WWEs at the end of autumn and in winter, propagating from 170°E to 210°E, work to strengthen warming in the eastern Pacific during its peaks in SST and in E-index.

JAS and ONDJ composites are different in their evolution and keep these evolutionary differences with climate change.

When comparing, in RCP8.5 simulations, ONDJ and FMA composites, the main differences appear along a diagonal longitudes-time, beginning around 180° in January and ending more or less abruptly in the eastern Pacific around the summer following the event, for the three studied variables. Even though the maximum values of SSTA in winter in the extreme east of the equatorial Pacific around 270°E and in early spring around 210°E are lower for RCP8.5 FMA composite than for RCP8.5 ONDJ composite, FMA composite shows a greater persistence in the extreme east as early as spring. Precipitation follows anomalous warming of SST and FMA composite is accompanied by more rain in particular in summer around 210°E and in next spring and summer in the extreme east until the decay of the event. These warming areas are associated each time with more westerly winds than in ONDJ composite.

Extreme El Niño The same analyse is applied to the extreme precipitation El Niño composite, defined by the rainfall threshold in the eastern Pacific.

The RCP8.5 extreme precipitation composite is clearly less intense in SSTA than that of historical climate. As discussed in the paragraph 5.3.3.2, it is mainly explained by the fact that extreme precipitation El Niño composite is composed of 34 % of events classified as moderate according to the E-index in a warmer climate. The ensemble mean decrease in the amplitude of the composite is also observed on the events of westerlies. However, the precipitation pattern does not show the same evolution, between historical and RCP8.5, partly because of the global SST warming in RCP8.5 simulations.

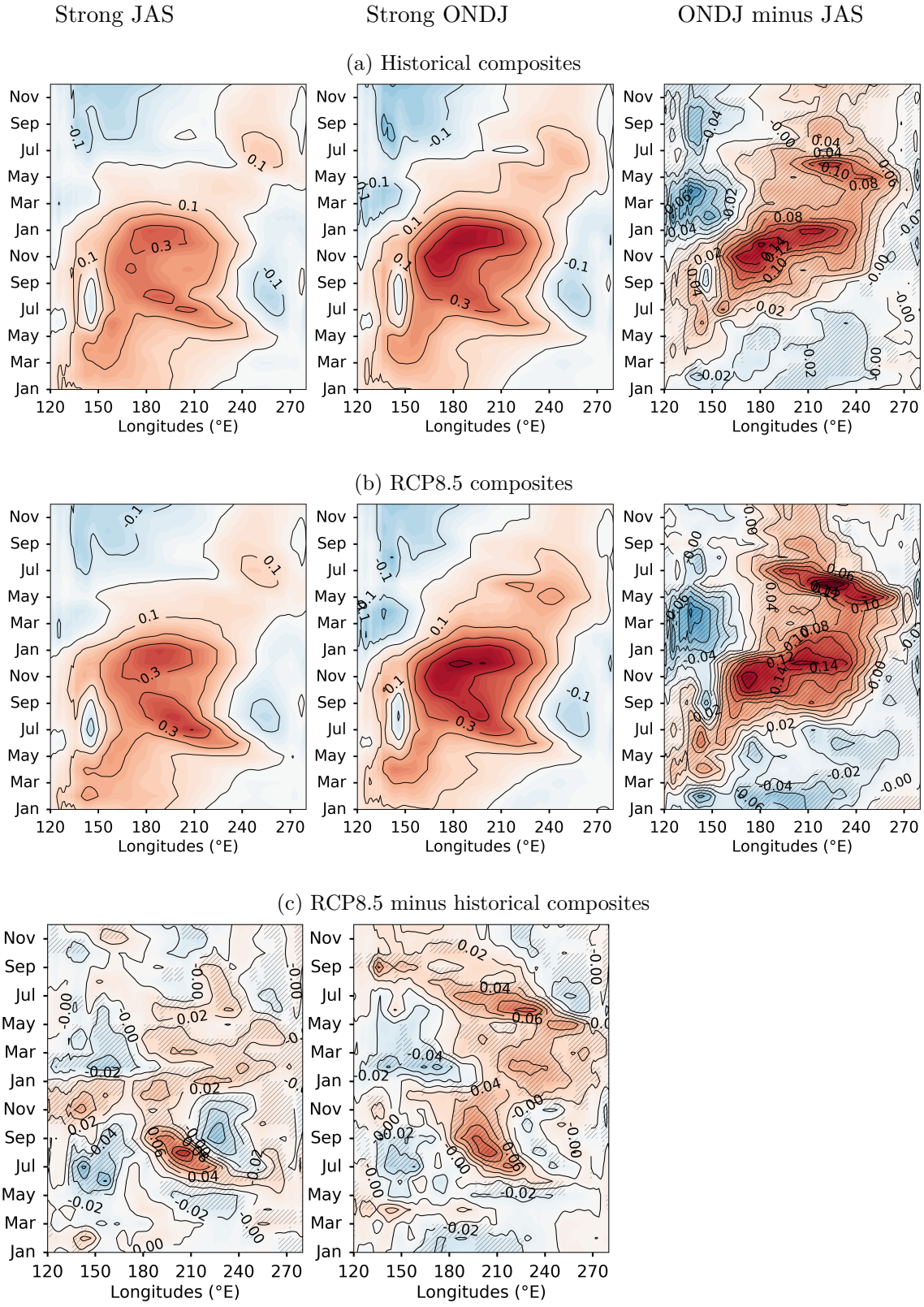

Figure 20 – Same as 19 but for the zonal wind stress ($10^{-1}N/m^2$).

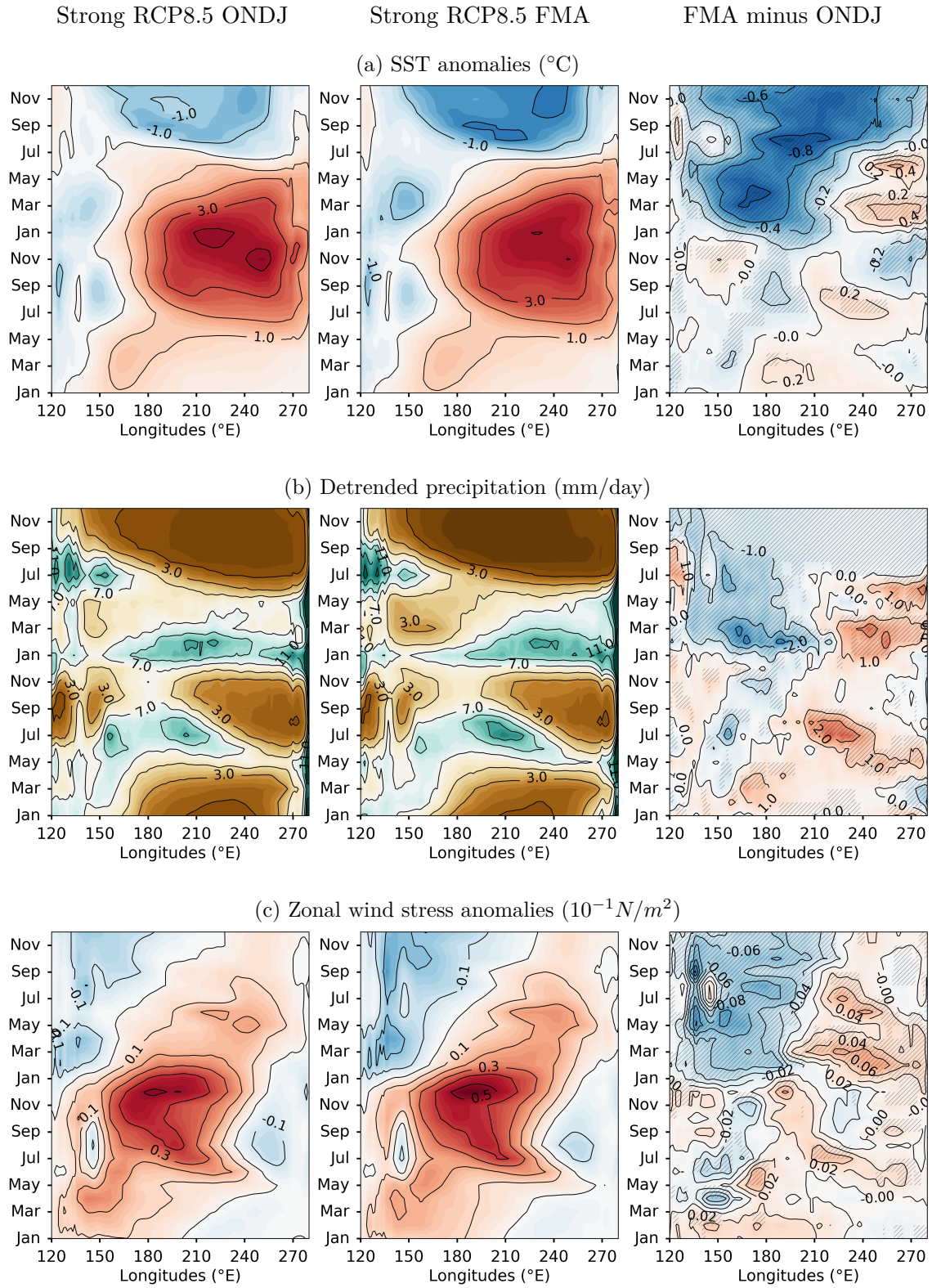

Figure 21 – Longitudes-time evolutions of (left column) ONDJ, (middle column) FMA and (right column) the difference between the FMA and ONDJ strong El Niño composites of RCP8.5 simulations for (21a) SSTA (celsius), (21b) detrended precipitation (mm/day) and (21c) zonal wind stress anomalies ($10^{-1}N/m^2$). The stippling on the latter column indicates where the values of the ensemble of the ONDJ composites are significantly positively or negatively larger than that of the ensemble of the JAS composites according to a Wilcoxon rank-sum test at 95 % confidence intervals. All the variables are averaged between 2°S-2°N.

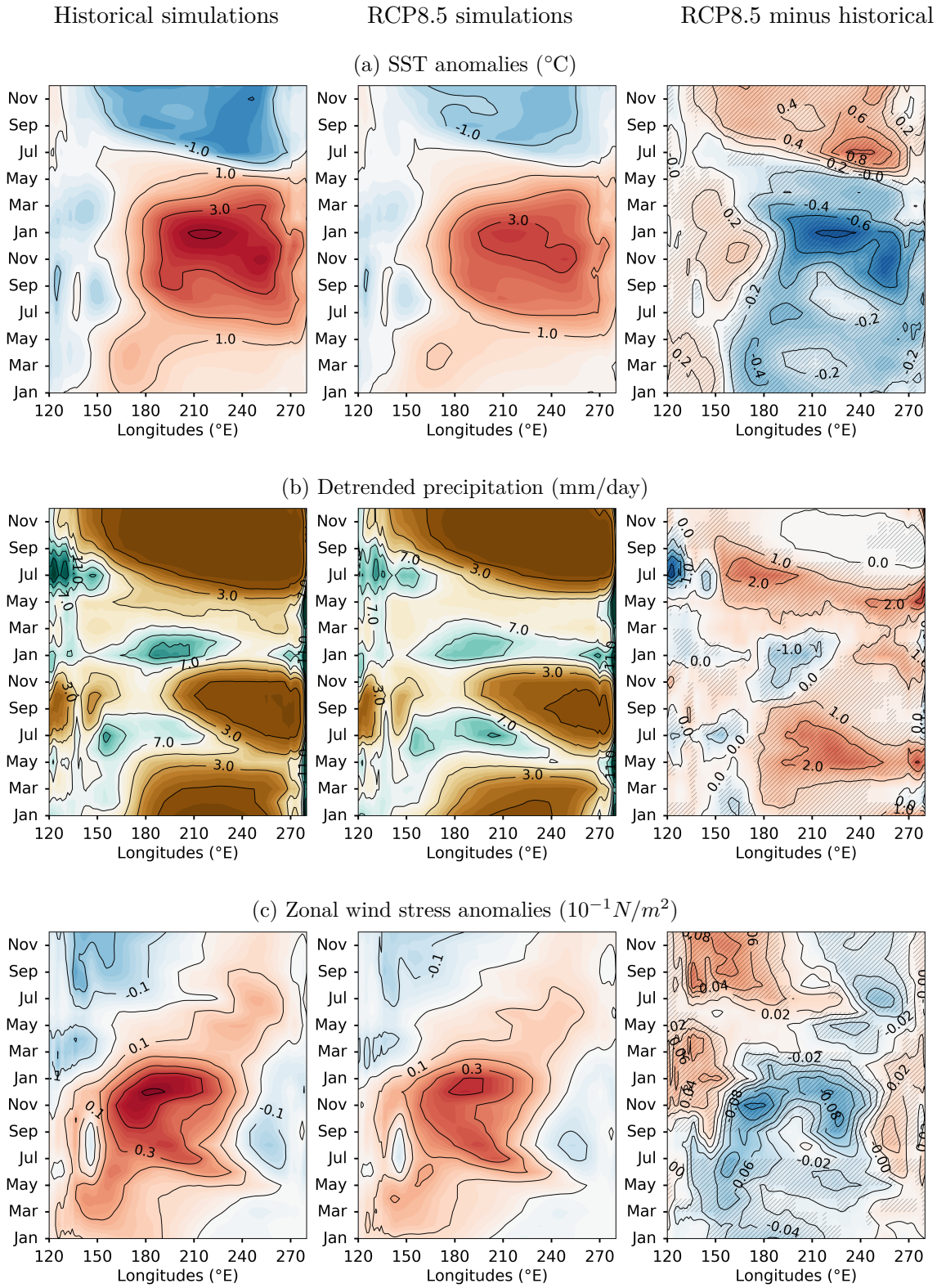

Figure 22 – Longitudes-time evolutions of (left column) the historical ensemble-mean composite, (middle column) the RCP8.5 ensemble-mean composite and (right column) the difference between RCP8.5 and historical extreme precipitation El Niño composites for (21a) SSTA (°C), (21b) detrended precipitation (mm/d mm/day) and (21c) zonal wind stress ($10^{-1}N/m^2$). The stippling on the latter column indicates where the values of the ensemble of the RCP8.5 composites are significantly positively or negatively larger than that of the ensemble of the historical composites according to a Wilcoxon rank-sum test at 95 % confidence intervals. All the variables are averaged between 2°S-2°N.

Bibliography

Abellán, E., S. McGregor, and M. H. England, 2017a: Analysis of the Southward Wind Shift of ENSO in CMIP5 Models. *Journal of Climate*, **30**, 2415–2435, doi:10.1175/JCLI-D-16-0326.1.

Abellán, E., S. McGregor, M. H. England, and A. Santoso, 2017b: Distinctive role of ocean advection anomalies in the development of the extreme 2015–16 El Niño. *Climate Dynamics*, 1–18, doi:10.1007/s00382-017-4007-0.

Adler, R. F., G. J. Huffman, A. Chang, R. Ferraro, P.-P. Xie, J. Janowiak, B. Rudolf, U. Schneider, S. Curtis, D. Bolvin, A. Gruber, J. Susskind, P. Arkin, and E. Nelkin, 2003: The Version-2 Global Precipitation Climatology Project (GPCP) Monthly Precipitation Analysis (1979–Present). *J. Hydrometeor.*, **4**, 1147–1167, doi:10.1175/1525-7541(2003)004<1147:TVGPCP>2.0.CO;2.

An, S.-I., 2008: Interannual Variations of the Tropical Ocean Instability Wave and ENSO. *Journal of Climate*, **21**, 3680–3686, doi:10.1175/2008JCLI1701.1.

— 2009: A review of interdecadal changes in the nonlinearity of the El Niño-Southern Oscillation. *Theor Appl Climatol*, **97**, 29–40, doi:10.1007/s00704-008-0071-z.

An, S.-I., Y.-G. Ham, J.-S. Kug, F.-F. Jin, and I.-S. Kang, 2005a: El Niño–La Niña Asymmetry in the Coupled Model Intercomparison Project Simulations. *Journal of Climate*, **18**, 2617–2627, doi:10.1175/JCLI3433.1.

An, S.-I., W. W. Hsieh, and F.-F. Jin, 2005b: A Nonlinear Analysis of the ENSO Cycle and Its Interdecadal Changes. *Journal of Climate*, **18**, 3229–3239, doi:10.1175/JCLI3466.1.

An, S.-I. and F.-F. Jin, 2000: An eigen analysis of the interdecadal changes in the structure and frequency of ENSO mode. *Geophysical Research Letters*, **27**, 2573–2576, doi:10.1029/1999GL011090.

— 2001: Collective Role of Thermocline and Zonal Advective Feedbacks in the ENSO Mode. *Journal of Climate*, **14**, 3421–3432, doi:10.1175/1520-0442(2001)014<3421:CROTAZ>2.0.CO;2.

— 2004: Nonlinearity and Asymmetry of ENSO. *J. Climate*, **17**, 2399–2412, doi:10.1175/1520-0442(2004)017<2399:NAAOE>2.0.CO;2.

An, S.-I., J.-S. Kug, Y.-G. Ham, and I.-S. Kang, 2008: Successive Modulation of ENSO to the Future Greenhouse Warming. *Journal of Climate*, **21**, 3–21, doi:10.1175/2007JCLI1500.1.

An, S.-I. and B. Wang, 2000: Interdecadal Change of the Structure of the ENSO Mode and Its Impact on the ENSO Frequency. *Journal of Climate*, **13**, 2044–2055, doi:10.1175/1520-0442(2000)013<2044:ICOTSO>2.0.CO;2.

Arakawa, A. and V. R. Lamb, 1977: Computational Design of the Basic Dynamical Processes of the UCLA General Circulation Model. *Methods in Computational Physics: Advances*

in Research and Applications, J. Chang, ed., Elsevier, volume 17 of *General Circulation Models of the Atmosphere*, 173–265.

Ashok, K., S. K. Behera, S. A. Rao, H. Weng, and T. Yamagata, 2007: El Niño Modoki and its possible teleconnection. *Journal of Geophysical Research*, **112**, doi:10.1029/2006JC003798.

Baldwin, M. P., D. B. Stephenson, and I. T. Jolliffe, 2009: Spatial Weighting and Iterative Projection Methods for EOFs. *J. Climate*, **22**, 234–243, doi:10.1175/2008JCLI2147.1.

Banzon, V., T. M. Smith, T. M. Chin, C. Liu, and W. Hankins, 2016: A long-term record of blended satellite and in situ sea-surface temperature for climate monitoring, modeling and environmental studies. *Earth System Science Data*, **8**, 165–176, doi:10.5194/essd-8-165-2016.

Battisti, D. S. and A. C. Hirst, 1989: Interannual Variability in a Tropical Atmosphere–Ocean Model: Influence of the Basic State, Ocean Geometry and Nonlinearity. *Journal of the Atmospheric Sciences*, **46**, 1687–1712, doi:10.1175/1520-0469(1989)046<1687:IVIATA>2.0.CO;2.

Bayr, T., M. Latif, D. Dommenget, C. Wengel, J. Harlaß, and W. Park, 2018a: Mean-state dependence of ENSO atmospheric feedbacks in climate models. *Climate Dynamics*, **50**, 3171–3194, doi:10.1007/s00382-017-3799-2.

Bayr, T., C. Wengel, M. Latif, D. Dommenget, J. Lübbecke, and W. Park, 2018b: Error compensation of ENSO atmospheric feedbacks in climate models and its influence on simulated ENSO dynamics. *Climate Dynamics*, doi:10.1007/s00382-018-4575-7.

Bejarano, L. and F.-F. Jin, 2008: Coexistence of Equatorial Coupled Modes of ENSO. *Journal of Climate*, **21**, 3051–3067, doi:10.1175/2007JCLI1679.1.

Bellenger, H., E. Guilyardi, J. Leloup, M. Lengaigne, and J. Vialard, 2014: ENSO representation in climate models: from CMIP3 to CMIP5. *Climate Dynamics*, **42**, 1999–2018, doi:10.1007/s00382-013-1783-z.

Belmadani, A., B. Dewitte, and S.-I. An, 2010: ENSO feedbacks and associated time scales of variability in a multimodel ensemble. *Journal of Climate*, **23**, 3181–3204. ISSN 0894–8755, doi:10.1175/2010jcli2830.1.

Bittner, M., H. Schmidt, C. Timmreck, and F. Sienz, 2016: Using a large ensemble of simulations to assess the Northern Hemisphere stratospheric dynamical response to tropical volcanic eruptions and its uncertainty. *Geophysical Research Letters*, **43**, 9324–9332, doi:10.1002/2016GL070587.

Bjerknes, J., 1969: Atmospheric teleconnections from the equatorial pacific. *Mon. Wea. Rev.*, **97**, 163–172, doi:10.1175/1520-0493(1969)097<0163:ATFTEP>2.3.CO;2.

Björnsson, H. and S. A. Venegas, 1997: A Manual for EOF and SVD Analyses of Climatic Data. CCGCR Report 97-1, Department of Atmospheric and Oceanic Sciences and Centre for Climate and Global Change Research, McGill University.

Bosc, C. and T. Delcroix, 2008: Observed equatorial Rossby waves and ENSO-related warm water volume changes in the equatorial Pacific Ocean. *Journal of Geophysical Research*, **113**, doi:10.1029/2007JC004613.

Boschat, G., P. Terray, and S. Masson, 2013: Extratropical forcing of ENSO. *Geophysical Research Letters*, **40**, 1605–1611, doi:10.1002/grl.50229.

Boucharel, J., 2010: *Modes de variabilité climatique dans l'océan Pacifique tropical : quantification des non-linéarités et rôle sur les changements de régimes climatiques*. phd, Université de Toulouse, Université Toulouse III - Paul Sabatier.

Boucharel, J., B. Dewitte, Y. du Penhoat, B. Garel, S.-W. Yeh, and J.-S. Kug, 2011: ENSO nonlinearity in a warming climate. *Climate Dynamics*, **37**, 2045–2065, doi:10.1007/s00382-011-1119-9.

Boucharel, J., B. Dewitte, B. Garel, and Y. du Penhoat, 2009: ENSO's non-stationary and non-Gaussian character: the role of climate shifts. *Nonlinear Processes in Geophysics*, **16**, 453–473, doi:10.5194/npg-16-453-2009.

Boucharel, J. and F.-F. Jin, 2020: A simple theory for the modulation of tropical instability waves by ENSO and the annual cycle. *Tellus A: Dynamic Meteorology and Oceanography*, **72**, 1–14, doi:10.1080/16000870.2019.1700087.

Boucharel, J., A. Timmermann, and F.-F. Jin, 2013: Zonal phase propagation of ENSO sea surface temperature anomalies: Revisited. *Geophysical Research Letters*, **40**, 4048–4053, doi:10.1002/grl.50685.

Boucharel, J., A. Timmermann, A. Santoso, M. H. England, F.-F. Jin, and M. A. Balmaseda, 2015: A surface layer variance heat budget for ENSO. *Geophysical Research Letters*, **42**, 3529–3537, doi:10.1002/2015GL063843.

Boulanger, J.-P., 2003: Reflected and locally wind-forced interannual equatorial Kelvin waves in the western Pacific Ocean. *Journal of Geophysical Research*, **108**, doi:10.1029/2002JC001760.

Boulanger, J.-P., E. Durand, J.-P. Duvel, C. Menkes, P. Delecluse, M. Imbard, M. Lengaigne, G. Madec, and S. Masson, 2001: Role of non-linear oceanic processes in the response to westerly wind events: New implications for the 1997 El Niño onset. *Geophysical Research Letters*, **28**, 1603–1606, doi:10.1029/2000GL012364.

Boulanger, J.-P. and C. Menkes, 1999: Long equatorial wave reflection in the Pacific Ocean from TOPEX/POSEIDON data during the 1992-1998 period. *Climate Dynamics*, **15**, 205–225, doi:10.1007/s003820050277.

Brainard, R. E., T. Oliver, M. J. McPhaden, A. Cohen, R. Venegas, A. Heenan, B. Vargas-Ángel, R. Rotjan, S. Mangubhai, E. Flint, and S. A. Hunter, 2018: Ecological Impacts of the 2015/16 El Niño in the Central Equatorial Pacific. *Bulletin of the American Meteorological Society*, **99**, S21–S26, doi:10.1175/BAMS-D-17-0128.1.

Bunge, L. and A. J. Clarke, 2014: On the Warm Water Volume and Its Changing Relationship with ENSO. *Journal of Physical Oceanography*, **44**, 1372–1385, doi:10.1175/JPO-D-13-062.1.

Cai, W., S. Borlace, M. Lengaigne, P. van Rensch, M. Collins, G. Vecchi, A. Timmermann, A. Santoso, M. J. McPhaden, L. Wu, M. H. England, G. Wang, E. Guilyardi, and F.-F. Jin, 2014: Increasing frequency of extreme El Niño events due to greenhouse warming. *Nature Climate Change*, **4**, 111–116, doi:10.1038/nclimate2100.

Cai, W., A. Santoso, G. Wang, S.-W. Yeh, S.-I. An, K. M. Cobb, M. Collins, E. Guilyardi, F.-F. Jin, J.-S. Kug, M. Lengaigne, M. J. McPhaden, K. Takahashi, A. Timmermann, G. Vecchi, M. Watanabe, and L. Wu, 2015a: ENSO and greenhouse warming. *Nature Climate Change*, **5**, 849–859, doi:10.1038/nclimate2743.

Cai, W., G. Wang, B. Dewitte, L. Wu, A. Santoso, K. Takahashi, Y. Yang, A. Carréric, and M. J. McPhaden, 2018: Increased variability of eastern Pacific El Niño under greenhouse warming. *Nature*, **564**, 201–206, doi:10.1038/s41586-018-0776-9.

Cai, W., G. Wang, A. Santoso, X. Lin, and L. Wu, 2017: Definition of Extreme El Niño and Its Impact on Projected Increase in Extreme El Niño Frequency. *Geophysical Research Letters*, **44**, doi:10.1002/2017GL075635.

Cai, W., G. Wang, A. Santoso, M. J. McPhaden, L. Wu, F.-F. Jin, A. Timmermann, M. Collins, G. Vecchi, M. Lengaigne, M. H. England, D. Dommenget, K. Takahashi, and E. Guilyardi, 2015b: Increased frequency of extreme La Niña events under greenhouse warming. *Nature Climate Change*, **5**, 132–137, doi:10.1038/nclimate2492.

Cane, M. A. and S. E. Zebiak, 1985: A theory for El Niño and the Southern Oscillation. *Science*, **228**, 1085–1087, doi:10.1126/science.228.4703.1085.

Capotondi, A., 2013: ENSO diversity in the NCAR CCSM4 climate model. *Journal of Geophysical Research: Oceans*, **118**, 4755–4770, doi:10.1002/jgrc.20335.

Capotondi, A. and P. D. Sardeshmukh, 2015: Optimal precursors of different types of ENSO events: Optimal Precursors of ENSO Events. *Geophysical Research Letters*, **42**, 9952–9960, doi:10.1002/2015GL066171.

Capotondi, A., A. Wittenberg, and S. Masina, 2006: Spatial and temporal structure of Tropical Pacific interannual variability in 20th century coupled simulations. *Ocean Modelling*, **15**, 274–298, doi:10.1016/j.ocemod.2006.02.004.

Capotondi, A., A. T. Wittenberg, M. Newman, E. Di Lorenzo, J.-Y. Yu, P. Braconnot, J. Cole, B. Dewitte, B. Giese, E. Guilyardi, F.-F. Jin, K. Karnauskas, B. Kirtman, T. Lee, N. Schneider, Y. Xue, and S.-W. Yeh, 2015: Understanding ENSO Diversity. *Bulletin of the American Meteorological Society*, **96**, 921–938, doi:10.1175/BAMS-D-13-00117.1.

Carton, J. A. and B. S. Giese, 2008: A Reanalysis of Ocean Climate Using Simple Ocean Data Assimilation (SODA). *Monthly Weather Review*, **136**, 2999–3017, doi:10.1175/2007MWR1978.1.

Castaño Tierno, A., E. Mohino, B. Rodríguez-Fonseca, and T. Losada, 2018: Revisiting the CMIP5 Thermocline in the Equatorial Pacific and Atlantic Oceans. *Geophysical Research Letters*, doi:10.1029/2018GL079847.

Chadwick, R., I. Boutle, and G. Martin, 2013: Spatial Patterns of Precipitation Change in CMIP5: Why the Rich Do Not Get Richer in the Tropics. *Journal of Climate*, **26**, 3803–3822, doi:10.1175/JCLI-D-12-00543.1.

Chang, P., L. Zhang, R. Saravanan, D. J. Vimont, J. C. H. Chiang, L. Ji, H. Seidel, and M. K. Tippett, 2007: Pacific meridional mode and El Niño-Southern Oscillation. *Geophysical Research Letters*, **34**, doi:10.1029/2007GL030302.

Chen, C., M. A. Cane, A. T. Wittenberg, and D. Chen, 2017a: ENSO in the CMIP5 Simulations: Life Cycles, Diversity, and Responses to Climate Change. *Journal of Climate*, **30**, 775–801, doi:10.1175/JCLI-D-15-0901.1.

Chen, D., M. A. Cane, A. Kaplan, S. E. Zebiak, and D. Huang, 2004: Predictability of El Niño over the past 148 years. *Nature*, **428**, 733–736, doi:10.1038/nature02439.

Chen, D., T. Lian, C. Fu, M. A. Cane, Y. Tang, R. Murtugudde, X. Song, Q. Wu, and L. Zhou, 2015a: Strong influence of westerly wind bursts on El Niño diversity. *Nature Geoscience*, **8**, 339–345, doi:10.1038/ngeo2399.

Chen, G., 2011: How Does Shifting Pacific Ocean Warming Modulate on Tropical Cyclone Frequency over the South China Sea? *Journal of Climate*, **24**, 4695–4700, doi:10.1175/2011JCLI4140.1.

Chen, G. and C.-Y. Tam, 2010: Different impacts of two kinds of Pacific Ocean warming on tropical cyclone frequency over the western North Pacific. *Geophysical Research Letters*, **37**, doi:10.1029/2009GL041708.

Chen, L., T. Li, and Y. Yu, 2015b: Causes of Strengthening and Weakening of ENSO Amplitude under Global Warming in Four CMIP5 Models. *Journal of Climate*, **28**, 3250–3274, doi:10.1175/JCLI-D-14-00439.1.

Chen, L., T. Li, Y. Yu, and S. K. Behera, 2017b: A possible explanation for the divergent projection of ENSO amplitude change under global warming. *Climate Dynamics*, doi:10.1007/s00382-017-3544-x.

Chen, S., W. Chen, B. Yu, and H.-F. Graf, 2013: Modulation of the seasonal footprinting mechanism by the boreal spring Arctic Oscillation. *Geophysical Research Letters*, **40**, 6384–6389, doi:10.1002/2013GL058628.

Chen, S. and R. Wu, 2018: Impacts of winter NPO on subsequent winter ENSO: sensitivity to the definition of NPO index. *Climate Dynamics*, **50**, 375–389, doi:10.1007/s00382-017-3615-z.

Chiang, J. C. H. and D. J. Vimont, 2004: Analogous Pacific and Atlantic Meridional Modes of Tropical Atmosphere–Ocean Variability. *Journal of Climate*, **17**, 4143–4158, doi:10.1175/JCLI4953.1.

Chikamoto, Y., A. Timmermann, J.-J. Luo, T. Mochizuki, M. Kimoto, M. Watanabe, M. Ishii, S.-P. Xie, and F.-F. Jin, 2015: Skilful multi-year predictions of tropical trans-basin climate variability. *Nature Communications*, **6**, 6869, doi:10.1038/ncomms7869.

Chiodi, A. M. and D. E. Harrison, 2013: El Niño Impacts on Seasonal U.S. Atmospheric Circulation, Temperature, and Precipitation Anomalies: The OLR-Event Perspective. *Journal of Climate*, **26**, 822–837, doi:10.1175/JCLI-D-12-00097.1.

Choi, J., S.-I. An, B. Dewitte, and W. W. Hsieh, 2009: Interactive Feedback between the Tropical Pacific Decadal Oscillation and ENSO in a Coupled General Circulation Model. *Journal of Climate*, **22**, 6597–6611, doi:10.1175/2009jcli2782.1.

Choi, J., S.-I. An, J.-S. Kug, and S.-W. Yeh, 2011: The role of mean state on changes in El Niño's flavor. *Climate Dynamics*, **37**, 1205–1215, doi:10.1007/s00382-010-0912-1.

Choi, J., S.-I. An, and S.-W. Yeh, 2012: Decadal amplitude modulation of two types of ENSO and its relationship with the mean state. *Climate Dynamics*, **38**, 2631–2644, doi:10.1007/s00382-011-1186-y.

Choi, J., S.-I. An, S.-W. Yeh, and J.-Y. Yu, 2013a: ENSO-Like and ENSO-Induced Tropical Pacific Decadal Variability in CGCMs. *Journal of Climate*, **26**, 1485–1501, doi:10.1175/JCLI-D-12-00118.1.

Choi, K.-Y., G. A. Vecchi, and A. T. Wittenberg, 2013b: ENSO Transition, Duration, and Amplitude Asymmetries: Role of the Nonlinear Wind Stress Coupling in a Conceptual Model. *Journal of Climate*, **26**, 9462–9476, doi:10.1175/JCLI-D-13-00045.1.

Chung, E.-S., A. Timmermann, B. J. Soden, K.-J. Ha, L. Shi, and V. O. John, 2019: Reconciling opposing Walker circulation trends in observations and model projections. *Nature Climate Change*, **9**, 405–412, doi:10.1038/s41558-019-0446-4.

Chung, P.-H. and T. Li, 2013: Interdecadal Relationship between the Mean State and El Niño Types. *Journal of Climate*, **26**, 361–379, doi:10.1175/JCLI-D-12-00106.1.

Cibot, C., E. Maisonnave, L. Terray, and B. Dewitte, 2005: Mechanisms of tropical Pacific interannual-to-decadal variability in the ARPEGE/ORCA global coupled model. *Climate Dynamics*, **24**, 823–842, doi:10.1007/s00382-004-0513-y.

Clarke, A. J., 1994: Why Are Surface Equatorial ENSO Winds Anomalously Westerly under Anomalous Large-Scale Convection? *Journal of Climate*, **7**, 1623–1627, doi:10.1175/1520-0442(1994)007<1623:WASEEW>2.0.CO;2.

— 2010: Analytical Theory for the Quasi-Steady and Low-Frequency Equatorial Ocean Response to Wind Forcing: The "Tilt" and "Warm Water Volume" Modes. *Journal of Physical Oceanography*, **40**, 121–137, doi:10.1175/2009JPO4263.1.

— 2014: El Niño Physics and El Niño Predictability. *Annual Review of Marine Science*, **6**, 79–99, doi:10.1146/annurev-marine-010213-135026.

Clarke, A. J., S. Van Gorder, and G. Colantuono, 2007: Wind Stress Curl and ENSO Discharge/Recharge in the Equatorial Pacific. *Journal of Physical Oceanography*, **37**, 1077–1091, doi:10.1175/JPO3035.1.

Clement, A., K. Bellomo, L. N. Murphy, M. A. Cane, T. Mauritsen, G. Rädel, and B. Stevens, 2015: The Atlantic Multidecadal Oscillation without a role for ocean circulation. *Science*, **350**, 320–324, doi:10.1126/science.aab3980.

Collins, M., S.-I. An, W. Cai, A. Ganachaud, E. Guilyardi, F.-F. Jin, M. Jochum, M. Lengaigne, S. Power, A. Timmermann, G. Vecchi, and A. Wittenberg, 2010: The impact of global warming on the tropical Pacific Ocean and El Niño. *Nature Geoscience*, **3**, 391–397, doi:10.1038/ngeo868.

Compo, G. P., J. S. Whitaker, P. D. Sardeshmukh, N. Matsui, R. J. Allan, X. Yin, B. E. Gleason, R. S. Vose, G. Rutledge, P. Bessemoulin, S. Brönnimann, M. Brunet, R. I. Crouthamel, A. N. Grant, P. Y. Groisman, P. D. Jones, M. C. Kruk, A. C. Kruger, G. J. Marshall, M. Maugeri, H. Y. Mok, O. Nordli, T. F. Ross, R. M. Trigo, X. L. Wang, S. D. Woodruff, and S. J. Worley, 2011: The Twentieth Century Reanalysis Project. *Quarterly Journal of the Royal Meteorological Society*, **137**, 1–28, doi:10.1002/qj.776.

Danabasoglu, G., S. C. Bates, B. P. Briegleb, S. R. Jayne, M. Jochum, W. G. Large, S. Peacock, and S. G. Yeager, 2012: The CCSM4 Ocean Component. *Journal of Climate*, **25**, 1361–1389, doi:10.1175/JCLI-D-11-00091.1.

Dawson, A., 2016: eofs: A Library for EOF Analysis of Meteorological, Oceanographic, and Climate Data. *Journal of Open Research Software*, **4**, doi:10.5334/jors.122.

Delcroix, T., G. Eldin, M. McPhaden, and A. Morlière, 1993: Effects of westerly wind bursts upon the western equatorial Pacific Ocean, February–April 1991. *Journal of Geophysical Research*, **98**, 16379, doi:10.1029/93JC01261.

Delworth, T. L., A. J. Broccoli, A. Rosati, R. J. Stouffer, V. Balaji, J. A. Beesley, W. F. Cooke, K. W. Dixon, J. Dunne, K. A. Dunne, J. W. Durachta, K. L. Findell, P. Ginoux, A. Gnanadesikan, C. T. Gordon, S. M. Griffies, R. Gudgel, M. J. Harrison, I. M. Held, R. S. Hemler, L. W. Horowitz, S. A. Klein, T. R. Knutson, P. J. Kushner, A. R. Langenhorst, H.-C. Lee, S.-J. Lin, J. Lu, S. L. Malyshev, P. C. D. Milly, V. Ramaswamy, J. Russell, M. D. Schwarzkopf, E. Shevliakova, J. J. Sirutis, M. J. Spelman, W. F. Stern, M. Winton, A. T. Wittenberg, B. Wyman, F. Zeng, and R. Zhang, 2006: GFDL's CM2 Global Coupled Climate Models. Part I: Formulation and Simulation Characteristics. *J. Climate*, **19**, 643–674, doi:10.1175/JCLI3629.1.

Deser, C., A. S. Phillips, and M. A. Alexander, 2010: Twentieth century tropical sea surface temperature trends revisited. *Geophysical Research Letters*, **37**, doi:10.1029/2010GL043321.

Deser, C., A. S. Phillips, R. A. Tomas, Y. M. Okumura, M. A. Alexander, A. Capotondi, J. D. Scott, Y.-O. Kwon, and M. Ohba, 2012: ENSO and Pacific Decadal Variability in the Community Climate System Model Version 4. *Journal of Climate*, **25**, 2622–2651, doi:10.1175/JCLI-D-11-00301.1.

Deser, C. and J. M. Wallace, 1990: Large-Scale Atmospheric Circulation Features of Warm and Cold Episodes in the Tropical Pacific. *Journal of Climate*, **3**, 1254–1281, doi:10.1175/1520-0442(1990)003<1254:LSACFO>2.0.CO;2.

Dewitte, B., 2000: Sensitivity of an Intermediate Ocean–Atmosphere Coupled Model of the Tropical Pacific to Its Oceanic Vertical Structure. *Journal of Climate*, **13**, 2363–2388, doi:10.1175/1520-0442(2000)013<2363:SOAIOA>2.0.CO;2.

Dewitte, B., J. Choi, S.-I. An, and S. Thual, 2012: Vertical structure variability and equatorial waves during central Pacific and eastern Pacific El Niños in a coupled general circulation model. *Climate Dynamics*, **38**, 2275–2289, doi:10.1007/s00382-011-1215-x.

Dewitte, B., C. Cibot, C. Périgaud, S.-I. An, and L. Terray, 2007: Interaction between Near-Annual and ENSO Modes in a CGCM Simulation: Role of the Equatorial Background Mean State. *Journal of Climate*, **20**, 1035–1052, doi:10.1175/JCLI4060.1.

Dewitte, B. and K. Takahashi, 2017: Diversity of moderate El Niño events evolution: role of air–sea interactions in the eastern tropical Pacific. *Climate Dynamics*, doi:10.1007/s00382-017-4051-9.

Dewitte, B., S. Thual, S.-W. Yeh, S.-I. An, B.-K. Moon, and B. S. Giese, 2009: Low-Frequency Variability of Temperature in the Vicinity of the Equatorial Pacific Thermocline in SODA: Role of Equatorial Wave Dynamics and ENSO Asymmetry. *Journal of Climate*, **22**, 5783–5795, doi:10.1175/2009JCLI2764.1.

Dewitte, B., S.-W. Yeh, and S. Thual, 2013: Reinterpreting the thermocline feedback in the western-central equatorial Pacific and its relationship with the ENSO modulation. *Climate Dynamics*, **41**, 819–830, doi:10.1007/s00382-012-1504-z.

Di Lorenzo, E., G. Liguori, N. Schneider, J. C. Furtado, B. T. Anderson, and M. A. Alexander, 2015: ENSO and meridional modes: A null hypothesis for Pacific climate variability. *Geophysical Research Letters*, **42**, 9440–9448, doi:10.1002/2015GL066281.

Dijkstra, H. A. and J. D. Neelin, 1995: Ocean-Atmosphere Interaction and the Tropical Climatology. Part II: Why the Pacific Cold Tongue Is in the East. *Journal of Climate*, **8**, 1343–1359, doi:10.1175/1520-0442(1995)008<1343:OAIATT>2.0.CO;2.

DiNezio, P., A. Clement, and G. Vecchi, 2010: Reconciling Differing Views of Tropical Pacific Climate Change. *Eos, Transactions American Geophysical Union*, **91**, 141–142, doi:10.1029/2010EO160001.

DiNezio, P. N., A. C. Clement, G. A. Vecchi, B. J. Soden, B. P. Kirtman, and S. K. Lee, 2009: Climate response of the equatorial pacific to global warming. *Journal of climate*, **22**, 4873–4892, doi:10.1175/2009JCLI2982.1.

DiNezio, P. N., B. P. Kirtman, A. C. Clement, S.-K. Lee, G. A. Vecchi, and A. Wittenberg, 2012: Mean Climate Controls on the Simulated Response of ENSO to Increasing Greenhouse Gases. *J. Climate*, **25**, 7399–7420, doi:10.1175/JCLI-D-11-00494.1.

Dommenget, D., T. Bayr, and C. Frauen, 2013: Analysis of the non-linearity in the pattern and time evolution of El Niño southern oscillation. *Climate Dynamics*, **40**, 2825–2847, doi:10.1007/s00382-012-1475-0.

Dommenget, D. and M. Latif, 2002: A Cautionary Note on the Interpretation of EOFs. *Journal of Climate*, **15**, 216–225, doi:10.1175/1520-0442(2002)015<0216:ACNOTI>2.0.CO;2.

Dommenget, D. and Y. Yu, 2016: The seasonally changing cloud feedbacks contribution to the ENSO seasonal phase-locking. *Climate Dynamics*, **47**, 3661–3672, doi:10.1007/s00382-016-3034-6.

Efron, B., 1982: *The Jackknife, the Bootstrap and Other Resampling Plans*. CBMS-NSF Regional Conference Series in Applied Mathematics, Society for Industrial and Applied Mathematics.

Eisenman, I., L. Yu, and E. Tziperman, 2005: Westerly Wind Bursts: ENSO's Tail Rather than the Dog? *Journal of Climate*, **18**, 5224–5238, doi:10.1175/JCLI3588.1.

Exarchou, E., C. Prodhomme, L. Brodeau, V. Guemas, and F. Doblas-Reyes, 2018: Origin of the warm eastern tropical Atlantic SST bias in a climate model. *Climate Dynamics*, **51**, 1819–1840, doi:10.1007/s00382-017-3984-3.

Eyring, V., S. Bony, G. A. Meehl, C. A. Senior, B. Stevens, R. J. Stouffer, and K. E. Taylor, 2016: Overview of the Coupled Model Intercomparison Project Phase 6 (CMIP6) experimental design and organization. *Geoscientific Model Development*, **9**, 1937–1958, doi:10.5194/gmd-9-1937-2016.

Fasullo, J. T., B. L. Otto-Bliesner, and S. Stevenson, 2018: ENSO's Changing Influence on Temperature, Precipitation, and Wildfire in a Warming Climate. *Geophysical Research Letters*, **45**, 9216–9225, doi:10.1029/2018GL079022.

Fedorov, A. V., 2002: The response of the coupled tropical ocean–atmosphere to westerly wind bursts. *Quarterly Journal of the Royal Meteorological Society*, **128**, 1–23, doi:10.1002/qj.200212857901.

— 2010: Ocean Response to Wind Variations, Warm Water Volume, and Simple Models of ENSO in the Low-Frequency Approximation. *Journal of Climate*, **23**, 3855–3873, doi:10.1175/2010JCLI3044.1.

Fedorov, A. V., S. Hu, M. Lengaigne, and E. Guilyardi, 2015: The impact of westerly wind bursts and ocean initial state on the development, and diversity of El Niño events. *Climate Dynamics*, **44**, 1381–1401, doi:10.1007/s00382-014-2126-4.

Fedorov, A. V. and S. G. Philander, 2000: Is El Niño Changing? *Science*, **288**, 1997–2002, doi:10.1126/science.288.5473.1997.

— 2001: A Stability Analysis of Tropical Ocean–Atmosphere Interactions: Bridging Measurements and Theory for El Niño. *Journal of Climate*, **14**, 3086–3101, doi:10.1175/1520-0442(2001)014<3086:ASAOTO>2.0.CO;2.

Fischer, H., K. J. Meissner, A. C. Mix, N. J. Abram, J. Austermann, V. Brovkin, E. Capron, D. Colombaroli, A.-L. Daniau, K. A. Dyez, T. Felis, S. A. Finkelstein, S. L. Jaccard, E. L. McClymont, A. Rovere, J. Sutter, E. W. Wolff, S. Affolter, P. Bakker, J. A. Ballesteros-Cánovas, C. Barbante, T. Caley, A. E. Carlson, O. Churakova, G. Cortese, B. F. Cumming, B. A. S. Davis, A. de Vernal, J. Emile-Geay, S. C. Fritz, P. Gierz, J. Gottschalk, M. D. Holloway, F. Joos, M. Kucera, M.-F. Loutre, D. J. Lunt, K. Marcisz, J. R. Marlon, P. Martinez, V. Masson-Delmotte, C. Nehrbass-Ahles, B. L. Otto-Bliesner, C. C. Raible, B. Risebrobakken, M. F. Sánchez Goñi, J. S. Arrigo, M. Sarnthein, J. Sjolte, T. F. Stocker, P. A.

Velasquez Alvárez, W. Tinner, P. J. Valdes, H. Vogel, H. Wanner, Q. Yan, Z. Yu, M. Ziegler, and L. Zhou, 2018: Palaeoclimate constraints on the impact of 2 °C anthropogenic warming and beyond. *Nature Geoscience*, **11**, 474–485, doi:10.1038/s41561-018-0146-0.

Flato, G. M., 2011: Earth system models: an overview: Earth system models. *Wiley Interdisciplinary Reviews: Climate Change*, **2**, 783–800, doi:10.1002/wcc.148.

Frauen, C. and D. Dommenget, 2010: El Niño and La Niña amplitude asymmetry caused by atmospheric feedbacks. *Geophysical Research Letters*, **37**, doi:10.1029/2010GL044444.

Friedlingstein, P., P. Cox, R. Betts, L. Bopp, W. von Bloh, V. Brovkin, P. Cadule, S. Doney, M. Eby, I. Fung, G. Bala, J. John, C. Jones, F. Joos, T. Kato, M. Kawamiya, W. Knorr, K. Lindsay, H. D. Matthews, T. Raddatz, P. Rayner, C. Reick, E. Roeckner, K.-G. Schnitzler, R. Schnur, K. Strassmann, A. J. Weaver, C. Yoshikawa, and N. Zeng, 2006: Climate–Carbon Cycle Feedback Analysis: Results from the C4mip Model Intercomparison. *Journal of Climate*, **19**, 3337–3353, doi:10.1175/JCLI3800.1.

Gadgil, S., P. V. Joseph, and N. V. Joshi, 1984: Ocean–atmosphere coupling over monsoon regions. *Nature*, **312**, 141–143, doi:10.1038/312141a0.

Gebbie, G., I. Eisenman, A. Wittenberg, and E. Tziperman, 2007: Modulation of Westerly Wind Bursts by Sea Surface Temperature: A Semistochastic Feedback for ENSO. *Journal of the Atmospheric Sciences*, **64**, 3281–3295, doi:10.1175/JAS4029.1.

Gent, P. R., G. Danabasoglu, L. J. Donner, M. M. Holland, E. C. Hunke, S. R. Jayne, D. M. Lawrence, R. B. Neale, P. J. Rasch, M. Vertenstein, P. H. Worley, Z.-L. Yang, and M. Zhang, 2011: The Community Climate System Model Version 4. *J. Climate*, **24**, 4973–4991, doi:10.1175/2011JCLI4083.1.

Giese, B. S. and S. Ray, 2011: El Niño variability in simple ocean data assimilation (SODA), 1871-2008. *Journal of Geophysical Research (Oceans)*, **116**, C02024, doi:10.1029/2010JC006695.

Gill, A. E., 1980: Some simple solutions for heat-induced tropical circulation. *Quarterly Journal of the Royal Meteorological Society*, **106**, 447–462, doi:10.1002/qj.49710644905.

Goddard, L. and M. Dilley, 2005: El Niño: Catastrophe or Opportunity. *Journal of Climate*, **18**, 651–665, doi:10.1175/JCLI-3277.1.

Graham, F. S., A. T. Wittenberg, J. N. Brown, S. J. Marsland, and N. J. Holbrook, 2017: Understanding the double peaked El Niño in coupled GCMs. *Climate Dynamics*, **48**, 2045–2063, doi:10.1007/s00382-016-3189-1.

Graham, N. E. and T. P. Barnett, 1987: Sea Surface Temperature, Surface Wind Divergence, and Convection over Tropical Oceans. *Science*, **238**, 657–659, doi:10.1126/science.238.4827.657.

Griffies, S., A. J. Adcroft, H. Hewitt, S. Boning, E. Chassignet, G. Danabasoglu, S. Danilov, E. Deleersnijder, H. Drange, and Matthew H. England, 2010: Problems and Prospects in Large-Scale Ocean Circulation Models. *Proceedings of OceanObs'09: Sustained Ocean Observations and Information for Society*, European Space Agency, 410–431.

Griffies, S. M., M. J. Harrison, R. C. Pacanowski, A. Rosati, Z. Liang, M. Schmidt, H. Simmons, and R. Slater, 2004: A Technical Guide to MOM4. GFDL group technical report No.5, 342.

Guan, C. and M. J. McPhaden, 2016: Ocean Processes Affecting the Twenty-First-Century Shift in ENSO SST Variability. *Journal of Climate*, **29**, 6861–6879, doi:10.1175/JCLI-D-15-0870.1.

Guilyardi, E., 2006: El Niño–mean state–seasonal cycle interactions in a multi-model ensemble. *Climate Dynamics*, **26**, 329–348, doi:10.1007/s00382-005-0084-6.

Guilyardi, E., P. Braconnot, F.-F. Jin, S. T. Kim, M. Kolasinski, T. Li, and I. Musat, 2009a: Atmosphere Feedbacks during ENSO in a Coupled GCM with a Modified Atmospheric Convection Scheme. *Journal of Climate*, **22**, 5698–5718, doi:10.1175/2009JCLI2815.1.

Guilyardi, E., A. Wittenberg, A. Fedorov, M. Collins, C. Wang, A. Capotondi, G. J. van Oldenborgh, and T. Stockdale, 2009b: Understanding El Niño in Ocean–Atmosphere General Circulation Models: Progress and Challenges. *Bull. Amer. Meteor. Soc.*, **90**, 325–340, doi:10.1175/2008BAMS2387.1.

Gushchina, D. and B. Dewitte, 2012: Intraseasonal Tropical Atmospheric Variability Associated with the Two Flavors of El Niño. *Monthly Weather Review*, **140**, 3669–3681, doi:10.1175/MWR-D-11-00267.1.

— 2019: Decadal modulation of the relationship between intraseasonal tropical variability and ENSO. *Climate Dynamics*, **52**, 2091–2103, doi:10.1007/s00382-018-4235-y.

Halpert, M. S. and C. F. Ropelewski, 1992: Surface Temperature Patterns Associated with the Southern Oscillation. *Journal of Climate*, **5**, 577–593, doi:10.1175/1520-0442(1992)005<0577:STPAWT>2.0.CO;2.

Ham, Y.-G. and J.-S. Kug, 2012: How well do current climate models simulate two types of El Niño? *Climate Dynamics*, **39**, 383–398, doi:10.1007/s00382-011-1157-3.

Hameed, S. N., D. Jin, and V. Thilakan, 2018: A model for super El Niños. *Nature Communications*, **9**, 2528, doi:10.1038/s41467-018-04803-7.

Harper, S., 2000: Thermocline ventilation and pathways of tropical–subtropical water mass exchange. *Tellus A: Dynamic Meteorology and Oceanography*, **52**, 330–345, doi:10.3402/tellusa.v52i3.12269.

Harrison, D. E. and G. A. Vecchi, 1997: Westerly Wind Events in the Tropical Pacific, 1986–95. *Journal of Climate*, **10**, 3131–3156, doi:10.1175/1520-0442(1997)010<3131:WWEITT>2.0.CO;2.

— 1999: On the termination of El Niño. *Geophysical Research Letters*, **26**, 1593–1596, doi:10.1029/1999GL900316.

Hayashi, M. and M. Watanabe, 2017: ENSO Complexity Induced by State Dependence of Westerly Wind Events. *Journal of Climate*, **30**, 3401–3420, doi:10.1175/JCLI-D-16-0406.1.

Hoerling, M. P., A. Kumar, and M. Zhong, 1997: El Niño, La Niña, and the Nonlinearity of Their Teleconnections. *Journal of Climate*, **10**, 1769–1786, doi:10.1175/1520-0442(1997)010<1769:ENOLNA>2.0.CO;2.

Holmes, R. M., S. McGregor, A. Santoso, and M. H. England, 2018: Contribution of tropical instability waves to ENSO irregularity. *Climate Dynamics*, doi:10.1007/s00382-018-4217-0.

Hong, L.-C., LinHo, and F.-F. Jin, 2014: A Southern Hemisphere booster of super El Niño. *Geophysical Research Letters*, **41**, 2142–2149, doi:10.1002/2014GL059370.

Hoyer, S. and J. J. Hamman, 2017: xarray: N-D labeled Arrays and Datasets in Python. *Journal of Open Research Software*, **5**, doi:10.5334/jors.148.

Hu, S. and A. V. Fedorov, 2017: The extreme El Niño of 2015–2016: the role of westerly and easterly wind bursts, and preconditioning by the failed 2014 event. *Climate Dynamics*, doi:10.1007/s00382-017-3531-2.

Hu, S., A. V. Fedorov, M. Lengaigne, and E. Guilyardi, 2014: The impact of westerly wind bursts on the diversity and predictability of El Niño events: An ocean energetics perspective. *Geophysical Research Letters*, **41**, 4654–4663, doi:10.1002/2014GL059573.

Hu, Z.-Z., A. Kumar, B. Jha, W. Wang, B. Huang, and B. Huang, 2012: An analysis of warm pool and cold tongue El Niños: air–sea coupling processes, global influences, and recent trends. *Climate Dynamics*, **38**, 2017–2035, doi:10.1007/s00382-011-1224-9.

Hu, Z.-Z., A. Kumar, J. Zhu, B. Huang, Y.-h. Tseng, and X. Wang, 2017: On the Shortening of the Lead Time of Ocean Warm Water Volume to ENSO SST Since 2000. *Scientific Reports*, **7**, doi:10.1038/s41598-017-04566-z.

Hunke, E. C. and W. Lipscomb, 2010: CICE: The Los Alamos sea ice model documentation and software user's manual version 4.0 LA-CC-06-012. *Tech. Rep. LA-CC-06-012*.

Hurrell, J., T. Delworth, G. Danabasoglu, H. Drange, S. Griffies, N. Holbrook, B. Kirtman, N. Keenlyside, M. Latif, J. Marotzke, G. Meehl, T. Palmer, H. Pohlmann, T. Rosati, R. Seager, D. Smith, R. Sutton, A. Timmermann, K. E. Trenberth, and J. Tribbia, 2009: Decadal climate prediction: opportunities and challenges. *Proceedings of OceanObs'09: Sustained Ocean Observations and Information for Society*.

Hurrell, J. W., M. M. Holland, P. R. Gent, S. Ghan, J. E. Kay, P. J. Kushner, J.-F. Lamarque, W. G. Large, D. Lawrence, K. Lindsay, W. H. Lipscomb, M. C. Long, N. Mahowald, D. R. Marsh, R. B. Neale, P. Rasch, S. Vavrus, M. Vertenstein, D. Bader, W. D. Collins, J. J. Hack, J. Kiehl, and S. Marshall, 2013: The Community Earth System Model: A Framework for Collaborative Research. *Bull. Amer. Meteor. Soc.*, **94**, 1339–1360, doi:10.1175/BAMS-D-12-00121.1.

Hwang, Y.-T. and D. M. W. Frierson, 2013: Link between the double-Intertropical Convergence Zone problem and cloud biases over the Southern Ocean. *PNAS*, 201213302, doi:10.1073/pnas.1213302110.

Izumo, T., M. Lengaigne, J. Vialard, I. Suresh, and Y. Planton, 2018: On the physical interpretation of the lead relation between Warm Water Volume and the El Niño Southern Oscillation. *Climate Dynamics*, doi:10.1007/s00382-018-4313-1.

Jauregui, Y. R. and K. Takahashi, 2018: Simple physical-empirical model of the precipitation distribution based on a tropical sea surface temperature threshold and the effects of climate change. *Climate Dynamics*, **50**, 2217–2237, doi:10.1007/s00382-017-3745-3.

Jekabsons, G., 2013: *ARESLab: Adaptive regression splines toolbox for Matlab. http://www.cs.rtu. lv/jekabsons/regression.html*.

Jeong, H.-I. and J.-B. Ahn, 2017: A new method to classify ENSO events into eastern and central Pacific types. *International Journal of Climatology*, **37**, 2193–2199, doi:10.1002/joc.4813.

Jin, F.-F., 1997a: An Equatorial Ocean Recharge Paradigm for ENSO. Part I: Conceptual Model. *J. Atmos. Sci.*, **54**, 811–829, doi:10.1175/1520-0469(1997)054<0811:AEORPF>2.0.CO;2.

— 1997b: An Equatorial Ocean Recharge Paradigm for ENSO. Part II: A Stripped-Down Coupled Model. *Journal of the Atmospheric Sciences*, **54**, 830–847, doi:10.1175/1520-0469(1997)054<0830:AEORPF>2.0.CO;2.

Jin, F.-F. and S.-I. An, 1999: Thermocline and Zonal Advective Feedbacks Within the Equatorial Ocean Recharge Oscillator Model for ENSO. *Geophysical Research Letters*, **26**, 2989–2992, doi:10.1029/1999GL002297.

Jin, F.-F., S.-I. An, A. Timmermann, and J. Zhao, 2003a: Strong El Niño events and nonlinear dynamical heating. *Geophysical Research Letters*, **30**, 20–1–20–1, doi:10.1029/2002GL016356.

Jin, F.-F., S. T. Kim, and L. Bejarano, 2006: A coupled-stability index for ENSO. *Geophysical Research Letters*, **33**, doi:10.1029/2006GL027221.

Jin, F.-F., J.-S. Kug, S.-I. An, and I.-S. Kang, 2003b: A near-annual coupled ocean-atmosphere mode in the equatorial Pacific ocean. *Geophysical Research Letters*, **30**, doi:10.1029/2002GL015983.

Jin, F.-F., L. Lin, A. Timmermann, and J. Zhao, 2007: Ensemble-mean dynamics of the ENSO recharge oscillator under state-dependent stochastic forcing. *Geophysical Research Letters*, **34**, doi:10.1029/2006GL027372.

Jin, F.-F. and J. D. Neelin, 1993: Modes of Interannual Tropical Ocean–Atmosphere Interaction—a Unified View. Part I: Numerical Results. *Journal of the Atmospheric Sciences*, **50**, 3477–3503, doi:10.1175/1520-0469(1993)050<3477:MOITOI>2.0.CO;2.

Jin, F.-F., J. D. Neelin, and M. Ghil, 1994: El Nino on the Devil's Staircase: Annual Subharmonic Steps to Chaos. *Science*, **264**, 70–72, doi:10.1126/science.264.5155.70.

Johnson, N. C., 2013: How Many ENSO Flavors Can We Distinguish? *Journal of Climate*, **26**, 4816–4827, doi:10.1175/JCLI-D-12-00649.1.

Johnson, N. C. and S.-P. Xie, 2010: Changes in the sea surface temperature threshold for tropical convection. *Nature Geoscience*, **3**, 842–845, doi:10.1038/ngeo1008.

Kang, I.-S. and J.-S. Kug, 2002: El Niño and La Niña sea surface temperature anomalies: Asymmetry characteristics associated with their wind stress anomalies. *Journal of Geophysical Research*, **107**, doi:10.1029/2001JD000393.

Kao, H.-Y. and J.-Y. Yu, 2009: Contrasting Eastern-Pacific and Central-Pacific Types of ENSO. *Journal of Climate*, **22**, 615–632, doi:10.1175/2008JCLI2309.1.

Karamperidou, C., P. N. Di Nezio, A. Timmermann, F.-F. Jin, and K. M. Cobb, 2015: The response of ENSO flavors to mid-Holocene climate: Implications for proxy interpretation. *Paleoceanography*, **30**, 2014PA002742, doi:10.1002/2014PA002742.

Karamperidou, C., F.-F. Jin, and J. L. Conroy, 2017: The importance of ENSO nonlinearities in tropical pacific response to external forcing. *Climate Dynamics*, **49**, 2695–2704, doi:10.1007/s00382-016-3475-y.

Kay, J. E., C. Deser, A. Phillips, A. Mai, C. Hannay, G. Strand, J. M. Arblaster, S. C. Bates, G. Danabasoglu, J. Edwards, M. Holland, P. Kushner, J.-F. Lamarque, D. Lawrence, K. Lindsay, A. Middleton, E. Munoz, R. Neale, K. Oleson, L. Polvani, and M. Vertenstein, 2015: The Community Earth System Model (CESM) Large Ensemble Project: A Community Resource for Studying Climate Change in the Presence of Internal Climate Variability. *Bulletin of the American Meteorological Society*, **96**, 1333–1349, doi:10.1175/BAMS-D-13-00255.1.

Kerr, R. A., 1999: Big El Niños Ride the Back of Slower Climate Change. *Science*, **283**, 1108–1109, doi:10.1126/science.283.5405.1108.

Kessler, W. S., 2002: Is ENSO a cycle or a series of events? *Geophysical Research Letters*, **29**, 2125, doi:10.1029/2002GL015924.

Kessler, W. S. and R. Kleeman, 2000: Rectification of the Madden–Julian Oscillation into the ENSO Cycle. *Journal of Climate*, **13**, 3560–3575, doi:10.1175/1520-0442(2000)013<3560:ROTMJO>2.0.CO;2.

Kessler, W. S. and M. J. McPhaden, 1995: Oceanic Equatorial Waves and the 1991–93 El Niño. *Journal of Climate*, **8**, 1757–1774, doi:10.1175/1520-0442(1995)008<1757:OEWATE>2.0.CO;2.

Khodri, M., T. Izumo, J. Vialard, S. Janicot, C. Cassou, M. Lengaigne, J. Mignot, G. Gastineau, E. Guilyardi, N. Lebas, A. Robock, and M. J. McPhaden, 2017: Tropical explosive volcanic eruptions can trigger El Niño by cooling tropical Africa. *Nature Communications*, **8**, 778, doi:10.1038/s41467-017-00755-6.

Kim, D., 2011: El Niño-Southern Oscillation sensitivity to cumulus entrainment in a coupled general circulation model. *Journal of Geophysical Research*, **116**, D22112, doi:10.1029/2011JD016526.

Kim, H.-M., P. J. Webster, and J. A. Curry, 2009: Impact of Shifting Patterns of Pacific Ocean Warming on North Atlantic Tropical Cyclones. *Science*, **325**, 77–80, doi:10.1126/science.1174062.

— 2011: Modulation of North Pacific Tropical Cyclone Activity by Three Phases of ENSO. *Journal of Climate*, **24**, 1839–1849, doi:10.1175/2010JCLI3939.1.

Kim, S. T., W. Cai, F.-F. Jin, and J.-Y. Yu, 2014: ENSO stability in coupled climate models and its association with mean state. *Climate Dynamics*, **42**, 3313–3321, doi:10.1007/s00382-013-1833-6.

Kim, S. T. and F.-F. Jin, 2011: An ENSO stability analysis. Part II: results from the twentieth and twenty-first century simulations of the CMIP3 models. *Climate Dynamics*, **36**, 1609–1627, doi:10.1007/s00382-010-0872-5.

Kim, S. T. and J.-Y. Yu, 2012: The two types of ENSO in CMIP5 models. *Geophysical Research Letters*, **39**, doi:10.1029/2012GL052006.

Kirchmeier-Young, M. C., F. W. Zwiers, and N. P. Gillett, 2016: Attribution of Extreme Events in Arctic Sea Ice Extent. *Journal of Climate*, **30**, 553–571, doi:10.1175/JCLI-D-16-0412.1.

Kug, J.-S., J. Choi, S.-I. An, F.-F. Jin, and A. T. Wittenberg, 2010: Warm Pool and Cold Tongue El Niño Events as Simulated by the GFDL 2.1 Coupled GCM. *Journal of Climate*, **23**, 1226–1239, doi:10.1175/2009JCLI3293.1.

Kug, J.-S., F.-F. Jin, and S.-I. An, 2009: Two Types of El Niño Events: Cold Tongue El Niño and Warm Pool El Niño. *J. Climate*, **22**, 1499–1515, doi:10.1175/2008JCLI2624.1.

Kumar, A. and Z.-Z. Hu, 2014: Interannual and interdecadal variability of ocean temperature along the equatorial Pacific in conjunction with ENSO. *Climate Dynamics*, **42**, 1243–1258, doi:10.1007/s00382-013-1721-0.

Kumar, K. K., 1999: On the Weakening Relationship Between the Indian Monsoon and ENSO. *Science*, **284**, 2156–2159, doi:10.1126/science.284.5423.2156.

Lai, A. W.-C., M. Herzog, and H.-F. Graf, 2015: Two key parameters for the El Niño continuum: zonal wind anomalies and Western Pacific subsurface potential temperature. *Climate Dynamics*, **45**, 3461–3480, doi:10.1007/s00382-015-2550-0.

Lamarque, J.-F., T. C. Bond, V. Eyring, C. Granier, A. Heil, Z. Klimont, D. Lee, C. Liousse, A. Mieville, B. Owen, M. G. Schultz, D. Shindell, S. J. Smith, E. Stehfest, J. Van Aardenne, O. R. Cooper, M. Kainuma, N. Mahowald, J. R. McConnell, V. Naik, K. Riahi, and D. P. van Vuuren, 2010: Historical (1850–2000) gridded anthropogenic and biomass burning emissions of reactive gases and aerosols: methodology and application. *Atmospheric Chemistry and Physics*, **10**, 7017–7039, doi:10.5194/acp-10-7017-2010.

Large, W. G., G. Danabasoglu, S. C. Doney, and J. C. McWilliams, 1997: Sensitivity to surface forcing and boundary layer mixing in a global ocean model: Annual-mean climatology. *Journal of Physical Oceanography*, **27**, 2418–2447.

Large, W. G. and S. G. Yeager, 2009: The global climatology of an interannually varying air–sea flux data set. *Climate Dynamics*, **33**, 341–364, doi:10.1007/s00382-008-0441-3.

Larkin, N. K. and D. E. Harrison, 2005a: Global seasonal temperature and precipitation anomalies during El Niño autumn and winter. *Geophysical Research Letters*, **32**, doi:10.1029/2005GL022860.

— 2005b: On the definition of El Niño and associated seasonal average U.S. weather anomalies. *Geophysical Research Letters*, **32**, doi:10.1029/2005GL022738.

Larson, S. M. and B. P. Kirtman, 2014: The Pacific Meridional Mode as an ENSO Precursor and Predictor in the North American Multimodel Ensemble. *Journal of Climate*, **27**, 7018–7032, doi:10.1175/JCLI-D-14-00055.1.

Larson, S. M., K. V. Pegion, and B. P. Kirtman, 2018: The South Pacific Meridional Mode as a Thermally Driven Source of ENSO Amplitude Modulation and Uncertainty. *Journal of Climate*, **31**, 5127–5145, doi:10.1175/JCLI-D-17-0722.1.

Latif, M., 1998: Dynamics of Interdecadal Variability in Coupled Ocean–Atmosphere Models. *Journal of Climate*, **11**, 602–624, doi:10.1175/1520-0442(1998)011<0602:DOIVIC>2.0.CO;2.

Latif, M., R. Kleeman, and C. Eckert, 1997: Greenhouse Warming, Decadal Variability, or El Niño? An Attempt to Understand the Anomalous 1990s. *Journal of Climate*, **10**, 2221–2239, doi:10.1175/1520-0442(1997)010<2221:GWDVOE>2.0.CO;2.

Lawrence, D. M., K. W. Oleson, M. G. Flanner, P. E. Thornton, S. C. Swenson, P. J. Lawrence, X. Zeng, Z.-L. Yang, S. Levis, K. Sakaguchi, G. B. Bonan, and A. G. Slater, 2011: Parameterization improvements and functional and structural advances in Version 4 of the Community Land Model. *Journal of Advances in Modeling Earth Systems*, **3**, doi:10.1029/2011MS00045.

Lee, S.-K., P. N. DiNezio, E.-S. Chung, S.-W. Yeh, A. T. Wittenberg, and C. Wang, 2014: Spring persistence, transition, and resurgence of El Niño: Two modes of inter-El Niño variability. *Geophysical Research Letters*, **41**, 8578–8585, doi:10.1002/2014GL062484.

Lee, T. and M. J. McPhaden, 2010: Increasing intensity of El Niño in the central-equatorial Pacific. *Geophysical Research Letters*, **37**, doi:10.1029/2010GL044007.

Lengaigne, M., J.-P. Boulanger, C. Menkes, G. Madec, P. Delecluse, E. Guilyardi, and J. Slingo, 2003: The March 1997 Westerly Wind Event and the Onset of the 1997/98 El Niño: Understanding the Role of the Atmospheric Response. *Journal of Climate*, **16**, 3330–3343, doi:10.1175/1520-0442(2003)016<3330:TMWWEA>2.0.CO;2.

Lengaigne, M., J.-P. Boulanger, C. Menkes, S. Masson, G. Madec, and P. Delecluse, 2002: Ocean response to the March 1997 Westerly Wind Event. *Journal of Geophysical Research: Oceans*, **107**, SRF 16–1–SRF 16–20, doi:10.1029/2001JC000841.

Lengaigne, M., J.-P. Boulanger, C. Menkes, and H. Spencer, 2006: Influence of the Seasonal Cycle on the Termination of El Niño Events in a Coupled General Circulation Model. *Journal of Climate*, **19**, 1850–1868, doi:10.1175/JCLI3706.1.

Lengaigne, M., E. Guilyardi, J.-P. Boulanger, C. Menkes, P. Delecluse, P. Inness, J. Cole, and J. Slingo, 2004: Triggering of El Niño by westerly wind events in a coupled general circulation model. *Climate Dynamics*, **23**, 601–620, doi:10.1007/s00382-004-0457-2.

Lengaigne, M. and G. A. Vecchi, 2010: Contrasting the termination of moderate and extreme El Niño events in coupled general circulation models. *Climate Dynamics*, **35**, 299–313, doi:10.1007/s00382-009-0562-3.

Levine, A., F. F. Jin, and M. J. McPhaden, 2016: Extreme Noise–Extreme El Niño: How State-Dependent Noise Forcing Creates El Niño–La Niña Asymmetry. *Journal of Climate*, **29**, 5483–5499, doi:10.1175/JCLI-D-16-0091.1.

Levitus, S., 1983: Climatological Atlas of the World Ocean. *Eos, Transactions American Geophysical Union*, **64**, 962, doi:10.1029/EO064i049p00962-02.

Li, G. and S.-P. Xie, 2014: Tropical Biases in CMIP5 Multimodel Ensemble: The Excessive Equatorial Pacific Cold Tongue and Double ITCZ Problems. *Journal of Climate*, **27**, 1765–1780, doi:10.1175/JCLI-D-13-00337.1.

Li, G., S.-P. Xie, Y. Du, and Y. Luo, 2016: Effects of excessive equatorial cold tongue bias on the projections of tropical Pacific climate change. Part I: the warming pattern in CMIP5 multi-model ensemble. *Climate Dynamics*, **47**, 3817–3831, doi:10.1007/s00382-016-3043-5.

Li, X., C. Li, J. Ling, and Y. Tan, 2015: The Relationship between Contiguous El Niño and La Niña Revealed by Self-Organizing Maps. *Journal of Climate*, **28**, 8118–8134, doi:10.1175/JCLI-D-15-0123.1.

Li, Y., J. Li, W. Zhang, Q. Chen, J. Feng, F. Zheng, W. Wang, and X. Zhou, 2017: Impacts of the Tropical Pacific Cold Tongue Mode on ENSO Diversity Under Global Warming. *Journal of Geophysical Research: Oceans*, **122**, 8524–8542, doi:10.1002/2017JC013052.

Lian, T. and D. Chen, 2012: An Evaluation of Rotated EOF Analysis and Its Application to Tropical Pacific SST Variability. *Journal of Climate*, **25**, 5361–5373, doi:10.1175/JCLI-D-11-00663.1.

Lian, T., D. Chen, Y. Tang, X. Liu, J. Feng, and L. Zhou, 2018a: Linkage Between Westerly Wind Bursts and Tropical Cyclones. *Geophysical Research Letters*, **45**, 11,431–11,438, doi:10.1029/2018GL079745.

Lian, T., D. Chen, J. Ying, P. Huang, and Y. Tang, 2018b: Tropical Pacific trends under global warming: El Niño-like or La Niña-like? *National Science Review*, **5**, 810–812, doi:10.1093/nsr/nwy134.

Liang, J., X.-Q. Yang, and D.-Z. Sun, 2017: Factors Determining the Asymmetry of ENSO. *Journal of Climate*, **30**, 6097–6106, doi:10.1175/JCLI-D-16-0923.1.

Liu, Y. and G. Chen, 2018: Intensified influence of the ENSO Modoki on boreal summer tropical cyclone genesis over the western North Pacific since the early 1990s. *International Journal of Climatology*, **38**, e1258–e1265, doi:10.1002/joc.5347.

Liu, Y., K. M. Cobb, H. Song, Q. Li, C.-Y. Li, T. Nakatsuka, Z. An, W. Zhou, Q. Cai, J. Li, S. W. Leavitt, C. Sun, R. Mei, C.-C. Shen, M.-H. Chan, J. Sun, L. Yan, Y. Lei, Y. Ma, X. Li, D. Chen, and H. W. Linderholm, 2017: Recent enhancement of central Pacific El Niño variability relative to last eight centuries. *Nature Communications*, **8**, 15386, doi:10.1038/ncomms15386.

Liu, Y., X. San Liang, and R. H. Weisberg, 2007: Rectification of the Bias in the Wavelet Power Spectrum. *Journal of Atmospheric and Oceanic Technology*, **24**, 2093–2102, doi:10.1175/2007JTECHO511.1.

Lloyd, J., E. Guilyardi, and H. Weller, 2011: The role of atmosphere feedbacks during ENSO in the CMIP3 models. Part II: using AMIP runs to understand the heat flux feedback mechanisms. *Climate Dynamics*, **37**, 1271–1292, doi:10.1007/s00382-010-0895-y.

— 2012: The Role of Atmosphere Feedbacks during ENSO in the CMIP3 Models. Part III: The Shortwave Flux Feedback. *Journal of Climate*, **25**, 4275–4293, doi:10.1175/JCLI-D-11-00178.1.

Lloyd, J., E. Guilyardi, H. Weller, and J. Slingo, 2009: The role of atmosphere feedbacks during ENSO in the CMIP3 models. *Atmospheric Science Letters*, **10**, 170–176, doi:10.1002/asl.227.

Long, J. and C. Robertson, 2018: Comparing spatial patterns. *Geography Compass*, **12**, e12356, doi:10.1111/gec3.12356.

Lorenz, E. N., 1963: Deterministic Nonperiodic Flow. *Journal of the Atmospheric Sciences*, **20**, 130–141, doi:10.1175/1520-0469(1963)020<0130:DNF>2.0.CO;2.

Lough, J., A. Sen Gupta, S. Power, M. Grose, and S. Mcgree, 2016: Observed and projected changes in surface climate of tropical Pacific Islands. *Vulnerability of Pacific Island agriculture and forestry to climate change*, M. Taylor, A. McGregor, and B. Dawson, eds., Pacific Community, 47–102.

Lu, Q., Z. Ruan, D.-P. Wang, D. Chen, and Q. Wu, 2017: Zonal Transport from the Western Boundary and Its Role in Warm Water Volume Changes during ENSO. *Journal of Physical Oceanography*, **47**, 211–225, doi:10.1175/JPO-D-16-0112.1.

Lu, Z., Z. Liu, J. Zhu, and K. M. Cobb, 2018: A Review of Paleo El Niño-Southern Oscillation. *Atmosphere*, **9**, 130, doi:10.3390/atmos9040130.

Lübbecke, J. F. and M. J. McPhaden, 2014: Assessing the Twenty-First-Century Shift in ENSO Variability in Terms of the Bjerknes Stability Index. *Journal of Climate*, **27**, 2577–2587, doi:10.1175/JCLI-D-13-00438.1.

L'Heureux, M. L., K. Takahashi, A. B. Watkins, A. G. Barnston, E. J. Becker, T. E. Di Liberto, F. Gamble, J. Gottschalck, M. S. Halpert, B. Huang, K. Mosquera-Vásquez, and A. T. Wittenberg, 2017: Observing and Predicting the 2015/16 El Niño. *Bulletin of the American Meteorological Society*, **98**, 1363–1382, doi:10.1175/BAMS-D-16-0009.1.

Ma, J. and S.-P. Xie, 2013: Regional Patterns of Sea Surface Temperature Change: A Source of Uncertainty in Future Projections of Precipitation and Atmospheric Circulation. *Journal of Climate*, **26**, 2482–2501, doi:10.1175/JCLI-D-12-00283.1.

Maes, C., J. Picaut, Y. Kuroda, and K. Ando, 2004: Characteristics of the convergence zone at the eastern edge of the Pacific warm pool. *Geophysical Research Letters*, **31**, n/a–n/a, doi:10.1029/2004GL019867.

Mann, H. B. and D. R. Whitney, 1947: On a Test of Whether one of Two Random Variables is Stochastically Larger than the Other. *Ann. Math. Statist.*, **18**, 50–60, doi:10.1214/aoms/1177730491.

Mantua, N. J. and D. S. Battisti, 1994: Evidence for the Delayed Oscillator Mechanism for ENSO: The "Observed" Oceanic Kelvin Mode in the Far Western Pacific. *Journal of Physical Oceanography*, **24**, 691–699, doi:10.1175/1520-0485(1994)024<0691:EFTDOM>2.0.CO;2.

Marathe, S., K. Ashok, P. Swapna, and T. P. Sabin, 2015: Revisiting El Niño Modokis. *Climate Dynamics*, **45**, 3527–3545, doi:10.1007/s00382-015-2555-8.

Matveeva, T., D. Gushchina, and B. Dewitte, 2018: The seasonal relationship between intraseasonal tropical variability and ENSO in CMIP5. *Geoscientific Model Development*, **11**, 2373–2392, doi:10.5194/gmd-11-2373-2018.

McGregor, S., A. Timmermann, M. H. England, O. Elison Timm, and A. T. Wittenberg, 2013: Inferred changes in El Niño–Southern Oscillation variance over the past six centuries. *Climate of the Past*, **9**, 2269–2284, doi:10.5194/cp-9-2269-2013.

McGregor, S., A. Timmermann, F.-F. Jin, and W. S. Kessler, 2016: Charging El Niño with off-equatorial westerly wind events. *Climate Dynamics*, **47**, 1111–1125, doi:10.1007/s00382-015-2891-8.

McGregor, S., A. Timmermann, N. Schneider, M. F. Stuecker, and M. H. England, 2012: The Effect of the South Pacific Convergence Zone on the Termination of El Niño Events and the Meridional Asymmetry of ENSO. *Journal of Climate*, **25**, 5566–5586, doi:10.1175/JCLI-D-11-00332.1.

McPhaden, M., A. Busalacchi, and D. Anderson, 2010: A TOGA Retrospective. *Oceanography*, **23**, 86–103, doi:10.5670/oceanog.2010.26.

McPhaden, M. J., 1999: El Niño: The child prodigy of 1997-98. *Nature*, **398**, 559–562, doi:10.1038/19193.

— 2012: A 21st century shift in the relationship between ENSO SST and warm water volume anomalies. *Geophysical Research Letters*, **39**, doi:10.1029/2012GL051826.

McPhaden, M. J., A. J. Busalacchi, R. Cheney, J.-R. Donguy, K. S. Gage, D. Halpern, M. Ji, P. Julian, G. Meyers, G. T. Mitchum, P. P. Niiler, J. Picaut, R. W. Reynolds, N. Smith, and K. Takeuchi, 1998: The Tropical Ocean-Global Atmosphere observing system: A decade of progress. *Journal of Geophysical Research: Oceans*, **103**, 14169–14240, doi:10.1029/97JC02906.

McPhaden, M. J., T. Lee, and D. McClurg, 2011: El Niño and its relationship to changing background conditions in the tropical Pacific Ocean. *Geophysical Research Letters*, **38**, doi:10.1029/2011GL048275.

McPhaden, M. J. and X. Yu, 1999: Equatorial waves and the 1997-98 El Niño. *Geophysical Research Letters*, **26**, 2961–2964, doi:10.1029/1999GL004901.

McPhaden, M. J., S. E. Zebiak, and M. H. Glantz, 2006: ENSO as an Integrating Concept in Earth Science. *Science*, **314**, 1740–1745, doi:10.1126/science.1132588.

McPhaden, M. J. and X. Zhang, 2009: Asymmetry in zonal phase propagation of ENSO sea surface temperature anomalies. *Geophysical Research Letters*, **36**, doi:10.1029/2009GL038774.

Meehl, G. A., P. R. Gent, J. M. Arblaster, B. L. Otto-Bliesner, E. C. Brady, and A. Craig, 2001: Factors that affect the amplitude of El Niño in global coupled climate models. *Climate Dynamics*, **17**, 515–526, doi:10.1007/PL00007929.

Meehl, G. A., W. M. Washington, J. M. Arblaster, A. Hu, H. Teng, J. E. Kay, A. Gettelman, D. M. Lawrence, B. M. Sanderson, and W. G. Strand, 2013: Climate Change Projections in CESM1(CAM5) Compared to CCSM4. *J. Climate*, **26**, 6287–6308, doi:10.1175/JCLI-D-12-00572.1.

Meinen, C. S. and M. J. McPhaden, 2000: Observations of Warm Water Volume Changes in the Equatorial Pacific and Their Relationship to El Niño and La Niña. *Journal of Climate*, **13**, 3551–3559, doi:10.1175/1520-0442(2000)013<3551:OOWWVC>2.0.CO;2.

Meinshausen, M., S. J. Smith, K. Calvin, J. S. Daniel, M. L. T. Kainuma, J.-F. Lamarque, K. Matsumoto, S. A. Montzka, S. C. B. Raper, K. Riahi, A. Thomson, G. J. M. Velders, and D. P. van Vuuren, 2011: The RCP greenhouse gas concentrations and their extensions from 1765 to 2300. *Climatic Change*, **109**, 213–241, doi:10.1007/s10584-011-0156-z.

Menkes, C. E., M. Lengaigne, J. Vialard, M. Puy, P. Marchesiello, S. Cravatte, and G. Cambon, 2014: About the role of Westerly Wind Events in the possible development of an El Niño in 2014. *Geophysical Research Letters*, **41**, 6476–6483, doi:10.1002/2014GL061186.

Min, Q., J. Su, and R. Zhang, 2017: Impact of the South and North Pacific Meridional Modes on the El Niño–Southern Oscillation: Observational Analysis and Comparison. *Journal of Climate*, **30**, 1705–1720, doi:10.1175/JCLI-D-16-0063.1.

Moon, B.-K., 2004: Vertical structure variability in the equatorial Pacific before and after the Pacific climate shift of the 1970s. *Geophysical Research Letters*, **31**, doi:10.1029/2003GL018829.

Moore, A. M. and R. Kleeman, 1999: Stochastic Forcing of ENSO by the Intraseasonal Oscillation. *Journal of Climate*, **12**, 1199–1220, doi:10.1175/1520-0442(1999)012<1199:SFOEBT>2.0.CO;2.

Morice, C. P., J. J. Kennedy, N. A. Rayner, and P. D. Jones, 2012: Quantifying uncertainties in global and regional temperature change using an ensemble of observational estimates: The HadCRUT4 data set. *Journal of Geophysical Research: Atmospheres*, **117**, doi:10.1029/2011JD017187.

Neelin, J. D., D. S. Battisti, A. C. Hirst, F.-F. Jin, Y. Wakata, T. Yamagata, and S. E. Zebiak, 1998: ENSO theory. *Journal of Geophysical Research: Oceans*, **103**, 14261–14290, doi:10.1029/97JC03424.

Neelin, J. D. and F.-F. Jin, 1993: Modes of Interannual Tropical Ocean–Atmosphere Interaction—a Unified View. Part II: Analytical Results in the Weak-Coupling Limit. *Journal of the Atmospheric Sciences*, **50**, 3504–3522, doi:10.1175/1520-0469(1993)050<3504:MOITOI>2.0.CO;2.

Neelin, J. D., F.-F. Jin, and H.-H. Syu, 2000: Variations in ENSO Phase Locking. *Journal of Climate*, **13**, 2570–2590, doi:10.1175/1520-0442(2000)013<2570:VIEPL>2.0.CO;2.

Neske, S. and S. McGregor, 2018: Understanding the Warm Water Volume Precursor of ENSO Events and its Interdecadal Variation. *Geophysical Research Letters*, **45**, 1577–1585, doi:10.1002/2017GL076439.

Newman, M., S.-I. Shin, and M. A. Alexander, 2011: Natural variation in ENSO flavors. *Geophysical Research Letters*, **38**, doi:10.1029/2011GL047658.

Okumura, Y. M. and C. Deser, 2010: Asymmetry in the Duration of El Niño and La Niña. *Journal of Climate*, **23**, 5826–5843, doi:10.1175/2010JCLI3592.1.

Oleson, W., M. Lawrence, B. Bonan, G. Flanner, E. Kluzek, J. Lawrence, S. Levis, C. Swenson, E. Thornton, A. Dai, M. Decker, R. Dickinson, J. Feddema, L. Heald, F. Hoffman, J.-F. Lamarque, N. Mahowald, G.-Y. Niu, T. Qian, J. Randerson, S. Running, K. Sakaguchi, A. Slater, R. Stockli, A. Wang, Z.-L. Yang, X. Zeng, and X. Zeng, 2010: Technical Description of version 4.0 of the Community Land Model (CLM). doi:10.5065/D6FB50WZ.

Otto-Bliesner, B. L., E. C. Brady, J. Fasullo, A. Jahn, L. Landrum, S. Stevenson, N. Rosenbloom, A. Mai, and G. Strand, 2016: Climate Variability and Change since 850 CE: An Ensemble Approach with the Community Earth System Model. *Bulletin of the American Meteorological Society*, **97**, 735–754, doi:10.1175/BAMS-D-14-00233.1.

Overpeck, J. T., G. A. Meehl, S. Bony, and D. R. Easterling, 2011: Climate Data Challenges in the 21st Century. *Science*, **331**, 700–702, doi:10.1126/science.1197869.

Paek, H., J.-Y. Yu, and C. Qian, 2017: Why were the 2015/2016 and 1997/1998 extreme El Niños different?: Contrasting 1997/1998 and 2015/2016 El Niños. *Geophysical Research Letters*, doi:10.1002/2016GL071515.

Park, T.-W., Y. Deng, M. Cai, J.-H. Jeong, and R. Zhou, 2014: A dissection of the surface temperature biases in the Community Earth System Model. *Climate Dynamics*, **43**, 2043–2059, doi:10.1007/s00382-013-2029-9.

Penland, C. and P. D. Sardeshmukh, 1995: The Optimal Growth of Tropical Sea Surface Temperature Anomalies. *Journal of Climate*, **8**, 1999–2024, doi:10.1175/1520-0442(1995)008<1999:TOGOTS>2.0.CO;2.

Pham, D. T., S. S. Dimov, and C. D. Nguyen, 2005: Selection of K in K-means clustering. *Proceedings of the Institution of Mechanical Engineers, Part C: Journal of Mechanical Engineering Science*, **219**, 103–119, doi:10.1243/095440605X8298.

Philander, S. G., 1990: *El Niño, La Niña, and the southern oscillation*. Number v. 46 in International geophysics series, Academic Press, San Diego.

Philander, S. G. and A. Fedorov, 2003: Is El Niño Sporadic or Cyclic? *Annual Review of Earth and Planetary Sciences*, **31**, 579–594, doi:10.1146/annurev.earth.31.100901.141255.

Philander, S. G. H., 1983: Anomalous El Niño of 1982-83. *Nature*, **305**, 16, doi:10.1038/305016a0.

Philip, S. and G. J. van Oldenborgh, 2006: Shifts in ENSO coupling processes under global warming. *Geophysical Research Letters*, **33**, doi:10.1029/2006GL026196.

Picaut, J., M. Ioualalen, T. Delcroix, F. Masia, R. Murtugudde, and J. Vialard, 2001: The oceanic zone of convergence on the eastern edge of the Pacific warm pool: A synthesis of results and implications for El Niño-Southern Oscillation and biogeochemical phenomena. *Journal of Geophysical Research: Oceans*, **106**, 2363–2386, doi:10.1029/2000JC900141.

Picaut, J., M. Ioualalen, C. Menkes, T. Delcroix, and M. J. McPhaden, 1996: Mechanism of the Zonal Displacements of the Pacific Warm Pool: Implications for ENSO. *Science*, **274**, 1486–1489, doi:10.1126/science.274.5292.1486.

Picaut, J., F. Masia, and Y. d. Penhoat, 1997: An Advective-Reflective Conceptual Model for the Oscillatory Nature of the ENSO. *Science*, **277**, 663–666, doi:10.1126/science.277.5326.663.

Planton, Y., J. Vialard, E. Guilyardi, M. Lengaigne, and T. Izumo, 2018: Western Pacific Oceanic Heat Content: A Better Predictor of La Niña Than of El Niño. *Geophysical Research Letters*, **45**, 9824–9833, doi:10.1029/2018GL079341.

Power, S., F. Delage, C. Chung, G. Kociuba, and K. Keay, 2013: Robust twenty-first-century projections of El Niño and related precipitation variability. *Nature*, **502**, 541–545, doi:10.1038/nature12580.

Puy, M., J. Vialard, M. Lengaigne, and E. Guilyardi, 2016a: Modulation of equatorial Pacific westerly/easterly wind events by the Madden–Julian oscillation and convectively-coupled Rossby waves. *Climate Dynamics*, **46**, 2155–2178, doi:10.1007/s00382-015-2695-x.

Puy, M., J. Vialard, M. Lengaigne, E. Guilyardi, P. N. DiNezio, A. Voldoire, M. Balmaseda, G. Madec, C. Menkes, and M. J. Mcphaden, 2017: Influence of Westerly Wind Events stochasticity on El Niño amplitude: the case of 2014 vs. 2015. *Climate Dynamics*, doi:10.1007/s00382-017-3938-9.

Puy, M., J. Vialard, M. Lengaigne, E. Guilyardi, A. Voldoire, and G. Madec, 2016b: Modulation of equatorial Pacific sea surface temperature response to westerly wind events by the oceanic background state. *Climate Dynamics*, doi:10.1007/s00382-016-3480-1.

Rasmusson, E. M. and T. H. Carpenter, 1982: Variations in Tropical Sea Surface Temperature and Surface Wind Fields Associated with the Southern Oscillation/El Niño. *Mon. Wea. Rev.*, **110**, 354–384, doi:10.1175/1520-0493(1982)110<0354:VITSST>2.0.CO;2.

Ray, S. and B. S. Giese, 2012: Historical changes in El Niño and La Niña characteristics in an ocean reanalysis. *Journal of Geophysical Research (Oceans)*, **117**, 11007, doi:10.1029/2012JC008031.

Rayner, N. A., 2003: Global analyses of sea surface temperature, sea ice, and night marine air temperature since the late nineteenth century. *Journal of Geophysical Research*, **108**, 4407, doi:10.1029/2002JD002670.

Ren, H.-L. and F.-F. Jin, 2011: Niño indices for two types of ENSO. *Geophysical Research Letters*, **38**, doi:10.1029/2010GL046031.

— 2013: Recharge Oscillator Mechanisms in Two Types of ENSO. *Journal of Climate*, **26**, 6506–6523, doi:10.1175/JCLI-D-12-00601.1.

Richter, I., 2015: Climate model biases in the eastern tropical oceans: causes, impacts and ways forward. *Wiley Interdisciplinary Reviews: Climate Change*, **6**, 345–358, doi:10.1002/wcc.338.

Rodgers, K. B., P. Friederichs, and M. Latif, 2004: Tropical Pacific Decadal Variability and Its Relation to Decadal Modulations of ENSO. *J. Climate*, **17**, 3761–3774, doi:10.1175/1520-0442(2004)017<3761:TPDVAI>2.0.CO;2.

Roemmich, D. and B. Owens, 2000: The Argo Project: Global Ocean Observations for Understanding and Prediction of Climate Variability. *Oceanography*, **13**, 45–50, doi:10.5670/oceanog.2000.33.

Rogers, J. C., 1981: The North Pacific Oscillation. *Journal of Climatology*, **1**, 39–57, doi:10.1002/joc.3370010106.

Ropelewski, C. F. and M. S. Halpert, 1987: Global and Regional Scale Precipitation Patterns Associated with the El Niño/Southern Oscillation. *Monthly Weather Review*, **115**, 1606–1626, doi:10.1175/1520-0493(1987)115<1606:GARSPP>2.0.CO;2.

Rädel, G., T. Mauritsen, B. Stevens, D. Dommenget, D. Matei, K. Bellomo, and A. Clement, 2016: Amplification of El Niño by cloud longwave coupling to atmospheric circulation. *Nature Geoscience*, **9**, 106–110, doi:10.1038/ngeo2630.

Saint-Lu, M. and J. Leloup, 2016: Petit précis de théorie pour comprendre El Niño. *La Météorologie*, doi:10.4267/2042/61615.

Saji, N. H. and T. Yamagata, 2003: Structure of SST and Surface Wind Variability during Indian Ocean Dipole Mode Events: COADS Observations*. *Journal of Climate*, **16**, 2735–2751, doi:10.1175/1520-0442(2003)016<2735:SOSASW>2.0.CO;2.

Sanabria, J., L. Bourrel, B. Dewitte, F. Frappart, P. Rau, O. Solis, and D. Labat, 2018: Rainfall along the coast of Peru during strong El Niño events. *International Journal of Climatology*, **38**, 1737–1747, doi:10.1002/joc.5292.

Santoso, A., S. McGregor, F.-F. Jin, W. Cai, M. H. England, S.-I. An, M. J. McPhaden, and E. Guilyardi, 2013: Late-twentieth-century emergence of the El Niño propagation asymmetry and future projections. *Nature*, **504**, 126–130, doi:10.1038/nature12683.

Santoso, A., M. J. Mcphaden, and W. Cai, 2017: The Defining Characteristics of ENSO Extremes and the Strong 2015/2016 El Niño. *Reviews of Geophysics*, **55**, 1079–1129, doi:10.1002/2017RG000560.

Schopf, P. S. and R. J. Burgman, 2006: A Simple Mechanism for ENSO Residuals and Asymmetry. *Journal of Climate*, **19**, 3167–3179, doi:10.1175/JCLI3765.1.

Schopf, P. S. and D. E. Harrison, 1983: On Equatorial Waves and El Niño. I. Influence of Initial States on Wave-induced Currents and Warming. *Journal of Physical Oceanography*, **13**, 936–948, doi:10.1175/1520-0485(1983)013<0936:OEWAEN>2.0.CO;2.

Seiki, A. and Y. N. Takayabu, 2007: Westerly Wind Bursts and Their Relationship with Intraseasonal Variations and ENSO. Part I: Statistics. *Monthly Weather Review*, **135**, 3325–3345, doi:10.1175/MWR3477.1.

Shin, S.-J. and S.-I. An, 2018: Interdecadal Change in the Relationship Between the North Pacific Oscillation and the Pacific Meridional Mode and Its Impact on ENSO. *Asia-Pacific Journal of Atmospheric Sciences*, **54**, 63–76, doi:10.1007/s13143-017-0060-1.

Singh, A. and T. Delcroix, 2013: Eastern and Central Pacific ENSO and their relationships to the recharge/discharge oscillator paradigm. *Deep Sea Research Part I: Oceanographic Research Papers*, **82**, 32–43, doi:10.1016/j.dsr.2013.08.002.

Singh, A., T. Delcroix, and S. Cravatte, 2011: Contrasting the flavors of El Niño-Southern Oscillation using sea surface salinity observations. *Journal of Geophysical Research: Oceans*, **116**, doi:10.1029/2010JC006862.

Smith, N., W. S. Kessler, S. Cravatte, J. Sprintall, S. Wijffels, M. F. Cronin, A. Sutton, Y. L. Serra, B. Dewitte, P. G. Strutton, K. Hill, A. Sen Gupta, X. Lin, K. Takahashi, D. Chen, and S. Brunner, 2019: Tropical Pacific Observing System. *Frontiers in Marine Science*, **6**, doi:10.3389/fmars.2019.00031.

Smith, R., P. Jones, B. Briegleb, F. Bryan, G. Danabasoglu, J. Dennis, J. Dukowicz, C. Eden, B. Fox-Kemper, P. Gent, and others, 2010: The parallel ocean program (POP) reference manual ocean component of the community climate system model (CCSM) and community earth system model (CESM). *Rep. LAUR-01853*, **141**, 1–140.

Smith, T. M., R. W. Reynolds, T. C. Peterson, and J. Lawrimore, 2008: Improvements to NOAA's Historical Merged Land–Ocean Surface Temperature Analysis (1880–2006). *Journal of Climate*, **21**, 2283–2296, doi:10.1175/2007JCLI2100.1.

Stein, K., A. Timmermann, N. Schneider, F.-F. Jin, and M. F. Stuecker, 2014: ENSO Seasonal Synchronization Theory. *Journal of Climate*, **27**, 5285–5310, doi:10.1175/JCLI-D-13-00525.1.

Stevenson, S., A. Capotondi, J. Fasullo, and B. Otto-Bliesner, 2017: Forced changes to twentieth century ENSO diversity in a last Millennium context. *Climate Dynamics*, 1–16, doi:10.1007/s00382-017-3573-5.

Stevenson, S., B. Fox-Kemper, M. Jochum, B. Rajagopalan, and S. G. Yeager, 2010: ENSO Model Validation Using Wavelet Probability Analysis. *Journal of Climate*, **23**, 5540–5547, doi:10.1175/2010JCLI3609.1.

Stevenson, S. L., 2012: Significant changes to ENSO strength and impacts in the twenty-first century: Results from CMIP5. *Geophysical Research Letters*, **39**, doi:10.1029/2012GL052759.

Storch, H. v. and F. W. Zwiers, 1999: *Statistical analysis in climate research*. Cambridge University Press, Cambridge ; New York.

Stuecker, M. F., 2018: Revisiting the Pacific Meridional Mode. *Scientific Reports*, **8**, 3216, doi:10.1038/s41598-018-21537-0.

Stuecker, M. F., A. Timmermann, F.-F. Jin, S. McGregor, and H.-L. Ren, 2013: A combination mode of the annual cycle and the El Niño/Southern Oscillation. *Nature Geoscience*, **6**, 540–544, doi:10.1038/ngeo1826.

Suarez, M. J. and P. S. Schopf, 1988: A Delayed Action Oscillator for ENSO. *Journal of the Atmospheric Sciences*, **45**, 3283–3287, doi:10.1175/1520-0469(1988)045<3283:ADAOFE>2.0.CO;2.

Takahashi, K. and B. Dewitte, 2016: Strong and moderate nonlinear El Niño regimes. *Climate Dynamics*, **46**, 1627–1645, doi:10.1007/s00382-015-2665-3.

Takahashi, K., C. Karamperidou, and B. Dewitte, 2018: A theoretical model of strong and moderate El Niño regimes. *Climate Dynamics*, doi:10.1007/s00382-018-4100-z.

Takahashi, K., A. Montecinos, K. Goubanova, and B. Dewitte, 2011: ENSO regimes: Reinterpreting the canonical and Modoki El Niño. *Geophysical Research Letters*, **38**, doi:10.1029/2011GL047364.

Taylor, K. E., R. J. Stouffer, and G. A. Meehl, 2012: An Overview of CMIP5 and the Experiment Design. *Bulletin of the American Meteorological Society*, **93**, 485–498, doi:10.1175/BAMS-D-11-00094.1.

Thomas, E. E. and D. J. Vimont, 2016: Modeling the Mechanisms of Linear and Nonlinear ENSO Responses to the Pacific Meridional Mode. *Journal of Climate*, **29**, 8745–8761, doi:10.1175/JCLI-D-16-0090.1.

Thual, S., B. Dewitte, S.-I. An, and N. Ayoub, 2011: Sensitivity of ENSO to Stratification in a Recharge–Discharge Conceptual Model. *Journal of Climate*, **24**, 4332–4349, doi:10.1175/2011JCLI4148.1.

Thual, S., B. Dewitte, S.-I. An, S. Illig, and N. Ayoub, 2013: Influence of Recent Stratification Changes on ENSO Stability in a Conceptual Model of the Equatorial Pacific. *Journal of Climate*, **26**, 4790–4802, doi:10.1175/JCLI-D-12-00363.1.

Timmermann, A., 2003: Decadal ENSO amplitude modulations: a nonlinear paradigm. *Global and Planetary Change*, **37**, 135–156, doi:10.1016/S0921-8181(02)00194-7.

Timmermann, A., S.-I. An, J.-S. Kug, F.-F. Jin, W. Cai, A. Capotondi, K. Cobb, M. Lengaigne, M. J. McPhaden, M. F. Stuecker, K. Stein, A. T. Wittenberg, K.-S. Yun, T. Bayr, H.-C. Chen, Y. Chikamoto, B. Dewitte, D. Dommenget, P. Grothe, E. Guilyardi,

Y.-G. Ham, M. Hayashi, S. Ineson, D. Kang, S. Kim, W. Kim, J.-Y. Lee, T. Li, J.-J. Luo, S. McGregor, Y. Planton, S. Power, H. Rashid, H.-L. Ren, A. Santoso, K. Takahashi, A. Todd, G. Wang, G. Wang, R. Xie, W.-H. Yang, S.-W. Yeh, J. Yoon, E. Zeller, and X. Zhang, 2018: El Niño–Southern Oscillation complexity. *Nature*, **559**, 535–545, doi:10.1038/s41586-018-0252-6.

Timmermann, A. and F.-F. Jin, 2002: A Nonlinear Mechanism for Decadal El Niño Amplitude Changes. *Geophysical Research Letters*, **29**, 3–1–3–4, doi:10.1029/2001GL013369.

Timmermann, A., F.-F. Jin, and J. Abshagen, 2003: A Nonlinear Theory for El Niño Bursting. *J. Atmos. Sci.*, **60**, 152–165, doi:10.1175/1520-0469(2003)060<0152:ANTFEN>2.0.CO;2.

Torrence, C. and G. P. Compo, 1998: A Practical Guide to Wavelet Analysis. *Bulletin of the American Meteorological Society*, **79**, 61–78, doi:10.1175/1520-0477(1998)079<0061:APGTWA>2.0.CO;2.

Torrence, C. and P. J. Webster, 1999: Interdecadal Changes in the ENSO–Monsoon System. *J. Climate*, **12**, 2679–2690, doi:10.1175/1520-0442(1999)012<2679:ICITEM>2.0.CO;2.

Trenberth, K. E., 1990: Recent Observed Interdecadal Climate Changes in the Northern Hemisphere. *Bulletin of the American Meteorological Society*, **71**, 988–993, doi:10.1175/1520-0477(1990)071<0988:ROICCI>2.0.CO;2.

— 1997: The Definition of El Niño. *Bulletin of the American Meteorological Society*, **78**, 2771–2777.

Trenberth, K. E. and D. P. Stepaniak, 2001: Indices of El Niño Evolution. *Journal of Climate*, **14**, 1697–1701, doi:10.1175/1520-0442(2001)014<1697:LIOENO>2.0.CO;2.

Tziperman, E., L. Stone, M. A. Cane, and H. Jarosh, 1994: El Nino Chaos: Overlapping of Resonances Between the Seasonal Cycle and the Pacific Ocean-Atmosphere Oscillator. *Science*, **264**, 72–74, doi:10.1126/science.264.5155.72.

van Oldenborgh, G. J., S. Y. Philip, and M. Collins, 2005: El Niño in a changing climate: a multi-model study. *Ocean Science*, **1**, 81–95.

Vannière, B., E. Guilyardi, G. Madec, F. J. Doblas-Reyes, and S. Woolnough, 2013: Using seasonal hindcasts to understand the origin of the equatorial cold tongue bias in CGCMs and its impact on ENSO. *Climate Dynamics*, **40**, 963–981, doi:10.1007/s00382-012-1429-6.

Vecchi, G. A. and D. E. Harrison, 2000: Tropical Pacific Sea Surface Temperature Anomalies, El Niño, and Equatorial Westerly Wind Events. *Journal of Climate*, **13**, 1814–1830, doi:10.1175/1520-0442(2000)013<1814:TPSSTA>2.0.CO;2.

— 2003: On the termination of the 2002-03 El Niño event. *Geophysical Research Letters*, **30**, doi:10.1029/2003GL017564.

— 2006: The Termination of the 1997–98 El Niño. Part I: Mechanisms of Oceanic Change*. *Journal of Climate*, **19**, 2633–2646, doi:10.1175/JCLI3776.1.

Vecchi, G. A. and B. J. Soden, 2007: Global Warming and the Weakening of the Tropical Circulation. *Journal of Climate*, **20**, 4316–4340, doi:10.1175/JCLI4258.1.

Vecchi, G. A., B. J. Soden, A. T. Wittenberg, I. M. Held, A. Leetmaa, and M. J. Harrison, 2006: Weakening of tropical Pacific atmospheric circulation due to anthropogenic forcing. *Nature*, **441**, 73–76, doi:10.1038/nature04744.

Vialard, J., C. Menkes, J.-P. Boulanger, P. Delecluse, E. Guilyardi, M. J. McPhaden, and G. Madec, 2001: A Model Study of Oceanic Mechanisms Affecting Equatorial Pacific Sea Surface Temperature during the 1997–98 El Niño. *J. Phys. Oceanogr.*, **31**, 1649–1675, doi:10.1175/1520-0485(2001)031<1649:AMSOOM>2.0.CO;2.

Vimont, D. J., J. M. Wallace, and D. S. Battisti, 2003: The Seasonal Footprinting Mechanism in the Pacific: Implications for ENSO*. *Journal of Climate*, **16**, 2668–2675, doi:10.1175/1520-0442(2003)016<2668:TSFMIT>2.0.CO;2.

Wang, B., 1995: Interdecadal Changes in El Niño Onset in the Last Four Decades. *Journal of Climate*, **8**, 267–285, doi:10.1175/1520-0442(1995)008<0267:ICIENO>2.0.CO;2.

Wang, C., 2001: A Unified Oscillator Model for the El Niño–Southern Oscillation. *Journal of Climate*, **14**, 98–115, doi:10.1175/1520-0442(2001)014<0098:AUOMFT>2.0.CO;2.

Wang, C. and J. Picaut, 2004: Understanding ENSO physics—a review. *Earth's Climate: The Ocean-Atmosphere Interaction*, C. Wang, S.-P. Xie, and J. A. Carton, eds., American Geophysical Union, Washington, D. C., volume 147 of *Geophysical Monograph Serie*, 21–48.

Wang, C. and R. H. Weisberg, 2000: The 1997–98 El Niño Evolution Relative to Previous El Niño Events. *Journal of Climate*, **13**, 488–501, doi:10.1175/1520-0442(2000)013<0488:TENOER>2.0.CO;2.

Wang, G., W. Cai, B. Gan, L. Wu, A. Santoso, X. Lin, Z. Chen, and M. J. McPhaden, 2017: Continued increase of extreme El Niño frequency long after 1.5 °C warming stabilization. *Nature Climate Change*, **7**, 568–572, doi:10.1038/nclimate3351.

Wang, R. and H.-L. Ren, 2017: The linkage between two ENSO types/modes and the interdecadal changes of ENSO around the year 2000. *Atmospheric and Oceanic Science Letters*, **10**, 168–174, doi:10.1080/16742834.2016.1258952.

Weisberg, R. H. and C. Wang, 1997: A Western Pacific Oscillator Paradigm for the El Niño-Southern Oscillation. *Geophysical Research Letters*, **24**, 779–782, doi:10.1029/97GL00689.

Weng, H., S. K. Behera, and T. Yamagata, 2009: Anomalous winter climate conditions in the Pacific rim during recent El Niño Modoki and El Niño events. *Climate Dynamics*, **32**, 663–674, doi:10.1007/s00382-008-0394-6.

Wengel, C., M. Latif, W. Park, J. Harlaß, and T. Bayr, 2018: Seasonal ENSO phase locking in the Kiel Climate Model: The importance of the equatorial cold sea surface temperature bias. *Climate Dynamics*, **50**, 901–919, doi:10.1007/s00382-017-3648-3.

Wilcoxon, F., 1945: Individual Comparisons by Ranking Methods. *Biometrics Bulletin*, **1**, 80–83, doi:10.2307/3001968.

Williams, I. N. and C. M. Patricola, 2018: Diversity of ENSO Events Unified by Convective Threshold Sea Surface Temperature: A Nonlinear ENSO Index. *Geophysical Research Letters*, doi:10.1029/2018GL079203.

Wittenberg, A. T., 2009: Are historical records sufficient to constrain ENSO simulations? *Geophysical Research Letters*, **36**, doi:10.1029/2009GL038710.

Wittenberg, A. T., A. Rosati, N.-C. Lau, and J. J. Ploshay, 2006: GFDL's CM2 Global Coupled Climate Models. Part III: Tropical Pacific Climate and ENSO. *J. Climate*, **19**, 698–722, doi:10.1175/JCLI3631.1.

Woelfle, M. D., S. Yu, C. S. Bretherton, and M. S. Pritchard, 2018: Sensitivity of Coupled Tropical Pacific Model Biases to Convective Parameterization in CESM1. *Journal of Advances in Modeling Earth Systems*, **10**, 126–144, doi:10.1002/2017MS001176.

Wyrtki, K., 1961: The thermohaline circulation in relation to the general circulation in the oceans. *Deep Sea Research (1953)*, **8**, 39–64, doi:10.1016/0146-6313(61)90014-4.

— 1975: El Niño—The Dynamic Response of the Equatorial Pacific Oceanto Atmospheric Forcing. *Journal of Physical Oceanography*, **5**, 572–584, doi:10.1175/1520-0485(1975)005<0572:ENTDRO>2.0.CO;2.

— 1985: Water displacements in the Pacific and the genesis of El Nino cycles. *Journal of Geophysical Research*, **90**, 7129, doi:10.1029/JC090iC04p07129.

Xiang, B., B. Wang, Q. Ding, F. Jin, X. Fu, and H.-J. Kim, 2012: Reduction of the thermocline feedback associated with mean SST bias in ENSO simulation. *Climate Dynamics*, **39**, 1413–1430, doi:10.1007/s00382-011-1164-4.

Xie, R. and F.-F. Jin, 2018: Two Leading ENSO Modes and El Niño Types in the Zebiak–Cane Model. *Journal of Climate*, **31**, 1943–1962, doi:10.1175/JCLI-D-17-0469.1.

Xie, S.-P., C. Deser, G. A. Vecchi, M. Collins, T. L. Delworth, A. Hall, E. Hawkins, N. C. Johnson, C. Cassou, A. Giannini, and M. Watanabe, 2015: Towards predictive understanding of regional climate change. *Nature Climate Change*, **5**, 921–930, doi:10.1038/nclimate2689.

Xie, S.-P., C. Deser, G. A. Vecchi, J. Ma, H. Teng, and A. T. Wittenberg, 2010: Global Warming Pattern Formation: Sea Surface Temperature and Rainfall. *Journal of Climate*, **23**, 966–986, doi:10.1175/2009JCLI3329.1.

Xie, S.-P., Q. Peng, Y. Kamae, X.-T. Zheng, H. Tokinaga, and D. Wang, 2018: Eastern Pacific ITCZ Dipole and ENSO Diversity. *Journal of Climate*, **31**, 4449–4462, doi:10.1175/JCLI-D-17-0905.1.

Xie, S.-P. and S. G. H. Philander, 1994: A coupled ocean-atmosphere model of relevance to the ITCZ in the eastern Pacific. *Tellus A: Dynamic Meteorology and Oceanography*, **46**, 340–350, doi:10.3402/tellusa.v46i4.15484.

Xu, J. and J. C. L. Chan, 2001: The Role of the Asian-Australian Monsoon System in the Onset Time of El Niño Events. *Journal of Climate*, **14**, 418–433, doi:10.1175/1520-0442(2001)014<0418:TROTAA>2.0.CO;2.

Xue, Y. and A. Kumar, 2017: Evolution of the 2015/16 El Niño and historical perspective since 1979. *Science China Earth Sciences*, **60**, 1572–1588, doi:10.1007/s11430-016-0106-9.

Xue, Y., C. Wen, A. Kumar, M. Balmaseda, Y. Fujii, O. Alves, M. Martin, X. Yang, G. Vernieres, C. Desportes, T. Lee, I. Ascione, R. Gudgel, and I. Ishikawa, 2017: A real-time ocean reanalyses intercomparison project in the context of tropical pacific observing system and ENSO monitoring. *Climate Dynamics*, **49**, 3647–3672, doi:10.1007/s00382-017-3535-y.

Yang, H. and F. Wang, 2009: Revisiting the Thermocline Depth in the Equatorial Pacific*. *Journal of Climate*, **22**, 3856–3863, doi:10.1175/2009JCLI2836.1.

Yeh, S.-W., Y.-G. Ham, and J.-Y. Lee, 2012: Changes in the Tropical Pacific SST Trend from CMIP3 to CMIP5 and Its Implication of ENSO. *Journal of Climate*, **25**, 7764–7771, doi:10.1175/JCLI-D-12-00304.1.

Yeh, S.-W. and B. P. Kirtman, 2004: Tropical Pacific decadal variability and ENSO amplitude modulation in a CGCM. *Journal of Geophysical Research: Oceans*, **109**, doi:10.1029/2004JC002442.

Yeh, S.-W., B. P. Kirtman, J.-S. Kug, W. Park, and M. Latif, 2011: Natural variability of the central Pacific El Niño event on multi-centennial timescales. *Geophysical Research Letters*, **38**, doi:10.1029/2010GL045886.

Yeh, S.-W., J.-S. Kug, B. Dewitte, M.-H. Kwon, B. P. Kirtman, and F.-F. Jin, 2009a: El Niño in a changing climate. *Nature*, **461**, 511–514, doi:10.1038/nature08316.

Yeh, S.-W., X. Wang, C. Wang, and B. Dewitte, 2015: On the Relationship between the North Pacific Climate Variability and the Central Pacific El Niño. *Journal of Climate*, **28**, 663–677, doi:10.1175/JCLI-D-14-00137.1.

Yeh, S.-W., B. Y. Yim, Y. Noh, and B. Dewitte, 2009b: Changes in mixed layer depth under climate change projections in two CGCMs. *Climate Dynamics*, **33**, 199–213, doi:10.1007/s00382-009-0530-y.

Ying, J., P. Huang, T. Lian, and H. Tan, 2019: Understanding the effect of an excessive cold tongue bias on projecting the tropical Pacific SST warming pattern in CMIP5 models. *Climate Dynamics*, **52**, 1805–1818, doi:10.1007/s00382-018-4219-y.

Yu, J.-Y. and H.-Y. Kao, 2007: Decadal changes of ENSO persistence barrier in SST and ocean heat content indices: 1958-2001. *Journal of Geophysical Research: Atmospheres*, **112**, doi:10.1029/2006JD007654.

Yu, J.-Y., H.-Y. Kao, and T. Lee, 2010a: Subtropics-Related Interannual Sea Surface Temperature Variability in the Central Equatorial Pacific. *Journal of Climate*, **23**, 2869–2884, doi:10.1175/2010JCLI3171.1.

Yu, J.-Y., H.-Y. Kao, T. Lee, and S. T. Kim, 2010b: Subsurface ocean temperature indices for Central-Pacific and Eastern-Pacific types of El Niño and La Niña events. *Theor Appl Climatol*, **103**, 337–344, doi:10.1007/s00704-010-0307-6.

Yu, J.-Y. and S. T. Kim, 2010: Three evolution patterns of Central-Pacific El Niño. *Geophysical Research Letters*, **37**, doi:10.1029/2010GL042810.

— 2011: Relationships between Extratropical Sea Level Pressure Variations and the Central Pacific and Eastern Pacific Types of ENSO. *Journal of Climate*, **24**, 708–720, doi:10.1175/2010JCLI3688.1.

— 2013: Identifying the types of major El Niño events since 1870. *International Journal of Climatology*, **33**, 2105–2112, doi:10.1002/joc.3575.

Yu, J.-Y., M.-M. Lu, and S. T. Kim, 2012: A change in the relationship between tropical central Pacific SST variability and the extratropical atmosphere around 1990. *Environmental Research Letters*, **7**, 034025, doi:10.1088/1748-9326/7/3/034025.

Yu, J.-Y. and H. Paek, 2015: Precursors of ENSO beyond the tropical Pacific. *Variations*, **13**, 15–20.

Yu, J.-Y., F. Sun, and H.-Y. Kao, 2009: Contributions of Indian Ocean and Monsoon Biases to the Excessive Biennial ENSO in CCSM3. *Journal of Climate*, **22**, 1850–1858, doi:10.1175/2008JCLI2706.1.

Zebiak, S. E. and M. A. Cane, 1987: A Model El Niño–Southern Oscillation. *Mon. Wea. Rev.*, **115**, 2262–2278, doi:10.1175/1520-0493(1987)115<2262:AMENO>2.0.CO;2.

Zelle, H., G. Appeldoorn, G. Burgers, and G. J. van Oldenborgh, 2004: The Relationship between Sea Surface Temperature and Thermocline Depth in the Eastern Equatorial Pacific. *Journal of Physical Oceanography*, **34**, 643–655, doi:10.1175/2523.1.

Zhang, H., A. Clement, and P. Di Nezio, 2014: The South Pacific Meridional Mode: A Mechanism for ENSO-like Variability. *Journal of Climate*, **27**, 769–783, doi:10.1175/JCLI-D-13-00082.1.

Zhang, T., X. Shao, and S. Li, 2017: Impacts of Atmospheric Processes on ENSO Asymmetry: A Comparison between CESM1 and CCSM4. *Journal of Climate*, **30**, 9743–9762, doi:10.1175/JCLI-D-17-0360.1.

Zhang, T. and D.-Z. Sun, 2014: ENSO Asymmetry in CMIP5 Models. *Journal of Climate*, **27**, 4070–4093, doi:10.1175/JCLI-D-13-00454.1.

Zhang, W., H. Li, F.-F. Jin, M. F. Stuecker, A. G. Turner, and N. P. Klingaman, 2015a: The Annual-Cycle Modulation of Meridional Asymmetry in ENSO's Atmospheric Response and Its Dependence on ENSO Zonal Structure. *Journal of Climate*, **28**, 5795–5812, doi:10.1175/JCLI-D-14-00724.1.

Zhang, X., H. Liu, and M. Zhang, 2015b: Double ITCZ in Coupled Ocean-Atmosphere Models: From CMIP3 to CMIP5. *Geophysical Research Letters*, **42**, 8651–8659, doi:10.1002/2015GL065973.

Zheng, X.-T., C. Hui, and S.-W. Yeh, 2018: Response of ENSO amplitude to global warming in CESM large ensemble: uncertainty due to internal variability. *Climate Dynamics*, **50**, 4019–4035, doi:10.1007/s00382-017-3859-7.

Zheng, X.-T., S.-P. Xie, L.-H. Lv, and Z.-Q. Zhou, 2016: Intermodel Uncertainty in ENSO Amplitude Change Tied to Pacific Ocean Warming Pattern. *Journal of Climate*, **29**, 7265–7279, doi:10.1175/JCLI-D-16-0039.1.

Zheng, Y., J.-L. Lin, and T. Shinoda, 2012: The equatorial Pacific cold tongue simulated by IPCC AR4 coupled GCMs: Upper ocean heat budget and feedback analysis. *Journal of Geophysical Research: Oceans*, **117**, doi:10.1029/2011JC007746.

Zuidema, P., P. Chang, B. Medeiros, B. P. Kirtman, R. Mechoso, E. K. Schneider, T. Toniazzo, I. Richter, R. J. Small, K. Bellomo, P. Brandt, S. de Szoeke, J. T. Farrar, E. Jung, S. Kato, M. Li, C. Patricola, Z. Wang, R. Wood, and Z. Xu, 2016: Challenges and Prospects for Reducing Coupled Climate Model SST Biases in the Eastern Tropical Atlantic and Pacific Oceans: The U.S. CLIVAR Eastern Tropical Oceans Synthesis Working Group. *Bulletin of the American Meteorological Society*, **97**, 2305–2328, doi:10.1175/BAMS-D-15-00274.1.

AUTEUR : Aude Carréric
DIRECTEURS DE THESE : Boris Dewitte et Virginie Guémas
LIEU ET DATE DE SOUTENANCE : Toulouse, le 5 juin 2019

LA DIVERSITE D'ENSO ET LE CHANGEMENT CLIMATIQUE

Résumé : El Niño-Southern Oscillation (ENSO) est le mode de variabilité dominant du Pacifique tropical à l'échelle inter-annuelle. Ce phénomène couplé océan-atmosphère est à l'origine d'événements météorologiques extrêmes qui affectent de nombreuses régions du monde. Compte tenu de ses conséquences socio-économiques, et pour pouvoir atténuer ses dommages potentiels, il est important de mieux le comprendre afin de prévoir son évolution avec le réchauffement climatique. Dans ce travail de thèse, nous nous sommes intéressés en premier lieu à réévaluer la caractérisation de la diversité des événements El Niño. Ils présentent en effet une grande diversité d'amplitude et de structures spatiales des anomalies de température de surface de l'océan (SST). Nous avons ensuite analysé le changement des statistiques de la diversité d'El Niño avec le réchauffement climatique. Nous avons pour cela utilisé les simulations du modèle de climat couplé CESM-LE qui fournit un grand ensemble de réalisations (40 simulations) du climat historique et futur (1920-2100) sous l'hypothèse du scénario RCP8.5 d'émission soutenue de gaz à effet de serre. Nous montrons que les événements El Niño forts, caractérisés par un réchauffement important dans le Pacifique oriental, voient leur pic d'anomalies en SST être décalé de l'hiver au début du printemps (Février-Mars-Avril, FMA). Nous proposons l'hypothèse selon laquelle ces changements de l'évolution temporelle des événements El Niño forts proviennent d'un processus de recharge plus important et d'une rétroaction de la thermocline plus efficace en situation future, du fait de l'augmentation de la stratification verticale du Pacifique équatorial.

Mots clés : Oscillation australe El Niño, Changement climatique, Large Ensemble CESM, Variabilité décennale, El Niño extrême.

ENSO DIVERSITY AND GLOBAL WARMING

Abstract: El Niño-Southern Oscillation (ENSO) is the dominant mode of variability in the tropical Pacific on inter-annual scale. This phenomenon affects weather events, ecosystems, agriculture and fisheries worldwide via atmospheric and oceanic teleconnections. This natural phenomenon is likely to be strongly impacted by global warming. In this thesis, we first assessed the characterisation of the diversity of El Niño events. They exhibit a wide range of amplitudes and spatial patterns of sea surface temperature (SST) anomalies. We then analysed the change in ENSO diversity statistics (amplitude, seasonality) with global warming. We used simulations from the coupled climate model CESM-LE, which provides multiple realisations (40 members) of the historical and future climate (1920-2100), under the assumption of the RCP8.5 scenario of sustained greenhouse gas emissions. We show that strong El Niño events, which display significant warming in the eastern Pacific, have their peak of SST shifted from winter to early spring (February-March-April, FMA) in the future climate. Finally, the impact of the increase in the mean vertical stratification of the equatorial Pacific on ENSO diversity is assessed in terms of dynamic processes. We propose the hypothesis that the greater persistence of strong El Niño events and the time lag of their warming peaks are due to a larger recharge process and more effective thermocline feedback in the eastern Pacific in a warmer climate as simulated by CESM-LE.

Keywords: El Niño Southern Oscillation, Climate Change, CESM Large Ensemble, Decadal Variability, extreme El Niño.